AES 2019 Lisbon - Portugal

The 7th Advanced Electromagnetics Symposium

Proceedings

ISSN 2491-2417

mysymposia.org

AES 2019 Lisbon - Portugal

The 7th Advanced Electromagnetics Symposium

Share your comments, photos & videos !

https ://www.facebook.com/aes.symposium

@aes_contact

Edited by

Said Zouhdi | Paris-Sud University, France
Antonio Topa | Instituto Superior Técnico, Portugal

CONTENTS

ABOUT AES

The Advanced Electromagnetics Symposium (AES) serves as an international multidisciplinary forum for deliberations on recent advances and developments in the entire broad field of electromagnetics, Antennas and Propagation. Included in this wide-ranging subject, pertinent to both researchers and industry professionals, are all aspects of electromagnetics, and all frequency ranges from static to optics. Of special interest are :

- Electromagnetic Theory
- Antennas
- Propagation theory, modelling and simulation
- Microwave and Millimeter Circuits and Systems
- Scattering, diffraction and RCS
- Electromagnetic Compatibility
- Computational Electromagnetics
- Optimization Techniques
- Coupled Field Problems
- Optics and Photonics
- Remote Sensing, Inverse Problems, Imaging Radar
- Electromagnetic and photonic Materials
- Bioeffects of EM fields, Biological Media, Medical electromagnetics
- Techniques and tools for RF material characterisation
- EMI/EMC/PIM chambers, instrumentation and measurements
- Educational Electromagnetics

Additionally, through its unique from-Conference-to-Journal-Publication concept, AES offers a rare opportunity for authors to submit papers to Advanced Electromagnetic (AEM) journal and then be considered for journal publication.

Following a now well-established tradition AES takes place in unique locations around the world.

Year	Organizers	Venue
2018	Said Zouhdi	Western Mediteranean Cruise
2017	Junsuk Rho, Said Zouhdi	Incheon, Korea
2016	Enrique Márquez Segura, Eva Rajo-Iglesias, Said Zouhdi	Torremolinos (Malaga), Spain
2014	Lingling Sun, Ke Wu, Said Zouhdi	Hangzhou, China
2013	Hamid M. K. Al-Naimiy, Said Zouhdi	Sharjah-Dubai, United Arab Emirates
2012	Xavier Begaud, Said Zouhdi	Paris, France

AES 2019 ORGANIZATION

Said Zouhdi, General Chair
Paris–Sud University, France

Antonio Topa, General Co-Chair
Instituto Superior Técnico, Portugal

LOCAL ORGANIZING COMMITTEE

David Fernandes, Portugal
Sylvain Lannebère, Portugal
Haffsaa Latiou, Portugal
Tiago Morgado, Portugal
Filipa Prudencio, Portugal
Solange Silva, Portugal
Mario Silveirinha, Portugal
Mouna Zouhdi, France

INTERNATIONAL ADVISORY COMMITTEE

Yahia Antar, Canada
Jean Chazelas, France
Wen-Shan Chen, Taiwan
Christos Christopoulos, UK
Tie Jun Cui, China
Peter de Maagt, Netherlands
Apostolos Georgiadis, Spain
Dave V. Giri, USA
Xun Gong, USA
Lixin Guo, China
Yang Hao, United Kingdom
Nathan Ida, USA
Koichi Ito, Japan
Andrzej Karwowski, Poland
Kwai Man Luk, Hong Kong
Adel Razek, France
Alain Sibille, France
Ari Sihvola, Finland
Paul Smith, Australia
C-K Clive Tzuang, China
J(Yiannis) C. Vardaxoglou, UK
Junhong Wang, China
Yong-Jun Xie, China
Yu Zhang, China

TECHNICAL PROGRAM COMMITTEE

Christos Argyropoulos, USA
Silvio Ernesto Barbin, Brazil
Muhammad Bawa'aneh, Jordan
Xavier Begaud, France
Pai-Yen Chen, USA
Qin Chen, China
Christophe Craeye, Belgium
Laurent Daniel, France
Salvador Gonzalez Garcia, Spain
Brahim Guizal, France
Tian Sen Jason Horng, Taiwan
Zhirun Hu, UK
Ruey-Bing Hwang, Taiwan
Mohd Faizal Jamlos, Malaysia
Sungtek Kahng, Korea
Ali Khenchaf, France
Ahmed Kishk, Canada
Ken-ichi Kitayama, Japan
Maciej Krawczyk, Poland
Sebastien Lallechere, France
Allen M. Larar, USA
Howard Lee, USA
Jean-Claude Levy, France
Jensen Li, UK
Jean-Marc Lopez, France
Andrea Massa, Italy
Ozlem Ozgun, Turkey
Oscar Quevedo-Teruel, Sweden
Eva Rajo-Iglesias, Spain
Blaise Ravelo, France
Junsuk Rho, Korea
Thomas Schneider, Germany
Josaphat Tetuko Sri Sumantyo, Japan
Mohamed Swillam, Egypt
Van Yem Vu, Viet Nam
Konstantin Vytovtov, Russia
Steve Hang Wong, Hong Kong
Amir I. Zaghloul, USA
Kuang Zhang, China
Qi-Jun Zhang, Canada
Linjie Zhou, China
Tao Zhou, China
Arkady Zhukov, Spain

SPECIAL SESSIONS ORGANIZERS

Yangjian Cai, Soochow University, China

PLENARY SPEAKERS

Alexandra Boltasseva

Purdue University, USA

Transdimensional Materials for Nanophotonics : From 2D to 3D

Alexandra Boltasseva is a Professor at the School of Electrical & Computer Engineering at Purdue University. She received her PhD in electrical engineering at Technical University of Denmark, DTU in 2004. Boltasseva specializes in nanophotonics, nanofabrication, optical materials, plasmonics and metamaterials. She is 2018 Blavatnik National Award for Young Scientists Finalist and received the 2013 IEEE Photonics Society Young Investigator Award, 2013 Materials Research Society (MRS) Outstanding Young Investigator Award, the MIT Technology Review Top Young Innovator (TR35), the Young Researcher Award in Advanced Optical Technologies from the University of Erlangen-Nuremberg, Germany, and the Young Elite-Researcher Award from the Danish Council for Independent Research. She is a Fellow of the Optical Society of America (OSA) and Fellow of SPIE. She served on MRS Board of Directors and is Editor-in-Chief for OSA's Optical Materials Express.

Sir John Brian Pendry

Imperial College London, UK

Singular plasmonic surfaces and their properties

Sir John B. Pendry is an English theoretical physicist educated at Downing College, Cambridge, UK, graduating with a Master of Arts degree in Natural Sciences and a PhD in 1969. He is a professor of theoretical solid - state physics at Imperial College London where he was Head of the Department of Physics (1998 – 2001) and Principal of the Faculty of Physical Sciences (2001 – 2002). John Pendry has made seminal contributions to surface science, disordered systems and photonics. His most famous work has introduced a new class of materials, metamaterials, whose electromagnetic properties depend on their internal structure rather than their chemical constitution. He discovered that a perfect lens manufactured from negatively refracting material would circumvent Abbe's diffraction limit to spatial resolution, which has stood for more than a century. His most recent innovation of transformation optics gives the metamaterial specifications required torearrange electromagnetic field configurations at will, by representing the field distortions as a warping of the space in which they exist. In its simplest form the theory shows how we can direct field lines around a given obstacle and thus provide a cloak of invisibility. John Pendry's outstanding contributions have been awarded by many prizes, among which the Dirac Prize(1996), the Knight Bachelor (2004), the Royal Medal (2006), the Isaac Newton Medal (2013) and the Kavli Prize (2014).

Eli Yablonovitch

UC Berkeley, USA

Optical Antenna Physics : Spontaneous Emission Faster than Stimulated Emission

Eli Yablonovitch introduced the idea that strained semiconductor lasers could have superior performance due to reduced valence band (hole) effective mass. With almost every human interaction with the internet, optical telecommunication occurs by strained semiconductor lasers. He is regarded as a Father of the Photonic BandGap concept, and he coined the term "Photonic Crystal". The geometrical structure of the first experimentally realized Photonic bandgap, is sometimes called "Yablonovite".

Prof. Yablonovitch is elected as a Member of the National Academy of Engineering, the National Academy of Sciences, the American Academy of Arts & Sciences, and is a Foreign Member of the Royal Society of London. He has been awarded the Buckley Prize of the American Physical Society, the Isaac Newton Medal of the UK Institute of Physics, the Rank Prize (UK), the Harvey Prize (Israel), the IEEE Photonics Award, the IET Mountbatten Medal (UK), the Julius Springer Prize (Germany), the R.W. Wood Prize, the W. Streifer Scientific Achievement Award, and the Adolf Lomb Medal.

Eli Yablonovitch is the Director of the NSF Center for Energy Efficient Electronics Science (E3S), a multi-University Center headquartered at Berkeley. He received his Ph.D. degree in Applied Physics from Harvard University in 1972. He worked for two years at Bell Telephone Laboratories, and then became a professor of Applied Physics at Harvard. In 1979 he joined Exxon to do research on photovoltaic solar energy. Then in 1984, he joined Bell Communications Research, where he was a Distinguished Member of Staff, and also Director of Solid-State Physics Research. In 1992 he joined the University of California, Los Angeles, where he was the Northrop-Grumman Chair Professor of Electrical Engineering. Then in 2007 he became Professor of Electrical Engineering and Computer Sciences at UC Berkeley, where he holds the James & Katherine Lau Chair in Engineering.

CONFERENCE TUTORIALS

META 2019 features several technical tutorials instructed by world-leading experts on various topics of interest to the META community. Tutorials are intended to provide a high quality learning experience to conference attendees. The tutorials address an audience with a varied range of interests and backgrounds : beginners, students, researchers, lecturers and representatives of companies, governments and funding agencies who wish to learn new concepts and technologies.
The tutorials are part of the conference technical program, and are free of charge for the conference attendees.

ORGANIZER

Prof. Ishwar Aggarwal, UNC Charlotte, USA

Tutorials & Instructors

Prof. Federico Capasso

Harvard University, USA

Wednesday 24th July
10:50 - 11:50 — Auditorium I

Flat optics

This tutorial focuses on how metasurfaces enable the redesign of optical components into novel thin and planar diffractive optical elements, that overcome the limitations of Fresnel and refractive optics, promising a major reduction in footprint and system complexity as well as the introduction of new optical functions. The planarity of flat optics will lead to the unification of semiconductor manufacturing and lens making, where the planar technology to manufacture computer chips will be adapted to produce CMOS-compatible metasurface-based optical components, ranging from metalenses to novel multifunctional phase plates.

Prof. Eli Yablonovitch

UC Berkeley, USA

Wednesday 24th July
14:00 - 15:00 — Auditorium II

The Electromagnetic Spectra of Ordinary Objects

There is an aspect of Electromagnetics that has been somewhat overlooked. Common everyday objects can act as electromagnetic resonators. Indeed ordinary objects have a series of resonant frequencies extending from radio waves up to optical frequencies. These resonant modes can be modeled as LC circuits. Thus every object that we encounter is an LC resonator. Since LC circuits support ac currents, and since ac currents imply electron acceleration, they inherently radiate into the far-field. Therefore ordinary objects that we come across, in our daily lives, can act as electromagnetic antennas. This means that ordinary object have a Q-factor and a radiation Q-factor for each resonant mode.The lowest frequency resonance is especially characteristic of the object geometry, but there is an entire spectrum of higher frequencies to work with, a spectral fingerprint for everyday objects. Many of the properties that have been attributed to plasmonic resonances are actually universal, and they arise already in ordinary electromagnetics.In communications technology, the antenna application is the most important. The antennas in cellphones, carried by almost everyone on the planet, are examples of multi-frequency resonant objects, enabling wireless connectivity.

Dr. Rachel Won

Nature Photonics, UK

Thursday 25th July
11:00 - 12:00 — Auditorium II

Writing and submitting your papers : Dos and Don'ts

In this tutorial, Rachel will talk you through the detailed information and guidelines on scientific paper preparation and submission. Guidelines and tips for writing an abstract and a paper will be provided. Submission, editorial and peer-review processes will be discussed. At the end of the tutorial, you will walk away knowing how to write an informative cover letter, an outstanding abstract and a comprehensive scientific paper. You will also get to know where to submit your papers to, what editors seek, how your papers are reviewed and how to make an appeal.

Prof. Michael Fiddy

DARPA, USA

Thursday 25th July
14:00 - 15:00 — Auditorium I

DARPA's interests in metamaterials

Almost twenty years ago, some of the earliest research into metamaterials and their applications was funded by DARPA. The field has grown enormously since, and DARPA still supports fundamental research into improving our understanding and modeling of these engineered materials. This talk will provide the background and context for research of current interests. These include the study of new material properties, including bianisotropy and nonlinearity, advancing flat optics, and developing nonreciprocal and tunable components, all of which may impact imaging and remote sensing capabilities.

AES 2019 VENUE

AES 2019 will be held at the Congress Center of **Instituto Superior Técnico (IST)**, situated at the Civil Engineering Building. All talks are scheduled for the Congress Centre of IST **except for the Plenary talks** which will be held in **Culturgest**, an independent conference center located 500m away from IST (see map).

Instituto Superior Técnico - Congress Center
Civil Engineering Building (Pavilhão de Civil)
Av. Rovisco Pais 1
1049-001, Lisbon

Website : https ://tecnico.ulisboa.pt/en/

Culturgest
Rua Arco do Cego 77
1000-300
Lisbon

Website : https ://www.culturgest.pt/en/

GETTING TO VENUE

Taxi

The quickest way to get from Lisbon Airport (LIS) to Instituto Superior Técnico is to taxi which costs 7€ - 9€ and takes 10mn.

Metro

Being close to the Lisbon city centre, IST is easily reached by metro (metro station **"Alameda"** - Red and Green lines ; metro sation **"Saldanha"** - Red and Yellow lines), from any location in town, including the airport (metro station **"Aeroporto"**- Red line).

Bus

The bus routes cover all Lisbon and extend to its outskirts. The tickets can be pre-paid, at the counters of Carris, the surface transportation operator for Lisbon, or bought aboard the bus, electric cars or funiculars. For IST hop off on one of the following bus stops :

- ☐ Av. Manuel da Maia
- ☐ Av. Rovisco Pais
- ☐ Arco do Cego

GENERAL INFORMATION

Registration

Registered participants may pick up their conference material at the registration desk which will be located at the IST Civil Engineering Building :

- Wednesday, July 24 (08 :30-18 :00)
- Thursday, July 25 (08 :30-17 :00)
- Friday, July 26 (08 :30-11 :00)

Plenary Lectures

Plenary Lectures will be held at the Main Auditorium of **Culturgest**, located 500m away from Instituto Superior Técnico Congress Center :

• Thursday, July 25 (08 :30-10 :15)

Banquet

Venue : KAIS Restaurant, Cais da Viscondessa, R. da Cintura – Santos, 1200-109 Lisboa, Portugal.
Schedule : Thursday, July 25 at 20 :00.

Free Shuttle bus service will be provided between the Instituto Superior Técnico Congress Center and the KAIS Restaurant.

Pick-up time : 18 :30 at the West IST Entrance located Av. Alves Redol (see map).

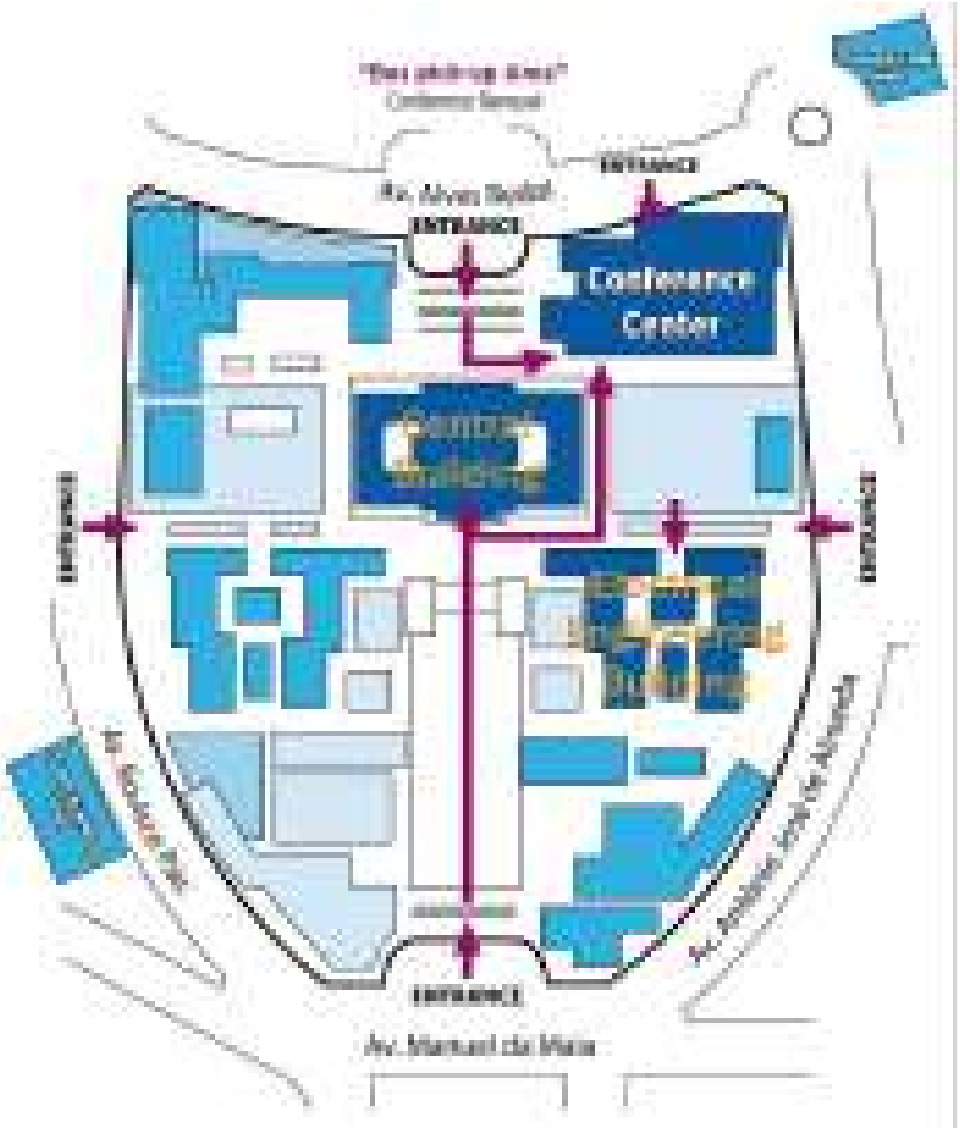

IST CONGRESS CENTER FLOOR PLANS

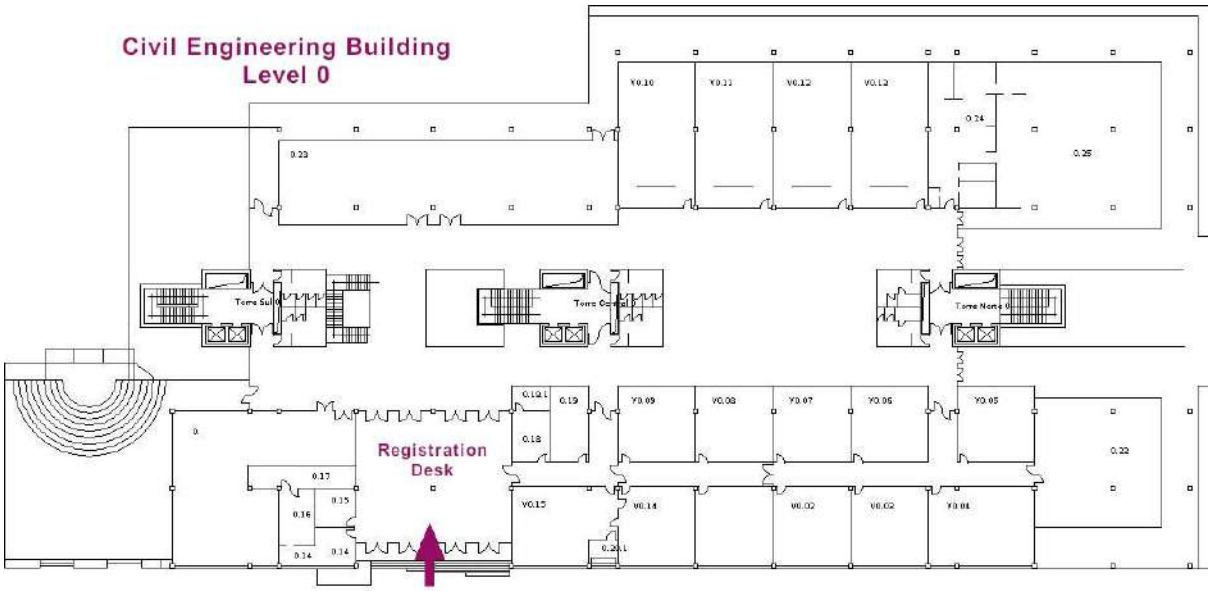

Civil Engineering Building - Level 0

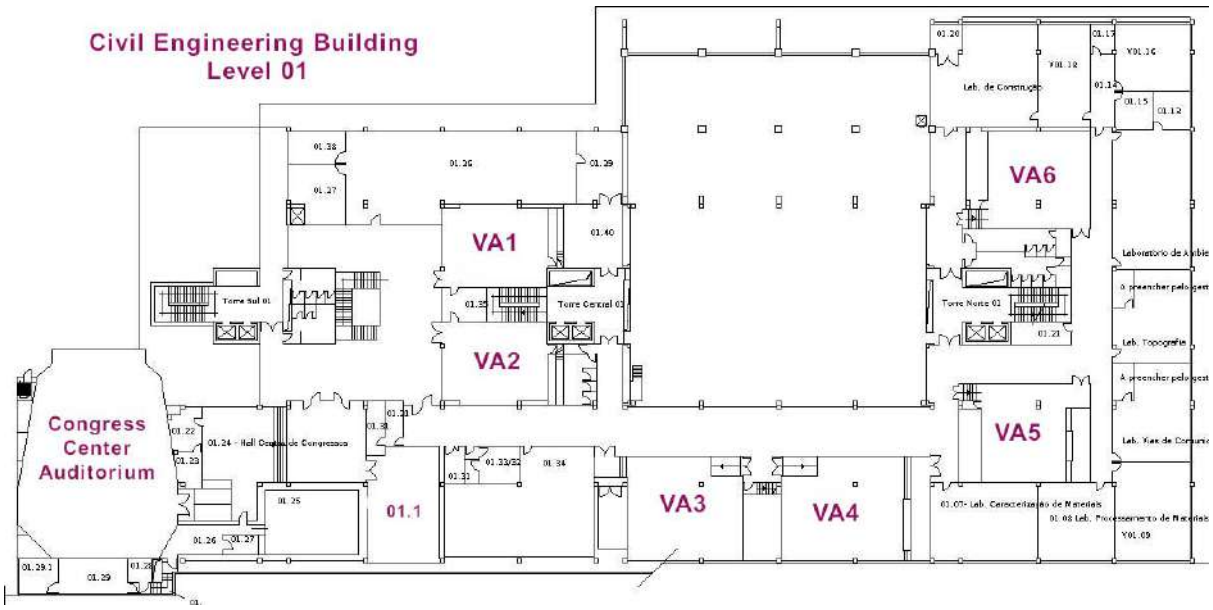

Civil Engineering Building - Level 01

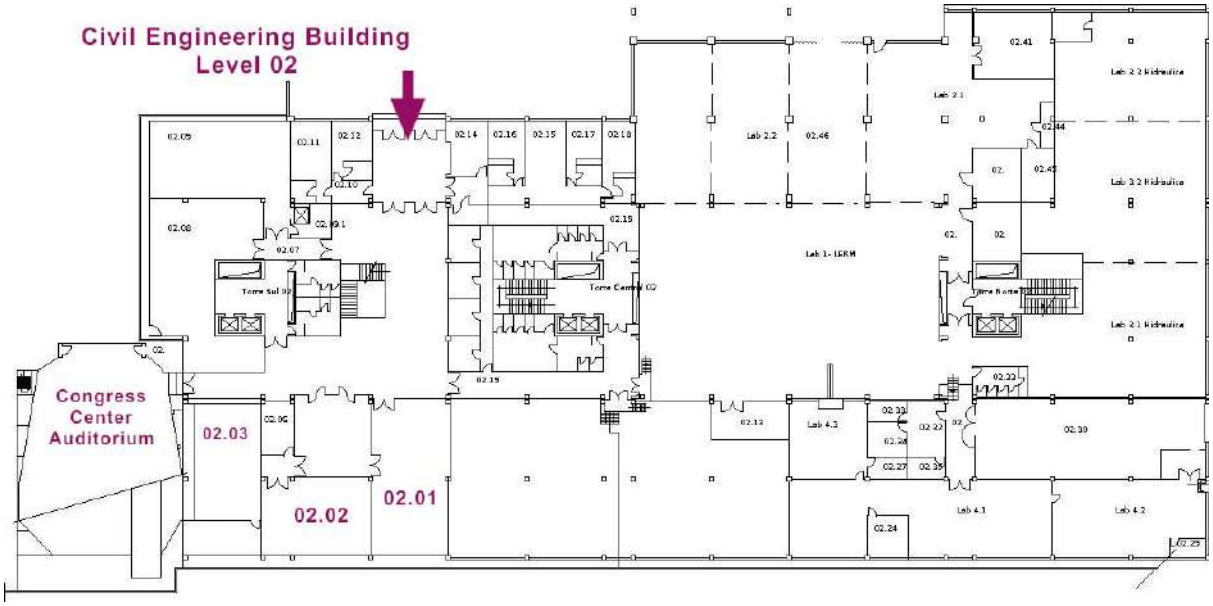

Civil Engineering Building - Level 02

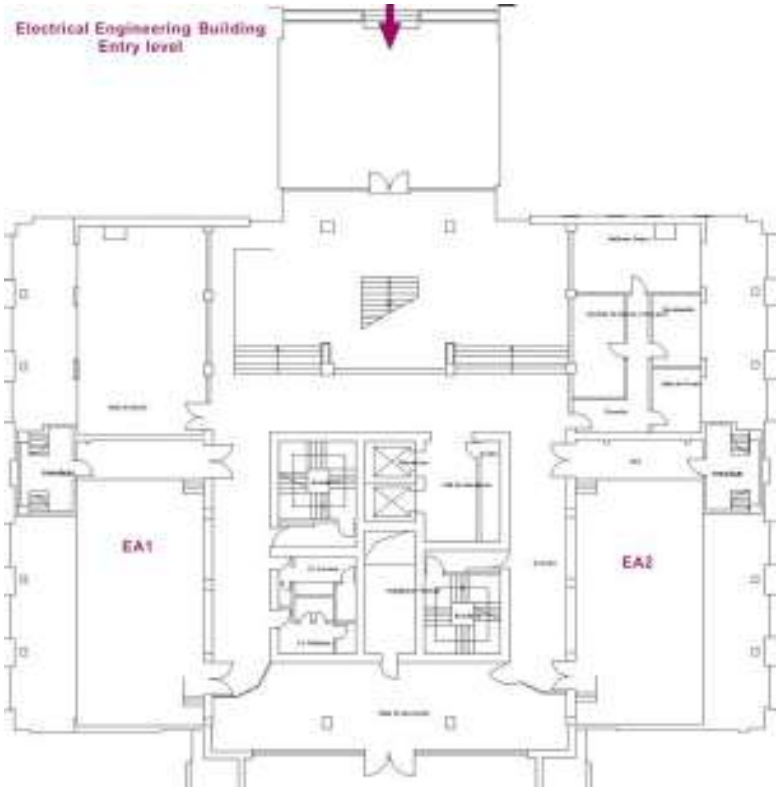

Electrical Engineering Building - Entry level

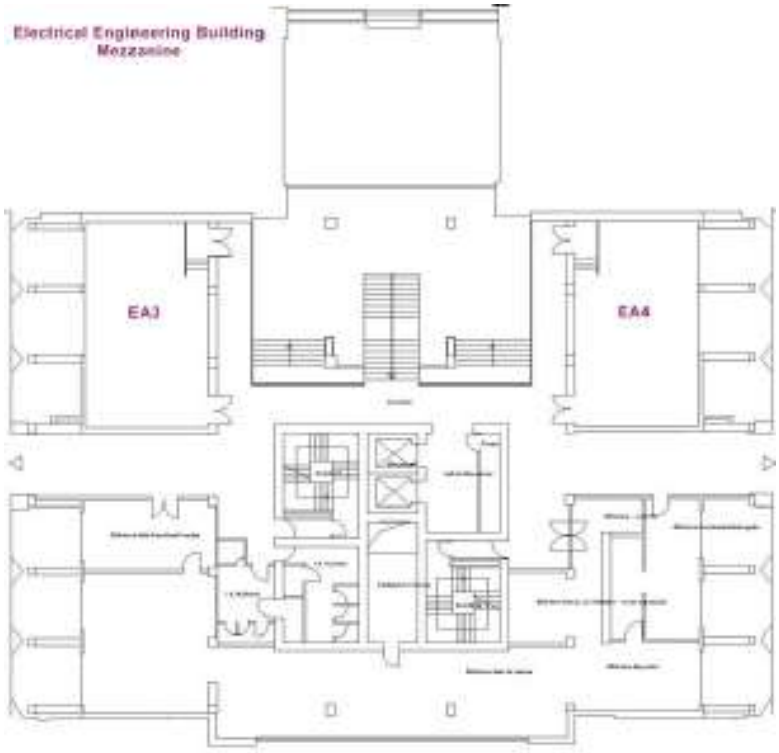

Electrical Engineering Building - Mezzanine

WI-FI INSTRUCTIONS

Wi-Fi instructions for **AES 2019** participants :

1. Browse available wireless networks and select as SSID "tecnico-guest" ;
2. Set IP to automatic (DHCP). This is usually the default setting, so you may probably skip this step ;
3. Open your browser and try to access any external website. You will be automatically redirected to the page **https ://wifi.ist.utl.pt/index_auth.php**. Follow the link 'Web based login' at the top of the page concerning short-time, conference and meetings accounts. Enter the following username/password when requested ;

   Username : **META2019**
   Password : **jwvr2f**

4. After step 3 you may freely browse and access the Internet. You may need to repeat the above steps if you close your browser or if the connection times out.

GUIDELINES FOR PRESENTERS

ORAL PRESENTATIONS

Each session room is equipped with a stationary computer connected to a LCD projector. Presenters must load their presentation files in advance onto the session computer. Technician personnel will be available to assist you.

Scheduled time slots for oral presentations are 15 mn for regular, 20 mn for invited presentations, 30 mn for keynote talks and 35 mn for plenary talks, including questions and discussions. Presenters are required to report to their session room and to their session Chair at least 15 minutes prior to the start of their session.

The session chair must be present in the session room at least 15 minutes before the start of the session and must strictly observe the starting time and time limit of each paper.

POSTER PRESENTATIONS

Presenters are requested to stand by their posters during their session. One poster board, A0 size (118.9 x 84.1 cm), in portrait orientation, will be available for each poster (there are no specific templates for posters). Pins or thumbtacks are provided to mount your posters on the board. All presenters are required to mount their papers 30mn before the session and remove them at the end of their sessions. Posters must prepared using the standard AES poster template (available on the symposium website).

TABLE OF CONTENTS

Light manipulations and applications

Antennas and propagation

Wave Propagation

Measurements

Electromagnetics

Microwaves, Millimeter Waves, and THz

EMC & EMI

Light manipulations and applications

Modulating the statistical properties of a vector partially coherent beam by a 4f optical system

Chenkun Mi[1], Chunhao Liang[1], Fei Wang[1], Lin Liu[1] and Yangjian Cai[1,2]

[1]School of Physical Science and Technology, Soochow University, Suzhou 215006, People's Republic of China
[2]Center of Light Manipulations and Applications & Shandong Provincial Key Laboratory of Optics and Photonic Device, School of Physics and Electronics, Shandong Normal University, Jinan 250014, China
*corresponding author, E-mail: liulin@suda.edu.cn, yangjiancai@suda.edu.cn

Abstract

A 4f optical system with an amplitude filter in the frequency plane is applied to modulate the statistical properties of a vector partially coherent beam. By controlling the parameters of the amplitude filter and the coherence length of the incident beam precisely, the shaped beam can display periodic spatial coherence in the source plane and form intensity lattices with radially polarization in the far field.

1. Introduction

The correlation function of the conventional partially coherent beam satisfies Gaussian distribution, and we call such beam as Gaussian correlated Schell-model (i.e., Gaussian Schell-model) beam.Ever since Gori and his collaborators put forward the sufficient conditions for devising the correlation functions of scalar and vector partially coherent beams [1,2], partially coherent beams with nonconventional correlation functions (i.e., non-Gaussian correlated Schell-model functions) have been studied extensively. In recent years, partially coherent beam with periodic spatial coherence has attracted increasing attention, and this beam is called optical coherence lattices (OCLs), which display unique property of periodicity reciprocity: the initial periodic degree of coherence transfers its periodicity to the periodic intensity distribution on propagation in free-space. The OCLs are expected to be useful for image transmission and optical encryption.

On the other hand, the coherence and polarization of a vector partially coherent beam are interrelated, the degree of polarization and the state of polarization of a vector partially coherent beam vary on propagation even in free space. Recently, vector OCLs were introduced as an extension of scalar OCLs, and were generated in experiment based on superposition of multiple Schell-model beams. In this paper, a new method for generating vector OCLs with periodical coherence properties and non-Gaussian intensity distribution is introduced. Different from the existing method, a 4f optical system with an amplitude filter in frequency plane is adopted to modulate the statistic properties of a vector partially coherent beam [i.e., radially polarized Gaussian Schell-model (RPGSM) beam]. By precisely controlling the parameters of the amplitude filter and coherence length of the incident RPGSM beam, the shaped beam can display periodic spatial coherence in the source plane and form intensity lattices with radially polarization in the far field, which is useful for particle trapping.

2. Theoretical model for a RPGSM beam passing through a 4f optical system

The elements of the CSD matrix of a RPGSM beam in the initial plane can be expressed as [3]

$$\Gamma_{\alpha\beta}(\mathbf{r}_1,\mathbf{r}_2)=\frac{\alpha_1\beta_2}{4w_s^2}\exp\left(-\frac{\mathbf{r}_1^2+\mathbf{r}_2^2}{4w_s^2}\right)\exp\left(-\frac{(\mathbf{r}_1-\mathbf{r}_2)^2}{2\delta_s^2}\right),(\alpha,\beta=x,y), \tag{1}$$

where w_s denotes the transverse beam width and δ_s denotes the transverse coherence width.

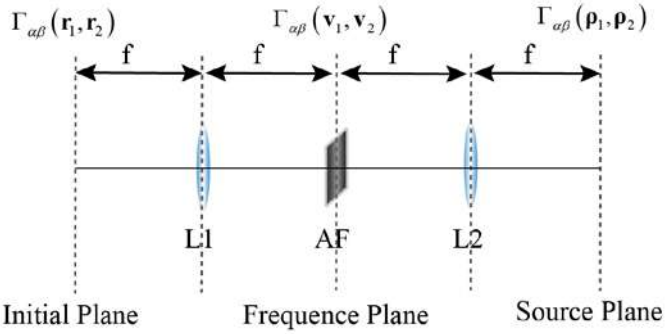

Figure 1: Scheme of a 4f optical system with an amplitude filter in the frequency plane. L1 and L2 are the thin lenses with identical focal length f. AF is amplitude filter.

With the help of Collins formula [4], we obtain the elements of the CSD matrix of a RPGSM beam propagating through the initial plane to the frequency plane (Fig.1) as follows

$$\Gamma_{\alpha\beta}(\mathbf{v}_1,\mathbf{v}_2)=\frac{1}{(\lambda B_1)^2}\exp\left[-\frac{ikD_1}{2B_1}(\mathbf{v}_1^2-\mathbf{v}_2^2)\right]\int_{-\infty}^{+\infty}\int_{-\infty}^{+\infty}\Gamma_{\alpha\beta}(\mathbf{r}_1,\mathbf{r}_2)$$
$$\times\exp\left[-\frac{ik}{2B_1}(A_1\mathbf{r}_1^2-2\mathbf{r}_1\cdot\mathbf{v}_1)+\frac{ik}{2B_1}(A_1\mathbf{r}_2^2-2\mathbf{r}_2\cdot\mathbf{v}_2)\right]d^2\mathbf{r}_1d^2\mathbf{r}_2, \tag{2}$$

The transfer matrix between the initial plane and the frequency plane reads as

$$\begin{pmatrix} A_1 & B_1 \\ C_1 & D_1 \end{pmatrix} = \begin{pmatrix} 1 & f \\ 0 & 1 \end{pmatrix} \begin{pmatrix} 1 & 0 \\ -1/f & 1 \end{pmatrix} \begin{pmatrix} 1 & f \\ 0 & 1 \end{pmatrix} = \begin{pmatrix} 0 & f \\ -1/f & 0 \end{pmatrix}. \quad (3)$$

The propagation of the RPGSM beam from the frequency plane to the source plane (as Fig.1) can be treated in a similar way by the following integral formula

$$\Gamma_{\alpha\beta}(\boldsymbol{\rho}_1, \boldsymbol{\rho}_2) = \frac{1}{(\lambda B_2)^2} \exp\left[-\frac{ikD_2}{2B_2}\left(\boldsymbol{\rho}_1^2 - \boldsymbol{\rho}_2^2\right)\right] \int_{-\infty}^{+\infty}\int_{-\infty}^{+\infty} \Gamma_{\alpha\beta}(\mathbf{v}_1, \mathbf{v}_2) A(\mathbf{v}_1) A^*(\mathbf{v}_2)$$

$$\times \exp\left[-\frac{ik}{2B_2}\left(A_2\mathbf{v}_1^2 - 2\mathbf{v}_1\cdot\boldsymbol{\rho}_1\right) + \frac{ik}{2B_2}\left(A_2\mathbf{v}_2^2 - 2\mathbf{v}_2\cdot\boldsymbol{\rho}_2\right)\right] d^2\mathbf{v}_1 d^2\mathbf{v}_2, \quad (4)$$

where $\boldsymbol{\rho}_i^2 = \rho_{xi}^2 + \rho_{yi}^2, (i = 1, 2)$ represents the position vector in the source plane, $A(\mathbf{v})$ represents the transmission function of the amplitude filter in the frequency plane and can be described by the following equation

3. Statistical properties of a RPGSM beam after passing through the 4f optical system

It is clear that the degree of coherence of the beam in the source plane displays lattices distribution (i.e., periodic coherence properties) and is controlled by the coherence width δ_s, a and d. As Fig.2 shows, with the increase of the coherence width δ_s, the lattice distribution of the degree of coherence disappears gradually and the nodes become larger.

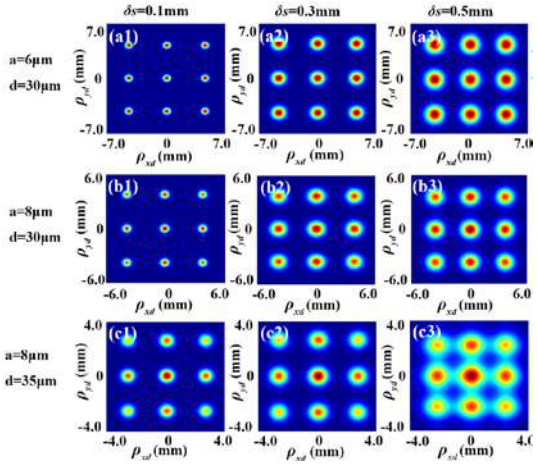

Figure 2 : Intensity plot of the squared modulus of the degree of coherence $|\mu(\rho_{xd}, \rho_{yd})|^2$ of the shaped RPGSM beam in the source plane for different values of coherence width δ_s, a and d with M=N=4.

As expected, the degree of coherence of the shaped beam transfers its periodicity to the intensity on propagation (Fig.3). The shaped beam evolves into lattices distribution with bright nodes in the far field. It is interesting to find that each node of the lattices displays radial polarization. One can see that the coherence width δ_s plays a major role in determining the latticest distribution and the parameter d has an effect on the size of nodes while the variation caused by variation of a within the range can be omitted.

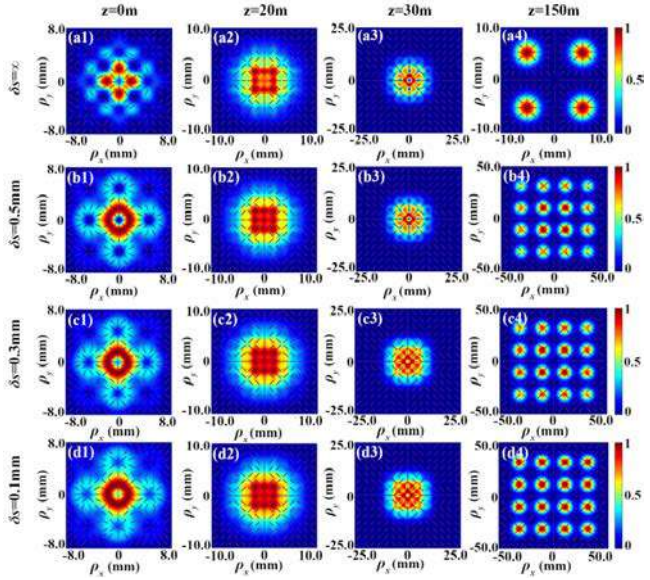

Figure 3: Intensity plot of the normalized intensity distribution and the SOP of the RPGSM beam shaped by the 4f optical system with an amplitude filer in the frequency plane at several propagation distances in free space for different values of δ_s with $a = 8\mu m, d = 35\mu m$, M=N=4.

4. Conclusions

A 4f optical system with an amplitude filter in frequency plane is applied to shape the intensity distribution and the degree of coherence of an incident RPGSM beam are shaped simultaneously, then we obtained the vector OCLs beam. The vector OCLs can generate intensity lattices with bright nodes and radially polarization in the far field if we precisely control the coherence width of the incident beam and parameters of the amplitude filter.

Acknowledgements

This work is supported by the National Natural Science Foundation of China under Grant Nos. 91750201 & 11525418 & 11774251 & 11474213, the Project of the Priority Academic Program Development of Jiangsu Higher Education Institutions

References

[1] Gori F, Santarsiero M, Devising genuine spatial correlation functions, Opt Lett 32:3531-3533, 2007.

[2] Gori F, Ramírez-Sanchez V, Santarsiero M, Shirai T, On genuine cross-spectral density matrices, J Opt A: Pure Appl Opt 11:085706, 2009.

[3] G. Wu, F. Wang, and Y. Cai, Coherence and polarization properties of a radially polarized beam with variable spatial coherence, Opt Express 20:28301-28318, 2012.

[4] S. A. Collins, Lens-system diffraction integral written in terms of matrix optics, J Opt Soc Am 60:1168-1177, 1970.

Optical imaging for Golay3 multi-mirror sparse aperture system

Quanying Wu [1], Junliu Fan[1], Baohua Chen[1], DaLing Cai[1,3] and Haiping Zhang[1,2]

[1] School of Mathematics and Physics, Suzhou University of Science and Technology, Suzhou 215009, China
[2] Soochow Mason Optics Co., Ltd. of Graduate Workstation in Jiangsu Province , Suzhou 215028, China
[3]Suzhou FOIF Co., Ltd. of Graduate Workstation in Jiangsu Province , Suzhou215006, China ,
*corresponding author, E-mail: wqycyh@mail.usts.edu.cn

Abstract

In order to better investigate sparse aperture optical systems a Goaly3 multi-mirror telescope is designed and the modulation transfer function (MTF) is given. Optical simulation imaging is researched. The experiment prototype is manufactured and optical imaging is also developed. The results between simulation and experiment are compared.

1. Introduction

The quest for finer angular resolution in astronomy will inevitably lead to larger apertures. Unfortunately, the primary mirror diameter for space telescopes is limited by volume and mass constraints of current launch vehicles as well as the scaling laws of manufacturing costs [1, 2]. Since the cost of monolithic optics increases proportionally to $D^{2.76}$ [2], efforts are ongoing to break this trend by employing breakthrough technologies such as deployed segmented mirror telescopes, and sparse aperture optics using interferometry. Sparse aperture systems can achieve the same information as full aperture systems, but their volume is smaller and the weight is lighter than the full aperture. It is the most useful optical systems because the aperture of the telescope is becoming larger. There are two kinds of methods for sparse aperture telescopes. One is the multi-mirror telescope (MMT) that the primary mirror is made of several small mirrors [3]. Another is the multi-telescope telescopes (MTT) that several telescopes make up a sparse aperture system [4]. In this paper we investigate the Golay3 MMT sparse aperture optical imaging.

2. Optical system for Golay3 MMT

The primary mirror of the telescope is made of three sub mirrors arranged by Golay3 in Figure 1. We design the Golay3 MMT and build the experiment prototype.
The parameters of the telescope are as follows
Parameters of the primary mirror

(1) Primary mirror: Spherical surface
(2) Radius of curvature: 1500mm
(3) Sub-Primary aperture: 80mm
(4) Distance between the primary mirror and secondary mirror: 500mm
(5) Surrounded aperture: 250mm, F number 8

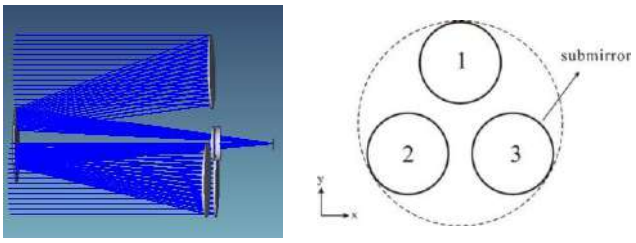

Figure 1: Scheme of a Golay3 MMT sparse aperture telescope.

Parameters of the secondary mirror

(1) Secondary mirror: hyperboloid conic coefficient :9.31
(2) Radius of curvature:800mm
(3) Secondary mirror aperture:88mm, thickness:15mm
(4) Distance between the secondary mirror and correction mirror: 500mm

The Golay3 MTF of the primary mirror is shown in Figure 2. There are nine sub-MTFs that three sub-MTFs are at the center and six sub-MTFs distribute in three directions at 60 °.

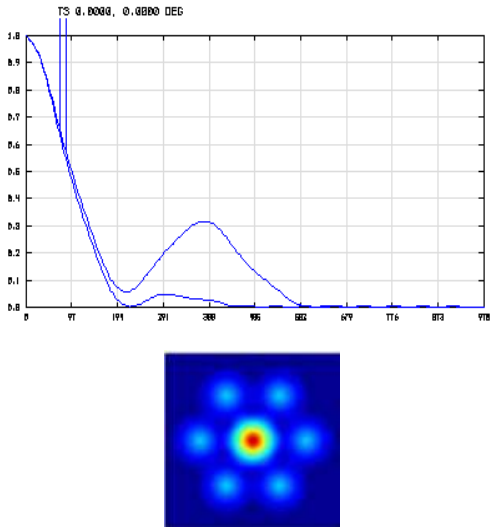

Figure 2 : MTF curves and two-dimension MTF.

Based on the parameters of the telescope the catoptrics system is designed. It has a spherical primary mirror, an aspherical secondary mirror, and two lenses. The simulation result is illustrated in Figure 3. Its aperture, point-spread

function (PSF), and modulation transfer function (MTF) output from Zemax are plotted as shown in Figure 4 when the field of view is 0 °. It shows that the sub-apertures seem to be circular because the relative aperture is still very small. The distributions of the PSF and MTF are in accordance with [5].

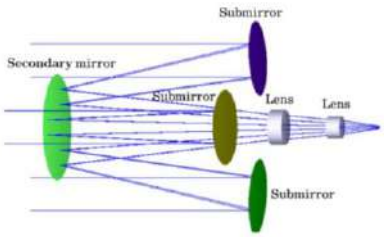

Figure 3 Simulation result of the Golay3 MMT with a spherical primary mirror.

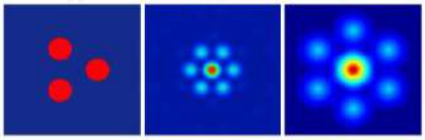

(a) (b) (c)

Figure 4: (a) Aperture, (b) PSF, and (c) MTF distribution of the Golay3 MMT with a spherical primary mirror.

3. Experiment and imaging for Golay3 MMT sparse aperture system

We built an experiment prototype illustrated in Figure 5.The resolution chart is imaged by the prototype. The results of the imaging are shown in Figure 6. Figure 6(a) illustrates the image from the experiment. Figure 6(b) is the image by recovering. Compared with Figure 6(a) and Figure 6(b) we can find that the image of Figure 6(b) becomes clearer than that of Figure 6(a).

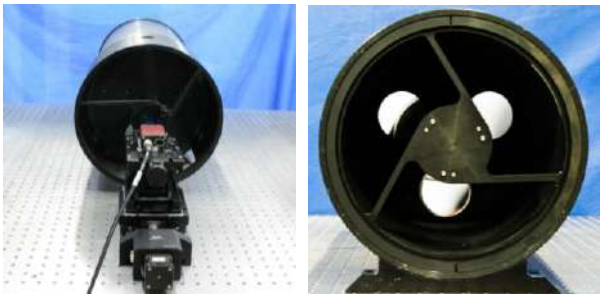

Figure 5: The experiment prototype of Golay3 MMT.

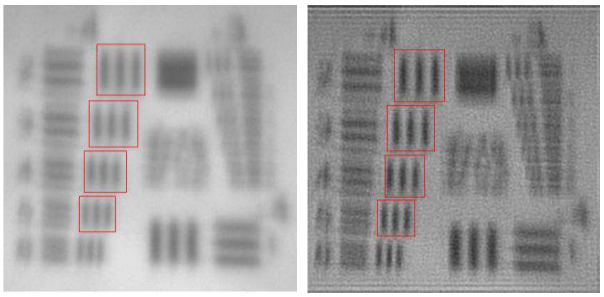

(a) (b)

Figure 6 : (a) The image of the experiment ,and (b) the recovered image.

Figure 7 shows the relationship between the image contrast and location of the focal plane. The abscissa stands for the distance away from the focal plane. It is shown that the image contrast is best at the focal plane according to Figure 7. It is clear that the contrast has obtained a great improvement.

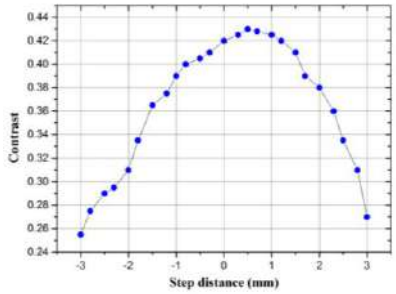

Figure 7 : The relationship between the image contrast and location of the focal plane.

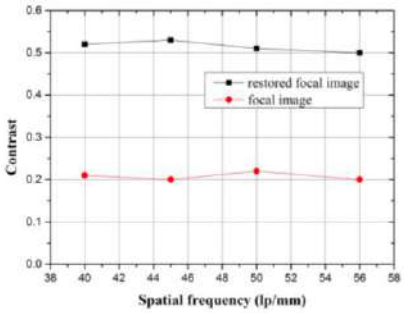

Figure 8 : The curves of the image contrast before and after recovering .

4. Conclusions

The MTF of Golay3 MMT is analyzed. The optical system of Golay3 MMT is designed and manufactured. The experiment result is given out and the image recovering is completed.

Acknowledgements

This work is supported by the National Natural Science Foundation of China under Grant Nos. 61875145& 1180 4243, Jiangsu Province Key Discipline of China′s 13th five-year plan (20168765),Jiangsu Key Laboratory of Advanced Optical Manufacture Technology (KJS1710).

References

[1] A.B. Meinel, Cost Scaling Laws Applicable to Very Large Telescopes, Proc. SPIE, 172, 1979.

[2] D. F. Robert, A. T. Theodore, Image quality of Sparse-aperture Designs for Remote Sensing, Opt. Eng. 41(8):1957-1968,2002.

[3] M. Johns, P. Mccarthy, K. Raybould, Giant Magellan Telescope: overview, Proc. SPIE, 8444(1):84441H_1-84441H_16, 2012.

[4] Z. L. Xie, H. T. Ma, B. Qi, Experimental demonstration of enhanced resolution of a Golay3 sparse-aperture telescope,"Chin. Opt. Lett. 15(4): 041101_1-041101_4, 2017.

[5] Q. Wu, F. Wu, L. Qian, and X. Zhu, Demonstration of the Golay 3 multiple-mirror telescope with a spherical primary mirror, Opt. Laser Technol.44, 749-755,2012.

Integration of Dielectric Fractals on Plasmonic Metasurfaces for Selective and Sensitive Optical Sensing of Volatile Compounds

Zelio Fusco[a], Mohsen Rahmani[b*], Renheng Bo[a], Ruggero Verre[c], Nunzio Motta[d], Mikael Käll[c], Dragomir Neshev[b] and Antonio Tricoli[a*]

[a] Nanotechnology Research Laboratory, College of Engineering and Computer Science, ANU, Australia
[b] Nonlinear Physics Centre, Research School of Physics and Engineering, ANU, Australia
[c] Department of Physics, Chalmers University of Technology, 412 96 Göteborg, Sweden
[d] Institute for Future Environments and School of Chemistry, Physics, and Mechanical Engineering, QUT, Australia

Abstract

Localized surface plasmon resonance has found widespread use in efficient optical transducers of local refractive index changes in liquids, leading to highly specific biomolecular sensors with sensitivity reaching the single molecule limit. However, it has proven challenging to translate these achievements to the selective detection of gases, which typically adsorb in an unspecific manner and induces refractive index changes below the detection limit. Here, we show first insights on the large-scale self-assembly of monocrystalline Au nano-islands with tunable size and separation, and their application as efficient LSPR surfaces. Highly homogeneous centimeter-sized Au metasurfaces are fabricated by one-step deposition and in situ coalescence of hot nanoparticle aerosols into a discontinuous monolayer of highly faceted monocrystals. Notably, these metasurfaces demonstrate high-quality and tunable LSPR, enabling the fabrication of highly performing optical gas sensors detecting down to 10^{-5} variations in refractive index at room temperature.

Next, we use our aerosol synthesis method to integrate tailored fractals of dielectric TiO_2 nanoparticles onto resonant plasmonic metasurfaces made by hole-colloidal mask lithography. We show how this integration strongly enhances the interaction between the plasmonic field and volatile organic molecules and provides a means for their selective detection. Notably, the superior optical response is due to the enhancement of the interaction between the dielectric fractals and the plasmonic metasurface for thickness of up to 1.8 μm, much higher than the spatial extension of the plasmonic near-field (~30 nm). Optimal dielectric-plasmonic structures allow measurements of changes in the refractive index of the gas mixture down to $<8x10^{-6}$ at room temperature and selective identification of three exemplary volatile organic compounds, acetone, toluene and ethanol. These findings provide a basis for the development of a novel family of dielectric-plasmonic materials with application extending from light harvesting and photocatalysts to contactless sensors for non-invasive medical diagnostics.

1. Introduction

Current technological advances demand more and more precise measurement of existence or absence of certain substances, with extremely low concentrations, in various environments. Sensing technology has already impacted many aspect of our daily lives; particularly, gas sensing is becoming considered as the key technology to avoid or reduce growing global challenges including global warming, pollution, safety and security. High sensitivity, fast response, and good selectivity are the target requirements for a high-throughput sensor in today's technology. Among all the nanotechnology-enabled gas sensors, the optical ones are most promising and attracting options thanks to their high selectivity, long lifetime, high resistivity to electromagnetic noise and the possibility to work at room temperature [1]. In this panorama, metal nanoparticles (NPs) have been extensively studied because of their characteristic localized surface plasmon resonance (LSPR) and it has been shown that they promptly react toward several compounds due to their catalytic activity or thanks to their high reactivity to the local environment parameter changes [2]. Gold NPs are the ideal candidates for plasmonic applications because of their stable and strong LSPR efficiency in the visible region. So far lots of gold morphologies have been proposed and synthesized in order to optimize the plasmonic properties and improve the sensibility. Despite the many attempts, the perfect plasmonic substrate that couples good efficiency and stability with the possibility to have a high reproducibility, cost-effectiveness and large-scale production is still object of research.

2. Discussion

Here, for the first time, we demonstrate the efficiency of a rapid high-temperature aerosol synthesis technique (flame spray pyrolysis, FSP) for the facile and scalable fabrication of an inexpensive resonant metasurface made of aperiodic monocrystalline Au nanoislands (Figure 1) in timeframes of seconds. Importantly, the morphology (particle size, interparticle distance and faceting degree) can be promptly tuned and hence a good control on the plasmonic properties is achievable. Furthermore, these substrates show a high-purity crystalline nature as demonstrated from the X-ray diffraction patterns, a feature that is important for the minimization of the grain boundaries.

Molecular dynamics simulations have been performed to investigate the driving mechanism that lead to the formation of disconnected nanoislands instead of a uniform thin film, and it has been found that a coalescence process drives the synthesis. Additionally, we have exploited these random metasurfaces toward the room temperature detection of gaseous volatile organic compounds, achieving the detection of refractive index changes as low as 10^{-5} [3].

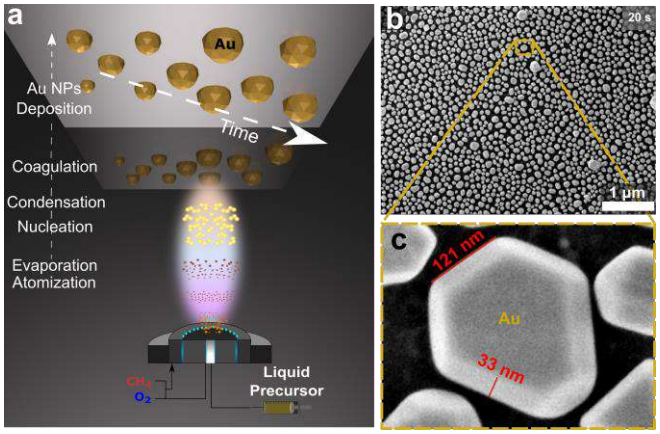

Figure 1: a, Schematic representation of the high-temperature aerosol setup and phenomenon during the Au deposition processes. b, Exemplary top-view scanning electron microscope (SEM) image of the Au NIs film, showing high uniformity on large scale. c, zoom into a single crustal, faceted Au nanoisland.

In order to improve the performances and build a more sensitive device, we then integrated an ultra-porous fractal layer on TiO_2 nanoparticles, deposited by using the same aerosol FSP technique, onto more regular plasmonic metasurfaces made by hole mask colloidal lithography, as shown in Figure 1a,c [4].

The intrinsic deposition properties of the FSP in the diffusion regime, lead to the self-assembly of the TiO_2 nanoparticles in a fractal morphology, showing an ultra-porous network with hierarchical pore size distribution (Figure 2a) and feature repeating at different magnifications.

Gas sensing performances have been investigated as a function of the fractal layer thickness (ranging from 0 to 5.5 µm) and we demonstrated the excellent sensitivity toward the room temperature detection of volatile organic compounds (VOCs), namely ethanol, acetone and toluene, measuring refractive index changes as low as $<8x10^{-6}$ at room temperature (Figure 2d-f).

The synergistic interplay between the tailored TiO_2 fractals and the plasmonic metasurfaces has been studied with electrodynamic simulations and shows a drastic Enhancement of the interaction between the plasmonic field and the volatile organic molecules.

Additionally, we exploited the VOCs condensation onto the high-surface area fractals to selectively discriminate the different gases. In fact, for any given VOCs the vapor pressure, which is directly correlated to the condensation rate, is a function of the temperature and the higher the concentration the higher is its vapor pressure. Indeed, by little increases of the temperature, is possible to reduce the amount of condensed VOCs, which in turn leads to a smaller plasmonic shift and providing a platform for the selective detection of gaseous molecules.

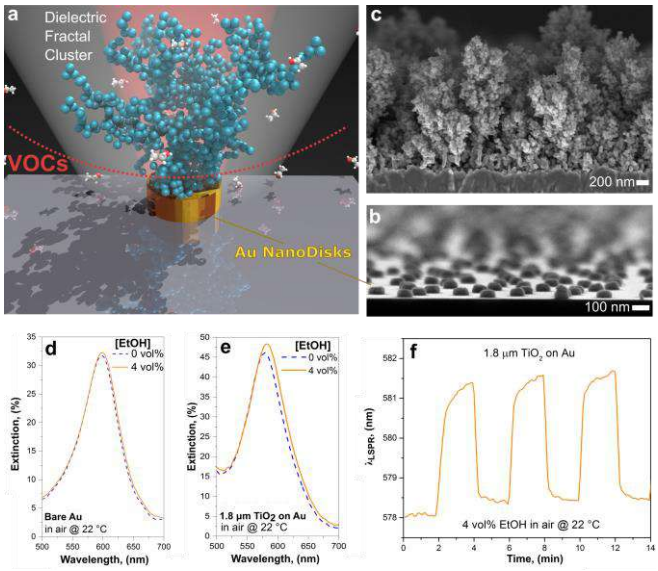

Figure 1: a, Schematic of the fractal TiO_2-Au nanodisks layout (not in scale). b, Cross-section SEM image in tilted view of a Au nanodisks metasurface with an in-plane diameter of 100 nm and a thickness of 40 nm. c, Cross-section SEM image of the engineered TiO_2 dielectric fractals with a porosity of 98% and a thickness of 1.8 µm. d,e, Extinction measurement in a 0% and 4% air-ethanol mixture for the bare Au substrate and the one with the integrated TiO_2, respectively. f, Dynamic responses of the same sample to different cycles of air/ethanol at room temperature show high repeatability and sensitivity.

3. Conclusions

We have synthesized tunable and plasmonic hybrid novel nanostructured material, comprising of resonant metasurfaces and tailored dielectric fractals, for enhancing the interaction of the plasmonic field with a gaseous environment. These findings could pave the way toward a new class of contactless optical sensors with applications ranging from non-invasive diagnostic to pollution monitoring and safety.

References

1. Eguchi, K., *Optical Gas Sensors*, in *Gas Sensors: Principles, Operation and Developments*, G. Sberveglieri, Editor. 1992, Springer Netherlands: Dordrecht. p. 307-328.
2. Anker, J.N., et al., *Biosensing with plasmonic nanosensors.* Nature materials, 2008. **7**(6): p. 442-453.
3. Fusco, Z., et al., *High-Temperature Large-Scale Self-Assembly of Highly Faceted Monocrystalline Au Metasurfaces.* Advanced Functional Materials, 2019. **29**(2): p. 1806387.
4. Fusco, Z., et al., *Nanostructured Dielectric Fractals on Resonant Plasmonic Metasurfaces for Selective and Sensitive Optical Sensing of Volatile Compounds.* Advanced Materials, 2018. **30**(30): p. 1800931.

Optical Design of the Goaly3 Multi-Mirror Telescope System with a Wide Field of View

Junliu Fan,[1] Quanying Wu,[*1] Baohua Chen,[1] DaLing Cai[1,3] and Haiping Zhang[1,2]

[1] School of Mathematics and Physics, Suzhou University of Science and Technology, Suzhou 215009, China
[2] Soochow Mason Optics Co., Ltd. of Graduate Workstation in Jiangsu Province , Suzhou 215028, China
[3]Suzhou FOIF Co., Ltd. of Graduate Workstation in Jiangsu Province , Suzhou215006, China ,
*corresponding author, E-mail: *wqycyh@mail.usts.edu.cn*

Abstract

A Golay3 Multi-Mirror Telescope (MMT) system is researched in this paper. An initial configuration is established according to the paraxial optical theory. A three-element aspheric corrector group is designed and placed in the converging light cone to enlarge the field of view (FOV) of the Golay3 MMT. The design results show that the fill factor *F* of the Golay3 MMT can be determined by a given CCD device. The FOV of the Golay3 MMT system can be increased to 1.5^0 with the insert of a three-element aspheric corrector group.

1. Introduction

The quest for finer angular resolution in astronomy will inevitably lead to larger apertures, which has pushed the limits of size and weight for monolithic primary mirrors. Large primary mirrors are increasingly difficult to fabricate and mount. In response, technologies such as segmented and sparse aperture systems are developed as the next generation of telescopes[1-4]. One type of the sparse aperture systems is the multiple-mirror telescope(MMT) in which several sub-mirrors resolve an object and share the same secondary mirror[5]. The major disadvantage of the MMT lies in its relative small FOV. In our paper we design a Golay3 MMT with a wide field of view. The configuration of the Golay3 MMT is based on a 300mm Cassegrain system. The FOV of the Golay3 MMT is enlarged to 1.5^0 by designing a three-element aspheric corrector group in the converging light cone.

2. Determination of the Fill Factor of the Golay3 MMT

The Golay3 MMT adopts the two-mirror Cassergrain configuration, and the primary mirror is made up of three spherical sub-mirrors which are arranged in the Golay3 form(Fig. 1). The secondary surface needs to be strongly deformed to remove spherical aberration from the primary surface. This design suffers from such severe coma that it is limited to a very narrow FOV.

The fill factor *F*, which is defined as the ratio of all sub-mirrors' area to that of the surrounding aperture can be obtained by

$$F = 3 \cdot D_{sub}\text{^}2 / D\text{^}2 \qquad (1)$$

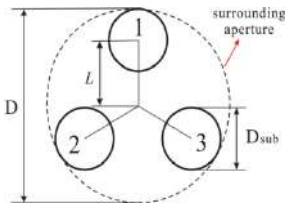

Fig.1 The Golay3 aperture

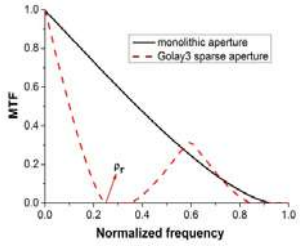

Fig.2 The MTF of the Golay3 aperture

Where D_{sub} and D are the diameters of the sub-mirrors and the surrounding aperture, respectively. Compared with the system with a monolithic primary, the Modulation Transfer Function(MTF) of a sparse aperture system suffers a contrast loss in the mid frequency range as shown in Fig. 2. For an aberration-free sparse aperture system, the first cutoff frequency denoted by ρ_r, is determined by the equivalent aperture D_{eq} of the sparse aperture system,

$$\rho_r = D_{eq} / (\lambda f) \qquad (2)$$

Where λ is the wavelength, *f* is the focal length of the optical system, and th D_{eq} for the Golay3 MMT is defined as,

$$D_{eq} = \frac{3L + \sqrt{4D_{sub}^2 - 3L^2}}{2} \qquad (3)$$

Where *L* is the distance between the centers of the surrounding aperture and the sub-mirror. Eq. (1), Eq. (2) and The frequency ρ_r should match with the Nyquist frequency of the CCD device. Once given a CCD device and the size of the surrounding aperture, the size of the sub-mirrors and the fill factor of the sparse aperture system can be determined through Eq. (1) and Eq. (3), respectively. In this paper, we select a CCD with pixels of 6.2 μm. It can be inferred that the semi-diameter of the sub-mirror is 46.2mm and the fill factor of the sparse aperture system is 29.6%. The detailed specifications for the Golay3 MMT are listed in Table1.

Table 1. The design specifications of the Golay3 MMT

Parameter	specification
Entrance pupil diameter(mm)	300
Focal length(mm)	2100
Focal ratio of the primary	3.5

Full field of view(degree)	1.5
Spectral range(μm)	0.486-0.656

3. Design of the Goaly3 MMT

The design of the Golay3 MMT begins from a coaxial two-mirror system with a monolithic primary which is set as the stop. With the increase of the FOV, off-axis aberrations such as coma and astigmatism of the Golay3 MMT become dominant and the image quality is getting worse. Thus a corrector group before the image plane is designed to enlarge the FOV.

Initially, the corrector group is designed with two normal glasses of BK7 and SF2. At a certain stage of the optimization, a third glass BK7 is added into the corrector group. At last, a hammer optimization is performed to choose the best glasses for the design. The final configuration of the corrector group is shown in Fig. 3.

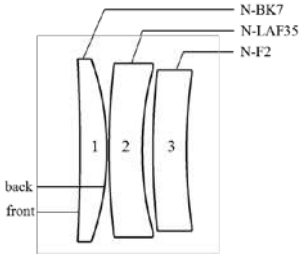

Fig. 3 The configuration of the corrector group

4. Analysis of the design result

Fig. 4 is the configuration of the Golay3 MMT with the optimized corrector group. The parameters of the final system are listed in Table 2. The thickness of the secondary mirror which refers to the distance between the secondary and the image plane is 869.69mm. The semi-diameter of the secondary is 62.5mm, which is slightly larger than the constraint of 60mm, but still results in a fill factor of 25.5%.

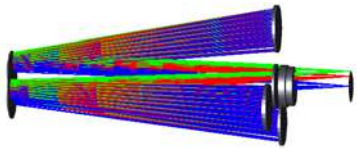

Fig. 4 The configuration of the Golay3 MMT with the corrector group

Table 2. The parameters of the final Golay3 MMT

Parameters	Primary	Secondary
Radius(mm)	-2100.00	-1291.34
Thickness(mm)	-674.22	869.69
Semi-diameter of sub-mirror(mm)	43.75	62.50
Conic constant	0.00	11.71

According to the design results, the maximum spot RMS radius in the 1.5^0 field is 4.808μm which is less than the pixel size of the CCD device. The MTF curves of the Golay3 MMT as shown in Fig.5 indicate that the first cutoff frequency ρ_r in each field of view is around 80 lp/mm, which corresponds to a resolving power of 5.9 μrad. Besides, the resolving power of different orientation in the mid and high frequency region (above 80 lp/mm) is different due to the distribution of sub-mirrors. Though the final system satisfies all the design specifications, it should be noted that the image size is 56.65mm in diameter, which means that the CCD size should at least be as large as 2.23×2.23 inches to cover a 1.5^0 target scene.

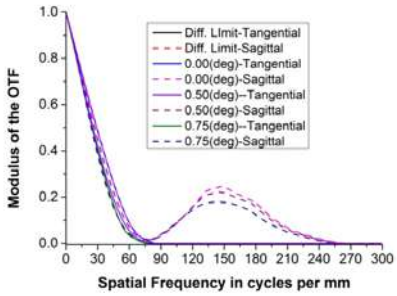

Fig.5 The MTF of the Golay3 MMT

5. Conclusions

In this paper, a Golay3 MMT which is based on the Cassegrain system is designed. The determination of the fill factor of the Golay3 MMT is analyzed in detail. A three-element aspheric corrector group is designed and placed in the converging light cone to enlarge the full FOV to 1.5^0 and balance the residual aberrations of the Cassegrain system. The final Golay3 MMT achieves a fill factor of 25.5% and the performance of the system satisfies all the requirements of the design specifications.

Acknowledgements

This work is supported by the National Natural Science Foundation of China under Grant Nos. 61875145& 11804243, Jiangsu Province Key Discipline of China's 13th five-year plan (20168765),Jiangsu Key Laboratory of Advanced Optical Manufacture Technology (KJS1710). the Six Talent Peaks Project of the Jiangsu Province (DZXX-026).

References

1. RobertD. F, Theodore A. T, "Image quality of Sparse-aperture Designs for Remote Sensing," Opt. Eng. **41**, 1957-1968(2002).
2. G. Andersen, "Holographic correction and phasing of large sparse-array telescopes", Appl. Opt. **44**(8), 1355-1359(2005)
3. R. Genet, D. Rowe, M. Clause, "Sparse-Aperture Quasi-Meridian Telescopes,"*Journal of Double Star Observation*, **12**, 287-294(2016).
4. T. J. Schulz, R. G. Paxman, "Piston alignment for a segmented-aperture imaging system by using piston-sweep phasing", Opt. Lett, **42**(15), 2922-2925(2017).
5. F. Wu, Q. Y. Wu, L. Qian, "Analysis of the characteristics of the Golay3 multiple-mirror telescope", Appl. Opt. **48**(3), 643-652(2009).

Cylindrically correlated partially coherent vector beams

Yahong Chen[1,*], Chengliang Zhao[1], Lin Liu[1], Fei Wang[1], and Yangjian Cai[1,2]

[1]School of Physical Science and Technology, Soochow University, Suzhou 215006, People's Republic of China
[2]Center of Light Manipulations and Applications & Shandong Provincial Key Laboratory of Optics and Photonic Device, School of Physics and Electronics, Shandong Normal University, Jinan 250014, China
*corresponding author, E-mail: yahongchen@suda.edu.cn

Abstract

We introduce a class of vector beams with inhomogeneous statistical and nontrivial far-field angular distributions which we term cylindrically correlated partially coherent vector beams. We find that the novel beams posses, in general, cylindrically polarized, far-field patterns of an adjustable degree of polarization, that can find important applications to e.g., simultaneous trapping of different kinds of neutral microparticles and multiple surface plasmon excitation.

1. Introduction

Optical coherence, as one of the fundamental properties of light, plays an important role in the light field manipulation and the light-matter interactions. Recent studies have shown that the light coherence structure [1] can be viewed as an indispensable degree of freedom to control the physical properties of propagating beams and surface waves. Several types of partially coherent fields with statistically nonuniform correlation functions have been introduced and generated via various coherence manipulation methods. These fields exhibit many interesting properties during propagation such as self-splitting, self-focusing, and self-shaping in either space or time domains, and are envisioned useful in a wealth of applications to free-space optical communications, super-resolution imaging, and longitudinal field shaping.

Polarization is another fundamental feature of light fields, reflecting their vector nature. Until recently, coherence and polarization of light fields had been treated separately for historical reasons. Since Gori and Wolf developed unified theories of coherence and polarization for the random electromagnetic beams, numerous studies have been devoted to partially coherent vector beams aiming to elucidate their fundamental properties and outline potential applications. Recently, increasing attention has been paid to the spatial coherence structure engineering of partially coherent vector beams. In 2014, Chen et al. introduced a class of nonuniformly correlated partially coherent vector beams [2]. A fully polarized intensity fraction of such beams is radially polarized in the far zone of the source. As the source spatial coherence decreases, a very pure radially polarized, partially coherent far field can be generated by the source, a feature combination especially conducive to reliable particle trapping and material thermal processing applications.

In this paper, we will we introduce a class of partially coherent vector beams with nonuniform correlations and nontrivial far-field features that we term cylindrically correlated partially coherent (CCPC) vector beams. We find such CCPC vector beams can create cylindrically polarized far fields of any degree of polarization, which can find applications to particle sorting and controllable surface plasmon excitation.

2. Generalized complex Gaussian representation of partially coherent vector beams

The statistical properties of a partially coherent vector beam, propagating close to the optical axis (i.e., along z-axis), are characterized by a 2 × 2 (space-frequency) cross-spectral density matrix or (space-time) coherence-polarization matrix. A straightforward complex Gaussian representation (CGR) extension to the vectorial case implies that the cross-spectral density matrix for any partially coherent vector fields can be represented as

$$\mathbf{W}(\mathbf{R}_1,\mathbf{R}_2,0)=\int \mathrm{d}^4\boldsymbol{\alpha}\,\mathcal{P}(\boldsymbol{\alpha})\Psi_{\boldsymbol{\alpha}}^{*}(\mathbf{R}_1,0)\Psi_{\boldsymbol{\alpha}}(\mathbf{R}_2,0). \quad (1)$$

Here we use the notation $\mathbf{R}\equiv(X,Y)$ to represent a dimensionless radius vector with $X=x/\sigma_I$, $Y=y/\sigma_I$, and σ_I being any characteristic spatial scale in the beam transverse plane. In particular, it is convenient to assume that σ_I coincides with a beam waist at the source plane. Next,

$$\mathcal{P}(\boldsymbol{\alpha})=\begin{bmatrix}\mathcal{P}_{xx}(\boldsymbol{\alpha}) & \mathcal{P}_{xy}(\boldsymbol{\alpha})\\ \mathcal{P}_{yx}(\boldsymbol{\alpha}) & \mathcal{P}_{yy}(\boldsymbol{\alpha})\end{bmatrix}, \quad (2)$$

is a nonnegative matrix that guarantees nonnegative definiteness of the cross-spectral density matrix, and $\{\Psi_{\boldsymbol{\alpha}}(\mathbf{R},0)\}$ are the complex Gaussian (pseudo) modes, given by

$$\Psi_{\boldsymbol{\alpha}}(\mathbf{R},0)=\frac{\mathrm{e}^{-\mathbf{v}^2/2}}{\sqrt{\pi}}\exp[-\frac{(\mathbf{R}-\sqrt{2}\boldsymbol{\alpha})^2}{2}]. \quad (3)$$

We Stress here that the cross-spectral density of **any** partially coherent vector source can be represented by Eq. (1). In addition, the generalized CGR can be applied to synthesize novel partially coherent vector beams via engineering the nonnegative matrix $\mathcal{P}(\boldsymbol{\alpha})$.

3. Cylindrically correlated partially coherent vector beams

As a particular example, we introduce cylindrically correlated partially coherent (CCPC) vector beams in this section by using the generalized CGR. The $\mathcal{P}$-matrix for an CCPC vector beam source has the form,

$$\mathcal{P}(\boldsymbol{\alpha}) = \delta(\mathbf{u})\exp(-\frac{\xi_c^2\mathbf{v}^2}{2})\begin{bmatrix} a^2(\mathbf{v}) & a(\mathbf{v})b(\mathbf{v}) \\ a(\mathbf{v})b(\mathbf{v}) & b^2(\mathbf{v}) \end{bmatrix}, \quad (3)$$

where $\xi_c = \sigma_c / \sigma_I$ stands for a relative coherence length; σ_c being the coherence length of the CCPC vector beam at the source, and

$$\begin{bmatrix} a(\mathbf{v}) \\ b(\mathbf{v}) \end{bmatrix} = \mathbf{M}(\theta)\begin{bmatrix} v_x \\ v_y \end{bmatrix}, \quad (4)$$

with $\mathbf{M}(\theta)$ being a clockwise rotation matrix and $0 \le \theta < 2\pi$. In the free space propagation case, the CCPC beam Stokes parameters can then be expressed as

$$S_0(\mathbf{R}, Z) = 2C_0 \exp\left(-\frac{\mathbf{R}^2}{S_0^2}\right)\left(\frac{1}{S_0^2} + \frac{2Z^2}{\xi_c^2 S_0^4} + \frac{2Z^2\mathbf{R}^2}{\xi_c^2 S_0^6}\right), \quad (5)$$

$$S_1(\mathbf{R}, Z) = \frac{4C_0 Z^2}{\xi_c^2 S_0^6}\exp\left(-\frac{\mathbf{R}^2}{S_0^2}\right) \times (X^2\cos 2\theta - Y^2\cos 2\theta + 2XY\sin 2\theta), \quad (6)$$

$$S_2(\mathbf{R}, Z) = \frac{4C_0 Z^2}{\xi_c^2 S_0^6}\exp\left(-\frac{\mathbf{R}^2}{S_0^2}\right) \times (-X^2\sin 2\theta + Y^2\sin 2\theta + 2XY\cos 2\theta), \quad (7)$$

$$S_3(\mathbf{R}, Z) = 0. \quad (8)$$

The polarized part of the CCPC beam polarization state is encapsulated in the three Stokes parameters: $S_1(\mathbf{R}, Z)$, $S_2(\mathbf{R}, Z)$, $S_3(\mathbf{R}, Z)$. For a CCPC vector beam, we have $S_3(\mathbf{R}, Z) = 0$, implying that the fully polarized part has linear polarization. Moreover, the ratio of $S_1(\mathbf{R}, Z)$ to $S_2(\mathbf{R}, Z)$ can be written as

$$\frac{S_1(\mathbf{R}, Z)}{S_2(\mathbf{R}, Z)} = \frac{X^2\cos 2\theta - Y^2\cos 2\theta + 2XY\sin 2\theta}{-X^2\sin 2\theta + Y^2\sin 2\theta + 2XY\cos 2\theta}, \quad (9)$$

indicating that the fully polarized part of the CCPC vector beam displays cylindrical polarization [3]. The polarization state distribution is controlled by the angle θ. In Fig. 1 we display the CCPC beam polarization distribution at the distance $Z = 1$ for different values of θ. We find that the beam is radially polarized for $\theta = 0$ and becomes azimuthally polarized for $\theta = \pi / 2$, while for $\theta = \pm\pi / 4$ the CCPC vector beam shows general cylindrical polarization.

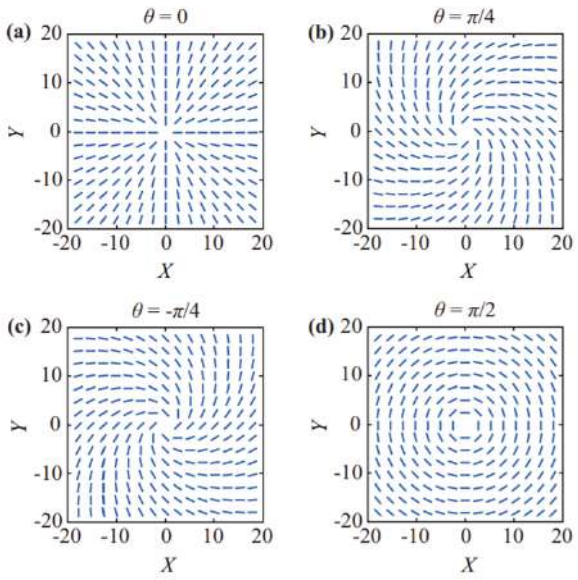

Figure 1: Distribution of the CCPC vector beam polarization states at the distance $Z = 1$ for (a) $\theta = 0$, (b) $\theta = \pi / 4$, (c) $\theta = -\pi / 4$, and (d) $\theta = \pi / 2$.

4. Conclusions

We proposed the concept of cylindrically correlated partially coherent (CCPC) vector beams and studied their free space propagation properties. The CCPC beams become progressively more polarized on propagation and they acquire doughnut shape profiles. Further, we found that very pure far-field cylindrical polarization states (with 99% polarization purity) can be created by the CCPC sources of low spatial coherence.

Acknowledgements

This work is partially supported by National Natural Science Foundation of China (NSFC) (11525418, 91750201, 61505046).

References

[1] Y. Cai, Y. Chen, and F. Wang, "Generation and propagation of partially coherent beams with nonconventional correlation functions: a review," J. Opt. Soc. Am. A **31**, 2083–2096 (2014).

[2] Y. Chen, F. Wang, L. Liu, C. Zhao, Y. Cai, and O. Korotkova, "Generation and propagation of a partially coherent vector beam with special correlation functions," Phys. Rev. A **89**, 013801 (2014).

[3] Q. Zhan, "Cylindrical vector beams: from mathematical concepts to applications," Adv. Opt. Photon. **1**, 1–57 (2009).

Non-iterative Method for Retrieving an Object Illuminated by Spatially Partially Coherent Beam

Chengliang Zhao[1], Xingyuan Lu[1], Lin Liu[1], Fei Wang[1], Yahong Chen[1], Yangjian Cai[1,2]

[1]School of Physical Science and Technology, Soochow University, Suzhou, China
[2]Center of Light Manipulation and Application, School of Physics and Electronics, Shandong Normal University, Jinan, China
*corresponding author, E-mail: zhaochengliang@suda.edu.cn

Abstract

Phase retrieval of objects using partially coherent illumination has been a long-lasting challenge due to the fact that propagation of the four-dimensional mutual coherence function is very complicated. The problem is especially challenging when the mutual coherence function is unknown. In this letter, a new non-iterative method for phase retrieval using partially coherent beams directly without coherence filtering is proposed and demonstrated experimentally. The effects of spatial coherence on the reconstructed object are discussed and studied in detail. Even for low degrees of coherence a reconstruction of good quality can be obtained by characterizing the partially coherent source. This method is also non-contact and can be used for phase imaging using all kinds of partially coherent beams with arbitrary coherence function and wavelength.

1. Introduction

When light is transmitted through a sample, the amplitude and phase of the light are modulated according to the object's complex-valued transmission function. If we want to reconstruct the transmission function completely, we need to find both its amplitude and phase. However, with detectors we can only measure the intensity directly, while the phase information is lost. Thus, to reconstruct the transmission function, one needs to use phase retrieval methods that reconstruct the phase from intensity measurements [1]. Especially when no high-quality lenses are available for imaging, reconstruction of the sample's transmission function through phase retrieval is important.

For short wavelengths, e.g. X-rays, light sources such as a free-electron laser or a third-generation synchrotron are not perfectly coherent [2, 3]. Therefore, it is necessary to study phase retrieval with partially coherent illumination. To the best of our knowledge, there have been no reports on explicitly non-iterative phase retrieval for partially coherent illumination, especially not for partially coherent beams with nonconventional correlation functions. The aim of this paper is to explore the possibility of using a non-iterative method in the case of partial coherence, to study the effect of partially spatial coherence on the reconstruction of the object's transmission function, and to overcome difficulties caused by partially spatial coherent illumination with nonconventional correlation functions. Advantages of our non-iterative reconstruction scheme are that it requires only few measurements, it is less computationally expensive, and it does not suffer from issues such as stagnation or non-unique solutions from which iterative algorithms tend to suffer.

2. Result

2.1. Description of the experiment

In the experiment, we choose our illuminating beam to be a Gaussian correlated Schell-model (GSM) beam. The experimental set-up for generating a GSM beam is shown in Fig. 1a. A coherent laser beam emitted by a solid-state laser is expanded and then focused by lens L1 on a rotating ground-glass disk, which produces a partially coherent beam with Gaussian statistics. The GSM beam is obtained by collimating the partially coherent beam by lens L2 and transmitting it through a Gaussian filter. Coherence width can be determined by the size of the focus spot as well as the roughness of the rotating ground-glass disk. In the experiment, the beam width is controlled by varying the size of the focused spot by translating back-and-forth lens L1.

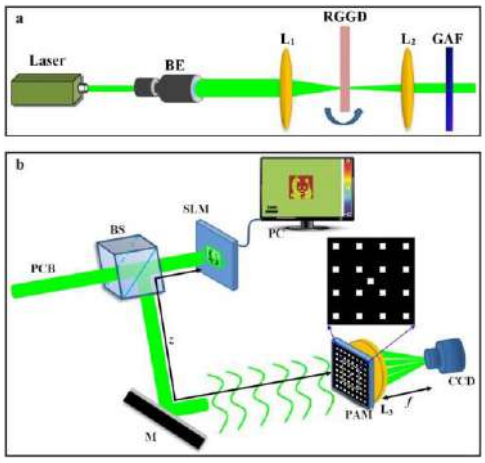

Figure 1: Experimental set-up for generating a GSM beam (a) and experimental set-up for retrieving the phase object (b).

Fig. 1b illustrates the experimental set-up for our non-iterative method. A phase object, whose amplitude is uniform, is displayed on the phase spatial light modulator (SLM). The phase object is illuminated by the GSM beam and the reflected light is reflected again by the beam splitter. The Fourier transform of the light transmitted by the PAM is performed using lens L3 and its intensity is captured by the camera.

2.2. Results of the experiment

The field-of-view of the object function retrieval is not only limited by the signal to noise ratio (SNR), but also by the coherence width of the illuminating beam: the less coherent the diffraction pattern gets the more blurred the retrieved object function becomes for larger fields of view. This reduces the field-of-view in object space. At positions where the retrieved field is below the noise level, the object function cannot be retrieved. This is illustrated in Fig. 2 where reconstruction results are shown for phase object with the perturbation point located at the head of the panda. Every row in Fig. 2 corresponds to a GSM beam with a certain coherence width that decreases from the upper row to the lower row. In the left two columns, the amplitude and the phase of the mutual coherence function are shown. The amplitude of a GSM beam obeys the Gaussian distribution with centre at the perturbation point and a phase which is uniform. It is seen that the size of the region is bigger than the SNR, is smaller when the coherence width decreases. In the right two columns, the logarithm of the amplitude and the phase of the retrieved field are shown. It is seen that the region around the perturbation point where the object function can be retrieved decreases for decreasing the coherence width, which is in accordance with the decrease of the size of the region where is larger than the SNR. This region can be enlarged either by increasing the SNR or by increasing the coherence width.

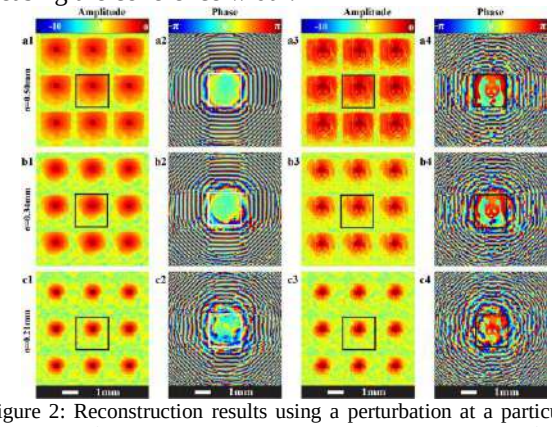

Figure 2: Reconstruction results using a perturbation at a particular point with (first and second column) and without (third and fourth column) object for a GSM beam with various coherence widths.

In Fig. 2, we have seen that for a GSM beam and for a given SNR, the region where the object field can be retrieved is approximately a disk centred at the perturbation point with the radius of the disk determined by the coherence width. For GSM beam illumination with low coherence width, the disk does not cover the entire object. However, the object can still be retrieved in the entire field-of-view of the object by using more perturbation points. This means that we need to repeat the procedure of object retrieval several times, each time introducing the perturbation at a different position. In Fig. 3 the reconstructed phase objects are shown for the case of lowest coherence width when six perturbation points are used. By comparing the retrieved object with the result shown in Fig.2 (c4), it is seen that the field-of-view of the retrieved object is larger when more perturbation points are used.

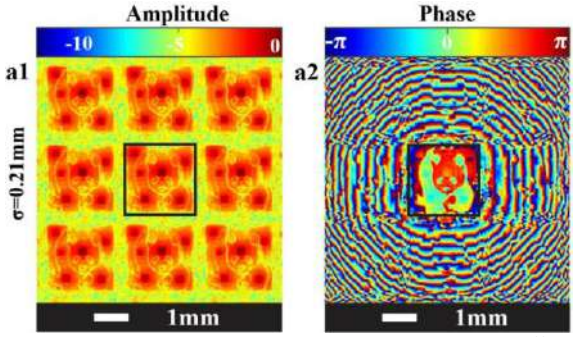

Figure 3: Reconstruction results using perturbations at different positions for GSM beam illumination. The perturbations are introduced sequentially at different positions and for each position the object is retrieved independently. The reconstruction result is the sum of all the retrieved objects.

3. Conclusions

We have introduced a new non-iterative method to retrieve the complex-valued object function of an object illuminated by an unknown partially coherent beam. By using a PAM placed at a certain distance from the object and by perturbing the object in a point, the direct relationship between the complex-valued object function and the intensity of the Fourier transform of the field transmitted by the PAM can be obtained. Our method is wavelength independent and can hence be applied to a wide range of wavelengths, from X-rays to infrared light, and overcomes several challenges of conventional iterative CDI. In particular, we do not need to decompose the mutual coherence function that describes the partially coherent illumination into a sum of coherent modes.

Acknowledgements

This work is supported by the National Natural Science Foundation of China (11774250, 91750201), National Natural Science Fund for Distinguished Young Scholar (11525418).

References

[1] J. Miao, et al. Quantitative image reconstruction of GaN quantum dots from oversampled diffraction intensities alone, *Phys. Rev. Lett*. 95: 085503, 2005.

[2] L. W. Whitehead, et al. “Diffractive imaging using partially coherent x rays,” *Phys. Rev. Lett.* 103: 243902, 2009.

[3] J. N. Clark, et al. Dynamic imaging using ptychography. *Phys. Rev. Lett*. 112: 113901, 2014.

A Goaly3 Multi-Mirror Telescope System Alignment Technology Based on Zernike Polynomials

Baohua Chen,[1] Quanying Wu,[*1]Junliu Fan,[1] DaLing Cai[1,3] and Haiping Zhang[1,2]

[1] School of Mathematics and Physics, Suzhou University of Science and Technology, Suzhou 215009, China
[2] Soochow Mason Optics Co., Ltd. of Graduate Workstation in Jiangsu Province , Suzhou 215028, China
[3]Suzhou FOIF Co., Ltd. of Graduate Workstation in Jiangsu Province , Suzhou215006, China ,
*corresponding author, E-mail: *wqycyh@mail.usts.edu.cn*

Abstract

Zernike polynomials with field of view(FOV) and pupil factors are derived.The first three polynomial coefficients are used to represent the alignment errors of a Golay3 Multi-Mirror Telescope (MMT) system.The effects of alignment errors under different FOV of the MMT optical system are analyzed and the process of imaging simulation based on this model is also discussed.Finally, the phase difference method(PD) is used to estimate the errors successfully and restore the images accurately.

1. Introduction

Sparse aperture systems can achieve the same information as full aperture systems, but their volume is smaller and the weight is lighter than the full aperture[1].One type of the sparse aperture systems is the multiple-mirror telescope(MMT) in which several sub-mirrors resolve an object and share the same secondary mirror[2].However,the major disadvantage of the MMT lies in its large alignment errors duing to the high degree of freedom of the sub-mirrors. In our paper we use the first three terms of Zernike polynomial which contain field of view(FOV) and pupil factors to express the system alignment errors[3]. Analyse the influence of alignment errors under different FOV and discuss the process of imaging simulation based on this model.Finally, the phase difference method(PD) is used to estimate the errors successfully and restore the images accurately.

2. Golay3 MMT and its alignment errors

The Golay3 MMT adopts the two-mirror Cassergrain configuration, and the primary mirror is made up of three spherical sub-mirrors which are arranged in the Golay3 form(Fig. 1). Because of the high degree of freedom of the sub-mirrors, this optical system produce large alignment errors easily,such as *Piston* error along the optical axis(*Z* axis)and *Tilt* error around the *x* or *y* axis[4].(Fig. 2)

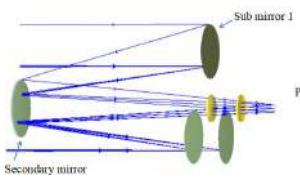

Fig.1 The Golay3 optical system

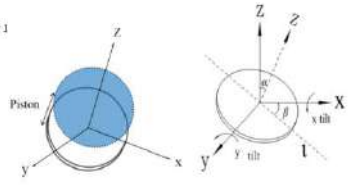

Fig.2 The *piston* and *tilt* error

Generally,people use the first three terms of traditional Zernike polynomial expressing the system alignment errors which is defined as Eq.(1),

$$\phi_n(x,y)=\frac{2\pi}{\lambda}\sum_{j=1}^{3}a_j z_j(x,y) \qquad (1)$$

where λ is the wavelength, $\phi_n(x,y)$is the Wavefront error and a_j is the Zernike polynomial coefficient,$Z_j(x,y)$ is the Zernike polynomial.

However,the traditional Zernike polynomial is only in a single FOV to reconstruct the wavefront error.Because of the lack of field parameters ,the corresponding Zernike term is not a real wave aberration function.the $Z_j(x,y)$ shows only pupil parameters.In the actual imaging, there are different FOV, which leads to the detection of the wavefront distortion inaccuracy and affects the final image restoration.

3.Zernike polynomials with field parameters

In an optical system with a circular pupil and a rotational symmetry, the wave aberration function is generally used to represent the wavefront aberrations of the FOV and pupil factors.Hopkins proposed the expression of the wave aberration function in polar coordinates as a power series expansion[5]：

$$W(h,\theta;\rho,\phi)=\sum_{j}\sum_{p=0}^{\infty}\sum_{n=0}^{\infty}\sum_{m=0}^{\infty}(W_{klm})_j h^k \rho^l \cos^m(\theta-\phi) \qquad (2)$$

Where $k=2p+m,l=2n+m$ are the power series of the FOV and the pupil term,W_{klm} is the coefficient,j is a number of optical components that affect the system's wavefront.

The FOV and pupil vector are shown in Fig.3.In the image plane, the field vector is pointing to the origin and the actual surface center,θ is the angle between the h and x axis and its direction is counterclockwise.In the exit pupil plane, the pupil's vector ρ is the center of the pupil's center and the point of the actual pupil.Φ is the angle between the ρ and x axis of the exit pupil and its direction is also counterclockwise.

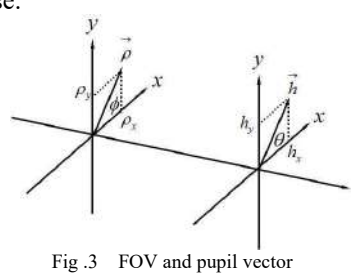

Fig .3 FOV and pupil vector

According to Seidel theory, the piston and tilt term of the

wave aberration function can be expressed as:

$$W_{piston} = \sum_j (W_{000} + W_{200} h^2) \tag{3}$$

$$W_{tilt} = \sum_j W_{111} h\rho\cos(\theta - \phi) = \sum_j W_{111} \vec{h} \cdot \vec{\rho} \tag{4}$$

Where $W_{000,}$ W_{200} and W_{111} are the aberration coefficients of the FOV and pupil， The tilt term in the wave aberration function can be attached to the error vector σ when there is alignment error in system,:

$$W_{tilt} = \sum_j W_{111} (\vec{h} + \vec{\sigma}) \cdot \vec{\rho} \tag{5}$$

Due to the image point coordinates of the plane will change with the FOV and the tilt of sub mirror，so when the system has a tilt error, the vector h of FOV will attach the error vector σ .Its formula is expanded into：

$$\begin{aligned} W_{tilt} &= \sum_j W_{111} (\vec{h} + \vec{\sigma}) \cdot \vec{\rho} \\ &= \sum_j (W_{111} h\rho\cos(\theta - \phi) + W_{111}\sigma\rho\cos(\theta - \phi)) \\ &= \sum_j ((W_{111} h\cos\theta + W_{111}\sigma\cos\theta)\rho\cos\phi) + \sum_j ((W'_{111} h\sin\theta + W_{111}{}'\sigma\sin\theta)\rho\sin\phi) \end{aligned} \tag{6}$$

Make the normalized FOV term like $h\cos\theta = hx$,$h\sin\theta = h_y$, $\beta_1 = W_{200}$,$\beta_2 = W_{111}$,$\beta_3 = W'_{111}$,$\alpha_1 = W_{000}$,$\alpha_2 = W_{111}\sigma\cos\theta$,$\alpha_3 = W'_{111}\sigma\sin\theta$.As shown in the following table1 that contains field parameters of the Zernike first three terms,where β_1, β_2 and β_3 are the simplified coefficients of the field terms,α_1,α_2 and α_3 are the additional error when the system has the alignment errors.

Table 1. Zernike polynomials with field parameters

Number of items	Polynomial	Coefficient
1	1	$\beta_1(h_x^2 + h_y^2) + \alpha_1$
2	$\rho\cos\Phi$	$\beta_2 h_x + \alpha_2$
3	$\rho\sin\Phi$	$\beta_3 h_y + \alpha_3$

With the coefficients are expressed, $\phi_n(x,y)$ in Eq. (1) is defined .The corresponding aberrations of the system can be obtained by using interferometer or Shack-Hartmann,so the FOV coefficients(β) can be obtained by using multiple sets of corresponding aberrations.

Then, in Fig.4,we use phase difference method to simulate imaging in the Golay3 MMT.Selecting two simulated FOV angle,respectively(0°,0.01°)and(0.1°,0.1°),set the sub mirror 1 contains 4λ piston and 0.1° x tilt and y tilt error, sub mirror 2and 3 as a reference without any error.Getting two images from the focal and defocus plane,the focal distance is77um,the defocusing amount is 1λ.Fig. 5 shows that restore the images accurately by PD,but because of the image noise there is a certain bias between the two results,and the restored image under the FOV(0.1°,0.1°) recovery a bit weak compared to FOV (0°,0.01°).

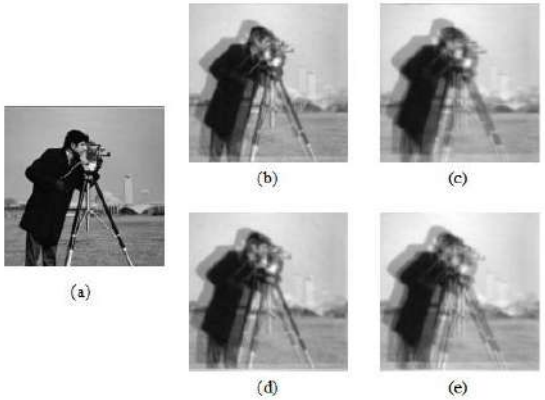

Fig .4 Object image (a),FOV(0°,0.01°) focal and defocus image(b),(c) FOV(0.1°,0.1°)focal and defocus image(d),(e)

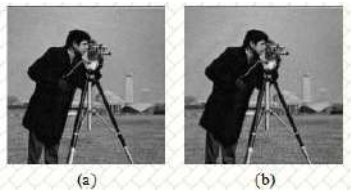

Fig .5 Restore image at FOV(0°,0.01°)(a) and (0.1°,0.1°)(b)

5. Conclusions

In this paper, Zernike polynomials with field of view(FOV) and pupil factors are derived.The first three polynomial coefficients are used to represent the alignment errors of a Golay3 Multi-Mirror Telescope (MMT) system.The effects of alignment errors under different FOV of the MMT optical system are analyzed and the process of imaging simulation based on this model is also discussed.Finally, the phase difference method(PD) is used to estimate the errors successfully and restore the images accurately.

Acknowledgements

This work is supported by the National Natural Science Foundation of China under Grant Nos. 61875145& 1180 4243, Jiangsu Province Key Discipline of China′s 13th five-year plan (20168765),Jiangsu Key Laboratory of Advanced Optical Manufacture Technology (KJS1710).

References

[1] RobertD. F, Theodore A. T, “Image quality of Sparse-aperture Designs for Remote Sensing,” Opt. Eng. **41**, 1957-1968(2002).

[2] F. Wu, Q. Y. Wu, L. Qian, “Analysis of the characteristics of the Golay3 multiple-mirror telescope”, Appl. Opt. **48**(3), 643-652(2009).

[3] Bolcar M . Phase diversity for segmented and multi-aperture systems[J]. Dissertations & Theses - Gradworks, 2008, 48(1):A5-A12.

[4] T. J. Schulz, R. G. Paxman, “Piston alignment for a segmented-aperture imaging system by using piston-sweep phasing”, Opt. Lett, **42**(15), 2922-2925(2017).

[5] Kwee I W, Braat J J M. Double Zernike expansion of the optical aberration function[J]. Pure & Applied Optics Journal of the European Optical Society Part A, 1993, 2(1):21.

Effects of Atmospheric Turbulence on Lensless Ghost Imaging with Partially Coherent Light

Xianlong Liu[1,*], Yaru Gao[1], Yangjian Cai[1]

[1]Shandong Provincial Engineering and Technical Center of Light Manipulations and Shandong Provincial Key Laboratory of Optics and Photonic Device, School of Physics and Electronics, Shandong Normal University, Jinan 250014, China
*corresponding author, E-mail: *xlliu1988@163.com*

Abstract

Ghost imaging with partially coherent light through monostatic and bistatic turbulence has been studied both theoretically and experimentally. Our results reveal that in bistatic turbulence, the visibility and quality of the image decrease with the increase of the turbulence strength, while in monostatic turbulence, the image quality remains invariant, only the visibility decreases with the increase of the strength of turbulence. Our results solve the controversy about the influence of atmospheric turbulence on ghost imaging.

1. Introduction

Ghost imaging (GI) is a novel technique to retrieve the image of an object by measuring the correlation function of light intensities from two distinct paths. The conventional GI geometry is that the light beam is first divided into two parts entering two optical paths; an object is located in one path, and a bucket detector with no spatial resolution collects the light intensity transmitting from the object; in another path, a spatial resolution detector receives the light intensity, but no object exists. By making a correlating calculation of the optical signals from two detectors, an image of the object can be obtained. This phenomenon was first observed using entangled photon pairs in spontaneous parametric down-conversion (SPDC) [1].

In 2009, Cheng first investigated GI through atmospheric turbulence and found that the quality of the image degraded due to turbulence [2]. Since then, considerable attention has been paid to GI through turbulence with classical or quantum light due to its important applications in remote sensing and communications [3,4]. The effects of turbulence on the visibility and quality of the image have been extensively studied both theoretically and experimentally [3,4]. The results in these studies are similar with that in [2], i.e., the turbulence has a negative effect of the quality of image in GI system. However, Meyers et al. found from experiment that the quality of ghost image seems to be immune to turbulence [5], while the visibility of the image decreases. This result is contradiction to the previous theoretical analysis [2-4]. The motivation in our manuscript is try to solve the controversy about the ghost imaging in atmospheric turbulence. Several studies in [2-4] declared that the turbulence has negative effects on the quality of the ghost image. However, the experiment results in [5] showed that the quality of the ghost image seems immune to the atmospheric turbulence. Up to now, there is still lack of a clear understanding about the different results between in [3,4] and in [5].

Here, we present our explanations that the different results are due to the different types of atmospheric turbulence, i.e., bistatic turbulence and monostatic turbulence. In bistatic turbulence, the visibility and the quality of the image all degrade, compared to those in free space. Our experimental results in bistatic turbulence are consistent with those reported in [2-4]. In monostatic turbulence, we have established the theoretical model for the four-order correlation function between the detector D_1 and D_2. With the help of this model, we theoretically predicted that the quality of the image is nearly immune to the atmospheric turbulence. Further, our experimental results in monostatic turbulence confirmed our theoretical prediction.

2. GI in monostatic turbulence and bistatic turbulence

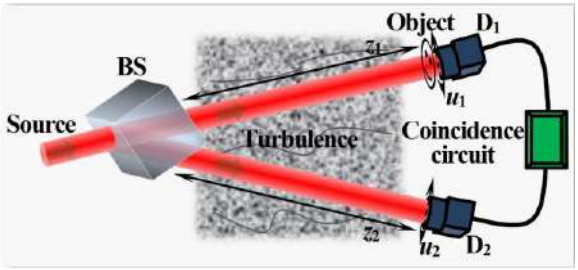

Figure 1: Schematic setup for lensless ghost imaging through turbulence.

The typical GI optical system is shown in Figure 1. The light source is first split into two twin portions by the intensity beam splitter (BS), and then two portions propagate through two distinct paths. One is a test path, which contains a bucket detector D_1 and an object. The object is close to D_1 and the distance from the source to the D_1 is z_1. Another is a reference path, where a high resolution detector D_2 is located at a distance z_2 from the source. Generally, both of the two paths are in turbulence. The output signal from D_1 and D_2 are sent to a coincidence circuit to measure the forth-order correlation function (FOCF), i.e., intensity fluctuations. In

order to observe the image information, the condition $z_2=z_1=z$ should be satisfied. As shown in Figure 1, the turbulence is introduced in two optical paths. $F_4\left(x_1,x_2,x_3,x_4;u_1,u_2\right)$ is the fourth-order coherence function of the turbulent medium, given by

$$F_4\left(x_1,x_2,x_3,x_4;u_1,u_2\right) = \left\langle \exp\left[\psi_1\left(x_1,u_1\right)+\psi_1^*\left(x_2,u_1\right)+\psi_2\left(x_3,u_2\right)+\psi_2^*\left(x_4,u_2\right)\right]\right\rangle_m , \quad , \quad (1)$$

In bistatic turbulence case, the complex phase perturbations in path one and path two are statistically independent. $F_4\left(x_1,x_2,x_3,x_4;u_1,u_2\right)$ can be simplified as

$$F_4\left(x_1,x_2,x_3,x_4;u_1,u_2\right) = \left\langle \exp\left[\psi_1\left(x_1,u_1\right)+\psi_1^*\left(x_2,u_1\right)\right]\right\rangle_m , \times\left\langle \exp\left[\psi_2\left(x_3,u_2\right)+\psi_2^*\left(x_4,u_2\right)\right]\right\rangle_m . \quad (2)$$

In monostatic turbulence case, $F_4\left(x_1,x_2,x_3,x_4;u_1,u_2\right)$ can't be separated by the product of the ensemble average over the second-order statistics of and that of due to that the turbulence in two paths are statistically correlated. There are some theoretical approximation models to describe this process [6]. Here, we adopt the theoretical model based on Wang's analysis. F_4 is expressed as [6]

3. Experimental measurement of the GI through monostatic and bistatic turbulence in lab

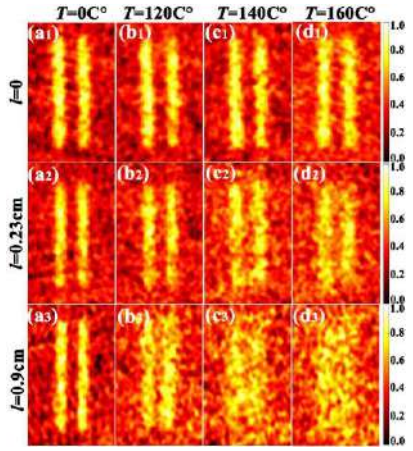

Figure 2: Normalized image of double slits with different l and temperature T of the hot plate. a1)-(a3): $T=0\ \mathrm{C}^\circ$, (b1)-(b3): $T=120\ \mathrm{C}^\circ$, (c1)-(c3): $T=140\ \mathrm{C}^\circ$ and (d1)-(d3): $T=160\ \mathrm{C}^\circ$.

Figure 2 shows our experimental measurements of the ghost imaging through turbulent atmosphere with l being the distance between two optical paths, T is the temperature of the hot plate (i.e., the strength of the turbulence). It can be seen in Figure 2(a1)-(d1) that the turbulence almost has no effect on the quality of the image in monostatic case when the temperature of the hot plate from 0 to $160^\circ\mathrm{C}$. As the distance l increases, the image gradually blurred by the turbulence-induced degradation as the strength of the turbulence increases [see in Figure 2(a2)-(d2)]. When l=0.9cm, the turbulences in two paths develop into bitatic case, no image information can be obtained for the temperate $T=140\ \mathrm{C}^\circ$ and $T=160\ \mathrm{C}^\circ$ [see in Figure 2(a3)-(d3)]. The distance l is closely related to the types of the turbulence. Our experimental results are consistent with the theoretical analysis.

4. Conclusions

We have studied the quality and visibility of the GI through monostatic and bistatic turbulence both in theory and experiment. Analytical expressions for the FOCFs which contain the background noise and the image information are derived for the case of monostatic and bistatic turbulence with the help of a tensor method. It was found that the visibility and the quality of the image in two types of turbulence lead to different results. In bistatic turbulence, the visibility and the quality of the image all degrade by the turbulence due to the statistical independence of the two paths in GI system. In monostatic turbulence, the quality of the image can keep invariant as that in free space in some range of the strength of turbulence whereas the visibility decreases with the increase of the turbulence. When the distance from the light source to the detection plane is an order of hundred meters, the GI information can remain longer distance in monostatic turbulence than that in bistatic case under the same condition. The experiment for the GI through monostatic and bistatic turbulence is also carried out in laboratory. Our results agree with the theoretical predictions and are consistent with the experiment results in [5]

References

[1] D.-V. Strekalov, A.-V. Sergienko, D.-N. Klyshko, Y. Shih, Observation of Two-photon "Ghost" interference and diffraction, *Phys. Rev. Lett.* 74: 3600-3603, 1995.

[2] J. Cheng, Ghost imaging through turbulent atmosphere, *Opt. Express* 17: 7916-7921, 2009.

[3] F. Wang, Y. Cai, O. Korotkova, Ghost imaging with partially coherent light in turbulent atmosphere, *Proc. SPIE* 7588, 75880F, 2010.

[4] P. Zhang, W. Gong, X. Shen, S. Han, Correlated imaging through atmospheric turbulence, *Phys. Rev. A* 82, 033817, 2010.

[5] R.-E. Meyers, K.-S. Deacon, Y. Shih, Turbulence-free ghost imaging, *Appl. Phys. Lett.* 98: 111115, 2011.

[6] S.-J. Wang, Y. Baykal, M.A. Plonus, Receiver-aperture averaging effects for the intensity fluctuation of a beam wave in the turbulent atmosphere, *J. Opt. Soc. Am* 73: 831-837, 1983.

Generation and application of partially coherent beam

Yangjian Cai[1,2*], Fei Wang[1], Chengliang Zhao[1], Lin Liu[1], and Xianlong Liu[2]

[1]School of Physical Science and Technology, Soochow University, Suzhou 215006, China
[2]Shandong Provincial Engineering and Technical Center of Light Manipulations & Shandong Provincial Key Laboratory of Optics and Photonic Device, School of Physics and Electronics, Shandong Normal University, Jinan 250014, China
*Corresponding author, E-mail: yangjiancai@suda.edu.cn

In the past decades, partially coherent beams with conventional correlation functions were explored extensively, and were applied in many applications, such as ghost imaging, remote detection, second-harmonic generation, and optical scattering. Recently, a great deal of attention is being paid to partially coherent beams with nonconventional correlation functions [1-3]. Manipulating the correlation functions of partially coherent beams will induce many extraordinary phenomena, such as self-focusing [4], self-shaping [5], self-splitting [6], self-steering [7] and super-strong self-reconstruction [8], which are useful for particle trapping [9], free-space optical communications [10, 11], and sub-Rayleigh imaging [12]. Through measuring the far-field correlation function of a partially coherent vortex beam, one also can determine its topological charge (i.e., orbital angular momentum) [13-14]. In this talk, we will introduce recent progress on generation and application of partially coherent beam.

References

[1] F. Gori and M. Santarsiero, "Devising genuine spatial correlation functions," Opt. Lett. **32**, 3531 (2007).
[2] Y. Cai, Y. Chen, and F. Wang, "Generation and propagation of partially coherent beams with nonconventional correlation functions: a review," J. Opt. Soc. Am. A **31**, 2083 (2014).
[3] Y. Cai, Y. Chen, J. Yu, X. Liu, and L. Liu, "Generation of partially coherent beams," Prog. Opt. **62**, 157 (2017).
[4] H. Lajunen and T. Saastamoinen, "Propagation characteristics of partially coherent beams with spatially varying correlations," Opt. Lett. **36**, 4104 (2011).
[5] S. Sahin and O. Korotkova, "Light sources generating far fields with tunable flat profiles," Opt. Lett. **37**, 2970 (2012).
[6] Y. Chen, J. Gu, F. Wang, and Y. Cai, "Self-splitting properties of a Hermite-Gaussian correlated Schell-model beam," Phys. Rev. A **91**, 013823 (2015).
[7] Y. Chen, S. A. Ponomarenko, and Y. Cai, "Self-steering partially coherent beams," Sci. Rep. **7**, 39957 (2017).
[8] F. Wang, Y. Chen, X. Liu, Y. Cai, and S. A. Ponomarenko, "Self-reconstruction of partially coherent light beams scattered by opaque obstacles," Opt. Express **24**, 23735 (2016).
[9] Y. Chen and Y. Cai, "Generation of a controllable optical cage by focusing a Laguerre-Gaussian correlated Schell-model beam," Opt. Lett. **39**, 2549 (2014).
[10] Y. Yuan, X. Liu, F. Wang, Y. Chen, Y. Cai, J. Qu, and H. T. Eyyuboğlu, "Scintillation index of a multi-Gaussian Schell-model beam in turbulent atmosphere," Opt. Commun. **305**, 57 (2013).
[11] S. Avramov-Zamurovic, C. Nelson, S. Guth, and O. Korotkova, "Flatness parameter influence on scintillation reduction for multi-Gaussian Schell-model beams propagating in turbulent air," Appl. Opt. **55**, 3442 (2016).
[12] C. Liang, G. Wu, F. Wang, W. Li, Y. Cai, and S. A. Ponomarenko, "Overcoming classical Rayleigh diffraction limit by controlling two-point correlations of partially coherent light sources," Opt. Express **25**, 28352 (2017).
[13] C. Zhao, F. Wang, Y. Dong, Y. Han, and Y. Cai, "Effect of spatial coherence on determining the topological charge of a vortex beam," Appl. Phys. Lett. **101**, 261104 (2012).
[14] X. Liu, T. Wu, L. Liu, C. Zhao, and Y. Cai, "Experimental determination of the azimuthal and radial mode orders of a partially coherent LG_{pl} beam (Invited Paper)," Chin. Opt. Lett. **15**, 030002 (2017).

Graphene based all-optical switch and tunable optical filter by using the thermo-optic effect

Ciyuan Qiu*, Tao Guo and Kan Wu

[1] State Key Lab of Advanced Optical Communication Systems and Networks, Department of Electronic Engineering, Shanghai Jiao Tong University, China
*corresponding author, E-mail: qiuciyuan@sjtu.edu.cn

Abstract

In this paper, we present our recent works on graphene based integrated devices by using the thermo-optic effect. We demonstrated an all-optical switch with a response time constant of 253.0 ns and a switching energy of ~50 nJ. Furthermore, we implemented a nanobeam based tunable optical filter with a tuning efficiency ~1.5 nm/mW by using a graphene micro-heater.

1. Introduction

Graphene is considered as a promising material for optoelectronic device integration due to its high carrier mobility, low optical loss and ultra-high thermal conductivity. Various optoelectronic devices based on graphene have been demonstrated, including electro-optic modulators [1-2] and photodetectors [3] which show merits, including low power consumption, high speed and broadband.

Since graphene has high thermal conductivity ~5,300 $Wm^{-1}K^{-1}$ and low optical loss, graphene can then be integrated onto the waveguides as a heater for fast thermo-optic tuning. In this paper, we show our recent works on this topic, including an all-optical switch [4] and a tunable optical filter [5] by using the thermo-optic effect.

2. All optical switch

We have proposed and demonstrated an all-optical switch [4] based on a silicon nitride (Si_3N_4) micro-ring (MRR) resonator and graphene, as shown in the Fig. 1(a). Pump light and probe light are combined and then injected into the chip. Part of the pump light will be absorbed by the graphene on the Si_3N_4 resonator if the light wavelength matches the resonant wavelength. The absorbed power by the graphene can be converted to heat and the temperature of the graphene increases. Then the graphene can heat the Si_3N_4 micro-ring resonator underneath and the resonant wavelength can be tuned. After passing through the chip, pump light and probe light can be separated by an optical filter for power detection.

The static thermo-optic tuning efficiency is measured to be 0.0079 nm/mW which is four times larger than that of the reported similar work for Si_3N_4 MRR without graphene. Then we modulate the pump light and test the probe light for dynamic switching process. The results are shown in Fig. 1(b). In the switching process, the response time constant is about 253.0 ns with a switching energy of ~50 nJ.

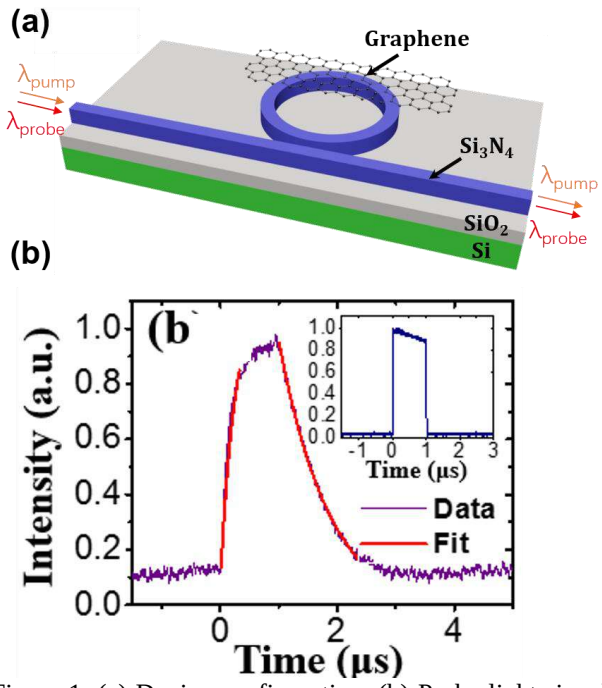

Figure 1: (a) Device configuration. (b) Probe light signal in all-optical dynamic switching, inset: normalized pump signal [4].

3. Tunable optical filter

We also demonstrated a tunable optical filter by using a nanobeam resonator and a graphene micro-heater [5]. The device configuration is shown in the Fig. 2 (a). By using the nanobeam resonator, the optical mode volume can be effectively shrunk to be 0.145 μm^3. To tune the resonance wavelength of the resonator, the graphene micro-heater only needs to heat the silicon within the mode volume, thus the heating energy can be reduced and the thermo-optic tuning efficiency can increase.

By applying electrical power on the graphene micro-heater, the resonance wavelength can be effectively tuned.

The tuning efficiency is measured to be 1.5 nm/mW which can be further increased to be 3.75 nm/mW with an optimized structure. The response time constants for the heating process is also measure with τ_{rise} = 1.11 μs and τ_{fall} = 1.47 μs for the rise and fall edges respectively.

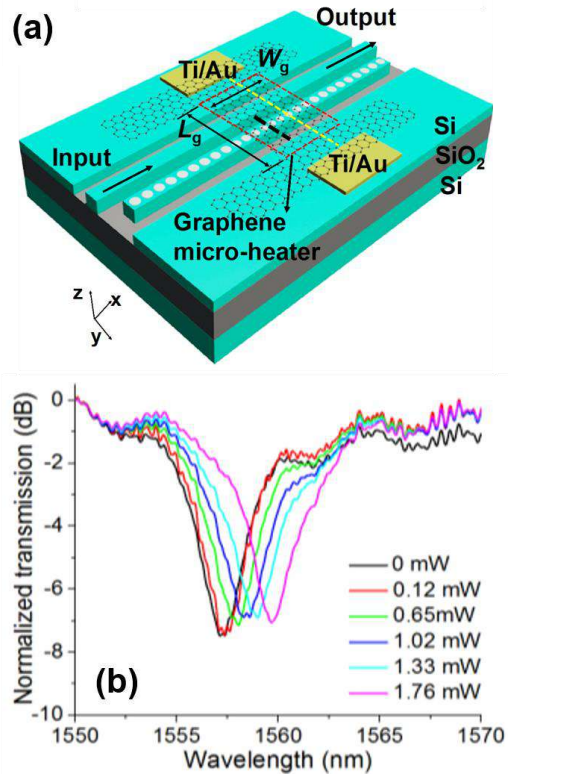

Figure 2: (a) Device configuration for the tunable filter. (b) Transmission spectra at different heating powers [5].

4. Conclusions

We demonstrated two graphene based integrated devices including an all-optical switch and a tunable optical filter. High tuning efficiency and fast thermo-optic tuning speed are achieved which would be useful for various application in optical communications and all-optical logic computing.

Acknowledgements

We acknowledge the support of device fabrication by the Center for Advanced Electronic Materials and Devices of Shanghai Jiao Tong University.

References

[1] M. Liu, X. B. Yin, E. Ulin-Avila, B. S. Geng, T. Zentgraf, L. Ju, F. Wang, and X. Zhang, A graphene-based broadband optical modulator, *Nature* 474:64-67, 2011.

[2] C. Qiu, W. Gao, R. Vajtai, P. M. Ajayan, J. Kono, and Q. Xu, Efficient Modulation of 1.55 μm Radiation with Gated Graphene on a Silicon Microring Resonator, *Nano Letters* 14:6811–6815, 2014.

[3] X. Gan, R. Shiue, Y. Gao, I. Meric, T. Heinz, K. Shepard, J. Hone, S. Assefa and D. Englund. Chip-integrated ultrafast graphene photodetector with high responsivity, *Nature Photonics*, 7:883–887, 2013.

[4] C. Qiu, Y. Yang, C. Li, Y. Wang, K. Wu and J. Chen. All-optical control of light on a graphene-on-silicon nitride chip using thermo-optic effect, *Scientific Reports*, 7:17046, 2017.

[5] Z. Xu, C.Qiu, Y. Yang, Q. Zhu, X. Jiang, Y. Zhang, W. Gao, and Y. Su, Ultra-compact tunable silicon nanobeam cavity with an energy-efficient graphene micro-heater, *Optics Express*, 25 :19479-19486, 2017

Manipulation of orbital angular momentum using structured photon sieves

Yuanjie Yang [1,2] *, Qi Zhao[1], Linli Liu[1], Yi-dong Liu[1], Carmelo Rosales-Guzman[3]

[1] School of Physics, University of Electronic Science and Technology of China, Chengdu 610051, China
[2] Department of Electrical and Computer Engineering, National University of Singapore, 117576, Singapore
[3] School of Physics, University of the Witwatersrand, Private Bag 3,Wits 2050, South Africa
*corresponding author, E-mail: dr.yang2003@uestc.edu.cn

Abstract

1. The generation of light beams carrying Orbital angular momentum (OAM) has attracted the interest of a wide community and in recent time it has been extended to the generation of matter beams, such as, electrons, neutrons or atoms. While most applications are centered on the use of beams carrying a unique OAM value, many of them will benefit from having a wider OAM spectrum. The reason being, each OAM component can provide different information. Here, we propose and demonstrate a simple way to produce, in a controlled way, OAM-carrying beams using pinhole structures, also known as photonics sieves. This study provides a new avenue for the flexible generation of beams carrying a well-defined OAM spectrum. This technique is not limited to light waves but can also apply to matter waves.

2. Introduction

Vortices are inherent to any wave phenomena and much interest has been focused on vortex fields in the past few years [1,2]. Vortices denote singular (zero intensity) points in a given field that have indeterminate phase, and a multiple of 2π phase circulation around the vortex in the plane transversal to the direction of wave propagation [1]. In a light wave, the phase singularity is known to form an optical vortex, which has an exp(ilθ) azimuthal phase structure and carry an orbital angular momentum (OAM) of lħ per photon, where l denotes the azimuthal mode of the field, and also called as topological charge. Recently, optical vortices have found numerous applications in optical micromanipulation [3], free-space communication [4], and quantum information [5], etc. Besides optical vortex beams, recent studies show that the some other beams, such as electron vortex beams [6], neutron vortex beams [7] and atom vortex beams [8], plasmonic vortices [9] can carry OAM as well and may lead to wide-ranging applications in new types of communication and memory devices as well as imaging [10,11].

So far, a variety of devices have been reported to produce vortex beam. Besides the classic methods, such as spiral phase plate , spiral zone plate , recently, pinhole masks, such as photon sieves and Vogel spiral arrays are adopted to produce vortex beams as well. While, most of these aforementioned methods, especially those based on the binary amplitude masks, showed how to produce vortex beams carrying OAM modes, but not presented the "whys" clearly. More recently, a general OAM mode selection principle of the rotationally symmetric superposition of chiral states was put forward, which explained the relationship between the OAM modes selected and the order of the rotationally symmetric binary amplitude chiral sieve masks. On the other hand, the ability to manipulate OAM states and OAM spectrum of structured light beams are crucial in many applications.

In this study, we propose and experimentally validate a simple method that achieves this goal using a structured photonics sieves.

3. Concept and theory.

3.1. Theory

We know that any arbitrary light beam can be expressed as the superposition of OAM states, and the OAM is associated with a helical or twisted wavefront. Now, we show that any asymmetrical aperture can convert a plane wave into a specific OAM spectrum. A simulated asymmetrical plate with one spiral of pinholes, is shown in Figs.1 (a). Then, if the plate is illuminated with a plane wave, the complex amplitude of the diffracted beam in the observation plane can be obtained by Fresnel diffraction integral.

Figures 1 (b) and (c) shows the intensity and phase patterns in the observation plane when the plate is illuminated with a plane wave, where the parameters are z=1m and λ=532.8nm. Due to the asymmetry of the plate, the intensity pattern of the generated beam is not symmetric either. Interestingly, although the phase pattern is asymmetric as well, we can still recognize the spiral phase distribution in the Fig.1(c). As a comparison, Figs. 1 (d)-(f) show the of the simulated results using a rotationally symmetrical plate with five spirals, and each of which is same as that in Fig.1(a). From Figs.1(a)-(f) we can see that both the intensity and the phase patterns are improved significantly when we replace the one-spiral pinholes plate with a five-spiral pinholes mask. We can see a clear bright ring the centre of the beam (Fig.1(e)), and Fig.1(f) shows the

phase increases by 5 × 2π around the center in clockwise direction clearly.

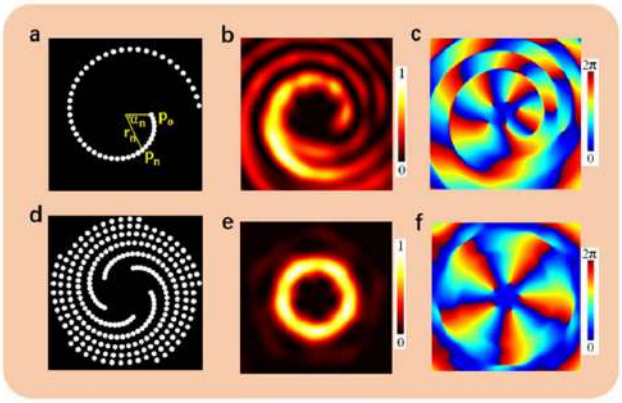

Figure 1 Schematics for the generation of vortex beams using a one-spiral pinholes plate and a structured plate with five spirals. (a) Simulated mask of one-spiral pinhole mask. (b) and (c) are the corresponding simulations of intensity and phase pattern of the diffracted beam at z=1m. (d)-(f) Same with (a)-(c) but for the plate with five spirals of pinholes.

3.2. Structured pinhole plate

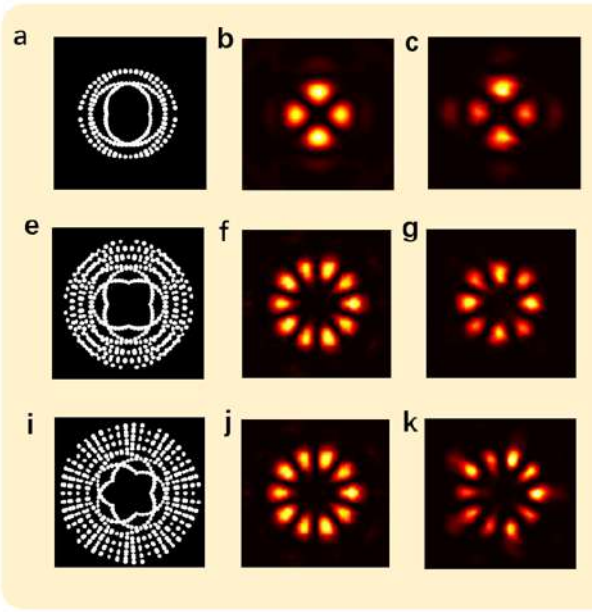

Figure 2: Structured photon sieves for generating of multiple OAM modes. (a) Simulated mask for producing the superposition of opposite 2 OAM; (b) Simulated intensity pattern; (d) Corresponding experimental results; (d) Power weight OAM spectrum; (e-h) Same with (a-d)

We can further explore the structured photon sieves for generating of multiple OAM modes. Without loss of generality, we consider the generated beam comprising two pairs of opposite OAM, as shown in Fig. 2. It is known that the superposition of two vortex beams with $\pm\ell$ can form a pattern like a 2ℓ-petal flower-like intensity distribution, and we can see this phenomenon clearly in Fig.2. For example, in Figs.2 (b) and 2(c), there are four petals in the intensity pattern. Therefore, Figure 2 shows that we need not use the superposition of two vortex beams, and just a simple pinhole-plate can convert a plane wave into multiple OAM modes. The corresponding OAM mode spectra show that the generated OAM modes are very pure using this method, and almost have no side lobes in the OAM spectra.

4. Conclusions

In conclusion, we have presented a structured photon sieves which can produce both a single OAM and a mixture of multiple OAM. Although this plate is verified in generating optical vortex beams, the general design approach and results obtained with the structured sieves are not confined to the opitcal waves alone, but are valid for generating of any scalar vortex beams such as electron vortex, neutron vortex and acoustic vortex.

Acknowledgements

This work was partially supported by the National Natural Science Foundation of China (11874102)

References

[1] J.F.Nye and M.V.Berry, Proceedings of the Society of London. Series A**336**, 165 (1974).

[2] L. Allen, M. W. Beijersbergen, R. J. C. Spreeuw, and J. P. Woerdman, Phys. Rev. A **45**, 8185 (1992).

[3] K. Dholakia and T. Cizmar, Nat. Photon. **5**, 335 (2011).

[4] J. Wang, J. Yang, I. Fazal, N. Ahmed, Y. Yan, H. Huang, Y. Ren, Y. Yue, S. Dolinar, M. Tur and A. Willner, Nat. Photon. **6**, 488 (2012).

[5] G. Molina-Terriza, J. P. Torres, and L. Torner, Nat. Phys. **3**, 305 (2007).

[6] J. Verbeeck, H. Tian, P. Schattschneider, Nature **467**, 301(2010).

[7] Clark, C. W. et al. Controlling neutron orbital angular momentum. Nature 525, 504–506 (2015).

[8] Lembessis, V. E., Ellinas, D., Babiker, M. & Al-Dossary, O. Atom vortex beams. Phys. Rev. A 89, 053616 (2014).

[9] Kim, H. *et al.* Synthesis and dynamic switching of surface plasmon vortices with plasmonic vortex lens. *Nano Lett.* **10,** 529–536 (2010).

[10] R. A. Herring, Science, **331**, 155 (2011).

[11] J. Harris, V. Grillo, E. Mafakheri, G. C. Gazzadi, S. Frabboni, R.W. Boyd and E. Karimi, Nature Phys, **11**, 629(2015).

Propagation characteristics of vortex beams in double-pass optical links with atmospheric turbulence

Fei Wang[1], Jiayi Yu[1], Lin Liu[1], Yahong Chen[1] Chengliang Zhao[1]and Yangjian Cai[1,2]

[1]School of Physical Science and Technology, Soochow University, Suzhou 215006, People's Republic of China
[2]Center of Light Manipulations and Applications & Shandong Provincial Key Laboratory of Optics and Photonic Device, School of Physics and Electronics, Shandong Normal University, Jinan 250014, China
*corresponding author, E-mail: fwang@suda.edu.cn

Abstract

We experimentally investigate the enhanced back scatter (EBS) of Laguerre-Gaussian (LG) vortex beams on double passage through turbulent air, reflecting from a retroreflector. It is found that only vortex beams with an even topological charge exhibit EBS, whereas beams with an odd topological charge maintain a dark-hollow shape. The physical mechanisms behind the aforementioned effects are explained using a ray model, and the results are further confirmed computationally using a multiple phase screen method. This work potentially allows the control of EBS through engineering of the phase in the transmitter plane.

1. Introduction

In recent years, considerable attention has been paid to vortex beams [1-2] due to their potential applications in FSOC communications and optical images. Such beams possess an intensity minimum on axis and a helical phase structure in the form of exp(i*l*φ), where *l* is the topological charge and φ is the azimuthal angle. As one knows, light beams will experience beam wander, scintillation and angle-of-arrival fluctuation when they propagate in atmospheric turbulence. However, some studies showed that vortex beams can greatly reduce these negative effects. In addition, as vortex beams with different charges are mutually orthogonal, they are being applied to increase the data rate in FSOC by multiplexing information on different vortex modes simultaneously. Mode mixing and the degradation of mode quality resulting in cross-talk between orbital angular momentum (OAM) modes were investigated when the phases of vortex beams suffered random fluctuation induced by turbulence. The possible use of vortex beams for communications in photon counting level was studied in [3]. Recently, Yuan et al. were proposed an optimized scheme to improve the detection probability of OAM of vortex both in Kolmogorov and non-Kolmogorov turbulence [4]. In this paper, we explore both the average and instantaneous behavior of vortex beams on double-passage through monostatic turbulence via a retroreflector. We find that EBS only appears for beams with even topological charge, while beams with odd charge maintain their intensity minimum. It is further found that Laguerre-Gauss (LG) vortex modes will convert to Hermite-Gauss (HG) modes under certain circumstances. Physical explanations of these effects are presented.

2. Experimental setup and results

The experimental arrangement is illustrated in Fig. 1. A linearly polarized Gaussian beam generated from a He-Ne laser (λ=632.8nm) is first passed through a beam expander (BE1) and then reaches a spatial light modulator (SLM) acting as a computer-controlled (PC1) phase screen. A standard fork grating is programmed onto the SLM to generate the desired vortex beam of azimuthal order l; a circular aperture (CA) is used to isolate only the desired vortex diffraction order from the SLM. The resulting vortex beam is then expanded and collimated by BE_2. After the expander BE2, the beam is well-represented as an LG mode with radial index 0 and azimuthal index *l*

$$E(r,\varphi,z=0)=A_l r^l \exp\left(-\frac{r^2}{\omega_0^2}\right)\exp(il\varphi), \qquad (1)$$

where $r=(x^2+y^2)^{1/2}$ and φ are the radial and azimuthal coordinates, respectively. A_l is a positive constant; l is the topological charge. When *l* =0, this expression reduces to a fundamental Gaussian mode. The measured beam width ω_0 after BE_2 is almost the same for *l* =1, 2, 3, with ω_0=2.5mm.

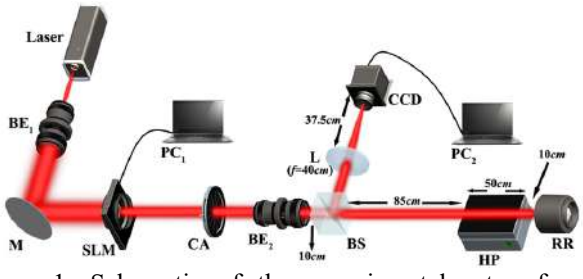

Figure 1: Schematic of the experimental setup for the generation of vortex beams and measurement of the intensity distributions through a monostatic double-passage channel.

A beam splitter (BS) sends half of the resulting intensity through atmospheric turbulence generated by a hot plate

(HP), after which it reflects off a retroreflector (RR), and then returns back via the same path. The backward beam is reflected by the BS and is focused by a lens (L) with focal length 40cm. A CCD with 1952×786 square pixels of side length 3.75μm is placed at the receiver plane to measure the average/instantaneous intensity distributions. The measured intensity was averaged over 2000 frames with frame per second (FPS) of the CCD being 25.

Figure 2 illustrates the experimental average intensity profiles of a Gaussian beam (*l*=0) and vortex beams with *l*=1, 2, 3 reflected by the flat mirror (first column) and the retroreflector (second column), respectively. One can see that the beam profiles of vortex beams degenerate to Gaussian-like shapes for the case of the flat mirror, irrespective of topological charge. When the retroreflector is used, the situation is different. The average intensity for *l*=0, 2 exhibits a sharp and bright peak in the beam center, indicative of an EBS enhancement. The central peak values for *l*=0 and 2 are about 2.46 and 1.60 compared to these for flat mirror target. For *l*=1 and *l*=3, however, the beam profiles still display dark-hollow shapes, with no EBS. Other experimental results for higher values of *l* indicate that EBS only occurs when the topological charge is an even number.

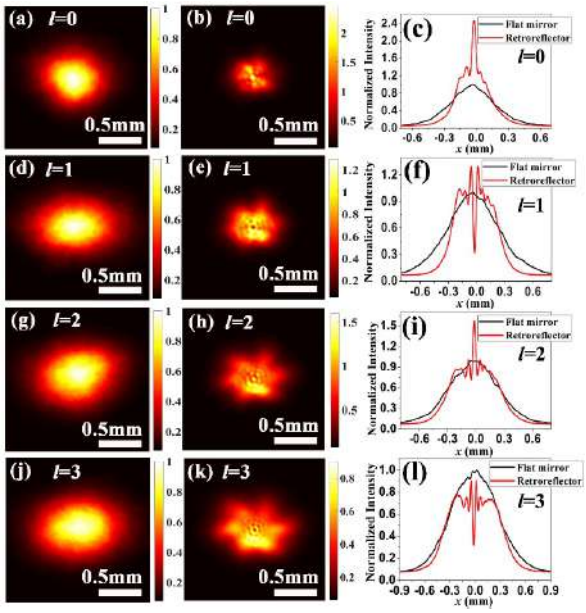

Figure 2: Density plot of the beam profiles of the Gaussian beam (*l*=0) and vortex beams for different values of topological charges reflected by a flat mirror (first column) and retroreflector (second column). The corresponding cross-line of the intensity distribution at y=0 is plotted in the third column.

3. Simulation results

Figure 3 illustrates average intensity distributions of the Gaussian beam (*l*=0) and vortex beams with l=1, 2 and 3 reflected by a flat mirror and a retroreflector. It can be seen that only when *l*=0, 2 (even number), a bright spot in the beam center appears, indicating the EBS effect. The simulation results agree well with the experimental results shown in Fig. 2.

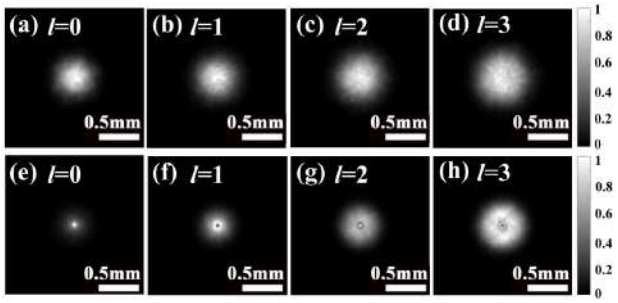

Figure 3: Simulations results of the average beam profiles of the Gaussian beam and vortex beams in the receiver plane. The structure constant is . The size of pictures is 1.5mm×1.5mm

4. Conclusions

In conclusion, we have experimentally measured the average/instantaneous intensity distributions of vortex beams on double-passage in monostatic turbulence using a retroreflector. The experimental results show that EBS occurs only when the topological charge is even, and this can be explained using a model of reciprocal ray pairs. Our finds may be useful in FSOC systems using vortex beams and point towards methods for controlling EBS by engineering the phase of the beam

Acknowledgements

This work is supported by the National Natural Science Fund for Distinguished Young Scholar (11525418); National Natural Science Foundation of China (NSFC) (91750201&11474213&11874046); Project of the Priority Academic Program Development of Jiangsu Higher Education Institutions; China Scholarship Council (CSC) (201706920103); Qing Lan Project of Jiangsu Province.

References

[1] Wang J, Yang J, Fazal I, Ahmed N, Yan Y, Huang H, Ren Y, Yue Y, Dolinar S, Tur M, Willner A. Terabit free-space data transmission employing orbital angular momentum multiplexing. Nature Photon. 6: 488, 2012.

[2] Lavery M, Peuntinger C, Gunthner K, Banzer P, Elser D, Boyd R, Padgett M, Marquardt C, Leuchs G. Free-space propagation of high-dimensional structured optical fields in an urban environment. Sci Adv. 3: e1700552, 2017.

[3] Paterson C. Atmospheric turbulence and orbital angular momentum of single photons for optical communication. Phys. Rev. Lett. 94: 153901, 2005.

[4] Yuan Y, Liu D, Zhou Z, Xu H, Qu J, Cai Y. Optimization of the probability of orbital angular momentum for Laguerre-Gaussian beam in Kolmogorov and non-Kolmogorov turbulence. Opt Express, 26: 21861-71, 2018.

Complex periodic beams generated by superposition of two sub periodic wave fields

Yuanmei Gao[1,*], Zhanghua Han[1], Yangjian Cai[1]

[1]Shandong Provincial Engineering and Technical Center of Light Manipulations and Shandong Provincial Key Laboratory of Optics and Photonic Device, School of Physics and Electronics, Shandong Normal University, Jinan 250014, China

*corresponding author, E-mail:gaoyuanmei@*sdnu.edu.cn*

Abstract

Complex periodic discrete non-diffracting beams (PDNBs) is produced by superposition of two sub simple PDNBs at a particular angle $\Delta\alpha$. As for special cases, we studied the superposition of the two identical squares (“4+4”) periodic wave fields at specific angles,and obtained a series of interesting complex PDNBs. New PDNBs were also obtained by modulating the initial phase difference between adjacent interfering beams.

1. Introduction

Due to a deeply rooted theory—diffraction is a natural phenomenon of light propagation—great attention of researchers has been attracted to the so called non-diffracting beams, which were firstly identified by Durnin et al. in 1987 [1]. Over the past three decades, different types of non-diffracting beams, for instance, Bessel beams, Mathieu beams, Weber beams and discrete non-diffracting beams, have a multitude of application fields, such as medical imaging, light microlithography as well as optical communications [2–6]. However, it is most noteworthy that discrete non-diffracting wave fields, among the four families of non-diffracting beams, are applied in weak light induced two-dimensional (2D) optical lattices most frequently [7,8]. Their band gap structure and beam transmission controlling ability make a significant research value [9].

Recently, non-diffracting patterns generated by two mutually rotated non-diffracting beams were introduced theoretically in reference [10], and the authors gives rigorous expressions for particular rotation angles, where periodicity of the pattern takes place. Although non-diffracting have infinite energy, only approximated DNBs can be obtained in experiment.

In the present work, we got a series of periodic discrete nondiffracting beams (PDNBs) through superposing two identical “child” periodic wave fields at specific angles decided by an expression, which is derived from the periodicity condition of the lattice field function after superposition. As for special cases, we studied the superposition of the two identical square or two hexagonal periodic wave fields at specific angles, respectively. Moreover, more PDNBs were generated by modulating the initial phase of each interfering beams.

2. Theoretical calculation and model

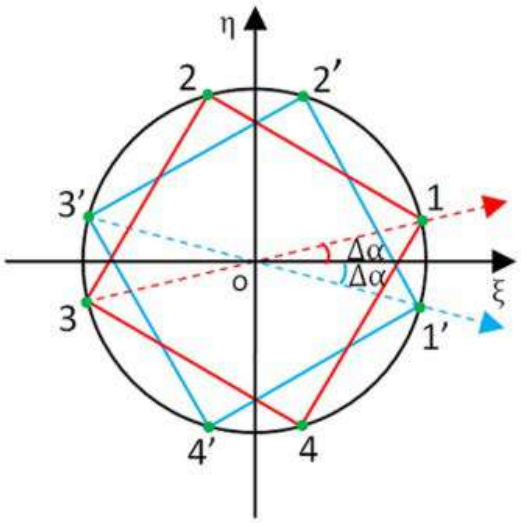

Fig. 1. Corresponding frequency change which was chosen by rotating two interfering wave field of square lattice.

The structure of lattice is a superposition of two equal sublattices (sublattice A and sublattice B).

$$\psi_{\mathrm{N+N}} = \sum_{j=0}^{n\text{-}1} \mathrm{E}_j e^{i(K_A \bullet r + \varphi_A)} + \sum_{j'=0}^{n'\text{-}1} \mathrm{E}_{j'} e^{i(K_B \bullet r + \varphi_B)} \quad \textbf{(1)}$$

where Ej and Ej′ are the amplitudes, φ_A and φ_A are initial phases of the sublattice A and sublattice B, respectively. and N represent the number of the interfering plane beams of sublattice fields. r is position vector of plane beams with $r = \sqrt{x^2 + y^2 + z^2}$ in Cartesian coordinates. In addition, k_A and k_B are wave vectors

$$K_A = [\cos(\frac{2\mathrm{j}\pi}{n} + \Delta\alpha)\sin\theta, \sin(\frac{2j\pi}{n} + \Delta\alpha)\sin\theta, \cos\theta]$$
$$K_B = [\cos(\frac{2j\pi}{n'} - \Delta\alpha)\sin\theta, \sin(\frac{2j\pi}{n'} - \Delta\alpha)\sin\theta, \cos\theta] \quad (2)$$

Where j is positive integer, and Δα is the angle between the sublattice A and sublattice B, and θ is the angle between direction of beam propagation and z-axis.

The wave fields produced by interference of "4+4" beams shown in Fig. 1 have a fourfold symmetric feature. Assuming $\varphi_{\mathrm{A}} = \varphi_{\mathrm{B}} = 0$ and $\mathrm{E}_{\mathrm{j}} = \mathrm{E}_{\mathrm{j}'}$, for all j, in x- y plane Eq. (1) can be rewritten as

$$\varphi(x, y) = 4|E|\cos(k\sin\theta\cos\Delta\alpha \cdot x)\cos(k\sin\theta\sin\Delta\alpha \cdot y) + 4|E|\cos(k\sin\theta\sin\Delta\alpha \cdot x)\cos(k\sin\theta\cos\Delta\alpha \cdot y) \quad (3)$$

When tan(Δα)=C, and C is an arbitrary real positive integer with range of 2 to positive infinite, the periodicity of the wave field is indicated.

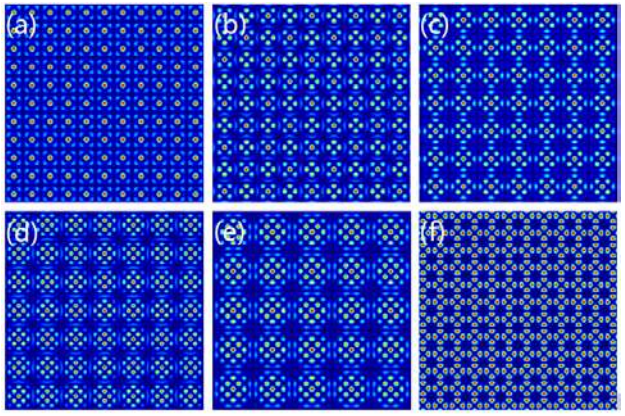

Fig. 2. Numerical simulation intensity realization of "4+4" PDNBs.

Fig. 2 shows experimental results of several PDNBs for the case of "4+4". With initial settings, $\varphi_j = \varphi_{j'} = 0$, $\mathrm{E_j} = \mathrm{E_{j'}} = 0$, PDNBs with intensity distributions are shown in Fig. 3(a)-(d). In addition, the foregoing discussion indicates that the periodic nature will not be changed if we modulate the initial phase of each plane beam [6]. For example, if $\varphi_j = \pi$, $\varphi_{j'} = 0$, different integer numbers C would lead to some new shapes of PDNBs as shown in Fig. 3(e) and (f). And size of the cell of PDNBs is about 250 μ m.

3. Conclusions

In conclusion, we got complex 2D PDNBs by superposition of two identical simple 2D PDNBs at a special angle. Subsequently, we acquired other new PDNBs with reprogrammable phase patterns for modulating the initial phase of each frequency component we have chosen. As for applications, these leave out entire wave fields can be utilized in research of light induced optical lattices because long non-diffracting distance satisfies the requirement of forming stable band gaps. In addition, as a prominent example[11], all these 2D PDNBs will become 3D periodic lattice fields which can be recorded by a photosensitive medium if we add one on-axis beam by reconfiguring phase patterns in SLM. Tasks above are reported with the expectation of facilitating exploring beam propagation behavior in 2D periodic optical lattices even in optical super lattices, which are increasingly required in controlling optical fields.

References

[1] J. Durnin, Exact solutions for nondiffracting beams. I. The scalar theory, J. Opt.Soc. Am. A. 4. 651-654, 1987.

[2] P. Rose, M. Boguslawski, C. Denz, Nonlinear lattice structures based on families of complex nondiffracting bea,. 46. 15-28, 2005.

[4] J.C. Gutiérrez, M.D. IturbeCastillo, G.A. Ramírez, E. Tepichín, R.M. RodríguezDagnino, S. ChávezCerda, G.H.C. New, Experimental demonstration of optical Mathieu beams, Opt. Commun. 195. 35-40, 2001.

[5] B.M. RodríguezLara, Normalization of optical Weber waves and Weber-Gauss beams, J. Opt. Soc. Am. A. 27 327-332, 2010.

[6] M. Boguslawski, P. Rose, C. Denz, Increasing the structural variety of discrete nondiffracting wave fields, Phys. Rev. A. 84. 013832(1-8), 2011.

[7] Yaroslav V. Kartashov, Victor A. Vysloukh, Lluis Torner, Soliton shape and mobility control in optical lattices, Prog. Opt. 52. 63‑148, 2009.

[8] Y.V. Kartashov, V.A. Vysloukh, L. Torner, Solitons in complex optical lattices, Phys. J. Spec. Top. 173.87‑105, 2009 .

[9] B. Terhalle, A.S. Desyatnikov, C. Bersch, D. Träger, L. Tang, J. Imbrock, Y.S. Kivshar, C. Denz, Anisotropic photonic lattices and discrete solitons in photorefractive media, Appl. Phys. B. 86. 399‑405, 2007.

[10] Changming Huang, Fangwei Ye, Xianfeng Chen, Yaroslav V. Kartashov, Vladimir V. Konotop, Lluis Torner, Localization-delocalization wavepacket transition in Pythagorean aperiodic potentials, Sci. Rep. 6,32546 2016.

[11] J. Xavier, S. Vyas, P. Senthilkumaran, C. Denz, J. Joseph, Sculptured 3D twister superlattices embedded with tunable vortex spirals, Opt. Lett. 36, 3512 ‑ 3514,2011.

Focusing Properties of an Apertured Bessel-Gaussian Correlated Schell-Model Beam

Yaru Gao[1,*], Xianlong Liu[1], Lina Guo[2], Yangjian Cai[1]

[1]Shandong Provincial Engineering and Technical Center of Light Manipulations and Shandong Provincial Key Laboratory of Optics and Photonic Device, School of Physics and Electronics, Shandong Normal University, Jinan, China
[2]School of Optoelectronic Engineering, Guangdong Polytechnic Normal University, Guangzhou, China
*corresponding author, E-mail: gaoyaru@sdnu.edu.cn

Abstract

The focusing properties of an apertured Bessel-Gaussian correlated Schell-model (BGCSM) beam are investigated theoretically in detail. An optical cage is formed by focusing BGCSM beam and it is moderately adjusted by the aperture radius, the spatial coherence width, and the parameter β of the BGCSM beam. Furthermore, the effect of these parameters on the effective beam size and the spectral degree of coherence are also analyzed. The optical cage can be useful for particle trapping and material thermal processing.

1. Introduction

The optical cage has attracted growing attention and has found wide applications in many fields. There are various techniques for generating the optical cage. However, all the optical cages produced by the techniques mentioned in the literature are completely coherent. A partially coherent optical cage may exhibit some advantages over those of a coherent optical cage, for example, a partially coherent optical cage is less sensitive to speckle [1]. Several approaches have been developed to generate partially coherent 3D optical cages, such as the axicon-lens system and the binary diffractive optical element. Furthermore, controlling the spatial coherence of a focused partially coherent source has also shown the possibility of forming an optical cage in the focal region.

Recently, partially coherent beams with nonconventional correlation functions (NCFs) have been widely investigated. The generation of several partially coherent sources with NCFs has been introduced[2,3]. These novel sources exhibit many interesting propagation properties, and are expected to be useful in many applications, such as optical trapping, free-space optical communications and so on. The Laguerre-Gaussian correlated Schell-model (LGCSM) beam and the Bessel-Gaussian correlated Schell-model (BGCSM) beam are two typical partially coherent beams with NCFs. These two types of beams have been introduced in theory [4], and later generated in experiment with the aid of a spatial light modulator or with a hologram and a diffuser. Their correlation functions are expressed in the form of Laguerre-Gaussian and Bessel-Gaussian functions, respectively. Both LGCSM and BGCSM beams display ring-shaped beam profiles in the far field in free space. Furthermore, Chen et al. demonstrated both theoretically and experimentally that by focusing an LGCSM beam with a thin lens and tailoring the source correlation function, a controllable partially coherent optical cage can be generated near the focal area [5]. Thus, how about generating an adjustable optical cage by focusing a BGCSM beam?

Here, we demonstrate that a partially coherent optical cage can be generated by focusing an apertured BGCSM beam and the circular aperture is located in front of the BGCSM beam. Based on the generalized Huygens-Fresnel integral and complex Gaussian function expansion, the analytical formula of the BGCSM beam passing through an apertured ABCD optical system is derived. Our numerical results show that the size and depth of the generated optical cage is adjustable by modulating the source spatial correlation function, the coherence width and the aperture radius. The effective beam width and spectral degree of coherence (SDOC) of the focused BGCSM beam in the focal region are also discussed. Our results may find uses in optical trapping and material thermal processing.

2. Propagation of an apertured BGCSM beam

The second-order correlation properties of a scalar partially coherent beam are generally characterized by the cross-spectral density (CSD) in the spatial-frequency domain. The CSD of the apertured BGCSM beam at two arbitrary points in the source plane is expressed as

$$W(r_1, r_2) = \exp(-\frac{r_1^2 + r_2^2}{4\sigma_0^2}) \exp[-\frac{(r_1 - r_2)^2}{2\sigma_0^2}] J_0(\beta \frac{|r_1 - r_2|}{\delta_0}) H(r_1) H^*(r_2) \quad (1)$$

where $r_j = (r_{jx}, r_{jy})$ $(j = 1, 2)$ denotes an arbitrary transverse position vector, σ_0 is the transverse beam waist width of the corresponding Gaussian beam, δ_0 is the transverse coherence width, β is a real constant, $J_0(x)$ is the zeroth-order Bessel function of first kind, and $H(r_i)$ is the transmission function of the circular aperture. Here

$$H(\mathrm{r}_i)=\sum_{m=1}^{M}A_m\exp(-\frac{B_m r_i^2}{a^2}) \tag{2}$$

where a is aperture radius, A_m and B_m are the expansion and Gaussian coefficients, respectively, which can be obtained through numerical optimization. With the help of extended Collins formula, the spectral density of the apertured BGCSM beam in the receiver plane as follows

$$I(\boldsymbol{\rho})=W(\boldsymbol{\rho},0)=$$
$$(\frac{k}{2B})^2\sum_{m=1}^{N}\sum_{n=1}^{N}\frac{A_mA_n^*}{\gamma\varsigma}\exp(-\frac{k^2}{\gamma B^2}|\boldsymbol{\rho}|^2-\frac{\beta^2}{4\delta_0^2\gamma})I_0(\frac{k\beta|\boldsymbol{\rho}|}{\delta_0 B\gamma}) \tag{3}$$

with

$$\varsigma=\frac{1}{2\sigma_0^2}+\frac{B_m}{a^2}+\frac{B_n^*}{a^2}$$
$$\gamma=\frac{\varsigma}{4}+\frac{1}{2\delta_0^2}-\frac{1}{4\varsigma}(\frac{ikA}{B}+\frac{B_m}{a^2}-\frac{B_n^*}{a^2})^2 \tag{4}$$

where $\rho_j=(\rho_{jx},\rho_{jy})\quad(j=1,2)$ denotes an arbitrary transverse position vector at the receiver plane, $k=2\pi/\lambda$ is the wave number related to the wavelength λ. The effective beam width and SDOC are obtained as

$$\omega=\frac{\sqrt{2\sum_{m=1}^{N}\sum_{n=1}^{N}\sum_{s=0}^{\infty}\frac{A_mA_n^*b^{2s}(\mathrm{s}+1)}{\gamma\varsigma s!2^{2s}\alpha^{2+s}}\exp(\frac{\beta^2}{4\delta_0^2\gamma})}}{\sqrt{\sum_{m=1}^{N}\sum_{n=1}^{N}\sum_{s=0}^{\infty}\frac{A_mA_n^*b^{2s}}{\gamma\varsigma s!2^{2s}\alpha^{1+s}}\exp(\frac{\beta^2}{4\delta_0^2\gamma})}} \tag{5}$$

with $\alpha=k^2/4\gamma B^2, b=k\beta/2\delta_0 B\gamma$.

$$\mu(\rho_1,\rho_2)=W(\frac{\rho_1+\rho_2}{2},\rho_1-\rho_2)/\sqrt{W(\rho_1,0)W(\rho_2,0)} \tag{6}$$

3. Numerical calculation results

We have studied numerically focusing characteristic of the intensity, the effective beam width, and the SDOC of an apertured BGCSM beam focused by a thin lens focusing system by applying the formula derived in Section 2. We calculated the normalized intensity distribution of an apertured BGCSM beam in the $\rho-z$ plane for different values of a, δ_0 and β (pictures are not shown here). With the decrease of a, the shape of the optical cage became much more uniform and the size of the cage became larger. With the small value of δ_0,a more uniform optical cage is formed. With the increase of δ_0, both transverse and longitudinal sizes, as well as the depth of the optical cage, decreased. The focal intensity profile gradually evolved from a peak-centered shape into an optical cage with the increase of β. However, the shape of the optical cage became less uniform with the increase of β. The effective beam width and the SDOC of an apertured BGCSM beam are shown in Fig.1 and Fig.2 with different parameters. With the increase of a and δ_0, the effective beam width first quickly decreased and then tended toward a minimum value. From Fig.2, the correlation singularities are formed when a decrease and the number of correlation singularities are not affected by δ_0 and β, while their locations are affected by δ_0 and β.

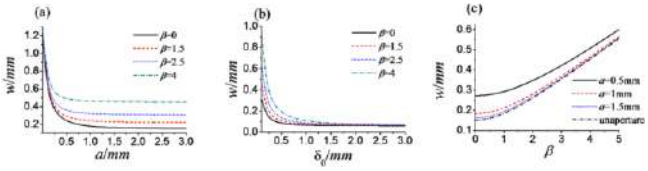

Figure 1: Effective beam waist width of an apertured BGCSM beams in the focal plane versus a, δ_0 and β.

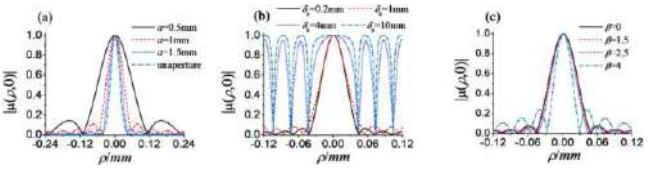

Figure 2: Dependence of modulus of the SDOC of apertured BGCSM beams in the focal plane.

4. Conclusions

The statistical properties of an apertured BGCSM beam focused by a thin lens have been explored. The adjustable size of a formed optical cage is the most attractive property. We found that the optical cage could be controlled by manipulating the initial spatial coherence width δ_0 ,the parameter β and the aperture radius a. The size and depth of the optical cage increased with the decrease of δ_0 or increase of β. The shape of the optical cage became much more uniform with small values of a and δ_0, or a moderate value of β. In addition, the effective beam width and the SDOC are also affected by these parameters. Our results will be rewarding in various applications, such as in particle trapping, dark field microscopy, and super-resolution fluorescence microscopy.

References

[1] C. Zhao, Y. Cai, F. Wang, X, Lu, Y. Wang, Generation of a high-quality partially coherent dark hollow beam with a multimode fiber, *Opt. Lett.* 33: 1389-1391, **2008**.

[2] J. Yu, Y. Cai, G. Gbur, Rectangular Hermite non-uniformly correlated beams and its propagation properties, *Opt. Express* 26: 27894-27906, **2018**.

[3] X. Peng, L. Liu, F. Wang, S. Popov, Y. Cai, Twisted Laguerre-Gaussian Schell-model beam and its orbital angular moment, *Opt. Express* 26: 33956-33969, **2018**.

[4] Z. Mei, O. Korotkova, Random sources generating ring-shaped beams, *Opt. Lett*. 38: 91-93, **2013**.

[5] Y. Chen, Y. Cai, Generation of a controllable optical cage by focusing a Laguerre-Gaussian correlated Schell-model beam, *Opt. Lett.* 39: 2549-2552, **2014**.

The statistical properties of a Hermite-Gaussian correlated Schell-model beam in a gradient-index fiber

Zhiheng Xu[1], Yangsheng Yuan[1], Yangjian Cai[1,*]

[1]Shandong Provincial Engineering and Technical Center of Light Manipulations and Shandong Provincial Key Laboratory of Optics and Photonic Device, School of Physics and Electronics, Shandong Normal University, Jinan 250014, China
*corresponding author, E-mail: yangjiancai@suda.edu.cn

Abstract

With the help of the extended Huygens-Fresnel principle, we derived analytical expressions for the cross-spectral density(CSD) and the second-order moments of a Hermite-Gaussian correlated Schell-model (HGCSM) beam propagating in a gradient-index (GRIN) fiber. It can be found that the distribution of the spectral intensity and the degree of coherence exhibit periodicity and the propagation factor of a HGCSM beam does not depend on the parameters of the GRIN fiber and propagation distance. As a result, we can modulate the state of the spectral intensity of the output beam in GRIN fiber by varying the length of fiber and the initial beam parameters of a HGCSM beam.

1. Introduction

Ever since Gori and his collaborators first discussed the sufficient condition for devising the genuine correlation function of partially coherent beams [1, 2], more and more attention is being paid to partially coherent beams with nonconventional correlation functions (i.e. non-Gaussian correlation functions). Among various nonconventional partially coherent beams, Hermite-Gaussian correlated Schell-model beams have been investigated in detail [3, 4]. It has been proved both in theory and experiment that the beam exhibits self-splitting properties on propagation in free space, which will be useful for attacking multiple targets, trapping multiple particles, and guiding atoms. By naturally extension, it inspires us to explore the propagation properties of Hermite-Gaussian correlated Schell-model beams in other medium.

On the other hand, optical fiber has been widely applied in optical sensing, optical imaging, optical communications, beam shaping, and biomedical engineering. It is of great significance to explore the beam's propagation properties in optical fiber. The gradient-index (GRIN) fiber whose index of refraction varies radially has an advantage of lower pulse dispersion over its step-index counterparts [5]. The ray varies sinusoidally along the fiber and never touches the edge. In this paper, we will concentrate on the beam's propagation in GRIN beam.

2. Cross-spectral and the propagation factor of a HGCSM beam propagating through a GRIN fiber

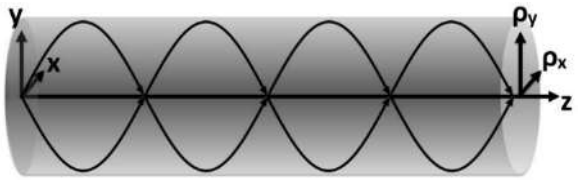

Figure 1: Schematic diagram of a GRIN fiber.

Figure 1 shows the schematic diagram of a GRIN fiber with its axis of symmetry along the z axis. The dependence of the square of the index of refraction has a parabolic profile given by [6].

$$n_r^2(x,y;\omega)=\begin{cases} n_0^2(\omega)\left[1-\alpha^2(\omega)\left(x^2+y^2\right)\right], & x^2+y^2\le R_0^2 \\ n_0^2(\omega)\left[1-\alpha^2(\omega)R_0^2\right], & x^2+y^2>R_0^2 \end{cases}, \quad , \tag{1}$$

$$\alpha(\omega)=\frac{1}{R_0}\left[1-\frac{n_1^2(\omega)}{n_0^2(\omega)}\right]^{1/2}, \tag{2}$$

The CSD of a HGCSM beam in the source plane (z=0) is expressed as follows

$$W^{(0)}(\mathbf{r}_1,\mathbf{r}_2)=G_0\exp\left(-\frac{\mathbf{r}_1^2+\mathbf{r}_2^2}{4\sigma_0^2}\right)\mu(\mathbf{r}_2-\mathbf{r}_1),, \tag{3}$$

$$\mu(\mathbf{r}_2-\mathbf{r}_1)=\frac{H_{2m}\left[(x_2-x_1)/\sqrt{2}\delta_{0x}\right]}{H_{2m}(0)}\frac{H_{2n}\left[(y_2-y_1)/\sqrt{2}\delta_{0y}\right]}{H_{2n}(0)} \times\exp\left[-\frac{(x_2-x_1)^2}{2\delta_{0x}^2}-\frac{(y_2-y_1)^2}{2\delta_{0y}^2}\right], \quad , \tag{4}$$

After tedious calculation, the spectral degree of coherence of a HGCSM beam in the output plane in a GRIN fiber is obtained as $\mu(\boldsymbol{\rho}_1,\boldsymbol{\rho}_2,z)$

$$\mu(\boldsymbol{\rho}_1,\boldsymbol{\rho}_2,z)=\frac{W(\boldsymbol{\rho}_1,\boldsymbol{\rho}_2,z)}{\sqrt{W(\boldsymbol{\rho}_1,\boldsymbol{\rho}_1,z)W(\boldsymbol{\rho}_2,\boldsymbol{\rho}_2,z)}},, \tag{5}$$

$$\begin{aligned}W(\boldsymbol{\rho}_1,\boldsymbol{\rho}_2)=&\frac{4G_0\sigma_0^2\pi^2\delta_{0x}\delta_{0y}}{H_{2m}(0)H_{2n}(0)\sqrt{ab}\lambda^2B^2}\left(1-\frac{1}{a}\right)^m\left(1-\frac{1}{b}\right)^n\\&\times H_{2m}\left[-\frac{c}{2a}\left(1-\frac{1}{a}\right)^{-1/2}\right]H_{2n}\left[-\frac{d}{2b}\left(1-\frac{1}{b}\right)^{-1/2}\right]\\&\times\exp\left[\frac{c^2}{4a}+\frac{d^2}{4b}-\frac{ikD}{B}\left(\rho_x\rho_{dx}+\rho_y\rho_{dy}\right)-\frac{k^2\sigma_0^2}{2B^2}\left(\rho_{dx}^2+\rho_{dy}^2\right)\right],\end{aligned} \tag{6}$$

$$a=2\delta_{0x}^2\left(\frac{1}{2\delta_{0x}^2}+\frac{1}{8\sigma_0^2}+\frac{k^2\sigma_0^2A^2}{2B^2}\right),b=2\delta_{0y}^2\left(\frac{1}{2\delta_{0y}^2}+\frac{1}{8\sigma_0^2}+\frac{k^2\sigma_0^2A^2}{2B^2}\right),,$$

$$c=\sqrt{2}\delta_{0x}\left(\frac{ik}{B}\rho_x+\frac{k^2\sigma_0^2A}{B^2}\rho_{dx}\right),d=\sqrt{2}\delta_{0y}\left(\frac{ik}{B}\rho_y+\frac{k^2\sigma_0^2A}{B^2}\rho_{dy}\right), \tag{7}$$

$$\begin{pmatrix}A & B\\ C & D\end{pmatrix}=\begin{pmatrix}\cos(\alpha z) & \dfrac{\sin(\alpha z)}{n_0\alpha}\\ -n_0\alpha\sin(\alpha z) & \cos(\alpha z)\end{pmatrix},, \tag{8}$$

The propagation factors of a HGCSM beam in the GRIN fiber is

$$M_x^2(z)=\left[1+\frac{4\sigma_0^2}{\delta_{0x}^2}(2m+1)\right]^{1/2},, \tag{9-a}$$

$$M_y^2(z)=\left[1+\frac{4\sigma_0^2}{\delta_{0y}^2}(2n+1)\right]^{1/2},, \tag{9-a}$$

One finds from Eq. (9) that the propagation factor of a HGCSM beam does not depend on the parameter of the GRIN fiber and a propagation distance *z*, and is determined only by the initial beam parameters.

3. Statistical properties of a HGCSM beam propagating in a GRIN fiber

In the following numerical examples, the parameters of the beam and the fiber are set as σ_0=10μm, δ_{0x}=δ_{0y}=4μm, δ_g=4μm, λ=632.8nm, R_0=50μm, n_1=1 and n_0=1.016. One finds from Fig. 2(a) that a HGCSM beam exhibits splitting properties at short propagation distance in a GRIN fiber. After a much more transmission distance, a HGCSM beam exhibits combing properties. If a HGCSM beam propagates in the GRIN fiber unceasingly, the phenomenon will repeat. Fig. 2(b) show the density plot of the modulus of the spectral degree of coherence and the corresponding cross line of a HGCSM beam at several propagation distances in the GRIN fiber with m=n=1. It exhibits array distribution in the source plane and the array distribution gradually disappears at short propagation distance in the GRIN fiber and evolves into diamond distribution. Then after propagating a certain more distance, it exhibits array distribution again. If a HGCSM beam propagates in the GRIN fiber unceasingly, the phenomenon will repeat.

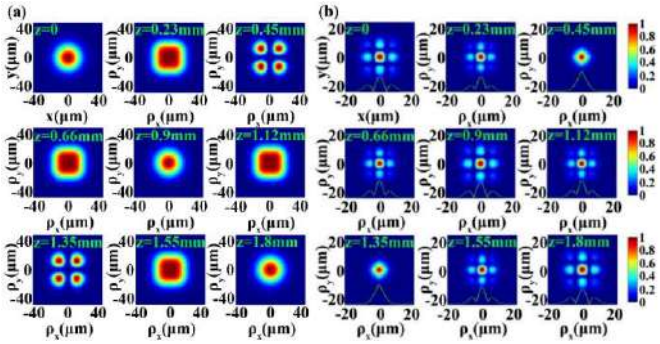

Figure 2: Intensity distribution (a) and the modulus of the spectral degree of coherence and the corresponding cross line (b) of a HGCSM beam at several propagation distances in a GRIN fiber with *m*=*n*=1.

4. Conclusions

The evolution properties and the propagation factor of the beams in a GRIN fiber have been illustrated numerically. It is found that the shape of the spectral intensity exhibits splitting and combining properties periodically in a GRIN fiber and the propagation factor of a HGCSM beam does not depend on the parameter of the GRIN fiber and the propagation distance *z*. One can modulate the state of the spectral intensity of the output beam in GRIN fiber by varying the length of fiber and the initial beam parameters of a HGCSM beam.

References

[1] F. Gori, M. Santarsiero, Devising genuine spatial correlation functions, *Opt. Lett.* 32(24): 3531-3533, 2007.

[2] F. Gori, V. R. Sanchez, M. Santarsiero and T. Shirai, On genuine cross-spectral density matrices, *J. Opt. A: Pure Appl. Opt.* 11(8): 085706, 2009.

[3] Y. Chen, J. Gu, F. Wang and Y. Cai, Self-splitting properties of a Hermite-Gaussian correlated Schell-model beam, *Phys. Rev. A* 91(1): 013823, 2015.

[4] J. Yu, Y. Chen, L. Liu, X. Liu and Y. Cai, Splitting and combining properties of an elegant Hermite-Gaussian correlated Schell-model beam in Kolmogorov and non-Kolmogorov turbulence, *Opt. Express* 23(10): 13467-13481, 2015..

[5] M. Van Buren, N. A. Riza, Foundations for low-loss fiber gradient-index lens pair coupling with the self-imaging mechanism, *Appl. Opt.* 42(3): 550–565, 2003.

[6] E. Siegman, Lasers University Science Books, Mill Valley, CA, 1986.

Optimization of orbital angular momentum spectra for Laguerre-Gaussian beam in Kolmogorov and Non-Kolmogorov turbulence

Yangsheng Yuan[1,*], Zhiheng Xu[1], Yangjian Cai[1]

[1]Shandong Provincial Engineering and Technical Center of Light Manipulations and Shandong Provincial Key Laboratory of Optics and Photonic Device, School of Physics and Electronics, Shandong Normal University, Jinan 250014, China
*corresponding author, E-mail: *yysheng@sdnu.edu.cn*

Abstract

We derive the probabilities of the signal OAM state and crosstalk OAM state for a Laguerre-Gaussian (LG) beam propagating through Kolmogorov and Non-Kolmogorov turbulence, and derive the accurate analytical function of the probability for the received OAM state modulated by an arbitrary receiver aperture. The analytical results show that the probability of the signal OAM state remains almost invariant when the radius of the receiver aperture varies. The probability of the crosstalk OAM state decreases with the decrease of the radius of a receiver aperture. Our results will be useful in free-space optical communications

1. Introduction

The vortex beams carrying orbital angular momentum (OAM) state are used in free space optical (FSO) communication and fiber optical communication to increase capacity and spectral efficiency [1]. In FSO communication, the vortex beams are inevitably disturbed by turbulent atmosphere [2], and then the initial OAM state induced by the turbulent atmosphere will be destroyed and spread to the neighbor OAM states [3]. Investigations on the probability of the receiver OAM state affected by atmospheric turbulence are helpful to improve FSO communication. Therefore the probability of the OAM state carried by vortex beams through turbulent atmosphere was studied in detail both theoretically and experimentally in [4]. Recently, the spiral spectrum of the OAM state of vortex beams induced by non-Kolmogorov turbulence was studied in [5], and the results showed that the probability of OAM state was degraded by non-Kolmogorov turbulence.

The spot size of the beams increases when they propagate through free space and turbulent atmosphere [6]. Usually, the sizes of the elements of the optical system are limited and an aperture is used at the receiver plane. The OAM states remain mutually orthogonal when a restricted angular aperture is used in the received plane for the OAM communications [7]. In this letter, we theoretically studied the probability of the detected OAM state of a LG beam induced by Kolmogorov and Non-Kolmogorov turbulence. The probability of the detected OAM state is restricted by a receiver aperture. The accurate analytical function of the probability for the received OAM state is derived. Our results show that the receiver aperture can optimize the probability of neighbor OAM state for a LG beam disturbed by atmospheric turbulence.

2. Probability of the received OAM state

The electric field will be disturbed by atmospheric turbulence, the cumulative effect induced by turbulence suppose as a pure phase perturbation on the OAM beam, as follows [3]

$$\psi(r,\theta,z)=R_{l_0}(r,z)\frac{\exp(il_0\theta)}{\sqrt{2\pi}}\exp\left[i\phi(r,\theta)\right]. \quad (1)$$

Here (r,θ) is the polar coordinates, $\phi(r,\theta)$ is the phase perturbation, $R_{l_0}(r,z)$ notes the amplitude distribution of the LG beam at the receiver plane and l_0 is the initial quantum number of the incident LG beam.

At received plane, the function of a circular aperture can be obtained by summing the complex Gaussian functions as follows

$$H(r)=\sum_{t=1}^{10}A_t\exp\left(-\frac{B_t}{a^2}r^2\right). \quad (2)$$

Here r is the polar coordinates at received plane, a denotes the radius of a circle aperture, A_t and B_t are the expansion and Gaussian coefficients, respectively.

Then we obtain the probability of the detected OAM states affected by a circular aperture and atmospheric turbulence as follows

$$\begin{aligned}P(l)=&\sum_{t=1}^{10}\sum_{t'=1}^{10}A_tA_{t'}^{*}\left(\frac{2}{\pi|l_0|!}\right)\left(\frac{k^2w_0^4}{k^2w_0^4+4z^2}\right)^{l_0+1}\\&\times\sum_{q=0}^{\infty}\frac{1}{q!\Gamma(q+\Delta l+1)}\left(\frac{1}{\rho_{0j}{}^2}\right)^{2q+\Delta l}\\&\times\frac{(l_0+2q+\Delta l)!}{2\left(\frac{B_t+B_{t'}^{*}}{a^2}+\frac{2}{\rho_{0j}{}^2}+\frac{2k^2w_0^2}{k^2w_0^4+4z^2}\right)^{l_0+2q+\Delta l+1}}\end{aligned} \quad (3)$$

Here $\rho_{0j} = \rho_{0T}$ or ρ_{0NT} is the spatial coherence length in Kolmogorov or Non-Kolmogorov turbulence, respectively.

3. Numerical analysis

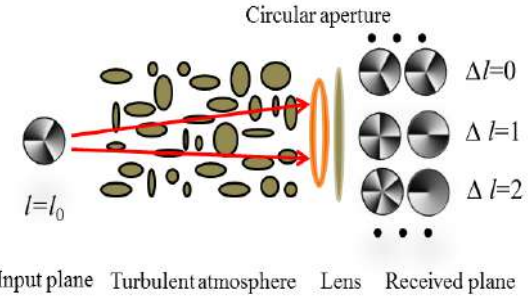

Figure 1: Schematic of the OAM state disturbed by a circular receiver aperture and turbulent atmosphere.

Figure 1 shows the schematic of the OAM state disturbed by a circular receiver aperture and turbulent atmosphere. From Fig. 1, there are many OAM states at the received plane, although the incident beam only has one OAM state. This phenomenon can be explained by the fact that the OAM state disturbed by atmospheric turbulence spreads to the neighbor OAM states. The initial OAM state will seriously spread to neighbor OAM states when atmospheric turbulence is strong and serious crosstalk occurs. A circular receiver aperture is used to filter the crosstalk.

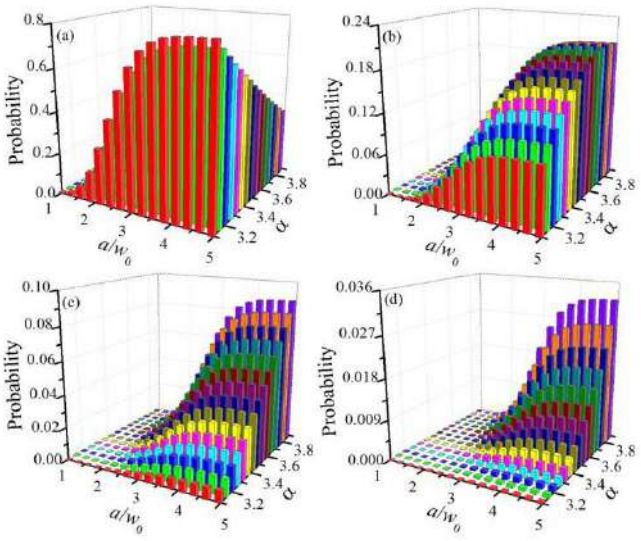

Figure 2: 3D-probability of a LG beam propagating through Non-Kolmogorov turbulence

Figure 2 shows 3D-probability of LG beam propagating through Non-Kolmogorov turbulence. In the numerical calculation, we set the propagation distance as 1km. When the radius of the receiver aperture increases or the arbitrary parameter decreases, the probability of the OAM state with Δl=0 for a LG beam propagating through Non-Kolmogorov turbulence will increase, and the probability will remain unchanged when the radius of the receiver aperture increases further (see Fig. 2(a)). When the arbitrary parameter and the radius of the receiver aperture increase, the probabilities of the OAM states with Δl=(1, 2 and 3) will increase and the probability of the OAM state with Δl=0 will decrease.

4. Conclusions

In summary, the probability of the received OAM state of a LG beam induced by Kolmogorov and Non-Kolmogorov turbulence has been derived, and the receiver aperture has been used to optimize the probability of the crosstalk modes. Our numerical results have shown that the low probability of the crosstalk OAM state correspond to small radius of the receiver aperture. The probability of the signal OAM state will approach to the same value as the radius of the receiver aperture increases or decreases. The probability of the signal OAM state decreases and the probability of the crosstalk OAM state increase when the propagation distance and an arbitrary parameter increase. Our results will be useful for FSO communications.

References

[1] J. Wang, J. Yang, I. M. Fazal, N. Ahmed, Y. Yan, H. Huang, Y. Ren, Y. Yue, S. Dolinar, M. Tur, and A. E. Willner, "Terabit free-space data transmission employing orbital angular momentum multiplexing," *Nat. Photon.* 6: 488-496, 2012.

[2] Y. Yuan, T. Lei, Z. Li, Y. Li, S. Gao, Z. Xie, and X. Yuan, "Beam wander relieved orbital angular momentum communication in turbulent atmosphere using Bessel beams," *Sci. Rep.* 7: 42276, 2017.

[3] C. Paterson, "Atmospheric turbulence and orbital angular momentum of single photons for optical communication," *Phys. Rev. Lett.* 94: 153901, 2005.

[4] Y. Ren, H. Huang, G. Xie, N. Ahmed, Y. Yan, B. I. Erkmen, N. Chandrasekaran, M. P. J. Lavery, N. K. Steinhoff, M. Tur, S. Dolinar, M. Neifeld, M. J. Padgett, R. W. Boyd, J. H. Shapiro, and A. E. Willner, "Atmospheric turbulence effects on the performance of a free space optical link employing orbital angular momentum multiplexing," *Opt. Lett.* 38(20): 4062-4065, 2013.

[5] M. Wei, J. Wang, Y. Zhang, and Z. Hu, "Orbital-angular-momentum photons for optical communication in non-Kolmogorov atmospheric turbulence," *Opt. Commun.* 416: 89–93, 2018.

[6] F. Wang and Y. Cai, "Second-order statistics of a twisted Gaussian Schell-model beam in turbulent atmosphere," *Opt. Express* 18(24): 24661–24672, 2010.

[7] S. Zheng, X. Hui, J. Zhu, H. Chi, X. Jin, S. Yu, and X. Zhang, "Orbital angular momentum mode demultiplexing scheme with partial angular receiving aperture," *Opt. Express* 23(9): 12251–12257, 2015.

Guide Star Catalog Establishment for Infrared Star Sensors

Feng Wu, Xifang Zhu, Ruxi Xiang , Qingquan Xu , Cheng Xu

School of Electrical Information Engineering, Changzhou Institute of Technology, Changzhou, China
*corresponding author, E-mail: dermindee@gmail.com

Abstract

Infrared star sensor provides accuracy navigation information to air vehicles which works in the infrared band. After constellation features are discussed, the idea that distributes stars in the local field of view to constellations is put forward. An optimization algorithm to establish the guide star catalog is proposed to achieve an evenly distributed guide stars. It proves that the proposed algorithm has the virtue of simple calculation and easy realization. The Boltzmann entropy of the guide star catalog drops 2 orders of magnitude.

1. Introduction

Star sensors calculate the attitudes by comparing the observed stars with the guide stars loaded in advance in the vehicles and identifying them according to star pattern identification algorithms. The establishment of guide star catalog is one of the key technologies in star sensor study. In the infrared band, much more stars appear with the same limiting magnitude [1]. However, redundant guide stars will harass the star pattern identification and lead to the slower speed and lower successful identification rates [2]. Therefore, the guide star optimal selection is preferred [3].
In this paper, an optimization algorithm to build the guide star catalog is proposed for the infrared star sensors to achieve an evenly distributed guide stars based on star clustering.

2. 2MASS and star distribution

Infrared star sensors run in the atmosphere close to the ground. Therefore, background interference and atmospheric attenuation are preferred to decrease as much as possible in order to obtain a high signal to noise ratio of the star maps. Fortunately, some near-infrared windows which permit star signals have less attenuation support the development of the infrared star sensors [4]. Furthermore, the sky radiations become weak, and their interferences will be negligible in the near-infrared bands. In this paper, we select 2MASS as the original star source to build the guide star catalog.
2MASS is the abbreviation of the Two Micron All Sky Survey, and stores nearly 47.1 million near-infrared stars of the entire sky in J, H, K bands.

When the J band is chosen and the limiting magnitude MI is chosen to be 3.5, 3694 stars are left after 2MASS is processed by magnitude threshold. Then star sensors with different FOVs traveling all over the celestial sphere and pointing to random directions are simulated. We implement the statistic of the numbers of stars appearing in the FOV, and calculate the capture probabilities with the given number of stars as shown in Fig.1. Thus, according to Fig.1 the FOV is chosen to be 12°×12°.

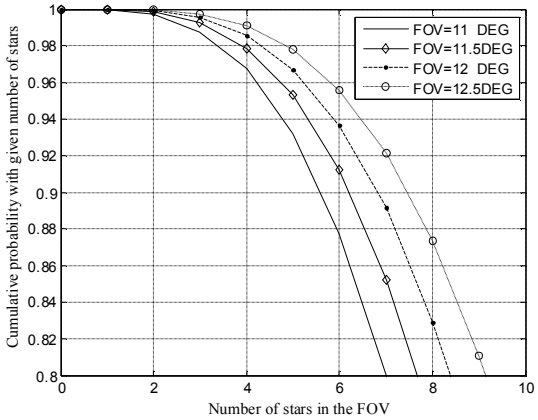

Figure 1: Star number cumulative probability when *MI* =3.5 in J band.

3. Guide star catalog establishment

The original star catalogue is filtered according to the magnitude threshold method which deletes stars brighter than the star with the limiting magnitude, and also deletes the binary stars and variable stars. The guide star catalog is optimized as follows, and illustrated in Fig.2.

- Step 1 The optical axis of the star sensor points to (α_i, δ_j) in the inertial coordinate system. Simulation of visiting every portion of the celestial sphere is performed by increasing α_i and δ_j gradually. i and j indicate the portion of the celestial sphere. They are both initialized to 1.
- Step 2 Stars in the current FOV are extracted. Suppose the total star number is N.
- Step 3 If $N \leq N_{th}$, all extracted stars are stored to be guide stars. Then i or j increases by 1, and the optical axis points to the next portion. Return to Step 2. Otherwise, go to Step 4. If the visiting is over, go to Step 6.

- Step 4 The remaining stars in the current FOV are clustered according to Section 3.1. Every star is assigned a constellation number.

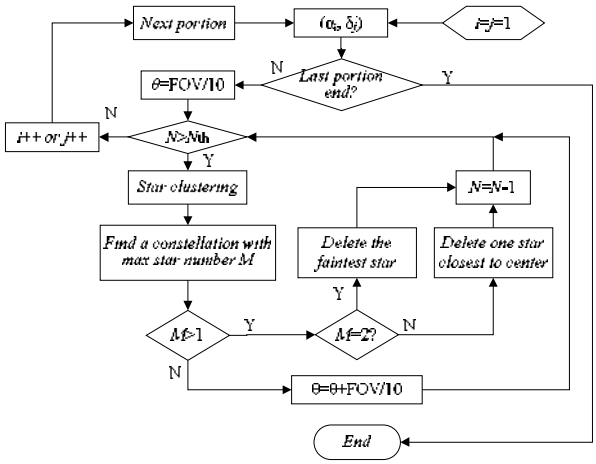

Figure 2: Flowing chart of guide star optimization.

- Step 5 Stars in each constellation are counted. The constellation with the largest number of stars is chosen. Its star number is denoted as M. N decreases by 1. Then return to Step 3. If M=1, the clustering angle θ increases by the 1/10 of FOV, and return to step 4.
- Step 6 The guide star catalog is built.

4. Simulations and results

When the limiting magnitude and FOV are selected to be 3.5 and 12°×12° respectively in J band, there are 3694 stars left after the original 2MASS catalog is processed by setting a limiting magnitude and deleting binary stars and variable stars. Their distribution on the celestial sphere is shown in Fig.3, and the Boltzmann entropy is 0.027. After the guide star catalog optimization in this paper, the distribution of obtained guide stars is shown in Fig.5. More than 1000 stars are deleted and only 2351 stars are left. The Boltzmann entropy drops to 7.4×10^{-4}. Therefore, the proposed algorithm achieves a better global uniformity. Tab.1 presents the star number statistics in FOV. It shows that the maximum star number decreases to 19, and the average number is 8.30 after optimization. The standard deviation drops from 6.91 to 1.84. It proves the local uniformity becomes better.

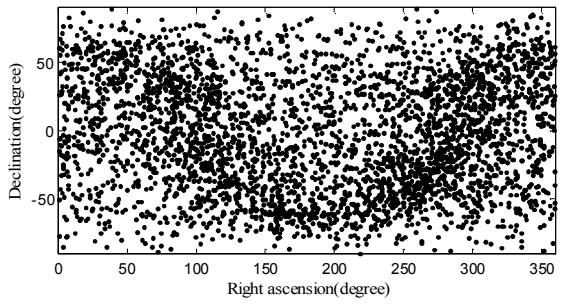

Figure 3: Star distribution before optimization.

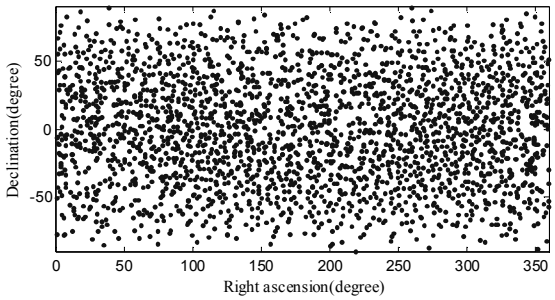

Figure 4: Star distribution after optimization.

5. Conclusions

Stars in the local FOV can be allotted into constellations by clustering stars when the mean shift algorithm is modified. The distribution of the stars will be more uniform when we delete one star closest to the center of the densest constellation. Guide star catalog optimization algorithm proposed in this paper achieves better local uniformity and better global uniformity.

Table 1: Comparison of guide star catalog before and after optimization.

Evaluation indexes	Before	After
Total	3694	2351
Maximum	59	19
Minimum	0	0
Average	13.25	8.30
Standard deviation	6.91	1.84
Boltzmann entropy	2.7×10^{-2}	7.6×10^{-4}

Acknowledgements

This work was supported by National Natural Science Foundation of China (No. 61640420), Top-notch Academic Programs Project of Jiangsu Higher Education Institutions (TAPP) under Grant No.PPZY2015B129, Changzhou Key Laboratory of Applied Technology on Intelligence & Unmanned Aerial Vehicle(No. CM20173003), and National Undergraduate Training Programs for Innovation and Entrepreneurship (No. 201811055072H) in China.

References

[1] Jun T., Shipeng S. Celestial bodies tracking identification for ship-borne star sensor. *Optics & Precision Engineering*, *25*(7),pp.1948-1953, 2017.

[2] Feng W.,Xifang Z.,Ruxi X., et al. Establishment of guide star database for the all-day star sensor. *Journal of Changzhou Institute of Technology* ,30(6), 26-29, 2017.

[3] Li, X., Yang, J., Zhang, L., Li, S., & Jin, G. A new simplified selection algorithm of the guide star catalogue for a star sensor. *Journal of Navigation*, 67(6), 984-994, 2014.

[4] Qing X., Chunhui Z., Xiao L. Current situation and key technologies of daytime star sensor. *Optical Technique*, 42(6), 523-528, 2016.

Mode Transformation in Perfect Optical Vortex

Xinzhong Li[1*], Haixiang Ma[1], Hao Zhang[1]

[1]School of Physics and Engineering, Henan University of Science and Technology, Luoyang 471023, China
*corresponding author, E-mail: xzli@haust.edu.cn

Abstract

Recently, perfect optical vortex (POV) whose radius is independent of the topological charge have been extensively studied. However, POV has only a single sample mode in the observation plane, which is challenging to satisfy the requirement to form a complex structured optical field. Here, we report three methods to breakthrough this limitation. i. the controllable mode transformation in POV. ii. the circular/elliptic optical vortex array by the superposition of POVs. iii. the close-packed POV lattices with controllable structures.

1. Introduction

In 2013, Ostrovsky et al. proposed the concept of a perfect optical vortex (POV), where the diameter is independent of the TCs. After this finding, research has been performed on POV's generation, verification, modulation, and applications. However, POV has only a single sample mode in the observation plane, i.e., a bright ring that has a constant diameter, independent of the TC. Therefore, it is challenging to satisfy the requirement to form a complex structured optical field. Versatile modes are significant for optical vortex beams, owing to the potentials for advanced applications, such as the optical cage formation, optical microfluidic sorting, and micro-particles regulation and acceleration. Therefore, it is of a key importance to realize a POV with multiple modes. In 2017, Mazilu et al. proposed a fractional POV with multiple gaps, which enriches the modes of POVs. Further, Kovalev et al. reported an elliptic perfect optical vortex (EPOV), and derived the exact analytical expressions for the total OAM and OAM density.

Here, we report three methods to breakthrough this limitation. i. the controllable mode transformation in POV which realize a single POV with diverse modes. ii. the circular/elliptic optical vortex array by the superposition of concentric POVs. iii. the close-packed POV lattices with controllable structures.

2. Controllable mode transformation in POV [1]

Intuitively, if we want to change a circle to an ellipse, in Cartesian coordinates, we can fix one axis and stretch out the other axis. One can ask the following question: Can we obtain an elliptic perfect optical vortex (EPOV) by stretching the Bessel–Gauss beam to an elliptic Bessel–Gauss beam and then apply an FT operation? In order to find the answer, the coordinates can be transformed as $mx = \rho\cos(\varphi)$ and $y = \rho\sin(\varphi)$, where m is a positive constant, called a scaling factor, and (x, y) denotes the Cartesian coordinates at the object plane. In this case, (ρ, φ) is a type of elliptic coordinate, and the polar coordinates are the particular case for $m = 1$. Via this technology, the POV could be transformed from circle to ellipse shown in Fig. 1 and the eccentricity e is determined by the stretching parameter m. In the process of transformation, the beam in each mode maintains a higher mode purity (> 0.9).

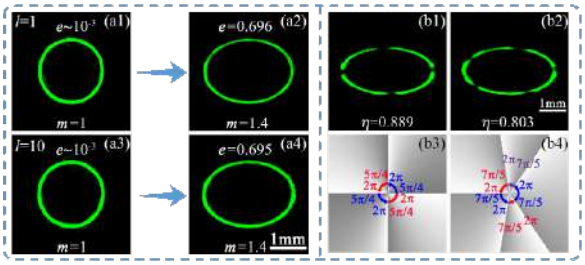

Fig.1 Elliptic perfect optical vortex.

By applying a spiral phase shown in Fig. 1(b3) and (b4), instead of the spiral phase $\exp(il\varphi)$ when generating the phase mask, the position and the quantity of the gap can be freely controlled.

3. Circular/elliptic optical vortex array [2, 3]

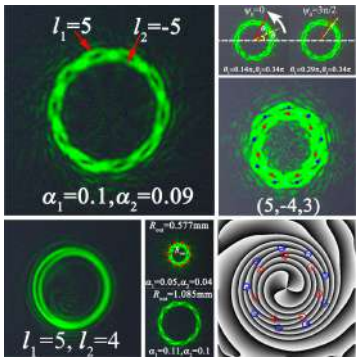

Fig. 2 Schematic of the circular optical vortex array.

Based on the light principle of independent propagation and hybrid phase encoding method, the concentric POVs are

generated. Via superposition of two concentric POVs with ring overlap of ~36%, a freely adjustable circular optical vortex array with a constant topological charge of +1 or −1 can be generated, shown in Fig. 2. The number and sign of the circular optical vortex array are determined by the topological charges of the two perfect optical vortices. Moreover, the radius of the circular optical vortex array is easily adjusted by using the cone angle of an axicon. Furthermore, the circular optical vortex array and multiple circular optical vortex array can be rotated by changing the initial phase difference of the perfect optical vortices on demand.

Furthermore, by applying the mode transformation technology shown in section 2, the elliptic annular optical vortex array can be generated, shown in Fig. 3. The control proporties are similar with the circular optical vortex array.

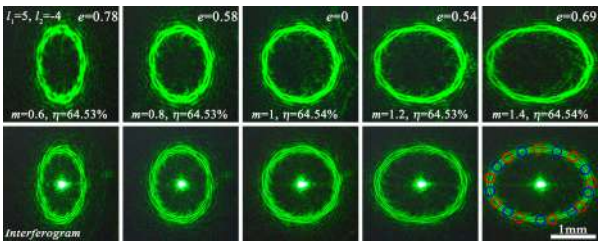

Fig. 3 Elliptic annular optical vortex array.

4. Close-packed POV lattices [4]

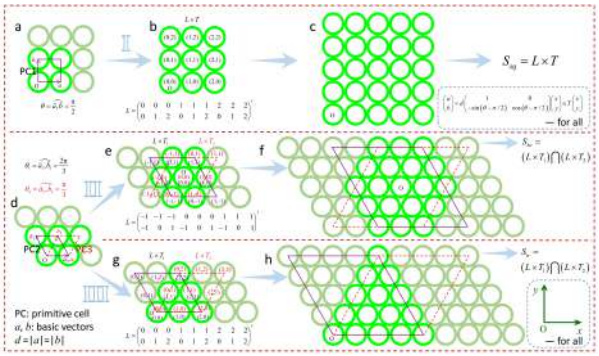

Fig. 4 Schematic of the close-packed POV lattices.

To produce close-packed POV lattices with controllable structures, the challenge is accurately determining the position of each lattice element and simultaneously ensuring the compact arrangement. To solve this problem, we borrow the crystal lattice theory and close-packed arrangement concept from solid-state physics, considering each individual optical vortex element as a Bravais net. As demonstrated in Fig. 4, there are two typical close-packed arrangements: the square close-packed arrangement shown as Route I and the most close-packed arrangement shown as Routes II and III. The lattice coordinates and corresponding matrix L are shown in Fig. 4(b), which is obtained via permutations with repetition of the integers. The Cartesian coordinates are deduced using the formula $S = L \times T$, where T is the transformation matrix. And then the close-packed POV lattices could be generated via global hybrid phase mask which is designed by the superposition of a series of phase masks with different phase-shift amounts obtained by S at the object plane according to the principle of independence of light propagation. Furthermore, the different structures can be obtained via some logic-operation (including “AND”, “OR”, and “NOT”), shown in Fig. 5.

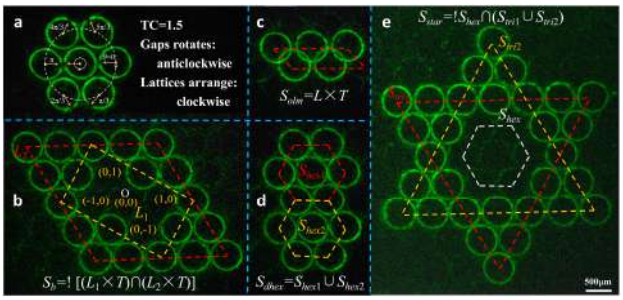

Fig. 5 More complex close-packed POV lattices with controlled structures: (a) fractional hexagonal lattice with multi-gaps, (b) hollow rhombus-shaped lattice, (c) “Olympic rings”-shaped lattice, (d) honeycomb-shaped lattice, and (e) hollow hexagram-shaped lattice.

5. Conclusions

We reported three methods and obtained three kinds of beams to overcome the drawback of the single mode distributions of POV. Firstly, the elliptic perfect optical vortex was generated via mode transformation. Secondly, the controllable circular/elliptic optical vortex array by the superposition of concentric POVs. Thirdly, close-packed arrangement OVLs with controllable structures by borrowing the crystal lattice theory. These works demonstrate some complex structured optical fields, which is of significance for applications such as optical tweezers, micro-particle manipulation, and optical imaging.

Acknowledgements

National Natural Science Foundation of China (Grant nos. 61775052).

References

[1] X. Z. Li, H. X. Ma, C. L. Yin, J. Tang, H. H. Li, M. M. Tang, J. G. Wang, Y, P. Tai, X. F. Li, Y. S. Wang, Controllable mode transformation in perfect optical vortices, *Opt. Express* 26: 651−662, 2018.

[2] H. X. Ma, X. Z. Li, Y, P. Tai, H. H. Li, J. G. Wang, M. M. Tang, J. Tang, Y. S. Wang, Z. G. Nie, Generation of circular optical vortex array, *Ann. Phys. (Berlin)* 529: 1700285, 2017.

[3] H. X. Ma, X. Z. Li, H. Zhang, J. Tang, Z. G. Nie, H. H. Li, M. M. Tang, J. G. Wang, Y, P. Tai, Y. S. Wang, Adjustable elliptic annular optical vortex array, *IEEE Photon. Technol. Lett.* 30: 813-816, 2018.

[4] X. Z. Li, H. X. Ma, H. Zhang, Y, P. Tai, H. H. Li, M. M. Tang, J. G. Wang, J. Tang, Y. J. Cai, Close-packed optical vortex lattices with controllable structures, *Opt. Express* 26: 22965−22975, 2018.

Optical Choppers: Classical, Eclipse, and with Shafts

Virgil-Florin Duma[1,2]

[1]3OM Optomechatronics Group, Aurel Vlaicu University of Arad, Romania
[2]Doctoral School, Polytechnic University of Timisoara, Romania
*corresponding author, E-mail: duma.virgil@osamember.org

Abstract

Optical choppers with rotational disks, in their classical configuration, with windows with linear margins were studied, for top-hat laser beam. Disks with windows with non-linear margins (e.g., circular or elliptic) were introduced and patented by our group. They were named 'eclipse' choppers, because of the way the beam section is obscured by the disk. Their modulation functions (of the transmitted light flux) were deduced and compared with those of classical choppers. Because of chop frequency limitations of disk choppers, we also introduced (patent pending) choppers with rotational shafts. They are presented, with their main optical characteristics. A multi-parameter analysis was carried out for each type of chopper, with regard to their constructive characteristics.

1. Introduction

Optical choppers are light modulators utilized in a wide range of applications, from lasers to radiometry, telescopes, spectral and biomedical apparatuses [1]. Choppers are employed mainly for light attenuation or for generating light (usually laser) impulses [2]. In photonic systems, they are almost as used as other basic components, such as lenses, mirrors, or filters. A brief overview of our contributions made in the last decade are presented in the following, structured on the three main research paths we have approached on this topic.

2. Classical choppers

This is the most common chopper configuration, which have rotational disks with windows with linear margins – Fig. 1(a). We developed their multi-parameter analysis [3,4], taking into account all the possible relationships between the angular width α of a window and the angular aperture 2δ of the laser beam.

The functions of the transmitted flux Φ was determined for top-hat (incident) laser beams (i.e., with a constant intensity over the entire beam section) with a Φ_S incident flux. Three main cases were approached [3]:

(i) *large wings* (with the angle of a wing $\gamma > 2\delta$), which can cover completely the beam section in the disk plane. If the beam is considered perfectly focused in this plane, than the output signal has rectangular impulses. In reality, the radius r of the beam section is finite therefore the light impulses produced have the profile shown in Fig. 2.

(ii) *a single wing is positioned at every moment in front of the beam section* (for $\gamma < 2\delta < \alpha$). In this case the output signal does not reach zero values; it reaches just minimum values corresponding to the moment when the wing passes through the central part of the beam section.

(iii) *two or more wings pass simultaneously through the beam section*. A summation of the obscured parts of the beam is extracted from the laser signal. The output signal has an approximately sinusoidal shape, with minimum and maximum values, as described in [3].

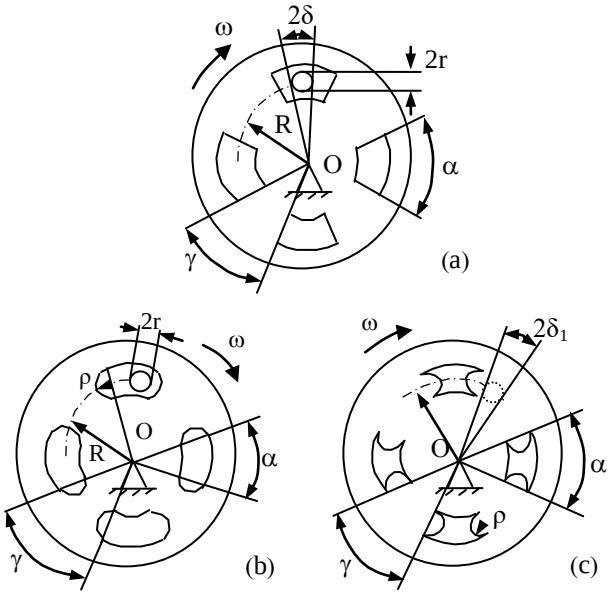

Figure 1: Optical choppers with rotational disks: (a) classical; eclipse, with outward (b) and inward (c) margins [3,4,6,7].

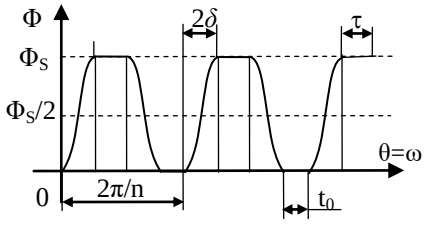

Figure 2: Transmission function of classical choppers for a single wing in the beam section – case (i) [3,4].

All the above cases are based on the assumption that the beam section enters entirely in the chopper window, i.e. $2r < R_2 - R_1$, where the latter represents the radial width of a window. One may consider the beam section cut in part by the window, which complicates the discussion, as approached in [5].

3. Eclipse choppers

These devices are a novel configuration of disk choppers that, to our knowledge, we have introduced [6] and patented [7]. They have non-linear margins of the windows, oriented outward – Fig. 1(b) or inward – Fig. 1(c). The name proposed is based on how the beam section is obscured by the window margin, similar to a planetary eclipse. For semi-circular margins of radius ρ - Fig. 1(b, c) - and for top-hat laser beams, such choppers produce laser impulses that are approximately triangular, i.e. with more linear transition portions of the impulses than in the case of classical choppers. The undesired portion of small energy transfer in the beginning of a laser impulse in Fig. 2(b) is thus avoided. The radius ρ (in general, the non-linear shape of a window margin) introduces another degree of freedom in the design of these choppers, to obtain a required profile of impulses. For $\rho \to \infty$, the particular case of classical choppers is obtained; eclipse choppers are their general configuration.

4. Choppers with shafts

Regardless of their configuration, choppers with disks are severely limited in term of chop frequency f – which corresponds to the frequency of the laser impulses produced. Macro-choppers have a maximum f of 10 kHz, but vibrations already occur from f equals 3 kHz. This issue has been tackled by developing Micro-Electro-Mechanical Systems (MEMS) choppers, usually with oscillatory, resonant elements [8]. We developed, for the first time to our knowledge, another solution, of macro-choppers with rotational shafts of different shapes (cylindrical, conical, or spherical) and with slits of different profiles [9]. Examples of choppers with shafts are shown in Fig. 3.

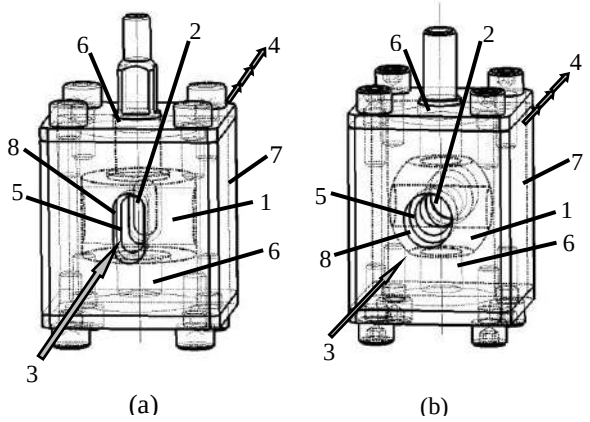

Figure 3: Optical choppers with rotational shafts [9]: (a) cylindrical with slits; (b) spherical with holes. Notations: 1, shaft; 2, slit; 3, incident laser beam; 4, emergent laser beam; 5, slot or hole; 6, bearings; 7, 8, cage.

A Finite Element Analysis (FEA) is necessary and we developed it to assess the structural integrity and the deformation level of the shaft of high rotational frequency, of up to 54 krpm, as utilized in polygon mirror-baser scanners, for example [10].

5. Conclusions

The three main directions of research in optical choppers in our group was reviewed. Current work includes design programs for the different types of choppers. Other types of laser beams, Gaussian or Bessel, are another topic on interest. An insight in these aspects concludes the presentation.

Acknowledgements

This study is supported by the European Union through the European Regional Development Fund under the Competitiveness Operational Program (Novel Bio-inspired Cellular Nano-architectures, POC-A1-A1.1.4-E nr. 30/2016), and previously by the Romanian Authority for Scientific Research, CNDI–UEFISCDI grant PN-III-P2-2.1-BG-2016-0297 (http://3om-group-optomechatronics.ro/).

References

[1] M. Bass, Ed., *Handbook of Optics*, 3rd Edition, Mc. Graw-Hill Inc., New York, 2009.

[2] K. Benjamin, A. Armitage, and R. South, Harmonic errors associated with the use of choppers in optical experiments, *Measurement* 39: 764-770, 2006.

[3] V.-F. Duma, Theoretical approach on optical choppers for top-hat light beam distributions, *J. of Opt. A: Pure and Appl. Opt.* 10: 064008, 2008.

[4] V.-F. Duma, Prototypes and modulation functions of classical and novel configurations of optical chopper wheels, *Latin American J. of Solids and Structures* 10: 5-18, 2013.

[5] V.-F. Duma, Optical attenuators with Risley prisms and disk choppers, *Proc. of the Romanian Academy, Series A* 20, 2019 – in print.

[6] V.-F. Duma, Optical choppers with circular-shaped windows: Modulation functions, *Comm. in Nonlin. Sc. and Num. Simulation* 16: 2218-2224, 2011.

[7] V.-F. Duma, M. F. Nicolov, C. Mnerie, L. Szantho, Optical modulator with rotating element, has role to generate light pulses of certain profile, Derwent No. 2011-J76364; *Romanian Patent* RO 126505, 2016.

[8] M. T. Ching, R. A. Brennen, R. M. White, Microfabricated optical chopper, *Opt. Eng.* 33: 3634-3642, 1994.

[9] V.-F. Duma, D. Demian, Optical modulator, has solid rotating shaft with some through slots of well-defined profiles, *Romanian Patent* RO129610-A0, 2014.

[10] V.-F. Duma, Polygonal mirror laser scanning heads: Characteristic functions, *Proc. of the Romanian Academy, Series A* 18: 25-33, 2017.

Energy Efficient Next Generation Passive Optical Network with Synchronized Watchful Sleep Mechanism

N. A. Ismail[1], A. M. Zin[1], S. M. Idrus[1*], F. Iqbal[1] and R. A. Butt[2]
[1]Universiti Teknologi Malaysia, Malaysia
[2]NED University of Engineering and Technology, Pakistan
*corresponding author: sevia@fke.utm.my

Abstract

We present an energy efficient XG-PON employing the synchronized watchful sleep mechanism. This sleep mode is combined with the available IACG DBA scheme to investigate the upstream delay for all traffic classes while utilizing the bandwidth resources efficiently. The sleep mechanism enables OLT to identify every state of ONUs and consequently only active ONUs have downstream transmission. We compare our simulation with CSM and observe improvements in upstream delays of the network.

1. Introduction

Various records have showed that, energy demand is continuously increasing year by year. According to the International Energy Agency (IEA), through the key world energy statistics, the global energy production and consumption is having a gradual increase from 1973-2015 [1]. One of the major consumers is the ICT sector, which requiring operating power, approximately 7% from the global electricity [2]. The currently developed 10-Gigabit PON (XG-PON) is 10 Gbps downstream while the Next-Generation PON (NG-PON) is planned for higher capacity in providing the access to an increasing number of network users. Referring to latest ITU statistics reported by 2016, the individuals using the internet have risen by 46% with 13.1 % increase in fixed broadband and 52.2 % increase in mobile service subscriptions [3].

As the global warming becomes the worlds' concern, the responsibility must be taken by all-hands to preserve the nature for our sustainable future living. Current record states that, ICT sectors contribute to 2% of global CO2 emission and surprisingly in the newest headlines, this figure would be 14% in 2040 if no improvement is done [4]. Thus, as the global electricity consumption is becoming the major concern, the International Telecommunication Union (ITU-T) has started working on the Gigabit-PON (GPON) power saving mechanism earlier and have published the ITU-T Series-G Supplement 45 "G-PON power conservation" in 2009 [5]. The four basic power saving methods that have been standardized in the specification are: power shedding, dozing, deep sleep and cyclic sleep. In 2015, the watchful sleep mode has been included in the XG-PON standard which simplify and able to emulates the mechanism of cyclic and doze modes [6]. However, these recommendations leave the decision to the network operators and researchers to implement the chosen saving method. Applying the power saving mechanism in ONU is essential since ONU in the access network takes the most percentage from the total power in telecommunication, followed by the IP core devices, Ethernet Aggregators (EA) and Optical Line Terminator (OLT) [7]. However, OLT as the network controller is also responsible for managing Optical Network Units (ONU) with this sleep activity especially when related to resource allocations.

2. The synchronized watchful sleep mode

The watchful sleep mode at the ONU is operated based on four power management states: Active held (AH), Active free (AF), Watch Sleep Aware (WA) and Watch as shown in Figure 1 [8]. The first two states constitute the active phase, and the latter two states comprise the power saving phase of an ONU. Watch state consist of Asleep and Listen interval. Asleep is full low power mode (Both Tx/Rx OFF). In Listen, the ONU regularly turns ON and OFF the receiver to check for any wake-up indicators. During Asleep, the ONU kept the incoming data in its buffer queue. Based on this queue status contained in Status Reports (SR) sent from ONU to OLT regularly, OLT will decide the allocation length to each ONU as practiced by the DBA scheme. In cyclic sleep mode (CSM), there are also four power states and the difference between watchful is it replaces Watch with Asleep state. In synchronized watchful sleep, the OLT learns every state of watchful sleep ONUs and consequently improve scheduling mechanism with aid of DBA. The IACG [9], [10] is a simple DBA scheme compared to other DBA schemes due to its extra remaining unassigned bandwidth (RBW) assignment phase at the end of each DBA cycle termed as Colorless Grant.

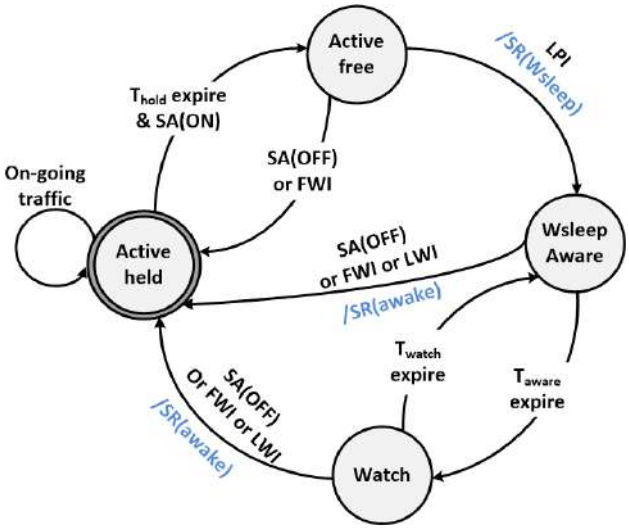

Figure 1: Watchful sleep state diagram for ONU

3. Performance evaluation

The simulation study was conducted using our simulation testbed developed in OMNET++ also used in our earlier PON studies [11]–[13]. This study comprised of a single OLT connected to total 16 ONUs through a passive optical splitter at a distance of 20 km. For simplicity, only one host and one user are configured per ONU. The downstream is varied from 0.1 to 0.7 network load corresponding to 15 Mbps to 350 Mbps per ONU with US load always being one fourth of DS, as in [14]. For traffic frame generation, we used the Broadcom CATV upstream and downstream frame distribution of [15]. The key parameters used in the simulation are listed in Table 1.

Table 1 Simulation parameters

Parameter	**Values / Details**
P_{AH}, P_{AF}, P_{WA}	100%
P_W	5%
ONU - OLT Line Rate	200 Mbps
RTT	200 us
US / DS Line Rates	2.5Gbps / 10Gbps
Downstream rate (λ_{DS})	15 Mbps to 350 Mbps per ONU.
Upstream rate (Λ_{US})	$\lambda_{DS}/4$

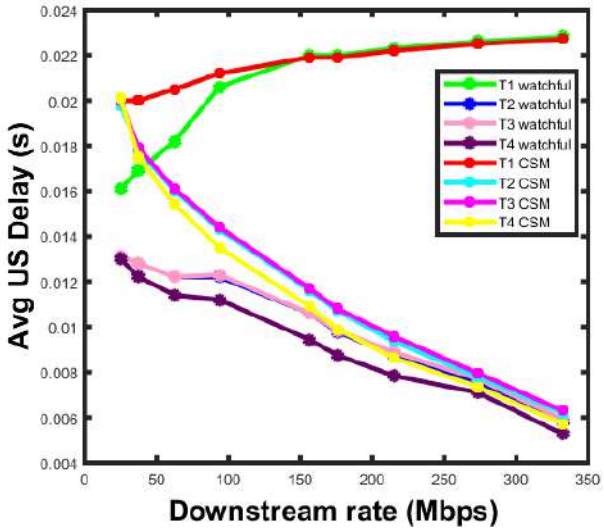

Figure 2: Average upstream delay for T1, T2, T3 and T4 for synchronized watchful and cyclic sleep mode

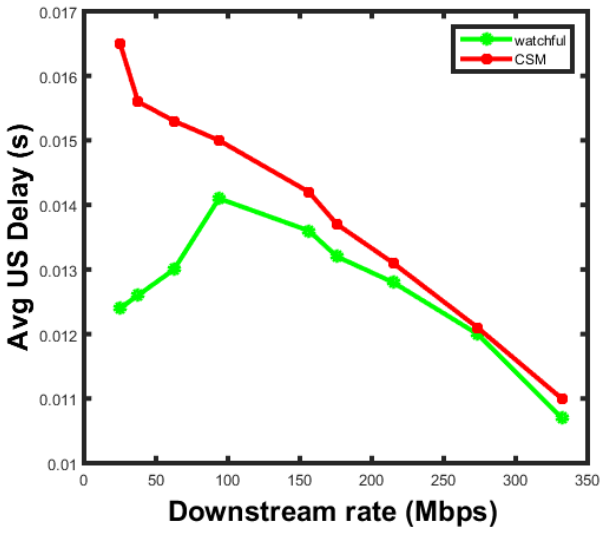

Figure 3: Overall average upstream delay for synchronized watchful and cyclic sleep mode

Based on Figure 2 and 3, the performance of average upstream delay for T2, T3 and T4 with synchronized watchful sleep outperforms CSM as the downstream rate increases. At lower downstream rate, synchronized watchful sleep has 35% lower delay compared to CSM. This proves that the suggested mechanism can improve performance while conserving energy of a XG-PON. However, for T1, the performance of upstream delay is better when downstream rate is lower which is in between 15 – 100 Mbps.

4. Conclusions

In this work, we have studied the synchronized watchful sleep technique and compare the performance with CSM. An existing reported dynamic bandwidth assignment scheme

was used and all the traffic classes T1 to T4, defined by ITU were considered. A Poisson distributed traffic generator with exponentially varying inter-arrival times was used to inject the traffic frames in the network. The simulation results show that upstream delay for T2,T3 and T4 applying synchronized watchful gives better performance as compared to CSM and also below the recommended delay which is 56ms. In future, we will study the impact of synchronized watchful sleep with different DBA scheme.

Acknowledgements

The authors acknowledge the financial support from Ministry of Education, Malaysia and the administration of the University of Technology Malaysia (UTM) for this research through FRGS Fund vot number 4F961.

References

[1] G. S. Lakshmi, G. S. Rathore, R. Sharma, A. Anand, S. Sharma, and A. S. Hada, "Energy Statistics," p. 121, 2017.

[2] M. Avgerinou, P. Bertoldi, and L. Castellazzi, "Trends in Data Centre Energy Consumption under the European Code of Conduct for Data Centre Energy Efficiency," *Energies*, vol. 10, no. 10, 2017.

[3] "ICT Facts and Figures 2017." [Online]. Available: https://www.itu.int/en/ITU-D/Statistics/Pages/facts/default.aspx. [Accessed: 30-May-2019].

[4] "'Tsunami of data' could consume one fifth of global electricity by 2025 | Environment | The Guardian." [Online]. Available: https://www.theguardian.com/environment/2017/dec/11/tsunami-of-data-could-consume-fifth-global-electricity-by-2025. [Accessed: 01-Nov-2018].

[5] G 987, "ITU-T SERIES G: TRANSMISSION SYSTEMS AND MEDIA, DIGITAL SYSTEMS AND NETWORKS Digital sections and digital line system – Optical line systems for local and access networks 10 Gigabit-capable passive optical networks (XG-PON): Reach extension," 2012.

[6] 987.1 ITU-T Recomendation, "10-Gigabit-capable passive optical network (XG-PON) systems: Definitions, abbreviations and acronyms," *ITU-T Recomm. G.987*, pp. 1–19, 2012.

[7] A. Otaka, "Power saving ad-hoc Report," *Contrib. to IEEE P802.3av Task Force*, pp. 1–7, 2008.

[8] A. M. Zin, S. M. Idrus, N. A. Ismail, A. Ramli, and R. A. Butt, "Energy Efficient Performance Evaluation of XG-PON for Sustainable Green Communication Infrastructure," *Prog. Electromagn. Res. Symp.*, vol. 2018-Augus, pp. 950–955, 2018.

[9] M.-S. Han, "Dynamic bandwidth allocation with high utilization for XG-PON," *16th Int. Conf. Adv. Commun. Technol.*, pp. 994–997, 2014.

[10] M.-S. Han, H. Yoo, B.-Y. Yoon, B. Kim, and J.-S. Koh, "Efficient dynamic bandwidth allocation for FSAN-compliant GPON," *J. Opt. Netw.*, vol. 7, no. 8, p. 783, Aug. 2008.

[11] R. A. Butt, S. M. Idrus, N. Zulkifli, and M. Waqar Ashraf, "Comprehensive bandwidth utilization and polling mechanism for XGPON," *Int. J. Commun. Syst.*, vol. 31, no. 3, 2018.

[12] R. Aslam Butt, S. Mahdaliza Idrus, K. Naseer Qureshi, P. M. A. Shah, and N. Zulkifli, "An energy efficient cyclic sleep control framework for ITU PONs," *Opt. Switch. Netw.*, vol. 27, no. January 2017, pp. 7–17, 2018.

[13] R. A. Butt, S. M. Idrus, S. Rehman, P. M. A. Shah, and N. Zulkifli, "Comprehensive Polling and Scheduling Mechanism for Long Reach Gigabit Passive Optical Network," *J. Opt. Commun.*, 2017.

[14] R. O. C. Hirafuji, K. B. Cunha, D. R. Campelo, A. R. Dhaini, and D. A. Khotimsky, "The Watchful Sleep Mode : A New Standard for Energy Efficiency in Future Access Networks," *IEEE Commun. Mag.*, vol. 58, no. 3, pp. 150–157, 2015.

[15] G. Kramer, B. Mukherjee, and A. Maislos, *Ethernet Passive Optical Network (EPON).*, 1st ed. New York, USA: McGraw-Hill Education, 2005.

Metasurface Empowered Wide-Angle Fourier Lens

Shuqi Chen*, Wenwei Liu, and Jianguo Tian

The Key Laboratory of Weak Light Nonlinear Photonics, Ministry of Education, School of Physics and TEDA Institute of Applied Physics, Nankai University, Tianjin 300071, China

**E-mail: schen@nankai.edu.cn*

Abstract

Fourier optics, the principle of using Fourier Transformation to understand the functionalities of optical elements, lies at the heart of modern optics, and has been widely applied to optical information processing, imaging, holography etc. Here, we experimentally demonstrate a dielectric metasurface consisting of high−aspect−ratio silicon waveguide array, which is capable of performing Fourier transform for a large incident angle range and a broad operating bandwidth. Thus our device significantly expands the operational Fourier space, benefitting from the large numerical aperture, and negligible angular dispersion at large incident angles. Our Fourier metasurface will not only facilitate efficient manipulation of spatial spectrum of free-space optical wavefront, but also be readily integrated into micro-optical platforms due to its compact size.

Reference

[1] J. W. Goodman, Introduction to Fourier optics, Roberts and Company Publishers, Greenwood Village, Colorado, USA (2005).

[2] B. E. A. Saleh, M. C. Teich, Fundamentals of photonics, Wiley, New York, USA (1991).

Fog Removal for Single Images by Optimizing DTCWT Coefficients

Qingquan Xu*, Xifang Zhu, Feng Wu, Ruxi Xiang , Cheng Xu

School of Electrical Information Engineering, Changzhou Institute of Technology, Changzhou, China
*corresponding author, E-mail: dermindee@gmail.com

Abstract

Outdoor imaging devices usually produce degraded images with low contrast, bad clearness and color distortion when they are disturbed by fog. It becomes difficult for the outdoor visual systems to detect and identify objects efficiently. Algorithms of removing fog from single images provide a useful solution. The dual tree complex wavelet transform (DTCWT) has advantages superior to the conventional wavelet transform. The characteristics of sub-band coefficients of DTCWT were analyzed. A DTCWT based algorithm to removing fog from the single images was proposed which optimizes sub-band coefficients according to the frequency relationships between scenery and fog in the images. Its detailed procedures were described. Some experiments were performed to verify the algorithm. It proves that the proposed algorithm achieves satisfactory results and is better than the dark channel prior and Retinex.

1. Introduction

The contrast and visibility tends to be degenerated by fog. Heavy fog brings great troubles to traffic and probably causes serious accidents [1]. Vehicles such as cars, buses and planes are expected to keep safe if some visual systems are loaded to enhance the images in the field of view when they are running in the fog. The technology on removing fog from single images by digital image processing attracts increasing interests in the recent decades [2]. Matan Sulami et al. developed a method for recovering the atmospheric light vector in hazy scenes and obtained a more successful recovery[3]. Raanan Fattal presented a method to estimate the optical transmission to increase scene visibility and improve the fog-free scene contrasts[4].

The dual tree complex wavelet transformation (DTCWT) has the prominent properties including improved angular resolution, approximate shift invariance and perfect reconstruction superior to the conventional wavelet transform. It is expected to divide information more accurately and reconstruct images with fewer losses. Hu et al proposed the algorithm which combines a dual tree complex wavelet transform with domain adaptation transfer least square support vector regression to remove cloud and fog[5]. In this paper, we propose a DTCWT based algorithm to optimize coefficients of sub-bands at high levels and at low levels respectively to remove fog from single images. It proves that the proposed algorithm achieves satisfactory results and is better than the wavelet transform processing and Retenix.

The remainder of this paper is organized as follows. In Section 2 the fundamental principle of DTCWT was reviewed. In Section 3, a novel DTCWT based algorithm to remove fog from single remote sensing images was proposed by analyzing the characteristics of sub-band coefficients of DTCWT. Procedures to optimize sub-band coefficients were described in detail. The processing steps were presented completely. In Section 4 some experiments were carried out to validate the proposed algorithm. Their results were compared and analyzed. Finally in Section 5 some important conclusions were drawn.

2. Dual tree complex wavelet transform

According to Kingsbury, the complex scaling function and the complex wavelet function in 1 dimension are defined as

$$\varphi^c(t) = \varphi_h(t) + j\varphi_g(t) \tag{1}$$

and $$\phi^c(t) = \phi_h(t) + j\phi_g(t) \tag{2}$$

where j is the imaginary unit, and $\phi_h(t)$ and $\phi_g(t)$ should be designed to be the Hilbert transform of each other approximately in order to achieve the prominent features of DTCWT. The real parts use a filter bank different from that of the imagery parts in Eq.(1) and Eq.(2). We call them real filter bank and imaginary filter bank. Suppose the analytical filters of the real filter bank are denoted as H_0 and H_1, and those of the imaginary filter bank are G_0 and G_1. The subscript 1 represents high pass filter and 0 represents low pass filter.

DTCWT can be implemented by carrying out the real wavelet transformations in a real tree and an imaginary tree respectively [6]. As for 2-D DTCWT, the relative sub-bands of two trees such as the horizontal, vertical and diagonal detailed coefficients perform addition and subtraction operations respectively to produce six directional sub-bands at each level. Their orientations of these sub-bands are 75°,15°,-45°, -75°,-15° and 45° respectively.

When an image is decomposed into n levels by DTCWT, we obtain high-frequency sub-bands at each level and low-frequency sub-bands at last level which is similar to the 2-D

real wavelet transform. The sub-bands at low levels have higher frequencies than those at high levels.

3. Fog removal from single images

3.1. Basic scheme

In images disturbed by fog, the fog has lower frequencies than the scenery. Therefore, we decompose the original image to n levels by DTCWT and select an appropriate integer l from 1 to n to separate fog from scenery in high frequency sub-bands according to their frequency relationships. Fog should be allotted to the high-level high frequency sub-bands and low frequency sub-band as more as possible. Then, fog removal will be achieved by processing these sub-bands. At the same time, low-level high frequency sub-bands are enhanced to sharpen the scenery and weaken the residual fog.

Furthermore, the fog is usually distributed uniformly in the images. The fog information has very low frequencies, and is mainly located in the low-frequency sub-band. Therefore, our basic scheme of fog removal is process the high-frequency sub-bands at low levels and low-frequency sub-band. Their coefficients are optimized. And the high-frequency sub-bands at high levels are unchanged.

3.2. High frequency sub-band enhancement

The guided filter proposed by He Kaiming performs as an edge-preserving smoothing operator. When it is modified as Eq.(3), a sharpening filter is obtained which enhances the detailed image information and preserves the approximated information.

$$J(x,y) = G\{I(x,y)\} + k \times [I(x,y) - G\{I(x,y)\}] \qquad (3)$$

where I is the input image, and J is the output image. $G\{\}$ stands for the guided filtering. k should be larger than 1 in order to strengthen information with high frequencies.

Since the scenery distributes mainly in the high-frequency sub-bands at low levels, we process their coefficients according to Eq.(3) to strengthen the scenery. At the same time, the residual fog in those sub-bands will also be weakened when the contrast is improved.

3.3. Sub-band coefficient optimization

The atmosphere transmission theory indicates that the imaging degradation process disturbed by fog can be described as

$$J(x,y)=I(x,y)\times t(x,y)+A\times(1-t(x,y)) \qquad (4)$$

where J is the degradation image, and I is the fog free image. t stands for the atmosphere transmission coefficient. A is the global atmospheric light which has three elements corresponding to three color channels.

The dark channel prior proposed by He Kaiming in 2009 pointes out the most pixels representing scenery in fog-free outdoor images have at least one color channel whose gray value is close to 0. Therefore, the dark channel of the image I can be assumed to be 0. When we calculate the dark channels of all images in Eq.(4), we obtain the atmosphere transmission coefficient among the neighborhood Ω centering at (x,y) is

$$t(x,y) = 1 - \min_{c \in \{r,g,b\}} \{ \min_{(i,j) \in \Omega} [\frac{J^c(i,j)}{A^c}] \} \qquad (5)$$

where c stands for one of the r, g and b channels.

Then, based on Eq.(4) the image I can be deduced as

$$I = \frac{J - A}{max(t, t_0)} + A \qquad (6)$$

where t_0 is the threshold value in order to acquire a better result.

High frequency sub-bands at low levers represent mainly scenery. After they are processed by guide filtering, the residual fog is rare. On the contray, the low frequency sub-band has most of the fog. Thus, according to Eq.(6), the correspoding scenry in these sub-band will be improved and the contained fog can be decreased significantly. Therefore, their coefficients are optimized.

3.4. Fog removal algorithm description

Fog removal algorithm proposed in this paper is as shown in Fig.1 where the numbers 1 to 6 stand for the six directional sub-bands.

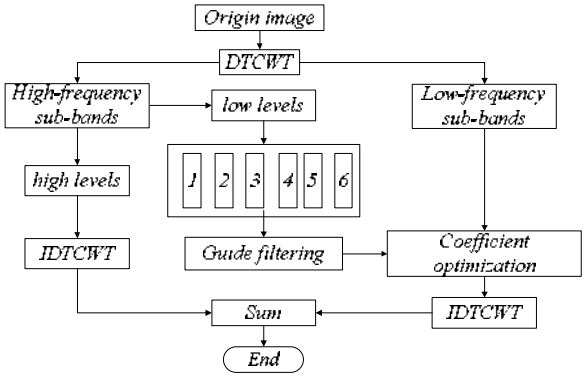

Figure 1: Flowing chart of fog removal algorithm

(1) The original image is decomposed to n levels by DTCWT. An integer l is chosen to separate the clouds from the scenery as far as possible. Suppose the pixel numbers along the column and the row of the image are M and N respectively, and then based on the theory of the DTCWT n is determined as

$$n = floor[\log_2 \min(M,N)] - 2 \qquad (7)$$

where *floor* is the function to calculate the nearest integer less than the number in the bracket.

(2) Process the low-level high frequency sub-bands in every direction and at each level. Each sub-band at 1 to l levels is processed according to Eq.(3).

(3) Low frequency sub-band and the processed sub-bands from Step (2) are combined together, and their coefficients

are optimized according to Eq.(6) before their combination is reconstructed by the inverse DTCWT.

(4) High-level high frequency sub-bands are reconstructed by the inverse DTCWT, and are added to the results from (3) to produce the final output image.

4. Experiments and results

Choose two original images as shown in Fig.2 in our experiments. These images have 512×512 pixels both. Therefore, their DTCWT decomposition levels are both 7.

Fig.2(a) is an image contaminated by a little thick fog. The buildings far away are much vaguer than the front figures and trees. They can not be distinguished easily. Fig.2(b) is a remote sensing image captured from a plane which is covered by thin fog. It looks to be bleached.

After they are processed according to the proposed algorithm, we obtain Fig.3(a) and Fig.3(c) respectively. The images become clear. Their details are sharpened at length. In Fig.3(a) all the scenery is improved although the image becomes a little dark. Since the fog appears bright, fog removal will darken the image. Fig.3(c) provides a very clear ground. The results prove the proposed algorithm is satisfactory.

Fig.3(b) and Fig.3(d) are obtained according to Retinex[7] which needs further improvement. Although the images are recovered in some degrees, the residual fog remains. Further, based on the dark channel prior we process Fig.3(a) and Fig.3(c) and obtain Fig.3(e) and Fig.3(f) respectively. It illustrates that the dark channel prior achieves a good fog removal effect. However, the details are still expected to be enhanced.

(a) (b)

Figure 2: Original images

The average brightness, the standard deviation, the entropy and the local phase coherence are used to evaluate the results above. When the images are processed by the fog removal algorithm, the average brightness will reduce, the standard deviation will increase. Larger entropy implies more information will be contained in the images. The normal value of the local phase coherence is less than 1, and greater values stands for better details. They are abbreviated to be B, S, E and LPC. Their values of the results in Fig.3 are presented in Table 1 where DCP is the abbreviation of the dark channel prior. It shows that the proposed algorithm based on DTCTWT has less average brightness than Retinex and the dark channel prior. As for Fig.2(a) , the proposed algorithm acquires better standard deviation and local phase coherence. In processing Fig.2(b), it has better entropy and local phase coherence. Therefore, the proposed algorithm based on DTCTWT achieves satisfactory results.

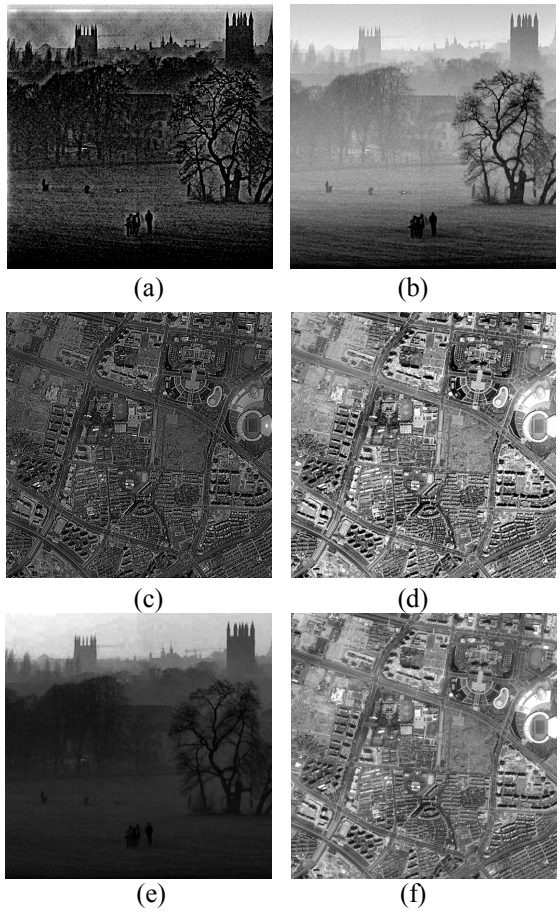

(a) (b)

(c) (d)

(e) (f)

Figure 3: Processing results

Table 1: Index comparison between algorithms.

Fig.2	Approach	B	S	E	LPC
(a)	Origin	127.06	51.02	5.98	0.8100
	DTCWT	17.32	**63.59**	5.56	**0.9476**
	Retinex	128.73	61.12	5.42	0.9207
	DCP	63.73	60.30	**6.41**	0.9175
(b)	Origin	155.46	26.08	3.23	0.8835
	DTCWT	62.69	44.85	**7.59**	**0.9423**
	Retinex	128.73	**61.12**	5.42	0.9207
	DCP	112.73	48.88	6.68	0.9193

5. Conclusions

Fog removal from single images by image processing can recover the clear scenery efficiently. Fog has lower frequencies than the scenery in the images disturbed by fog. Images will be decomposed to produce six directional sub-bands by 2-D DTCWT once. Sub-bands at low levels have higher frequencies than those at high levels after the image is decomposed by 2-D DTCWT with multiple levels.

Setting a number will separates fog from scenery and distributes them to high frequency sub-bands at high levels and those at low levels. The guided filtering is helpful to enhance the scenery information. Fog removal is satisfactory by implementing the DTCWT based algorithm by optimizing the coefficients.

Acknowledgements

The work was sponsored by the National Natural Science Foundation of China under Grant No. 61475027 and No. 61875022, the Top-notch Academic Programs Project of Jiangsu Higher Education Institutions (TAPP) under Grant No.PPZY2015B129, Changzhou Key Laboratory of Applied Technology on Intelligence & Unmanned Aerial Vehicle under Grant No. CM20173003, Jiangsu Collaborative Innovation Center for Cultural Creativity under Grant No. XYN1701, National Natural Foundation of Colleges and Universities under Grant No. 201711055003 , and National Undergraduate Training Programs for Innovation and Entrepreneurship under Grant No.201911055006 in China.

References

[1] Qingsong Zhu,, Jiaming Mai, and Shao, Ling, A fast single image haze removal algorithm using color attenuation prior, *IEEE Transactions on Image Processing* 24:3522-3533, 2015.

[2] I.W. Selesnick, R.G. Baraniuk, N.G. Kingsbury, The dual-tree complex wavelet transform, *IEEE Signal Processing Magazine* 22: 123-151,2005.

[3] Sulami, Matan, et al., Automatic recovery of the atmospheric light in hazy images, *Proc. IEEE Int. Conf. on Computational Photography* ,IEEE, USA, pp.1-11, 2014.

[4] Fattal R, Dehazing using Color-Lines ,*ACM TRans. Graph.* , 34,1 ,pp.1-14 ,2014.

[5] Hu, Gensheng, X. Li, and D. Liang, Thin cloud removal from remote sensing images using multidirectional dual tree complex wavelet transform and transfer least square support vector regression, *Journal of Applied Remote Sensing* 9, 1: 095053, 2015.

[6] Singh D , Kumar V., Single image haze removal using integrated dark and bright channel prior, *Modern Physics Letters B* 32:1850051, 2018.

[7] Yao L, Lin Y, Muhammad S., An Improved Multi-Scale Image Enhancement Method Based on Retinex Theory, *Journal of Medical Imaging & Health Informatics* 8:122-126, 2018.

Antennas and propagation

A numerical simulator for transmit-array antenna design and performance evaluation

Jeanne Pagés-Mounic[1], Hamza Kaouach[2], André Barka[1],

[1]ONERA/DEMR, Université de Toulouse, 2 avenue Edouard Belin 31055 Toulouse, France
[2] LAPLACE laboratory, Toulouse INP-ENSEEIHT, University of Toulouse, CNRS, Toulouse 31071, France
E-mail: jeanne.pages_mounic@onera.fr

Abstract

This paper describes a hybrid simulation method devoted to quick design and simulation of transmit-array antennas operating in the Ka band. The simulated radiation patterns of a 30 dBi gain discrete lens antenna [1] computed with this simulator will be compared with full-wave simulations and measurements [2].

1. Introduction

Many applications nowadays use beam-reconfigurable antenna commands that provide fast and accurate beam-steering. Currently, the applications are mainly related to the space sector, from L-band to Ka-band, short-range and high-rate communication systems in V and W bands, radar and driving assistance. To meet these needs, the solution investigated by several authors is the use of planar arrays in transmission (transmit-arrays) [3, 4].

A transmit-array antenna consists of two arrays of radiating elements illuminated by a focal source. The two arrays are interconnected by intermediate circuits which serve to modify the phase quantization and the amplitude of the wave and thus to control the direction and the shape of the antenna radiation pattern. This lens can be moved along one direction (x) and the primary source is placed on one side of the lens (Figure 1).

The focal source illuminates the first array with a spherical wave front that will be reradiated by the second array with a plane wave front. The direction α(a) of the wave depends on the position of the source with respect to the array [1].

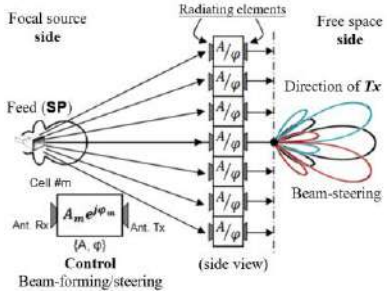

Figure 1: Principle of a transmit-array in transmit mode

A hybrid analytical tool has been developed for a quick design and computation of the performance of transmit-arrays. First the electromagnetic characteristics of the elementary cell and the focal source are obtained with commercial software (such as Ansoft HFSS, CST MWS or FEKO for example). The complex radiation pattern of the focal source is first used to determine the electric field distribution illuminating the receive antennas array (*Rx*). The complex radiation patterns and S-parameters of each elementary cell are then used to evaluate the radiation performances of the transmit-array.

The simulator is also of interest to study the impacts of the different design parameters (focal length, cells size, phase quantization ...) on the transmit-array performances (directivity, gain, side lobes level, beam steering ...).

2. Equations governing the simulator

The main challenge of the transmit-array design is the ability to generate the appropriate phase-shift for each unit cell in order to transform the incoming spherical wave radiated by the focal source into a plane wave on the free-space side. The objective is to generate a given phase gradient depending on the main beam direction.

2.1. Perfect quantization

Consider a generic unit cells array illuminated by a focal source placed at (0, 0, -F) where F is the focal distance. The phase distribution of the incident electric field on the receive array is given by:

$$\Phi_{inc}(x,y) = -k_0\sqrt{(x-a)^2+y^2+F^2} \quad \text{(Eq. 1)}$$

where a represents the shifting distance of the focal source along the x axis. The transmit-array is designed so as to introduce the required phase correction $\Phi_{lens}(x,y)$ to transform the spherical phase front into a plane wave front. The phase correction provided by the lens is then defined by:

$$\Phi_{lens}(x,y) = k_0\sqrt{x^2+y^2+F^2} - k_0\, x\, sin(\alpha_0) \quad \text{(Eq. 2)}$$

The phase distribution in the second array level (free space side) is given by:

$$\Phi_{out}(x,y) = \Phi_{inc}(x,y) + \Phi_{lens}(x,y)$$

$$\Phi_{out}(x,y) = -k_0\sqrt{(x-a)^2+y^2+F^2} + k_0\sqrt{x^2+y^2+F^2} - k_0\, x \sin(\alpha_0) \quad \text{(Eq. 3)}$$

For the central position $a = 0$ (reference point), the phase of the reradiated wave is:

$$\Phi_{out}(x,y) = -k_0\, x \sin(\alpha_0) \quad \text{(Eq. 4)}$$

This phase corresponds to a α_0-orientation of the beam in elevation as desired.

$\Phi_{lens}(x,y)$ defines the perfect compensation, but in reality it is very complex to realize it. In order to simplify the design process, it is recommended to get the optimal compromise between the phase quantization and the transmit-array performances.

2.2. N-bit quantization

The principle of this compensation is to provide the elementary cells with a number of phase states allowing them to create a more or less precise phase shift as a function of the number N of bits chosen [5]. The link in terms of number of bits, phase states (PE) and phase shift is given in the table below. For this case, a maximum range between 0° and 360° and a variable k which is a natural integer between 0 and 2^N -1 have been chosen.

Table 1: Link between the number of bits, phase states and phase shifts

N number of bits	Number of PE	Phase shifts
$N \in \mathbb{N}^*$	2^N	$k \times \frac{360}{2^N}$
1	2	0° - 180°
2	4	0° - 90° - 180° - 270°
3	8	0° - 45° - 90° - 135° - 180° - 225 ° - 270° - 315°

3. Effects of the overall system

This tool is better adapted for a periodic array and it allows to evaluate the radiation in free space side, that is, in the red area of the figure 2, when $\theta \in [-90°; 90°]$. Outside this range, it is a reflect-array effect instead of a transmit-array.

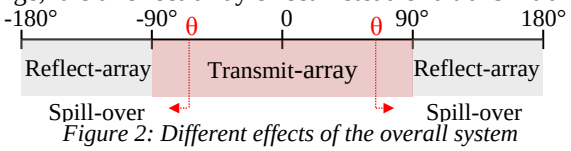

Figure 2: Different effects of the overall system

4. Simulation of a 30 GHz lens antenna [1]

The full wave simulation of the Fresnel lens presented in [1] requires considerable computation effort. Indeed, the lens is composed by 77 columns and 57 rows of unit cells of in-plane width P=2.5 mm. The dimensions of the lens is 192.5 mm x 142.5 mm (19.25λ x 14.25λ at 30 GHz) corresponding to a maximum directivity of 35.4 dBi and the electromagnetic problem to be solved is non-periodic. The single band lens we would like to calculate with the hybrid analytical tool is composed of 4389 phase-shifting cells chosen among 63 different constitutive unit cells. These unit cells are composed by five metallized layers of concentric squared patches on four substrate layers of Rogers Duroid 5880 (ε_r=2.2 and tan δ = 0.0009). The periodic simulation methods are therefore unusable here, whereas conventional full wave simulators require very important computing times and RAM memory.

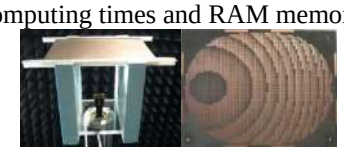

Figure 3: Single band 30 dBi lens antenna [1] (DOI:10.1109/TAP.2015.2484419)

The lens is illuminated with a standard 14.5 dBi horn antenna oriented such that the E-field is parallel to the shortest side of the horn. The horn is positioned at the focal distance F=100 mm below the lens and the analysis is done at 30 GHz (Figure 3). The 30 dBi full lens problem including the horn source is calculated with the hybrid tool. The gain diagrams obtained are considered acceptable compared to measurements, and simulations using CST MWS (Finite Difference Time Domain solver), ANSYS HFSS (Finite Element solver) and ONERA FACTOPO (Finite Element Tearing and Interconnecting solver) softwares [6] (Figure 4). Indeed, the main lobe position and level is well captured by all the methods but the hybrid tool does not take into account the lens's edges diffractions which induce very low side lobes (corresponding to grazing incidences).

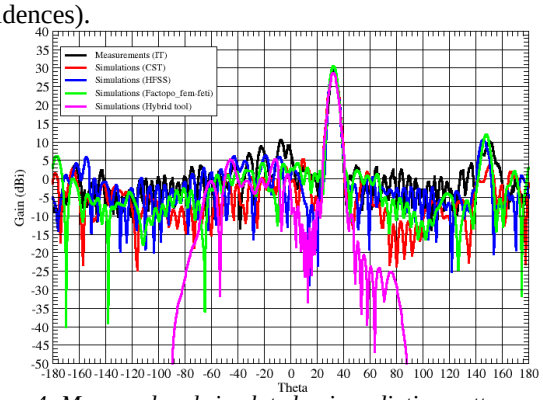

Figure 4: Measured and simulated gain radiation patterns with a centered horn source

5. Conclusions

The hybrid simulator developed in this study calculates efficiently the performances of transmit-arrays without taking into account the lens's edge diffractions. In the future, the simulator will be used to optimize the design of transmit-array antennas with limited ratio F/D in the aim of improving the compactness. The tool will be improved to take into account spill-over losses in the gain diagrams.

References

[1] E. B. Lima, S. A. Matos, J. R. Costa, C. A. Fernandes, and N. J. G. Fonseca, « Circular Polarization Wide-Angle Beam Steering at Ka-Band by In-Plane Translation of a Plate Lens Antenna », IEEE Trans. Antennas Propag., vol. 63, no 12, p. 5443‑5455, Dec. 2015.

[2] A. Barka, S. Matos, J. R. Costa, and C. A. Fernandes, « Assessment of FETI DDM methodologies for the simulation of high gain Ka-band transmit arrays », in 2017 International Symposium on Antennas and Propagation (ISAP), 2017.

[3] S. Ye, X. Liang, W. Wang, R. Jin, J. Geng, T. S. Bird, and Y. J. Guo, "High-Gain Planar Antenna Arrays for Mobile Satellite Communications," IEEE Antennas and Propag. Mag., vol. 54, No. 6, pp. 256 - 268, Dec. 2012.

[4] J. R. Costa, C. A. Fernandes, G. Godi, R. Sauleau, L. Le Coq, and H. Legay, "Compact Ka-Band Lens Antennas for LEO Satellites", IEEE Trans. Antennas and Propag., vol. 56, pp. 1251 - 1258, May 2008.

[5] H. Kaouach, L. Dussopt, R. Sauleau, and T. Koleck, « Design and demonstration of 1-bit and 2-bit transmit-arrays at X-band frequencies », in 2009 European Microwave Conference (EuMC), 2009, p. 918‑921.

[6] F. Roux and A. Barka, « Block Krylov Recycling Algorithms for FETI-2LM Applied to 3-D Electromagnetic Wave Scattering and Radiation », IEEE Transactions on Antennas and Propagation, vol. 65, no 4, p. 1886‑1895, April. 2017.

A Helically Shaped With Open Ended Reflector Probe Design For ISM Band Microwave Ablation System

Caner Murat[1], Merih Palandöken[1], Adnan Kaya[1], Irfan Kaya[2]

[1]Department of Electric and Electronic Engineering, Izmir Katip Celebi University, Izmir, Turkey,
[2]Department of Mechanical Engineering, Eskisehir Technical University, Eskisehir, Turkey
caner.murat35@gmail.com

Abstract

This paper purposes a Helically Shaped With Open Ended Reflector Probe (HSOERP) design as a part of microwave ablation (MWA) system operating at Industrial Scientific Medical (ISM) band for the local destruction of tumor cells with high microwave power. HSOERP is designed by wrapping the helix geometry around a dielectric material of the probe and building an open ended reflector structure around the helix geometry.

1. Introduction

Breast cancer is one of the most vital problems epitomized by unrestrained cell proliferation in complex and unpredictable ways today [1]. Because of the proliferation of the cancer cell to the circulatory or lymphatic system, a metabolic derangement called metastasis occurs [2]. The purpose of treatment is to stop the undesirable cell proliferation resulting metastasis, to prevent migration by execution these beleaguered cells [3, 4]. A major issue in classical clinical therapies is to overdose with the drug, which can be harmful for healthy cells [5]. In classical treatment, extermination of tumorous cells cannot be achieve due to the development of drug resistance that gets to diminish the effectiveness of tumorous cells, and metastatic formations, particularly [6]. Hence, there has been a need to develop methods to support classical therapy, reduce the dose of the drug and provide less damage to normal cells.

In microwave ablation, a microwave probe placed around the tumorous cells in near field region in order that microwave energy supplied by the probe at 2.45 GHz, leads to the tumorous cell to die with a temperature above 60 °C [7-10]. For the purpose of generation a microwave power which can heat the tumor above 60 °C, it is required to localize the electromagnetic radiation of the microwave ablation probe placed near the radiation edge section (Figure1.a). HSOERP modeled from the knowledge of directional electromagnetic radiation of helix radiator geometry and open ended reflector structure so that obtain high electromagnetic power in the near field area.

In this paper, HSOERP is proposed for microwave ablation systems operating in 2.45 GHz ISM band with the numerical computation and optimization results. The paper is structured in the following manner. The proposed probe geometry and S parameters are presented in Section 2. The numerical computation results of the electric field SAR values are demonstrated in Section 3 along with the numerical computations of various geometric parameters. The concluding remarks and discussions are presented in Section 4.

2. Microwave Probe Design

In order to create the localized electromagnetic radiation to the area to be ablated, the microwave ablation probe is designed by wrapping the helical wire which is 1mm diameter around the probe part called radiation edge placed inside an open ended reflector . By integrating helix geometry and open ended reflector structure into the probe model, HSOERP generates localized electromagnetic radiation. The number of windings of 1mm diameter copper wire, which forms the helix shape, is one of the points settling the frequency value that HSOERP resonates. Numerical computations for the deciding of the number of windings that provide the resonance frequency in the ISM band are shown in section 3. The modeled HSOERP is shown in Figure 1

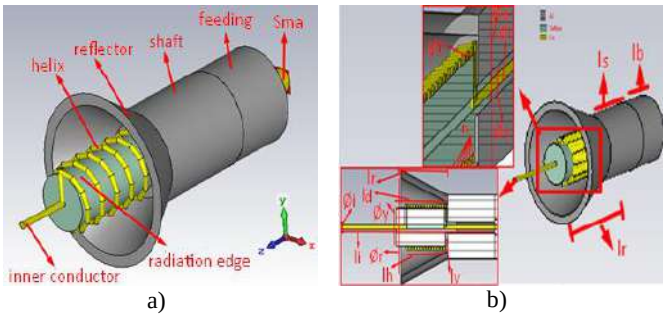

a) b)

Figure 1: a) HSOERP sections b) Material and length information of HSOERP

The optimized parameters of HSOERP whose number of windings are determined in an attempt to obtain minimal S parameter at 2.45 GHz are indicated into a table. The optimized parameters of HSOERP specified in Table 1.

Table 1: Dimensions of HSOERP and the number of windings in the helix section.

lb (mm)	ls (mm)	ld (mm)	lr (mm)	li (mm)	lv (mm)	lh (mm)
22.5	30	20	20	78.5	1	17
Øo (mm)	Øi (mm)	Øs (mm)	Ød (mm)	Ør (mm)	Øt (mm)	n
17	1.25	3	10	30	1	14

3. Numerical Computation Results

Numerical calculations have been made in order to determine the number of windings so that the return loss of HSOERP is minimum at the frequency of 2.45 GHz. As specified in Figure 2, the S parameters of the HSOERP models that have a different number of windings are respectively; 13.56 dB, 13.52 dB and -12.66 dB for the number of windings are 13, 14 and 15. Despite the fact that the numerical calculation results shown in Figure 2 are close to each other, the number of windings is selected to 14 because the center frequency of HSOERP is at 2.45 GHz.

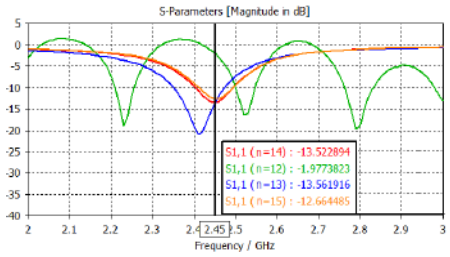

Figure 2: S parameters of HSOERP with changing the number of windings

Once designing a probe to be ablated in microwave ablation systems, it is required to calculate the S parameter of HSOERP with optimised parameters. Therefore, HSOERP is numerically computed in CST Microwave Studio with the parameters shown in Table1

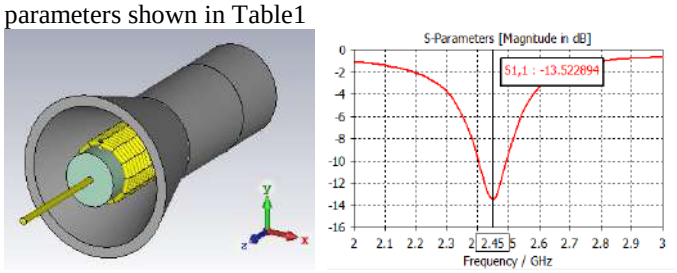

a) b)

Figure 3: a) Simulation mechanism of HSOERP b) S parameter of HSOERP

As specified in Figure 3.b, the resonant frequency of HSOERP is at ISM band with -13.52 dB return loss value.

4. Conclusions

In this paper, HSOERP design is suggested to operate in ISM band in high power medical applications. The HSOERP structure is combined with radiation edge, a helical radiator, and open ended reflector in order to allow microwave energy to be delivered into the ablation region with increased electric field density. The numerical model of HSOERP structure has been optimized for the microwave ablation applications at 2.45 GHz. In future work, electric field and SAR values of HSOERP in the center of tumor surface can be observed as satisfactory high value.

Acknowledgements

This work has been supported by the Project 117E811 of TUBITAK (Scientific and Technological Research Council of Turkey).

References

[1] R. Doll and R. Peto, "The causes of cancer: quantitative estimates of avoidable risks of cancer in the United States today," Journal of the National Cancer Institute, vol. 66, pp. 1192-1308, 1981.

[2] Liu, G., Guo, J., Li, Y., Fan, Z., Chen, T., Wang, C., ... & Wei, X. (2010, December). Studying cancer metastasis potential by in-vivo flow cytometry and imaging. In Communications and Photonics Conference and Exhibition (ACP), 2010 Asia (pp. 375-376). IEEE.

[3] G. R. Mundy, "Metastasis: Metastasis to bone: causes, consequences and therapeutic opportunities," Nature Reviews Cancer, vol. 2, pp. 584-593, 2002.

[4] M. Vanneman and G. Dranoff, "Combining immunotherapy and targeted therapies in cancer treatment," Nature Reviews Cancer, vol. 12, pp. 237-251, 2012

[5] D. E. Fisher, "Apoptosis in cancer therapy: crossing the threshold," Cell, vol. 78, pp. 539-542, 1994.

[6] K. Miller, M. Wang, J. Gralow, M. Dickler, M. Cobleigh, E. A. Perez, et al., "Paclitaxel plus bevacizumab versus paclitaxel alone for metastatic breast cancer," New England Journal of Medicine, vol. 357, pp. 2666-2676, 2007.

[7] J. P. McGahan, J. M. Brock, H. Tesluk, W.-Z. Gu, P. Schneider, and P. D. Browing, "Hepatic ablation with useof radiofrequency electrocautery in the animal model." J. Vasc. Inter. Radiol., vol. 3, pp. 291-297, 1992.

[8] REIMANN, Carolin, et al. Microwave Ablation Applicator with Sensing Capabilities for Thermal Treatment of Malignant Tissue. In: 2018 IEEE/MTT-S International Microwave Symposium-IMS. IEEE, 2018. p. 1278-1281.

[9] SCHENA, E.,et al.Thermometry based on computed tomography images during microwave ablation:Trials on ex vivo porcine liver. In: Instrumentation and Measurement Technology Conference (I2MTC), 2017 IEEE International. IEEE, 2017. p. 1-6.

[10] TAL, Nikolay; LEVIATAN, Yehuda. A minimally invasive microwave ablation antenna. In: Microwaves, Antennas, Communications and Electronic Systems (COMCAS), 2017 IEEE International Conference on. IEEE, 2017. p. 1-3.

A Helically Shaped With Closed Ended Reflector Probe Design For ISM Band Microwave Ablation System

Caner Murat[1], Merih Palandöken[1], Adnan Kaya[1], Irfan Kaya[2]

[1] Department of Electric and Electronic Engineering, Izmir Katip Celebi University, Izmir, Turkey
[2]Department of Mechanical Engineering, Eskisehir Technical University, Eskisehir, Turkey
caner.murat35@gmail.com

Abstract

This paper purposes a Helically Shaped With Closed Ended Reflector Probe (HSCERP) design as a part of microwave ablation (MWA) system operating at Industrial Scientific Medical (ISM) band for the local extirpation of tumor cells with high microwave power. HSCERP is designed by wrapping the helix geometry around a dielectric material of the probe and building a close ended reflector structure around the helix geometry.

1. Introduction

Nowadays, breast cancer is one of the most crucial problems characterized by uncontrolled cell proliferation in complex and unpredictable ways [1]. Owing to the proliferation of the cancer cell to the circulatory or lymphatic system, a metabolic derangement called metastasis occurs. [2]. The purpose of treatment is to stop the unpleasant cell proliferation resulting from metastasis, to prevent migration by killing these beleaguered cells [3, 4]. A major difficulty in classical clinical therapies is to overdose with the drug, which can destroy healthy cells [5]. In classical treatment, the destruction of tumorous cells cannot be achieve due to the development of drug resistance that is get to dilute the effectiveness of tumorous cells, and metastatic formations, specifically. [6]. Thus, there has been a need to develop methods to support classical therapy, reduce the dose of the drug and provide less damage to normal cells.
In microwave ablation, a microwave probe positioned around the tumorous cell in near field region in order that microwave energy supplied by the probe at 2.45GHz, brings the tumorous cells about to die with a temperature above 60°C [7-10]. In order to produce a microwave power that can heat tumorous cells above 60°C, it is essential to localize the electromagnetic radiation of the microwave ablation probe positioned near the radiation tip section (Figure1.a). HSCERP modeled from the knowledge of directional electromagnetic radiation of the model of helix radiator and closed ended reflector structure for the purposes of achievement high electromagnetic power in the near field region.

In this paper, HSCERP is proposed for microwave ablation systems operating in 2.45 GHz ISM band with the numerical computation and optimization results. The paper is structured in the following manner. The proposed probe geometry and S parameters are presented in Section 2. The numerical computation results of the electric field SAR values are demonstrated in Section 3 along with the numerical computations of various geometric parameters. The concluding remarks and discussions are presented in Section 4.

2. Microwave Probe Design

In order to make the concentrated electromagnetic radiation to the area to be ablated, the microwave ablation probe is designed by wrapping the helical wire which is 1mm diameter around the probe part called propagation tip placed inside a close ended reflector. By integrating helix geometry and closed ended reflector structure into the probe model, HSCERP generates localized electromagnetic radiation. The number of windings of 1mm diameter copper wire, which forms the helix shape, is one of the features deciding the frequency value that HSCERP resonates. Numerical calculations for the settling of the number of windings that provide the resonance frequency in the ISM band are shown in section 3. The modeled HSCERP is shown in Figure 1

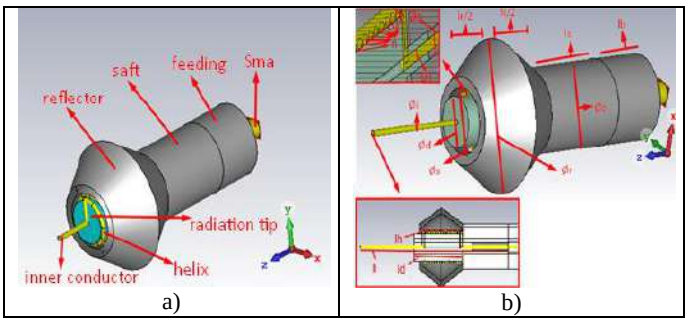

Figure 1: a) HSCERP sections b) Material and length information of HSCERP

The optimized parameters of HSCERP whose number of windings are determined in order to obtain minimal return loss at 2.45GHz are specified into a table. The optimized parameters of HSCERP are indicated in Table 1.

Table 1: Dimensions of HSOERP and the number of windings in the helix section.

lb (mm)	ls (mm)	ld (mm)	lr (mm)	li (mm)	lv (mm)	lh (mm)
22.5	30	20	20	80	1	17
Øo (mm)	Øi (mm)	Øs (mm)	Ød (mm)	Ør (mm)	Øt (mm)	n
17	1.25	3	10	30	1	14

3. Numerical Computation Results

Numerical calculations have been made in order to determine the number of windings so that the return loss of HSCERP is minimum at the frequency of 2.45 GHz. As indicated in Figure 2, the S parameters of the HSOERP models that have a different number of windings are respectively; -19.26dB, -16.32dB and -15.23dB for the number of windings are 13, 14 and 15. Though the numerical calculation results shown in Figure 2 are close to each other, the number of windings is selected to 14 because the center frequency of HSOERP is at 2.45GHz.

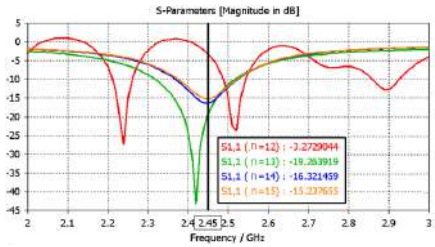

Figure 2: S parameters of HSOERP with changing the number of windings

While designing a probe to be ablated in microwave ablation systems, it is needed to compute the S parameter of HSCERP with optimised parameters. Therefore, HSOERP is simulated in CST Microwave Studio with the parameters specified in Table1

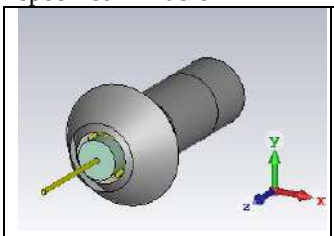

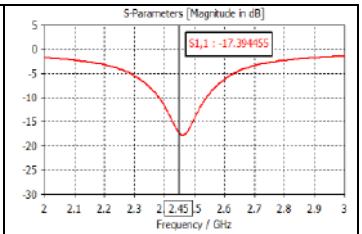

Figure 3: a) Simulation mechanism of HSCERP b) S parameter of HSCERP

As shown in Figure 3.b, the return loss value of HSOERP is -13.52dB with the resonant frequency is at ISM band.

4. Conclusions

In this paper, HSCERP design is put forward to operate in the ISM band in high power medical applications. The HSCERP structure is combined with radiation tip, a helical radiator and closed ended reflector in an attempt to allow microwave energy to be delivered into the tumorous cells placed in petri dishes with increased electric field density. The numerical model of HSCERP geometry has been optimized for the microwave ablation applications at 2.45 GHz. The electric field and SAR values of HSOERP in the center of tumor surface can be observed as satisfactory high value in future work.

Acknowledgements

This work has been supported by the Project 117E811 of TUBITAK (Scientific and Technological Research Council of Turkey).

References

[1] R. Doll and R. Peto, "The causes of cancer: quantitative estimates of avoidable risks of cancer in the United States today," Journal of the National Cancer Institute, vol. 66, pp. 1192-1308, 1981.

[2] Liu, G., Guo, J., Li, Y., Fan, Z., Chen, T., Wang, C., ... & Wei, X. (2010, December). Studying cancer metastasis potential by in-vivo flow cytometry and imaging. In Communications and Photonics Conference and Exhibition (ACP), 2010 Asia (pp. 375-376). IEEE.

[3] G. R. Mundy, "Metastasis: Metastasis to bone: causes, consequences and therapeutic opportunities," Nature Reviews Cancer, vol. 2, pp. 584-593, 2002.

[4] M. Vanneman and G. Dranoff, "Combining immunotherapy and targeted therapies in cancer treatment," Nature Reviews Cancer, vol. 12, pp. 237-251, 2012

[5] D. E. Fisher, "Apoptosis in cancer therapy: crossing the threshold," Cell, vol. 78, pp. 539-542, 1994.

[6] K. Miller, M. Wang, J. Gralow, M. Dickler, M. Cobleigh, E. A. Perez, et al., "Paclitaxel plus bevacizumab versus paclitaxel alone for metastatic breast cancer," New England Journal of Medicine, vol. 357, pp. 2666-2676, 2007.

[7] J. P. McGahan, J. M. Brock, H. Tesluk, W.-Z. Gu, P. Schneider, and P. D. Browing, "Hepatic ablation with useof radiofrequency electrocautery in the animal model." J. Vasc. Inter. Radiol., vol. 3, pp. 291-297, 1992.

[8] REIMANN, Carolin, et al. Microwave Ablation Applicator with Sensing Capabilities for Thermal Treatment of Malignant Tissue. In: 2018 IEEE/MTT-S International Microwave Symposium-IMS. IEEE, 2018. p. 1278-1281.

[9] SCHENA, E.,et al.Thermometry based on computed tomography images during microwave ablation:Trials on ex vivo porcine liver. In: Instrumentation and Measurement Technology Conference (I2MTC), 2017 IEEE International. IEEE, 2017. p. 1-6.

[10] TAL, Nikolay; LEVIATAN, Yehuda. A minimally invasive microwave ablation antenna. In: Microwaves, Antennas, Communications and Electronic Systems (COMCAS), 2017 IEEE International Conference on. IEEE, 2017. p. 1-3.

Wideband Curved Patch Antenna

Vesna Radisic[1*], Jimmy Hester[1,2], Stéphane Larouche[1]

[1]Northrop Grumman Corporation, Redondo Beach, CA, USA
[2]School of Electrical and Computer Engineering, Georgia Tech, Atlanta, GA, USA
*corresponding author, E-mail: vesna@ieee.org

Abstract

In this paper, we introduce a concept to engineer and extend the bandwidth of patch antennas by controlling and designing substrate thickness profile. This concept was validated by HFSS simulation. A concave patch with sinusoidal substrate height profile shows good simulated return loss from 10 to 20 GHz. Simulated three-dimensional radiation patterns are also shown. This antenna can be fabricated using additive manufacturing

1. Introduction

A patch antenna is a type of printed antenna that is used heavily due to its low profile and easy fabrication. It consists of a metal sheet separated from a groundplane by a dielectric substrate forming a resonant cavity with a length of about half wavelength ($\lambda/2$) at the operating frequency. The resonant nature of this type of antenna results in narrowband performance, which is a drawback of this type of antenna.

For some applications, there is a need to place a patch antenna on a curved surface, such as a cylinder. Common applications include the surface of an aircraft, car radio antennas, and cellular base station antennas. As these applications focus on convex surfaces, prior research involved theory and simulation of placing traditional patch antennas on curved, mostly convex, surfaces [1-5]. For example, patch antennas on convex, cylinder type surface were analyzed in [1-2] and the authors observed that the bandwidth increased with increased curvature.

In this work, we modify the design of a traditional patch antennas by engineering the substrate thickness profile to control the bandwidth of the patch antenna. We have observed that the bandwidth can be controlled and that both ultra-narrowband and wideband frequency responses can be obtained. Our work focuses mainly on concave profiles, where the best bandwidth control has been observed. This unique structure can be fabricated using additive manufacturing (AM).

Additive manufacturing technologies have been the subject of attention in engineering and research. They have the unique capability to convert a digital model into an arbitrary 3D physical counterpart. One of the great advantages of AM in RF, microwave, and general engineering areas is exploiting additional degrees of freedom to create innovative designs that cannot be obtained using conventional manufacturing. Examples of unique microwave structures that are enabled by AM are: "roller coaster" transmission line [6] and compact composite right/left-handed transmission line [7].

2. Curved patch design and simulation

Fig. 1 shows the concept for the curved patch antenna. It consists of a rectangular metal patch fed using a microstrip line just like any traditional microstrip patch antennas. The main difference in our design is that the substrate is concave and has a sinusoidal change in thickness. This change in thickness allows for a gradual impedance change in the direction of the fundamental mode. This enables control of antenna's bandwidth from ultra-wideband to ultra-narrow.

This concept was validated by simulating a wideband curved patch. The antenna was simulated using ANSYS's High Frequency Structure Simulator (HFSS). The simulation assumed a 2.5 mm thick substrate with a dielectric constant (ε_r) of 2.1. The patch antenna is 12.3 mm × 14 mm with a cosine thickness profile with minimum thickness of 0.1 mm. The metal conductivity is assumed to be 1×10^7 S/m. The feed line from Fig. 1 was deembedded from the simulation results, therefore the reference plane is at the input of the patch antenna for all simulations.

Fig. 2 shows the simulated input return loss for the curved patch antenna. An excellent return loss ($\leq$ 10 dB) is achievable from about 10 to 20 GHz. Fig. 2 also shows the simulated three-dimensional far field radiation patterns at 10, 12, 13.4, 16.7 and 18.3 GHz. There is some variability in the radiation pattern through frequencies

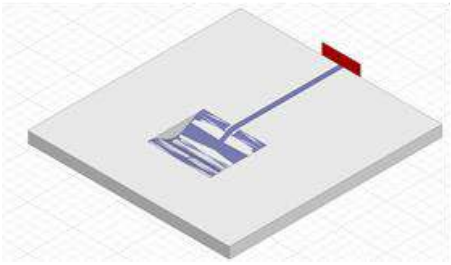

Figure 1: HFSS drawing of the curved (concave) patch antenna.

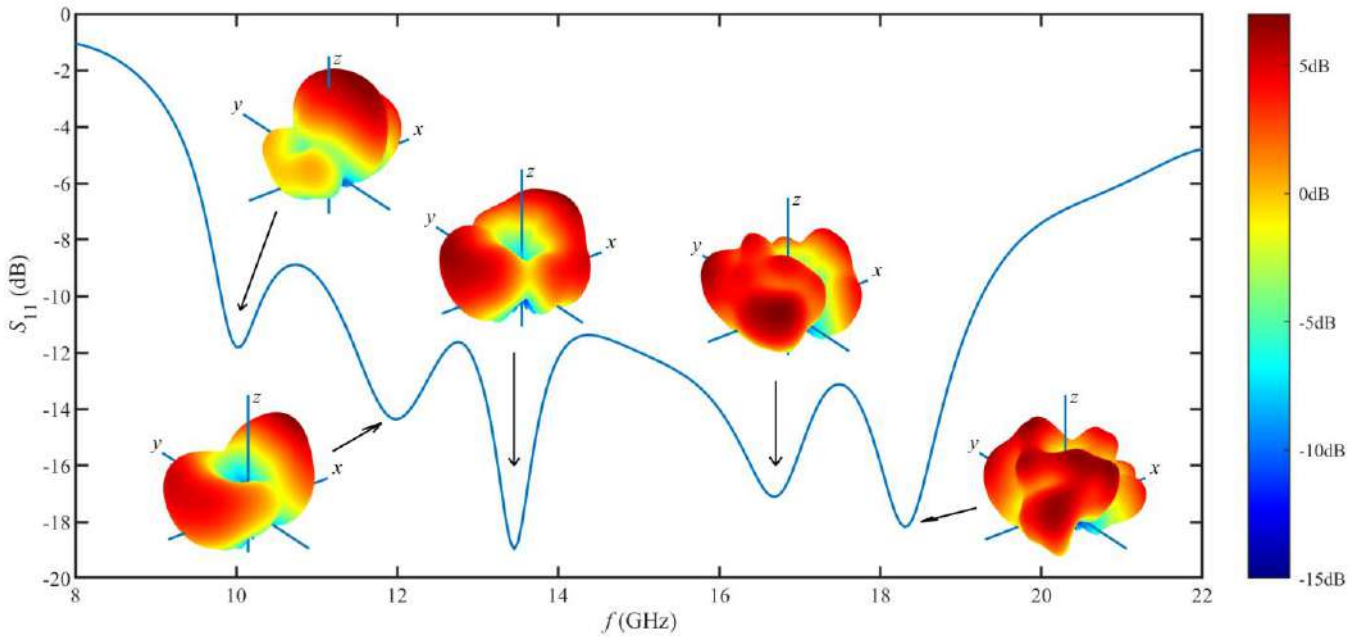

Figure 2: Simulated input return loss (S_{11}) of the curved patch antenna. Simulated three-dimensional radiation patterns are shown at frequencies of 10, 12, 13.4, 16.7 and 18.3 GHz.

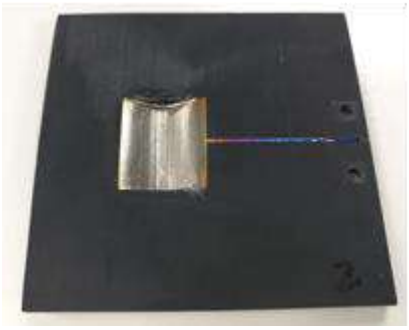

Figure 3: Photograph of the patch antenna fabricated using additive manufacturing.

A proof of concept curved antenna structure that was fabricated using additive manufacturing is shown in Fig. 3. This demonstrates that this concept can be realized using additive manufacturing. Here the substrate was printed using Form 2 SLA printer from Formlabs using their standard black resin, while the feed microstrip line and metal patch were printed using Optomec aerosol jet printer and silver nano particle ink. Our current work includes improving the fabrication method and testing the antenna.

3. Conclusions

We have demonstrated a new concept that enables control of the bandwidth of patch antennas. It is based on curving the substrate thickness, which allows for gradual impedance change in the direction of the fundamental mode.
This concept is enabled by advances in additive manufacturing, where arbitrary 3D structures can be manufactured.

References

[1] J.S. Dahele, R.J. Mitchell, K.M. Luk, K.F. Lee, "Effect of curvature on characteristics of rectangular patch antenna," *Electronics Letters,* vol. 23, no. 14, pp. 748-749, July 1987.

[2] K.-M. Luk, K.-F. Lee, J.S. Dahele, "Analysis of the cylindrical-rectangular patch antenna," *IEEE Trans. on Antennas and Propagation,* vol. 37, no. 2, pp. 143-147, Feb. 1989.

[3] L. Li, L. Luk, "A wideband patch antenna with cross-polarization suppression," *IEEE Antennas and Wireless Propagation Letters,* vol. 3, pp. 211-214, 2004.

[4] P. Li, K.L. Lau, K.M. Luk, " A study of the wide-band L-probe fed planar patch antenna mounted on a cylindrical or conical surface," *IEEE Trans. On Antennas and Propagation,* vol. 53, no. 10, pp. 3385-3389, Oct. 2005.

[5] T. Yuan, C.-W. Qiu, L.-W. Li, M.S. Leong, Q. Zhang, "Elliptically shaped ultra-wideband patch antenna with band-notch features," *Microwave and Optical Technology Letters,* Jan. 2008.

[6] J. Hester, E. Nguyen, J. Tice, V. Radisic, "A novel 3D-printing enables "roller coaster" transmission line," *IEEE Intern. Symposium on Antennas and Propagation & USNC/URSI National Radio Science Meeting,"* July 2017.

[7] J. Hester, E. Nguyen, R. Shishido, J. Tice, V. Radisic, "A fully-3D-printed complementary right/left-handed transmission line," *IEEE Intern. Symposium on Antennas and Propagation & USNC/URSI National Radio Science Meeting,"* July 2018.

Compact Switchable Mono/dual Band Reject Monopole Antenna for Ultrawideband Applications

Khelil Fertas[1], Fateh Benmahmoud[2], Farid Ghanem[3], Ali Mansoul[4], Smail Tedjini[2] and Rabia Aksas[1]

[1]Ecole Nationale Polytechnique, Electronics Dept., El-Harrach, Algiers, Algeria
[2]Univ. Grenoble Alpes, Grenoble INP, LCIS, 26000, Valence, France
[3]Telecom Product Direction, R&D&I, Brandt Group, Cevital Industry Pole, Garidi II, Algiers, Algeria
[4]Centre de Développement des Technologies Avancées, Algiers 16000, Algeria
E-mail: khelil.fertas@g.enp.edu.dz

Abstract

The proposed antenna is capable to operate in the ultra-wideband mode with a bandwidth of (2.9 – 15.65 GHz), in the ultra-wideband mode with single notched-band at 5.8GHz (WLAN) or 7.2GHz (X-band) and in the ultra-wideband mode with dual notched-band. The rate of rejection achieved in the two bands is close to -1.5dB. Three ideal switches are used to achieve the reconfigurability. The two states on/off of the switch are modelled by the presence/absence of a conductor respectively. The results obtained by simulations are presented and discussed

1. Introduction

These last years, with the evolution of the modern communications systems, frequency reconfigurable antennas have obtained a lot of attention; due to their attractive features such as capability to incorporate numerous operating services with a large frequency flexibility (cognitive and multiservice radios), reducing size and interference in wireless communication [1-3].

Currently, to achieve frequency reconfigurability, different switches can be used like pin diodes, varactor diodes, RF MEMS switches, FETs switches. The UWB antenna is one of the keys to increasing the number of features in a single small device compared to conventional narrowband antennas described in the literature. However, the use of UWB antenna can cause interferences with another device operating in one standard such as WLAN, WiMAX and X-band. To solve this problem, generally, we introducing a filter (notched band) in these frequency bands [4-6]. Many interesting and novel concepts have been developed to achieve this property. Notched band can be obtained by using split ring resonators (SRRs), defected microstrip structure (DMS), defected ground structure (DGS) and etching in feeding line. We can also achieve reconfigurable UWB response with one notch or multiple notches.

In this paper, we propose a switchable frequency reconfigurable monopole antenna. The bandwidth of the proposed prototype is from 2.9 GHz to more than 15.65 GHz. It is capable to switch between an UWB mode, an UWB mode with single notched band and an UWB mode with dual notched band in the WLAN and X-band frequencies. Moreover, the rate of notched bands is appreciable. The first notched band is achieved by integrating hexagonal ring shaped slot with four slots on the patch and the second notched band is obtained by a pair of modified hexagonal SRR, which are located close to a 50Ω microstrip feed line. Frequency reconfiguration is achieved by controlling the state of the three switches. With this approach, four different modes of operation can be selected.

2. Antenna structure and Design

Fig. 1 describes the schematic of the proposed antenna. The antenna geometry consists of a hexagonal patch fed by a microstrip line and a pair of modified hexagonal SRR (MH-SRR) which are positioned close to a 50-Ω microstrip feed line. The location of the pair of MH-SRR is important as it determines the level of suppression in the band-cut, represented by the magnitude of the module of the reflection coefficient ($|S_{11}|$dB>-10 dB). The size of MH-SRR is optimized to achieve band-cut filtering at the resonant frequency of 7.2GHz. The purpose to employ a pair of MH-SRR is to improve the rejection rate. This improvement is due to the enhancement in the coupling with proximity between the cells and the feeding line.

The hexagonal slot introduced into the lower part of the radiating patch acts as a filter that captures frequencies proportional to its electrical length. The result obtained on the frequency behavior of the antenna is the appearance of a cutoff band at 5.8 GHz. The ideal switches used in this work for reconfiguration have dimensions of 0.5 mm x 0.5 mm.

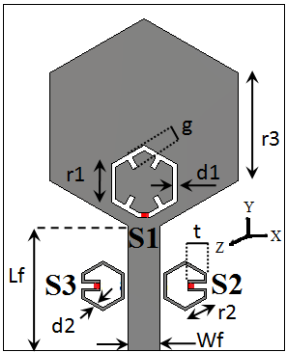

(a)

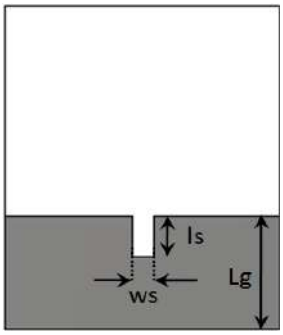

(b)

Figure 1. Geometry of the proposed antenna (a) front view, (b) back view (Lf=11.57mm, Wf=3mm, r1=3.5mm, r2=2.3mm, r3=10mm, d1=0.5mm, d2=0.23mm, t=1.76mm, g=1.5mm, Lg=11.2mm, ls=4mm, ws=2mm.

The ON state is modeled by the presence of a copper bridge and the OFF state by the absence of a copper bridge. The use of ideal switches as the first reconfiguration approach before using actual switches is widely reported in the literature as in [7-9]. The first switch (S1) used in this search is placed in the lower part of the hexagonal slot. When the switch S1 is in the ON state (metal presence), the rejected frequencies correspond to the WLAN at 5.2 GHz. The other two switches (S2, S3) are located in the empty spaces of the MH-SRR placed near the power line. When both switches are OFF, the rejected frequencies are those of the X band (7.2 GHz). The closing of the two switches (ON states) and the opening of S1 give the radiating structure its ultra wide band performance. This developed approach makes it possible to obtain four different modes of operation described in Table 1.

Table 1: Different configuration states of the proposed antenna.

States	S1	S2 & S3	Operation mode
State 1	ON	OFF	UWB with dual rejected bands (WLAN, X-band) at 5.8GHz and 7.2GHz respectively
State 2	ON	ON	UWB with WLAN notch band at 5.8GHz
State 3	OFF	OFF	UWB with X-band notch at 7.2GHz
State 4	OFF	ON	UWB (2.9 – 15.65 GHz)

The antenna is printed on a Teflon glass substrate, with a thickness of 1.6 mm, a relative permittivity of 2.5 and a tangent loss of 0.002. The simulator used here is the CST Microwave Studio. The total size of the antenna is (31 x 34) mm2.

3. Results and discussion

The different curves of the reflection coefficient for the four modes of operation, summarized in Table 1, are illustrated in Figure 2. Despite the introduction of the cut-off bands, the antenna retains a fairly substantial bandwidth (up to 16 GHz). The rejection level in both 5.8GHz and 7.2GHz cut-off bands is quite high and is close to -1.52dB. The location of the cut-off bands is fixed despite switching between the different operating modes. In ultra wide band mode the antenna has a relative bandwidth of about 136% (5.33:1).

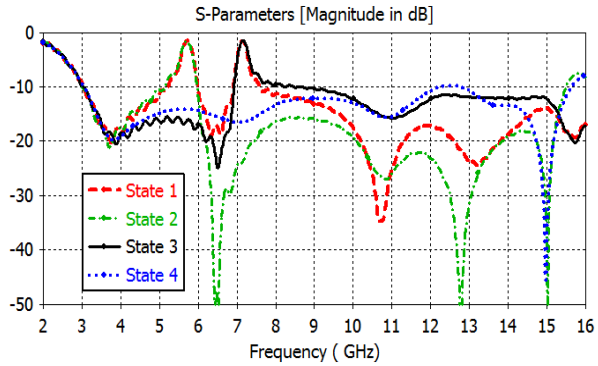

Figure 2. Simulated reflection coefficient for four different states.

In order to demonstrate the operation of the two types of filter introduced into the antenna structure, a study on the current distribution in the two cut-off bands was carried out, as shown in Figure 3. For the first band at 3.5 GHz when the filtering is active (S1 is in the ON state) it is clear that the surface currents are mainly concentrated around the hexagonal slot (Fig. 3 a), confirming the capture of these frequencies (5.8 GHz) by the slot introduced on the radiating patch.

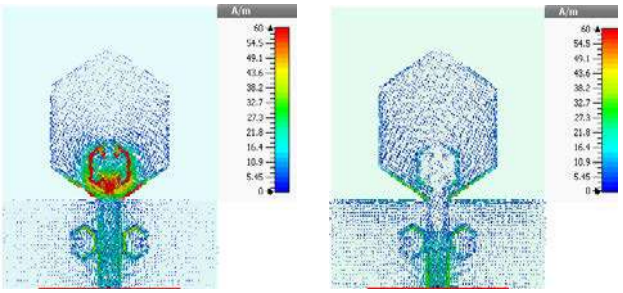

(a) (b)

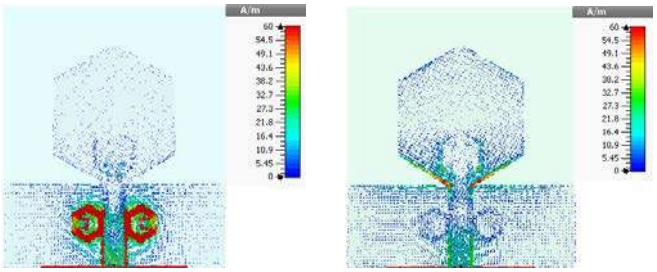

(c) (d)

Figure 3. Current distribution of proposed antenna for different states (a) state 1 at 5.7 GHz, (b) state 3 at 5.7 GHz, (c) state 1 at 7.2 GHz, (d) state 2 at 7.2 GHz

Now when S2 and S3 are in the OFF state, the second 7.2 GHz cutoff band is active and a high current concentration is noted on the MH-SRR pair near the feed line, as shown in Figure 3 (c). Fig. 4 shows the normalized radiation pattern in the E-plane (yz) and the H-plane (xz) at 3.8 GHz and 10.7 GHz for state 1.

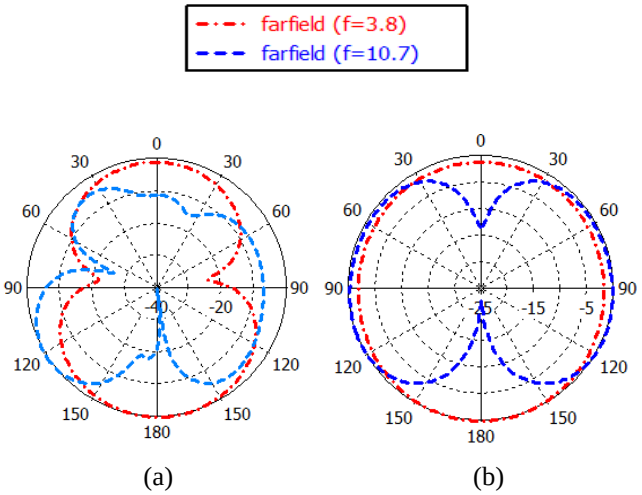

(a) (b)

Figure 4. Simulated radiation pattern at 3.8 GHz and 10.7 GHz for state1 (a) E-plan, (b) H-plan.

It is deduced from the radiation pattern that the proposed antenna has an omnidirectional radiation pattern in the H-plane at 3.8 GHz. In the E- plane the radiation pattern is bidirectional.

The performance of the proposed antenna compared to previous works reported in the literature is illustrated in Table 2. It can be concluded from these results that the proposed antenna offers good performance in terms of bandwidth, level of selectivity, miniaturization and reconfigurability in frequency.

Table 2: Comparison of proposed and reference antennas.

	[9]	[6]	[5]	This work
Substrate εr/h (mm)	2.55 / 0.77	10.2 / 0.635	4.3 / 1.62	2.5 / 1.6
UWB (GHz)	3.1 – 10.6	3.1 - 11	2.57 – 11.3	2.9 – 15.65
Rejection levels dB	-1.9 / -1.1	-1.6 / -3	-2.5	-1.5
Size (W x L) mm2	40 x 40	39.9 x 34.1	23 x 32	31 x 34
Reconfigurability	yes	no	no	yes

4. Conclusion

In this work, a compact frequency reconfigurable UWB antenna has been introduced. Frequency reconfiguration allows switching between an ultra-wide band mode (2.9 - 15.65 GHz), an ultra-wideband mode with a cutoff band (WLAN or X-band), and ultra-wideband mode with two cutoff bands. In total, the antenna has four different modes of operation. For cut bands, the rejection level reached is close to 0 dB. For the reconfiguration mechanism a first approach with ideal switches was used before proceeding to prototype fabrication with actual switches. The proposed antenna is suitable for multi-service radios and UWB applications.

References

[1] A. Mansoul, F. Ghanem, M. R. Hamid, and M. Trabelsi, “A selective frequency-reconfigurable antenna for cognitive radio applications,” IEEE antennas Wirel. Propag. Lett., vol. 13, pp. 515–518, 2014.

[2] H. F. Abutarboush, R. Nilavalan, S. W. Cheung, K. M. Nasr, T. Peter, D. Budimir, and H. Al-Raweshidy, “A Reconfigurable Wideband and Multiband Antenna Using Dual-Patch Elements for Compact Wireless Devices,” IEEE Trans. Antennas Propaga. vol. 60, pp. 36-43, 2012.

[3] T. Aboufoul, A. Alomainy, and C. Parini, “Reconfiguring UWB monopole antenna for cognitive radio applications using GaAs FET switches,” IEEE Antenna Wirel. Propag. Lett. vol. 11, pp. 392–394, 2012.

[4] L. C. Tsai, and W. J. Chen, “A UWB antenna with bandnotched filters using slot type split ring resonators,” Microwave Opt. Technol. Lett., vol. 58, pp. 2595-2598, 2016.

[5] F. Guichi, M. Challal, and T. A. Denidni. “A novel dual band-notch ultra-wideband monopole antenna using parasitic stubs and slot,” Microw. and Opt. Technol. Lett., vol. 60.(7), pp. 1737-1744, 2018.

[6] , O. Abu Safia, M. Nedil, and L. Talbi “Coplanar waveguide-fed rose-curve shape UWB monopole antenna with dual-notch characteristics,” IET Microw., Antennas & Propag., vol. 12(7), pp. 1112-1119, 2018.

[7] M. N. Osman, M. K. Rahim, P. Gardner, et al. “An electronically reconfigurable patch antenna design for polarization diversity with fixed resonant frequency,” Radioengineering, vol. 24(1), pp. 45-53, 2015.

[8] A. Mansoul, F Ghanem, “Frequency reconfigurable antenna for cognitive radios with sequential UWB mode of perception and multiband mode of operation,” Intern. Journal of Microw. and Wirel. Technol., pp. 1-7, 2018

[9] V. Asha, and M. S. Parihar. “Multifunctional Antenna with Reconfigurable Ultra-Wide Band Characteristics,” Radioengineering, vol. 26(3), 2017.

Extending the Bandwidth of UWB Monopole Antenna using Genetic Algorithm with 5-6 Ghz Notched Band

Khelil Fertas[1], Fateh Benmahmoud[2], Farid Ghanem[3], Ali Mansoul[4], Smail Tedjini[2] and Rabia Aksas[1]

[1]Ecole Nationale Polytechnique, Electronics Dept., El-Harrach, Algiers, Algeria
[2]Univ. Grenoble Alpes, Grenoble INP, LCIS, 26000, Valence, France
[3]Telecom Product Direction, R&D&I, Brandt Group, Cevital Industry Pole, Garidi II, Algiers, Algeria
[4]Centre de Développement des Technologies Avancées, Algiers 16000, Algeria
E-mail: khelil.fertas@g.enp.edu.dz

Abstract

Abstract— An ultra-wideband (UWB) antenna with band-rejection by using genetic algorithm optimization (GAO) is developed and presented in this paper. This is achieved by adequate combination of a radiating patch element with an area divided into 2x2 mm^2 where each one is allocated by presence or absence of conductor property and an inverted Π-shaped defected ground structure (DGS) filter. The optimization process is programmed in visual basic script and implemented in CST Microwave software as a macro. The presented antenna, printed on Teflon substrate of dielectric constant 2.4 with loss tangent of 0.002, operates over a wide range of frequency bands, i.e., from 2.7 to 20 GHz. By etching an inverted Π-shaped slot in the ground plane, a rejection of WLAN frequency band is achieved. Extremely interesting numerical results for the return loss, current distribution, radiation patterns and gain are illustrated and discussed. The proposed antenna is prototyped to investigate the measurement performance where a good agreement is observed with the simulated results.

***Index Terms*— Ultra-wideband (UWB) antenna, Genetic algorithm optimization (GAO), Defected ground structure (DGS) filter, Wireless local area network (WLAN) frequency band.**

1. Introduction

Nowadays, the technologies of communication present fast and immense evolution. Therefore, the obligation to include a large number of functionalities in the communication systems and to respond the needs of cohabit several standards on the same antenna is very crucial. Among of the efficient solutions for this requirement is the implementation of ultra-wide band (UWB) antenna [1, 4]. Moreover, numerous interfering narrow band communication systems operate in this large bandwidth such as wireless local area network (WLAN: 5-6 GHz) and worldwide interoperability for microwave access (WiMAX: 3.5 GHz). Many research works have been conducted to reduce interferences with other users through introducing filters [5-7]. Though, the antenna optimization performance becomes complicatedness in the case of integrating several frequency bands. The antenna design, with desired requirements, using conventional methods is more intricate compared to non-conventional ones and as well takes more time. Various techniques have been investigated to optimize antennas [8-16]. In [10], a particle swarm optimization algorithm (PSOA) was used in UWB monopole antenna. In [12], the authors were exploited the Taguchi's method in the area of Electromagnetics and as well antennas. In [13] and [14], wearable antennas parameters were automatically adjusted, respectively, using the evolution strategy based algorithm EStra and the hierarchical optimization paradigm. In [15], a surrogate with multi-objective optimization algorithm was applied in the antenna design. Among these techniques, we find the optimization by genetic algorithm (GA) [17-20]. The GA technique presents an immense prospective in research of no-predictable solutions to antennas design. On the other hand, the use of GA helps to design antennas for the needs of different application domains. Generally, optimization problems in the antenna design for a specific application and for a given frequency band can be classified into two categories: continuous and binary problems. The first category can be used to optimize the geometrical parameters of the antenna [18], the second one can be employed to check the presence or the absence of a metal to find the appropriate patch shape or the geometry pixels [19].

2. Design and Optimization of Ultra-Wideband Antenna

The antenna geometry shown in Figure 1 is designed on two sides over a Teflon substrate of height 1.58 mm and relative permittivity of 2.4. The 50 Ω microstrip line is used to feed the antenna. The basic structure of radiating element consists of a 20 x 20 mm^2 rectangular patch antenna. In order to be able to apply a GA, the radiating element is formed by a matrix of 10 x 10 square compartments as shown in Figure 2.

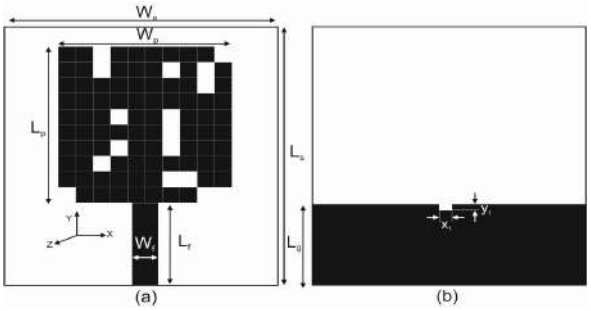

Figure 1: Schematic of the proposed UWB antenna based on GA: a) Front view and, b) Back view. (x1 =1.5mm, y1 =1mm, Lg =17.5mm, Lf =18mm, Wf=3.1mm Ws=33mm, Ls=43mm, Wp=20mm, Lp=20mm).

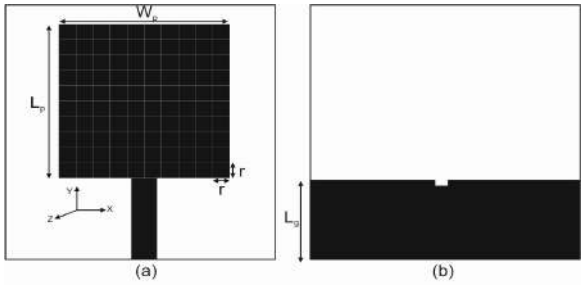

Figure 2: Schematic of the basic structure (r= 2 mm): a) Front view and,b) Back view.

A binary coding is used by affecting the value "1" to the cells containing metal and "0" to the cells without metal. The resulting structure is composed of 100 fragment cells which correspond to a matrix of 10 x 10 over which a GAO can be run to find the configurations that allow achieving the frequency optimization. The GA code developed in visual basic interface and implemented in CST simulator. The cost function of this code was useful to attain excellent matching of the magnitude of the reflection coefficient module (in dB) (|S11|dB < -10 dB) at the band starting from 3 GHz to 20 GHz. The goal here is to calculate and minimize the average value of the cost function, given by expression (1).

$$\cos t = \frac{\sum_{i=1}^{A} |S_{11}(f_i)|_{dB}}{A} \qquad (1)$$

In expression (1), the parameter A is the number of frequency that points in the desired frequency band. In the same perspective, to reduce the number of iterations, which correspond to all possible shape combinations and over which the GA is run, the percentage of no-metallic and metallic subdivisions were chosen to be 10% and 90%, respectively.
The population size is composed of 20 chromosomes per generation in all designs. Selection with a preference for the individuals with better cost function value is used to fill the new generation. The probability of crossover is 100% from the selection individuals and the single point crossover method was used with mutation probability of 0.1%. The next generation is formed from the current generation. The number of generations used in this work is 30.
The simulation result of the VSWR parameter versus frequency is depicted in Figure 3.

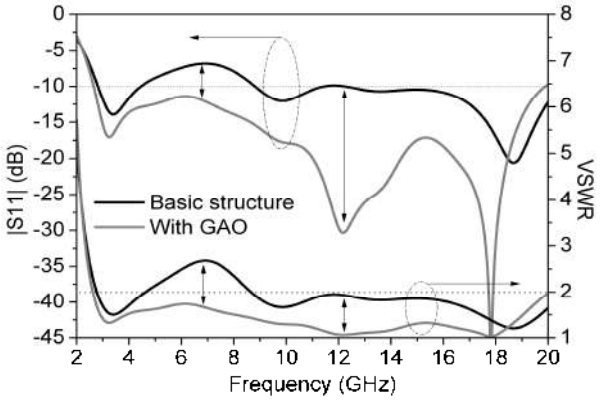

Figure 3: The S11-parameter and VSWR of UWB antenna.

From Figure 3, the presence of UWB characteristic is noticed where a good matching is satisfied in the band starting from 2.7 GHz to 20 GHz.

3. Implementation of the Band-Stop Filter

3.1. Inverted Π shaped filter design

The proposed shape of the band-stop filter (BSF) is shown in Figure 4. The design is a 50 Ω microstrip line along with an inverted Π shaped slot embedded into the ground plane.

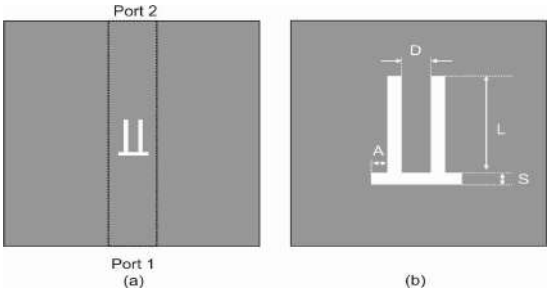

Figure 4: Schematic of the band-stop filter.

The parameters for optimal BSF design are illustrated in Table 1 whereas the S-parameters of the filter are shown in Figure 5.

Table 1: Band-stop filter dimensions.

Parameter	Value (mm)
L	10.3
D	1.0
A	0.7
S	0.3

From Figure 5, it is noticed that the response confirms the band-stop behavior where its central frequency is around 5.2 GHz.

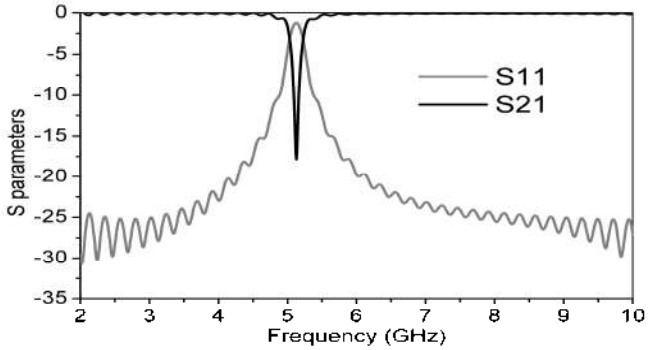

Figure 5: S-parameters of the band-stop filter.

3.2. Band-notched UWB antenna with band-rejected element

In order to achieve an UWB-antenna with a band-rejection, an inverted Π-shaped DGS slot is embedded in the ground plane as shown in Figure 6.

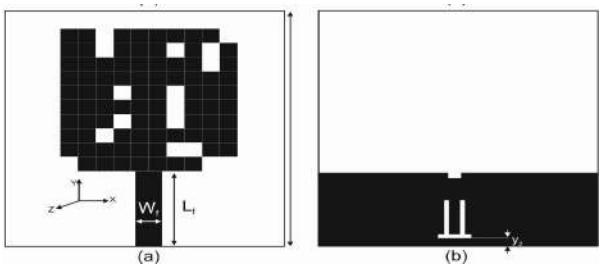

Figure 6: Integration of the DGS on the UWB antenna (y2 =1mm).

Figure 7 illustrates the antenna VSWR parameter. From this result, a band-rejection at the range starting from 5 GHz to 6 GHz is observed.

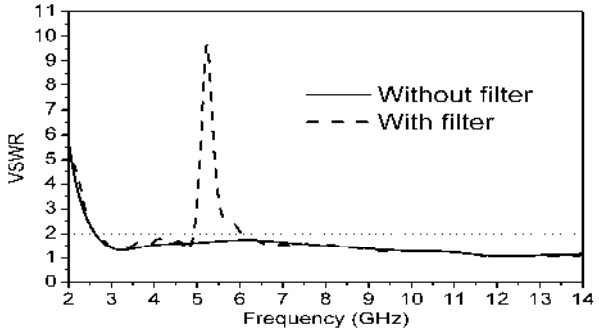

Figure 7: VSWR of the antenna with and without filter.

The current distributions at 5.2 GHz and 3.5 GHz are presented in Figure 8. This figure demonstrates the effect of introducing the BSF where the surface current distribution is concentrated around the DGS-BSF at 5.2 GHz. At this frequency, the antenna does not radiate and the introduced BSF captures waves that have a wavelength proportional to the wavelength of the WLAN (at 5.2 GHz).

The realized gain is illustrated in Figure 9. At frequency of 5.2 GHz, the gain decreases quickly which indicates clearly the effect of the embedded BSF.

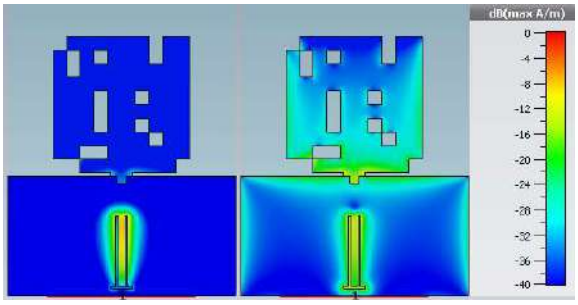

(a) (b)

Figure 8: Current distributions at: (a) 5.2 GHz and, (b) 3.5 GHz.

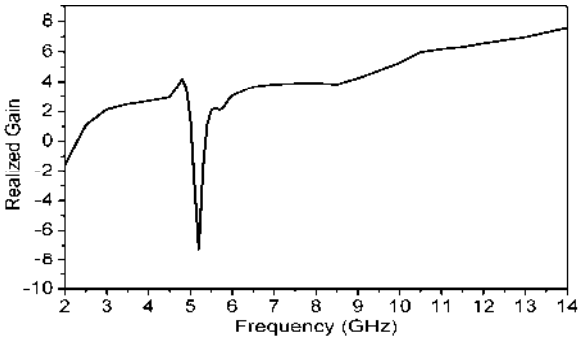

Figure 9: Gain of the proposed antenna.

4. Experimental Results

To validate the proposed UWB antenna with WLAN rejection-band, an experimental antenna prototype was fabricated and tested. The photograph of the fabricated antenna is shown in Figure 10 where the simulated and measured results of the return losses are presented in Figure 11.

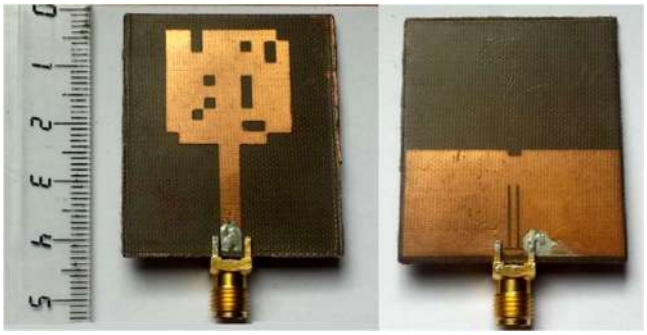

(a) (b)

Figure 10: Photograph of the fabricated antenna (a) Front view and, (b) Back view.

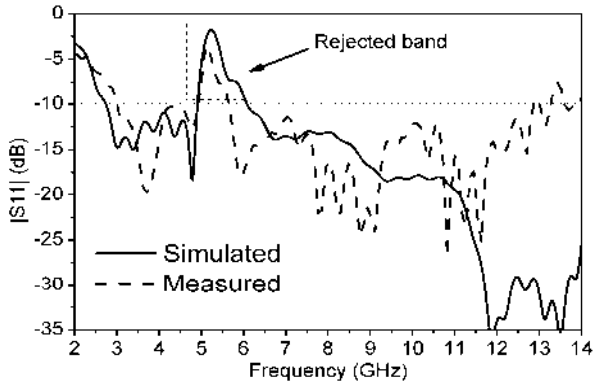

Figure 11: Comparison between measured and simulated S11-parameter.

From Figure 11, good agreement is realized between the measured and simulated results with slight differences. These small discrepancies can be attributed to possible mismatching in the SMA connectors and may possibly to the fabrication tolerances.

Figure 12 shows the measured and simulated radiation patterns for both E and H planes at 3.5 GHz and 10 GHz. The eight shape of the radiation pattern (E-plane) is clearly visible in Figure 12-a. The antenna has an omnidirectional radiation as shown in Figure 12-b and Figure 12-d.

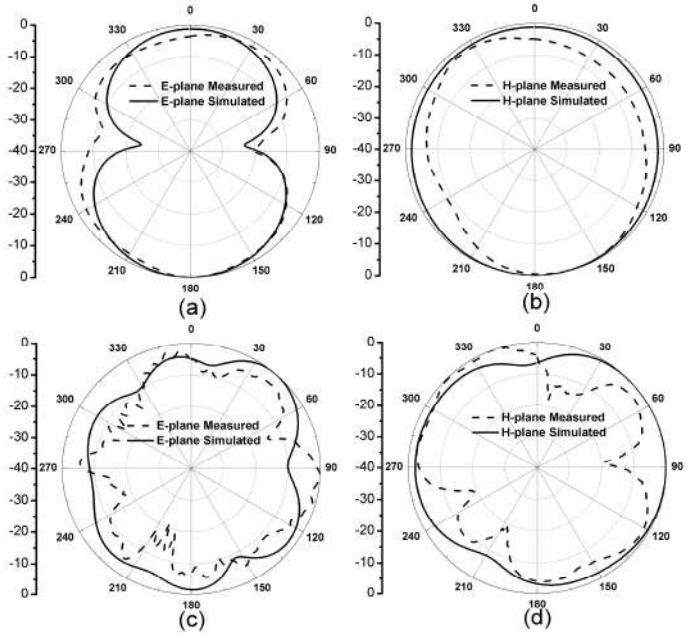

Figure 12: Radiation patterns of the proposed antenna at different frequencies. a) E-plane at 3.5GHz, b) H-plane at 3.5 GHz, c) E-plane at 10 GHz, and d) H-plane at 10 GHz.

5. Conclusions

An UWB antenna with band-notch characteristic has been designed, simulated and tested. The proposed antenna shape has been optimized by a GA code, using the visual basic interface, implemented in *CST MICROWAVE SOFTWARE*. By inserting an inverted Π-shaped DGS slot, a band-rejection is achieved in the frequency range starting from 5 GHz to 6 GHz. The measured results have shown an acceptable agreement with the simulation. The presented antenna provides good radiation patterns in both E and H-planes. It has a simple shape that is easy to manufacture and can be easily embedded in diverse UWB wireless communication systems.

References

[1] M. M. Bait-Suwailam, and O. M. Ramahi, Ultrawideband mitigation of simultaneous switching noise and EMI reduction in high-speed PCBs using complementary split-ring resonators, *IEEE Trans. Electromag. Compatib.*, 54(2), 389-396, 2012.

[2] A. Bekasiewicz, and S. Koziel, Compact UWB monopole antenna for internet of things applications, *Electron. Lett.*, vol. 52, no. 7, 492-494, 2016.

[3] F. Guichi, M. Challal and T. A. Denidni, A Novel Dual Band-Notch Ultra-Wideband Monopole Antenna using Parasitic Stubs and Slot, *MOTL – Microw. and optic. Technol. Lett.*, vol. 60(7), 1737-1744, Jul. 2018.

[4] T. Aboufoul; A. Alomainy, and C. Parini, Reconfiguring UWB monopole antenna for cognitive radio applications using GaAs FET switches, *IEEE Antennas and Wireless Propag. Lett.*, vol. 11, 392 – 394, 2012.

[5] L. C. Tsai, and W. J. Chen, A UWB antenna with bandnotched filters using slottype split ring resonators, *Microwave Opt. Technol. Lett*., vol. 58, 2595-2598, 2016.

[6] C. Sim, W. Chung and C. Lee, An octagonal UWB monopole antenna with 5 GHz band-notch function, *Microwave Opt. Technol. Lett.* Vol. 51, 74-78, 2009.

[7] H. Hosseini, H. R. Hassani, and M. H. Amini, Miniaturised multiple notched omnidirectional UWB monopole antenna, *Electron. Lett.*, vol. 54, no. 8, 472-474, 2018.

[8] J. Zhao, D. Psychoudakis et al, Design optimization of a low-profile UWB body-of-revolution monopole antenna, *IEEE Trans. Antennas and Propag.*, vol. 60, no 12, 5578-5586, 2012.

[9] L. Zhang, Z. Cui, Y. Jiao, and F. Zhang, Broadband patch antenna design using differential evolution algorithm, *Microwave Opt. Technol. Lett.*, vol. 51, 1692-1695, 2009.

[10] A. Bhattacharya, B. ROY et al, An UWB monopole antenna with hexagonal patch structure designed using particle swarm optimization algorithm for wireless applications, *Microelectronics, Computing and Communications (MicroCom), 2016 International Conference on. IEEE*, 1-5, 2016.

[11] F. J. Villegas, T. Cwik, Y. Rahmat-Samii, and M., Majid, A parallel electromagnetic genetic-algorithm optimization (EGO) application for patch antenna design, *IEEE Trans. Antennas and Propag.*, vol. 52, no 9, 2424-2435, 2004.

[12] W. Wei-Chung, Y., Fan, and A. Elsherbeni, Electromagnetics and antenna optimization using Taguchi's method, *Synthesis Lectures on Computational Electromagnetics*, vol. 2, no 1, 1-94, 2007.

[13] Ł. Januszkiewicz, P. Barba, and S. Hausman, Optimization of wearable microwave antenna with

simplified electromagnetic model of the human body, *Open Physics*, vol. 15(1), 1055-1060, 2017.

[14] L. Januszkiewicz, P. Barba, and S. Hausman, Hierarchical paradigm for automated optimal design of dual-band wearable antenna with simplified human body models, *COMPEL - The international journal for computation and mathematics in electrical and electronic engineering*, vol. 37 (5), 1597-1608, 2018.

[15] P. Singh, M. Rossi, I. Couckuyt, D. Deschrijver, H. Rogier, and T. Dhaene, Constrained multi-objective antenna design optimization using surrogates, *Int. J. Numer. Model. Electron. Netw. Devices Fields*, vol. 30, 2017.

[16] Chen, Y.S., Performance enhancement of multiband antennas through a two-stage optimization technique, *Int. J. RF Microw. Comput.-Aided Eng*., vol. 27, 2016.

[17] J. M. Johnson, and V. Rahmat-Samii, Genetic algorithms in engineering electromagnetics, *IEEE Magazine AP.*, vol. 39, 7-21, 1997.

[18] E. J. Rodrigues, A. G. D'Assunção, H. W. Lins, and C. Peixeiro, Genetic algorithm optimization of a CPW fed UWB circular ring monopole with modified ground plane, *Microwave Opt. Technol. Lett.*, vol. 58, 1319-1323, 2016.

[19] S. Song, and R. D. Murch, An efficient approach for optimizing frequency reconfigurable pixel antennas using genetic algorithms, *IEEE Trans. Antennas and Propagation*, vol. 62, no. 2, 609-620, 2014.

[20] K. Fertas, H. Kimouche, M. Challal, H. Aksas, R. Aksas and A. Azrar, Design and optimization of a CPW-fed tri-band patch antenna using genetic algorithms, *ACES-Applied Computat. Electromag. Society Journal*, 30(7), 2015.

CUDA-Based Particle Swarm Optimization in Reflectarray Antenna Synthesis

Amedeo Capozzoli*, Claudio Curcio, Angelo Liseno

Universitá di Napoli Federico II, Dipartimento di Ingegneria Elettrica e delle Tecnologie dell'Informazione
via Claudio 21, I 80125 Napoli (Italy)
*corresponding author, E-mail: a.capozzoli@unina.it

Abstract

We show how reflectarray antenna synthesis can take profit from parallel computing on Graphics Processing Units (GPUs). The presented approach uses an implementation of Particle Swarm Optimization in CUDA language and accelerates the computation of the field radiated by the reflectarray using a GPU-implemented Non-Uniform FFT routine. Numerical results show how computing time can be kept convenient for the application at hand.

1. Introduction

Microstrip reflectarrays (RAs) have attracted much interest in the last years [1, 2].

The design of high performance microstrip reflectarrays requires the ability of exploiting all the degrees of freedom (DoFs) of the antenna as the positions, the orientations, the characteristics of the scattering elements or the shape of the reflecting surface.

Managing a large number of DoFs requires a proper synthesis strategy trading-off effectiveness and efficiency through efficient and effective numerical algorithms guaranteeing reliability, keeping the computational complexity low and exploiting highly performing computing hardware.

To guarantee reliability and accuracy, a multistage approach has been devised [3, 4, 5]. The idea is to employ a rough modeling of the structure to enable robustness against suboptimal solutions at the early stages and then refining the model from stage to stage. The success of the whole procedure is submitted to the capability of the early stages to mitigate the false solution issue. To this end, the unknowns of the problem are given proper representations enabling a progressive enlargement of the parameters space as well as a modulation of the computational complexity of the approach [3, 4, 5]. At the beginning of the whole procedure, few properly chosen polynomials are employed for the command phases and the element positions (Zernike polynomials for the phases and Lagrange polynomials for the positions in this paper) and progressively increased in number [3, 4, 5].

The success of the whole procedure is submitted to the capability of the early stages to mitigate the false solution issue. To this end, a global optimizer should be adopted. However, choosing the global optimization algorithm is not a simple task and a wide discussion is contained in [6]. The No Free Lunch Theorems [6] provide insight in choosing the strategy to get a successful algorithm for the problem at hand. They explore the relationship between an efficient optimization algorithm and the problem that it is asked to solve. These results state that a general purpose algorithm that can be efficiently used in all optimization problems does not exist: on average, the performances of any two optimization algorithms are the same across all the possible optimization problems [6]. Explicitly or implicitly inserting some a priori information on the structure of the problem at hand should improve the performance. It is suggested that an algorithm can be "aligned" to the structure of the problem because of an implicit tuning procedure due to training and/or to the years of research [6].

On the other side, the high dimensionality of a problem is the main obstacle towards effective global optimization. The amount of computing time required to get a reliable solution becomes inordinate as long as the number of variables increase [7, 8]. In particular, the dependence of the performances of a global optimization algorithm versus the dimension of the searching space can be rigorously established thanks to Nemirovsky and Yudin Theorem [8]. It proves the exponential dependence of the number of minimization steps on the dimensionality of the problem.

Accordingly and once again, the number of unknowns of the problem must be modulated during the design by using a proper representation of the unknowns enabling its progressive enlargement [3, 4, 5]. Then, global optimization can be exploited as starting stage, while local tools can be employed in the subsequent ones.

In this paper, we use a Particle Swarm Optimization (PSO) approach [9]. PSO, indeed, is a simple, but powerful optimization algorithm which searches for the optimum of a function following rules inspired by the behavior of flocks of bees looking for food. PSO has recently gained more and more popularity due to its robustness, effectiveness, and simplicity. Furthermore, PSO enables a very efficient implementation since it maps into a highly parallelizable computing pattern and is amenable of acceleration using Graphics Processing Units (GPU) computing.

We show how PSO can take profit from this technology. In particular, we provide an implementation of PSO in CUDA language, the NVIDIA Compute Unified Device Architecture that represents the NVIDIA extension of C++ to let a large class of users able to program GPUs for numerical computing applications. We show how computing time can be kept at very convenient durations for the application at hand.

The presented approach is further accelerated by the use of Non-Uniform FFTs [10] for the evaluation of the field radiated by the RA [11, 12]. The Authors have been the first employing NUFFT algorithms for the calculation of the field radiated by aperiodic arrays and RAs [11, 12]. They have presented an improved version of [10] in [13].
The paper is organized as follows. In Section II, the approach is sketched. In particular, the radiative model is described along with its calculation by a NUFFT. Furthermore, the NUFFT algorithm is briefly described along with its GPU implementation. Section III is devoted to discuss the GPU-based PSO implementation. In Section IV, the results are presented. Finally, in Section V, the conclusions are drawn.

2. The approach

A simplified layout of the multi-stage synthesis approach is illustrated in Fig. 1. We refer to [3, 4, 5] for a complete description of the approach.
In the initial stages, an approximate radiative model, namely, the Phase-Only (PO) model, is adopted leading to the Phase-Only Synthesis (POS) stage. For a POS, the unknowns to be determined are the element positions as well as the command phases. Then, an accurate model exploiting all the DoFs refines the results from the POS stages and leads to the Accurate Synthesis (AS). For the AS, the unknowns turn to be the internal DoFs of each element. The element positions can be further refined or, for the sake of simplicity, the result of the POS, in terms of element positions, can be kept fixed. In this paper, attention is focused to the POS only.
In order to limit the number of unknowns and make the use of a global optimizer affordable to generate a good initial guess, in stage 1), few polynomials are exploited to represent command phases and element positions. In stage 2), the number of the unknowns is progressively enlarged by increasing the order of the involved polynomials and a local optimizer is considered. Stage 3) exploits an impulsive representation of the unknowns involving all the effective DoFs at disposal for the command phases.
In this paper, for the sake of brevity, only some implementation details of the POS stages are discussed.

2.1. The radiative model and the NUFFT

We refer to a flat aperiodic RA, made up by N elements, illuminated by a feed located at the origin of the $Oxyz$ reference system as shown in Fig. 2. The feed is assumed to have the typical $\cos^{m_f}(\theta_n)$ pattern, where θ_n is the angle under which the feed sees the n-th element having coordinates (x_n, y_n, z_0) and located at a distance r_n from the feed. In this way, the 2D aperiodic array factor F is:

$$F_{kl} = \sum_{n=1}^{N} e^{j\varphi_n} \cos^{m_f}(\theta_n) \frac{e^{-j\beta r_n}}{r_n} e^{j2\pi\left(\frac{k\Delta u}{\lambda}x_n + \frac{l\Delta v}{\lambda}y_n\right)} \tag{1}$$

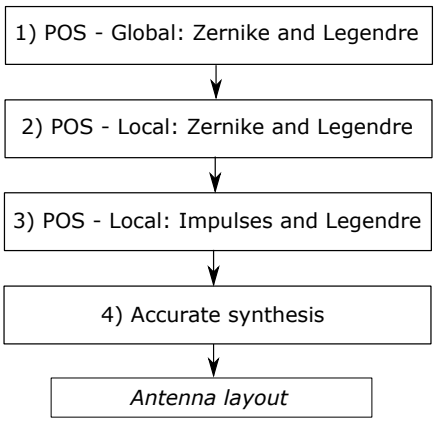

Figure 1: Stages of RA synthesis approach.

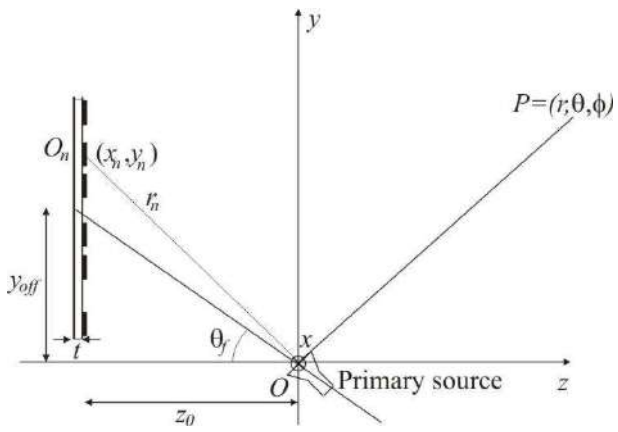

Figure 2: RA geometry.

when evaluated at a regular spectral grid $(u_k, v_l) = (k\Delta u, l\Delta v)$, with $k = -N_1/2, \ldots, N_1/2 - 1$ and $l = -N_2/2, \ldots, N_2/2 - 1$, the φ_n's being the element control phases, λ being the wavelength and $\beta = 2\pi/\lambda$ the wavenumber.
Apart from an unessential conjugation, F has the same expression of a 2D Non-Uniform Discrete Fourier Transform (NUDFT) of NED (Non-Equispaced-Data) type whose expression is

$$\hat{z}_{kl} = \sum_{i=1}^{N} z_i e^{-j2\pi\widetilde{x}_i\frac{k}{N_1}} e^{-j2\pi\widetilde{y}_i\frac{l}{N_2}}. \tag{2}$$

In eq. (2), the z_i's represent the sequence to be transformed, sampled at the non-uniform spatial coordinates $(\widetilde{x}_i, \widetilde{y}_i)$, and the $\hat{z}_{kl}$'s represent the transformed one. Accordingly, the array factor (1) can be effectively and efficiently evaluated using a 2D NED-NUFFT algorithm [10, 11, 12, 13].

2.2. The 2D NED-NUFFT algorithm

To guarantee a fast and accurate processing, the "non-uniformly sampled" exponentials $\exp(-j2\pi\widetilde{x}_i k/N_1)$ and $\exp(-j2\pi\widetilde{y}_i l/N_2)$ appearing in eq. (2) need to be properly interpolated. The idea behind NED NUFFTs is to use "uniformly sampled" exponentials $\exp(-jm\xi)$.
The exponential representation is made possible by the use of the Poisson summation formula [13, 14]. Indeed, under general hypotheses, given a function f, then $\sum_{m\in\mathbb{Z}} f(\xi + 2m\pi)$ converges absolutely almost everywhere to the 2π-periodic locally integrable function simply expressed through a Fourier series

$$\sum_{m\in\mathbb{Z}} f(\xi + 2m\pi) \sim \sqrt{2\pi} \sum_{m\in\mathbb{Z}} \hat{f}(m) e^{jm\xi}, \qquad (3)$$

where $\hat{f}(m) = \mathcal{F}[f; m]$ is the Fourier transform of f calculated at m.
Let us then consider a window function $\phi(\xi)$ having compact support in $(-\xi_M, \xi_M)$. The Poisson formula can be then applied to the function $\phi(\xi)\exp(-jx\xi)$:

$$e^{-j\xi x} = \sqrt{2\pi} \frac{\sum_{m\in\mathbb{Z}} \mathcal{F}\left[\phi(\xi) e^{-j\xi x}; m\right]}{\sum_{m\in\mathbb{Z}} \phi\left(\xi + 2m\pi\right) e^{-j2m\pi x}}. \qquad (4)$$

In order to obtain a computationally convenient expression of $\exp(-jx\xi)$, the denominator must be factored in the variables x and ξ. A straightforward way to achieve factorization is to avoid that the replicas $\phi(\xi + 2m\pi)\exp(-j2k\pi\xi)$ overlap, which is related to the replication period 2π of the Poisson summation formula in eq. (4) and to a proper choice of the support of $\phi(\xi)$. In particular, we have:

$$e^{-j2\pi\widetilde{x}_i \frac{k}{N_1}} \simeq \frac{\sqrt{2\pi}}{\phi\left(\frac{2\pi k}{cN_1}\right)} \sum_{m=\mu_i-K}^{\mu_i+K} \hat{\phi}\left(cx_i - m\right) e^{-j2\pi m \frac{k}{cN_1}}, \qquad (5)$$

where ϕ is the window function with support in $(-\pi/c, \pi/c)$ having Fourier transform $\hat{\phi}$ with support in $(-K, K)$, c is an oversampling factor, and $\mu_i = Int[c\widetilde{x}_i]$, $Int[\cdot]$ denoting he integer part. A similar expression can be obtained for the exponential with $\widetilde{y}_i$, by introducing $\nu_i = Int[c\widetilde{y}_i]$.
By denoting with

$$\begin{cases} \phi_k^1 = \phi\left(2\pi\frac{k}{cN_1}\right) & \phi_k^2 = \phi\left(2\pi\frac{l}{cN_2}\right) \\ \hat{\phi}_{it} = \frac{\hat{\phi}(cx_i - (\mu_i + t))}{\sqrt{2\pi}} & \hat{\psi}_{it} = \frac{\hat{\phi}(cy_i - (\nu_i + t))}{\sqrt{2\pi}} \end{cases}, \qquad (6)$$

by assuming that both $\hat{\phi}_{it}$ and $\hat{\psi}_{it}$ vanish outside $0 \le i \le M$ and $-K \le t \le K$ and by exploiting the fact that $\exp(-j2\pi(m + cN_1)k/(cN_1)) = \exp(-j2\pi mk/(cN_1))$ and $\exp(-j2\pi(n+cN_2)l/(cN_2)) = \exp(-j2\pi nl/(cN_2))$, eq. (2) can be written as

$$\hat{z}_{kl} = \frac{1}{\phi_k^1 \phi_l^2} \sum_{m=-cN_1/2}^{cN_1/2-1} \sum_{n=-cN_2/2}^{cN_2/2-1} u_{mn} e^{-j2\pi m \frac{k}{cN_1}} e^{-j2\pi n \frac{k}{cN_2}}, \qquad (7)$$

where

$$u_{mn} = \sum_{i=-\infty}^{+\infty} \sum_{p=-\infty}^{+\infty} \sum_{q=-\infty}^{+\infty} z_i \hat{\phi}_{i\ m+cpN_1-\mu_i} \hat{\psi}_{i\ n+cqN_2-\nu_i}. \qquad (8)$$

Therefore, eq. (7) is essentially given by the three steps [13]:

- interpolation to obtain u_{mn} (eq. (8));
- standard two-dimensional FFT on $cN_1 \times cN_2$ points;
- scaling and decimation.

It should be noticed that, in eq. (8), the u_{mn}'s receive contribution only from a very limited number of terms. Indeed, the $\hat{\phi}$ and $\hat{\psi}$ in eq. (8) are different from zero only for

$$|m+cpN_1-\mu_i| \le K \ll cN_1 \quad |n+cqN_2-\nu_i| \le K \ll cN_2, \qquad (9)$$

where typical values for K are 3 and 6.
Finally, let us highlight that the obtained overall computational complexity is $\mathcal{O}((cN)^2 \log(cN))$ for $N \sim N \sim N_2$, N_1, N_2, $M \gg K$.

2.3. Acceleration of the pattern evaluation

Once described the 2D NED-NUFFT algorithm, let us briefly sketch the GPU acceleration.
The most difficult step to be implemented on GPU is the interpolation stage [5, 12]. Accordingly, only for this stage, we present some details of the strategy exploited to profit of the available massive parallelism.
If we denote the input index with i and output indices with m and n, according to eq. (9), a given input index contributes only to a small number of output terms. The adopted solution assigns each GPU thread to an input index. Unfortunately, with such a choice, race conditions occur since different inputs can contribute to the same output. The problem is solved by profiting of a special feature of GPU: the atomic operations. They make the access of different threads to the same output location (in the GPU global memory) serial.
Dynamic Parallelism has been exploited to perform the two nested "for loops" with indices p and q occurring in eq. (8), each one spanning only $2K + 1$ cycles. Indeed, the CUDA Dynamic Parallelism allows each CUDA function (kernel) to give work to itself, thus making the easy implementation of recursive algorithms possible, exploiting different levels of parallelism.
We present now some codes to let the Reader take a closer

look at the details of the adopted coding strategy. In the Listing 1, each parent thread is assigned to an input index i. The parent thread (first level of parallelism) generates $(2K+1)\times(2K+1)$ children (second level of parallelism), by calling the "series terms" kernel shown in Listing 2. Each child thread takes into account for a single loop cycle (double summation).
The implemented NUDFT NED provides a significant speedup of the array factor calculation, of one order of magnitude with respect to a CPU code, for a RA made of 100×100 elements [15].

```
__global__ void InterpolationNFFT2_2DGPUKernel(_)
{
   int i = threadIdx.x + blockDim.x * blockIdx.x;
   double cc_points1=cc*x[i];
   // It is the mu
   double r_cc_points1=rint(cc_points1);
   const double cc_diff1 =
         cc_points1-r_cc_points1;

   double cc_points2=cc*y[i];
   // It is the nu
   double r_cc_points2=rint(cc_points2);
   const double cc_diff2 =
         cc_points2-r_cc_points2;

   double2 temp_data = data[i];
   dim3 dimBlock(13,13); dim3 dimGrid(1,1);
   series_terms<<<dimGrid,dimBlock>>>(_); }
```

Listing 1: CUDA interpolation Kernel using the dynamic parallelism.

```
__global__ void series_terms(_) {
    int m = threadIdx.x;
    int n = threadIdx.y;

    double tempd, phi_cap;

    double P = K*K-(cc_diff1 -(m-K))*
               (cc_diff1 -(m-K));

    if(P<0.) {
       tempd=rsqrt(-P);
       phi_cap = (1./pi_double)*
             ((sin(alpha/tempd))*tempd);   }
    else if(P>0.) { tempd=rsqrt(P);
       phi_cap = (1./pi_double)*
             ((sinh(alpha/tempd))*tempd); }
    else phi_cap = alpha/pi_double;

    P = K*K-(cc_diff2 -(n-K))*
        (cc_diff2 -(n-K));

    if(P<0.) {tempd=rsqrt(-P);
    phi_cap = phi_cap*(1./pi_double)*
          ((sin(alpha/tempd))*tempd);   }
    else if(P>0.) {tempd=rsqrt(P);
    phi_cap = phi_cap*(1./pi_double)*
          ((sinh(alpha/tempd))*tempd); }
    else phi_cap = phi_cap*alpha/pi_double;

    int PP1 = modulo((r_cc_points1+
              (m-K)+N1*cc/2),(cc*N1));
    int PP2 = modulo((r_cc_points2+
              (n-K)+N2*cc/2),(cc*N2));
    atomicAdd(&result[IDX2R(PP1,PP2,cc*N2)].x,
          temp_data.x*phi_cap);
    atomicAdd(&result[IDX2R(PP1,PP2,cc*N2)].y,
          temp_data.y*phi_cap); }
```

Listing 2: CUDA summation kernel invoked by the interpolation one.

3. PSO

PSO [9] is a global optimization algorithm working according to the behavior of flocks of bees in search of food. It shows appealing convergence properties that can be obtained by tuning its parameters in order to align the algorithm to the problem at hand. PSO shows a highly parallelizable computing pattern, making its implementation amenable of acceleration using GPUs [16]. This mitigates the need of large number of iterations and of particle updates and fitness evaluations [9].
The search space dimension in PSO equals the overall number of unknowns N_{unkn}, i.e., the number of polynomial coefficients used to represent the command phase and the element coordinates. The particles' position and the so-called "velocity" $\underline{X}(t)$ and $\underline{V}(t)$, respectively, at the iteration step fictitiously represented by the time variable t are N_{unkn}-dimensional vectors whose update rule is given by

$$\begin{cases} \underline{V}(t) = & w\underline{V}(t-1)+ \\ & C_1R_1\left[\underline{X}_{best}(t-1)-\underline{X}(t-1)\right]+ \\ & C_2R_2\left[\underline{X}_{gbest}(t-1)-\underline{X}(t-1)\right] \\ \underline{X}(t) = & \underline{X}(t-1)+\underline{V}(t) \end{cases} \quad (10)$$

In eqs. (10), the velocity is actually dealt with as a "displacement" vector. Furthermore, in eqs. (10), C_1 and C_2 are proper positive constants, R_1 and R_2 are two random numbers uniformly distributed in $[0,1]$, $\underline{X}_{best}(t-1)$ is the best-fitness position (local best) reached by an individual particle at the time $t-1$ and $\underline{X}_{gbest}(t-1)$ is the best-fitness position (global best) ever found by the whole swarm up to $t-1$. Moreover, the term $\underline{X}_{best}(t-1)-\underline{X}(t-1)$ represents the *cognitive contribution* while $\underline{X}_{gbest}(t-1)-\underline{X}(t-1)$ is the *social contribution*. Finally, w is the so-called *inertia weight* [17] balancing global and local search.
According to eq. (10), the processing consists of four steps: a) Global best update kernel; b) Positions update; c) Fitness evaluation function; d) Local best update kernel. The four steps are detailed in the following Subsections.

3.1. Global best update kernel

Following the initial random generation of the population achieved by the cuRAND library or after a generic iteration step has been accomplished, the best-fitness position $\underline{X}_{gbest}(t-1)$ is determined by a direct CUDA Thrust call.

3.2. Positions update

Concerning the positions update, eq. (10) shows that, once the information related to the global best has been achieved,

there is no need for any further communication among the particles. Accordingly, the update can occur in parallel both across the particles and across the particle dimensions. The kernel function performing the position update is schematically reported in Listing 4. For the execution of such a kernel, different blocks are assigned to handle different particles, while their corresponding block threads manage the particle dimensions. Care has been taken to store as much as possible local (to the thread) temporary data within the registers while avoiding register spilling. It is noted that the kernel function in Listing 4 also performs the update of the best personal particle position. However, to save global memory storage time, such update is performed only if the neighboring particles have better personal best positions than the particle at hand. The particle neighborhood is evaluated by storage of the relevant arrays in the texture memory. Further global memory loads are saved by storing the Boolean update information in the shared memory.

3.3. Fitness evaluation function

Regarding the fitness evaluation, the far field pattern and, then, the fitness, are calculated for each particle by using different parallel kernels, including the one implementing the 2D NED NUFFT.

3.4. Local best update kernel

The local best update kernel is meant to update the personal best fitness value. In this case, a different thread manages a different particle. Again, to save global memory storage time, the update is executed only provided that the neighboring particles have better personal fitness. The necessary minimum value calculations are obtained by in-kernel Thrust calls.

```
__global__ void g_positionsUpdate(...){

   unsigned int tid = blockIdx.x * blockDim.x
                    + threadIdx.x;

   __shared__ unsigned int s_update;
   __shared__ unsigned int s_bestID;

   if(threadIdx.x == 0){
      s_update = d_to_be_updated[blockIdx.x];
      s_bestID = d_localBestIDs[blockIdx.x]
               * blockDim.x;
   }
   __syncthreads();

   float pos = d_positions[tid];
   float bestPos = d_best_personal_positions[tid];
   float vel = d_velocities[tid];

   float R1, R2;
   R1 = curand_uniform(&devStates[tid]);
   R2 = curand_uniform(&devStates[tid]);

   if (s_update){
      bestPos = pos;
      d_best_personal_positions[tid] = bestPos; }

   __threadfence();
```

```
   vel *= W;
   vel += C1 * R1 * (bestPos - pos);
   vel += C2 * R2 *
   (d_best_personal_positions[s_bestID
       + threadIdx.x] - pos);

   d_velocities[tid] = vel;
   pos += vel;
   pos = min(pos, c_maxValues[threadIdx.x]);
   pos = max(pos, c_minValues[threadIdx.x]);

   d_positions[tid] = pos; }
```

Listing 3: Positions update kernel function.

4. Results

The computational performance of the GPU implementation of the 2D NED-NUFFT algorithm has been compared with that of an analogous CPU implementation for 2D RAs having randomly located elements as well as random command phases [15]. The codes have been run on an Intel Core i7-6700K, 4GHz, 4 cores (8 logical processors), equipped with an NVIDIA GTX 960 card, compute capability 5.2. Fig. 4 shows the GPU vs. CPU speedup when RAs having N elements are considered. The achieved speedup is larger than 10 even though atomic operations are employed: atomic operations on modern GPU architectures are indeed very fast. The speedup also saturates for values of N approaching millions of elements due to the saturation of the GPU resources.

Let us now turn to the results of the RA synthesis. The antenna here considered is an aperiodic RA working at $14.25GHz$, with a circular footprint, $z_0 = 58.3cm$, θ_f equal to about 11.2°, $y_{off} = 11.6cm$, feed shape factor $m_f = 12$.

The POS synthesized according to stages 1-3 of Fig. 1 provides the number of elements, their coordinates, and the corresponding command phase. Indeed, the optimization of the spatial distribution of the elements moves them freely, but only those elements falling within the assigned circular antenna footprint are effectively considered as scatterers. However, constraints on the minimum and the maximum spacing, equal to 0.49λ and 0.7λ, respectively, are enforced in all the stages, by discarding solutions not satisfying the requirements.

A target coverage of South America has been adopted for the test case, and enforced by two mask functions having a flat top behavior on the coverage, and a nominal sidelobe level lower than $40dB$. PSO has been executed with a swarm of 100 particles, by using 56 unknowns, $w = 0.721$, $C_1 = C_2 = 1.193$. The optimization on 100 iterations takes about $2hours$ on a PC equipped with a NVIDIA GTX 960.

A total number of 2032 elements has been considered for the synthesized RA. The directivity pattern synthesized by the first stage is reported in Fig. 4, together with the mask functions (black lines). Finally the synthesized pattern at the end of stage 3) is shown in Fig. 4.

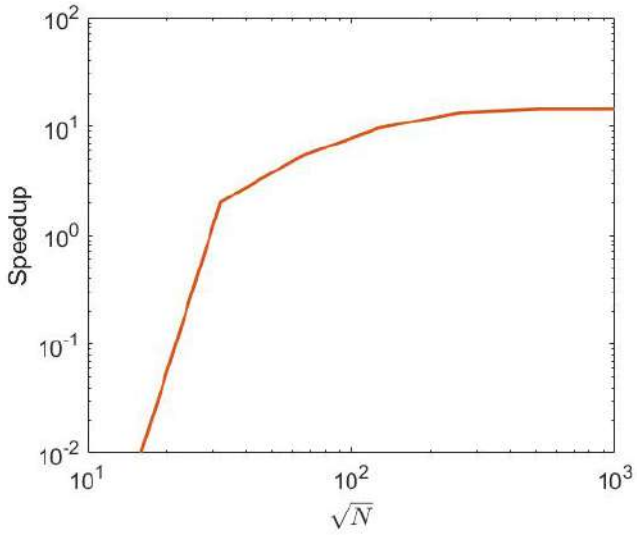

Figure 3: Speedup in log-scale of the 2D NED NUFFT implementation.

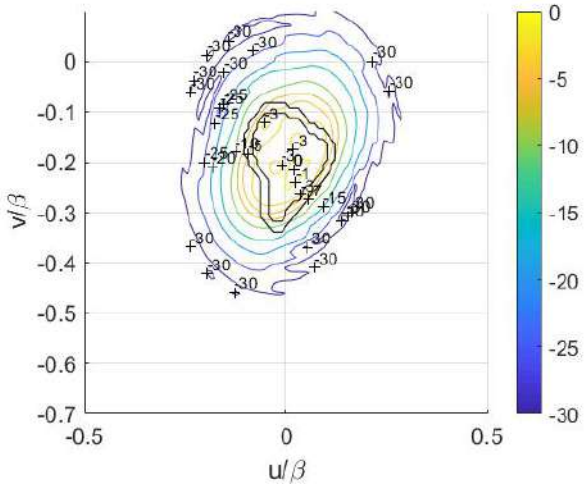

Figure 4: Directivity pattern synthesized by the PSO.

5. Conclusions

In this paper, the use of GPU computing in reflectarray antenna synthesis has been discussed.
The described approach uses a multi-stage synthesis structure, using global and local optimizers. Global optimization is afforded by a GPU-based implementation of Particle Swarm Optimization. To reduce the computational burden, the evaluation of the aperiodic array factor is performed by a GPU-implemented Non Uniform FFT routine.

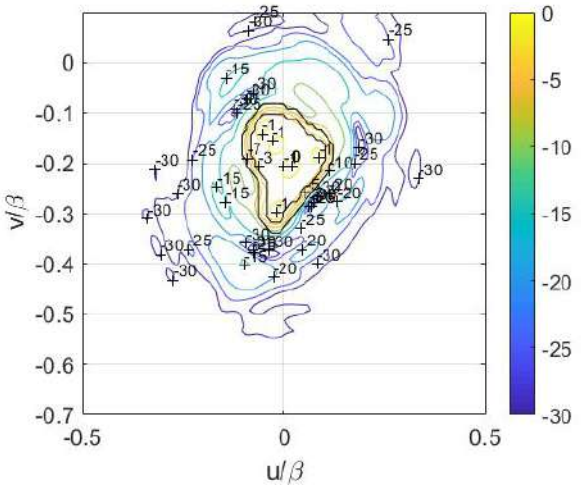

Figure 5: Directivity pattern synthesized after stage 3).

References

[1] J. Huang, J.A. Encinar, *Reflectarray Antennas*, J. Wiley & Sons, Hoboken, NJ, 2008.

[2] J.A. Encinar, M. Arrebola, and G. Toso, A parabolic reectarray for a bandwidth improved contoured beam coverages, *Proc. of the Europ. Conf. on Antennas Prop.*, Edinburgh, UK, Nov. 1116, 2007, pp. 15.

[3] A. Capozzoli, C. Curcio, G. D'Elia, A. Liseno, P. Vinetti, G. Toso, *Aperiodic and non-planar array of electromagnetic scatterers, and reflectarray antenna comprising the same*, World Patent Nr. WO/2011/033388.

[4] A. Capozzoli, C. Curcio, A. Liseno, G. Toso, Fast, Phase-only synthesis of flat aperiodic reflectarrays, *Progr. Electromagn. Res.* 133: 53–89, 2013.

[5] A. Capozzoli, C. Curcio, A. Liseno, G. Toso, Fast, Phase-Only synthesis of aperiodic reflectarrays using NUFFTs and CUDA, *Progr. Electromagn. Res.* 156: 83–103, 2016.

[6] A. Capozzoli, G. D'Elia, Global optimization and antennas synthesis and diagnosis, part one: concepts, tools, strategies and performances, *Progr. Electromagn. Res.* 56: 195-232, 2006.

[6] D.H. Wolpert, W.G. Macready, No free lunch theorems for optimization, *IEEE Trans. Evolutionary Comput.*, vol. 1, n. 1, pp. 67-82, Apr. 1997.

[7] S.A. Vavasis, *Nonlinear Optimization: Complexity Issues*, Oxford Science Publication, New York, 1991.

[8] A. S. Nemirovsky, D.B. Yudin, *Problem Convexity and Method Efficiency in Optimization*, John Wiley & Sons, New York, 1983.

[9] J. Kennedy, R. Eberhart, Particle swarm optimization, *Proc. of the IEEE Int. Conf. on Neural Networks*, Perth, WA, Nov. 27-Dec. 01, 1995, pp. 1942-1948.

[10] K. Fourmont, Non-Equispaced Fast Fourier Transforms with applications to tomography, *J. Fourier Anal. Appl.*, vol. 9, n. 5, pp. 431-450, 2003.

[11] A. Capozzoli, C. Curcio, G. D'Elia, A. Liseno, P. Vinetti, FFT & aperiodic arrays with phase-only control and constraints due to super-directivity, mutual coupling and overall size, *Proc. of the 30th ESA Antenna Workshop*, May 27-30, 2008, pp. 213-216.

[12] A. Capozzoli, C. Curcio, G. D'Elia, A. Liseno, P. Vinetti, Fast CPU/GPU pattern evaluation of irregular arrays, *ACES J.*, vol. 25, n. 4, pp. 355-372, Apr. 2010.

[13] A. Capozzoli, C. Curcio, A. Liseno, Optimized nonuniform FFTs and their application to array factor computation, *IEEE Trans. Antennas Prop.*, vol. 67, n. 6, pp. 3924-3938, Jun. 2019.

[14] R.M. Tribug, E.S. Belinsky, *Fourier Analysis and Approximation of Functions*, Springer Science+Business Media, Dordrecht, NL, 2004.

[15] A. Capozzoli, C. Curcio, A. Liseno, Non-Uniform FFT (NUFFT) Algorithms for Antenna Radiation, *Proc. of the 23rd Int. Conf. on Appl. Electromagn. and Commun.*, Dubrovnik, Croatia, Sept. 30-Oct. 2, 2019.

[16] L. Mussi, F. Daolio, S. Cagnoni, Evaluation of particle swarm optimization algorithms within the CUDA architecture, *Information Sciences* 181: 4642–4657, 2011.

[17] Y. Shi, R. Eberhart, A modified particle swarm optimizer, *Proc. of the IEEE Int. Conf. on Evolutionary Comput.*, Anchorage, Ak, May 4-9, 1998, pp. 6973.

Wave Propagation

Aberration Analysis of Four-lens Slit Spatial Filter for High-power Lasers

Han Xiong*, Quanying Wu

School of Mathematics and Physics, Suzhou University of Science and Technology, Suzhou, China
*corresponding author, E-mail: xh1980xh@126.com

Abstract

For better investigating of the four-lens slit spatial filter to be potentially used in high-power lasers, effect of aberrations to the filter is numerically studied and analyzed, and the corresponding tolerance of each kind of aberration is obtained.

1. Introduction

Spatial filter [1] is used to improve laser beam quality by cleaning off the harmful middle and high spatial frequencies, especially in inertial confinement fusion lasers that have higher intensities. In addition, spatial filter also bears the functions of image relaying and aperture matching. Traditional spatial filter consists of two convex lenses with a pinhole aperture placed at the common focal plane of the two lenses, which is used for cutting off the spatial spectra. However, the pinhole diameter has to be small enough for efficient spectrum cutoff, therefore it has to withstand intense focal spot and result into pinhole closure [2]. To lower the focal intensities and postpone the pinhole closure time, the focal lengths of the lenses in high power lasers have to be long enough, which always leads to large-scaled high-power lasers. Besides, high vacuum environment is need due to the air breakdown brought from peak focal intensity. Fortunately, slit spatial filter, as a kind of novel spatial filter, solved the above problems. The slit spatial filters can focus the laser beam into a line instead of the original spot by introducing cylindrical lenses into filters, which can greatly enlarge the focal area and lower the focal intensity. As a result, the pinhole closure problem in present high-power lasers can be significantly eased or even avoided. As for now, four-lens [3], three-lens and two-lens slit spatial filters had been proposed, and relative characteristics of image relay model and spatial filtering had already been studied theoretically and experimentally. Since the intense focus in high-power lasers, little deviations in wavefront could induce large turbulence in pinhole closure time. In this paper, the effect of aberrations to four-lens slit spatial filter is studied based on the diffraction theory of aberration [4].

2. Numerical simulation of aberration analysis

As shown in Fig. 1, the four-lens slit spatial filter consists of two pairs of cylindrical lenses and two slit apertures, in which Lens-v-I, Lens-v-II and Slit-I are for the vertical focusing and collimation, and Lens-h-I, Lens-h-II and Slit-II are for the horizontal with corresponding focal lengths of $f_{v,1}$, $f_{v,2}$, $f_{h,1}$ and $f_{h,2}$, respectively.

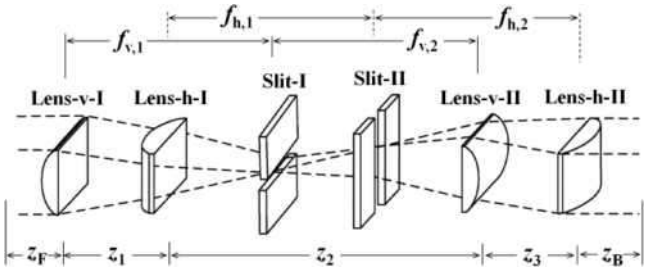

Figure 1: The schematic diagram of the four-lens slit spatial filter.

The incident laser is a 20th super-Gaussian beam with diameter of 100 mm, wavelength of 1053 nm, pulse width of 10 ns and pulse energy of 1 KJ for single beam, which incidents the four-lens slit spatial filter after being modulated with Sinc function and then undergoing a 3-meter-long free propagation. Focal lengths of the lenses in filter are all 5 meter, and the cutoff frequency of slit apertures is set as 30 times of the diffraction limitation. Due to the introduced cylindrical lens, the focusing in meridian plane is separated from that in sagittal plane. Distortion, astigmatism and coma in meridian or sagittal plane will show different effect to the system from each other, so that they are all considered individually in the two directions. The aberrations are added into the incident laser beam one kind for each time. Assuming the wavefront error is $\phi(x,y)$, which, with Zernike polynomials, can be expanded as shown below:

$$\begin{aligned}\phi(\rho,\theta) = {} & Z_0 + Z_1\cdot\rho\cos\theta + Z_2\cdot\rho\sin\theta + Z_3\cdot(2\rho^2-1) \\ & + Z_4\cdot\rho^2\cos^2\theta + Z_5\cdot\rho^2\sin^2\theta \\ & + Z_6\cdot(3\rho^3-2\rho)\cos\theta + Z_7\cdot(3\rho^3-2\rho)\sin\theta \\ & + Z_8\cdot(6\rho^4-6\rho^2+1)\end{aligned} \quad (1)$$

where ρ is the normalized polar radius and θ is the polar angle, Z_0, Z_1, …Z_7 and Z_8 are the Zernike polynomials, in which Z_0 is the translation value of the whole wavefront and can be omitted here, the others polynomials are shown below:

Table 1. Zernike polynomials

Items	Corresponding aberrations	Cartesian coordinate system
Z_1	Distortion-x	x
Z_2	Distortion-y	y
Z_3	Field curvature	$-1+2(x^2+y^2)$
Z_4	Astigmatism-x	x^2-y^2
Z_5	Astigmatism-y	$2xy$
Z_6	Coma-x	$-2x+3x(x^2+y^2)$
Z_7	Coma-y	$-2y+3y(x^2+y^2)$
Z_8	Spherical aberration	$6(x^2+y^2)^2-6(x^2+y^2)+1$

The introduced aberrations will affect beam quality and far-field distributions. Near-field contrast and near-field modulation are important parameters of beam quality, peak intensity is related with the high vacuum environment of spatial filter, and the intensity irradiated on inner edge of slit apertures seriously involves the pinhole closure time and is an important parameter for normal running of high-power lasers. According to simulation, the near-field contrast and the inner edge intensity are the main affected parameters, which will be used to determine the tolerance of each aberration. For near-field contrast, 10% is the tolerant change, and 50% is for the inner edge intensity since intensity change within 10% has no apparent effect on the ablation of aperture material and closure time.

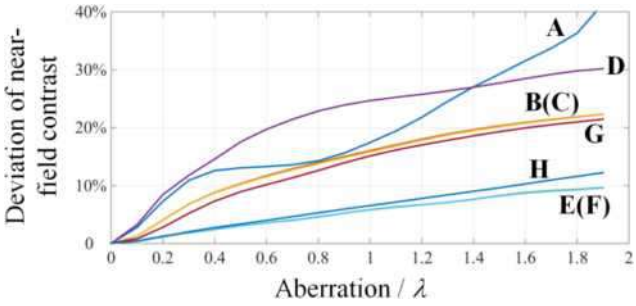

Figure 2: Deviations of near-field contrast change along with the aberrations (A: spherical aberration, B: coma-x, C: coma-y, D: field curvature, E: distortion-x, F: distortion-y, G: astigmatism-x, H:astigmatism-y).

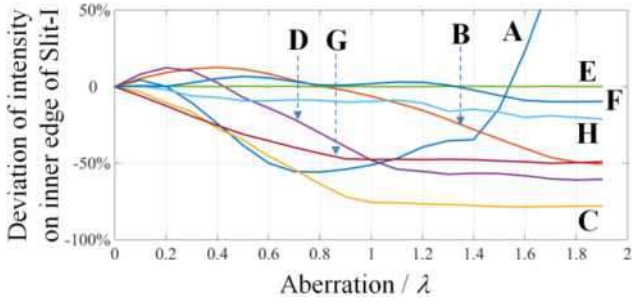

Figure 3: Deviations of intensity on inner edge of slit-I change along with the aberrations.

As shown in Fig. 2, all kinds of aberrations drop down the beam quality, in which the spherical aberration and field curvature are the most influenced factors. It can be seen that both the coma and the distortion shows no difference in x- and y-directions. As shown in Fig. 3 and Fig. 4, the introduction of coma-x, coma-y and astigmatism-y changed little on the inner edge intensities of both Slit-I and Slit-II, and spherical aberration and astigmatism-x show almost the same effect on inner edge intensities of Slit-I and Slit-II.

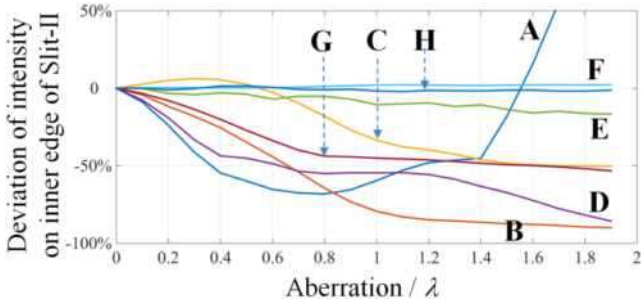

Figure 4: Deviations of intensity on inner edge of slit-II change along with the aberrations.

According to the above results, the tolerances of aberrations are summarized, as listed in Table. 2.

Table 2. Tolerance values of aberrations

Aberration	Tolerance	Aberration	Tolerance
Distortion-x	1.90λ	Astigmatism-x	0.58λ
Distortion-y	1.90λ	Astigmatism-y	1.55λ
Field curvature	0.22λ	Spherical aberration	0.27λ
Coma-x	0.48λ	Coma-y	0.48λ

3. Conclusions

In this paper, the influence of aberrations to four-lens slit spatial filter is numerically studied based on diffraction theory of aberration, and the tolerance of all kinds of aberrations are obtained according to near-field contrast and intensities on inner edge of slit apertures of slits.

Acknowledgements

This work is supported by the National Natural Science Foundation of China under Grant Nos. 11504255, Jiangsu Province Key Discipline of China′s 13th five-year plan (20168765), Jiangsu Key Laboratory of Advanced Optical Manufacture Technology (KJS1710).

References

[1] A. J. Campillo, S. L. Shapiro, B. R. Suydam, Periodic breakup of optical beams due to self-focusing, *Applied Physics Letters* 23: 628−630, 1973.

[2] J. E. Murray, D. Milam, C. D. Boley, et al, Spatial filter pinhole development for the national ignition facility, *Applied Optics* 39:1405−1420, 2000.

[3] J. Wang, H. Xiong, X. Zhang, X. Yuan, Beam propagation characteristics in four-cylindrical-lens slit spatial filter, *Acta Optica Sinica* 35: 0907001, 2015.

[4] M. Born, E. Wolf, *Principles of optics*, University press, Cambridge, pp.517−547, 2005.

A Hybrid Electromagnetic Propagation Model for Predicting Ground Multipath Effects

Gul Yesa ALTUN[1,2], Ozlem OZGUN[2]

[1]HBT – PHDTM, Aselsan Inc., Ankara, Turkey
[2]Department of Electrical and Electronics Engineering, Hacettepe University, Ankara, Turkey
*corresponding author, E-mail: yesaaltun@msn.com

Abstract

This paper presents a novel hybrid propagation model for solving electromagnetic wave propagation over an irregular terrain by incorporating the ground multipath effects into the solution efficiently. The proposed method combines the advantages of the Two-Way Split-Step Parabolic Equation (2W-SSPE) method with the Method of Moments (MoM). The 2W-SSPE is used to propagate the waves over long distances with less computational load, and the MoM is employed to obtain the scattered waves from slanted/curved surfaces more accurately compared to the 2W-SSPE formalism which employs staircasing approximation for terrain modeling. The numerical results of a representative example, which has been modeled by the hybrid SSPE+MoM, as well as by the standard 2W-SSPE, are also presented.

1. INTRODUCTION

The Split-Step Parabolic Equation (SSPE) method is an efficient method which can be used to solve electromagnetic wave propagation over terrain by taking some tropospheric, especially ducting, effects into account [1]. It can easily be employed for long-range propagation problems because it can obtain the field distribution in an electrically-large computational domain with less computational burden, which cannot be handled by standard full-wave solvers due to the necessity for small mesh resolution to obtain accurate results. The SSPE method solves an initial-value problem starting from an initial range and marching out in range by obtaining the field at each range step. In this manner, long-range propagation problems can be solved in a relatively-short CPU time with less memory. However, since the standard SSPE is a one-way method, which models only forward-propagating waves, it cannot take account of backward-propagating waves which are important for modeling multipath effects in a terrain environment. The Two-Way SSPE (2W-SSPE) method has been introduced by using a forward-backward formalism to incorporate the effects of multipath effects into the solution [2]. The 2W-SSPE method was implemented in PETOOL [3] by using a staircase approximation over an irregular terrain. Although the staircase approximation provides reliable results in most cases, the accuracy of the 2W-SSPE method can be improved by modeling curved/slanted surfaces by using a more efficient approach rather than the staircase approach.

In this study, a novel hybrid method is proposed for modeling electromagnetic wave propagation over an irregular terrain, by combining the 2W-SSPE method with the Method of Moments (MoM). The MoM is an integral equation-based full-wave method, and can successfully be used to mitigate the staircasing error by solving the scattered field problem over the irregular part of the Earth's surface. Therefore, the hybridization of the two methods is done as follows: The MoM is used to obtain the scattered waves from slanted/curved surfaces, whereas the 2W-SSPE is used to propagate the waves over long distances. In this manner, a more efficient propagation model is developed by combining the strengths of both methods. After briefly summarizing the proposed method, the numerical results of some representative examples are presented.

2. FOURIER-BASED SPLIT-STEP SOLUTION OF PARABOLIC EQUATION

The parabolic equation is derived from the two-dimensional Helmholtz equation by using a paraxial approximation. The rapidly varying phase term is separated, and a reduced function that varies slowly in range for propagation angles close to the paraxial direction is obtained. The details of the parabolic equation modeling and the SSPE methods can be found in [1-3]. In Cartesian coordinates (x, y, z), in accordance with the expansion of the pseudo-differential operator, the wide-angle split-step solution of the scalar wave equation for forward and backward propagation for horizontal polarization is determined by (assuming $e^{-i\omega t}$ time-dependence)

$$u(x \pm \Delta x, z) = e^{ik(n-1)\Delta x}\, F^{-1}\{e^{-\frac{ip^2\Delta x}{k}\left(\sqrt{1-\frac{p^2}{k^2}}+1\right)^{-1}} F[u(x,z)]\} \quad (1)$$

where *u(x, z)* is the propagating wave, *x* and *z* are the range and the height respectively, $k = 2\pi/\lambda$ is the wave number where λ is the wavelength, n is the refractive index, F indicates the Fourier transform, F^{-1} is the inverse Fourier transform, $p = ksin\theta$ is the transform variable (θ is the propagation angle) and Δx is the range step size.

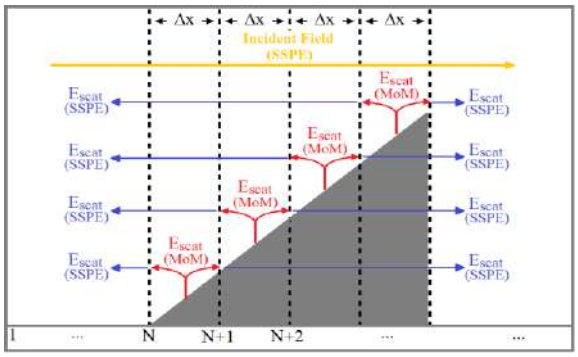

Figure 1: Modeling by the SSPE+MoM hybrid method.

3. METHOD OF MOMENTS

For horizontal polarization, the Electric Field Integral Equation (EFIE) with $e^{j\omega t}$ time-dependence is expressed by

$$\frac{k\eta}{4}\int_{C'} J_z(\mathbf{r}')\ H_0^{(2)}(k|\mathbf{r}-\mathbf{r}'|)dl' = E_z^i(\mathbf{r}) \qquad (2)$$

In this equation, $H_0^{(2)}$ is Hankel function of second kind (zero-order), $\mathbf{r}'$ and $\mathbf{r}$ are the source point vector and observation point vector respectively, J_z is the induced current density on the surface, η is the intrinsic impedance of the free-space, C' is the boundary of the surface and $E_z^i(\mathbf{r})$ is the incident wave which is computed by the SSPE in (1).

4. THE HYBRID METHOD

The hybrid method is illustrated in Fig. 1. The first step in the hybrid method is to use the SSPE to obtain the field in the computational domain assuming that the flat Earth exists in the absence of terrain irregularities. The computed field is used as the excitation/incident field in MoM at the surface of the terrain. In the second step, the MoM is solved by using the incident field derived from the SSPE method, and the induced current densities are determined on the terrain surface. Afterwards, the induced currents lying on the surface between two consecutive range steps are radiated to obtain the fields at the corresponding range steps (i.e., dashed lines). For example, the currents on the surface lying between $N\Delta x$ and $(N+1)\Delta x$ range steps are used to determine the fields at these ranges steps. Finally, the SSPE is employed to propagate the fields at the range steps back and forth to obtain the field distribution in the whole computational domain by superposing all field components. Note that the scattered field at $N\Delta x$ range step is marched back by reversing the paraxial direction and, the scattered field at $(N+1)\Delta x$ range step is marched in the forward direction.

5. NUMERICAL EXAMPLES

A numerical example is considered, where a triangular terrain profile exists over the Earth as shown in Fig. 2. The transmitter antenna's beam pointing angle is 0 degree, and the 3dB beamwidth is 0.5 degree. The antenna is located at $x = 0$ km range and $z = 25$ m height. The frequency is 600MHz. The propagation factor (PF) maps are shown in Fig. 2. The PF is plotted at $x = 1.65$km range as a function of height in Fig. 3(a), and at $z = 100$m height as a function of range in Fig. 3(b). It is clearly observed from Fig. 2 that the multipath effects from the slanted face of the triangular terrain are modeled more accurately by the hybrid method.

6. CONCLUSIONS

A new hybrid method has been presented for modeling electromagnetic wave propagation by using the 2W-SSPE and MoM methods. It is observed that the backscattered waves are modeled more effectively by the hybrid method when there are curved/slanted objects on the Earth's surface. In the near future, this method will be applied to more general electromagnetic problems which include ducting conditions.

(a)

(b)

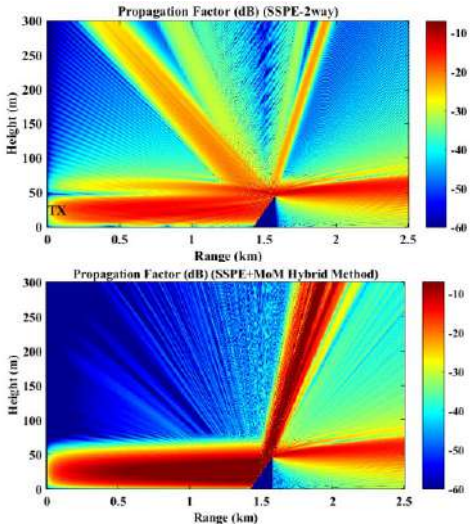

Figure 2: PF maps: (a) 2W-SSPE, (b) SSPE+MoM. ($\Delta x = 5$ m, $\Delta z = 0.35$m)

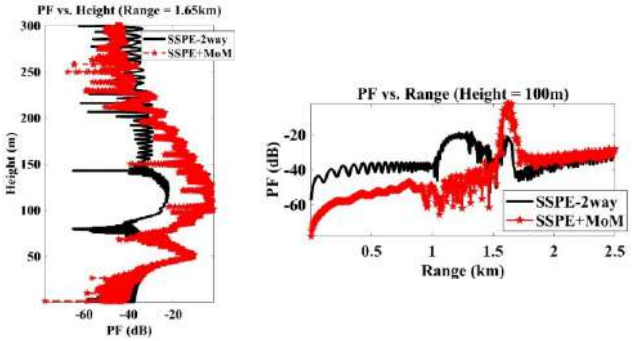

(a) (b)

Figure 3: PF plots: (a) At x = 1.65km, (b) at z =100m.

REFERENCES

[1] M.F. Levy, Parabolic equation methods for electromagnetic wave propagation, *IEEE Electromagnetic Wave Series* 45, London, 2000.

[2] O. Ozgun, "Recursive two-way parabolic equation approach for modeling terrain effects in tropospheric propagation," *IEEE Trans Antennas Propag*., vol. 57, no. 9, pp. 2706-2714, 2009.

[3] O. Ozgun, G. Apaydin, M. Kuzuoglu, L. Sevgi, "PETOOL: MATLAB-based one-way and two-way split-step parabolic equation tool for radiowave propagation over variable terrain", *Comput. Phys. Commun*., vol. 182, pp. 2638-2654, 2011.

Lumped energy absorbers and sinks in optics and electronics of metamaterials

Vasily Klimov[1]

[1]Lebedev Physical Institute, Leninskij Prospect 53, Moscow, 119991 Russia
*corresponding author, E-mail: klimovvv@lebedev.ru

Abstract

A new paradigm for investigations in nano-optics and optics of metamaterials is put forward. This paradigm is based on simultaneous use of notions of both sources and sinks of energy and allows one to realize rich potential of metamaterials.

1. Introduction

Usually, to describe optical and electromagnetic phenomena, the notion of an energy source is used. However, due to energy conservation the energy sinks should also be taken into account. Usually, the energy flow is going from the source to infinity, and in this case the infinity point can be considered as the energy sink. In my talk, I will present a new paradigm for investigation of nano-optics and optics of metamaterials. This paradigm is based on simultaneous use of notions both of sources and sinks of energy and allows one to realize rich potential of metamaterials.

2. Sources, sinks, and lumped absorbers in free space

Let me start with discussion of how the energy radiated by an excited atom (one photon) can be fully absorbed by another atom and how the energy sink notion can be useful to describe this process. In Fig.1a, one can see streamlines for the emitting dipole and the absorbing nanoparticle

$$H_z(\mathbf{r}) = H_0^{(1)}\left(k_0|\mathbf{r}+\mathbf{r}_0|\right) + \alpha H_0^{(1)}\left(k_0|\mathbf{r}-\mathbf{r}_0|\right), \quad (1)$$

where $H_0^{(1)}$ stands for the Hankel function of the first kind, (outgoing waves) and α stands for the polarizability of the absorber.

From Fig.1a, one can see that the power outgoing from the dipole source is almost fully absorbed by a passive nanoparticle due to interference effects. As a result, we have a perfect lumped absorber.

In Fig.1b, the streamlines for the radiating source (outgoing waves, $H_0^{(1)}$) and the power sink (incoming waves, $H_0^{(2)}$)

$$H_z(\mathbf{r}) = H_0^{(1)}\left(k_0|\mathbf{r}+\mathbf{r}_0|\right) + \beta H_0^{(2)}\left(k_0|\mathbf{r}-\mathbf{r}_0|\right) \quad (2)$$

are shown.

Comparing these pictures, one can see that the streamlines are almost the same although the systems are very different from the physical point of view.

Then, I will discuss how Perfect Electric Conductor (PEC) or Photonic Crystal (PC) cavity can improve the efficiency and localization of photon absorption process.

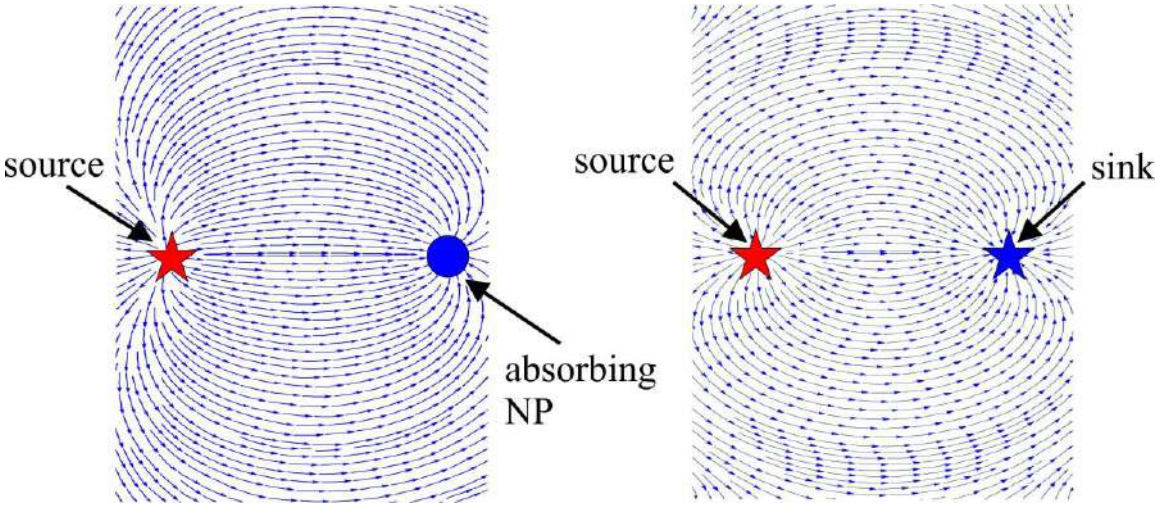

Figure 1: Streamlines for a dipole source and a point absorber (eq. (1), a) and for a dipole source and a sink (eq. (2), b)

3. Lumped absorbers and power sinks in a Negative Index Metamaterial (NIM)

It is known that a dipole source near the NIM interface (ε,μ < 0) with small losses results in resonance excitation of surface waves of infinite amplitude. However, the excitation of the surface waves can be suppressed if one put a (ghost) sink of energy inside the NIM. In this case, the exact analytical solutions can be written as [1,2]:

$$H_z = \begin{cases} \frac{\partial}{\partial x} H_0^{(1)}\left(k_0 |\mathbf{r}+\mathbf{r}_0|\right), x<0 \\ -\frac{\partial}{\partial x} H_0^{(1)}\left(k_0 |\mathbf{r}-\mathbf{r}_0|\right), x>0 \end{cases} \quad (3)$$

The corresponding streamlines of Poynting vector are shown in Fig. 2.

vacuum NIM

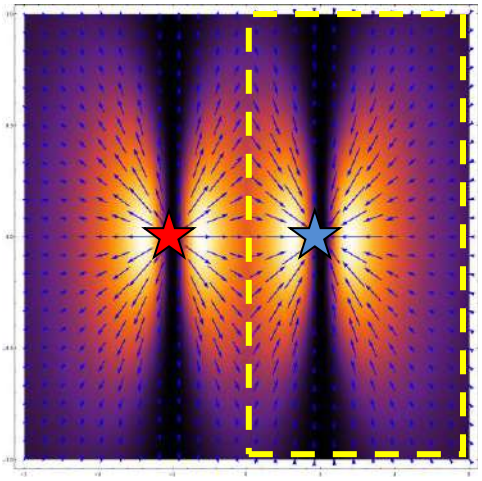

Figure 2: Streamlines for a dipole source and a sink

From Fig.2, one can see that the power emitted by the source is fully absorbed by the sink.
The solution (3) is not fully physical. However, if one put a point absorber instead of a sink, one will have the same picture of streamlines [3,4]. That is why one can design perfect lumped absorbers with making use of the NIM interface.
A fully analogous situation takes place in the case of a NIM slab of a finite thickness [1,5] and some other geometries.

4. Sources and sinks for electrons in graphene

The interplay between power sources and sinks is a very general phenomenon, and one can observe it in different branches of physics. In this section, we will show that an analogous situation occurs in graphene half of which has negative refraction for electrons due to external potential *V=2E* applied [2]:

$$\begin{matrix} \left[i\boldsymbol{\sigma}\cdot\nabla+\mathrm{E}\right]\psi = j_{source}\delta^{(2)}\left(\mathbf{r}-\mathbf{r}_0\right), x<0 \\ \left[i\boldsymbol{\sigma}\cdot\nabla-\mathrm{E}\right]\psi = 0, \qquad\qquad x>0 \end{matrix}, \quad (4)$$

where $\boldsymbol{\sigma} = \{\sigma_x, \sigma_y\}$ are the Pauli matrices and $j_{source} = [1,0]$.
The solution of eq. (4) is very similar to eq. (3) and has the following form ($j_{\text{sink}} = [0,1]$):

$$\psi = \begin{cases} \left(\begin{matrix} \frac{i}{4}\left(\left[i\boldsymbol{\sigma}\cdot\nabla-\mathrm{E}\right]H_0^{(1)}\left(E|\mathbf{r}+\mathbf{r}_0|\right)\right) j_{source} \\ -\frac{i}{4E}\frac{\partial}{\partial y}\left[i\boldsymbol{\sigma}\cdot\nabla-\mathrm{E}\right] j_{\text{sink}} H_0^{(1)}\left(E|\mathbf{r}-\mathbf{r}_0|\right) \end{matrix}\right), x<0 \\ \frac{1}{4E}\frac{\partial}{\partial x}\left[i\boldsymbol{\sigma}\cdot\nabla+\mathrm{E}\right] j_{\text{sink}} H_0^{(1)}\left(E|\mathbf{r}-\mathbf{r}_0|\right), x>0 \end{cases} \quad (5)$$

The current flows for (5) are shown in Fig.3.

V=0 V=2E

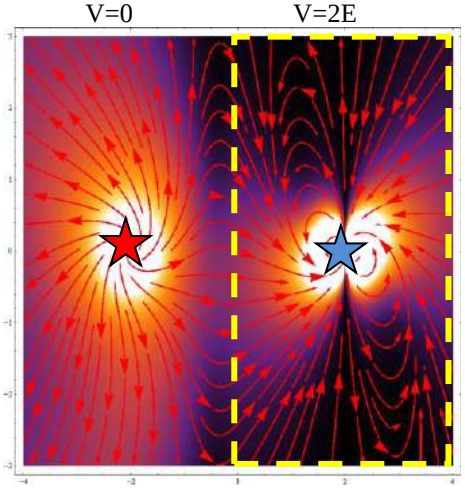

Figure 3: Streamlines for a source and a sink for electrons in graphene.

It is interesting to note that in contrast to an electrodynamics case, there is a field reflected from a sink in the domain of a source.
It is very important that the notion of sink in electronics is fully physical and there is no need to use absorbers instead of sinks.

5. Conclusions

Our results show that lumped power sinks and perfect absorbers are natural and universal phenomena at large. They can be used for development of new optical and electronic nanodevices on the base of new metamaterials.

Acknowledgements

The author is grateful to the Russian Foundation for Basic Research (Grant No.18-02-00315).

References

[1] V. Klimov, Novel approach to a perfect lens, *JETP Letters* 89(5): 270-273, 2009.
[2] V. Klimov, J. Baudon and M. Ducloy, Comparative focusing of Maxwell and Dirac fields by negative refraction half-space, *Europhys. Letters* 94: 20006, 2011.
[3] G.-Y. Guo, V. Klimov, S. Sun, W.-J. Zheng, Metamaterial slab-based super-absorbers and perfect nanodetectors for single dipole sources, *Optics Express* 21: 11338, 2013.
[4] V. Klimov, S. Sun, G.-Y. Guo, Coherent perfect nanoabsorbers based on negative refraction, *Optics Express* 20: 13071-13081, 2012.
[5] V. Klimov,Energy Flow in a Negative-Index Material, http://demonstrations.wolfram.com/EnergyFlowInANegativeIndexMaterial/, *Wolfram Demonstrations Project*.

Learning Approaches to Solve Full-Wave Inverse Scattering Problem

Zhun Wei[1] and Xudong Chen[1]

[1]Department of Electrical & Computer Engineering, National University of Singapore, Singapore, 117583
*corresponding author, E-mail: elechenx@nus.edu.sg

Abstract

This paper discusses machine learning approaches to solve full-wave inverse scattering problem and gives a brief review on this topic. In terms of representing scatterers, both parameterization representation and pixel-bases representation are discussed. This paper primarily focuses on pixel-bases representation since it is more versatile. Learning approaches for solving ISPs are categorized into three types. Each type is introduced, together with its advantages and disadvantages. We also give some guidelines that are useful in applying learning approaches to solve inverse scattering problems.

1. Introduction

Inverse scattering problems (ISPs) consists of determining the property of an unknown scatterer, such as its shape, position, size, and electrical properties from the measurement data that record how it scatters off incoming wave fields. Due to the contactless property of wave propagation, the imaging techniques based on ISPs have wide real-world applications, such as geophysics, biomedical imaging, nondestructive evaluation, through-wall imaging, remote sensing, and security checks. The ISPs are well-known to be challenging since they are intrinsically ill-posed and usually highly nonlinear.

ISPs can be solved by either traditional optimization approaches or learning approaches where neural network is first trained and then is used for reconstruction.

In early stage of machine learning approach for solving ISPs, neural network is able to extract rather general information of scatterers that is parameterized by only few parameters, such as the positions, sizes, shapes (such as radius for a circle), and piecewise-constant permittivities. However, the scope of such a parameterization approach is quite limited since scatterers' shape can be irregular, their number can be arbitrary, and scatterers can be spatially inhomogeneous.

A more powerful and versatile approach to represent scatterers is to use nature pixel basis, i.e., pulse basis, where the value of permittivity/conductivity of each pixel is an independent parameter. Learning approaches for solving ISPs are categorized into three types: direct application of learning; leaning a routine or step that is within the framework of iterative inversion solvers; new design of input-output pair for neural network. Each type is introduced, together with its advantages and disadvantages.

Summaries should be submitted electronically via http://mysymposia.org as a processed PDF. Acknowledgement of receipt of the submission will be sent to the contact-author e-mail address.

2. Conclusion

When applying machine learning to solve an inverse problem, a deep understanding of the corresponding forward problem is desirable. In solving ISPs, the concept of induced current plays an essential role in machine learning approaches, which enables us to design architecture of learning machine such that unnecessary computational effort spent in learning wave physics is minimized or avoided. The following guidelines are found useful in applying learning approaches to solve ISPs: (1) To construct input-output pairs in a way such that output depends in a much less nonlinear way on input. (2) To avoid directly dealing with measurement data, where neural network has to spend unnecessary cost to train and learn underlying wave physics. We should extract out as much as possible what people can do and leave the remaining to machine.

Propagation within Vegetation Issues towards New Frontiers

Iñigo Cuiñas*

Dept. Teoría do Sinal e Comunicacións, Universidade de Vigo, Vigo, Spain
*corresponding author, E-mail: inhigo@uvigo.es

Abstract

For several years, research on radio wave propagation within vegetation areas was something like a byproduct of radio science groups. The growing needs of connectivity everywhere, including rural, forest and vegetation areas, boosted the interest on such research during the beginnings of 21st century.
Nowadays, having even an ITU-R recommendation, it seems that it is an almost close field of interest. However, future needing would re-open the interest on such ambit, and this invited talk focus on different possibilities arising.

1. Introduction

Radio wave propagation still represents an important issue in deployment of a radio system. Although most research focus on indoor or outdoor-to-indoor propagation, as this kind of environments concentrate most of the users of radio communications (cellular and wireless systems), other rural or suburban areas are gaining interest: digitization of agriculture and livestock activities, sensing of forests and crops, Internet of the Things applications, emergency communications, and so on. Such activities could occur within forest or, at least, vegetated areas. Thus, a good knowledge of propagation conditions in such scenarios becomes interesting and deserves a deep study. The interest will grow in the immediate future, as deployment of new communication networks based on Fifth Generation (5G) paradigms will increase exponentially the possibilities of communication and, with them, the applications everywhere a wireless link can help in providing a new or traditional service.
Research on propagation within vegetation includes several experimental works, involving measurements and analysis of gathered data; some propagation models, with different origins both theoretical and based on real world data; and even an ITU-R recommendation [1]. Besides those researches focused on improving the coverage or the range within vegetation, there are also some contributions that get advantages on the attenuation or scattering induced by trees and shrubbery to provide security or privacy to the network users. Thus, the effect of vegetation is both interesting in terms of radio propagation aspects and in terms of cybersecurity at OSI model's Physical layer.
It could seem that this research area is closed. But, which are the new challenges for future communication systems in vegetation environments? The deployment of 5G mobile systems opens a new gate in rural and suburban outdoor areas. The worldwide connectivity, reaching remote wild areas, is another field of interest when vegetation cuts satellite to land links. Higher and higher frequencies expected to be used for communications, as terahertz bands, could be explored even in rural links. And the ITU-R Recommendation must be, at least, tested for being used at such new frequencies of operation. Thus, the research area is still open to new proposals, ideas, and developments.
On the other hand, the possible use of vegetation elements as a way to control or limit the non-desired access to a wireless network in order to improve information security and to protect data and systems from external attacks is a field with development possibilities.
All those opportunities deserve a future-eyed analysis, reflecting on the future trends of radio links within forests and vegetation areas, and this is the focus of this invited talk.
The organization, after this introduction, begins with a summary of past contributions in terms of measurements in section 2, and then of models in section 3, classifying the last years' activities in different categories to organize and explain the various insights. Then, an analysis of the open scenarios towards future work configures section 4, in a personal view of the ways of development within the topic. Finally, section 5 depicts the main conclusions, acting as a summary for this contribution.

2. Measurement-based research

During decades, different research groups provided a collection of experimental contributions regarding propagation within vegetation environments. Although most of them followed narrowband principles, there are few wideband-based.
The variety of published results is very wide, from very pitched studies, which put the focus on the specific effects of a particular vegetation variety, to wider researches including several species, a selection of specimen, various configurations or environments, and then provide a more general insight on their proposals.
Next subsections analyze some of these contributions, those considered more relevant in a personal optics.

2.1. Narrowband results

Older studies focused on the attenuation induced by individual specimen of different tree species, analyzing the effect of the specific characteristics (wood density, water content, size and shape of the leaves, canopy density, and so on) on the received power within the shadow area behind the vegetal element [2].

There are several developments within this category, as different authors used a variety of methods to provide insight on the behavior of isolated specimen. Experiments are made in both bi-static [3] or monostatic configuration [4], and taking into account the effect of wind at different speeds on the electromagnetic performance of the vegetation in terms of attenuation and scattering.

The scattering is also the focus of some previous works as [5] or [6].

With the explosion of cellular mobile systems, the interest moved to analyze the effect of groups of trees, or even forests, at frequencies used to provide such services [7].

There are also proposals to use vegetation barriers or fences (composed only by trees or combined with lattice or other supported structures) [8-11] to reduce the electromagnetic pollution in specific areas (kinder gardens, geriatric hospitals, primary schools, playing parks, and similar), which included large measurement campaigns involving several species and environments. Some of those experiments were performed within real world scenarios [9], whereas most of them used controlled environments [8, 11] and even anechoic chambers [10].

There are also some experiences in analyzing groups of trees in actual scenarios, involving the use of complex measurement vans [12].

In recent years, when internet of things and sensing applications discover its usefulness in forest areas for detecting fires, for helping in connecting emergency staff during or after catastrophic events, etc., the interest on propagation models for predicting radio propagation behavior re-grow. And most of these models are based on large measurement campaigns [13-16]. The analysis of such measurement outcomes provide attenuation data [13-15] or short-term evolutions [16]

As a result of such publications, we have attenuation data at different frequency bands for several isolated vegetation specimens or for a combination or group of trees.

2.2. Wideband results

Measurement campaigns on wideband bases are less popular due to the increased complexity of such measurement systems, and its requirements in terms of power supply and, what is not less important, on stability of that supply. Urban parks could be as complex as streets for doing wideband measurements, but when moving to wild forests, complexity grows and less research groups worldwide performed this kind of research.

An example of such kind of results is [17], where the use of a complex measurement system allowed the researchers to provide wideband data at 60 GHz band.

3. Models for radio wave propagation within vegetation

Most of the models belong to the group of experimental models; this means that they come from measurements which outcomes are used to tune mathematical equations or, directly, to extract values for the variables of statistics expressions.

Although, in the limit, deterministic models directly arising from Maxwell equations could be defined, and so that Electromagnetic simulation tools based on method of moments or finite elements method would provide exact solutions, the own nature of a forest or even a tree, with highly complex structures and natural variability of many parameters (seasonal evolution, moisture contents, wind movement, etc.) discard these solutions compared to those involved some probabilistic elements that deal with such unpredictable variations [18].

More complex models, including fractal techniques as Lindemayer systems [19], has been also proposed in the past, although they did not experiment a long evolution.

Along last years, different research groups have presented models from simple attenuation with distance within forests of different vegetal species to artificial intelligence proposal based on neural networks [20-22], passing through more or less complex mathematical proposals.

4. The open scenarios

Future systems (or near future applications) would involve also future research. Propagation within vegetation appear as one of the scenarios to be considered as technology extends far away initial places, and city centers are not the only deployment areas. In such conditions, some ideas arise related to different near future developments:

- *5G.* The main issue would be the selected frequency band. As previously investigated, the 3.5 GHz band seems viable for transmitting even within a forest or a densely vegetated area. However, millimeter wave bands suffer strong propagation problems in very dispersive places, with deep multipath phenomena. In such places, an *a priori* estimation based on experience would not be too optimistic in terms of usability.
- *Autonomous car.* Cars driving by themselves, using radio communication and radio location systems intend to be the future of human mobility. A confident system must base on a full-assured connectivity independently of the environment: it has to work at cities, but also at rural forested environments.
- *Terahertz bands.* Looking for clean bands, some proposals move communication systems towards terahertz bands. The behavior of trees and forests at these bands, which are in the frontiers of radio waves and fotonics, needs to be studied and deserves deeper research.
- *Internet of Things.* Sensing everywhere, with more and more interconnected sensors, seems to be the future of our living standards. All among those that

are intended to be installed within forests or parks will need the support of clear and simple propagation models in order to provide the expected performance.

- *Cybersecurity*. Another collateral application of such research could be the definition of coverage areas for wireless LANs in such a way that the vegetation would protect the system and its related information from malicious or non-desired access that could compromise the security or the integrity of data and equipment. In the modern context, any proposal contributing to improve cybersecurity of radio system must be considered and deserves a deep analysis.

In fact, there would be many other scenarios related to future and present radio systems interacting with vegetation environments. In most of them, new research, new measurements and new models would be required. And, then, the floor is open for new contributions.

5. Conclusions

Although propagation within vegetation has been an up-to-the-date topic in the beginnings of the 21st century, it seems that everything has been done in such research area.

This invited talk goes through that has been done during last decades, but it also analyses some open scenarios that allows the researchers in this field to maintain the interest and to work in providing solutions to current and also future problems.

The proposal is to analyze what it has been done, and where are the possible new actions to be taken in the near future to provide advances in this domain: the extension of radio systems to unexpected scenarios or applications represents an opportunity to spread also the pitch of the research on radio propagation within vegetation areas or elements.

Acknowledgements

This work was supported by the Spanish Government, Ministerio de Ciencia, Innovación y Universidades, Secretaría de Estado de Investigación, Desarrollo e Innovación, (project TEC2017-85529-C3-3R), Xunta de Galicia (project GRC2015/019), atlanTTic Research Center and the European Regional Development Fund (ERDF).

References

[1] Recommendation ITU-R P.833-5 – Attenuation in Vegetation, 2005.

[2] S. Morgadinho, R. F. S. Caldeirinha, M. O. Al-Nuaimi, I. Cuiñas, M. G. Sanchez, T. R. Fernandes, J. Richter, “Time-Variant Radio Channel Characterisation and Modelling of Vegetation Media at Millimetre-Wave Frequency”, IEEE Transactions on Antennas and Propagation, vol.60, no.3, pp.1557-1568, March 2012.

[3] R.F.S. Caldeirinha, M.O. Al-Nuaimi, Propagation Modelling of Bistatic Scattering of Isolated Trees for Micro- and Millimeter Wave urban Microcells, PIMRC, pp. 135-139, 2002.

[4] Paula Gomez, Iñigo Cuiñas, Ana V. Alejos, Manuel García Sánchez, Rafael FS Caldeirinha, “Shrub-Blown-Time Variability in Attenuation and Scattering at Cellular Frequencies”, IET Microwaves, Antennas and Propagation, vol.4, no.4, pp. 526-542, April 2010

[5] R.M. Narayan, S.E. Nelson, J.P. Dalton, “Azimuthal Scattering Pattern of Trees at X-Band”, IEEE Transactions on Aerospace and Electronic Systems, vol.29, no.2, pp. 588-593, Abril 1993.

[6] Y.I. Nechayev, C.C. Constantinou, M.J. Mughal, “Scattering by Trees in Microcellular Environments”, 11th IEE International Conference on Antennas and Propagation, pp. 511-515, Abril 2001.

[7] C. Oestges, B. M. Villacieros, and D. Vanhoenacker-Janvier, “Radio channel characterization for moderate antenna heights in forest areas,” IEEE Trans. Veh. Technol., vol. 58, no. 8, pp. 4031–4035, Oct. 2009.

[8] Iñigo Cuiñas, Ana Vázquez Alejos, Manuel García Sánchez, "Vegetal barriers for minimizing electromagnetic pollution at cellular phone bands", Electronics Letters, vol. 41, no. 6, pp. 340-341, March 2005

[9] Paula Gomez, Iñigo Cuiñas, Ana Vázquez Alejos, Manuel García Sánchez, José Antonio Fernández-Gay, “Analysis of the performance barriers of vegetation to reduce electromagnetic pollution”, IET Microwaves, Antennas & Propagation, vol. 5, no. 6, pp. 651-663, April 2011

[10] Iñigo Cuiñas, Paula Gómez, Ana Vázquez Alejos, Manuel García Sánchez, “Reducing Electromagnetic Pollution by Shrub Lines Supported by Lattice Structures”, IET Electronics Letters, vol. 45, no. 13, pp. 664-666, June 2009

[11] Iñigo Cuiñas, Paula Gómez, “A Method to Compare the Stability of Electromagnetic Attenuation Induced by Soft Barriers”, IEEE Antennas and Wireless Propagation Letters, vol. 13, pp. 690-693, December 2014

[12] M.O. Al-Nuaimi, A.M. Hammoudeh, Measurements and Predictions of Attenuation and Scatter of Microwave Signals by Trees, IEE Proceedings Microwaves, Antennas and Propagation, vol. 141, no. 2, pp. 70-76, April 1994.

[13] Gay-Fernandez, J.A.; Cuinas, I., “Peer to Peer Wireless Propagation Measurements and Path-Loss Modeling in Vegetated Environments”, IEEE Transactions on Antennas and Propagation, vol.61, no.6, pp.3302,3311, June 2013.

[14] Jose Antonio Gay-Fernández, Manuel G. Sanchez, Iñigo Cuiñas, Ana V. Alejos, Javier G. Sánchez, José Luis Miranda-Sierra, “Propagation Analysis and Deployment of a Wireless Sensor Network in a Forest”, Progress In Electromagnetics Research (PIER), vol. 106, pp. 121-145, July 2010

[15] G. Durgin, T.S. Rappaport, H. Xu, Measurements and Models for Radio Path Loss and Penetration Loss in and

around Homes and Trees at 5.85 GHz, IEEE Transactions on Communications, vol. 46, no. 11, pp. 1484-1496, Noviembre 1998.

[16] Jose Antonio Gay-Fernández, Iñigo Cuiñas, “Short-Term Vegetation Modeling in Wireless Network Media at Frequency Bands”, IEEE Transactions on Antennas and Propagation, vol. 62, no. 6, pp. 3330-3337, June 2014

[17] D.A. Scammell, A.M. Hammoudeh, M.G. Sánchez, “Characterisation of 62.4 GHz Radiowave Propagation Through a Single Tree Using Wideband Measurements”, 11th IEE International Conference on Antennas and Propagation, pp. 184-187, Abril 2001.

[18] J. Richter, R. F. S. Caldeirinha, M. O. Al-Nuaimi, A. Seville, N. C. Rogers, and N. Savage, “A generic narrowband model for radiowave propagation through vegetation," Vehicular Technology Conference, 2005. VTC 2005-Spring. 2005 IEEE 61st, Vol 1, no., pp. 39-43, 30 May-1 June 2005.

[19] G. Zhang, L. Tsang, Wave Scattering and Scene Image of Trees Generated by Lindenmayer Systems, IGARSS '96 Remote Sensing for a Sustainable Future., pp. 728-729, May 1996.

[20] P. Gómez-Pérez, R.F.S. Caldeirinha, T.R. Fernandes, I. Cuiñas, “Using Artificial Neural Networks to Scale and Infer Vegetation Media Phase Functions”, Neural Computing and Applications, vol. 29, no. 12, pp. 1563-1574, 2018.

[21] Paula Gómez-Pérez, Rafael F.S. Caldeirinha, Telmo R. Fernandes, Iñigo Cuiñas, “Retrieving Vegetation Re-Radiation Patterns by means of Artificial Neural Networks, IEEE Antennas and Wireless Propagation Letters, vol. 15, pp.1097-1100, December 2016

[22] Paula Gómez-Pérez, Marcos Crego-García, Iñigo Cuiñas, Rafael F.S. Caldeirinha, “Modelling and inferring the attenuation induced by vegetation barriers ar 2G/3G/4G cellular bands using Artificial Neural Networks”, Elsevier Measurement, vol. 98C, pp. 262-275, 2017

Sparse Polynomial-Chaos Models for Stochastic Problems with Filtering Structures

Theodoros Zygiridis[1*], Aristeides Papadopoulos[2], Nikolaos Kantartzis[3], and Elias Glytsis[2]

[1]Department of Electrical and Computer Engineering, University of Western Macedonia, Kozani, Greece
[2]School of Electrical and Computer Engineering, National Technical University of Athens, Athens, Greece
[3]Department of Electrical and Computer Engineering, Aristotle University of Thessaloniki, Thessaloniki, Greece
*corresponding author, E-mail: tzygiridis@uowm.gr

Abstract

This work develops sparse polynomial models for investigating the response of electromagnetic filtering structures, when the design of the latter is affected by a number of uncertain variables. The proposed approach describes an improved implementation framework for contemporary Compressed Sensing techniques, which are known for their capacity to reconstruct sparse signals with a limited number of samples. Unlike typical implementations, the necessary set of basis functions is formulated after performing an initial estimation of partial variances that, despite being computationally cheap, provides sufficient information for the impact of each variable on the output. A number of numerical tests on different filter configurations verify the reliability of the presented methodology, display its efficiency, and unveil the performance of the considered structures, when operated under uncertainty.

1. Introduction

Electromagnetic (EM) filtering structures appear in numerous classic and modern applications spanning diverse parts of the spectrum, including the radio- [1], microwave- [2], millimeter- [3], THz- [4] and optical- [5] frequency bands, to name a few representative instances. In most cases, the consistent operation of such configurations requires the compliance with specific – and probably firm – design guidelines, and deviations from the latter are likely to cause performance degradation or even failures. Consequently, the ability to predict the response of filtering structures under uncertainty conditions appears to be a matter of importance, due to the necessity for assessing key features, such as their functionality sensitivity on potential manufacturing flaws.

Given the aforementioned framework, the computation of generalized polynomial-chaos (PC) expansions [6] of stochastic quantities of interest (QoIs) is considered an attractive solution, as these are used extensively in the construction of surrogate models for problems with uncertainties. When a QoI depends on a small or moderate number of random variables, PC approaches are proven to perform more efficiently than traditional methodologies, among which Monte-Carlo (MC) techniques [7] constitute common choices. On the other hand, these high-performance levels of the PC expansions are not always guaranteed and their computation may require more advanced approaches, in case of several random inputs or expensive deterministic models. This stems from the fact that the computational cost for the determination of the pertinent expansion coefficients is directly related to the number of basis functions used in the PC formulae. In general, finding efficient solutions for multi-dimensional stochastic problems is a non-trivial, but of crucial importance, issue and a number of different solutions have been proposed, including sparse grids [8], alternative construction methodologies for the basis sets [9], adaptive schemes [10], etc.

Regarding the development of sparse PC models (i.e. models with a low number of terms), Compressed Sensing (CS) is known to be more cost-effective than standard methodologies (e.g. least-squares techniques), provided that the PC coefficients form a sufficiently sparse vector [11]. The efficiency of CS stems from the fact that the reconstruction of sparse vectors is possible using a limited number of samples, which can be smaller than the number of unknowns. As regression methodologies commonly require increased amounts of samples (two to three times the number of unknowns) to formulate an over-determined system, one easily recognizes the advantages that CS has to offer. These capabilities have been recently exploited with success in the context of PC methodologies [12–14], and will be also used extensively in the present work.

In this paper, we adopt a CS approach for the study of stochastic problems involving filters, considering that their responses are commonly affected by several EM or geometric factors. We propose the incorporation of an extra stage before the computation of the PC expansion coefficients, within which an approximate variance analysis is conducted in a cost-effective fashion. Thus, an initial estimation of the importance of each input is formed, according to which unnecessary basis functions may be dropped without accuracy compromise, improving eventually the overall efficiency. Until today, only a limited number of works have given attention to the truncation scheme of the PC expansions, in the context of CS techniques (for instance, [14] develops an adaptive basis-selection methodology that can be used in conjunction with ℓ_1-minimization). A number of numerical tests display the reliability of the suggested

approach for the development of sparse PC models, when filtering configurations operate under uncertain conditions, and useful statistics characterizing their stochastic behavior are computed.

2. Methodology

2.1. Polynomial-Chaos Expansions

Suppose that the QoI y is a function of d independent random variables $\boldsymbol{\xi} = [\xi_1 \ \dots \ \xi_d]^T$, as well as of some deterministic variables represented by $\boldsymbol{\zeta}$ (e.g. frequency). A truncated PC representation of y has the form

$$y(\boldsymbol{\zeta};\boldsymbol{\xi}) \simeq \hat{y}(\boldsymbol{\zeta};\boldsymbol{\xi}) = \sum_{\boldsymbol{\alpha}\in\mathcal{A}} c_{\boldsymbol{\alpha}}(\boldsymbol{\zeta})\Psi_{\boldsymbol{\alpha}}(\boldsymbol{\xi}) \tag{1}$$

where $\boldsymbol{\alpha} = (\alpha_1,\dots,\alpha_d) \in \mathbb{N}_0^d$ is a multi-index, $c_{\boldsymbol{\alpha}}$ are the expansion coefficients, $\Psi_{\boldsymbol{\alpha}}$ are the basis functions, and $\mathcal{A}$ is the set of basis indices [6]. The basis functions are constructed via

$$\Psi_{\boldsymbol{\alpha}}(\boldsymbol{\xi}) = \prod_{i=1}^{d} \psi_{\alpha_i}(\xi_i) \tag{2}$$

where ψ_{α_i} is a univariate polynomial of degree α_i, selected according to the Askey scheme [6], which matches the basis functions with the distribution of the input variables for optimum performance. In this work, we consider uniformly distributed random variables, and the suitable choice in this case corresponds to Legendre polynomials. The basis functions are orthogonal with respect to the joint probability density function (pdf),

$$f(\boldsymbol{\xi}) = \prod_{i=1}^{d} f_i(\xi_i) \tag{3}$$

where $f_i(\xi_i)$ is the pdf of the i-th variable. Consequently, it is $\left\langle \Psi_{\boldsymbol{\alpha_i}}(\boldsymbol{\xi}), \Psi_{\boldsymbol{\alpha_j}}(\boldsymbol{\xi}) \right\rangle = \|\Psi_{\boldsymbol{\alpha_i}}(\boldsymbol{\xi})\|^2 \delta_{\boldsymbol{\alpha_i}\boldsymbol{\alpha_j}}$, where

$$\left\langle \Psi_{\boldsymbol{\alpha}_i}(\boldsymbol{\xi}), \Psi_{\boldsymbol{\alpha}_j}(\boldsymbol{\xi}) \right\rangle = \int_{\Omega} \Psi_{\boldsymbol{\alpha}_i}(\boldsymbol{\xi})\Psi_{\boldsymbol{\alpha}_j}(\boldsymbol{\xi}) f(\boldsymbol{\xi})\, d\boldsymbol{\xi} \tag{4}$$

$\|\Psi_{\boldsymbol{\alpha}_i}(\boldsymbol{\xi})\|^2 = \langle \Psi_{\boldsymbol{\alpha}_i}(\boldsymbol{\xi}), \Psi_{\boldsymbol{\alpha}_i}(\boldsymbol{\xi}) \rangle$, $\delta_{\boldsymbol{\alpha}_i\boldsymbol{\alpha}_j} = 1$ if $\boldsymbol{\alpha}_i = \boldsymbol{\alpha}_j$ and $\delta_{\boldsymbol{\alpha}_i\boldsymbol{\alpha}_j} = 0$ in any other case, and Ω is the d-dimensional random space.

Furthermore, $\mathcal{A}$ is constructed according to a certain truncation rule. For example,

$$\mathcal{A}_q = \{\boldsymbol{\alpha} \in \mathbb{N}_0^d : \|\boldsymbol{\alpha}\|_q \leq p\} \tag{5}$$

where p is the selected polynomial order and

$$\|\boldsymbol{\alpha}\|_q = (\alpha_1^q + \dots \alpha_d^q)^{1/q} \tag{6}$$

with $q \leq 1$. The cardinality $N+1$ of $\mathcal{A}_1$ ($q = 1$) in (5), which corresponds to the total-degree rule, is

$$N + 1 = \frac{(p+d)!}{p!d!} \tag{7}$$

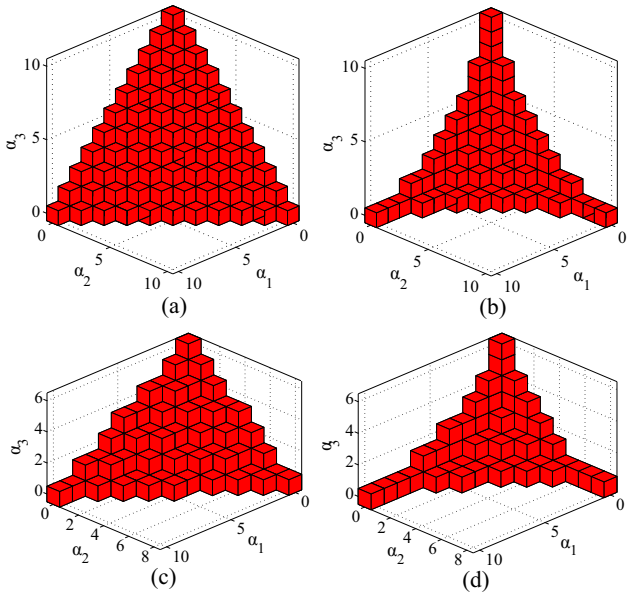

Figure 1: Index sets for different truncation schemes when $d = 3$: (a) isotropic truncation with $p = 10$ and $q = 1$ (286 functions), (b) isotropic truncation with $p = 10$ and $q = 0.7$ (120 functions), (c) anisotropic truncation with $p_1 = 10$, $p_2 = 8$, $p_3 = 6$ and $q = 1$ (139 functions), and (d) anisotropic truncation with $p_1 = 10$, $p_2 = 8$, $p_3 = 6$ and $q = 0.7$ (72 functions).

and attains large values in case of stochastic problems with several dimensions. The reduction of the number of basis function is possible by resorting to hyperbolic indexing [9], which amounts to selecting $q < 1$. In this way, functions describing complex contributions are excluded from the basis set. Furthermore, anisotropic index sets may be constructed by enforcing a different maximum polynomial order $(p_1,\dots,p_d)$ for each variable. Such an approach can be useful, when information about the impact of each input on the QoI is already available [15]. It is noted that the anisotropic and hyperbolic truncation rules can be easily combined and adapted to a problem's needs. Some representative examples of the aforementioned truncation schemes when $d = 3$ can be found in Fig. 1.

Finally, the availability of a PC expansion enables the direct computation of fundamental statistics, such as the expected value and the variance of y, according to

$$\mathrm{E}\{y\} = c_{\boldsymbol{\alpha}_0} \tag{8}$$

$$\sigma^2\{y\} = \sum_{\boldsymbol{\alpha}\in\mathcal{A}\setminus\{\boldsymbol{\alpha}_0\}} c_{\boldsymbol{\alpha}}^2(\boldsymbol{\zeta})\|\Psi_{\boldsymbol{\alpha}}(\boldsymbol{\xi})\|^2 \tag{9}$$

respectively, where $\boldsymbol{\alpha}_0 = (0,0,\dots,0)$.

2.2. Compressed Sensing

The computation of the expansion coefficients of a PC series necessitates the availability of a number of deterministic samples y_i, $i = 1,\dots,N_t$, for which an equal number of

input vectors $\boldsymbol{\xi}^{(i)}$ needs to be selected. Using (1), a system of the form

$$\boldsymbol{\Psi}\mathbf{c} = \mathbf{y} \tag{10}$$

is derived, where

$$\boldsymbol{\Psi} = \begin{bmatrix} \Psi_{\boldsymbol{\alpha}_0}(\boldsymbol{\xi}^{(1)}) & \Psi_{\boldsymbol{\alpha}_1}(\boldsymbol{\xi}^{(1)}) & \dots & \Psi_{\boldsymbol{\alpha}_N}(\boldsymbol{\xi}^{(1)}) \\ \Psi_{\boldsymbol{\alpha}_0}(\boldsymbol{\xi}^{(2)}) & \Psi_{\boldsymbol{\alpha}_1}(\boldsymbol{\xi}^{(2)}) & \dots & \Psi_{\boldsymbol{\alpha}_N}(\boldsymbol{\xi}^{(2)}) \\ \vdots & \vdots & \ddots & \vdots \\ \Psi_{\boldsymbol{\alpha}_0}(\boldsymbol{\xi}^{(N_t)}) & \Psi_{\boldsymbol{\alpha}_1}(\boldsymbol{\xi}^{(N_t)}) & \dots & \Psi_{\boldsymbol{\alpha}_N}(\boldsymbol{\xi}^{(N_t)}) \end{bmatrix} \tag{11}$$

$\mathbf{c}$ is the vector of expansion coefficients, $\boldsymbol{\alpha}_0, \dots, \boldsymbol{\alpha}_N$ are the $N+1$ elements of $\mathcal{A}$, and $\mathbf{y} = [y(\boldsymbol{\zeta};\boldsymbol{\xi}^{(1)})\, y(\boldsymbol{\zeta};\boldsymbol{\xi}^{(2)}) \dots y(\boldsymbol{\zeta};\boldsymbol{\xi}^{(N_t)})]^{\mathrm{T}}$ is the vector of the output samples. In a standard line of work, the system (10) is overdetermined by selecting $N_t = (2 \sim 3) \times (N+1)$, and a typical least-squares approach can be applied. Evidently, the computational cost involved in the construction of $\mathbf{y}$ may become undesirably large, in case of several random dimensions and/or computationally expensive deterministic models. On the other hand, CS may be selected in case of under-determined systems ($N_t < N+1$), as long as the vector $\mathbf{c}$ is sparse (i.e. only a few elements are non-zero). Naturally, PC expansions are rarely sparse, yet they feature expansion coefficients with rapidly decaying magnitude in most cases. Thus, the information regarding the stochastic properties of a QoI is concentrated in a limited number of terms, and a sparse formula can be sufficient.

Specifically, CS approaches determine the PC coefficients by solving the ℓ_0-minimization problem

$$\hat{\mathbf{c}} = \arg\min_{\mathbf{c}} \|\mathbf{c}\|_0 \quad \text{subject to} \quad \boldsymbol{\Psi}\mathbf{c} = \mathbf{y} \tag{12}$$

where $\|.\|_0$ is the number of non-zero elements contained in the argument. Given that (17) is an NP-hard problem, a direct solution is not realistic. On the other hand, an approximate solution can be found with the Orthogonal Matching Pursuit (OMP), which is a greedy algorithm. OMP features an iterative procedure, according to which a set of active-column indices $\mathcal{B}^{(i)}$ (initially, $\mathcal{B}^{(0)} = \emptyset$) is enriched after the i-th iteration, until the required number of non-zero coefficients is reached, or when the residual $\mathbf{r}^{(i)}$ satisfies a specific criterion (initially, $\mathbf{r}^{(0)} = \mathbf{y}$). In more detail, the column $\mathbf{v}$ of $\boldsymbol{\Psi}$ that is most correlated with the current residual, excluding those whose indices are already in $\mathcal{B}^{(i-1)}$, is selected at each iteration. The index of the most suitable column is identified via

$$j^* = \arg\max_{j \notin \mathcal{B}^{(i-1)}} \frac{\boldsymbol{\Psi}_j^{\mathrm{T}} \mathbf{r}^{(i-1)}}{\|\boldsymbol{\Psi}_j\|_2} \tag{13}$$

and the active column-index set is updated by adding the aforementioned element:

$$\mathcal{B}^{(i)} = \mathcal{B}^{(i-1)} \cup \{j^*\} \tag{14}$$

The coefficients are updated via

$$\mathbf{c}^{(i)} = \arg\min \left\| \mathbf{y} - \boldsymbol{\Psi}^{(i)}\mathbf{c} \right\|_2 \tag{15}$$

where $\boldsymbol{\Psi}^{(i)}$ comprises only those columns of $\boldsymbol{\Psi}$ described by $\mathcal{B}^{(i)}$. The solution of (15) is computed via least-squares. In the final step of the iterative procedure, the residual is updated via

$$\mathbf{r}^{(i)} = \mathbf{y} - \boldsymbol{\Psi}^{(i)}\mathbf{c}^{(i)} \tag{16}$$

As several studies have shown, the most significant features of OMP are its simplicity and rapid implementation.

Alternatively, the ℓ_1-minimization problem can be solved,

$$\hat{\mathbf{c}} = \arg\min_{\mathbf{c}} \|\mathbf{c}\|_1 \quad \text{subject to} \quad \boldsymbol{\Psi}\mathbf{c} = \mathbf{y} \tag{17}$$

where $\|\boldsymbol{\alpha}\|_1 = \sum_{i=1}^{d} |\alpha_i|$ (this problem is commonly referred to as Basis Pursuit). In case of non-exact representations, a non-zero error threshold ϵ can be defined (in order to avoid the strict condition $\boldsymbol{\Psi}\mathbf{c} = \mathbf{y}$) and the minimization problem is formulated as

$$\hat{\mathbf{c}} = \arg\min_{\mathbf{c}} \|\mathbf{c}\|_1 \quad \text{subject to} \quad \|\boldsymbol{\Psi}\mathbf{c} - \mathbf{y}\|_2 \leq \epsilon \tag{18}$$

This is known as Basis Pursuit Denoising. In the present study, we use the SPGL1 package [16] for performing ℓ_1-minimization, which is based on the Spectral Projected Gradient algorithm [17], and has been already utilized in several pertinent publications [12, 13, 18].

2.3. Basis Selection via Variance Analysis

Typical PC approaches involve the a priori selection of the basis set, according e.g. to the total-degree rule or a hyperbolic truncation scheme. Instead of choosing the basis functions in this manner, we propose performing a preliminary screening of the input variables, so that their potential impact on the QoI is assessed, at least in an approximate fashion. Towards this goal, one may consider computing the first-order Sobol indices S_i, $i = 1, \dots, d$, as proposed in other similar strategies [19], before proceeding to the final calculation of the PC expansion. It is reminded that the Sobol indices constitute a standard measure for global sensitivity analysis. If a PC representation of the QoI y is available, then the Sobol index that corresponds to the i-th variable is computed via

$$S_i = \frac{\sum\limits_{\boldsymbol{\alpha} \in \mathcal{A}_i} c_{\boldsymbol{\alpha}}^2 \|\Psi_{\boldsymbol{\alpha}}\|^2}{\sigma^2\{y\}} \tag{19}$$

where $\mathcal{A}_i = \{\boldsymbol{\alpha} \in \mathcal{A} : \alpha_i \neq 0, \alpha_{j \neq i} = 0\}$. The numerator in (19) corresponds to the conditional variance due to the ξ_i variable only, without taking into account combined interactions of ξ_i with other variables. Evidently, computing the variance in the denominator of (19) requires the availability of all but one PC coefficients. To enable a more practical solution, we assume a sparse initial PC approximation that comprises only univariate polynomials:

$$\mathcal{A}^* = \{\boldsymbol{\alpha} \in \mathbb{N}_0^d : \|\boldsymbol{\alpha}\|_0 = 1, \alpha_i \leq p\} \tag{20}$$

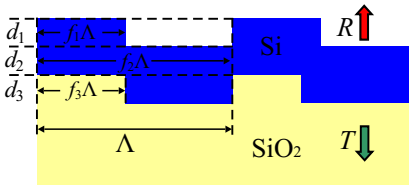

Figure 2: Geometry of the periodic-grating optical filter, depicting the geometric parameters that are considered stochastic.

where the cardinality of $\mathcal{A}^*$ is $(p \times d + 1)$, which is quite small. As we need the S_i values just for screening purposes, only the conditional variances in the numerator of (19) affect the ordering (according to their significance) of the input variables. In this way, it is possible to identify the least important variables at a small computational cost. These variables can be safely assigned to lower polynomial degrees, or even be treated as deterministic, thus reducing the cardinality of the basis set.

3. Numerical Results

We first examine a periodic-grating optical structure [20], which is designed to produced flat, high-efficiency and broad reflection spectra. The geometry of the considered filter is shown in Fig. 2, and its nominal geometric parameters are: $f_1 = f_3 = 0.283$, $f_2 = 1$, $\Lambda = 846.4$ nm, $d_1 = d_3 = 375$ nm, and $d_2 = 175$ nm [20]. We are interested in investigating the properties of the reflectance for normal incidence, as a function of the wavelength, when the aforementioned parameters are treated as stochastic. Specifically, this problem features 7 geometric random variables with uniform distributions, in the range within $\pm 1\%$ of the corresponding mean (nominal) values. The computation of the reflectance is performed with the Rigorous Coupled Wave Analysis [21], a frequency-domain convergent solver that has become a standard tool for problems with periodic-grating structures. As described earlier, the proposed methodology features a two-stage implementation. For the initial step, the 1-D basis functions of a total-degree PC expansion with $p = 4$ are selected, whose overall number is $4 \times 7 + 1 = 29$ basis functions. By performing only 27 simulations and implementing CS, an estimation of the Sobol indices at every wavelength is derived, based on which the selection of the three most important variables is carried out. Next, a new, total-degree truncation set is constructed, considering only the dominant factors. The new set comprises 35 basis functions, and the corresponding coefficients are recovered by CS and another 27 deterministic samples. Overall, $27 + 27 = 54$ simulations are performed.

Fig. 3 plots the mean value and the standard deviation of the reflectance, when computed with a standard MC approach and two CS methodologies. The MC curves are obtained after $10,000$ simulations and used as the reference data. The comparison clearly verifies that the sparse solutions provide credible statistics for the QoI, despite using

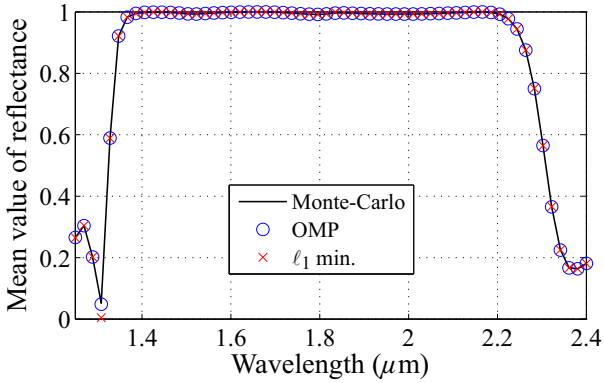

(a)

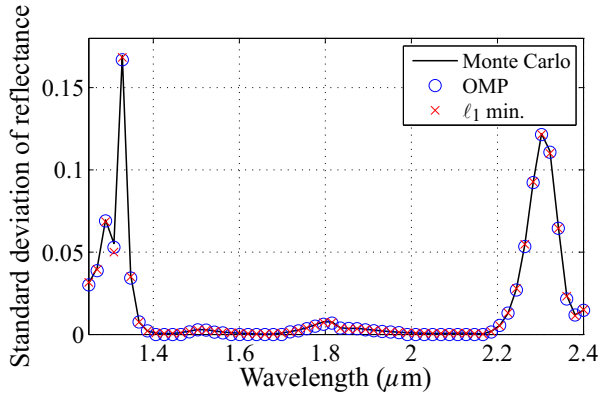

(b)

Figure 3: (a) Mean value and (b) standard deviation of the reflectance of the periodic-grating optical filter of Fig. 2 for normal incidence.

only a small number of deterministic samples. The results also prove that, for the considered level of uncertainty, the flatness of the reflectance is maintain to a high degree, and the most notable variability is noted at the two ends of the spectrum, where the transition of the reflectance between high and low values takes place. In addition, we compute the pdf of the reflectance at the wavelength where the highest standard deviation is observed (around 1.328 μm). The comparison of the different curves (computed via kernel-density estimation [22]) is shown in Fig. 4, and good agreement of the sparse models with the reference solution can be noted again.

A dielectric-stack filter is examined next, which consists of 10 lossless slabs, each one with a mean relative permittivity $\epsilon_r = 3.5$, and width equal to 1.2 cm. The slabs are placed apart, at a distance of 3.6 cm. We examine the transmission coefficient upon normal incidence, when the ϵ_r of each slab varies within $\pm 10\%$ of the mean value. Now, the deterministic solver is based on the finite-difference time-domain method [23]. We select $p = 3$ for the initial basis set, which comprises 286 functions. The first step of the proposed procedure enables the computation of the partial variances of all variables throughout the considered frequency band. This action requires a basis set with only

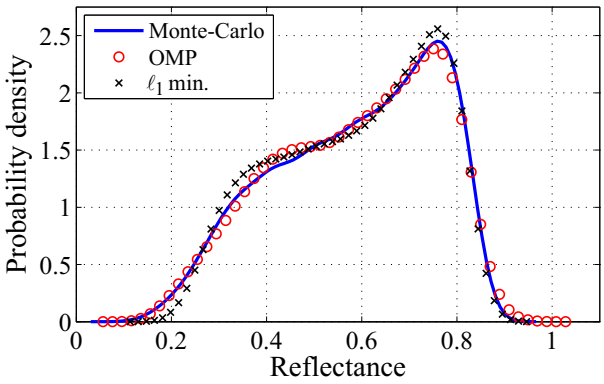

Figure 4: Probability-density function of the reflectance at the wavelength of maximum variance (approximately 1.328 μm).

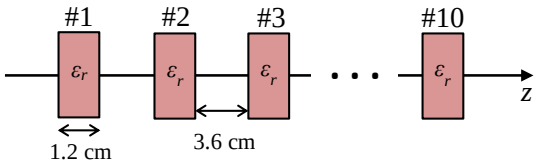

Figure 5: Geometry of the dielectric-stack filter, comprising 10 slabs with stochastic electric permittivities.

$3 \times 10 + 1 = 31$ functions. Unlike the first problem, we implement a least-squares approach, and then average the partial variances over all frequencies. In this way, we determine each variable's importance considering the average values, and the same reduced basis set is used at all frequencies. In fact, we choose to construct an anisotropic basis set (instead of simply rejecting the weaker variables), where the order p is set to 3 for the 4 most important variables, to 2 for other 4 variables, and to only 1 for the least influential factors. The resulting basis set comprises 67 elements, and the amount of random samples is selected equal to 50 for both the OMP and the ℓ_1-minimization approaches.

Before proceeding with some numerical results for the configuration of Fig. 5, we pay attention to the reliability of the first stage of the proposed technique. Table I compares the average partial variances, when obtained via full total-degree PC expansions with $p = 3$, or the suggested line of work. In essence, the former are used as a reference for assessing the reliability of the latter. As the approximation of the partial variances is conducted using a basis set of 31 basis functions, 62 simulations are required for the calculation of the expansion coefficients, in the context of a least-squares approach. For this problem, we compute the partial variance $\mathrm{var}_i(f)$ for the i-th variable, $i = 1, \ldots, 10$ as a function of frequency, and then obtain the corresponding averages over all frequencies $f \in [f_{\min}\ f_{\max}]$, via

$$\langle \mathrm{var}_i \rangle = \frac{1}{f_{\max} - f_{\min}} \int_{f_{\min}}^{f_{\max}} \mathrm{var}_i(f)\, df \qquad (21)$$

Table 1: Estimated average partial variances ($\times 1000$) for the stack-dielectric problem.

Significance	Variable	Full PC	PC (1D bases)
1	ϵ_{r6}	5.42	6.76
2	ϵ_{r5}	5.37	6.04
3	ϵ_{r4}	3.61	4.37
4	ϵ_{r7}	3.57	4.17
5	ϵ_{r3}	2.75	3.58
6	ϵ_{r8}	2.74	3.24
7	ϵ_{r9}	1.65	2.10
8	ϵ_{r2}	1.64	1.62
9	ϵ_{r10}	0.35	0.57
10	ϵ_{r1}	0.35	0.33

As the comparison in Table I verifies, the computation of the partial variances with the reduced basis set can be considered reliable, in the sense that it can be used for ordering the random variables according to their significance, despite some discrepancies with the actual values, obtained with the full PC expansion.

The mean value and the standard deviation of the transmission coefficient T are shown in Fig. 6, where satisfactory matching with the reference data, based on $30,000$ MC simulations, is evident. This accuracy comes at a much lower computational cost, since the derivation of the sparse solution requires $50 + 62 = 112$ simulations, whereas the full PC expansion necessitates at least $2 \times 286 = 572$ samples. It can be noted that, similarly to the previous problem, the highest variability is observed at the transition area of the transmission coefficient, while the flatness is maintained in the band $2.2 - 3$ GHz, as practically no variability is encountered therein. An illustration of the PC coefficients, computed by the OMP algorithm and the ℓ_1-minimization approach, is given in Fig. 7. It can be deduced that the sparse solutions maintain, to a satisfactory degree, the most important elements of the total-degree PC expansion, and neglect several terms of low significance at the same time. It can be also noted that the OMP solution is sparser than the corresponding one of the ℓ_1-minimization technique.

We also calculate the distribution of the 6-dB roll-off frequency, whose value is affected by the uncertainty in the electric parameters of the stack filter (Fig. 8 depicts a fraction of different transmission-coefficient curves, computed by the MC method, and illustrates this phenomenon). A comparison of the pdfs computed via MC, OMP, and ℓ_1-minimization is depicted in Fig. 9. Although some deviations may be observed, compared to the results of the

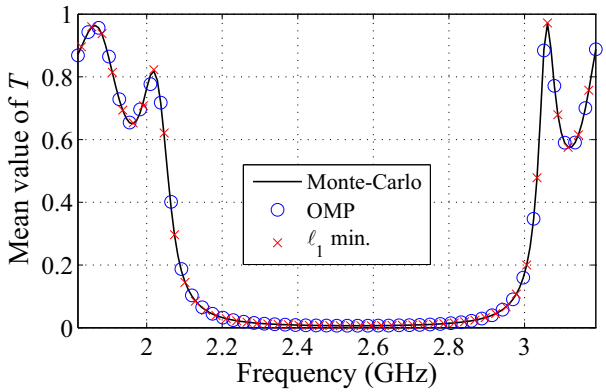

(a)

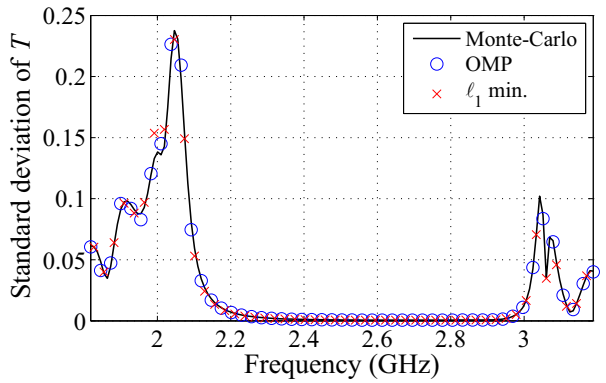

(b)

Figure 6: (a) Mean value and (b) standard deviation of the transmission coefficient T of the dielectric-stack filter of Fig. 5 for normal incidence.

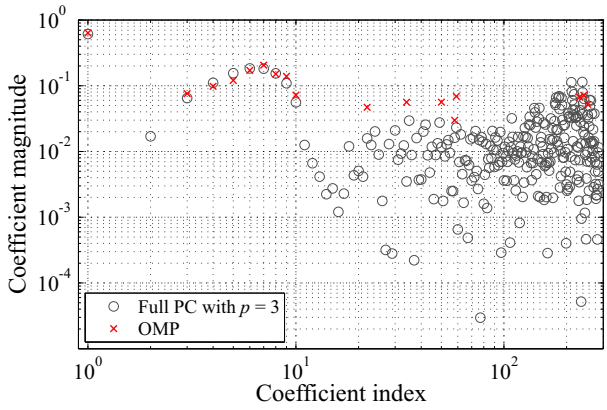

(a)

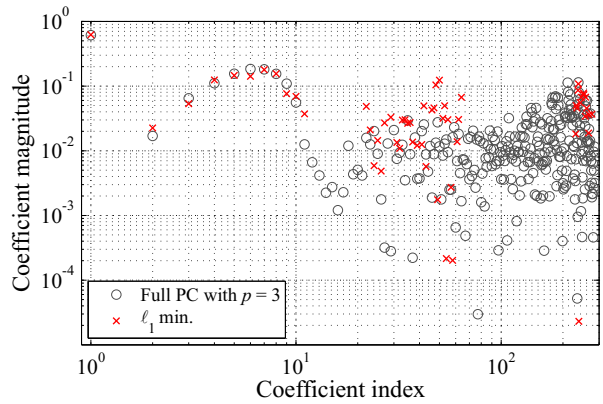

(b)

Figure 7: Magnitude of PC coefficients obtained via (a) OMP and (b) ℓ_1-minimization.

previous example (probably due to the higher dimensionality and stronger input variability), it appears that the sparse polynomial surrogates correctly incorporate the most fundamental statistical properties of the physical QoI. Thus, they can be safely utilized, without resorting to alternatives with higher computational cost. It is interesting to notice that the considered levels of uncertainty in the values of the dielectric constants results in randomness in the 6-dB roll-off frequencies that span a band of almost 100 MHz.

4. Conclusion

This paper has focused on developing sparse PC models for the investigation of stochastic problems involving EM filters with various uncertain parameters. The implementation of known CS solvers has been further facilitated by a preliminary variance analysis, which provides sufficient information regarding the influence of each input and enables a more consistent choice of the basis set, unlike standard methodologies. A number of numerical experiments have verified the validity of the proposed approach and exemplified its efficiency. Finally, the impact of uncertainty on the performance of the examined filtering structures has been assessed, and it has been deduced than non-trivial variability may emerge, even in the presence of weak uncertainties.

Acknowledgement

A. D. Papadopoulos acknowledges support from the framework of the EUROfusion Consortium and has received funding from the Euratom research and training programme 2014-2018 and 2019-2020 under grant agreement No 633053. The views and opinions expressed herein do not necessarily reflect those of the European Commission.

References

[1] A. Tombak, J. . Maria, F. T. Ayguavives, Zhang Jin, G. T. Stauf, A. I. Kingon, and A. Mortazawi, "Voltage-controlled RF filters employing thin-film barium-strontium-titanate tunable capacitors," *IEEE Trans. Microw. Theory Tech.*, vol. 51, no. 2, pp. 462–467, Feb. 2003.

[2] D. Swanson and G. Macchiarella, "Microwave filter design by synthesis and optimization," *IEEE Microw. Mag.*, vol. 8, no. 2, pp. 55–69, Apr. 2007.

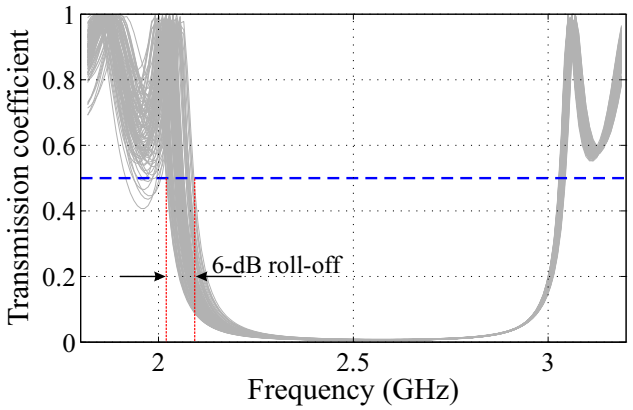

Figure 8: Uncertainty in the 6-dB roll-off frequency (100 MC curves are depicted).

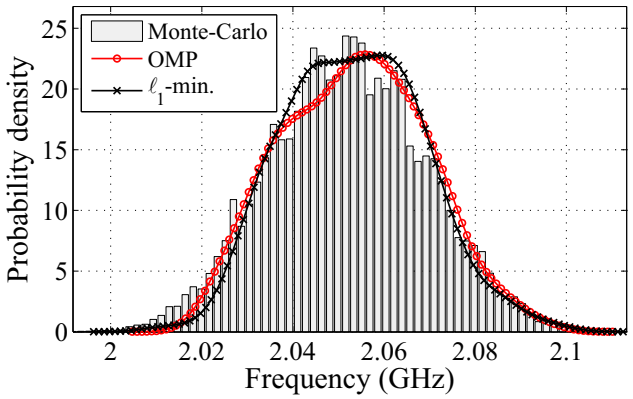

Figure 9: Probability-density functions of the 6-dB roll-off frequencies, in the case of the dielectric-stack filter.

[3] P. Blondy, A. R. Brown, D. Cros, and G. M. Rebeiz, "Low-loss micromachined filters for millimeter-wave communication systems," *IEEE Trans. Microw. Theory Tech.*, vol. 46, no. 12, pp. 2283–2288, Dec. 1998.

[4] I. H. Libon, S. Baumgrtner, M. Hempel, N. E. Hecker, J. Feldmann, M. Koch, and P. Dawson, "An optically controllable terahertz filter," *Appl. Phys. Lett.*, vol. 76, no. 20, pp. 2821–2823, 2000.

[5] R. Magnusson and S. S. Wang, "New principle for optical filters," *Appl. Phys. Lett.*, vol. 61, no. 9, pp. 1022–1024, 1992.

[6] D. Xiu and G. Karniadakis, "The Wiener–Askey polynomial chaos for stochastic differential equations," *SIAM J. Sci. Comput.*, vol. 24, no. 2, pp. 619–644, 2002.

[7] C. P. Robert, *Monte Carlo Methods*. John Wiley & Sons, Ltd, 2014.

[8] D. Xiu and J. Hesthaven, "High-order collocation methods for differential equations with random inputs," *SIAM J. Sci. Comput.*, vol. 27, no. 3, pp. 1118–1139, 2005.

[9] G. Blatman, "Adaptive sparse polynomial chaos expansions for uncertainty propagation and sensitivity analysis," Ph.D. dissertation, 2009, thse de doctorat dirige par Sudret, Bruno Gnie mcanique Clermont-Ferrand 2 2009.

[10] G. Blatman and B. Sudret, "Adaptive sparse polynomial chaos expansion based on least angle regression," *Journal of Computational Physics*, vol. 230, no. 6, pp. 2345 – 2367, 2011.

[11] L. Yan, L. Guo, and D. Xiu, "Stochastic collocation algorithms using ℓ_1-minimization," *International Journal for Uncertainty Quantification*, vol. 2, no. 3, pp. 279–293, 2012.

[12] J. Peng, J. Hampton, and A. Doostan, "A weighted ℓ_1-minimization approach for sparse polynomial chaos expansions," *J. Comput. Phys.*, vol. 267, pp. 92–111, 2014.

[13] J. Hampton and A. Doostan, "Compressive sampling of polynomial chaos expansions: Convergence analysis and sampling strategies," *J. Comput. Phys.*, vol. 280, pp. 363 – 386, 2015.

[14] J. Jakeman, M. Eldred, and K. Sargsyan, "Enhancing ℓ_1-minimization estimates of polynomial chaos expansions using basis selection," *J. Comput. Phys.*, vol. 289, pp. 18 – 34, 2015.

[15] I. Kapse, A. K. Prasad, and S. Roy, "Generalized anisotropic polynomial chaos approach for expedited statistical analysis of nonlinear radio-frequency (rf) circuits," in *2016 IEEE 20th Workshop on Signal and Power Integrity (SPI)*, May 2016, pp. 1–3.

[16] E. van den Berg and M. P. Friedlander, "SPGL1: A solver for large-scale sparse reconstruction," http://www.cs.ubc.ca/labs/scl/spgl1, June 2007.

[17] E. van den Berg and M. Friedlander, "Probing the pareto frontier for basis pursuit solutions," *SIAM J. Sci. Comput.*, vol. 31, no. 2, pp. 890–912, 2009.

[18] N. Alemazkoor and H. Meidani, "A near-optimal sampling strategy for sparse recovery of polynomial chaos expansions," *J. Comput. Phys.*, vol. 371, pp. 137 – 151, 2018.

[19] G. Blatman and B. Sudret, "Anisotropic parcimonious polynomial chaos expansions based on the sparsity-of-effects principle," in *Proc ICOSSAR'09, International Conference in Structural Safety and Reliability*, 2009.

[20] M. Shokooh-Saremi and R. Magnusson, "Leaky-mode resonant reflectors with extreme bandwidths," *Opt. Lett.*, vol. 35, no. 8, pp. 1121–1123, Apr. 2010.

[21] M. G. Moharam, E. B. Grann, D. A. Pommet, and T. K. Gaylord, "Formulation for stable and efficient implementation of the rigorous coupled-wave analysis of binary gratings," *J. Opt. Soc. Am. A*, vol. 12, no. 5, pp. 1068–1076, May 1995.

[22] B. W. Silverman, *Density Estimation for Statistics and Data Analysis*. London: Chapman & Hall, 1986.

[23] A. Taflove and S. C. Hagness, *Computational electrodynamics: The finite-difference time-domain method*. Norwood MA: Artech House, 2005.

Measurements

On the use of 3D printed targets for diffraction, scattering and radar measurements

Jean-Michel Geffrin[1*], Hassan Saleh[1,2], Christelle Eyraud[1], Hervé Tortel[1]

[1] Aix Marseille Univ, CNRS, Centrale Marseille, Institut Fresnel, Marseille, France
[2] Centre Commun de Ressources en Microondes (CCRM), 5 Rue Enrico FERMI, 13012, Marseille, France
*corresponding author, E-mail: Jean-Michel.Geffrin@fresnel.fr

Abstract

This paper presents how additive manufacturing was used at CCRM in scattering, diffraction and radar measurements, to make cross validations of models and measurements. We show, with a few examples, how 3D printing can help to control both the geometry and the permittivity even locally. Some trends and expectations on new printable materials are also discussed.

1. Introduction

Those last years, many experimental studies of diffraction, scattering, and radar have been conducted in the anechoic chamber of the CCRM. This paper is focusing on the interest of additive manufacturing for such applications, as it allows in certain limits to control shape, global and local permittivity. The paragraph 2 is reminding the principle of the Scale Invariance Rule (SIR). The paragraph 3 depicts some scattering studies on aggregates. The paragraph 4 proposes two methods for the global and local control of permittivity. The last paragraph is devoted to the new trends and expectations of new printable materials.

2. Microwave Analogy

Already used in radar applications for a while especially with metallic objects, the scaling of scenes is a powerful tool to study the interaction of wave with targets. Enounced as the scale invariance rule in [1], it consists in scaling the dimensions of the objects with the same factor than the wavelength (in other words keeping wavelength over dimension ratio constant) while keeping the dielectric characteristics of the object unchanged. Even if this principle, sometimes called "microwave analogy", is rather simple to state, it is often rather difficult to handle practically because it supposes the control of both the geometry and the dielectric constant of the target under test. This may be very tricky, but we took profit of 3D printing capabilities, to overcome at least partly such difficulties even if there are always certain limitations.

3. Aggregates analogs

Many particles like pollutants dust or the soot particles produced by any combustion are composed of aggregates of different monomers. To help in the understanding of the light scattering of such aggregates we build upscaled objects (Figure 1) with a scaling factor of about 10^6 and we measured them with microwave (in the 2-18 GHz range).

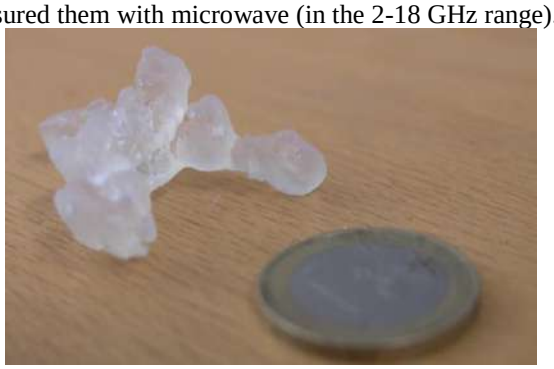

Figure 1: Upscale aggregate realized in acrylate resin ($\varepsilon_r = 3 + j*0.1$) with an additive fabrication printer based on Stereo Lithography (SL)

3.1. Numerical aggregates

The geometry of our first two analogs of aggregate was generated numerically to assess the validity of certain approximations of the scattering models that are currently used in such applications. The first one was made to test the influence of the interpenetration of the spherical monomers [2] (it is made of 6 mm spheres with a spacing of 5 mm between their centers). The second aggregate was designed to test the influence of the necking and overlapping that can be present in soot particles [3].

3.2. Real aggregates

The third aggregate analog is the upscaled version of a real aggregate collected in a real flame and scanned with a 3D electronic microscope. It was used to test the impact of the real shape of the monomers which is rather far from spheres and also for a comparison of two EM models (Discrete Dipole Approximation and Method of Moments).

4. Global and local control of the permittivity

The previous aggregate analogs were made using acrylate, the standard resin material provided for this 3D printer. Its permittivity has been measured and is $\varepsilon_r = 3 + j*0.1$ and it is almost constant in the 2-18 GHz range. However, other

materials, mixtures, or additives are needed to mimic targets having different permittivity values.

4.1. Trees analogs

In radar applications developments, like for canopy monitoring or vehicles detection in forests, it is important to build analogs with realistic dielectric characteristics. In the VHF band, trees present a permittivity around 10+j*10. The idea here was to downscale the trees from meter to centimeter scale and to move from MHz to GHz. 3D printing was used to build void containers shaped in the form of the modelled trees and then fill them with a liquid of the expected permittivity (Figure 2).
The measurements made in the CCRM's anechoic chamber were used to validate the DEMOS model [4] and confirmed the impact of the polarization on the vehicle detection possibility.

Figure 2: Downscaled tree realized in PLA with a Fused Deposition Modeling (FDM) 3D printer and filled with a liquid (glycerol plus water) having a permittivity of ε'_r=8 to 10 and ε''_r=6 to 9 in the considered frequency range.

4.2. Microalgae analogs

In biophotoreactors the microalgae are low contrast objects; they can also have various shapes and can be very large compared to the wavelength of the light used in their characterization. As a huge number of microalgae are contained in such reactors, the model describing their scattering parameters must be fast and accurate to account for the high number scatterers.
To mimic such complex morphologies, the idea was to control the porosity of the material, playing with the proportion of air included in the printed material to control its effective permittivity. A meshing of the object is made and, replacing the edges of each tetrahedron by a cylinder of controlled radius enabled us to control the permittivity from the plain material one down to to 1.1 (with 0.5 mm diameter cylinders) [5]. One of the strengths of such a design is that it also enables to locally control the permittivities as it was made with some microalgae samples, including a kernel or a mantel (Figure 3).

5. Trends and expectations

Additive manufacturing is a very active domain and new printable materials are appearing "every day" but they are unfortunately rarely designed with respect to their dielectric characteristics. The FDM technology almost dominates over the other ones for being the lowest in cost; however, it is a low precision 3D printing technique with limitations in printable shapes. But we have recently used materials with carbon particles that allowed to manufacture solid trees analogs. The seek for higher permittivity materials is still ongoing. Ceramic printing could satisfy partly such needs in term of permittivity characteristics, but it is not yet very widespread and may require high temperature curing processes that can deform the parts.

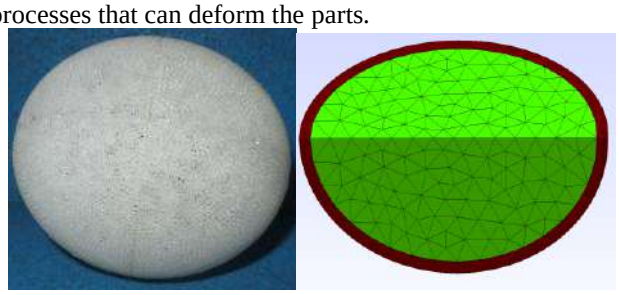

Figure 3: Upscaled microalgae realized in "porous" acrylate with two different permittivities for the inner part and for the mantel (resp. ε_r= 1.2 and ε_r=1.4).

6. Conclusions

Taking profit of the microwave analogy, 3D printing may be of very helpful for diffraction, scattering and radar applications. Experiments and simulation results for each of the previously mentioned examples will be discussed during the talk. There is still a need for new materials and the development of higher permittivity resins and composites would be of great interest for the ongoing research topics.

Acknowledgements

R Vaillon (IES), O. Merchiers (CETHYL), J Yon (CORIA), F Enguehard & G Okyay (EM2C), H Roussel and L Hettak (L2E), O Meyer (GEEPS), A Coudreuse & C Leroux (CTTM), J Dauchet & J-F Cornet (Institut Pascal), A Maalouf (UBO) A. Litman, B. Stout (Institut Fresnel).

References

[1] Mishchenko MI. Scale invariance rule in electromagnetic scattering. J Quant Spectrosc Radiat Transf 2006 ; 101:411–5

[2] Vaillon R, Geffrin JM. Recent advances in microwave analog to light scattering experiments. J Quant Spectrosc Radiat Transf 2014 Oct 1;146:100-5.

[3] Yon J, Bescond A, Liu F. On the radiative properties of soot aggregates part 1: Necking and overlapping. J Quant Spectrosc Radiat Transf 2015 Sep 1;162:197-206.

[4] Hettak L, et al H. DEMOS: A domain decomposition model for scattering in forest environments compared with mono and bistatic measurements on scaled models. In Electromagnetics in Advanced Applications, 2017 (pp. 726-728). IEEE.

[5] H. Saleh *et al*, Approach to Control Permittivity and Shape of Centimeter-Sized Additive Manufactured Objects: Application to Microwave Scattering Experiments, submitted to IEEE-TAP

Aerosol Characterization with Digital Holography

Matthew J. Berg[1*], Yuli W. Heinson[2], Osku Kemppinen[1], Ramesh Giri[1], Claudia Morello[1], Stephen Holler[3] and Gorden Videen[4,5,6]

[1]Department of Physics, Kansas State University, 1228 N. 17th St., Manhattan, KS, 66506, USA
[2]Department of Energy, Environmental & Chemical Engineering, Washington University in Saint Louis, One Brookings Drive, Box 1180, Saint Louis, MO, 63130, USA
[3]Department of Physics & Engineering Physics, Fordham University, 441 E. Fordham Rd., Bronx, NY, 10458, USA.
[4]U.S. Army Research Laboratory, 2800 Powder Mill Road, Adelphi, Maryland 20783, USA
[5]Space Science Institute, 4750 Walnut Street Suite 205, Boulder, Colorado 80301, USA
[6]Deptartment of Astronomy and Space Science, Kyung Hee University, 1732, Deogyeong-daero, Giheung-gu, Yongin-si, Gyeonggi-do 17104, South Korea
*corresponding author, E-mail: matt.berg@phys.ksu.edu

Abstract

Light-scattering techniques are commonly used to characterize micron and submicron particulate matter in a contact-free way. A common example is inferring particle morphology information from light-scattering patterns. An alternative methodology is to use digital holography to obtain particle images that can provide such information in a less ambiguous manner. This presentation will discuss our recent work with digital holography applied to aerosols. We will describe our laboratory experiments and the development of a field instrument.

1. Introduction

Methods to determine the physical properties of aerosol particles is important in a vast array of scientific and applied contexts [1]. Due in part to the difficulty of collecting such particles, a variety of contact-free techniques have been developed to infer information about particles in an indirect manner. A popular example is elastic light scattering in which the angular pattern of light scattered from a particle is analyzed to estimate particle properties like shape and size [1]. This approach is similar to the ill-posed light-scattering inverse problem. Fundamentally, this problem cannot be solved because of the loss of optical phase information in such measurements.

An alternative is to image particles with holography. By placing a digital image-sensor in an optical beam containing particles, the interference pattern produced by scattered and unscattered light can be resolved [2]. The pattern constitutes a digital hologram of the particles and much useful information can be extracted from it, since the phase information is encoded. For example, applying the Fresnel-Kirchhoff diffraction integral to the hologram yields a silhouette-like image of the particle, thus revealing its shape and size without need for *a priori* information [3]. From the silhouette, Huygens's principle can provide a limited portion of the scattering pattern [4]. Also, the extinction cross section can be obtained directly from the hologram [5]. Thus, digital holography is a versatile technique and avoids the difficulties of the classic inverse problem.

While most of our work has focused on proof-of-principle research in the laboratory, we have also developed a field instrument applying holographic imaging techniques. Our instrument, called the Holographic Aerosol Particle Imager (HAPI), obtains *in situ* images of particles in the atmosphere from an unmanned aerial vehicle (UAV), i.e., a drone. This presentation will highlight our laboratory and field work with the HAPI instrument as summarized below.

2. Measuring Holograms and Scattering Patterns

One example where hologram-derived images of aerosol particles is measured along with scattering patterns is our work in [2]. Here, an aerosol is generated from a dried powder source such as pollen or mineral dust. Particles flow from a nozzle into a region where two laser beams of different wavelength intersect. Scattering of both colors indicates a particle is in position to be observed. The coincidence event queues emission of a single green pulse from a ND:YLF laser at λ_g=526.5 nm, which illuminates the free-flowing particle. Simultaneously, a red pulse is emitted from a λ_r=640 nm diode laser co-propagating with the green pulse such that both illuminate the particle at the same time from the same direction. The beam profiles are much larger than the particles; thus, the majority of light passes the particle undisturbed, with a comparatively small portion scattered. Unscattered and scattered red light proceed to a color CCD sensor facing the oncoming light where they interfere, yielding a digital hologram in the sensor's red channel. The green light, however, is diverted by a dichroic filter after interaction with the particle. A spatial filter then removes the strong unscattered portion from the scattered portion, which is then relayed to the sensor.

Thus, the sensor's green channel records a portion of the particle's 2D scattering pattern for the green light, λ_g. The

spatial filter is a mirror with a 500 μm diameter through-hole oriented at 45° to the mirror axis, called the spatial-filter mirror (SFM). A positive lens is used to focus the unscattered light into the SFM hole while collimating the scattered light. In this way, the particle's scattering pattern is separated from the unscattered light except for the small portion of the pattern also lost through the mirror hole.

To render an image of a particle from the measured hologram, Fresnel-Kirchhof (FK) diffraction theory is applied [3]. This simulates the step in conventional analog holography where the chemically developed film hologram is re-illuminated with the light used to record the hologram except with the object (particle) present. Here, the FK theory amounts to a Fourier-transform-like integral applied to the digital hologram. An example of the image resulting from a hologram of a free-flowing aerosol particle and its scattering pattern is presented in Fig. 1.

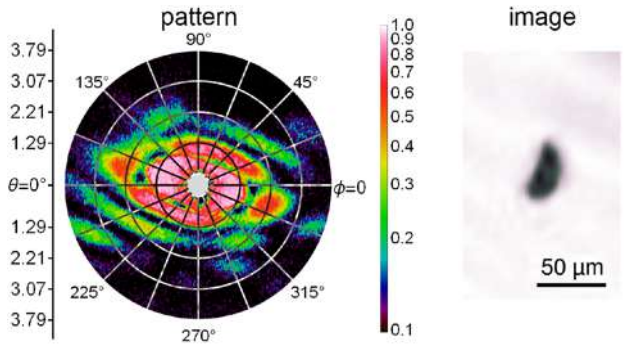

Figure 1: Angular scattering pattern (left) and hologram-derived particle image (right) for a TiO_2 aerosol particle from [2]. The forward scattering direction is at the center of the polar grid overlaid on the pattern where a small region is missing due to the spatial filter. The pattern is measured with green light (λ_g) simultaneously with the hologram in red light (λ_r). The hologram, not shown here, yields the gray-level particle image at right following application of FK diffraction theory.

3. Digital Holography with a UAV

The HAPI instrument we have developed allows us to apply holographic particle-characterization techniques to atmospheric aerosols in the field. The design of this instrument is based on our prior laboratory work in [2, 4-5]. In short, HAPI consists of two optical paths. One path is used to detect when particles reside in the sensing volume and the other produces a hologram of the particles, as in Fig. 2. The optics and electronics are housed in a 3D printed structure made of a UV-cured polymer material. A two-centimeter air gap extends through the instrument allowing aerosol particles to enter as the UAV carries the instrument through an aerosol-laden region of the atmosphere.

To enable operation on a small-scale UAV (DJI Matrice 600 Pro), the laser sources and other key components used have small form factors. Holograms are recorded on a CCD sensor and are temporarily stored on a Raspberry Pi single-board computer. In all, the HAPI instrument weighs ~3 kg, which includes the Li-ion batteries it requires for operation. An example of a particle image obtained during field operation of HAPI is also shown in Fig. 2.

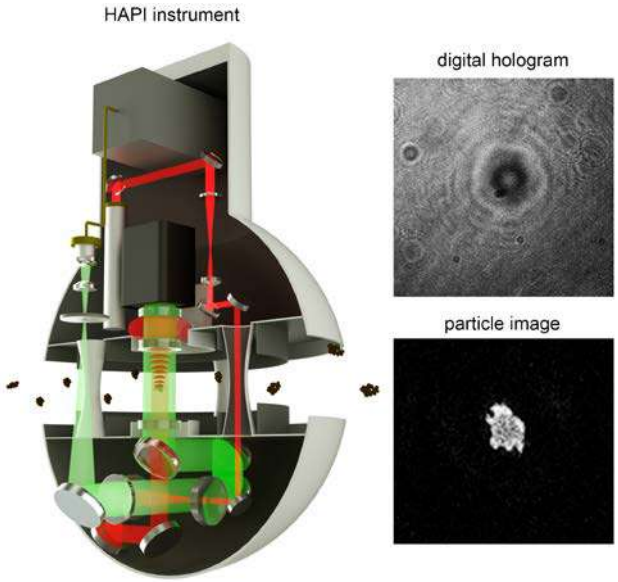

Figure 2: The Holographic Aerosol Particle Imager, HAPI, and an example of its measurement ability. At left is an artist's illustration of the instrument. The red and green-laser beam paths for the optical trains can be seen in this cutaway view along with the air gap extending through the instrument where particle pass. At top right is an example of a digital hologram measured with HAPI when tested with road-dust particles. Application of the FK integral yields the particle image (bottom right). The scale of this particle is approximately 100 μm in its largest dimension.

Acknowledgements

This work was funded by the National Science Foundation (1665456), the U.S. Army Research Office (W911NF-15-1-0549), and the U.S. Air Force Office of Scientific Research (FA9550-19-1-0078).

References

[1] Kulkarni, P., Baron, P. A., Willeke, K. (eds.) *Aerosol Measurement: Principles, Techniques, and Applications*, Wiley, Hoboken, pp. 269-312, 2011.

[2] M.J. Berg, Y.W. Heinson, O. Kemppinen, S. Holler, "Solving the inverse problem for coarse-mode aerosol particle morphology with digital holography, *Sci. Rep*. 7:9400, 2017.

[3] T. Kreis, *Handbook of Holographic Interferometry: Optical and Digital Methods*, Wiley-VCH, Weinheim, 2005.

[4] R. Giri, C. Morello, Y.W. Heinson, O. Kemppinen, G. Videen, M.J. Berg, "Generation of aerosol-particle light-scattering patterns from digital holograms," *Opt. Lett.* **44**(4): 819-822, 2019.

[5] M.J. Berg, N.R. Subedi, P.A. Anderson, “Measuring extinction with digital holography: Nonspherical particles and experimental validation” *Opt. Lett.* **42**(5): 1011-1014, 2017.

Wi-Fi Computer Communication in IEEE 802.11 Protocols N and AC: An Analysis of the User's Exposure using Real-Time Spectrum Analyzer Power Statistics Capability

Andrei Cristian Bechet[1], Annamaria Sarbu[2], Robert Helbet[1], Simona Miclaus[2*], Paul Bechet[2], and Iulian Bouleanu[2]

[1]Department of Electromagnetics and Measurements, Technical University of Cluj-Napoca, Romania
[2]Department of Technical Sciences, Land Forces Academy, Sibiu, Romania
*corresponding author, E-mail: simo.miclaus@gmail.com

Abstract

The agility of the complementary cumulative distribution function mode implemented in a real-time spectrum analyzer is tested for tracing quasi-stochastic radio signals with the aim of expressing the exposure level due to wireless transfer of data in two protocols belonging to IEEE 802.11 communication standard (n and ac), at 2.4 and 5.2 GHz.

1. Introduction

Devices using Wireless Fidelity (WiFi) technology are sources of specific radiofrequency emissions in the form of short-duration pulses, quasi-stochastic in nature. Assessing the user's exposure to such signals during the use of the devices, in an accurate way, requires high performance spectrum analyzers and measurement procedures adequate to trace such behavior. In papers [1] and [2], measurement procedures have been proposed for wireless local area network (WLAN) source devices, based on measuring the maximum power of the channel and on the weighting of it with a factor that depends on the signal's variation in time and in amplitude.

A very proper method that could trace WLAN signals variability is an instrument-integrated statistical one. Practically, by using the Complementary Cumulative Distribution Function (CCDF) capability of a real-time spectrum analyzer, such a method have already shown its ability to accurately express exposure level in case of WiMax signals [3] and in case of mobile communications that use 4G/LTE standard [4]. Present paper proposes a comparative study of exposure levels when a user transfers the same data file under IEEE 802.11 standard family, either using n or ac protocols. Practically, electric (E) field strength was measured in a point in the vicinity of a laptop. Both WLAN protocols use the Orthogonal Frequency Division Multiplexing (OFDM) channel access method for which a high Peak to Average Ratio exist (PAR). This is why the measurement method made use of CCDF, which is destined to underline tail distributions or exceedance.

2. Materials and methods

For the exposure assessment, a simplified operating scenario was implemented. It comprised of an EAP330 Access Point (AP) and two workstations (laptops), one wirelessly-connected to it and the other wire-connected to the Gigabit Switch AP. In the n-protocol, AP was set on channel 8, at the frequency f_n = 2447 MHz; in the ac-protocol AP was set on channel 38, at f_ac = 5190 MHz. In both situations the channel bandwidth was of 40 MHz. All measurements were made in a single point (at 17 cm from the edge of the laptop's keyboard and at 25 cm above the keyboard plane). A data file was transferred, while E-field was measured separately, in case of upload or download. The measurement system included a Rohde & Schwarz FSVR7 spectrum analyzer, an E-field probe (Aaronia EMC Sniffer Set PBS 1: DC-9GHz) and an automatic rotator system for the probe (3 orthogonal directions). The spectrum analyzer was set on CCDF power mode, always being centered on the channel's central frequency while the resolution bandwidth (RBW) was of 40 MHz. The raw results were presented as mean (average) powers and as peak powers. The acquisition time duration was equal to a number of 8226 symbols transferred, each of 4 μs long.

3. Results and discussions

The statistical analysis has shown significant differences in E-field strengths due to different protocols of wireless transfer. During upload, much higher exposure is observed than during download (Figure 1). No matter of the communication protocol, the median values of the field are higher than the averages. Transmission when using IEEE 802.11n signals conduct to a higher exposure of the user than when using IEEE 802.11ac.

To show the time variation of the E-field strengths, in Figure 1 we present a 32.9 ms long field capture, either as peak values or as averages. Short spikes are observable on the traces, mainly on the peak ones. For example, over the Peak_n trace, momentary (<40 ns) E-field strengths peaks, as high as 12-14 V/m, have been captured during transferring data in the "n" protocol, while its momentary

maxima along the average trace, AVG_n, does not exceed 1.7 V/m. Figure 2 shows the time-evolution of E-field level with the highest technological fidelity up-to-now, in each communication protocol and by following the highest possible, or the average exposure, respectively.

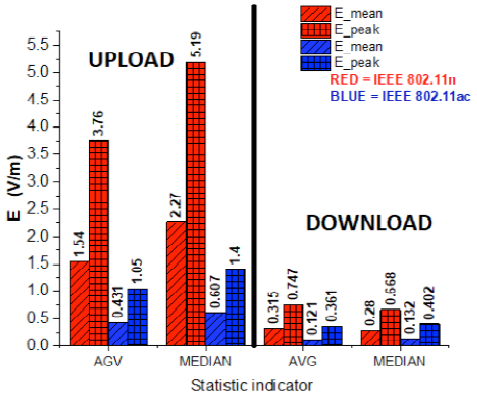

Figure 1: Comparative statistics over repeating measurements in IEEE 802.11 protocols "n" and "ac": mean and peak E-field levels, presented as average and as median, respectively, over the repetition cycles: data file UPLOAD – left side; data file DOWNLOAD – right side.

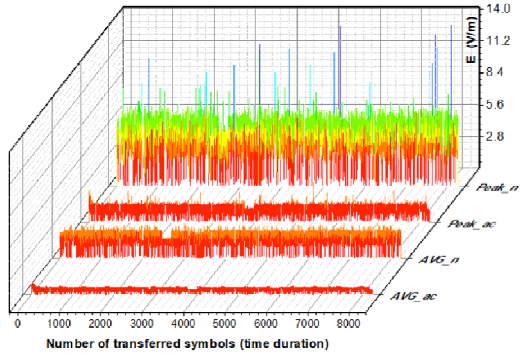

Figure 2: Comparison between the variability of the E-field levels during data UPLOAD in IEEE 802.11 ac & n protocols, for the CCDF averaged ("AVG") channel power and for the peak ("Peak") power respectively, during 32.9 ms (8226 symbols) transfer.

In the statistics graphs of Figure 3 we have represented with the box and whiskers plots (with outliers) the peak and the average field level distributions over a set of 8226 samples recorded. In "n" protocol, the most spread peak values are observed, while the ratio between peaks of "n" and peaks of "ac" signals is of about 4 times. The ratio between averages "n" and "ac" signals is of about 3 times. A deepen analysis of the E-field strengths distributions is shown in Figure 3 by histograms and field-distribution curves. Both curves corresponding to IEEE 802.11ac protocol signals are much narrower than for n protocol. Comparing the two field level distributions, we observe very dissimilar kurtosis but similar skewness.

If one is interested not only in the total absorbed dose of energy due to such exposures, but also in the dose rate evolution, then this type of assessment is a first step of such an approach. Information regarding field versus time and field statistics provide valuable information for realistic quantification of human exposures to quasi-stochastic WiFi radiofrequency signals.

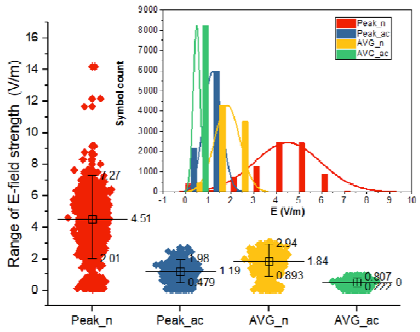

Figure 3: The distributions of E-field strength values during file UPLOAD, for each of the communication standard and in case of average ("AVG") and peak ("Peak") powers determination: box and whiskers plot with outliers (coefficient 1) – lower side; field strengths histograms and distribution curves – upper side.

4. Conclusions

Electromagnetic exposure of a user in front of a laptop transferring data in IEEE 802.11 WLAN standard is higher when using "n" than when using "ac" protocol. In either protocols upload brings much higher exposure (8.3 times in "n" protocol and 5.3 times in "ac" protocol) than download. While peak values as large as 12-14 V/m may be emitted for short periods (< 0.01 % of data transfer duration) in "n" protocol, average values are in the 1.7 V/m ranges, in a point where a person usually seats. Since "ac" protocol conducts to consistently lower exposure, it is preferred to the "n" protocol. All the field levels reported here are much lower than the safe limit of 61 V/m. The CCDF method proved its agility in tracing WiFi signals for exposure assessment aims.

References

[1] Verloock Leen, Wout Joseph, Günter Vermeeren, and Luc Martens, Procedure for assessment of general public exposure from WLAN in offices and in wireless sensor network testbed, *Health Phys.*, 98 (4): 628-638, 2010.

[2] P. Bechet, S. Miclaus, and A. C. Bechet, Improving the accuracy of exposure assessment to stochastic-like radiofrequency signals, *IEEE Trans. EMC*, 54(5): 1169-1177, 2012.

[3] T. Letertre, V. Monebhurrun, and Z. Toffano, Accurate measurement of RF exposure from emerging wireless communication systems, *IOP Conf. Series: Mater. Sci. Eng.* 44 12015, 2013.

[4] A. Sârbu, A. Bechet, T. Balan, D. Robu, P. Bechet, and S. Miclaus, Using CCDF statistics for characterizing the radiated power dynamics in the near field of a mobile phone operating in 3G+ and 4G+ communication standards, *Measurement*, 134: 874-887, 2019.

Magnetic Properties of Magnetosomes Chains Extracted from Magnetotactic Bacteria in the (20 Hz – 2 MHz) Frequency Range

Simona Miclaus[1*], Cristina Moisescu[2], Lucian Barbu-Tudoran[3], Ioan I. Ardelean[2]

[1]"Nicolae Balcescu" Land Forces Academy, Sibiu, Romania
[2]Institute of Biology Bucharest, Romanian Academy, Bucharest, Romania
[3]Institute for R&D of Isotopic and Molecular Technologies, Cluj-Napoca, Romania
*corresponding author, E-mail: simo.miclaus@gmail.com

Abstract

The complex magnetic permeability of three samples containing chains of magnetosomes was measured, to predict any specificity of the magnetic hyperthermia response due to chained structures. Two Brownian relaxation peaks were indeed revealed on the curves of the imaginary magnetic permeablity, at 20 Hz and at 20 kHz, and they may be connected to the short and long chains presence, respectively.

1. Introduction

Magnetotactic bacteria (MTB) are producing natural and highly pure magnetite nanoparticles enveloped in a biological membrane, this entity being called magnetosome (MS). Inside MTB, MS are present in the form of chains. The presence of biogenic magnetite nanoparticles inside cells attracted much attention in the last decade, mainly because of various potential bio-medical uses [1]. One of the most important is the magnetic hyperthermia. Until recently, just synthetic magnetic nanoparticles have been studied. However, some special properties of chained nanoparticles have recently attracted attention of researchers [2].

From such a perspective, present work aimed at the description, from experimental determination, of the complex magnetic permeability relaxation over a low frequency range, between 20 Hz – 2 MHz, of three liquid suspensions of chains of MS extracted from one species of MTB. Also, some differences from data in the literature referring to behavior of individual magnetite nanocrystals suspensions may be emphasized.

2. Materials and methods

Magnetospirillum gryphiswaldense (DSM-6361) cells were grown under microaerobic conditions at pH 7.0 and 30℃, in a flask standard medium [3]. When reached the stationary growth phase, the cells were harvested by centrifugation, washed twice with TrisHCl and the cell pellet was resuspended in fresh TrisHCl buffer to a concentration of 2.5×10^9 cells/ml (determined spectrophotometrically using a calibration curve at 565 nm of optical density, OD_{565}, versus direct cell counts). This bacterial suspension was further used to prepare three different samples containing either individual or chains of MS.

To extract the chains of MS (sample C), the cell suspension was sonicated to lyse the cells, then the suspension was magnetically separated over night by using a strong magnet and the magnetic material was collected as a pellet. The pellet of MS chains was washed twice and finally resuspended in TrisHCl buffer to OD_{480} of 1.123 (0.224 mg/ml).

For the samples containing individual MS (samples A and B), the bacterial suspension was centrifuged again and the cell pellet was resuspended in NaOH 10%, heated at 90℃ to lyse the cells and release the MS, and centrifuged again to collect the MS. The MS pellet was washed three times in deionized water, after each washing a centrifugation step being performed. The extracted MS were resuspended in TrisHCl. The final OD_{480} for sample A was of 0.2646 (0.025 mg/ml), while for sample B it was of 0.6724 (0.056 mg/ml). A weighing method provided then the magnetite concentration in each of the samples: c_A=25 μg/ml; c_B=59 μg/ml; c_D=210 μg/ml.

The samples were inspected by a field-emission-gun scanning transmission electron microscope (STEM), model Hitachi HD2700 and the dimensional profile of the MS was obtained. The average and standard deviation of a MS dimension was (39.93±9.23) nm while the median dimension was 40.73 nm.

Complex magnetic susceptibility measurements in the frequency range (20 Hz - 2 MHz) were made using an Agilent LCR meter (E4980A type) in conjunction with a coil containing a vial as sample holder [4].

3. Results and discussion

Figure 1 shows transmission electron micrographs of MS present in the three different samples. They revealed that, in all three samples, particle chains of various geometry and lengths are present. Besides, sample C still contains a lot of biological floating debris. Figure 2 and figure 3 present the frequency dependence of real and imaginary part of magnetic permeability, on sub-ranges. The imaginary part of the frequency dependence of complex magnetic permeability, $\mu''(f)$, revealed two relaxation peaks for each

sample. Magnetic colloids with magnetite particles of nanometric size usually have two relaxation peaks.

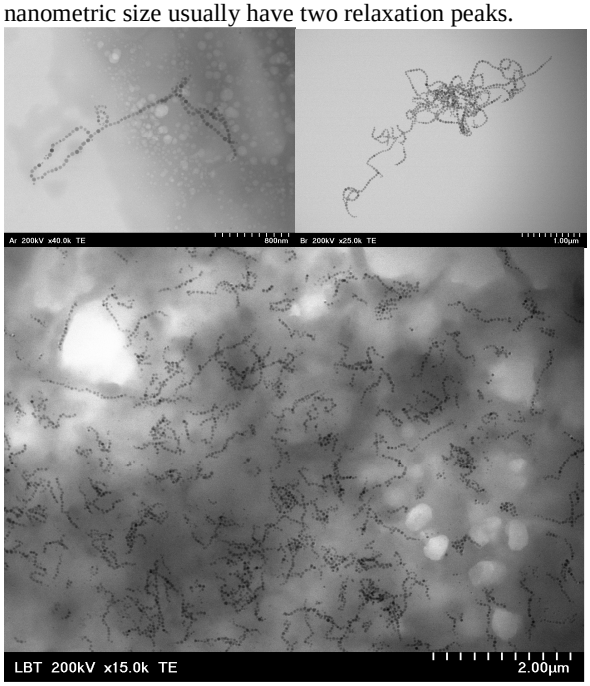

Figure 1: Three representative TEM images of MS chains in the samples: A (left, up); B (right, up); C (down).

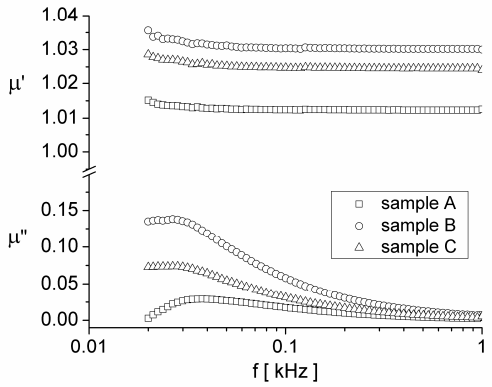

Figure 2: Components of complex magnetic permeability of samples between 20 Hz and 1 kHz.

One (corresponding to Brownian relaxation) is correlated to the rotation of aggregates or large particles within the carrier liquid and the second (corresponding to Nèel relaxation) is correlated to the rotation of the magnetic moment inside each magnetic particle [5]. The Nèel relaxation peak of magnetite nanoparticle systems occurs at frequencies of the order of tens of MHz [5], therefore the relaxation peaks revealed in the analyzed samples are attributed to the Brownian relaxation process. The relaxation peak at frequencies of tens of Hz is assigned to the large chains, and that at frequencies in the order of tens of kHz is attributed to the small chains or small chain aggregates.

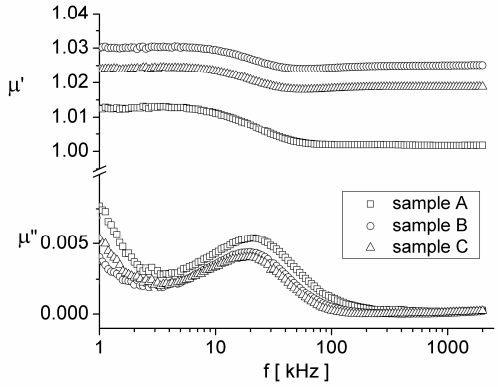

Figure 3: Components of complex magnetic permeability of samples between 1 kHz and 2 MHz.

4. Conclusions

Three liquid suspensions of chains of MS extracted from one species of MTB were obtained and frequency dependence of their complex magnetic permeability was measured. Each sample exhibits two Brownian relaxation peaks (one assigned to the rotation of large chains and the second attributed to the rotation of small aggregates). The result is of potential interest for magnetic hyperthermia applications.

Acknowledgements

We address special thanks to Associate Professor Catalin N. Marin from West University of Timisoara, Romania, for the fruitful discussions and support in writing this paper.

References

[1] E. Alphandery, Applications of magnetosomes synthesized by magnetotactic bacteria in medicine, *Front. Bioeng. Biotechnol.*, 2: art. 5, 2014.

[2] E. Alphandery, I. Chebbi, F. Guyot, M. Durand-Dubief., Use of bacterial magnetosomes in the magnetic hyperthermia treatment of tumours: A review, *Int. J. Hypertherm.*, 29(8): 801-809, 2013.

[3] O. Raschdorf, D. Schüler, R. Uebe, Preparation of Bacterial Magnetosomes for Proteome Analysis, In: Becher D. (eds), Microbial Proteomics. Methods in Molecular Biology, vol 1841, Humana Press, New York, 2018.

[4] C.N. Marin, P.C. Fannin, I. Malaescu, Time solved susceptibility spectra of magnetic fluids, *J. Magn. Magn. Mater*., 388: 45–48, 2015.

[5] P.C. Fannin, C.N. Marin, C. Couper, Investigation of magnetic fluids exhibiting field-induced increasing loss peaks, *J. Magn. Magn. Mater*., 322 (9-12): 1677-1681, 2010.

Empirical detection of bias and variances discrepancies in an RCS case

Amelie Litman[1*], Antoine Roueff[1], Jean-Michel Geffrin[1]

[1]Aix Marseille Univ, CNRS, Centrale Marseille, Institut Fresnel, Marseille
*corresponding author, E-mail: amelie.litman@fresnel.fr

Abstract

When comparing two sets of data when paired with uncertainties, the question arises of providing a meaningfull satisfaction indicator. Some promising criteria have been selected with probabilistic and information theories backgrounds: the Kullback divergence and the Bhattacharyya distance. These criteria remain constant for large sets of parameters. We thus first define reduced parameters to simplify the description of the problem. Then, we use them to analyse a Radar Cross Section (RCS) case where measurements and simulations are available.

1. Introduction

When analysing and comparing different datasets, the first idea is to compute the mean square error between two sets of curves. But if error bars are available, the comparisons are more complicate to handle. Nevertheless these uncertainties should be incorporated in the criteria as they can bring a better insight on the observed discrepancies. Moreover, this is in line with the notion of tolerance and improvement of measurement and/or simulation accuracies.

We propose to analyze two different information-theoretic measures: the Kullback divergence and the Bhattacharyya distance, which have been proved to be of interest to define contrast parameters [1]. We will also take advantage of the fact that we can derive some reduced parameters, similar to the methodology proposed in [2], to simplify the analysis of the problem. These reduced parameters are then applied to a dual set of Radar Cross Section (RCS) data corresponding to the scattering of an homogeneous sphere measured at a fixed frequency but in a bistatic configuration.

The Kullback divergence and the Bhattacharyya distance are parts of the ones currently investigated by the CDIIS Working Group from GDR Ondes [3] which involves several industrial, governmental or academic research laboratories and whose goal is to perform a national study of criteria able to provide a satisfaction indicator when comparing data from electromagnetic measurement and/or simulation, taking into account their associated uncertainties.

2. Discrepancy criteria

Let us assume that we have two sets of curves X_1 and X_2, defined by their mean μ_1 (resp. μ_2) and variance σ_1^2 (resp. σ_2^2) with density of probability p_1 (resp. p_2). To simplify, we assume that they are both normally distributed and uncorrelated. In the following, the criteria are normalized between 0 (no difference) and 1 (major differences).

The first criterion is based on the Bhattacharyya distance [4] which can be seen as an extension of the Mahalanobis distance that takes into account the presence of bias as well as variabilities in the variances

$$\begin{aligned} D_B(p_1,p_2) &= 2\left(1-\int\sqrt{p_1(x)p_2(x)}dx\right) \\ &= 2-2\sqrt{\frac{\sigma_1\sigma_2}{\sigma^2}}\exp\left(-\frac{1}{8}\frac{(\mu_1-\mu_2)^2}{\sigma^2}\right) \end{aligned}$$

where σ^2 is the average variance $\sigma^2=\frac{1}{2}(\sigma_1^2+\sigma_2^2)$. Another criterion for comparing probability density distributions, well-spread in the information theory community [4], is the Kullback-Leibler divergence defined as

$$\begin{aligned} D_{KL}(p_1,p_2) &= 1-\exp\left(-\int p_1(x)\ln\frac{p_1(x)}{p_2(x)}dx\right) \\ &= 1-\frac{\sigma_1}{\sigma_2}\exp\left(-\frac{(\mu_1-\mu_2)^2}{2\sigma_2^2}-\frac{\sigma_1^2-\sigma_2^2}{2\sigma_2^2}\right) \end{aligned}$$

The distributions p_1 and p_2 do not play symmetric roles in the Kullback-Leibler measure, which may be an undesirable property if the two datasets are assumed to be of equal trust, but which can also be a wanted property if one of the datasets is considered as a reference.

3. Reduced parameters

In the previous expressions, 4 parameters $(\mu_1,\mu_2,\sigma_1,\sigma_2)$ come into play which renders the analysis of the behavior of D_B and D_{KL} quite tedious. Moreover, D_B and D_{KL} will remain constant for large set of values. It is in fact possible to provide a reduced set of only 2 parameters which are sufficient to cover all the possible values of D_B and D_{KL}. Indeed, if we want to compare X_1 with X_2,

$$X_1\sim\mathcal{N}(\mu_1,\sigma_1^2) \qquad X_2\sim\mathcal{N}(\mu_2,\sigma_2^2)$$

The constrast between X_1 and X_2 remains unchanged when one applies the same affine transformation on X_1 and X_2. Thus a different physical situation with equivalent contrast is

$$\frac{X_1-\mu_1}{\sqrt{\sigma_1\sigma_2}}\sim\mathcal{N}(0,\tilde{\sigma}^2) \qquad \frac{X_2-\mu_1}{\sqrt{\sigma_1\sigma_2}}\sim\mathcal{N}(\tilde{\mu},\frac{1}{\tilde{\sigma}^2})$$

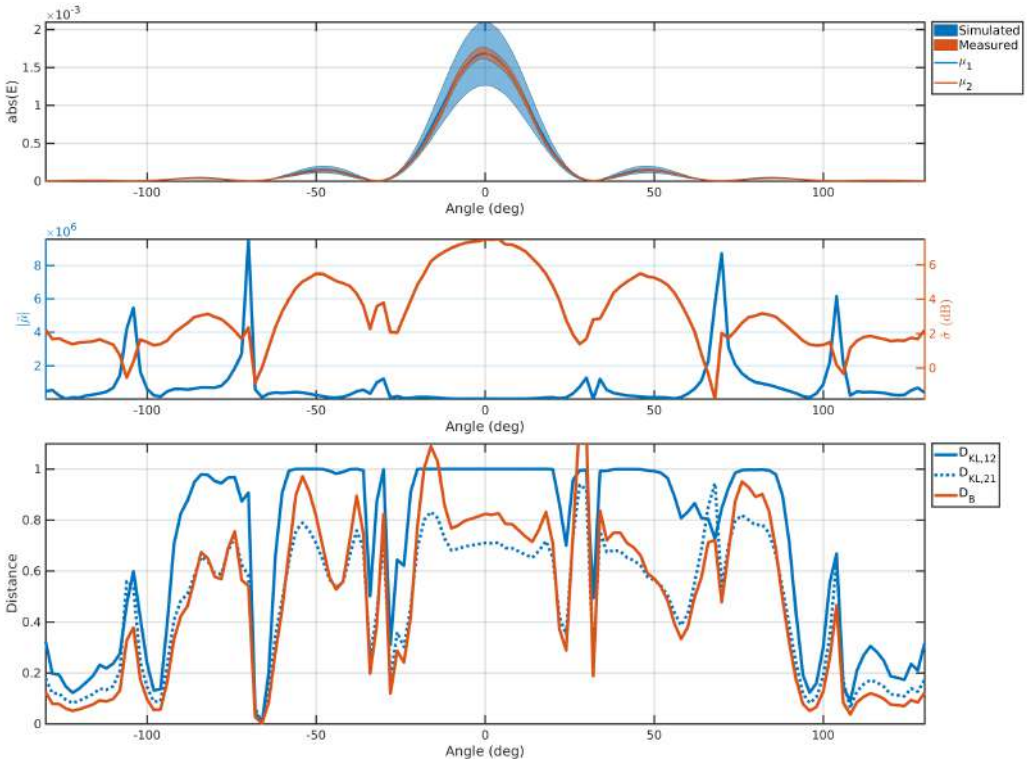

Figure 1: (Up) Amplitude with a $\pm 3\sigma$ area of the measured and simulated scattered fields according to the bistatic angle, at 12.6 GHz. (Middle) Reduced mean $\tilde{\mu}$ and variance $\tilde{\sigma}$. (Down) Comparison criteria.

where we have defined the following reduced parameters

$$\tilde{\sigma}^2 = \frac{\sigma_1}{\sigma_2}, \qquad \text{and} \qquad \tilde{\mu} = \frac{\mu_2 - \mu_1}{\sqrt{\sigma_1 \sigma_2}}$$

Thus D_{KL} and D_B remain invariant with such a change of variables. Parameter $\tilde{\mu}$ and $\tilde{\sigma}$ represent difference in mean and variance respectively.

4. Application to a RCS dataset

Let us now calculate the criteria D_{KL} and D_B and the reduced parameters $\tilde{\mu}$ and $\tilde{\sigma}$ for an RCS configuration. The datasets correspond to scattered fields acquired in a bistatic configuration. We assume that there are no correlation between the bistatic angles. Therefore, we can compute at each bistatic angle the previously defined criteria.

The first set corresponds to measurements. The field scattered by an homogeneous sphere of PMMA is collected in an anechoic chamber, in far-field, under VV polarization with an angle of incidence at $180°$. The permittivity of the sphere, the mean and variances of the scattered fields have been determined as explained in [5] [6]. The second set corresponds to simulated fields, computed using Mie formalism combined with a Monte-Carlo method assuming an uncertainty on the sphere permittivity and its radius, in order to derive the means and variances.

In Figure 1, the mean value and error bars of the amplitude of the scattered field is plotted along the bistatic angle. The reduced parameters and the selected criteria are plotted as well along the same bistatic angle. Even if the measurement and simulation appear to be close by, the criteria are able to detect some discrepancies. The reduced parameters shows whether these discrepancies originate from difference of mean or from difference of variance.

5. Conclusions and acknowledgements

Detecting some bias and variances discrepancies with Bhattacharyya or Kullback-Leibler divergence is possible and reduced parameters complete the information by revealing whether these discrepancies originate from bias or variance. The next step will be to combine these criteria with some decision rules, based for example on false alarm ratio.

The authors gratefully acknowledge the support of GdR Ondes and the Centre Commun de Ressources en Microonde (CCRM).

References

[1] F Goudail et al. *JOSA A*, 21(7):1231–1240, 2004

[2] Ph Refregier, F Goudail *JOSA A*, 19(6):1223–1233, 2002

[3] G Maze-Merceur et al. *Eucap*, 2019

[4] TM Cover, JA Thomas *Elements of Information Theory*, Wiley, 1991

[5] C Eyraud et al. *IEEE AWPL*, 14:309– 312, 2015

[6] JM Geffrin et al. *Radio Science*, 44:RS2007, 2009

Electromagnetics

Modeling and Analysis of Sea Clutter by a Novel Numerical Method

Ozlem Ozgun[1], and Mustafa Kuzuoglu[2]

[1]Department of Electrical & Electronics Engineering, Hacettepe University, Ankara, Turkey
[2]Department of Electrical & Electronics Engineering, Middle East Technical University, Ankara, Turkey
*corresponding author, E-mail: ozlem@ee.hacettepe.edu.tr

Abstract

The statistical behavior of sea clutter is obtained by employing a numerical method, which is called Finite Element Domain Decomposition (FEDD) method, in conjunction with the Monte Carlo technique. A set of sea surfaces are generated by using Pierson-Moskowitz spectrum. The FEDD method is used to accurately and efficiently solve the electromagnetic scattering problem over each surface. In the FEDD method, the computational domain is divided into a number of subdomains, and hence, the computational load decreases during each realization of the Monte Carlo technique. The results of Monte Carlo simulations are compared with the results of some empirical approaches and measurement data for different polarizations and grazing angles.

1. Introduction

Radar performance is affected by clutter signals, which are known as undesired signals backscattered from environment or untargeted objects. The characterization of clutter effects over sea is vital in radar applications since the largest part of the Earth's surface is covered by oceans. The characteristics of sea clutter can be deduced from some analytical, empirical or numerical methods. Since the interaction of radar signals with sea is quite complicated due to the random and ever-changing behavior of the sea surface, most of the sea clutter works in the literature are based on simplified analytical methods or empirical methods [1-3]. However, the accuracy of these methods is limited to certain ranges of parameters, such as higher grazing angle, lower surface roughness, etc. Although numerical methods can be used to obtain accurate results for a wider range of parameters characterizing the problem, they have been rarely used in the literature due to higher computational load [4, 5].

In this paper, the statistical characteristics of sea clutter is studied by a new full-wave numerical method, which combines the finite element method with domain decomposition principles. This method, which is called Finite Element Domain Decomposition (FEDD) method, divides the computational domain including the sea surface into a number of subdomains, and obtains the solution by solving each sub-problem corresponding to each subdomain only once without any iteration [6]. The non-iterative nature is achieved by using the Locally-Conformal Perfectly Matched Layer (LC-PML) method which truncates the subdomains without any artificial reflections [7]. In this manner, the computation time and memory decrease considerably. Another advantage of the FEDD method is that it overcomes the difficulties in handling low grazing angles and higher surface roughness levels. The FEDD method is employed at each realization of the Monte Carlo technique to extract the statistical behavior of the sea clutter phenomenon. The results of Monte Carlo simulations are presented and compared against some empirical models and measurement data from the literature.

2. Implementation of the Method

The statistical behavior of reflectivity (namely, the backscattered Radar Cross Section (RCS) per unit area) is obtained in average sense by using the Monte Carlo technique. A number of sea surfaces are generated randomly by using the Pierson-Moskowitz spectrum. For each surface realization, the problem is solved by the FEDD method, and the reflectivity is computed. The reflectivity values obtained from all surfaces are aggregated, and the statistical parameters (such as mean, variance, etc.) are computed from the family of these reflectivity values.

The FEDD method is implemented by dividing the computational domain into a number of overlapping subdomains. The method is illustrated in Fig. 1 for three subdomains. The most distinguished feature of the FEDD method is that each sub-problem, except the last one, is solved by attaching a LC-PML region to the truncation boundary of the corresponding subdomain. The LC-PML method is different from the standard PML methods because it can be applied to irregular PML regions in an easier manner [7]. After solving the first sub-problem by attaching a LC-PML region to the leftmost boundary of the first subdomain, the second sub-problem is solved by using the fields of the first sub-problem along the rightmost boundary and by attaching a LC-PML region to the leftmost boundary the second subdomain. The last sub-problem is solved by using the fields of the second sub-problem along the rightmost boundary of the last subdomain. The method can be generalized to arbitrary number of subdomains in a straightforward manner.

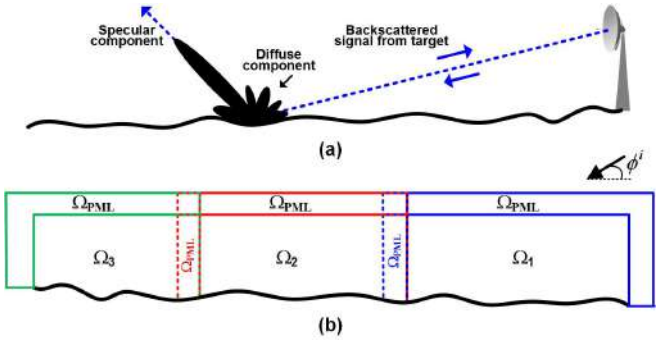

Figure 1: Illustration of (a) the sea clutter problem and (b) the FEDD method.

3. Simulation Results

For the Monte Carlo simulations, 100 rough surfaces are generated. Each surface is 100m long (i.e., 500λ where λ = 0.2 m) at 1.5 GHz. The sea state of each surface is taken as 3 in the context of Douglas sea scale. The sea state of 3 corresponds to the wind speed u = 7 m/s. In the FEDD method, the domain is divided into ten subdomains. In Fig. 2 and Fig. 3, the mean reflectivity is plotted for horizontal and vertical polarizations, respectively, as a function of grazing angle and compared with some well-known empirical methods [2, 3] and measurement data [1]. The empirical methods are GIT (Georgia Institute of Technology), TSC (Technology Service Corporation), HYB (Hybrid method) and NRL (Naval Research Laboratory). It is known that early empirical methods (such as GIT, TSC) are valid for a range of grazing angles and frequencies. It is observed that the FEDD method provides results closer to the measured data and the NRL model. In vertical polarization, the FEDD and NRL methods differ slightly in the quasi-specular region (i.e., around 90° grazing angle). In fact, it is expected that horizontal and vertical polarizations should show similar behavior in this region, and the FEDD results almost verify this behavior.

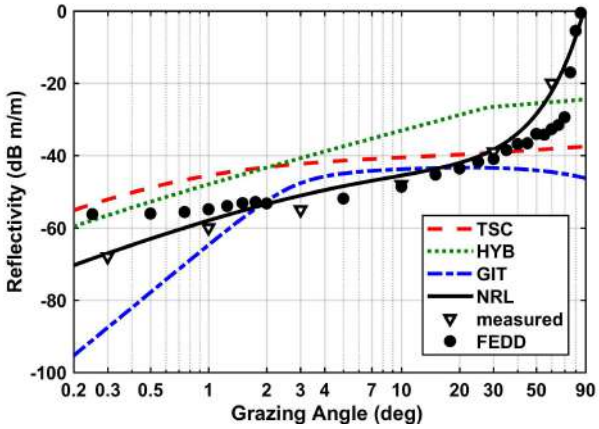

Figure 2: Mean clutter reflectivity at 1.5 GHz and sea state of 3 for horizontal polarization. (Horizontal axis is logarithmic.)

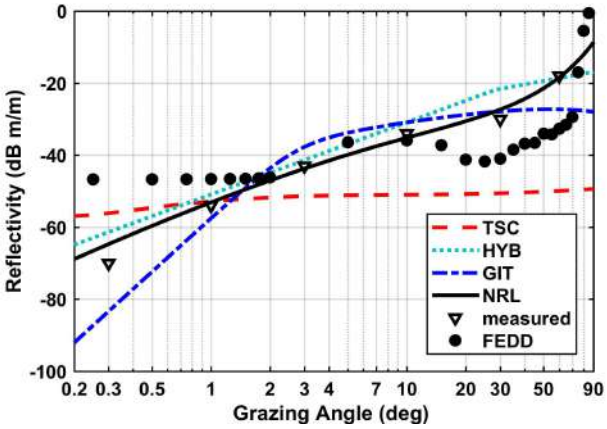

Figure 3: Mean clutter reflectivity at 1.5 GHz and sea state of 3 for vertical polarization. (Horizontal axis is logarithmic.)

4. Conclusions

The sea clutter problem has been solved by the FEDD method in conjunction with the Monte Carlo simulations. The results show that the FEDD method can reliably be used with reduced computational load. In the near future, the sea clutter phenomenon will be investigated in detail by the FEDD method from the radar engineer point of view.

References

[1] F. E. Nathanson, *Radar design principles*. McGraw Hill, New York, 1969.

[2] K. D. Ward, R.J.A. Tough, S. Watts, *Sea Clutter: Scattering, the K Distribution, and Radar Performance*. Institution of Engineering and Technology, 2006.

[3] V. G. Hansen, and R. Mital, "An improved empirical model for radar sea clutter reflectivity," *Naval Research Lab. Tech. Rep*., 2012.

[4] C.S. Chae, J.T. Johnson, "A study of sea surface range-resolved Doppler spectra using numerically simulated low-grazing-angle backscatter data," *IEEE Trans. Geosci. Remote Sens.,* 51: 3452-3460, 2013.

[5] D. Miret, G. Soriano, M. Saillard, "Rigorous Simulations of Microwave Scattering From Finite Conductivity Two-Dimensional Sea Surfaces at Low Grazing Angles," *IEEE Trans. Geosci. Remote Sens*., 52: 3150-3158, 2014.

[6] O. Ozgun, M. Kuzuoglu, "A domain decomposition finite element method for modeling electromagnetic scattering from rough sea surfaces with emphasis on near-forward scattering," *IEEE Trans. Antennas Propagat.*, to appear in 2019.

[7] O. Ozgun, M. Kuzuoglu, "Non-Maxwellian locally-conformal PML absorbers for finite element mesh truncation," *IEEE Trans. Antennas Propagat.*, 55: 931-937, 2007.

Improvement of Textile Antenna System Wireless Link Budget with Parabolic Textile Reflector

Benoît Agnus[1], Stephane Carras[2], Blaise Ravelo[3]

[1] SCIENTEAMA, 27 rue des Glengarrians, 14610 Villons Les Buissons, France
[2] FILIX SAS, Rue Saint-Aventin, 10150 Creney-prés-Troyes, France
[3] Normandy Université UNIROUEN, ESIGELEC, IRSEEM EA 4353, 76000 Rouen, France
*corresponding author, E-mail: agnusbenoit@yahoo.fr

Abstract

This paper presents a design of a fully textile antenna system with interesting electromagnetic performance over a wide frequency band. This research work is carried out by an innovative approach of realization of textile structures combining physical, electrical, structural and environmental specificities. The proposed structure consists originally of a source antenna associated with a parabolic reflector manufactured with textile materials supplied by the FILIX® company. After a description of the concept, an example of a prototype device is presented. An experimental result with a Wi-Fi terminal that operates around 2.45 GHz illustrates the possibility of receiving radiated EM energy. The present study shows that the parabolic reflector improves the level of power captured by the textile antenna.

1. Introduction

In the last few decades, with the tremendous progress of smart connected objects and wearable devices, intelligent textile systems have been emerging more and more. These systems cover various applications such as connected clothing and GPS tracking systems [1-2]. To adapt to the shape of implementation structures, the design of these systems uses new approaches such as flexible antennas [3-4]. More recently, various topologies of textile antennas have been proposed according to the application environments [2,5]. This technology also allows the realization of RF and microwave systems with acceptable performance for high-speed radiocommunications with flexible structures that are not only surface-based but in three dimensions. Flexible antennas are generally designed using microstrip planar technology or screen printing using conductive inks [3-4]. The main limitations of these technologies in the context of textiles is the degradation over time because the use is extremely severe for structures (torsions degrading the bonds, chemicals, mechanical stress, thermal peaks ...). In the framework of the FIL HARMONIQUE project, all these constraints were integrated right from the concept definition so that the systems are reliable and durable on the stress gauges of a garment.

Starting from these specific textile constraints, the difficulties resulting from the process of adapting electronic systems to a textile environment are avoided. This adaptive approach generally leads to a degradation of performance, an increase in cost by the addition of specific functions and an integration and engineering task that can sometimes be very heavy. On the other hand, in the FIL HARMONIQUE project, the question posed is related to accessible performance in a directly textile structure.

2. Wireless communication proofs-of-concept

Prototypes of textile planar antenna and innovative parabolic reflector are designed and tested as proofs-of-concept.

2.1. Antenna and parabolic reflector design description

The proposed textile antenna (A) is designed in planar microwave technology based on F-inverted topology. It is associated to the innovative reflector (R) presenting parabolic shape shown in Fig. 1. This reflector is originally designed with fully textile structure made fabricated with the materials fabricated by FILIX® introduced in Fig. 2. The reflectors are used to improve the power received by the antenna in free space communication.

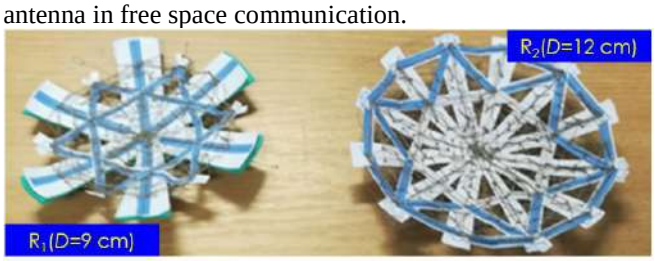

Figure 1: Photograph of the parabolic textile reflectors: R_1(D=9 cm, in left) and R_2(D=12 cm, in right).

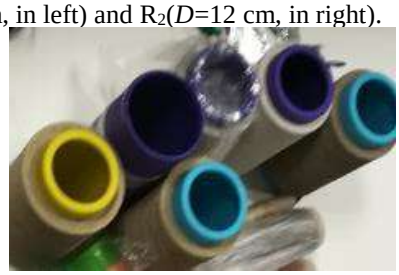

Figure 2: Coil of thread and textile web used to make the antenna.

This improvement can be quantified preliminary from the theoretical value of gains achievable with parabolic geodesies 6.5 dB for a diameter of D=9 cm and 8.5 dB for D=12 cm to operate at 2.5 GHz targeted to 80% efficiency.

2.2. Experimental results

To demonstrate the design feasibility of the textile A+R system in the realistic environment, indoor free space communication tests were carried out.

2.2.1. Wi-Fi emission power spectrum experimentation

As seen in Fig. 3(a), a Wi-Fi Tx terminal emitting pulses is considered. The textile Rx antenna is connected to a spectrum analyzer for reconstructing the received signal spectrum. For further understanding about the relevance of EM wave transmission in function of the reflector radius, Table 1 summarizes the received average power.

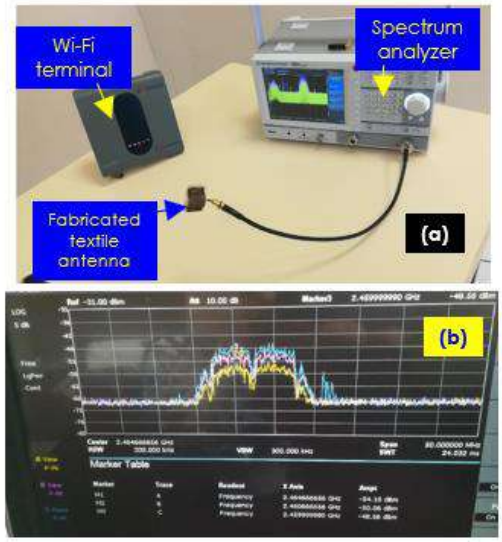

Figure 3: Measured power spectrums of the textile A+R system receiving system: source alone in yellow, in blue A+R_1 and in violet A+R_2.

Table 1: Theoretical and measured antenna gain and average power level.

System	Th. gain	Meas. power	Meas. gain
A	-	-54.16 dBm	-
A+R_1	6.5 dBi	-50.06 dBm	4.1 dBi
A+R_2	8.5 dBi	-48.56 dBm	5.6 dBi

2.2.2. S-parameter measurement

Fig. 4(a) show the S-parameter measurement of free space Rx-Tx communication performed with vector network analyzer (VNA) E5071C from Agilent technologies®. It consists of two Rx and Tx antennas positioned face to face at about 60 cm. Different cases of A and A+R terminals are considered. The measured transmission coefficients from 0.1 GHz-4 GHz are monitored in Fig. 4(b).

3. Conclusions

A novel design of an innovative antenna system with parabolic reflector is introduced. The RF/microwave communication system consists entirely of textile materials. The design method of the proposed textile antenna system is described. The implementation technique to use the conductor fiber is explained. The innovative technique to sew the parabolic reflector is defined in function of the expected working frequency.

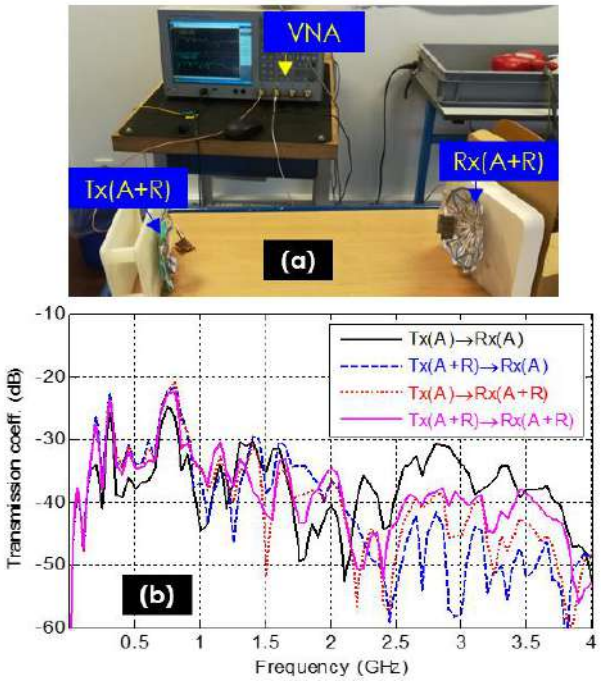

Figure 4: (a) Experimental test scenario and (b) measured transmission coefficients.

Acknowledgements

Acknowledgement is made to the France Normandy Region for the "FIL HARMONIQUE" project grant no. 18E00151 2017-2019 support of this research work, research and publication of the present article.

References

[1] H. Sun, Y.-X. Guo, M. He, Z. Zhong, A dual-band rectenna using broadband Yagi antenna array for ambient RF power harvesting, *IEEE Ant. Wireless Propag. Lett.*, 12: 918-921, 2013.

[2] G. Monti, L. Corchia, L. Tarricone, UHF Wearable rectenna on textile materials, *IEEE Ant. Propag. Mag.*, 61: 3869-3873, 2013.

[3] Y. G. Rabobason, et al., Design of flexible passive antenna array on Kapton substrate, *PIER C*, 63: 105-117, 2016.

[4] Y. G. Rabobason, et al., Design and synthesis of flexible switching 1 × 2 antenna array on Kapton substrate, *Eur. Phys. J. Appl. Phys*., 74: 1-10, 2016.

[5] H.-S. Zhang, S.-L. Chai, K. Xiao, L. F. Ye, Numerical and experimental analysis of wideband E-shape patch textile antenna, *PIER C*, 45: 163-178, 2013.

Chiral silicon photonic integrated circuits

(Invited Talk)

Jian Wang*

Wuhan National Laboratory for Optoelectronics, School of Optical and Electronic Information, Huazhong University of Science and Technology, Wuhan 430074, Hubei, China. *Corresponding author, E-mail: jwang@hust.edu.cn

Abstract

In this talk, we report recent advances in chiral silicon photonic integrated circuits. Ultra-directional high-efficient chiral coupling is demonstrated in the designed and fabricated silicon photonic circuits based on low-order to high-order mode conversion and interference mechanisms. The directionality of chiral coupling, in principle, can approach ±1. The chiral coupling efficiency can exceed 70%, which is much higher than conventional coupling mechanisms. The demonstrations open up the possibility of on-chip chirality determination to further flourish the development of chiral optics.

1. Introduction

Chiral light-matter interaction enables new fundamental researches and applications of light. The photonic chiral behavior has been extensively studied on different platforms of metasurfaces [1], nanostructures [2], and various optical interfaces [3]. As for the nanophotonic waveguides, the strongly confined guided-modes naturally manifest as nonnegligible longitudinal polarization component. It gives rise to the large intrinsically transverse spin, and thus induces the remarkable spin-momentum locking phenomenon of light [4]. Accordingly, the on-chip chiral resolving, chiral photonic circuit emission and non-reciprocal phenomenon have been recently revealed and investigated via silicon microdisk [5], dipole emission [6], and photonic crystal waveguides with embedded quantum dots [7]. Note that most of the reported photonic chiral behaviors face challenges in low directionality and low efficiency, fundamentally limited by their chiral mechanisms. In this talk, we report our recent demonstration on ultra-directional and high-efficient chiral coupling in silicon photonic circuits [8], which are based on low-order to high-order mode conversion and interference mechanisms.

2. Working principle and device design

The chiral effect of light-matter interactions is illustrated in Fig. 1(a), characterized by spin-dependent splitting of light. The proposed chiral photonic device is formed on silicon platform. As shown in Fig. 1(b), incident light with left- or right-handed circular polarization (LCP or RCP) is injected into a polymer (SU8)-assisted inversely tapered Y-branch silicon waveguide for chiral coupling. The device is divided into three parts, i.e. a thick wire polymer waveguide covering an inversely tapered silicon waveguide at the bottom (part I), a subsequent adiabatic inverse taper structure after the polymer waveguide (part II), and a Y-branch waveguide at the end of the inverse taper structure (part III). For incident light, the x-pol. component excites TE_0 mode of the polymer waveguide. It is then coupled into the inversely tapered silicon waveguide and maintained in a subsequent adiabatically tapered silicon waveguide as TE_0 mode. Meanwhile, the y-pol. component excites TM_0 mode. The adiabatic inverse taper structure converts TM_0 mode into TE_1 mode [9], as shown in Fig. 1(c). In the adiabatic inverse taper structure, TE_0 and TE_1 modes produce spatial interference, giving rise to quasi-periodic up and down field oscillation along propagation and determining directional coupling to output of the followed Y-branch waveguide.

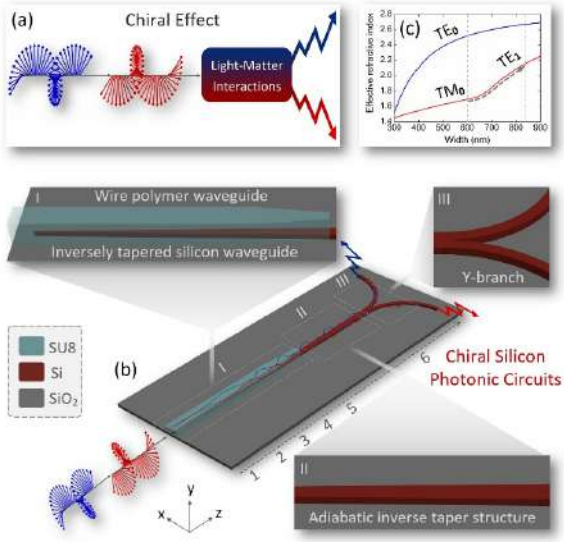

Figure 1: Principle and design of chiral silicon photonic circuits. (a) Illustration of chiral effect of light-matter interactions. (b) 3D view of chiral silicon photonic circuits (polymer-assisted inversely tapered Y-branch silicon waveguide) (c) Calculated effective refractive index versus the silicon waveguide width.

3. Experimental results

We fabricate the chiral photonic device on silicon platform and demonstrate the chiral coupling effect. The setup and results are shown in Fig. 2. The inset of Fig. 2(a) shows the measured optical microscope image of the fabricated chiral silicon photonic circuits. The input and two output ports of the silicon photonic circuits are all covered by a square polymer (SU8) waveguide (3.5 μm × 3.5 μm) to facilitate efficient excitation and output of light. The handedness-dependent output from chiral silicon photonic circuits is photographed by a camera under different polarization

handedness of incident light with helicity σ = -1, -0.5, 0, 0.5 and 1, respectively, at two wavelengths of λ_1 in Figs. 2(b)-2(f) and λ_2 in Figs. 2(g)-2(k) with opposite directionality. One can clearly see the distinct chiral coupling to different output ports of the Y-branch waveguide that is determined by the helicity of incident polarization handedness.

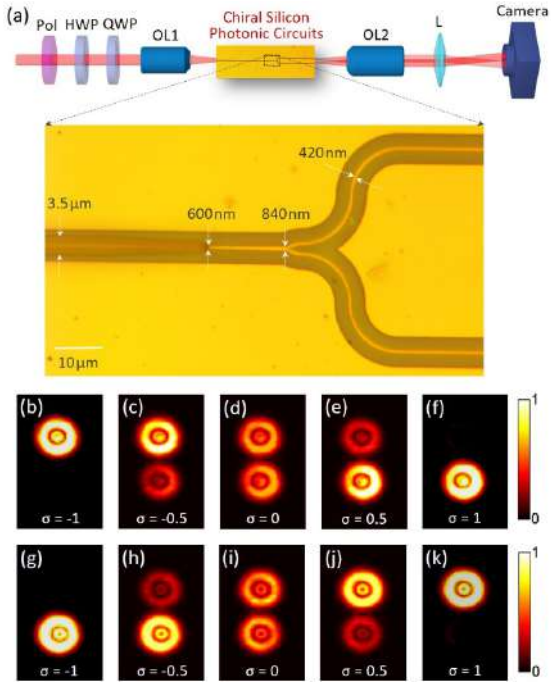

Figure 2: Experimental setup and results to measure the chiral coupling outputs. (a) Experimental schematic diagram with an inset of optical microscope image. Pol: polarizer; HWP: half-wave plate; QWP: quarter-wave plate; OL: objective Lens; L: lens. (b)-(k) Measured spin-dependent output from chiral silicon photonic circuits under different incident polarization handedness with helicity σ =-1 (b, g), -0.5 (c, h), 0 (d, i), 0.5 (e, j) and 1 (f, k), respectively, at two wavelengths (λ_1: (b)-(f), λ_2: (g)-(k)) with opposite directionality.

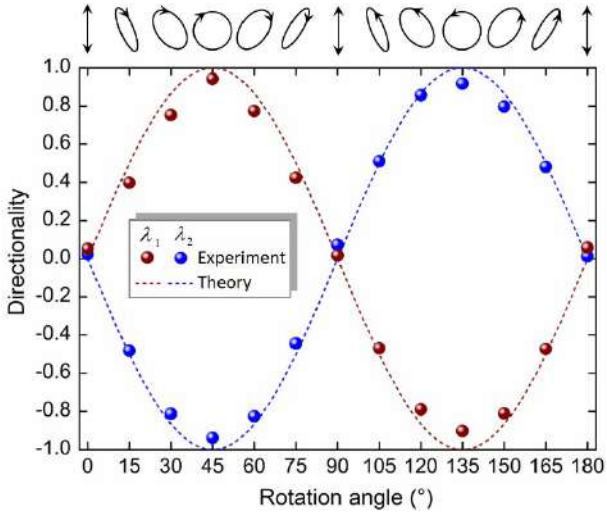

Figure 3: Measured directionality of chiral coupling under different incident polarization handedness at two wavelengths (λ_1, λ_2) with opposite directionality.

We characterize the directionality of chiral coupling in silicon photonic circuits and measure power from two output ports of the Y-branch waveguide, as shown in Fig. 3. The adjustable polarization state of incident light by controlling the rotation angle of the QWP is illustrated on top of Fig. 3. The measured results under different incident polarization handedness at two wavelengths (λ_1, λ_2) with opposite directionality are in good agreement with predicted values by theory. In particular, the absolute values of measured directionaliy $|D|$ exceed 0.92 under complete LCP (σ^{-1}) and RCP (σ^{+1}) inputs, indicating the achievable high directionality of chiral silicon photonic circuits. We also simulate chiral silicon photonic circuits, showing an ultra-high directionality approaching ±1 and high efficiency larger than 70%.

4. Conclusions

We demonstrate simple silicon photonic circuits for on-chip chiral coupling with superior performance based on low-order to high-order mode conversion and interference. It is believed that photonic integrated circuits will play an increasingly important role in chip-scale chiral optics and more chirality-related emerging applications.

Acknowledgements

National Natural Science Foundation of China (NSFC) (61761130082, 11774116, 11574001); Royal Society-Newton Advanced Fellowship, Natural Science Foundation of Hubei Province of China (2018CFA048); Program for HUST Academic Frontier Youth Team (2016QYTD05).

References

[1] S. Xiao, J. Wang, F. Liu, S. Zhang, X. Yin, J. Li, Spin-dependent optics with metasurfaces, *Nanophotonics* 6: 215–234, 2017.

[2] J. Petersen, J. Volz, A. Rauschenbeutel, Chiral nanophotonic waveguide interface based on spin-orbit interaction of light, *Science* 346: 67–71, 2014.

[3] K. Y. Bliokh, A. Niv, V. Kleiner, E. Hasman, Geometrodynamics of spinning light, *Nature Photon.* 2: 748–753, 2008.

[4] L. Fang, J. Wang, Intrinsic transverse spin angular momentum of fiber eigenmodes, *Phys. Rev. A* 95: 053827, 2017.

[5] F. J. Rodríguez-Fortuño, I. Barber-Sanz, D. Puerto, A. Griol, A. Martínez, Resolving light handedness with an on-chip silicon microdisk, *ACS Photon.* 1: 762–767, 2014.

[6] B. L. Feber, N. Rotenberg, L. Kuipers, Nanophotonic control of circular dipole emission, *Nature Commun.* 6: 6695, 2015.

[7] I. Söllner, S. Mahmoodian, S. L. Hansen, L. Midolo, A. Javadi, G. Kiršanskė, T. Pregnolato, H. El-Ella, E. H. Lee, J. D. Song, S. Stobbe, P. Lodahl, Deterministic photon–emitter coupling in chiral photonic circuits, *Nature Nanotechnol.* 10: 775–778, 2015.

[8] L. Fang, H. Luo, X. Cao, S. Zheng, X. Cai, J. Wang, Ultra-directional high-efficiency chiral silicon photonic circuits, *Optica* 6: 61-66, 2019.

[9] D. Dai, J. E. Bowers, Novel concept for ultracompact polarization splitter-rotator based on silicon nanowires, *Opt. Express* 19: 10940–10949, 2011.

Giant Magnetoimpedance Materials

Arcady Zhukov[1,2,3]*, Paula Corte-León[1,2], Lorena González-Legarreta[1], Mihail Ipatov[1,2], Juan M. Blanco[2], Julian Gonzalez[1] and Valentina Zhukova[1,2]

[1]Dpto. Fisica de Materiales, Fac. Quimicas, UPV/EHU, Paseo Manuel Lardizabal, 3, San Sebastian, 20018, Spain
[2]Dpto. de Física Aplicada, EIG, UPV/EHU, San Sebastian, Europa Plaza, 1,20018, Spain
[3]IKERBASQUE, Basque Foundation for Science, Bilbao, 48011, Spain
*corresponding author, E-mail: arkadi.joukov@ehu.es

Abstract

We present an overview of the factors affecting giant magnetoimpedance (GMI) effect and post processing tools allowing optimization of the GMI effect of soft magnetic wires. Generally, high GMI effect has been observed in Co-rich magnetic microwires. Annealing at adequate conditions allows manipulation the magnetic properties of amorphous ferromagnetic microwires. Stress-annealing allows induction of transverse magnetic anisotropy and GMI effect improvement in Fe-rich magnetic microwires.

1. Introduction

Soft magnetic materials and especially magnetic wires can present giant magnetoimpedance (GMI) effect suitable for industrial applications [1]-[5]. GMI effect can be observed either in crystalline or in amorphous magnetic wires, but amorphous magnetic wires present several advantages, such as superior mechanical and magnetic properties [2]-[5]. For these reasons, amorphous wires have attracted considerable attention since the 70-s [2]-[5].

Magnetic microwires prepared using the Taylor-Ulitovsky technique with thin metallic nucleus (typically with diameters from 0.5 to 50 μm) covered by flexible, insulating and biocompatible glass are quite demanded for a great number of applications [2],[6].

In amorphous materials the magnetoelastic anisotropy becomes one of the most important parameters that determine the magnetic properties [2]. In the case of glass-coated microwires the magnetoelastic anisotropy contribution is even more relevant since the preparation process involves not only the rapid quenching itself, but also simultaneous solidification of the metallic nucleus surrounded by the glass-coating with rather different thermal expansion coefficients [2].

Fe-rich glass-coated microwires are less-expensive and present a number of advantages, i.e. higher saturation magnetization [2]. Additionally, Co belongs to critical raw materials [7]. As a consequence, the insecure supplies of Co could hinder the development of new technologies related to massive applications. Accordingly, Fe-based microwires are preferable for large scale applications. But generally as-prepared Fe-rich microwires present much lower GMI effect than Co-rich microwires [2], [5]-[8]. Therefore, certain efforts have been recently paid to optimization of the magnetic softness and GMI effect in Fe-rich microwires [2], [10].

Consequently, we present our recent experimental results on post- processing of magnetic microwires with aim to achieve better magnetic softness and GMI effect.

2. Materials and methods

We selected typical Fe-rich ($Fe_{75}B_9Si_{12}C_4$) and Co-rich ($Co_{69.2}Fe_{4.1}B_{11.8}Si_{13.8}C_{1.1}$) alloys in which the phase diagram presents deep eutectic. Such chemical compositions were used previously for preparation of amorphous Fe-rich and Co-rich microwires [2].

2.1. Experimental technique

Hysteresis loops have been measured using fluxmetric method previously described elsewhere [9]. We represent the normalized magnetization, M/M_0 versus magnetic field, H, where M is the magnetic moment at given magnetic field and M_0 is the magnetic moment of the sample at the maximum magnetic field amplitude, H_m.

For GMI characterization we used GMI ratio, $\Delta Z/Z$, defined as:

$$\Delta Z/Z = [Z(H) - Z(H_{max})]/Z(H_{max}) \qquad (1)$$

where H_{max} is the maximum axial *DC* magnetic field (usually up to few kA/m).

We used micro-strip sample holder placed inside a sufficiently long solenoid that creates a homogeneous magnetic field, H. The sample impedance, Z, was measured using vector network analyzer from the reflection coefficient S_{11} using expression [7]:

$$Z = Z_0(1 + S_{11})/(1 - S_{11}) \qquad (2)$$

where Z_0=50 Ohm is the characteristic impedance of the coaxial line. Employed GMI measurements method allows evaluation of the GMI effect up to GHz frequencies.

3. Results and discussion

Studied Co-rich and Fe-rich as-prepared microwires present rather different magnetic properties and hence GMI effect: $Fe_{75}B_9Si_{12}C_4$ microwires present rectangular hysteresis loops with coercivity, H_c, (about 55 A/m) an order of magnitude higher that of $Co_{69.2}Fe_{4.1}B_{11.8}Si_{13.8}C_{1.1}$ microwires.

$Co_{69.2}Fe_{4.1}B_{11.8}Si_{13.8}C_{1.1}$ microwires present linear hysteresis loops with low H_c (see Fig. 1a and Fig. 1b)..

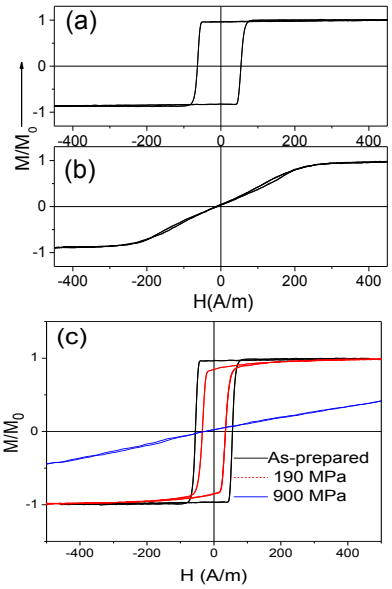

Figure 1. Hysteresis loops of as-prepared $Fe_{75}B_9Si_{12}C_4$ (a) and (b) $Co_{69.2}Fe_{4.1}B_{11.8}Si_{13.8}C_{1.1}$ microwires. (c) Hysteresis loops of as-prepared and stress-annealed at T_{ann}=300° C (190 and 900 MPa) $Fe_{75}B_9Si_{12}C_4$ microwires.

Accordingly, magnetically softer $Co_{69.2}Fe_{4.1}B_{11.8}Si_{13.8}C_{1.1}$ microwires exhibit an order of magnitude higher GMI ratio than $Fe_{75}B_9Si_{12}C_4$ microwires (see Fig. 2).

Stress annealing of Fe based microwires allowed considerable magnetic softening (coercivity decreasing) and induction of transverse magnetic anisotropy as can be observed from hysteresis loops measured in stress-annealed $Fe_{75}B_9Si_{12}C_4$ microwires (Fig. 1c). Magnetic properties are considerably affected by the stress, σ_m, applied during the stress annealing: induced transverse magnetic anisotropy

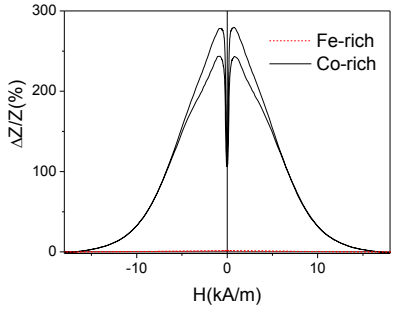

Figure 2. *ΔZ/Z(H)* dependences of as-prepared $Co_{69.2}Fe_{4.1}B_{11.8}Si_{13.8}C_{1.1}$ and $Fe_{75}B_9Si_{12}C_4$ measured at 100 MHz.

becomes more noticeable with increasing of σ_m -values.

Accordingly, remarkable improvement of GMI ratio is observed in stress-annealed $Fe_{75}B_9Si_{12}C_4$ microwires: improvement of *ΔZ/Z* –values by an order of magnitude is achieved (Fig. 3).

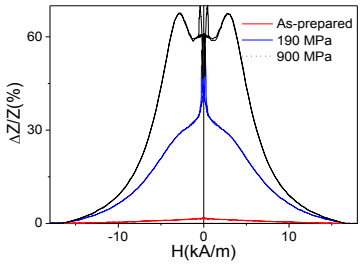

Figure 3. *ΔZ/Z(H)* dependencies of as-prepared and stress-annealed at T_{ann}=350° C (190 and 900 MPa) $Fe_{75}B_9Si_{12}C_4$ microwires measured at 100 MHz.

4. Conclusions

We observed that the stress-annealing allows remarkable improvement of GMI effect in Fe-rich microwires : an order of magnitude GMI ratio and magnetic softness improvement in Fe-rich microwires is demonstrated.

The future scope of our research will be focused on magnetic wires miniaturization and further development of appropriate post-processing.

References

[1] E.P. Harrison. G. L. Turney and H. Rowe, Electrical Properties of Wires of High Permeability, *Nature* 135: 961, 1935.

[2] A. Zhukov, M. Ipatov and V. Zhukova, *Advances in Giant Magnetoimpedance of Materials*, Handbook of Magnetic Materials, ed. K.H.J. Buschow, Vol. 24, 2015, pp. 139-236 (chapter 2).

[3] L.V. Panina and K. Mohri, Magneto-impedance effect in amorphous wires, *Appl Phys Lett.* 65: 1189-1191, 1994.

[4] S. Gudoshnikov, N. Usov, A.Nozdrin, M. Ipatov, A. Zhukov, and V. Zhukova, Highly sensitive magnetometer based on the off-diagonal GMI effect in Co-rich glass-coated microwire, *Phys. Stat. Sol. (a)* 211: 980–985, 2014.

[5] K. Mohri, T. Uchiyama, L. P. Shen, C. M. Cai, L. V. Panina, Amorphous wire and CMOS IC-based sensitive micro-magnetic sensors (MI sensor and SI sensor) for intelligent measurements and controls, *J. Magn. Magn. Mater.* 249: 351-356, 2002.

[6] A. Zhukov, A. Talaat, M. Ipatov and V. Zhukova, Tailoring of High Frequency Giant Magnetoimpedance Effect of amorphous Co-rich microwires, *IEEE Magn. Lett.* 6: 2500104, 2015.

[7] R.G. Eggert, Minerals go critical, *Nature Chemistry* 3:688–691, 2011

[8] A. Zhukov, M. Ipatov, M.Churyukanova, A. Talaat, J.M. Blanco and V. Zhukova, Trends in optimization of giant magnetoimpedance effect in amorphous and nanocrystalline materials, *J. Alloys Compound.* 727: 887-901, 2017

Novel Sensing Technique for Non-destructive Composites Monitoring

Valentina Zhukova[1,2], Paula Corte-León[1,2], Aleksandra Allue[3], Koldo Gondra[3], Mihail Ipatov[1,2], Juan M. Blanco[2], Julian Gonzalez[1] and Arcady Zhukov[1,2,3]*

[1]Dpto. Fisica de Materiales, Fac. Quimicas, UPV/EHU, Paseo Manuel Lardizabal, 3, San Sebastian, 20018, Spain
[2]Dpto. de Física Aplicada, EIG, UPV/EHU, San Sebastian, Europa Plaza, 1,20018, Spain
[3]Gaiker Technological Centre, 48170, Zamudio, Spain
[4]IKERBASQUE, Basque Foundation for Science, Bilbao, 48011, Spain
*corresponding author, E-mail: arkadi.joukov@ehu.es

Abstract

We observed evolution of the transmission and reflection parameters of the composites containing magnetic microwire inclusions during the composites matrix polymerization. A remarkable change of the reflection and transmission in the range of 4-7 GHz upon the matrix polymerization is observed. Obtained results are considered as a base for novel sensing technique allowing non-destructive and non-contact monitoring of the composites utilizing ferromagnetic glass-coated microwire inclusions with magnetic properties sensitive to tensile stress and temperature.

1. Introduction

Amorphous magnetic materials can present an unusual combination of excellent magnetic properties (e.g. high magnetic permeability, giant magnetoimpedance, GMI, effect, magnetic bistability, Matteucci and Widemann effects,) and superior mechanical properties (plasticity, flexibility) making them suitable for numerous industrial applications [1]-[2]. Furthermore the preparation method involving rapid melt quenching is quite fast and cheap and above mentioned magnetic softness can be realized without any complex post-processing treatments [1].

The development of novel applications of amorphous materials requires new functionalities, i.e. reduced dimensions, enhanced corrosion resistance or biocompatibility [1]. Glass-coated microwires prepared using the Taylor-Ulitovsky method fit to most of aforementioned expectation: such magnetic microwires have micro-nanometric diameters (typically 0.5-50 μm) covered by thin, insulating, biocompatible and flexible glass-coating [1] and can present excellent magnetic softness or magnetic bistability [1],[3].

These features of glass-coated microwires allow development of new exciting applications in various magnetic sensors [1]-[3], as well as in smart composites with tunable magnetic permittivity [2]-[3]. A few years ago the stress dependence of the GMI effect is proposed for the mechanical stresses monitoring in fiber reinforced composites (FRC) containing microwires inclusions [2]-[4]. A novel sensing technique involving free space microwave spectroscopy utilizing ferromagnetic microwire inclusions presenting the high frequency impedance is quite sensitive to tensile stress and magnetic field [4].

In this work we provide our recent results on study of the stresses arising during the polymerization of the matrix in FRCs on permittivity of the FRC with embedded microwire inclusions.

2. Materials and methods

We used glass-coated $Fe_{3.8}Co_{65.4}Ni_1B_{13.8}Si_{13}Mo_{1.35}C_{1.65}$ (metallic nucleus diameter, d=18.8 μm, total diameter, D=22.2 μm, ρ =d/D= 0.88) microwires with low negative magnetostriction coefficients, λ_s, prepared by Taylor-Ulitovsky technique described elsewhere [2]. The temperature during the polymerization process has been measured by a standard thermocouple.

For the composite matrix we used a vinylester resin (DERAKANE 8084) resin, accelerated with Cobalt Octoate (0,3 pph) and catalyzed with Methyl Ethyl Ketona (MEK 60%, 1,5 pph).

We used the free space measurement system previously described in details in [4]. The reflection (*R*) and transmission (*T*) coefficients were measure in free-space. The experimental set-up consists of a pair of broadband horn antennas (1-17 GHz) and a vector network analyzer. The composite was placed in 20 x 20 cm^2 window to avoid the edge effects. This window limits the applicable frequency range in 4-17 GHz. More detailed description of the free space systems is given in our previous publications [4]. The composites with ordered glass coated amorphous wires embedded in the thermoset matrix polymerization were prepared (Fig.1).

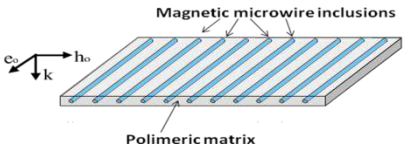

Figure 1 Sketch of a FRC with embedded microwires .

The polymerizing matrix provides external stimuli for the microwire inclusions (Fig. 1), which affects the magnetic properties and the GMI effect of microwires.

3. Results and discussion

During the polymerization process of the resin, volume shrinkage of about 8.2 % occurs and solid cured resin is obtained. The mechanical properties of the cured resin are the following: tensile strength of 76 MPa, tensile modulus of 2.9 GPa, and tensile elongation of 8-10%. However, apart of the matrix shrinkage considerable heating takes place. Therefore, in order to understand the processes during the polymerization of the composite that can affect the microwires we have measured the evaluation of temperature using a thermocouple. Obtained temperature changes during the polymerization represented at temperature, *T*, versus time, *t*, are sown in Fig.2.

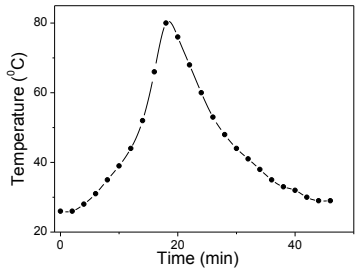

Figure 2. Evolution of temperature upon the polymerization.

As can be observed from the Fig.2, the matrix polymerization produces a heating of the composite up to 80 °C. As described above, we measured the transmission, *T*, and reflection, *R*, parameters of the composite containing Co-rich microwires ($Fe_{3.8}Co_{65.4}Ni_1B_{13.8}Si_{13}Mo_{1.35}C_{1.65}$) using the free space system.

As can be appreciated from Fig.3, considerable variation of the *T*-parameter is observed in the range frequency, *f*, of 4-7 GHz upon thermoset matrix polymerization (Fig.3). A non-monotonic variation of *T*-parameter upon polymerization is observed (Fig.3a). Additionally, some changes of *R*-parameter are also observed in a wide *f*- range (Fig.3b).

Observed changes of electromagnetic properties can be related to two main phenomena arising during the composite matrix polymerization: heating and mechanical stresses. As we mentioned above, apart of the matrix heating, the polymerization is accompanied by change of density and shrinkage. Therefore we can assume that the matrix shrinkage produces compressive stresses in magnetic nucleus of glass-coated microwires. Observed *T(f)* dependencies with are non- monotonic: some increase of *T* observed up to *t*=15 min (at *f* ≈4-7 GPa) followed by *T* decrease at *t*>15 min. Such evolution of *T*-parameter can be therefore associated to the heating and consequent cooling of the FRC.

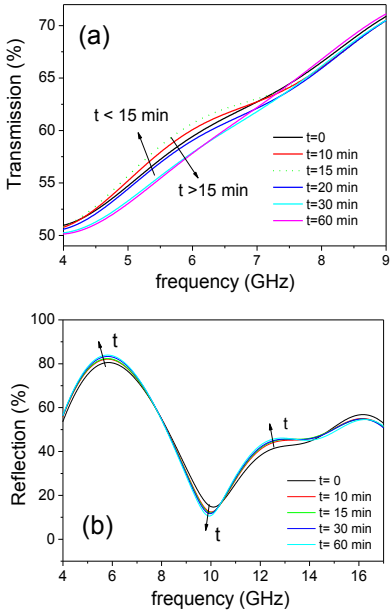

Figure 3. The Transmission, T (a) and reflection, R (a) parameters measured using free-space system during the composite polymerization.

4. Conclusions

We propose a novel sensing technique for non-destructive composites monitoring utilizing ferromagnetic microwire inclusions with magnetic properties sensitive to tensile stress and temperature. We have studied in-situ the impact of matrix polymerization on the evolution of the *T*- and R-parameters of the composites with microwire inclusions. We observed considerable variation of the *T*-parameter (in the range of 4-7 GHz) and *R*-parameter upon composite polymerization. Observed dependencies are discussed considering the matrix shrinkage during the polymerization and heating during the matrix polymerization and their influence on magnetic properties of glass-coated microwires.

References

[1] A. Zhukov, M. Ipatov and V. Zhukova, *Advances in Giant Magnetoimpedance of Materials*, Handbook of Magnetic Materials, ed. K.H.J. Buschow, Vol. 24, 2015, pp. 139-236 (chapter 2).

[2] K. Mohri, T. Uchiyama, L. P. Shen, C. M. Cai, L. V. Panina, Amorphous wire and CMOS IC-based sensitive micro-magnetic sensors (MI sensor and SI sensor) for intelligent measurements and controls, *J. Magn. Magn. Mater*. 249: 351-356, 2002.

[3] M.H. Phan, and H.X. Peng, Giant magnetoimedance materials: fundamentals and applications, *Prog. Mater. Sci.*, **53,** 323-420 (2008).

[4] D. Makhnovskiy, A. Zhukov, V. Zhukova, J. Gonzalez, Tunable and self-sensing microwave composite materials incorporating ferromagnetic microwires, *Advances in Science and Technology*, 54 (2008) pp. 201-210

High Q-factor Optofuidic Laser based on Fabry-Perot Resonator

Francesco Simoni[1], Silvio Bonfadini[2], and Luigino Criante[2]

[1]Department SIMAU, Università Politecnica delle Marche, Ancona, Italy
[2]Center for Nano Science and Technology, Istituto Italiano di Tecnologia, Milano, Italy

Recently we have demonstrated that robust optofluidic lasers based on standard Fabry-Perot (FP) optical cavity, made by two plane parallel mirrors, can be realized coupling two direct writing techniques: femtosecond micromachining technology and high resolution ink-jet printing. The chip design includes two parallel and empty pockets where metallic mirrors are printed and a central microfluidic channel where the active material flows. The device geometry is completed by additional microchannels necessary to insert microtubes and an optical fiber used to collect the output laser light.

Pumping is obtained by exploiting the 2nd harmonics of a linearly polarized Nd:YAG laser (5 ns pulse) focused on the sample through a cylindrical lens. The corresponding linear spot is completely absorbed by the dye solutio flowing in the microfluidic channel at a constant rate of 3.3 μL/min. The emission light, collected by the integrated fiber, is delivered to a high-resolution spectrometer.

The realized dye lasers show good performances allowing achieving state of the art low pumping threshold down to 2 μJ/mm^2 using a solution of Rh-6G in ethanol as active medium [1]. The obtained linewidth of 0.5 nm corresponds to a quality factor Q >10^3 that overcomes by about one order of magnitude the value obtained by other optofluidic laser based on FP resonator [2].

With the aim of improving the laser mode stability and the performances of the laser oscillator we have exploited the same technology in order to develop a hemispherical cavity, where one plane mirror acts as output coupler. The curvature radius R of the spherical mirror and the cavity length L were adjusted in order to fulfill the cavity stability condition R > L. Additionally, optimization of critical alignment of the device was carried out. Ultra-fine and user-friendly control of the pumping line spot on the cavity microchannel was achieved by exploiting a diffraction pattern detection method. Since an integrated optical fiber has been used for collecting the laser output, at the same time we have studied the effect of its alignment on the detected signal. We implemented a high resolution control of its location inside the chip by checking its position and tilt angle with respect to the mirror orthogonal axis. In this

way remarkable improvements have been demonstrated in laser performances with respect to devices previously realized.

Moreover, visualization of the emitted laser beam and intensity profile (Fig.1) was obtained, while a high-resolution spectrometer allowed measuring an emission line as narrow as 0.05nm, ten times lower than in the former demonstration [1]. The quality factor of this device has been measured to be $Q > 10^4$ and overcomes by one order of magnitude the state-of-the-art of any previous optofluidic laser based on a typical FP cavity. Moreover, it is very close to the values obtained in conventional optofluidic ring laser exploiting the WGM resonances. The reported results make attractive this robust glass embedded microlaser for applications related to biosensing, security and environment control.

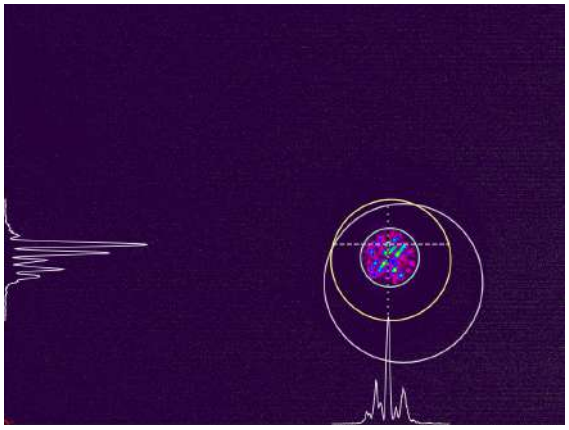

Fig.1 - Image and beam profile of the laser spot.

REFERENCES

1. Simoni F., Bonfandini S., Spegni P., Lucchetta D. E., Lo Turco S. and Criante L., Optics Express, Vol. 24, 17416, 2016.

2. Q. Kou, I. Yesilyurt, and Y. Chen, Appl. Phys. Lett., Vol. 88, 091101, 2006

Accelerating linear and nonlinear electromagnetic computations of nanostructures under a focused beam

P. Bouchon[1, *]

[1] DOTA, ONERA, Université Paris-Saclay, F-91123 Palaiseau, France

[*]corresponding author: Patrick.bouchon@onera.fr

Abstract- The linear and non linear responses of nanostructures are investigated with the B-spline modal method. The study is depicted for both plane waves and focused beam illumination. The simulation of a focused beam can be used to simulate the real conditions of experiments. I will show how computations can be accelerated, using either specific implementations of the modal equations, sparse matrices or learning.

Focusing the light onto nanostructures thanks to spherical lenses is a first step to enhance the field, and is widely used in applications, in particular for enhancing non-linear effects like the second harmonic generation.

Nonetheless, the electromagnetic response of such nanostructures, which have subwavelength patterns, to a focused beam can not be described by the simple ray tracing formalism. Here, we present a method to compute the response to a focused beam, based on the B-spline modal method, which is known to be fast thanks to a non-uniform mesh and sparse matrices. The eigenmodes are computed in each layer for both polarizations in conical mounting and are then combined for the computation of scattering matrices. The simulation of a gaussian focused beam is obtained thanks to a truncated decomposition on plane waves computed on a single period, which limits the computation burden.

A specific formalism is developed to compute the second harmonic field under the undepleted pump approximation. The nonlinear polarization induced by a fundamental plane wave or a focused beam generates a source term at the doubled frequency. The latter is divided into a finite number of sub-sources and the second harmonic field is subsequently computed by integration of these sub-sources contributions.

Through this presentation, I will show various strategies to hasten the computations, either through the implementation of the modal method itself, or by using specific strategies involving sparse matrices or learning of scattering matrices.

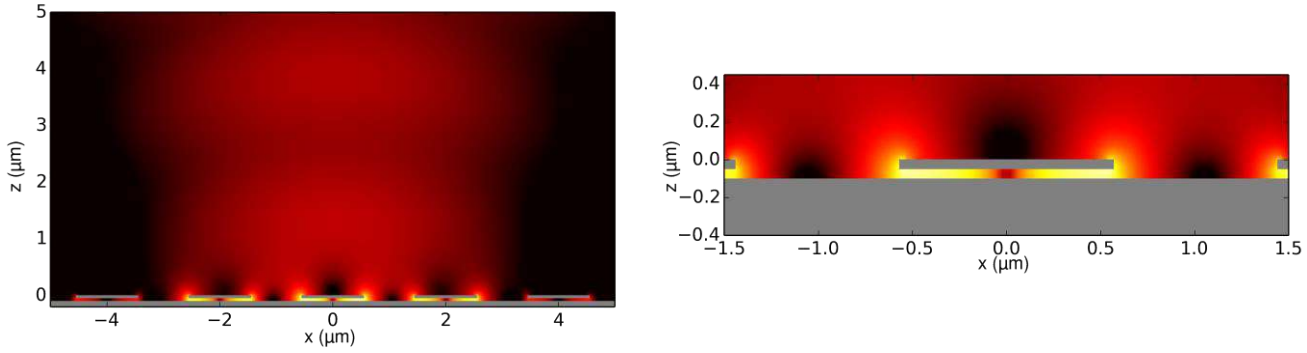

Figure 1: Metal-insulator-metal resonators array under a focused beam at the resonance wavelength. The beam is impinging on mainly three resonators of the array.

REFERENCES

1. Bouchon, P., F. Pardo, R. Haïdar, and J.L. Pelouard, "Fast modal method for subwavelength gratings based on B-spline formulation," *Journal of the Optical Society of America A*, Vol. 27, No. 4, 696–702, 2010.
2. Chevalier P., P. Bouchon, F. Pardo, and R. Haïdar, "Electromagnetic modelization of spherical focusing on a one-dimensional grating thanks to a conical B-spline modal method," *Journal of the Optical Society of America A*, Vol. 31, No. 8, 1692–1697, 2014.
3. Héron S., F. Pardo, P. Bouchon, J.L. Pelouard, and R. Haïdar, "Modal method for second harmonic generation in nanostructures," *Journal of the Optical Society of America B*, Vol. 32, No. 2, 275–280, 2015.

Thin-film Germanium Perfect Absorber for High-responsivity Photodetection

Xiyuan Cao [1, 2], Yijin Zhang [1], Yi Jin[3], Aimin Wu*[1, 2]

[1] State Key Laboratory of Functional Materials for Informatics, Institute of Microsystem and Information Technology, Chinese Academy of Sciences, Shanghai, P.R. China

[2]Center of Materials Science and Optoelectronics Engineering, University of Chinese Academy of Sciences, Beijing, 100049, P.R. China

[3] Department of optoelectronic information engineering, Zhejiang University, Hangzhou, P.R. China

*corresponding author, E-mail: wuaimin@mial.sim.ac.cn

Abstract

Strong energy harvesting in suspended nanopatterned germanium (Ge) thin-film is characterized in the near-infrared. Specifically, perfect light absorption can be achieved in nano-hole arrays based on guided resonance of the thin film when illuminated from a single side. Its response is both angle insensitive and polarization independent, with over 95% absorption at an incident angle up to 20°. The ultrathin design allows the active area with a short carrier diffusion length, i.e., the efficiency of the detection will be improved, paving a way for small footprint high-speed and high-responsivity photon detection.

1. Introduction

Instead of intrinsic layer with large thickness then hindering the fast response devices, light absorption by a semiconductor thin layer has become practically and fundamentally important in recent decades, such extensive works have found appealing applications such as solar cells and photon detection [1,2]. Various physical mechanisms give rise to absorption enhancement with thin-layer artificially dielectric structures [2, 3]. It is well known that the concept of high-refractive index dielectric metasurfaces exhibiting Mie resonances is adopted to construct super absorbing, based on the interference between simultaneously induced electric and magnetic dipoles [3]. While periodically structured surfaces or other plasmonic nanoantenna structures [4] are employed to increase absorption, nanohole arrays structures exhibit a significant improvement of the light absorption that exceeds [5] or approaches [6] the theoretical Yablonovitch limit, here we mean that the thin layer itself is patterned. In addition, nanohole arrays have an efficiency superior to nanopost arrays to some extent [7].

In this summary, investigation of the light absorption enhancement of nanohole arrays in suspended Ge thin-film is carried out to numerically verify the optical response, aiming to use these films in photon detection applications for their minimization size and compatibility with CMOS technology, which will be beneficial for future monolithic integration.

2. Simulation methods and results

Fig. 1 shows the structure of the proposed freestanding Ge absorber. The period (a), dimeter (d), and thickness (h) of the air holes are 540 nm, 408 nm, and 230 nm, respectively. The designed wavelength is 1310nm with normal incidence and optical constants of Ge are from Palik's handbook [8]. The light trapping structures were performed using the S^4 implementation [9] based on Rigorous Coupled Mode Analysis (RCWA) [10]. The absorption, transmittance and reflectance are satisfied A=1-T-R.

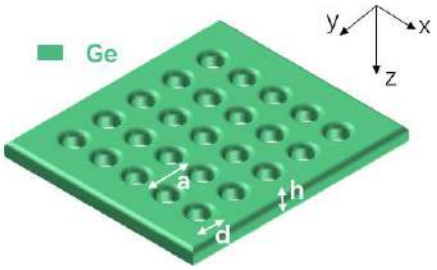

Figure 1: Three-dimensional schematic of the proposed freestanding Ge air hole absorber. The lattice constant in both x and y directions is a=540 nm, the dimeter of air holes is d=408 nm and the thicknesses of the film is h=230nm for perfect absorption (A=1-T-R=100%).

For a two-port resonator system, the one-side incident wave can be completed absorbed provided the resonator support two frequency-degenerate resonances which has opposite symmetry properties simultaneously as described in Piper and Fan's paper [3]. And from the point view of critical coupling, the incident power will be absorbed on resonance when the dissipation rate in the resonator is equal to the leakage rate of energy. In our theoretically infinite Ge air hole configuration, each face (top and bottom) of the Ge film acts as a port, and the material itself acts as appearance of dissipation to the system, so perfect absorption can be obtain through optical optimization of structural parameters

as shown in Fig. 2(a). Fig. 2(b) shows the intensity distribution through the centerline of the unit cell in a certain set of perfect absorption configurations from fig. 2(a). The strongly confined local field in the film is favorable condition for separation of charge-carrier pairs which is beneficial for high-responsivity and high-speed transport behaviors.

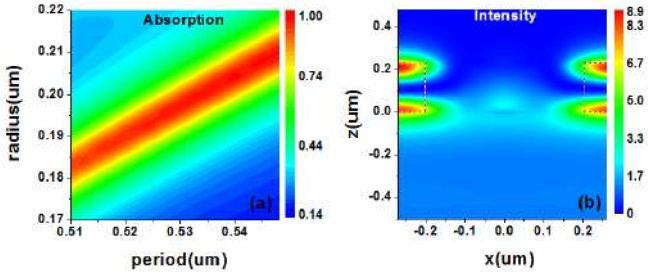

Figure 2: (a) Contour plots of absorption with variations of the radius and lattice constant of air holes, the film thickness is fixed as 230nm. Panel (b) shows the intensity distribution through the centerline of the unit cell in the perfect absorption configuration. The dashed line here shows envelop of the air hole structure.

The dependence of the absorption of such a thin film absorber on the incident wavelength and angle is also studied. In Fig. 3(a), it is worth noting that the absorption spectra exhibit a relatively narrow spectrum bandwidth which is approximately 30nm with over 95% absorption. The cross-shaped air hole or bilayer structures are the potential solutions for extending the bandwidth. Fig. 3(b) shows the property of angle insensitive with over 95% absorption at an incident angle up to 20°.

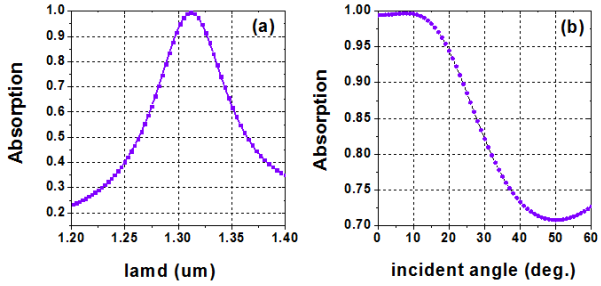

Figure 3: (a) Absorption spectra under normal incidence and (b) incident angle tolerance at 1310nm with period, dimeter, and thickness of the air holes are 540 nm, 408 nm, and 230nm, respectively.

3. Conclusions and outlook

In conclusion, a freestanding Ge thin film absorber with periodic air hole configuration in the near-infrared region is theoretically demonstrated. It is shown that perfect absorption can be achieved in such subwavelength-thin structures without the aid of traditional metal-dielectric scheme and rarely due to guided resonance of the film. A thinner film also has the added advantage of efficient charge-carrier transport. Those appealing features makes the thin film a good candidate for high-speed and high-efficiency photodetectors. The structure also has potential prospect to improve the absorption 2D material devices for photo detection and sensing.

Acknowledgements

This work is supported by the National Key Research and Development Program of China (No.2016YFE0130000), the Science Foundation of Shanghai (No. 16ZR1442600), “Strategic Priority Research Program” of Chinese Academy of Sciences (Grant No. XDB24020400).

References

[1] A. Polman, H. A. Atwater, Photonic design principles for ultrahigh-efficiency photovoltaics, *Nat. Mater.* 11, 174-177, 2012.

[2] J.Y. Tian, H. Luo, Q. Li, X.L. Pei, K.K. Du, M. Qiu, Near-infrared super-absorbing all-dielectric metasurface based on single-layer germanium nanostructures, *Laser Photonics Rev.* 1800076, 2018.

[3] J.R. Piper, V. Liu, S.H. Fan, Total absorption by degenerate critical coupling, *Appl. Phys. Lett.* 104, 251110, 2014.

[4] K. Aydin, V.E. Ferry, R.M. Briggs, H.A. Atwater, Broadband polarization-independent resonant light absorption using ultrathin plasmonic super absorbers, *Nat. Mater.* 2, 517, 2011.

[5] N.A. Yahaya, N. Yamada, Y. Kotaki, T. Nakayama, Characterization of light absorption in thin-film silicon with periodic nanohole arrays, *Opt. Express.* 21, 5924-5930, 2013.

[6] S.B. Mallick, M. Agrawal, P. Peumans, Optimal light trapping in ultra-thin photonic crystal crystalline silicon solar cells, *Opt. Express.* 18, 5691-5706, 2010.

[7] S.E. Han, G. Chen, Optical absorption enhancement in silicon nanohole arrays for solar photovoltaics, *Nano Lett.* 10, 1012-1015, 2010.

[8] E.D. Palik, *Handbook of Optical constants of Solids*, Academic Press, San Diego, 1998.

[9] V. Liu and S.H. Fan, *Comput. Phys. Commun.* 183, 2233, 2012.

[10] M.G. Moharam, T.K. Gaylord, Rigorous coupled-wave analysis of planar-grating diffraction, *J. Opt. Soc. Am.* 71, 811, 1981.

New numerical instability of the coordinate transformation method when applied to thinly coated deep gratings and methods to avoid it

Lifeng Li* and Xihong Xu

Department of Precision Instrument, Tsinghua University, Beijing 100084, China
*corresponding author, E-mail: lifengli@mail.tsinghua.edu.cn

Abstract

The coordinate transformation method in electromagnetic theory of gratings (the C method) has been improved recently so that it can model smooth-profile gratings of groove depth to period ratio up to 10. However, if such a grating is coated with a thin dielectric layer, the C method encounters a new type of numerical instability. This work reveals the origin of the instability and offers two solutions.

1. Introduction

The coordinate transformation method in electromagnetic theory of gratings (the C method) was first proposed by Chandezon et al [1] in 1980. Since then, the works of many researchers have enabled it to model dielectric and metallic gratings, isotropic and anisotropic gratings, one-dimensional and two-dimensional (crossed) gratings, and the grating profiles can be almost arbitrary. Nowadays it is truly one of the most efficient and simple methods for modelling surface-relief gratings, especially coated gratings [2-4]. However, the C method is not perfect. Only a few years ago, on the one hand, a grating with sharp edges had slow but steady numerical convergence even if the grooves were deep. On the other hand, a shallow and smooth grating had quick initial convergence but eventual divergence as the truncation number increased; for deep and smooth gratings, convergence was impossible when numerical computation was done in double precision.

Five years ago, we began an in-depth study of the C method. By focusing on the condition numbers of the eigenvalues and eigenvector matrix of the matrix eigenvalue problem in the C-method and studying their relationships with the continuity properties of the grating profile function, we found ways to improve the C method greatly. It now can be used to model accurately smooth bare gratings of groove depth to period ratio up to 10, and the truncation number range practically has no upper limit [5, 6]. As we extended our research, we found for deep and smooth bare gratings coated with a thin dielectric layer, the C method equipped with many well-tested numerical algorithms, e.g. the S matrix algorithm, to solve the boundary-matching equations exhibited strong numerical instability. In this paper, we show the newly discovered numerical instability, reveal its origin, and offer two solution methods.

2. Presentation of the problem

Due to page limitation, we give only one example, a distorted sinusoidal grating with profile function $a(x) = \sin^2[\pi f(x)]$, $f(x) = 5x/4$ if $0 \le x < 0.4$ and $f(x) = (5x+1)/6$ if $0.4 \le x \le 1$. The refractive indices of the incident medium, the conformally coated layer, and the substrate are 1.0, 1.5, and 1.7, respectively. The angle of incidence is arcsin(1/3). The optical wavelength, grating groove depth, and the coating thickness t are 0.6328, 1.0, and 0.01, respectively, all in unit of grating period. Figure 1 shows the convergence of error of energy balance vs truncation number N for a ***bare*** grating (when the coated layer is absent), where Σ stands for sum of diffraction efficiencies of all propagating orders. The negative of the vertical axis gives the number of accurate decimal places of individual diffraction orders (this is true for the C method). Therefore, the C method converges very well. Figure 2 shows the convergence of the C method for almost the same grating, now ***coated***. For clarity, only TM polarization is shown. In the figure legend, FM stands for the full-matrix algorithm, WsS for the $W \rightarrow s \rightarrow S$ variant of the S-matrix algorithm [7], WS for the $W \rightarrow S$ variant of the S-matrix algorithm [8], and ET for the enhanced transmittance algorithm [9]. The full-matrix algorithm is one that solves the whole system of linear equations as is, keeping all unknown field amplitudes. One can immediately see that with the FM algorithm the C method works for the coated grating as well as for the bare grating, but the three recursive algorithms show strong numerical instability.

3. Origin of the new numerical instability

The numerical instability shown in Figure 2 is clearly not due to the exponential growth of the modal fields in the coated layer because the layer thickness is very small. Although not shown here, our numerical test for zero coated layer thickness led to similar numerical instability. Our theoretical analysis and numerous numerical tests revealed that the origin of the problem is in the poor condition of the matrix that is formed by the eigenvectors of the matrix eigenvalue problem of the C method. For gratings of smooth and deep profiles, the condition numbers of some leading evanescent eigenvalues and the eigenvector matrix grow exponentially. Then round-off error creates numerical instability in matrix manipulations like matrix inversion, even though actual inverse matrices are never calculated. When t is

large, this effect is damped out by the exponential decay of the modal fields. When t is small, coupling between numerically contaminated upward and downward eigenvectors is strong, hence giving rise to numerical instability. Apparently, different recursive algorithms have different vulnerabilities to a given poor condition of eigenvector matrix. The FM algorithm contains no matrix inversion; therefore, it has the best resistance to poor condition of the eigenvector matrix.

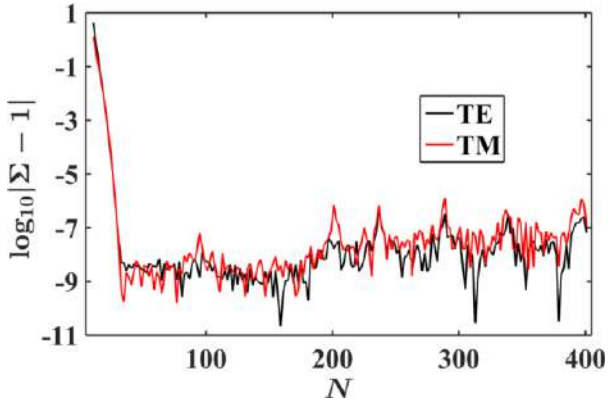

Figure 1: Convergence of the C method for the distorted sinusoidal bare grating.

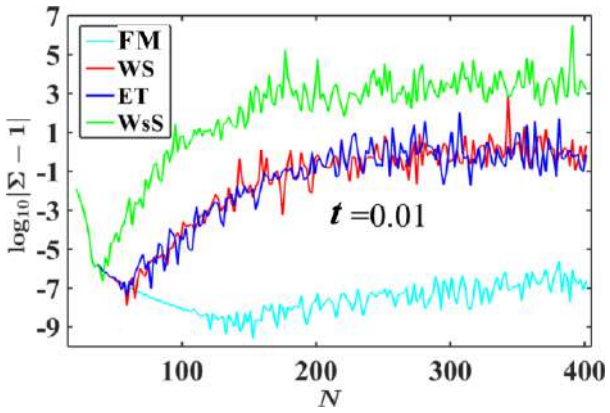

Figure 2: Convergence of the C method for the distorted sinusoidal thinly coated grating.

4. Methods to overcome the numerical instability

From Section 2, it is already obvious that one of the methods to overcome the numerical instability is to use the full-matrix algorithm. The second method we have found is to use the perturbative preconditioning method that we developed in [6]. We first solve the matrix eigenvalue problem with perturbative preconditioning as described in [6]. Then, we apply the preconditioning to the matrix inversions in the recursive algorithms. Specifically, we convert the matrix to be inverted, which has been calculated in double precision, in a k-digit data representation, where $5 \le k \le 7$. Then, we store the matrix back in the double precision data representation, and proceed with a recursive algorithm normally in double precision. The above data precision conversions can be easily done by using the MATLAB toolbox Advanpix [10]. Figure 3 shows the convergence of the transmitted -1^{st}-order diffraction efficiency, computed with k = 5. The change of vertical axis is because after perturbative preconditioning energy balance is no longer automatically satisfied. The reference value T_{-1}^{s} is obtained by using the FM algorithm. The figure shows that from a practical point of view all three recursive algorithms work well. The drawbacks of this method are that it relies on having a means of converting data precision and the selection of k value may be grating problem dependent.

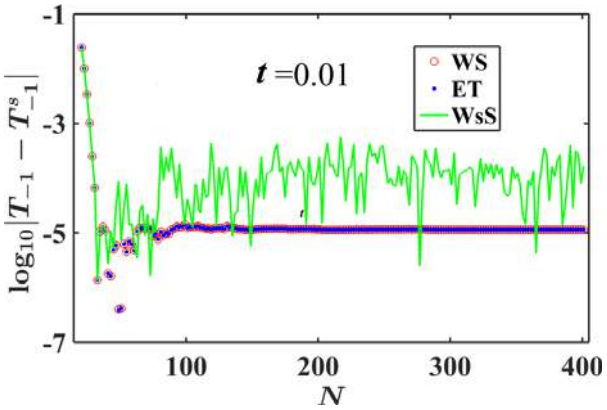

Figure 3: Improved convergence of the C method for the thinly coated distorted sinusoidal grating, obtained by applying perturbative preconditioning to the matrices to be inverted.

5. Conclusions

We have presented the newly discovered numerical instability of the C method when it is applied to thinly coated gratings of smooth and deep grooves, revealed its origin, and offered two solution methods.

References

[1] J. Chandezon, D. Maystre, and G. Raoult, *J. Opt.* (*Paris*) 11: 235-241, 1980.

[2] J. Chandezon, M. T. Dupuis, G. Cornet, and D. Maystre, *J. Opt. Soc. Am* 72: 839-846, 1982.

[3] L. Li, J. Chandezon, G. Granet, and J.-P. Plumey, *Appl. Opt*. 38: 304-313, 1999.

[4] Gérard Granet, Chap. 8 in *Gratings: Theory and Numeric Applications*, 2nd revisited edition, E. Popov ed. (Institut Fresnel, AMU, Marseille, 2014).

[5] X. Xu and L. Li, *Opt. Lett*. 39: 6644-6647, 2014.

[6] X. Xu and L. Li, *J. Opt. Soc. Am. A* 34: 881-891, 2017.

[7] L. Li, *J. Opt. Soc. Am. A* 13: 1024-1035, 1996.

[8] L. Li, *J. Opt. Soc. Am. A* 20: 655-660, 2003.

[9] M. G. Moharam, D. A. Pommet, E. B. Grann, and T. K. Gaylord, *J. Opt. Soc. Am. A* 12: 1077-1086, 1995.

[10] http://www.advanpix.com/

Detection and Recognition of Buried Conducting Objects Using Subsurface Microwave Images Constructed by Down-Looking GPR Measurements and by Energy-Based Target Features

Selman Dinç[1], Hande Elibol[1], Rutkay Güneri[1], Ali Bahadır Özdöl[1], Furkan Şık[1], İsmail Taylan Yeşilyurt[1] , Mesut Dogan[1,2] and Gonul Turhan-Sayan[1]

[1]Middle East Technical University, Dept. of Electrical and Electronics Engineering 06800 Ankara, Turkey
[2] Ardahan University, Dept. of Electrical and Electronics Engineering, 75000 Ardahan, Turkey
*Gonul Turhan-Sayan, E-mail: gtsayan@metu.edu.tr

Abstract

Detection of buried objects using ultra-wideband ground penetrating radar measurements have been a challenging area of research aiming for high detection probabilities while assuring low false alarm rates. In this paper, conducting objects of similar size but different geometries are buried very close to ground surface. Effective preprocessing and energy-based electromagnetic features are used to detect and recognize buried targets from their subsurface microwave images constructed from real-time A-scan measurements conducted in cross-track and down-track directions.

1. Introduction

Ground Penetrating Radar (GPR) is a well-known ultra-wideband electromagnetic sensor which has a large area of applications such as landmine or improvised explosive device (IED) detection in military applications, detection of people or animals trapped behind walls or under demolished buildings in rescue operations, detection of archeological sites or mineral deposits buried in soil etc. [1-2]. Subsurface detection of buried objects is a challenging problem due to many factors including antenna coupling effects, powerful reflections from the air-ground boundary, absorption of electromagnetic power by soil, and interferences of clutter signals caused by the heterogeneous structure of the soil and the clutter objects like rocks, metal and non-metal trash in the environment. The time-domain signals (A-Scan signals) measured by a GPR system provides us the time-localized (hence space-localized) information about the reflected and scattered signals coming from all kinds of discontinuities and objects placed in the measurement environment. The two-dimensional and three-dimensional GPR data can be obtained by scanning the ground in cross-track and down-track directions resulting in the B-Scan and C-Scan data, respectively. Such data, after proper preprocessing, can be used to construct microwave images or to extract energy-based target features for the detection and identification of buried objects.

In this paper, a preprocessing method based on the use of cumulative energy curves [3-4] is used to remove the air-ground reflections from raw GPR A-Scan signals because such strong reflections can increase the false alarm rate and decrease the detection rate by masking and deteriorating the desired signals coming from buried targets. Then, the preprocessed C-Scan data set is used to obtain microwave images of the buried targets which are basically thin conducting discs with circular, rectangular and triangular cross-sections. While the total energy values of preprocessed A-Scan signals are used to construct the images, the cumulative energy curves belonging to A-scan signals are also used as additional target features for improved recognition when the image resolution is not good enough.

2. Design of Experiments and Image Construction

In this study, down-looking GPR type stepped frequency measurements are recorded by using a computerized set up composed of a portable vector network analyzer, a wideband (1 to 18 GHz) horn antenna, and an all-wooden soil box of planar dimensions 2 meters by 3 meters with a depth of 1.2 meters as shown in Fig. 1.

Figure 1: General view of experimental setup for subsurface measurements.

The test targets are as large as to fit a cross-sectional area of 10x10 cm and all has the same thickness of 2 cm. They are buried just 1 cm below the air-ground boundary as described in Fig. 2 below.

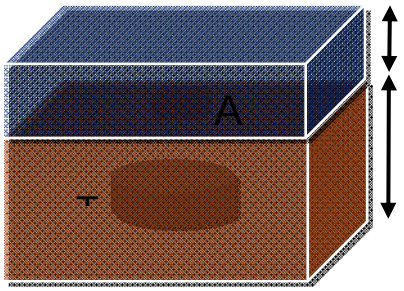

Figure 2: The circular disc type target (T) is buried 1 cm below the air (blue)-soil (brown) boundary. The aperture of the antenna (A) is 10 cm above the ground.

The A-Scan signals are recorded at each one of 225 measurement points taken by 2 cm scanning steps in both cross-track and down-track directions within a 30 cm by 30 cm measurement domain. To provide sufficient spatial image resolution, S11 scattering parameter measurements are recorded over the frequency band extending from 15 GHz to 16 GHz as the horn antenna has a relatively narrow HPBW of about 14 degrees over this band. First, the ground reflections are removed from the raw data by improved preprocessing techniques to facilitate the detection of buried objects [3]. Sample A-Scan measurements with and without a target is shown in Fig. 3. Next, the target images are obtained by computing the total energy E_T of each recorded A-scan signal x(t) with the formula

$$E_T = \int_0^\infty |x(t)|^2 \, dt \qquad (1)$$

The contour plot for the GPR image obtained for the buried triangular conducting disc is given in Fig. 4 as an example of the results. The location and shape of the actual target is overlaid in the image.

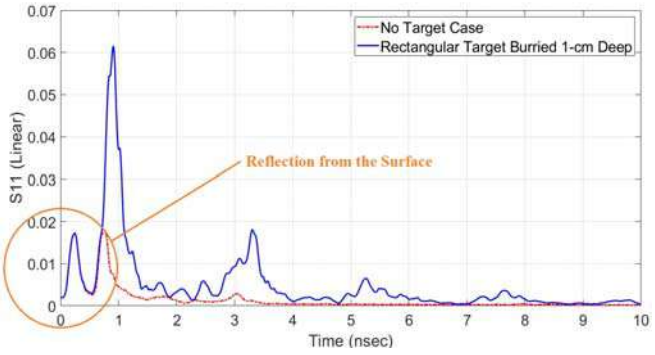

Figure 3: Raw A-Scan signals for no target case (red curve) and for rectangular target (blue curve).

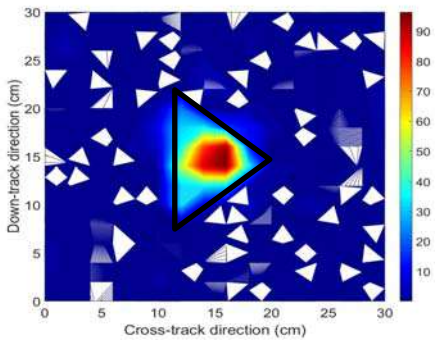

Figure 4 : Image obtained for the triangular conducting disc.

3. Conclusions

It has been observed in this study that the directivity of the antenna beam-width is critical to obtain a good spatial resolution in subsurface imaging. It is also noticed that detection of thin targets buried very close to the air-soil boundary may be very tricky as the returns coming from the target may be removed unintentionally while removing the ground reflections. Improved methods for ground reflection removal need to be used instead of the simple thresholding technique to avoid such critical errors.

Acknowledgements

The experimental data used in this study is collected in the *Subsurface Target Detection Lab*oratory of the Dept. of Electrical and Electronics Engineering of METU in the course of a STAR Project directed by Prof. G. Turhan-Sayan, which is a part of the undergraduate research program of the department.

References

[1] G.S. Smith, and R.S. Waymond, "A scale model for studying ground penetrating radars." IEEE transactions on geoscience and remote sensing 27.4, 1989, 358-363.

[2] L.P. Peters, J.J. Daniels and J.D. Young, "Ground Penetrating Radar as a Subsurface Environmental Sensing Tool," in Proceedings of the IEEE, vol. 82, no. 12, Dec 1994, pp. 1802-1822.

[3] M. Dogan and G. Turhan-Sayan, “Preprocessing of A-Scan GPR Based on Energy Features,” Conference #9823 “Detection and Sensing of Mines, Explosive Objects, and Obscured Targets XXI” at the SPIE Defense+Security Symposium 2016, Baltimore, Maryland, USA, 17-21 April 2016.

[4] M. Dogan, O. Yesilyurt and G. Turhan-Sayan, “Inside-the-wall detection of objects with low metal content using the GPR sensor: effects of different wall structures on the detection performance,” SPIE Defense+Security and Commercial Sensing Symposium 2018, Orlando, Florida, USA, 17-19 April 2018.

Electromagnetically induced transparency and lattice resonances in metasurfaces composed of silicon nanocylinders

Saeid Jamilan, George Semouchkin, Navid Gandji, and Elena Semouchkina

Department of Electrical and Computer Engineering, Michigan Technological University, Houghton, MI, 49931, USA
*corresponding author, E-mail: esemouch@mtu.edu

Abstract

Densely packed metasurfaces composed of cylindrical silicon nano-resonators were found to demonstrate the phenomenon of electromagnetically induced transparency at electric dipolar resonances. It was shown that this phenomenon is not related to overlapping of dipolar resonances or to the Kerker's effects. The observed transparency appeared to be related to interference between waves scattered by nano-resonators and by additional scattering centers including the electric branch of lattice resonances. Coupled resonance fields were also found to contribute to observed phenomena.

1. Introduction

We have recently shown [1, 2] that electromagnetic responses of metasurfaces (MSs) composed of cylindrical silicon nano-resonators (NRs) drastically depend on the lattice constant characterizing the periodicity of these arrays. At fixed diameters of nano-resonators, chosen to be 240 nm, densely packed MSs with the lattice constant Δ of about 300 nm revealed strong interactions between neighboring NRs. On the contrary, in sparsely packed MSs with Δ = 450 nm, meta-atoms conserved autonomous behavior and remained unaffected by neighboring resonances.

From the analysis of recent literature devoted to studies of silicon MSs [3, 4] it could be concluded that most intriguing results, such as full transmission and 2π phase control at specific NR and MS geometries, providing for coincidence of electric (EDR) and magnetic (MDR) dipolar resonances, could be obtained only in densely packed MSs. However, varying resonator geometry in [3, 4] was accompanied by simultaneous varying of array lattice constant that complicated the interpretation of the results. Our studies of the influence of NR geometry on MS responses at fixed lattice constants did not confirm the benefits observed in [3, 4] at overlapping of EDR and MDR in NRs. In particular, spectral changes in waves scattered from MSs did not demonstrate effects, which could be related to π-value jumps in phases at two dipolar resonances and did not testify in favor of realizing the Kerker's condition at joint resonance frequency. In addition, we have found that full transmission through MSs at Δ = 300 nm could be obtained at various NR geometries, irrelevant to coincidence of the resonance frequencies of EDR and MDR. Here we present the results of investigation of this newly observed phenomenon.

2. Electromagnetically induced MS transparency

S-parameter spectra of MS with Δ = 275 nm, presented in Fig. 1, reveal narrowband full transmission at 633 nm. Sharp peak of S21 is accompanied by a deep drop of S11 that is typical for observation of electromagnetically induced transparency (EIT) in metamaterials [5]. Another S11 drop seen at 900 nm is defined by destructive interference of waves backscattered from red tails of EDR and MDR at the 1st Kerker's condition [6].

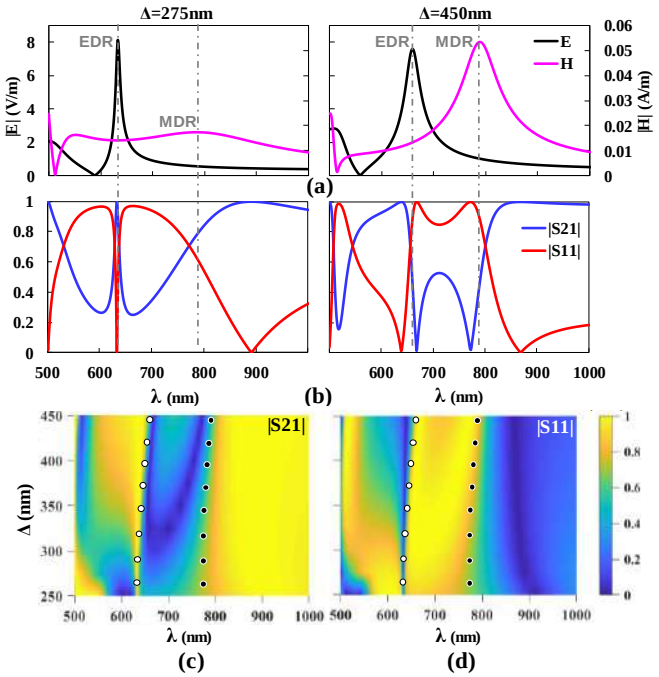

Fig. 1. (a) Spectra of signals from field probes in NRs of MSs with Δ=275nm and Δ=450nm at NR heights of 160 nm; (b) S-parameter spectra; (c) and (d) spectra of |S21| and |S11| coefficients in dependence on MS lattice constant.

As seen in Fig. 1, S-parameter spectra of MS at Δ = 450 nm also demonstrate similar Kerker's effect, however, near EDR, these spectra has nothing in common with EIT-like response of dense MS at 633 nm. Presented in Fig. 1c changes of spectral distributions of S21 values at varying MS lattice constants show that the bandwidth of EIT-like

phenomenon becomes especially narrow at Δ less than 325 nm. At higher Δ, the bandwidth increases while S21 plot loses its symmetry. As seen in Fig. 1d, S11 spectra conserve deep drops at EDRs at increasing values of Δ up to 350 nm.

3. Bright and dark resonance modes

Although EIT has been originally detected in atomic systems at destructive interference of parallel electron transitions, it is now recognized as the phenomenon similar to that observed in metamaterials at interference between waves scattered from so-called bright resonance modes, coupled with incident waves, and from dark modes, participating due to coupling with bright modes. I was shown in [7] that EIT in metamaterials with electric dipole response could be described by using the two oscillator model. While EDRs in NRs could be considered as bright oscillators, to apply the model, dark oscillators should also be defined. Recently, it was shown [8] that EDRs in MSs can be coupled with so-called lattice resonances (LRs) originating from interaction of surface waves with the lattice. This coupling was assumed affecting the formation of EDRs and causing changes of EDR frequency at varying Δ, similar to our earlier observations [1].

Fig. 2a presents E-field pattern in the planar cross-section of dense MS at the EDR frequency and Fig. 2b - similar pattern at the frequency corresponding to zero signal in the spectrum of the probe placed at NR center (at point P1 in the inset of Fig. 2c). As seen in the figures, the pattern obtained at the EDR frequency demonstrates confined in resonators dipolar fields along with E-fields in the gaps between NRs in X-oriented rows of MS. The latter fields are apparently due to LRs interacting with EDRs in a wide range of Δ restricted only by the Rayleigh anomaly [8].

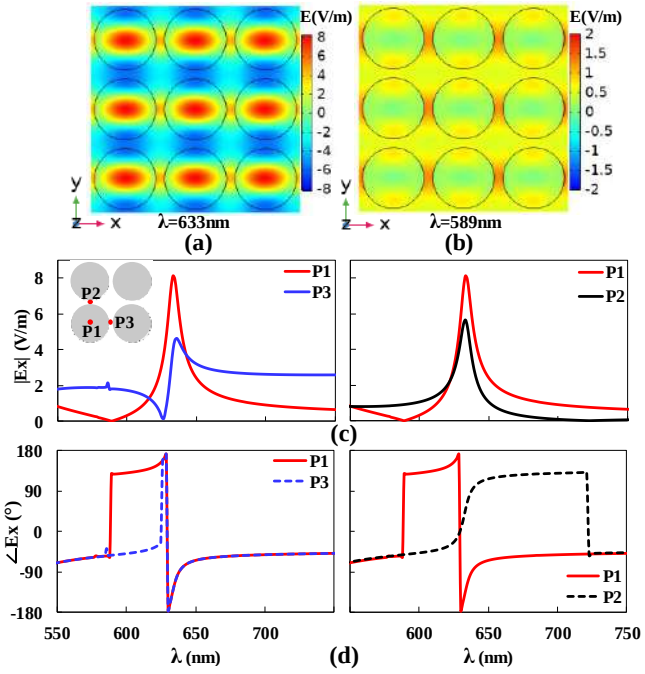

Fig. 2. (a) and (b) E-field patterns in XY cross-section of dense MS at EDR frequency (a) and at the frequency of zero probe signal at point P1(b); (c) spectra of probe signals in the points shown in the inset; (d) spectral changes of signal phases in points P1-P3.

It is interesting to note that LRs remain visible in the field patterns obtained at $\lambda<\lambda_{EDR}$ (Fig. 2b), when EDRs cannot be registered. Fig. 2c (left) shows that the probe signal in the point P3 centered in the area of LS responses has Fano shape. This fact is in favor of suggestion that LSs interfere with waves scattered from other sources. Fig. 2d (left) confirms the possibility of destructive interference between waves scattered by LSs and EDRs, as it demonstrates the π-value phase difference of probe signals characterizing responses of these resonances below the EDR frequency.

The field pattern presented in Fig. 2a allows for suggesting that additional involvement in the interference phenomena can be expected from dipolar-type fields concentrated in the gaps between resonators in Y-oriented columns of MSs. Presented in Fig. 2c (right) spectrum of signal from the probe placed in such gap (at point P2 shown in the inset of Figs. 2c) also has Fano shape, which looks as mirrored with respect to the shape of signal spectrum for the probe placed inside NR (at point P1). This specifics could be related to the π-value difference between phases of E-fields inside NRs and in the Y-oriented gaps that is illustrated by Fig. 2d. Such difference is capable of causing destructive interference between waves scattered in backward direction from NRs and from fields in the gaps.

4. Conclusion

Conducted studies have demonstrated an opportunity for realizing EIT-like phenomenon in dense silicon MSs and have identified centers of scattering capable of providing in destructive interference of waves backscattered from MS.

Acknowledgements

This work was supported by the National Science Foundation under Award ECCS-1709991.

References

[1] N. P.Gandji, *et al*., Electromagnetic responses from planar arrays of dielectric nano-disks at overlapping dipolar resonances, *IEEE RAPID Conference*, 2018.

[2] S. Jamilan, G. Semouchkin, N. P. Gandji, E. Semouchkina, Specifics of scattering and radiation from sparse and dense dielectric meta-surfaces, *JAP*, 2019

[3] Y.F. Yu, *et al*, High-transmission dielectric metasurface with 2π phase control at visible wavelengths, *Laser Photonics Rev*., 9 (4), pp. 412–418, 2015.

[4] A.I. Kuznetsov, *et al.*, Optically resonant dielectric nanostructures, *Science*, 354, 6314, 2016.

[5] N. Papasimakis and N. Zheludev, Metamaterial-Induced Transparency: Sharp Fano Resonances and Slow light, *Optics and Photonics News*, Vol. 20,Iss.10, pp.22-27, 2009.

[6] M. Kerker, et al, Electromagnetic scattering by magnetic spheres, *J. Opt. Soc. Am*., 73, pp. 765–767, 1983.

[7] P. Tassin, et al, Electromagnetically Induced Transparency and Absorption in Metamaterials: The Radiating Two-Oscillator Model and Its Experimental Confirmation, *PRL*, 109,187401,2012.

[8] V.E. Babicheva and A.B. Evlyukhin, Resonant Lattice Kerker Effect in Metasurfaces With Electric and Magnetic Optical Responses, *Laser Photonics Rev*. 11, 1700132, 2017.

A terahertz polarisation modulator with gate-controlled graphene metamaterials

Soojeong Baek[1], Hyeon-Don Kim[2], Jagang Park[1], Kanghee Lee[3], Bumki Min[1]

[1]Department of Mechanical Engineering, Korea Advanced Institute of Science and Technology, Daejeon, Republic of Korea
[2]Department of Nano-Convergence Mechanical Systems, Korea Institute of Machinery and Materials, Daejeon, Republic of Korea
[3]Department of Physics, Korea Advanced Institute of Science and Technology, Daejeon, Republic of Korea
*corresponding author, E-mail: bmin@kaist.ac.kr

Abstract

Electrical control of polarisation can have a beneficial impact on the development of an application in telecommunication and signal processing. However, in the terahertz (THz) regime, it has still been inaccessible due to the lack of efficiently active materials. Here, we demonstrate a terahertz polarisation modulator where anisotropy is reconfigurable via hybridization of metamaterials with mono- and bi- layer graphene patterns.

1. Introduction

Electrical access to manipulation of the polarisation state has attracted attention for the potential application such as polarisation-multiplexed communication, polarisation-dependent signal processing, polarisation-sensitive imaging and sensing[1]. To control the polarisation states of transmitted waves, the anisotropy of microscopic constituents in materials has been employed as a general means. However, for THz waves, it still remains a challenge on account of little efficiently interaction with natural media. Even, active modulation of THz polarisation has been limited to the bulky and sensitive way[2].

In recent year, metamaterials research has been progressed where unnatural optical properties can be realized via resonance. The resonant feature entails that a strong phase shift is enabled within a deep subwavelength thickness. Based on this, numerous devices for control of THz polarisation states have been proposed[3][4]. More recently, research on hybridization of metamaterials with active materials has been proposed[5]. Among this, experimental implementation of electrical modulation of THz polarisation states was abled through mechanical achitecture under the complicated fabricaiton[6][7].

Here, we demonstrate a terahertz polarisation modulator operated in an electrically controllable manner by an interaction between metamaterials and mono- and few layer graphene micropatterns. We present that transmission characteristics of one among two eigenpolarisations can be controlled by selectively modulating coupling between meta-atoms related to resonance with gating voltage. In result, based on independent control of response on two eigenpolarisations, we numerically and experimentally show the functionalities for THz polarisation control.

2. Result

2.1. Design of tunable anisotropic metamaterials

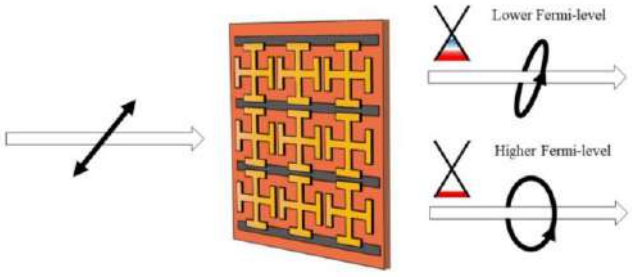

Figure 1 Schematic of Graphene tunable anisotropic metamaterials. Under 45-degree linearly polarised incidence, the polarisation states of transmitted THz waves are changed with respect to Fermi-level of graphene.

As shown in figure 1, Graphene tunable anisotropic metamaterials (GTAMs) are constituted by unit cell where there are two meta-atoms merged perpendicularly to each other and patterned graphene placed at the gaps between adjacent meta-atoms only in one principal axis, but not in the other. Namely, it is in the very direction that the degree of capacitive coupling between them can be adjusted so as to control the conductivity of graphene, thus imposing controllable function.

2.2. Experimental characterization of GTAMs

In order to experimentally demonstrate control of anisotropy with GTAMs, we fabricated the graphene metamaterials through conventional microfabrication. To increase the gating efficiency of graphene, Iongel which is reported to maximize the capacitance by forming a nanogap was exploited as a gating dielectric. The transmission characteristics of GTAMs are measured through terahertz

time-domain spectroscopy (THz-TDs). Figure 2 shows the measured spectra of the x and y-polarized light and transmitted via the GTAMs when various static gating voltage is applied. From that result, this structure support feasibility that transmission characteristics of two eigenpolarisations can be controlled independently. Interestingly, we turned out that there is the specific frequency with almost no change in transmittance but in phase for y-polarisation incidence regardless of changing a gating voltage V_g. It means that in the very frequency, only the phase difference of the two orthogonal polarisation can be controlled. In other words, the transmitted polarisation ellipse of incident light with 45-degree linear polarisation can be modulated after passing through GTAMs.

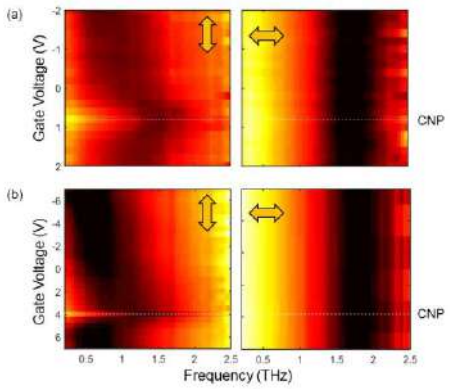

Figure 2 Experimental amplitude transmission of GTAMs with (a) mono- and (b) bi- layer graphene micro-patterns according to Fermi-level. Arrows represent incident polarisation direction. (CNP: Charge Neutral Point)

2.3. Modulation of the polarisation state of transmitted THz

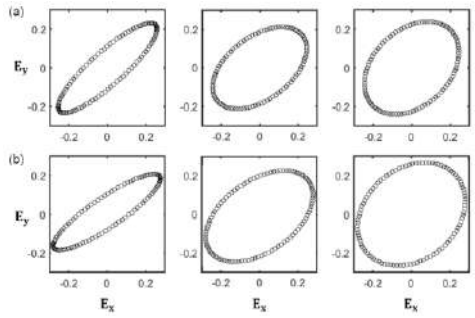

Figure 3 Experimental evolution of polarisation for the transmitted THz waves with respect to difference between gate and CNP voltage $|V_g - V_{CNP}|$ with (a) mono- and (b) bi-layered graphene patterns at 1.25 THz. $|V_g - V_{CNP}|$ increases from left to right panel.

When 45-degree linear-polarised THz waves are incident, transmitted THz polarisation states can be calculated via Jones matrix formalism. As illustrated in figure 3, it is confirmed that as the $|V_g - V_{CNP}|$ increases, transmitted polarisation states are modulated into circular polarisation.

3. Discussion

Graphene has been well-known as a material capable of changing conductivity with respect to the Fermi-level in the THz regime. However, it is only possible to make modulation of terahertz wave with graphene itself having good scattering time and efficient Fermi-level modulation. But, in proposed structure, attributed to strongly capacitive coupling of I-shaped meta atoms to each other, THz response of metamaterials can also be largely adjusted by inducing carrier leakage via contact with conductive graphene to coupling region. Furthermore, now that graphene leakage channel is placed in only one principal axis direction, under incident terahertz field, two eigenpolarisations can experience different transmission characteristics from each other. From this, we show functionalities for polarisation modulation based on that while transmission can be less changed, the phase delay between two linear eigenpolarisations orthogonal to each other can be modulated in the frequency range.

4. Conclusions

We experimentally present electrical modulation of THz polarisation states with graphene hybridized metamaterials. As graphene patterns are formulated into the coupling region related to only one principal axis, we realized electrically controlled anisotropy. In addition, the use of stacked graphene patterns can expand modulation range.

References

[1] T. Nagatsuma, G. Ducournau, and C. C. Renaud, Advances in terahertz communications accelerated by photonics, *Nat. Photonics* 10: pp. 371–379, 2016

[2] J. Dai, N. Karpowicz, and X.-C. Zhang, Coherent Polarization Control of Terahertz Waves Generated from Two-Color Laser-Induced Gas Plasma, *Phys. Rev. Lett* 103, p. 023001, 2009.

[3] L. Cong, N. Xu, W. Zhang, and R. Singh, Polarization Control in Terahertz Metasurfaces with the Lowest Order Rotational Symmetry, *Adv. Opt. Mater.* 3, pp. 1176–1183,2015.

[4] L. Cong, N. Xu, W. Zhang, and R. Singh, Polarization Control in Terahertz Metasurfaces with the Lowest Order Rotational Symmetry, *Adv. Opt. Mater.* 3, pp. 1176–1183, 2015.

[5] D. Wang *et al.*, Switchable Ultrathin Quarter-wave Plate in Terahertz Using Active Phase-change Metasurface, *Sci. Rep.*5, p. 15020, 2015.

[6] W. M. Zhu *et al.*, Microelectromechanical Maltese-cross metamaterial with tunable terahertz anisotropy, *Nat. Commun.*3, p. 1274, 2012.

[7] X. Zhao *et al.*, Electromechanically tunable metasurface transmission waveplate at terahertz frequencies, *Optica* 5, p. 303, 2018.

Fast tomography with pyCUDA

Amedeo Capozzoli*, Claudio Curcio, Angelo Liseno

Universitá di Napoli Federico II, Dipartimento di Ingegneria Elettrica e delle Tecnologie dell'Informazione
via Claudio 21, I 80125 Napoli (Italy)
*corresponding author, E-mail: a.capozzoli@unina.it

Abstract

We present a 3D tomographic reconstruction algorithm, programmed on a Graphics Processing Unit (GPU) by means of pyCUDA. pyCUDA, indeed, enables the combination of a dynamic, high-level scripting language with the massive performance of a GPU. The performance of the approach are numerically analyzed.

1. Introduction

Many tomographic reconstruction algorithms that are routinely used in applications are based on simple models and so on simple reconstruction approaches. Although they are typically successfully employed in 2D scattering scenarios, their 3D extension requires a computationally heavy reconstruction process.
In 3D, the increase in computing time with the amount of data required to obtain images with the desired accuracy often clashes with the need of having real time (or quasi-real time) reconstructions. Two approaches are then possible:

- Using computationally efficient algorithms and/or accelerating critical parts of the existing ones by fast routines;
- Exploiting high performance, massively parallel hardware and parallelizing the existing software.

Concerning the second point, modern Graphics Processing Units (GPUs) reach high parallelism levels by hundreds of processing cores. Furthermore, the introduction of multicore functionalities in high-level platforms for technical computing, as the Parallel Computing Toolbox and the multicoreaware functions in Matlab, the Matlab code GPU accelerators, or pyCUDA [1] is raising the interest of the radar community into parallel programming.
In this paper, we present a 3D tomographic reconstruction algorithm [2, 3], programmed on a Graphics Processing Unit (GPU) by means of pyCUDA. pyCUDA, indeed, enables the combination of a dynamic, high-level scripting language with the massive performance of a GPU.

2. The approach

Many tomographic reconstruction approaches have been developed throughout the literature for 3D imaging.
In many applications, however, the main purpose is to reveal the presence and localize the scattering objects, while providing also some geometrical information on the scatterers [4]. In these circumstances, approximated model can be sufficient, while dramatically simplifying the involved algorithms. The typically used approximations are the Born and Kirchhoff ones.
Let us then consider a 3D scatterer embedded, for simplicity, into free space within the investigation domain $D = [-x'_M, x'_M] \times [-y'_M, y'_M] \times [-z'_M, z'_M]$ centered at the origin of the $Oxyz$ reference system, see Fig. 1. The measurement configuration is multi-monostatic, namely, the same antenna transmits the illuminating wave and receives the scattered field, while occupying different positions in space. Furthermore, the illumination is multifrequency with band $[f_{min}, f_{max}]$.
Under the above hypotheses, and using a linearizing approximation, the generic component of the scattered field at the reception point can be written, apart from unessential factors and assuming the objects' reflectivity independent of the illumination direction, as

$$E_s(\underline{r}, f) = \int_D f(\underline{r}') e^{-j2k_0 R} d\underline{r}', \qquad (1)$$

where f is the operating frequency, k_0 is the wavenumber, $R = |\underline{r} - \underline{r}'|$ and $f(\underline{r}')$ is a function describing the scatterers' properties.
Eq. (1) can be discretized as

$$E_s(\underline{r}_p, f_q) = \sum_n f(\underline{r}'_n) e^{-j2k_0 R_{pn}} \Delta x \Delta y \Delta z, \qquad (2)$$

where Δx, Δy and Δz are discretization steps, $\underline{r}_p$ is the p-th position of the transmitting/receiving antenna, f_q is the q-th employed frequency and $R_{pn} = |\underline{r}_p - \underline{r}'_n|$.
According to eq. (2), the tomographic reconstruction problem amounts at the solution of a linear system of equations. Due to the large dimensions of involved linear system, in this paper, the problem is solved, in a regularized way, by reformulating it as the optimization of the error functional [5]

$$\|\underline{E}_s - \underline{\underline{A}}\underline{f}\|^2, \qquad (3)$$

where $\underline{E}_s$ is the data vector, $\underline{f}$ is the unknown vector and $\underline{\underline{A}}$ is the system matrix.
In order to estimate the speedup achievable thanks to the simple parallel scheme offered by pyCUDA, the optimization of functional (3) is here performed by a Conjugate Gradient (CG) approach as a first approach.

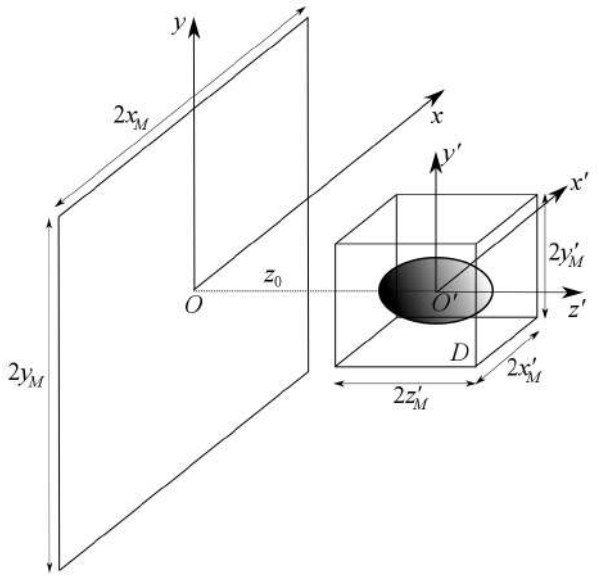

Figure 1: Geometry of the problem.

3. pyCUDA

As the name suggests, pyCUDA fuses the high-level Python programming language with the NVIDIA CUDA language. The justification for the choice of pyCUDA as the development platform is related to the fact that the major factors in choosing a high-level programming language over a potentially better-performing, low-level one is the complementarity of tasks between the GPU and the host processor. The GPU, indeed, is optimally suited to carrying out throughput-oriented parts of a program. The CPU is then freed from this duty, so that it is responsible for essentially control and communication and consequently it is appointed of tasks with a higher level of abstraction. Therefore, a high-level scripting language (such as Python) can perform this higher-level job equally well, simply because the performance demands to the CPU are reduced.
Furthermore, pyCUDA uses the GPU run-time code generation (RTCG) technique which enables automated tuning at run-time, namely, at the right time when all the information for a successful tuning is available.
Finally, and as compared to Matlab, pyCUDA is free and is more flexible in the interaction with CUDA.
The pyCUDA implementation of the approach consists of two steps:

- filling of the system matrix $\underline{\underline{A}}$;
- functional optimization by CG.

The first step is effectively implemented by a properly developed parallel kernel, compiled by CUDA and linked under python using the pyCUDA interfaces.
The second step is effectively solved by cuBLAS level 1, 2 and 3 routines thanks to the simple and very thin wrappers offered by pyCUDA.

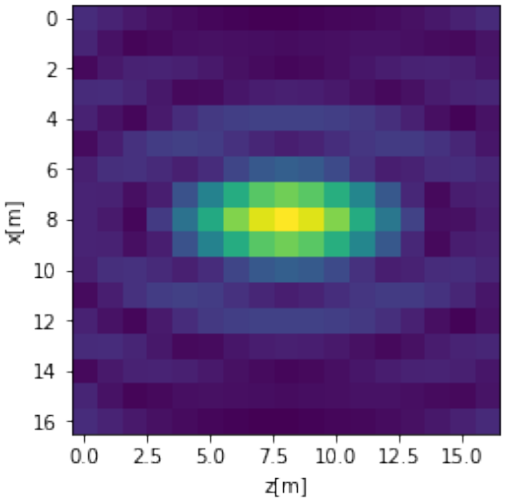

Figure 2: Reconstruction of a point-like scatterer.

4. Numerical results

Fig. 2 illustrates a slice of the reconstruction of a point-like scatterer. Three frequencies have been used, namely, $1GHz$, $1.5GHz$ and $2GHz$. The transmitting/receiving antennas occupy a region of $10\lambda_{max} \times 10\lambda_{max}$, with λ_{max} the largest employed wavelength, moving on a grid with a step of $\lambda_{min}/2$, λ_{min} being the minimum employed wavelength. The investigation domain D has been discretized with a $\lambda_{min}/4$ sampling step.
The algorithm has been run on an NVIDIA P100 card having compute capability equal to 6.0. Its performance has been compared to that of a sequential approach, run on an Intel i5-4590 CPU @3.30GHz with 16GB of RAM, and a speedup of about 30 has been observed.

References

[1] A. Klöckner, N. Pinto, Y. Lee, B. Catanzaro, P. Ivanov, A. Fasih, *PyCUDA: GPU run-time code generation for high-performance computing*, arXiv:0911.3456v1 [cs.DC] 18 Nov 2009.

[2] A. Capozzoli, C. Curcio, A. Di Vico, A. Liseno, Nufft-& GPU-based Fast imaging of vegetation, *IEICE Trans. Commun.*, E94-B: 2092-2103, 2011.

[3] A. Breglia, A. Capozzoli, C. Curcio, A. Liseno, CUDA expression templates for electromagnetic applications on GPUs, *IEEE Antennas Prop. Mag.*, 55: 156-166, 2013.

[4] K.J. Langenberg, R. Bärmann, R. Marklein, S. Irmer, H. Müller, M. Brandbaß, B. Potzkai, Electromagnetic and elastic wave scattering and inverse scattering applied to concrete, *NDT&Int.*, 30: 205-210, 1997.

[5] G.H. Golub, C.F. Van Loan, *Matrix Computations, Third Edition*, The Johns Hopkins University Press, 1996.

Waveform Design for Dispersive SAR

Natalie Cartwright[1*], **Kaitlyn Muller**[2]

[1]State University of New York at New Paltz, Department of Mathematics, New Paltz, NY, USA
[2]Villanova University, Department of Mathematics and Statistics, Villanova, PA, USA
*corresponding author, E-mail: cartwrin@newpaltz.edu

Abstract

We study waveform design for synthetic-aperture radar imaging through dispersive media. Under the assumptions of scalar wave propagation through a causal dielectric medium and single-scattering from an isotropic point scatterer, we use asymptotic analysis to derive an asymptotic approximation to the scattered electric field. From this asymptotic approximation, we define a *scattering precursor* that we propose for the transmit waveform for SAR imaging through dispersive material. We compare our scattering precursor with previously defined optimal waveforms in terms of both propagation and scattering capabilities, as well as imaging performance.

1. Introduction

It has been hypothesized that the slow decay rate of the so-called Brillouin pulse can be used to advantage in radar detection and imaging applications [1, 2]. The question of whether or not the Brillouin precursor is the ideal waveform for synthetic aperture radar imaging through dispersive material was partially addressed by Varslot, Morales, and Cheney in a pair of papers appearing in 2010 and 2011 [3, 4]. These authors used a filtered back-projection algorithm to derive an optimal filter and its associated optimal waveform. The optimization is based upon minimizing the mean square error of the L^2-norm between the ideal image and the reconstructed image. The authors conclude that the optimal minimum-phase waveforms have a "transmit spectrum that is concentrated around the frequencies which are conducive to the generation of precursors" [4], but no conclusive statement could be made.

Here, we provide an asymptotic expansion of the electric field component of the impulse response due to scattering by an isotropic point source in a frequency-dependent dispersive (and lossy) material. We subsequently define a *scattering precursor* based on this asymptotic expansion. We compare the propagation and imaging performance of this *scattering precursor* to that of the optimal waveform derived by Varslot et al. [4]. Our results show that the higher frequencies retained by the optimal waveform provide enhanced target detection as compared to our scattering precursor.

2. Formulation

We adopt the formulation of [3, 4] and assume that the sensor and scatterers are embedded in a homogeneous, isotropic, locally linear dispersive material with a known dielectric permittivity. With the additional assumptions of stationary targets comprised of linear materials with known dispersion residing on a known surface, and an isotropic point-like antenna moving along a path $\gamma(s)$ parametrized by slow-time s, using the start-stop approximation and the Born approximation, the solution of the scattered field may be written in terms of the Green's function as

$$E^{sc}(\gamma(s),t,s) = \int \frac{e^{-i\omega(t-2n(\omega)|\mathbf{r}_{s,\mathbf{y}}|/c_0)}}{(16\pi^3|\mathbf{r}_{s,\mathbf{y}}|)^2}\,\omega^2 P(\omega)d\omega\tilde{T}(\mathbf{y})d\mathbf{y}. \quad (1)$$

Here, $\tilde{T}$ is a modified target that accounts for both the target reflectivity and non-planar surface area, $\mathbf{y} = (y_1, y_2)$ is a two dimensional vector position, $\mathbf{r}_{s,\mathbf{y}} = |\mathbf{\Psi}(\mathbf{y}) - \gamma(s)|$ is the distance between the antenna $\gamma(s)$ and the target $\mathbf{\Psi}(\mathbf{y})$, the spectrum of the transmit pulse is $P(\omega)$, and $n(\omega)$ is the index of refraction of the dispersive material.

2.1. The Scattering Precursor

We consider an impulse response with spectrum $P(\omega) = 1$ and a Debye-type dielectric with permittivity given by

$$\epsilon(\omega)/\epsilon_0 = \epsilon_\infty + \frac{\epsilon(0) - \epsilon_\infty}{1 - i\omega\tau}, \quad (2)$$

with material parameters where chosen to model leafy vegetation: $\epsilon_\infty = 1.45, \epsilon(0) \approx 2.43$, and $\tau = 8$ ns. The scattering integral Eq. (1) may be evaluated using asymptotic methods of Bleistein [5]. With those results, we define a *scattering precursor pulse*

$$p^{sc}(t - z\sqrt{\epsilon_\infty}/c) = a_0 W_2\left(\gamma\sqrt{\frac{2d}{c_0}}\right) + a_1\left(\frac{2d}{c_0}\right)^{-1/2} W_3\left(\gamma\sqrt{\frac{2d}{c_0}}\right), \quad (3)$$

with

$$a_0 = \left(\frac{\omega^2}{t^2}\right) P(\omega) \frac{d\omega}{dt}\bigg|_{t=0,\omega=0}, \tag{4a}$$

$$a_1 = \frac{1}{\gamma}\left[a_0 - \left(\frac{\omega}{t}\right)^2 P(\omega)\frac{d\omega}{dt}\bigg|_{t=-\gamma,\omega=\omega_{sp}}\right], \tag{4b}$$

$$\gamma = \sqrt{2\phi(\omega_{sp}(\theta);\theta)}, \tag{4c}$$

$$W_n(\xi) = \sqrt{2\pi}\left(-\frac{d}{d\xi}\right)^n e^{\xi^2/2} \text{ for } n = 0, 1, 2, \ldots. \tag{4d}$$

and $\omega_{sp}(\theta)$ are saddle points of the complex phase function

$$\phi = i\omega\left[\sqrt{\epsilon(\omega)/\epsilon_0} - \theta\right], \tag{4e}$$

with $\theta = \frac{ct}{2|\mathbf{r}_{s,\mathbf{y}}|}$ a space-time parameter.

2.1.1. Comparisons

The transmit waveforms for an eight-cycle rectangular-modulated sinusoid of carrier frequency 0.1 GHz (dash-dotted black), the optimal waveform of Varslot et al. [4] with SNR $= -40$ dB (dashed blue), and the scattering precursor [Eq. (3)] with $d = 70$ m (solid red) and their spectra are shown on the top left and right in Fig. 1, respectively. The scattered waveforms and their spectra, corresponding to each transmit waveform, are shown on the bottom left and right in Fig. 1, respectively.

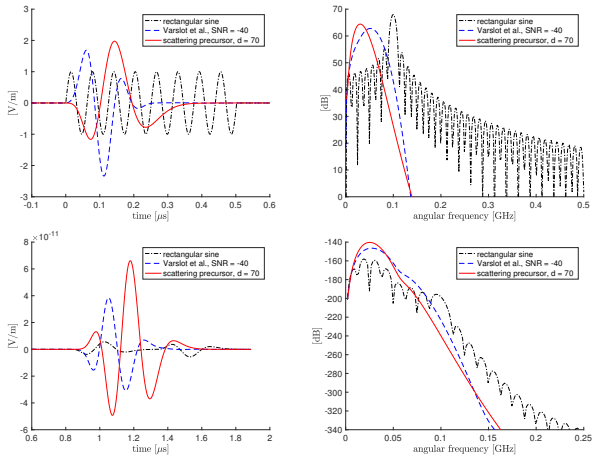

Figure 1: Transmit waveforms (left) and corresponding spectra (right). A rectangular-modulated sinusoid of carrier frequency 0.1 GHz (dash-dotted black), the optimal waveform of Varslot et al. for SNR $=-40$ dB (dashed blue), and the scattering precursor with $d = 70$ m (solid red).

Reconstructions of the target scene using the rectangular-modulated sinusoid, the optimal waveform of Varslot et al., and the scattering precursor with $d = 40$ m, are given in columns one, two, and three of Fig. 2, respectively. The noise level decreases from top to bottom with SNR = 40, 0, -40.

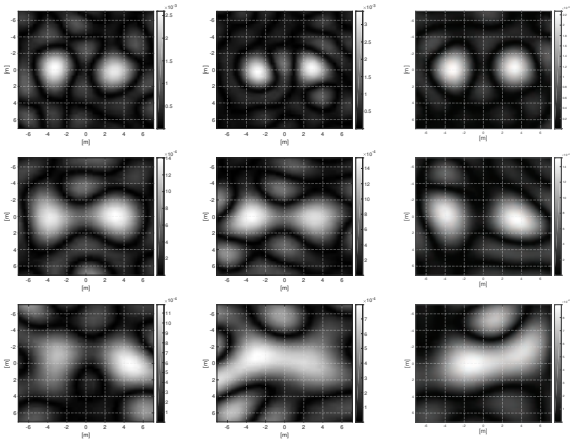

Figure 2: Reconstructions of the target scene using a rectangular-modulated sinusoid (left column), the optimal waveform (middle column), and the scattering precursor with $d = 40$ m (right column), for SNR = 40 (top row), SNR = 0 (middle row), and SNR = -40 (bottom row).

Acknowledgement

This manuscript is based upon work supported by the Air Force Office of Scientific Research under award number FA9550-16-1-0241.

References

[1] M. Dawood, H. U. R. Mohammed, and A. V. Alejos, "Method, technique, and system for detecting Brillouin precursors at microwave frequencies for enhanced performance in various applications," u. S. patent US 8570207 B1.

[2] K. E. Oughstun, "Dynamical evolution of the Brillouin precursor in Rocard-Powles-Debye model dielectrics," *IEEE Trans. Antennas Propag.*, vol. 53, no. 5, pp. 1582–1590, 2005.

[3] T. Varslot, J. H. Morales, and M. Cheney, "Synthetic-aperture radar imaging through dispersive media," *Inverse Problems*, vol. 26, no. 2, 2010.

[4] ——, "Waveform design for synthetic-aperture radar imaging through dispersive media," *SIAM J. Appl. Math.*, vol. 71, no. 5, pp. 1780–1800, 2011.

[5] N. Bleistein, "Uniform asymptotic expansions of integrals with many nearby stationary points and algebraic singularities," *J. Math. Mech*, vol. 17, no. 6, pp. 533–559, 1967.

Projective Space and Analytical Coordinate Systems

S. L. Vesely[1*], A. A. Vesely[2], C. A. Dolci[2], M. E. Vesely[2], and S. R. Dolci[3]

[1]ITB–CNR, Segrate, Italy
[2]Milan, Italy
[3]UNIMI-VESPA, Milan, Italy
*corresponding author, E-mail: sara.vesely@cnr.it

Abstract

Experimental physics is based on observations. Once, that literally meant "using one's own (perhaps aided) eyes", while now one mostly relies on computer processed measurements, data, and images obtained from electromagnetic/optic instruments. The interpretation of measurements can be eased by comparing the signals which convey information on the observed object with ordinary visual experience. We take a look at a geometric background that would allow transforming those signals so they are displayed like those directly seen by the naked eye.

1. Introduction

The mathematics known as geometry was collected as a logical-deductive system in Euclid's *The Elements* not much after the foundation of Alexandria by Alexander the Great in 332 BC. The story goes that land surveying had been practiced by Egyptian priests without significant changes since the first legendary Scorpion King (about 3200 BC) when Tales of Miletus (624-546 BC) embodied it in Greek philosophy. Euclid's thirteen books of *The Elements* witness to the extent of the Greek endeavor. According to a commentator living in the late antiquity, the philosopher Proclus (412-485 AD), the curator of *The Elements* had been a pupil of Plato at the Academy, and had approached the world of forms as an essential basis of reality. As such, Euclid was also a peer of Aristotle.[1] He neither struggled to measure the Earth radius, as the first geographer, Eratosthenes of Cyrene (276-194 BC) did, nor conceived his work as a Platonic way to access a higher realm of transcendental realities, other than providing reasoning tools and processes. Intriguingly, he provided a glimpse of his line of reasoning by ways of constructions with straightedge and collapsible compass. Despite conjectures by later commentators, just about nothing is known today on Euclid's life and thoughts.

During the late European Renaissance Euclid's geometry enjoyed a revival taht entailed applications of algebra to geometry, and comparison of the powers of both methods to perform practical calculations. Back then, the allegedly measurable geometric magnitudes were handled numerically. Positive numbers were conceived as extensive quantities, and constructions were understood as participating in both intellectual and sensible forms. Re-investigation of the relationships among geometric constructions, magnitudes, and arithmetic operations helped to streamline the deductive Euclidean structure, and brought algorithmic insights. However, conventional wisdom still had it that the actual world matches our geometric intuition, and often the results of drawings were accepted as physical evidence —without proofs.

Apart from the algebraic understanding of Euclid's geometry, during the Renaissance, naturalist studies driven by painters and architects also led to amendments consisting in generalizations of geometric constructions. The ensuing formalization of drawing methods, starting with Desargues, Pascal, and L. Carnot, resulted in the *geometry of position*, also called projective geometry, a new relational geometry of *space*. Its major features are, (A) construction instruments limited to straightedge; (B) foundation on geometric motions (transformations); and (C) first appearance of the principle of point-plane duality.

At the turn of 1900, logicism affirmed that thought is self-sustaining, thereby reducing the weight attributed to observations. Logicism rejected all geometrically based approaches to numbers and measurements, and turned down the role of graphic methods. Moreover, it strove to provide geometry with a logical foundation, based on the abstract concept of algebraic number field. The axiomatic program resulted in the disappearance of all outstanding issues concerning the analytical representations of space, especially projective space. Notwithstanding logicism, F. Klein took the view that application to physics of a mathematical theory validates it. He showed that the developments in projective geometry he had pursued since 1872 can be applied to the system of Maxwell's equations in a vacuum, the first field theory.[2] Short thereafter he showed that Minkowski

[1]It is known that Demetrius Phalereus (350-280 BC,) who was entrusted with the planing of the Bibliotheca Alexandrina by Ptolemy I Soter, was one of the first followers of the Peripatetic school founded by Aristotle (384-322). On the opposite, there is no record of any relationship involving Euclid.

[2]Klein's first claim refers to the representation of a field of force in projective space. As a rule, when forces are represented by vectors, the equilibrium condition is given by $\boldsymbol{R} = 0$ and $\boldsymbol{M} = 0$ for the resultant force and moment respectively. Its projective counterpart, which is called null system of statics, sets equal to zero a bilinear equation in six parameters $R_1, R_2, R_3, M_1, M_2, M_3$. When R_i is identified with the electric field, and M_i with the magnetic one, the two above equations assume the form of Ampère-Maxwell and Faraday equations respectively. The null

space is a drastically simplified application of his *Erlangen Program*.[3] Upon recognition of his program, that brings transformations decidedly to the fore, all representations became relationalist with respect to the ontology of space. A projective metric replaced the projective relationship between transformations and constructions, and the key to faithfully associate visual images to the analytic solutions to Maxwell's equations was lost. Here we try to dig out some cues.

2. Projective geometry

In Euclid's geometry, postulates follow definitions of the elements dealt with, each belonging to a category – starting from the point and the line – and precede propositions. The postulates themselves are the assumptions necessary to demonstrate all the propositions we need. They must be in sufficient number, and they must be consistent. The propositions establish relations between geometric elements, deducing them neatly as consequences of the postulates and of further logical statements, called common notions.

As anticipated, projective geometry differs from Euclid's one because:

1. it discards the collapsible compass and uses only the straightedge;[4]
2. the principle of continuity of figures set out by L. Carnot and systematized by Poncelet prevents the definition of geometric elements;[5]
3. the constructions that illustrate propositions are not elementary geometric figures but configurations of incidence.[6]

As concerns the configurations of incidence, some of them are implicitly defined by the postulates, and others can be constructed by using the relations established in the theorems and problems. The overwhelming majority of propositions are constructive, and can be shown in many ways.

Although projective geometry is intended to differ in principle from Euclid's one, in practice only minor differences appear. We next point out some reasons.

2.0.1. Synthetic versus analytic geometry

Both, Euclid's and projective geometry are based on constructions. Projective geometry became self-standing in the 1600s. It was formalized in order to generalize Euclid's hypothetical-deductive system, and in opposition to analytic (Cartesian) geometry. It was planned to deepen the mathematical rendition of constructions rather than to use algebra to unify all thinkable geometries under its umbrella. Perhaps, the name *synthetic* was introduced by Steiner. Since analytic geometry was more successful, its methods and the calculus were extended from Euclidean to projective geometry.[7] For example, integrals were applied to calculate distances, areas, and volumes rather then to implement geometric transformations. Nowadays, axiomatic projective geometry assumes from the outset the existence of an isomorphism between geometric and mathematical space, thanks to which the algorithmic aspects outweigh the constructive.

2.0.2. Structure of space versus algebra of transformation groups

Solid geometric figures are shapes enclosing a certain portion of space. Euclid supposes *that* space to be homogeneous and isotropic, i.e. rigid. Furthermore, he doesn't allow for displacements, but only for the notion of congruence of figures.[8] By the sixteenth century, in order to endow line segments with lengths, the editors of *The Elements* understood a segment of a line in the kinematic sense. The numerical continuity between start and endpoint of a line segment was extended beyond its boundaries, and the inadequacy of the notion of congruence started to appear. To get out of this mess a standalone geometry of position was set forth, based on geometric transformations.[9] The subsequent emergence of algebraic geometry gave rise to a role reversal between geometry and algebra, and brought us the concept of an abstract variety defined over an arbitrary number field. Based on it, besides having an algebraic structure, the geometric space devoid of figures can be required to possess topological and differentiability constraints.

2.0.3. Projective metrics and models of non-Euclidean geometries

By von Staudt's definition, projective geometry is independent of the metric properties of figures. So no metric function is defined on the projective space, nor can cross-ratios

system itself is a projetive invariant. It, or rather Plücker's linear system, gives rise to the above more general force equations as long as no orthogonality condition is imposed.

[3] Klein's second claim hinges on the classification of all geometries of constant curvature in the setting of projective geometry. It is achieved by imposing a so called projective metric on each space. Minkowski had just shown that invariance of the signal propagation front from a point source links space and time, and that Maxwell's equations become form-invariant in space-time. In turn, Klein claimed that the latter become form-invariant under the 10-parameter group of coordinate transformations because the signal-invariance measures the geometry of space-time. Initially Einstein conveyed an absolute meaning to the metric and curvature of the underlying space. But in general relativity theory he relaxed substantialism.

[4] Limitations of constructions date back to Plato. They possibly were exploited to keep a logical overview over the demonstrations.

[5] After the *Erlangen Program*, the property of being invariant under projective transformations replaces the principle of continuity of the figures.

[6] Poncelet distinguished between a drawn figure and a general figure. Plücker (On a new geometry of space) made clear that the general elements are aggregates or configurations of point-planes and/or of lines, *all unbounded by definition*. If illustrated on paper a figure ends at the edge of the sheet, while the "whole space" filled up is displayed on an optical support.

[7] Plücker took the straight line as generating element, because the projective lines are self-dual elements of space. Today line geometry has merged with Pieri's system.

[8] The congruence theorems of triangles, propositions 7 and 8 in Euclid's Book I are logically acceptable, but not demonstrable.

[9] Before differential geometry was established, the concept that the geometric space is rigid was firmly secured.

or unitary transformations be used to define a projective distance. Furthermore, no scaling and translation properties in the Euclidean sense can be introduced. Nevertheless projective geometry was used to model Euclidean and non-Euclidean geometries in the sense of inducing the relevant distances and angles associated with them. The relation – non-projective! – that lets us develop these geometries in the projective setting has been called *projective metric*, and has also been used to represent function spaces over $\mathbb{C}$.

2.1. Postulates of projective geometry

Projective *first species figures*, i.e. linear figures, are formed by (denumerable) elements point-planes and lines.[10] We can construct figures with as many elements as we wish, satisfying the axioms of incidence and the principle of duality. The latter principle expresses the fact that consistently replacing the word point with the word plane, and vice versa, always leads to a valid postulate/proposition. When, as happened, the notions of point, and indefinitely extended line and plane were drawn from experience it was customary to write the postulates and their duals on the same line in two contiguous columns. For example in Young's book we find:

I	Any two distinct points determine one and only one line on which they both lie.	I'	Any two distinct planes determine one and only one line through which they both pass.
II	Three points, which are not on the same line, determine one and only one plane on which they all lie.	II'	Three planes, which do not pass through the same line, determine one and only one point through which they all pass.
III	A point and a line not containing the point determine one and only one plane on which they both lie.	III'	A plane and a line not on the plane determine one and only one point through which they both pass.
IV	Any two distinct lines in the same plane intersect in one and only one point.	IV'	Any two distinct lines having a point in common determine one and only one plane.

As axiomatization grew to an end in itself, projective geometry reduced to a vestigial tail. For example, in 1911 N. J. Lennes gives a complete set of six consistent and logically independent axioms for projective geometry. In the same year, he proposes a different set of axioms, which will "form a more natural sequel to Euclidean geometry than the developments resulting from" the former set.

Hilbert brings the postulates concerning constructions, and the axioms concerning magnitudes (common notions) together. He classifies axioms into different groups for the purpose of determining the area of influence of each group. He adds to the incidence axioms of geometry of position: four axioms of betweeness (intermediacy), three congruence axioms, the parallel axiom, and two axioms of continuity. In this context geometry gets an algebraic interpretation of the axioms. Finally, he introduces the Cartesian plane as the standard graphic representation method.

Given that the exact formulation of the geometric axioms depends on the meaning we want to assign to geometry, we enunciate a set of non-independent statements mainly taken from Coxeter [1, 2]. In brackets, we specify a catchword related with the axiom.

1. (ray): For any two distinct points there is exactly one line incident with them;[11]
2. (axis): Any two distinct planes meet in a line;[12]
3. (triangle): Given a line and a point, not incident, there is exactly one plane with which both are incident;[13]
4. (quadrangle): If A, B, C, D are four distinct points such that AB meets CD, then AC meets BD;[14]
5. (Carnot's transversal): If a line – the transversal – intersects two sides of a triangle it also intersects the third side;[15]
6. (tetrahedron): Taken three points not on a line, there is at least one point not in their plane;[16]
7. (projectivity): The cross ratio of four elements is invariant under projective transformations.[17]

[10] In axiomatic geometry, points, lines and planes are notions left unspecified, but distinct. To obtain a model we need only specify them. On the contrary, in projective geometry the incidence relation and the duality principle alone are never enough to distinguish a point from a plane regardless of the used construction.

[11] This axiom does not differ from the Euclidean analogue. Thus, we can line up as many dots as we wish on a line of points.

[12] This axiom defines the pencil of planes. It dualizes the element ray defined in (1). When given in analytic geometry it takes on the meaning of a *closure axiom*, i.e. it entails a three-dimensional space.

[13] This axiom says that all triangles belong to planes. Topologically, the projective plane is a one-sided, doubly connected surface, different from the Cartesian plane. We accept that, while an assigned projective plane can always be projected on a sheet, the general projective plane lets us model both Euclidean and non-Euclidean planes.

[14] A quadrangle is a planar figure only if its points are in a plane. Through four points we can trace six straight lines: 2 pairs of opposite sides and 2 diagonals. The confluence of both, the diagonals and the sides occurs because there is no parallelism. The dual figure of the quadrangle, the quadrilateral, has 4 sides and 6 vertices. The points where sides intersect are six because they extend indefinitely and parallelism fails.

[15] This is Pasch's axiom in the Veblen-Young form (1908). Pasch used the axiom on the intersections of a straight line with two sides of a triangle, to demonstrate a theorem on the order in which points are intercepted. Veblen included this among the projective axioms to indicate that the sides of a projective triangle extend indefinitely.

[16] The tetrahedron is a quadrangle whose points are not in a plane. It is a self-dual figure: replacing point with plane, it is seen to be formed by three planes belonging to a bundle of planes, and by a further plane not part of that bundle. Each point is obtained as an intersection of three planes and each plane contains three points. We must not think "self-dual" means that the points are vertices and the planes the faces of the same tetrahedron.

[17] Pappus was perhaps the first to see that the cross ratio of the segments formed on a transversal cutting four concurrent lines is independent on the place of cutting. In the "motion postulate" the cross ratio fixes the meaning of congruence in projective geometry.

8. (Fano's axiom): The three diagonal points of a complete quadrangle are never collinear;[18]

9. (Pappus' theorem): If the six vertexes of a hexagon lie alternatively on two lines, the three points of intersection of pairs of opposite sides are collinear.

In synthetic projective geometry, the sole axioms are those of incidence (1) – (6), that differ from the Euclidean axioms of the same name, and the axiom (7) characterizing projective transformations. At a difference with Euclid's geometry, projective geometry is intrinsically spatial and lacks the definition of perpendicularity. Vice versa there is no duality principle in Euclid's geometry. We note that, if we pick up axioms (II) and (II'), the constructions involved – a pencil of lines and a bundle of planes respectively – are not dual one of the other in the same vein as (1) and (2). Indeed the interchangeability between point and plane in the statements does not necessarily imply constructions dual between themselves.

Plane axiomatic geometry isn't generated from synthetic projective geometry by central projection. Coxeter distinguishes between synthetic and axiomatic plane projective geometry, in which he states a new duality principle between point and line elements. As an important difference between the synthetic and the plane axiomatic geometry we mention *Desargues' theorem*:

- If two planes containing each a set of three points not in a line meet in an axis, the two three-points sets are perspective, and can be joined in twos by lines from a point. Conversely, if the two three-points sets are perspective from a center, their planes have a common axis.

A three-points set always belongs to a projective plane. If two of them are not perspective, they are projectively related, and cannot be projected from the same point on the same plane. In fact, projective planes are flat in their own way. As Hilbert shows, Desargues' theorem needs not hold within $\mathbb{P}^2(\mathbb{R})$, and must be postulated.

2.1.1. Axiomatic projective geometries

Axiomatic plane projective geometry models the abstract algebras that satisfy the point-line duality [3]. For the axiomatic geometry in $\mathbb{P}^2(\mathbb{R})$ Coxeter enunciates axioms almost equivalent to (1), (3), (4) and (5),[19] adding (8) and (9) to represent the algebras $\boldsymbol{GL}(n,p)$.[20] Within finite geometries, Fano needs to introduce axiom (8) after showing that, weakening axiom (4), that deals with four coplanar points, a finite configuration of points can be found, called the *Fano configuration*, in which (8) is no longer valid.

Axiom (9) is a special case of *Pascal's theorem*.[21] Dealing with self intersecting hexagons, and supposing the vertices to be alternate, i.e. that the odd and even numbers belong to distinct lines, the Pappus line of intersections is not unique, but there are six thereof (fig. 1). As a rule, a fixed order is used in numbering when the theorem is stated as an axiom for the purpose of endowing the plane with analytic coordinates. With this aim in mind that theorem is also enunciated as:

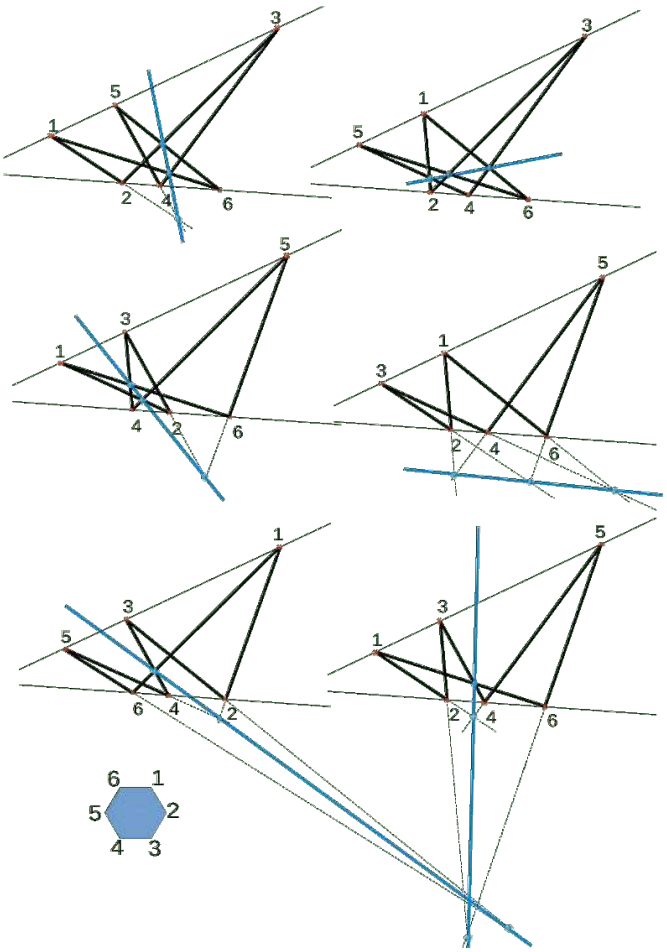

Figure 1: Pappus lines. Pappus' hexagons are self-intersecting. A regular hexagon is shown at the bottom. Opposite sides are $1-2/4-5$, $2-3/5-6$, $3-4/6-1$.They match the order of the Pappus' hexagon down to the right, with the two sets of collinear points $135/246$. The other permutations giving rise to the same Pappus line are: $135/642$; $315/264$; $351/462$; $513/624$ and $531/426$ (not shown). Each of the further drawings shows one member out of a class of six permutations.

9b. If a projection leaves invariant each of three distinct points on a line, it leaves invariant every point of

[18] We call *diagonal points* of a complete quadrangle those differing from the vertices. For $ABCD$ they are the crosses $AB \cdot CD$, $AC \cdot BD$ and $AD \cdot BC$. If they are collinear we cannot construct the fourth harmonic point on a straight line.

[19] Axiom (5) is usually weakened, or the remaining axioms are modified to make this superfluous.

[20] Each line in the finite plane of a geometry $\boldsymbol{GL}(n,p)$ contains $p+1$ points, where p is a prime number to the power of k. It can be shown that the Fano configuration is isomorphic to the group of degree 3 $\boldsymbol{GL}(3,2)$.

[21] Pascal's hexagon theorem states that if an hexagon is inscribed in a conic, the points of intersection of pairs of opposite sides are collinear. Pappus' theorem is the special case in which the conic becomes a couple of lines.

the line.

Then it is called *fundamental theorem of projective geometry*. Finally, analytic n-dimensional projective geometries, with $n \in \mathbb{N}_+$ and $n < \infty$ are a generalization of axiomatic plane projective geometry. In Veronese's view spaces with n dimensions are geometric entities that can conceptually be generated from ordinary three-dimensional space by recursively adding a point outside of the just generated one. The sets of independent axioms are likewise recursively introduced. The duality principle is re-interpreted as a closure axiom (mentioned in note 12). The geometry on any axiomatic projective space is not categorical,[22] but rather depends on the relationship between the manifold M, whose points are elements of a finite or infinite number-system, and the algebra with which the latter is equipped. As an alternative, geometry can be developed as an algebra of linear transformations.

3. Zahlen der Geometrie

With the title of this paragraph we wish to stress that in the present case we would invert Minkowski's strategy of tailoring geometry on numbers, exposed in his book *Geometrie der Zahlen*. He represents the numerical space as a finite dimensional lattice of integers, and uses geometrical insights in the theory of numbers to understand theorems on quadratic forms. For the key word "geometrical insights" we refer to the book by Hilbert and Cohn-Vossen *Anschauliche Geometrie* (Geometry and the Imagination). On the opposite, we propose to associate a suitable mathematical analysis with synthetic projective geometry, and apply it to electromagnetism and image recognition. In order to interpret displayed images of received signals according to visual experience, the signals need to be transformed into images recognizable with the naked eye. The final step consists in "identifying" some of the recognized features with elements of the original signal. To that purpose we may take advantage of a key feature of projective geometry, that was dubbed "continuity of figures" by Carnot, and consists of following invariants across *finite transformations* of figures. To the best of our knowledge, the finite transformations of projective geometry were negligibly exploited to extract information on the extension from general electromagnetic signals. Provided that one deals with signal reception, the integral approach to space typical of projective geometry enables applying it to Fourier and diffractive optics, in microscopy, and to display medical imagery and land surveying in radiation ranges different from the optical one. Advanced reception techniques may require general linear projective spatial transformations.

Below, we briefly sketch the historical faith of practical applications of geometry to optics to show how reductionism prevailed over geometric signal analysis in this field.

[22] A set of axioms is categorical if with it is given essentially a single representation of the geometry.

3.1. From visual experience to geometric optics

Euclid seems to have conceived speculative geometry as a reasoned approach to realize what one needs to look at. Beside availing of graphic methods to prove theorems in his treatise *The Elements*, he is known to have applied geometric reasoning to visual experience, providing some constructions and cues to model the outer world as viewed.[23] Euclid's booklet on sight is titled *Optics* [4, 5]. Since Herophilos was notoriously studying the physiology of the eye at the same time in the same place, that booklet must have been hailed as a mathematical treatise on optics. Judged by actual criteria it is no foundational work on optics, but rather a fair starting point when interpreting (received) images. In daylight, opaque envelopes standing out from a background are capable of being cut/projected as simple shapes on smooth surfaces from a given viewpoint. Nets cast over those envelopes allow an experienced observer to reproduce the course and depth from textures. The mutual relationships of the web's nodes under transformation to a different viewpoint, are perhaps the most easily tracked features.[24]

Euclid's geometry and optics were jumbled in the Middle Ages' expositions, like in the best-seller *Perspectiva* by Vitellio [6]. The first treatises on the techniques of linear perspective by Alberti and Della Francesca during Renaissance Humanism drew on Euclid's legacy. Especially in naturalistic art visual experience, called *perspectiva naturalis*, co-existed with the representations availing of linear perspective and with workshop traditions. After 1600 projective geometry started to be formalized from that bunch of ideas within the framework of the only known geometry so far. It was still too early to formally analyze images obtained with optical instruments within the projective framework, and the notion of *similarity* between object and image, that cannot be kept in projective geometry, was implicitly accepted.[25]

Suddenly, the rise of mechanics caused optics to take a reductionist wrinkle. While it is still not quite understood what makes diffused Sun light give rise to the perception of geometrically disposed objects in void space, it was clarified that the optical responses formed by transparent and/or polished objects of plane or rounded shape are perceived in the same way.[26] Experiments with narrow light beams

[23] Not dealing with catoptrics and dioptrics, Euclid is left with perspective. While projective geometry doesn't really allow to reckon distances, in perspective there are criteria to select a scale.

[24] Networks used to model geodetic reference frames are rather conceived as materializations of a coordinate system that would otherwise be attached to void space.

[25] The definition of similarity introduced in the 6th book of *The Elements* reads: "Similar rectilinear figures are such as have their angles severally equal and the sides about the equal angles proportional." Yet, his Optics is about angular magnitudes.

[26] First, calculations for optical instruments are performed for centered systems, thin lenses, and in paraxial ray approximation, while the angle of vision of the human eye is much larger. Second, the lens of the eye is neither thin nor homogeneous. Last, sharp images can also be obtained beyond the paraxial approximation from concave mirrors and inside crystal spheres. Images by a pinhole camera are formed differently from those by a concave mirror devoid of narrow aperture.

resulted in a new understanding of Euclid's "visual rays" as autonomous "light rays". Henceforth, the optics of light replaced that of sight.

In terms of rays Snell's law can be stated in projective form. It says that $\frac{\sin\varphi}{\sin\psi} = n$, where n is the relative index of refraction, and the line e shown in fig. 2

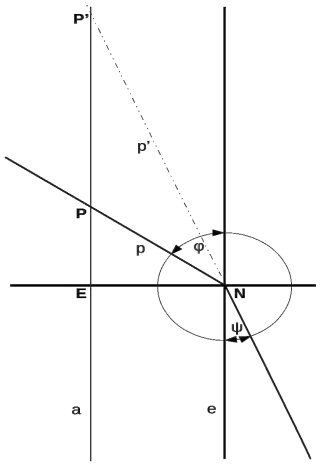

Figure 2: Snell-Descartes law of refraction.

is the perpendicular to the interface EN at the incidence point. Taking a line a parallel to e it is $\sin\varphi = \frac{\overrightarrow{EP}}{\overrightarrow{NP}}$ and $\sin\psi = \frac{\overrightarrow{EP'}}{\overrightarrow{NP'}}$, but the same relationship holds whatever the angle between e and a, and thus in general $n = \frac{\overrightarrow{EP}}{\overrightarrow{NP}} : \frac{\overrightarrow{EP'}}{\overrightarrow{NP'}}$.[27] A purely projective stating of Snell's law would be expressed as an anharmonic ratio, i.e. putting $n = 1$ which is obvious for mirrors.[28] Since, based on dioptrics, the "phantasms" of physical objects capsize when proceeding through the eye, $n \geq 1$ corroborated the idea that the outer world doesn't match visual experience, and that humans only realize reality in their mind's eye. The realized reality about light rays was called *geometric optics*. The stigmatic image of a point was constructed in the Cartesian plane by drawing lines (the so called *light-rays*) joining the object point to the image point. Conversely, graphical determinations of the image of a point source laid a particular emphasis on the focus properties.[29] With very few exceptions, the condition of stigmatism, i.e. the condition that rays issuing from a point-object converge to a point-image, is not fulfilled. Usually, a family of non-homocentric rays named caustic issues, fig. 3.

[27]For $a \parallel e$ it is $\overrightarrow{NE} = \overrightarrow{NP}\sin\varphi = \overrightarrow{NP'}\sin\psi$ as well. But there is no orthogonality in projective geometry.

[28]Since no metric structure can be introduced in projective geometry, neither can similarity theorems be stated. The requirement $n = cost$ is mandatory, though. Geometry hardly lends itself to the design of aspherical lenses, which is rather a subject of advanced technical optics.

[29]It was left for Abbe to discover that on the focal surface there is a whole pattern besides the luminous central point, and that the former causes the formation of the image.

Figure 3: Cut of a reflected beam through the focus. At the top the back of a concave mirror reflecting sunlight on black paper. A wisp of smoke rises from the focus. The insert shows the reflective caustic as an envelope of rays.

3.2. Inception of the analytical program

In the 1800s caustics were increasingly envisaged as systems of light paths. Reflection and refraction were studied in themselves, independently from imaging. Examples are Kummer and Fresnel surfaces. An effort was also made to introduce dynamical magnitudes independently from perception. The sloppy ray-tracing was taken for the graphic counterpart of Fermat's law of propagation of systems of rays, and subsequently formalized in this capacity, especially by Hamilton. The ensuing representation of light propagation through optical systems is as trajectories in phase space, a geometry tailored on optics.

The overall evolution of constructions in projective geometry seems to have pretty much followed the same approach. One striking difference between geometric optics and projective geometry is that, while during the reductionist process ray optics was integrated with physical/wave optics, projective geometry was stripped of duality. Otherwise, geometry was switched from synthetic to analytic hand in hand with the development of optics. Since a heap of configurations can be specified by a simple algebraic equation $\Omega \equiv 0$, the mathematical study of invariant properties prevailed over the attempts to analytically tackle space. A kind of motional interpretation not specifically involving propagation became predominating.[30] For instance, studying the stability of trusses Möbius considered all possible virtual motions, and Plücker in turn, sought to ground ray optics on projective congruences of lines.

[30]As stressed many times from Poincaré on, when stating dynamical laws, the space is not just an arena. It impacts on the internal structure of the physical theory concerned.

3.3. Isotropic rays

At some time the issue about how a geometrically transformed, distortion-free, image should be related to its original was connected with the algebraic invariants. Monge made a start in his book *Applications de l'analyse à la géométrie* of 1850, relating normal congruences of rays to the curvature of surfaces. A congruence defines a one-to-one point correspondence between surfaces. His mathematical problem was integration, and he wished to visualize families of solutions. For that purpose he chose a method akin to that of characteristics. Albeit there is no need of defining either orthogonality or differential relationships in optics, the notion of normal congruence was soon transplanted into it. It was shown that, as long as media are homogeneous and isotropic, a congruence of light rays normal to a surface can undergo reflections and refractions without loosing the property of remaining normal to wave-fronts. Kummer discussed focal properties in 1860, and explained the high density of rays at the focus.

To analytically define the rays belonging to a congruence G, let's consider their intersection with a reference plane $f(u, v)$, which a net (u, v) of coordinates defined on it.[31] Indicating a general ray $g \in G$ by three Cartesian coordinates x, y, and z, and three direction cosines ξ, η, and ζ, the latter variables take on the same values on a sphere $x^2 + y^2 + z^2 = 1$, that can be set to be the spherical image of f. Two "infinitely near rays" $g, g' \in G$ describe an arch $d\sigma^2 = d\xi^2 + d\eta^2 + d\zeta^2 = \sum \Xi^2$.[32] A moment $-\rho d\sigma = -\mu = dx d\xi + dy d\eta + dz d\zeta$ can also be assigned to the couple of rays, where ρ is the minimum distance between g and g'. Like the former equation, the latter too can be written as a function of u and v as $D du^2 + 2D' du\, dv + D'' dv^2$. The coefficients, that are functions of the same variables, are given by Sannia [7]. The above couple of differential equations are sufficient to characterize the congruence of rays, and are therefore called the two *fundamental forms of the congruence*. Concentrating on local properties, if for some set of rays of the congruence the curvature $\kappa = \frac{-\rho}{d\sigma} = \frac{-\mu}{d\sigma^2}$ of a normal cut is zero, i.e., if $D du^2 + 2D' du\, dv + D'' dv^2 = 0$, the ruling constituting that set is developable. At a distance $r = |\boldsymbol{r}|$ from the reference surface f the general ray has coordinates $x' = x + r\xi$, $y' = y + r\eta$, and $z' = z + r\zeta$. If it is $\xi dx' + \eta dy' + \zeta dz' = 0$ for all rays for some distance r, the rays happen to be all normal to a surface f'. By substituting $dx' = dx + dr \cdot \xi + r d\xi$, and similar expressions for dy' and dz' in it, we obtain the integrable equation $-dr = \xi dx + \eta dy + \zeta dz$ for the distance between f and f'. This allows integrating the distance $-dr = (a\xi + b\eta + c\zeta) du + (a'\xi + b'\eta + c'\zeta) dv$ on the reference surface $f(u, v)$. The equation $\frac{\partial(a\xi+b\eta+c\zeta)}{\partial v} = \frac{\partial(a'\xi+b'\eta+c'\zeta)}{\partial u}$ allows determining the family of surfaces to which the congruence of rays is normal.

As another example, if the curvature is constant, i.e. if it is $\frac{D}{E} = \frac{D'}{F} = \frac{D''}{G}$, a transformation with $D' = F = 0$ can be obtained in infinitely many ways, giving rise locally to a set of circular or isotropic rays. The rulings characterized by them are not developable. However, it has been shown that the planes on which the middle points of the rays fall envelope a real minimal surface.

While the isotropic rays found in optics are related to minimal surfaces, those found in projective geometry are related to a quadratic invariant. The *null system of statics*, a brainchild of Möbius, is a complex of ∞^3 lines defined by an algebraic equation $\Omega \equiv 0$, and likewise, Plücker's congruence is the doubly infinite system of rays obtained by intersection of two complexes of lines, $\Omega + \mu\Omega' \equiv 0$. Although, in principle, every algebraic invariant could be defined in terms of lines, in practice, these can be impossible to construct. If this happens, the lines are called imaginary lines. As an application of invariants to physics, Klein identified the (real) light-rays in Einstein's special relativity with isotropic rays from the origin, that are mapped on real lines. In Minkowski's four dimensional pseudo-Euclidean interpretation of special relativity, the invariant hypercone $\Omega \equiv x^2 + y^2 + z^2 - c^2t^2$ defines real isotropic rays. Reverting to three dimensions, the imaginary rays associated to the form $\Omega \equiv x^2 + y^2 + z^2$(called elliptic invariant) become real on performing an imaginary linear transformation $(x, y, z) \to (X, Y, iZ)$ to a pseudo-Euclidean space. Upon transformation the locus of the quadratic form becomes real, and therefore the lines go through real points.[33] Without having recourse to the above imaginary transformation, the imaginary rays are characterized by the property that, taking two points whatever $P = x_1 : x_2 : x_3 : x_4$ and $P' = x'_1 : x'_2 : x'_3 : x'_4$ on a ray, with $x_4, x'_4 \neq 0$, the expression $r = \pm\frac{\sqrt{(\sum_{i=1}^{3} x_i x'_4 - x_4 x'_i)^2}}{x_4 x'_4}$ relating them vanishes. Since in Cartesian spatial coordinates one has $x = \frac{x_1}{x_4}$, $y = \frac{x_2}{x_4}$, and $z = \frac{x_3}{x_4}$, it is tempting to read $r = 0$ as a null distance. In such event, the isotropic rays are called minimal rays. To see why they are isotropic, take the point $x'_1 : x'_2 : x'_3 : x'_4$ in the origin of a Cartesian reference frame. The $r = 0$ condition becomes analogous to a canonical quadratic form $\Omega(x_i^2) = 0$ with no real locus.[34] Moreover, the imaginary rays from whatever fixed real point not at infinity through the variable (imaginary) one on the invariant quadratic form constitute a cone of lines generating that $\Omega(x_i^2) = 0$. Since the latter is an invariant, the cones are independent on the fixed point, and the rays are called isotropic. The relationship between the projective transformation invariant associated with Minkowski's space and the locally defined Riemannian quadratic form $ds^2 = \sum_{i,j} g_{ij}\, dx_i\, dx_j$, or the invariant interval of special relativity, are marred by the topological and group theoretical definition of continuity [8].[35]

[31] The net is related to the congruence. A ruled surface normal to f cuts it on geodesics.

[32] On $f(u, v)$, as on the unit sphere, the arch is the first fundamental formula of the surface $d\sigma^2 = E du^2 + 2F du\, dv + G dv^2$, with $E = \sum(\frac{\partial \Xi}{\partial u})^2$, $F = \sum \frac{\partial \Xi}{\partial u} \frac{\partial \Xi}{\partial v}$, and $F = \sum(\frac{\partial \Xi}{\partial v})^2$.

[33] The so called hyperbolic transformations of projective geometry are associated with this kind of invariant.

[34] Klein calls "nullteilig" the quadric with index of inertia 4.

[35] Projective connections were studied after defining projective local

4. Cross ratio and coordinates

After this look-back over the geometric representations of light rays, let's take a better look at the way projective coordinates are introduced.

The *fundamental theorem of projective geometry*:

9b. If a projection leaves invariant each of three distinct points on a line, it leaves invariant every point of the line,

is formulated for extending the one-point perspective drawing to cover the most general projective transformation. We mentioned that it often stands in for Pappus theorem. It is also closely linked to the projective anharmonic ratio.[36] In fact, the graphic methods deployed in simple perspective fall short of describing a general chain of perspective transformations, i.e. a projective transformation. The extension to projective transformations consists in accounting for chains of subsequent perspectives by simply sticking with the transformation between the first and the last members of the chain. The criterion of invariance of the cross ratio of four harmonically divided elements then allows deciding independently on the chain of perspectivities when two configurations are projectively equivalent, i.e. when one is the result of a projective transformation of the other.

4.1. Cross ratio and harmonic division

Chasles and Steiner were among the first to study the cross ratio as a numerical relation between four elements of the same kind $X = \frac{P_1-P_2}{P-P_1}\frac{P-P_3}{P_3-P_2}$ when $X = |1|$ in homographies between first species figures.[37] Four elements in this relation are called *anharmonically related* if $X = -1$. That the relation is applicable to length and angle ratios, can be demonstrated by applying Menelaus' theorem.[38] Yet, that theorem depends on magnitudes, for it compares either lengths of segments of a line or dihedral angles belonging to the same pencil of planes. To be independent on intrinsic magnitudes, von Staudt chose to determine the fourth harmonically related point in the cross ratio $X = |1|$ starting from the graphic construction of a complete quadrangle/quadrilateral, as shown in fig. 4).

Any diagonal of a complete quadrangle is harmonically divided by the other diagonal and the two concurrent pairs of sides. The sign of the cross ratio between harmonically related points $X = \pm 1$ identifies a graphic property. Moreover, that construction can be extended from the line to the conic.

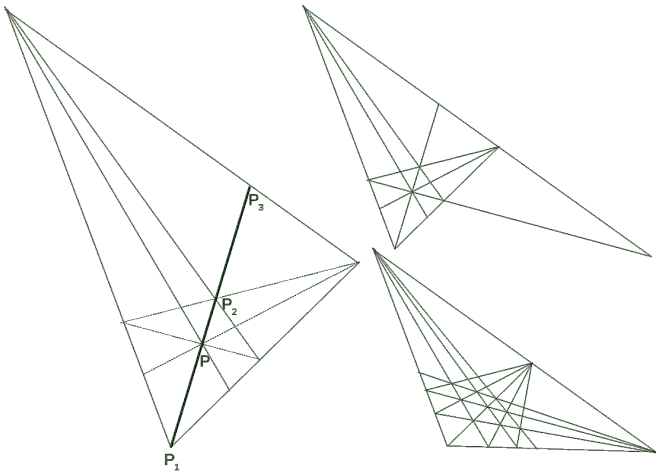

Figure 4: Harmonically divided points and Möbius net. Left: The value -1 is not a numerical value, although Staudt defines 4 elements whose cross ration is $X = -1$ "in harmonic position". Though the harmonic position of the elements on a support is independent of the element selected to construct it, effectively the construction exploits the properties of complete quadrangle/quadrilateral. Associating with the index i some elements P_i the order $P_1P_2PP_3$, there are two interpretations of the negative sign. (1) if we consider the pair $\overrightarrow{P_1P}$ oriented $\overrightarrow{P_2P_3}$, while we associate them with $\overrightarrow{P_1P_2}$ and $\overrightarrow{P_2P_3}$ opposite orientations; (2) we orient all pairs of points in the same direction. Then $X = -1$ says that the pair P_1P separates P_2P_3 in the order $P_1P_2PP_3$. Right: A way to draw a Möbius net is shown.

The cross ratio by harmonic division, $X = \pm 1$, can be introduced in projective geometry independently on any metric relations. Starting from it, a Möbius net lets us create a binary relationship between points on a line, called involution.[39] An example of Möbius net is shown in fig. 5.

Examples of a double ordering of points on a line are shown in fig. 6.

Möbius nets allow determining by construction a sequence of as many ordered points as we wish. A pair in involution chosen beforehand can be kept fixed or not during recursive construction of the following points. In fact, it can be useful to change the mesh step during construction either to achieve more detail, or to reach a given area more quickly. So far only synthetic geometry is concerned.

spaces. Weyl made a start by using the notion of parallel transport to show that the lengths of vectors are absolutely incomparable among themselves. He thus generalized Riemannian differential geometries. Afterwards he, Fubini and Čhech, and many others studied the projective structure in the context of Lie groups.

[36] The anharmonic ratio is the projective invariant.

[37] Fundamental first species figures are: the range of points, the pencil of lines and the sheaf of planes. These three forms can be put in perspective with one another. Thus they can be derived from one another without changing the mutual relationships between their elements.

[38] Menelaus' theorem in the plane. ABC is a triangle. D, E and F are points on the lines through BC, AC and AB respectively. The points D, E and F are collinear if and only if $BD{\cdot}CE{\cdot}AF = CD{\cdot}AE{\cdot}BF$. The theorem uses Thales theorem in the proof. Measures of lengths and angles are dual of each other in this context.

[39] The Möbius net consists of an iteration of the construction of the complete quadrilateral to find the next point in the sequence. By contrast, the Möbius transformation $z \to \frac{az+b}{cz+d}$ with $ad - bc{\neq}0$ can be regarded as an analytic expression in non-homogeneous coordinates that projectively transforms the complex plane. It is conformal and preserves orientation. With this distinction, the cross ratio remains invariant for the Möbius transformations too (collineations).

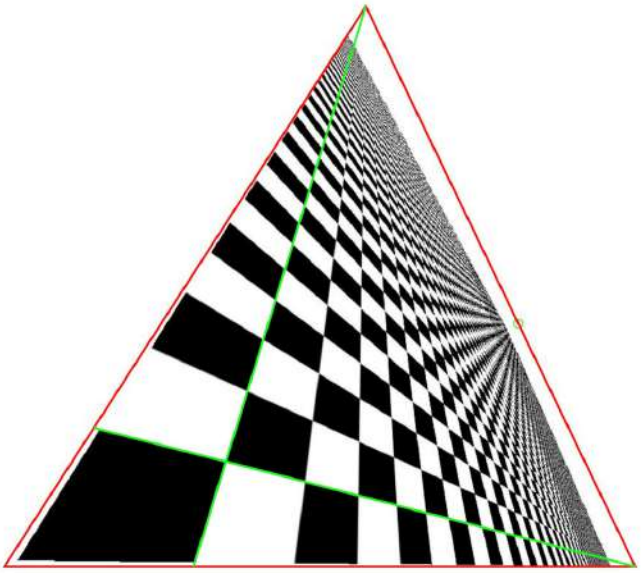

Figure 5: Möbius net.

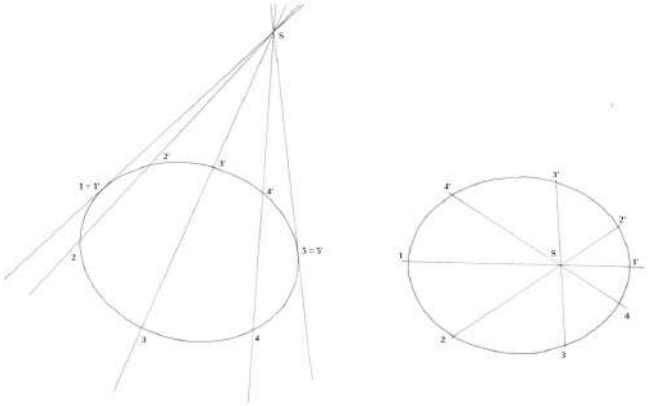

Figure 6: Double ordering of points on a conic (line). A double ordering of points on a line is called involutory. The line is intersected by a pencil of rays in pairs of corresponding points. Left: inverse projective correspondence of N and N' with two fixed poins. Those are called in involution. Right: direct projective correspondence of N and N' without fixed points (with imaginary fixed points.)

4.1.1. Numbers from cross ratios

We are not aware of a standard procedure to invert the construction of Möbius nets.[40] Once a net is constructed, it is quite possible to naively associate ordinal numbers with the sequence of net-points P on a line. However, numbers cannot be glued to points, segments cannot be moved, and the incidence relation doesn't identify the sizes of free vectors. To shed some further light on cross ratios, let's pick three points P_i, $i = 1, 2, 3$, on a line. Attributing numeric values to selected points, i.e. putting $P = P_1 \Rightarrow X = 0$, $P = P_2 \Rightarrow X = 1$, and $P = P_3 \Rightarrow X = \infty$, the values taken on by cross ratios $X \neq \pm 1$ are in the range $[0, \infty]$.[41] However, the cross ratios $X \neq \pm 1$ can no longer be called projectively invariant, and are devoid of meaning. An alternative association of numbers to points, uses the operation of harmonic conjugation. The cross ratio X always assumes the numeric value ± 1, and the points are allowed to cluster when $P \to P_3$, which is supposed to be kept fixed. This operation requires that the steps of unitary size be congruent to each other in the sense of being equivalent. Since a generic projective line is topologically different from the Euclidean straight line, that unitarity is an extra requirement.

To obviate those problems, in algebra a scale for cross ratios is introduced by associating labels to two fixed points Q_1 and Q_2 on the line[42] such that $\forall P$ be identified by the expression $\lambda x_{Q_1} + \mu x_{Q_2}$. The real number obtained from the relation $\xi = \frac{\mu}{\lambda}$ is independent of the selection of any two new reference points Q_1' and Q_2'. While that makes sense in algebra, the projective construction of a Möbius net can hardly be replaced with any scale $\xi \equiv \sigma X$ of the numerical line.[43]

Again, notice that four distinct points have six distinct numerical cross ratios, and that upon a projective transformation any of them can obtained.[44] A choice of the order of the four points allowing to construct a net was named "Wurf", litterally throw or cast, by von Staudt. Some examples of perspective harmonic Würfe are shown in fig. 7.

The shift in the ordering of points arises because of the topology of the general projective line.[45] In addition, a general projective transformations can lead to permutations of the points with the assigned coordinates 0, 1 and ∞, preventing orientation of the line.

Fig. 8 shows that, while the harmonic division is invariant after three steps, the order is not. Perhaps, because of his representation of imaginary, or hypercomplex numbers, by means of involutions, von Staudt was convinced he could once and for all equip projective lines with a direction along them. Once the axioms of order are admitted besides those of incidence, the axiomatic projective plane geometry is easily conflated with the absolute or neutral geometry.

[40] There is no "unity".

[41] This is about von Staudt's way to associate coordinates with the cross ratio. The cross ratio reduces to a ratio with unitary denominator $\frac{P}{1} \frac{1-\infty}{P-\infty} = P = X$.

[42] Pieri deduced 3-dimensional projective geometry from the indefinite notions of *point* and *line segment joining two points*. According to Pieri an order relationship can be extended to the projective line by iterating the segment construction, and is conserved under homography. But a projective transformation of the space in itself is not an ordered sequence of a small number of perspective homographies applied to one "segment".

[43] To account for projective transformations von Staudt generalized his X coordinates to Würfe (mentioned next in the text.) He developed an algebra – the "Wurftheorie", that is deemed to be isomorphic to the algebra of numbers.

[44] Numerically the ratios are X, $\frac{1}{X}$, $1 - X$, $\frac{1}{1-X}$, $\frac{X-1}{X}$, and $\frac{X}{X-1}$. They constitute a group. Klein extensively studied the representations of quotients of two hyperelliptic functions, for they are invariant under the same transformation group. In $\mathbb{R}$ $X = -1$ reduces the number of different values to three -1, $\frac{1}{2}$ and 2. They are not comparable to the roots of an algebraic equation.

[45] Allowing the projective line to be orientable, the problem of orientability of the projective plane was discussed both for $\mathbb{P}^1(\mathbb{C})$ which is obtained adding a point to plane $\mathbb{C}$, and for $\mathbb{P}^1(\mathbb{R})$, obtained compacting $\mathbb{R}^2$.

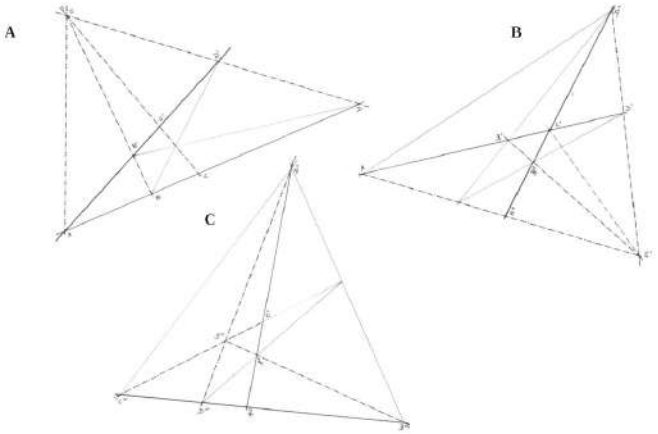

Figure 7: Wurf in relation to harmonic division. Perspectively related harmonically divided ranges from a center S. Harmonic division $\frac{A-C}{B-A} \cdot \frac{B-D}{D-C}$ is invariant. In A a side of the quadrilateral is perspective to the other. In B the point C' is a united point of the perspectivity. In C the point A'' is united, and the order of the points in the harmonically divided range is changed to $CDAB$.

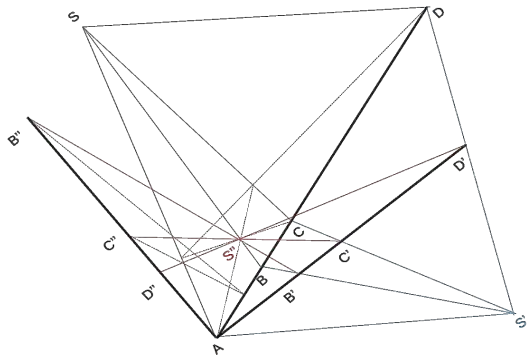

Figure 8: Projective transformation of a set of four harmonically dived point. A sequence of two perspective transformations $S \to S' \to S''$ that inverts the points B and D.

4.1.2. Klein's algebraic classification of projective transformations

To meet Staud's requirement while allowing for projective transformations, Klein postulated that a real quadratic homogeneous polynomial, that is a *quadratic form*, must remain invariant [9].[46] Thus, he gave an additional constraint to harmonic division. To clarify the meaning of invariant quadrics, let's recall that since Poncelet the homography of figures has an interpretation in terms of geometric motion. Poncelet himself developed the method of *polar reciprocation*: he drew the section of a quadric on a sheet of paper,[47] and constructed the dual element of each element assigned relying on this.[48] For him the fixed quadric was a graphic means to perform a projective transformation of geometric elements. In Klein's context fixed is taken to mean transformation-invariant. A property associated with a geometric locus of points $\Omega(x) = 0$, which is unchanged by all non-singular transformations $\Omega(x') = \Omega(x)$, where $x \to x'$ are linear coordinate substitutions, is called an invariant with regard to a given set of transformations. In projective geometry an invariant $\Omega(u) = 0$ can be defined as a locus of planes or of lines, as well. However, we shall limit ourselves to loci defined by points.

Coming to Klein, he asked himself how to establish a direction along von Staudt's lines. Differing from Poncelet, instead of transforming single points or entire figures – which would also have been possible – he chose to study the transformations of projective space themselves by classifying all possible canonical forms of polynomials of second degree. His quadratic form written without coefficients, and in canonical form $\Omega(x_i^2) \equiv 0$, [49] where x_i are homogeneous point coordinates, is invariant under the projective general linear group $PGL(4, \mathbb{R})$ in the algebraic sense. As well as the quadric whose points are kept fixed, as many quadric loci as we like remain projectively invariant. The points belonging to the latter loci shift along them by effect of the transformation, and there can be two fixpoints or none, depending on whether the motions correspond to true or to "hyperbolic" rotations. Klein called *self-conjugate* the loci of the quadrics that have the invariance property in the narrow sense. If the transformations are real, i.e. the variables in the quadratic polynomial are real, the geometric loci yield a distinction into four subgroups of transformations. The canonical forms $\Omega(x_i^2) = 0$ can be indexed by the so-called *index of inertia*, i.e. the modulus of the difference between the number of positive and negative signs in the equation. (1) If all four squares have the same sign the index is 4. The transformations are called *elliptical*, and there are no (real) loci of the self-conjugate quadrics. (2) If the form has three equal signs the index is 2. The transformations are called *hyperbolic*, and the real self-conjugate geometric loci consist of a system of round, or (3) ruled quadrics.[50] (4) If the difference of the signs in the expres-

[46] A form is a homogeneous polynomial $\Omega(x) \equiv 0$. We take the chance to note that, differently from unimodular invariants, projective invariants do not depend on numerical coefficients, and their algebraic expressions are identically null.

[47] The polar reciprocation, or polarity, is an involutory correlation that, besides transforming an element changes it into its dual. Projection and section operations are necessary in drawings, but as projective transformations they are degenerate.

[48] The auxiliary conic is a legacy from the Arab algebraists, who traced ellipses to construct algebraic curves of higher order. Conceived as drawing help, ellipses are distinct from the instruments allowed by Euclidean geometry to construct curves. Poncelet's drawn invariant conic has two properties: (1) it allows construction of the transformed (dual) element of each chosen element; (2) by definition the dual line of each point on it is incident with that point. However, a line touching the invariant conic is neither tangent to it nor is a trigonometric tangent. The first meaning requires the mathematical definition of continuity, while the second needs us to know how to construct a circle with a given center C. Steiner showed that Euclidean geometry can be formulated with a ruler and a fixed circle.

[49] Algebraically the canonical quadratic form is a sum of squares $\sum_{i=1}^{4} x_i^2 = 0$, with $x_i \neq 0$. It is obtained by solving an eigenvalue problem. In analytic projective geometry the reference frame is a tetrahedron, and the invariant quadric is transformed. It takes the canonical form when referred to one of its polar tetrahedra. Although orthogonality is not defined in projective geometry, there are no covariant or contravariant forms. These were introduced in both non-Euclidean geometry and in tensor calculus.

[50] Projective ruled quadrics are somewhat like twisted tori.

sion of the quadric is 0, the system of quadrics takes the name *null system*.[51] All elements are self-conjugate, i.e. all lines are conjugate of themselves, and all points belong to their conjugate planes.[52] Although in projective geometry constructions are generated by means of transformations in agreement with the *Helmholtz-Lie Raumproblem*, the algebraic approach to transformations taken by Klein focuses on the transformation paths without ever facing the construction of figures.[53]

Turning to Klein's way of meeting von Staudt's requirement and establishing a direction along first species figures, e.g. a line of points, his classification solves it once the invariant quadric is fixed. To clarify the problem for a general quadric let's do an example reducing to a sheet of paper. A not yet drawn ellipse will switch to a hyperbola during construction, if it closes at a point, where it undergoes a torsion similar to that of the more well-known Möbius strip.[54] As in that case, if on the ellipse we choose the anticlockwise direction, the torsion inverts it along one of the branches of the hyperbola. In conclusion we can orientate a given conic, but the general line in projective space cannot be orientated. Finally, the treatment of projective space just discussed is valid so long as the $\Omega(x_i^2) = 0$ have real expressions. If we admit complex transformations, there is no subdivision.

4.1.3. Relevance of the Erlangen Program to optics

In the *Erlangen Program* Klein chose projective geometry as a unifying framework containing the Euclidean and non-Euclidean geometries as subgroups. His recasting of Carnot's *principle of continuity of figures* in the framework of transformation groups solves the long standing problem of defining congruence in geometry. Euclidean congruence can be based on isometries, the length preserving transformations. Now, consider the geometrical optics counterpart of this development. We stressed that Poncelet's fixed trace of the quadric is conceptually different from the projective figures transformed with the help of it. In geometric optics, given the object point, the rays serve to construct the image point without belonging either to the object space or to the image space. Klein's choice to study the system of invariant quadrics has the same meaning. As a matter of fact:

- states of motions can be analytically described in a space whatever, as evidenced by Copernicus' heliocentric approach to the Ptolemaic model of the movement of celestial bodies;
- Stars are physical points. Still they are not the sole objects under study.

Clearly, there is no gist of interpreting images if they are deemed not to be signals, but rather deceptive appearances.

5. Relative positions and coordinates

Since the *absolute space* was conceived as immovable and unpierced, for a long time after Euclid, the issues of continuity and of transformations of space in itself were neglected in geometry. During 1600, while the infinitesimal calculus was still in its infancy, the use of arithmetic multitudes was extended to geometric magnitudes. Descartes' method of coordinates came into use to measure space, and the relationship $d(x_1, x_2) = |x_2 - x_1|$ between Cartesian coordinates x_i and distance d was supposed to always hold.[55] More and more often geometric loci were matched point-by-point with coordinates, until numerical values were biunivocally associated to the points of a line.

The possibility of having recourse to homogeneous coordinates in projective geometry was noticed by Plücker within his analytical understanding of duality. In fact, writing the equation of a plane incident with a point as $u_1x_1 + u_2x_2 + u_3x_3 + u_4 = 0$, and regarding it as a bilinear expression, the set $u_1 : u_2 : u_3 : u_4$ can be used to define a plane. One can achieve complete symmetry of writing between plane u_i and point x_i coordinates depending on which ones are kept fixed. Correspondingly, in projective geometry a point-coordinate is the value attributed to a parameter $k = \frac{x}{x_4}$, expressed by the ratio of two homogeneous coordinates, and is in fact an equivalence class. To have $k \in \mathbb{R}$, it is required that $x, x_4 < \infty$ and not both equal to zero. The formula $(k_1k_2k_3k_4) := \frac{k_1-k_3}{k_2-k_3} : \frac{k_1-k_4}{k_2-k_4}$

[51] We recollect that null system is the name given in statics to the *linear complex* studied by Plücker. The transformations of the projective space of lines are described assigning equations, that give an indication of the "degrees of freedom" of transformation. For line-elements, the condition $\Omega \equiv 0$ is satisfied by ∞^3 lines, and the structure takes the name linear complex. An expression of the type $\Omega + \mu\Omega' \equiv 0$, is satisfied by ∞^2 lines, and the structure is a linear congruence. If we cut the ∞ combinations of lines that satisfy $\Omega + \mu\Omega' + \nu\Omega'' \equiv 0$, the resulting structure is a ruled surface. Last, $\Omega + \mu\Omega' + \nu\Omega'' + \tau\Omega''' \equiv 0$ identifies a pair of skew lines. In Cartesian coordinates the space defined by those lines is four-dimensional. If $\boldsymbol{A}$ and $\boldsymbol{B}$ are two ordinary vectors, algebraic geometry admits that the lines of the null system be represented by the pseudovector $(\boldsymbol{A} - \boldsymbol{B}, \boldsymbol{A} \times \boldsymbol{B})$ which satisfies the quadratic relation $(\boldsymbol{A} - \boldsymbol{B}) \cdot (\boldsymbol{A} \times \boldsymbol{B}) = 0$. Klein showed that the lines belonging to the null system can be parametrized by points belonging to a quadratic four-dimensional variety embedded in a five dimensional linear space that, in this context, is called quadratic complex. Roger Penrose identified a slight generalization of the above quadratic form in $\mathbb{P}^5$ $(\mathbb{C}^6)$ with space-time corresponding to complexified three-dimensional "twistor space". The other two types of transformation quadrics mentioned in the text, ellipsoid and two-sheet hyperboloids, are not rules surfaces in three-dimensional projective space, but have quadratic form. They become complexes of lines only if admitting imaginary lines. More in general in projective algebraic geometry we talk of complexes and congruences of order n or class n, respectively considered as loci of points.

[52] When the supports of the invariants are projected on the plane, there we find nothing corresponding to the null system.

[53] The paths are linked to the transformation properties of polynomials. In algebra each symmetric matrix S identifies a quadratic form $Q(x) = x^T Sx$ on $\mathbb{R}^n$ uniquely. Thus here one considers the action $S \to ASA^T$ of the group $GL(\mathbb{R}^4)$ on the space $\mathcal{S}$ of real symmetric 4×4 matrices, representing real quadratic forms with the same signature. This time the inertia law is enunciated so as to include all of the degenerate forms.

[54] The point where this happens, which can lie on the paper, is called improper in retrospect. Being unable to distinguish between ellipse and hyperbola, the distinction is canceled, between inside and out of the conic.

[55] The distance $d(x_1, x_2)$ satisfies the three properties:

1. $d = 0$ implies $x_1 = x_2$;
2. $d(x_1, x_2) = d(x_2, x_1)$;
3. $d(x_1, x_3) \leq d(x_1, x_2) + d(x_2, x_3)$ (triangle inequality).

involving four numerical values k_1, k_2, k_3 and k_4 is called cross ratio. For variable $k \in \mathbb{R}$, $\xi = (k_1 k_2 k_3 k)$ is a function $\xi(k) = \frac{ak+b}{ck+d}$, which differs from zero provided that $\Delta = ad - bc$.[56] Clearly, both k and ξ can be used as projective coordinates of the points on a line. Moreover, putting $k_1 = \infty$, $k_2 = 0$, $k_3 = 1$ it can be shown that $\xi = k$. This is the reason why, in a projective space, the coordinates are indicated by the analytical notation $\xi_1 : \xi_2 : \xi_3 : \xi_4$, reminiscent of the anharmonic ratio. Nowadays, the strong link to Möbius nets and projective transformation invariants has lapsed, and that notation is regarded as an alternative to representing coordinates by an ordered quadruplet $(\kappa x_1, \kappa x_2, \kappa x_3, \kappa x_4)$, where $\kappa \neq 0$ is a real number. Like for the line on the Cartesian plane, the variables x_i $(i = 1, \ldots, 4)$ don't have any direct projective significance, and could be thought of as real Cartesian coordinates.

Homogeneous coordinates allow extending the Cartesian plane and the algebraic operations on it to improper elements, also called infinite or ideal, and therefore are being used ever since to represent projective space. Moreover, we repeatedly observed that Poncelet availed of projective transformations to carry out projective constructions, which implies a correspondence between the analytical representation of space and that of transformations. Even if projective transformations (in fact collinations) can be written out in terms of coordinates, exactly the correspondence between projective constructions and their analytical representation gets lost. As regards proposals for improved coordinate systems, J. Gray observes that "there is no such thing as advanced coordinate geometry. There are either differential or algebraic projective geometry".

5.1. Cross ratio and metrics

When the fundamental theorem of projective geometry is derived solely from $X = \frac{P_1 - P_2}{P - P_1} \frac{P - P_3}{P_3 - P_2}$ and $X = |1|$ a non exhaustive Möbius net can be constructed in different ways starting from three given elements. Whereas multiple possible outcomes are approved in connection with probability theory, a handful of different alternatives are banned from projective geometry. So, under pressure from the growing importance of algebraic methods, a fresh start was made to relate whatever picked element P with a unique P' and with numbers. Rejoin was achieved by introducing a point algebra on a set of points equipped with order. The one-to-one projective transformations were linked to the rules of the one-valued composition operations on pairs of real valued variables. From this vantage point a Möbius net becomes a *net of rationality*. Topological reasoning ensures that, once points are well ordered and their sequences are convergent, one can prove that, for each pair of elements in harmonic relation, there is no third pair in such a relation with both. The cross ratio so defined is logically equivalent to the fundamental theorem of projective geometry in the form: "A projective transformation between two projective ranges of points is uniquely determined by three pairs of corresponding points and the order of their correspondence." The meaning of that equivalence is shown in fig. 9, where the quadrangle/quadrilateral construction is reinterpreted as a point-correspondence on first species figures.

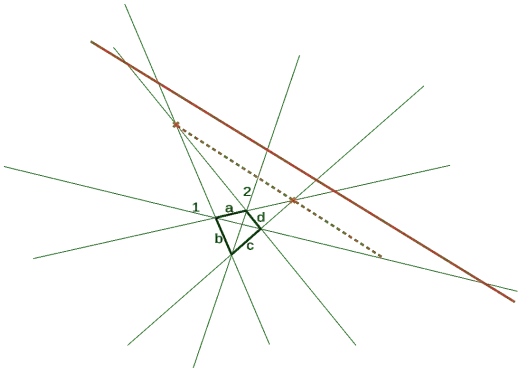

Figure 9: Harmonic relation and involutory order. On the dashed line the opposite sides of the quadrilateral $abcd$ pairwise meet. Those points and the incidence points of the diagonals are harmonically divided. On any other line, such as the continuous line nearby, given three pairs of corresponding points, one can intrinsically determine a double ordering of points in involution. Von Staudt used the involutory relationship to induce a direction on a line.

The continuity axiom involved in the assumption that all total functions of the continuum is continuous, is Dedekind's,[57] who convincingly showed that the construction of numerical systems has no geometric basis. As it may be, since by definition projective geometry is independent of the metric properties of figures, if by effect of the introduction of coordinates we can discuss distances, this is because continuity is induced from that defined on the field $\mathbb{R}$, and the other axioms established for $\mathbb{R}$ go to complete those of incidence, As a consequence, the algebraic interpretation of projective geometry also allows Archimedes' axiom,[58] that Hilbert intentionally called *Axiom des Messens* (axiom of measure). He thought it to be experimentally verifiable, and dualizable in the sense of the length-angle duality. Accepting the latter axiom, it is possible to fix a metric scale unit at least locally, and lead back from cross ratios to simple relations between the measures of the segments identified by the harmonic points.

5.2. Projective space

Synthetic projective geometry allows visualizing as many *entire figures* as wished by constructing each of them. At a difference the deduction of the properties of projective space by the analytical methods used to represent the Eu-

[56] That is the notation for a Möbius transformation on the real plane.

[57] The axiom says that, if all points on a line are separable into two classes so that each point of the first class falls to the right of all points o the second class, then there is one and only one point that produces the division into two classes. The hypothesis is certainly not verified in projective geometry if we do not establish that all points that fall on top of each other are to be considered as a single point.

[58] The axiom says that, if $b > a$ and $a \neq 0$, then $\exists n$ such that $na > b$. In projective geometry this is not valid because lines have the topology of conics.

clidean space fails because the space including the above figures cannot be accommodated in Cartesian 3D space. It could be argued that emptiness defies whatever representation, so that introduction of a Cartesian coordinate system is just as unfit for the void Euclidean space. In addition, however, the very convention adopted for Euclid's geometry, that all figures belong to one and the same geometric space, cannot be transferred as is to projective geometry, because each projective figure is itself a view of the whole space.

Many different lines of research helped pairing projective space and coordinates. Either projective representations of numbers were algebraically explored, or the loci corresponding to polynomials $\Omega \equiv 0$ of higher order and degree than the second were studied in the complex space $\mathbb{C}^n$, conceiving an "algebraic curve" as a kind of "Riemann surface", or projective transformations were represented by linear coordinate substitutions. An example of the first type of approach was von Staudt's handling of "Würfe". The second type of approach taught us that the duality principle cannot be easily extended beyond quadrics (via the clarification of Cramer's paradox about the intersections of curves). The third type of approach led to group theory and to n-dimensional representations of space.[59] However, the aim to produce more general proofs in Euclidean geometry tops the list of research lines.[60] In so far as the same meaning is attributed to the cross ratio and to the Cartesian quadruplet $(kx_1^H, kx_2^H, kx_3^H, kx_4^H)$, ($k{\neq}0$, and excluding $(0,0,0,0)$), the projective point transformations of space can be represented by linear homogeneous substitutions of 4 variables x'_k $kx_i = \sum_{k=1}^{4} c_{ik}x'_k$, with $i = 1, \cdots, 4$, and $D = |c_{ik}| \neq 0$. These transformations belong to the projective general linear group $PGL(4, \mathbb{R})$, which has the structure of a Lie group, say, and are linked to coordinates of points of the projective space $\mathbb{P}^3$ over $\mathbb{R}$.[61] As no representation of $\mathbb{R}^4 \setminus \{0\}$ in 3D can be given, matching with special constructions and space generation through transformations become second-level issues. Rather, leaning on 4D transformations, $PGL(4, \mathbb{R})$ leads to methods of reasoning *more geometrico* about sets of numbers and algebraic equations.

Sometimes, the affine space is told to provide an intuitive visualization of the projective space.[62] An example of affine mapping of the projective space consists of intersecting $\mathbb{R}^4$ with the hyperplane $x_4^H = 1$ by putting $k = \frac{1}{x_4}$, and of defining the non homogeneous coordinates $x := x_1^H/x_4$, $y = x_2^H/x_4$, $z = x_3^H/x_4$ in the affine space $(x, y, z, 1)$.[63] More in general, the section can be any hyperplane of $\mathbb{R}^4 \setminus \{0\}$. However, the affine space is topologically inconsistent, and formalizations tend to set straight its relevant mathematical features. Thus, in the end, algebraic geometry identifies a projective smooth three-dimensional manifold M over $\mathbb{R}$ with the vector space generated by central projection by four independent one-dimensional subspaces of $\mathbb{R}^4$ projected from the origin O. The homogeneous coordinates of the point $P{\in}M$ are defined as the equivalence class $(x, y, z, t){\sim}(kx, ky, kz, kt)$ of the vector v with $k \in \mathbb{R} \setminus \{0\}$. This representation is not isomorphic to that of Plücker's ruled space, which is itself represented as a quadratic hypersurface of $\mathbb{P}^5$. Since, doing algebraic geometry over an algebraically closed field of characteristic 0 is essentially equivalent to doing it over the complex numbers, projective algebraic complex geometry has been considerably developed. In this case differential geometry deals with the same objects as algebraic geometry. Finally, besides real and complex numbers, quaternions and other hypercomplex numbers are being used too.

5.3. Euclidean metric from projective geometry

Cayley, a convinced supporter of the primacy of the projective framework, formalized the notion of *absolute metric* in the case of Euclidean geometry. He wrote the equation of the circumference in homogeneous Cartesian coordinates as $x^2 + y^2 + cxt + dyt + et^2 = 0$, with any c, d, and e, and observed that, when $t = 0$, the equation degenerates into two algebraic curves $x^2 + y^2 = 0$ and $t^2 = 0$.[64] Cayley's absolute consists of the points at infinity that belong to the two imaginary lines with slopes i and $-i$, i.e. of the points of complex conjugate coordinates $(1, +i, 0)$ and $(1, -i, 0)$. The two imaginary lines are isotropic lines of the type we met when discussing geometric optics.[65] The two points, called circular points, are double points of an involution, are common to all circumferences, and belong to the line at infinity – the boundary of the Euclidean plane.[66] On this oc-

[59] Although three dimensions were allotted to the physical space, convenience soon suggested to decompose figures into geometric elements that require more than three Cartesian coordinates. For instance, Plücker represented congruences in the projective space by means of the line element, that requires at least four coordinates. Any other element or first species figure would do. For example, if one chooses to describe constructions in projective space using a suitable class of functions, the projective void will look like an abstract "space of functions".

[60] In practice, succeeding to Cantor's set theory problems, constructions and models of both geometries were set aside in favor of abstract topological research.

[61] If we adopt a non-homogeneous system of Cartesian coordinates to represent transformations of $\mathbb{P}^3$ in itself, these are three quotients of linear functions with identical denominator, a particular type of Cremona transformations.

[62] Projective space is modeled by the affine space if we postulate that the elements at infinity of projective geometry are improper points distinct from the proper ones. Yet, synthetic projective geometry has its own constructions. By contrast, the non-Euclidean geometries were set up logically (negating the parallel postulate), and as such have got no native graphic basis. We refer in particular to the interpretation of the geometry at the boundary ∂H^4 of hyperbolic hyper-space. Lobatschewsky showed that a Euclidean geometry can be defined on the horosphere ∂H^3 of hyperbolic space H^3. In the projective model ∂H^3 is interpreted as locus of the metric quadric.

[63] Affine transformations are parallel projections. Lowering by one the dimensions involved, the general point $P = (X, Y)$ in the plane $x = X$, $y = Y$, $z = 1$, become (tx, ty, t) when $z = t$, ($t{\neq}0$). If the general projective plane is embedded in an orthogonal Cartesian reference frame (x, y, z), parallelism is already embodied in the projective coordinates $x_1^H : x_2^H : x_3^H \to (kx_1^H, kx_2^H, kx_3^H)$. It can be shown that there is no embedding of $\mathbb{P}^2(\mathbb{R})$ as a submanifold of $\mathbb{R}^3$, i.e. without singularities.

[64] Klein calls it a degenerate canonical form $\Omega(x_i^2) = 0$.

[65] In space the absolute consists of a spherical circle, and there are infinitely many isotropic lines through each point.

[66] The main idea is that the limit of a sphere, when the radius tends to infinity, is a plane. Poncelet reached this result observing that two ellipses

casion, however, the canonical form $\Omega(x_i^2) \equiv 0$ (including $t^2 = 0$) is taken to mean specifically the Euclidean projective metric.

Klein put Cayley's absolute in relation with the projective determinations of the metric he associated with elliptical and hyperbolic geometries.[67] He renamed the Euclidean geometry parabolic geometry, to mean that it can be understood as a limiting, degenerate case between the two classes of non-Euclidean geometries. The special forms identified with the invariant boundaries $\Omega(x_i^2) \equiv 0$ don't really shape the space. Rather they are set to the projective models of homogeneous space used to study (mechanical) motion. In the parabolic plane the circular points remain invariant under translation, rotation, for reflection – their exchange, and under similarity transformations. Non-Euclidean geometries do not allow this last degree of freedom but just isometries[68]. If one were to believe that the structure of the specified empty geometric space can be recovered, he would conclude that, within the framework of projective geometry, the standard Euclidean metric becomes connected with points at infinity. Rather, in the light of rubber sheet geometries, the metric of Euclidean space is connected to Pythagoras' theorem.[69] Anyway, since, contrary to non-Euclidean geometries, Euclid's geometry is originally synthetic, it can be compared with its projective parabolic model. Through the absolute the Euclidean plane acquires a boundary. Thus, the axiom that two parallel lines meet at the boundary does not interpret Euclid's postulate V,[70] but corresponds to a different interpretation of it. Euclid himself assumed nothing as to the space between geometric figures.

intersect in four points at most while, without considering the imaginary points, the maximum number of points where two circumferences intersect is two.

[67] We must avoid confusing systems of projective invariants with the metric quadric that characterizes each projective non-Euclidean model. The metric is a relationship among points, that leaves invariant just the *one* non-degenerate metric quadric.

[68] Similarity transformations are invariant exclusively in Euclidean geometry. Non-Euclidean 3D rigid motion must leave invariant the non-degenerate quadric of the metric. The loss of the degree of freedom corresponding to similarity transformations is compensated by the extra degree of freedom in the choice of the system of homogeneous coordinates. The independent parameters of the group G of rigid transformations are calculated with the formula $\frac{n(n+1)}{2}$, where n is the dimension of the matrix that represents the transformation. For n odd, the inversions are excluded, because they do not correspond to "continuous" motions. By these arguments, the conformal group has 10 free parameters, ad the group of rigid motions in space is G_7. The same analysis fixes the group G_{16} of projective transformations. The space-time transformations in Nordström's conformal theory allow the same number of parameters as the projective transformations of space.

[69] Conversely, projective space is considered metrizable via a naturally induced topology, being it an underlying topological space of a metric space.

[70] "If a line segment intersects two straight lines forming two interior angles on the same side that sum to less than two right angles, then the two lines, if extended indefinitely, meet on that side on which the angles sum to less than two right angles."

6. Conclusions

Geometry is a very old branch of mathematics, the substrate of which has changed repeatedly in the course of the historical development. There is some evidence that Euclid's geometry provided a visual basis for thinking. Vice versa, as Euclid's *Optics* seems to suggest, geometric constructions may serve to enable a logical interpretation of optical sensations. Anyway, during Renaissance Humanism the traits bound to constructions were enhanced in the newly created projective geometry. A certain amount of further study was required if only to find out that projective geometry is based on axioms and postulates different from those laid down in *The Elements*. After formalization, provided that the graphic element typical of each geometry is given up, their two sets of axioms can be compared in order to determine which one is more inclusive. Yet, formal comparison is only possible at the price of some reinterpretation, as we set out to show on Euclid's parallel postulate.

Surely, mathematics is a human endeavor. However, in developing a common understanding in electromagnetism and telecommunications, the graphic element of projective geometry could be worth investigating more closely as an alternative to probabilistic field theories. When linked to an analytic apparatus more suited to projective constructions than Cartesian coordinates, projective geometry could supply a common ground on which to start learning how to compare not-encoded signals taken with modern, technically sophisticated instruments – also in other frequency ranges – with the images seen with the naked eye, to which our brain is accustomed.

References

[1] H. S. M. Coxeter, *Introduction to Geometry (II Ed.),* John Wiley & Sons, Inc., New York, 1969.

[2] H. S. M. Coxeter, *Projective Geometry (II Ed.),* Springer Verlag, New York, 2003.

[3] G. Birkhoff, Current trends in algebra, *Amer. Math. Monthly* 80(7): 760–782, 1973.

[4] H. E. Burton, The optics of Euclid, *JOSA* 35(5): 357–372, 1945.

[5] H. Siebert, Transformation of Euclid's Optics in Late Antiquity, *Nuncius* 29: 88–126, 2014.

[6] R. A. Houstoun, Kepler and the Law of Refraction, *Phys. Bull.* 9: 3–6, 1958.

[7] G. Sannia, Geometria differenziale delle congruenze rettilinee, *Math. Ann.* 68(8): 409–416, 1910.

[8] H. Weyl, On the foundations of general infinitesimal geometry, *Bull. Amer. Math.* 35(5): 716–725, 1929.

[9] F. C. Klein, *Vorlesungen über nicht-Euklidische Geometrie,* Springer, Berlin, 1928.

Electromagnetic Characterization of Sea Ice Using Low Frequency Electromagnetic Waves

M. Shifatul Islam[1,2,*], Sadman Shafi[1,2], Mohammad Ariful Haque[1,2]

[1]Anyeshan Limited, Dhaka, Bangladesh
[2]Department of Electrical and Electronic Engineering, Bangladesh University of Engineering and Technology, Dhaka, Bangladesh
*E-mail: shifatul@anyeshan.com

Abstract

The plane wave electromagnetic response of sea ice is an important electric characterization of sea ice. However, there is no existing sea ice model in the literature to conduct this study. In this work, we develop three different dielectric models of sea ice and use those to investigate the plane wave electromagnetic response of a sea ice bulk of varying thickness. This study can aid in monitoring sea ice using electromagnetic waves, which can be useful in marine navigation, meteorology, environmental studies etc.

1. Introduction

Much work has been done to quantify different properties of sea ice. The salinity, porosity, electrical permittivity, conductivity etc. and several relations among them have been studied in [1-7]. But to date, there is no known work that combines all the knowledge to develop a systematic layered model of sea ice to predict its properties. Such a model is necessary for investigating the electromagnetic (EM) characterization of sea ice. This model should incorporate the relations among different properties of sea ice, such as the relation between conductivity and depth or between salinity and temperature.

In this paper, we have developed three dielectric models of sea ice to generate profiles of its electrical properties, and then we use them to investigate the low-frequency EM plane wave response of a sea ice bulk following [8], [9].

2. Methodology

2.1. Sea ice properties and models

Several properties of sea ice, such as salinity, porosity, conductivity etc. change with depth. We have considered these changes in our models by assuming sea ice to be composed of many layers, with the properties changing from one layer to another. The effect of age of sea ice on its properties has been taken into account by considering two types of sea ice – one-year old ice and multiyear ice. These two types have differences in their properties that have been taken into account in one of our models.

Fig. 1 presents the schematic diagram of the proposed models. The complex permittivity at any point at any depth, d in the sea ice bulk is $\tilde{\epsilon} = \epsilon + i\epsilon' = \epsilon + i\frac{\sigma}{\omega}$, where ω is the frequency of the incident electromagnetic wave. The temperature of the sea ice bulk is θ (in $°C$).

2.1.1. Model 1

The first one is a simple ice bulk of thickness t present on top of sea water, and above the ice is air. $\tilde{\epsilon}$ is constant over the whole bulk. The variations of porosity, salinity and conductivity have not been considered in this model.

2.1.2. Model 2

In this model, the sea ice bulk, of thickness t, is assumed to consist of n layers, each layer having thickness h. The effects of porosity and salinity on the permittivity and

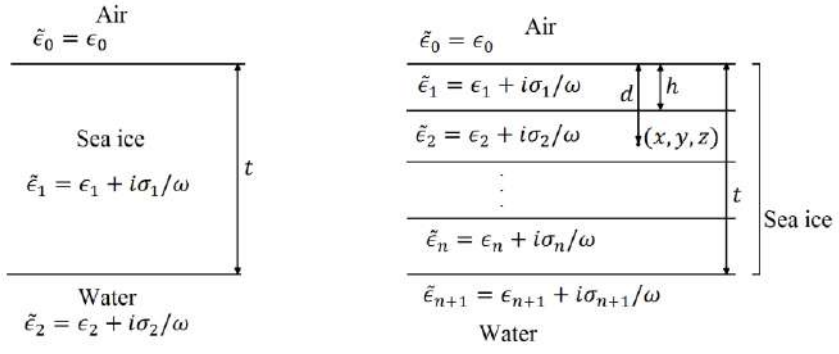

Figure 1: Geometric configuration of the media for (a) model 1 and (b) for models 2 and 3.

conductivity of sea ice are considered in this model, and the variations of these quantities with depth are included. In order to find out the relation of the permittivity with depth, we first consider the effect of porosity on permittivity. The porosity (due to the presence of air bubbles or other impurities) of any dielectric affects the value of the total permittivity of the material. It is known that sea ice contains air bubbles within, and so the real permittivity, ϵ, of the sea ice bulk is mainly determined by its porosity. Although there is no clear relation between depth vs porosity within a sea ice bulk, Kharitonov et al conducted some experiments [2] and, through the observations, came to a conclusion that the porosity variation is not completely random with the variation of depth, and a quantifiable trend can be observed. Fig. 2 shows the variation of the porosity, p, at any depth, d, in sea ice.

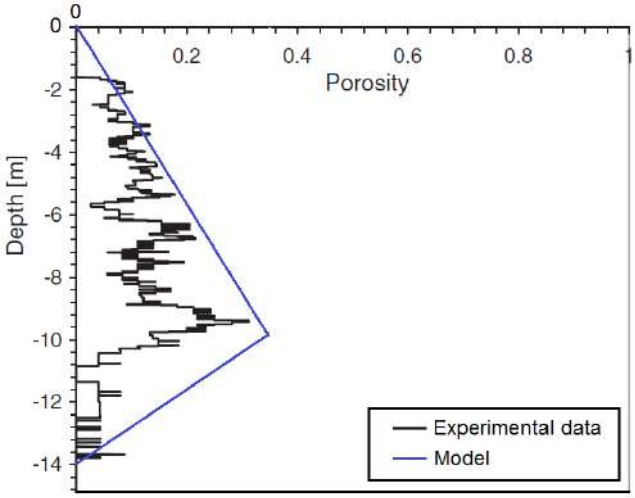

Figure 2: Depth-wise distribution of the porosity of sea ice [experimental data is the courtesy of [2]]

We approximate the relation between p and d using a linear approximation, as shown in Fig. 2, which assumes that p is 0 near the air ice interface, and gradually increases maintaining a linear slope with a maximum porosity value of 35%, and then again decreases with a linear profile, eventually reaching zero at the flat ice-water interface. Thus our proposed linear approximation is given by the following piece-wise linear function

$$p = \begin{cases} \frac{0.5}{t} d & 0 \le d \le 0.7t \\ 0.35 - \frac{1.17}{t}(d - 0.7t) & 0.7t < d \le t \end{cases} \quad (1)$$

The porosity p at a depth d determines the real permittivity ϵ at that depth. For a given porosity, the real permittivity of a dielectric can be calculated using the Maxwell Garnett (MG) equation for two dielectrics [3]. The MG equation assumes that a dielectric material contains spherical impurities (the impurities are another dielectric) which are disconnected from one another. In our case, we use the MG equation on the assumption that the air bubbles in the sea ice bulk are spherical in shape and disconnected from one another. The MG equation for the porous sea ice bulk is given as

$$\epsilon_{MG} = \left[\frac{2\epsilon_{\text{pure ice}} + \epsilon_0 + 2p(\epsilon_0 - \epsilon_{\text{pure ice}})}{2\epsilon_{\text{pure ice}} + \epsilon_0 - p(\epsilon_0 - \epsilon_{\text{pure ice}})}\right] \epsilon_{\text{pure ice}} \quad (2)$$

where $\epsilon_{\text{pure ice}} = 3.15\epsilon_0$ is the permittivity of pure ice, and it is almost constant for electromagnetic frequencies within 100 KHz - 100 MHz. Using this equation, we determine an approximate real permittivity $\epsilon = \epsilon_{MG}$ of the sea ice bulk for porosity p at depth d. Since p varies with d and ϵ depends on p, hence ϵ will also vary with d.

Unlike air volume, the salinity S of sea ice is more clearly dependent on the depth d of the ice. If we ignore the surface meltwater flushing during summer seasons, it is found that the salinity vs. depth curve is concave shaped, reaching its minimum at a certain depth and rising again [1] [4]. Such a variation of salinity with depth is shown in Fig. 3.

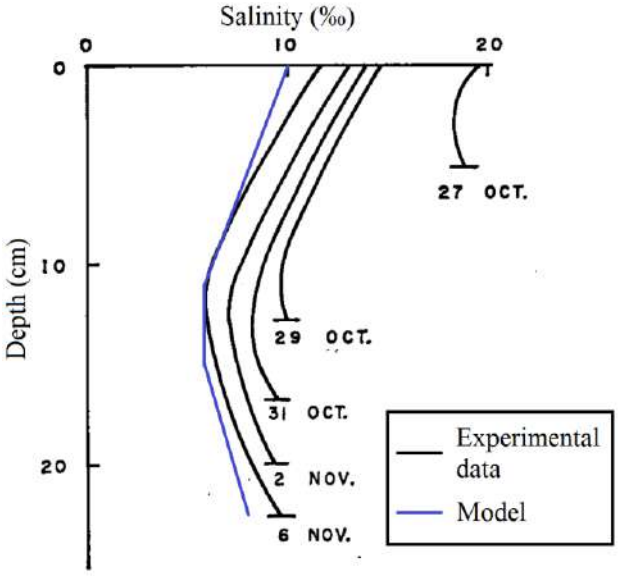

Figure 3: Depth-wise distribution of the salinity of sea ice [experimental data is the courtesy of [4]]

We approximate this concave shaped salinity profile using a linear piecewise function – the salinity decreases to two-thirds of its initial surface value, S_0, at a depth equal to half of the thickness (t) of the bulk; S then remains constant for some depth and then increases to 80% of S_0 as we go down to the bottom. An instance of the model is shown in Fig. 3. We thus model the depth dependency of salinity with the following relation

$$S = \begin{cases} S_0 - \frac{0.1d}{t} & 0 < d \le 0.5t \\ \frac{2S_0}{3} & 0.5t < d \le 0.7t \\ \frac{2S_0}{3} + \frac{d - t}{15t} & 0.7t < d \le t \end{cases} \quad (3)$$

Here, S_0 is the salinity at $d = 0$. In model 2, we assume that $S_0 = 5‰$.

The conductivity, σ, at any point of the sea ice depends on the salinity, S, at that point. We use the data in [5] to create

an empirical equation relating the conductivity σ at a point with temperature, θ (in $°C$), and S as follows

$$\frac{1}{\sigma} = -107 + 58\,exp\big(-(26S + 0.0818\theta)\big) \quad (4)$$

Since S depends on d and σ depends on S, we obtain a σ vs. d profile using equations (3) and (4).

2.1.3. Model 3

In this model, the characteristics of one-year old ice and multiyear ice are included and a model is generated using [6]. Unlike model 2, this model considers the dependence of ϵ_r on the relative brine volume, V_{br}, of sea ice. As before, we generate an MG air-ice model and compute its ϵ_{MG} using equation (2). The dependence of S on d is again modelled using equation (3). One-year old ice is mainly composed of frazil ice, and so we have characterized one-year old ice by the properties of frazil ice. The surface salinity of frazil ice is different from that of multiyear ice. Frazil ice tends to be more saline, with a surface salinity of $5 - 16‰$ while for multiyear ice, the surface salinity is typically $< 1‰$ [10]. In model 3, we take into account this difference and consider $S_0 = 10‰$ and $1‰$ for frazil and multiyear ice respectively while using equation (3). The relation between V_{br} with S and θ is approximated according to [7] by the following relation

$$V_{br} = S\left(\frac{49.185}{|\theta|} + 0.532\right);\ -22.9°C \le \theta \le -0.5°C \quad (5)$$

We then calculate ϵ using [6] as

$$\epsilon = \frac{\epsilon_{MG}}{1 - 3V_{br}} \quad (6)$$

Finally, we separately compute $\epsilon' = \frac{\sigma}{\omega}$ for frazil and multiyear ice respectively as per [6] with the following relations

$$\epsilon'(\text{frazil}) = (0.0316 + 9.26V_{br})\epsilon_0 \quad (7)$$

$$\epsilon'(\text{multiyear}) = (0.00633 + 9.98V_{br})\epsilon_0 \quad (8)$$

Then we obtain σ from ϵ'. Here, ϵ' (and thus σ) depend on V_{br}, which varies with S, which in turn varies with d. Thus we obtain a relation between σ and d.

2.2. Electromagnetic waves in layered structures

We have used the electrical properties of the different layers of the ice bulk obtained from models 1, 2 and 3 in section 2.1 to compute the generalized reflection coefficient R^{TM} (for the transverse magnetic component of EM waves) of the entire ice bulk using [8], [9]. Suppose a plane electromagnetic wave of angular frequency ω is incident on the sea ice bulk consisting of n layers (in case of model 1, $n = 1$). This wave will be partially transmitted and partially reflected by each layer of the sea ice bulk. Let the wave propagation vector of the EM wave in the m-th layer be $\vec{k}_m = k_{x,m}\hat{x} + k_{y,m}\hat{y} + k_{z,m}\hat{z}$. In that case, R^{TM} is given by

$$R^{TM} = \frac{K_0 - Z_1}{K_0 + Z_1} \quad (9)$$

where

$$K_m = \frac{ik_{z,m}}{\sigma_m + i\omega\epsilon_m};\ m = 0,1,2,\dots,n,n+1 \quad (10)$$

$$Z_m = K_m \frac{Z_{m+1} + K_m\,tanh(ik_{z,m}h)}{K_m + Z_{m+1}\,tanh(ik_{z,m}h)};\ m = 1,2,\dots,n \quad (11)$$

Here, $m = 0$ corresponds to the air (also called the "source medium") above the sea ice, while $m = n + 1$ corresponds to the sea water below the sea ice. For the bottommost $(n + 1)$-th layer (sea water), $Z_{n+1} = K_{n+1}$, and hence Z_{n+1} can be calculated by equation (10). Thus, starting from this, $Z_n, Z_{n-1}, \dots, Z_2, Z_1$ can be recursively computed using equations (11), (10). Using K_0 and Z_1, we compute R^{TM} using equation (9). This method is applicable for a wide range of EM frequencies, including the low-frequency range.

3. Simulation results

The magnitudes of R^{TM} of the ice bulk are observed in the three ice models separately. Their variations with the bulk's thickness for a 5 MHz incident EM wave are plotted in Fig. 4. For models 2 and 3, the temperature of the bulk is assumed to be $-20°C$ in Fig. 4 (a) and $-10°C$ in Fig. 4 (b). In model 3, if the ice bulk's thickness is less than 2 m, it is considered as frazil ice, while bulks of greater thicknesses are considered as multiyear ice.

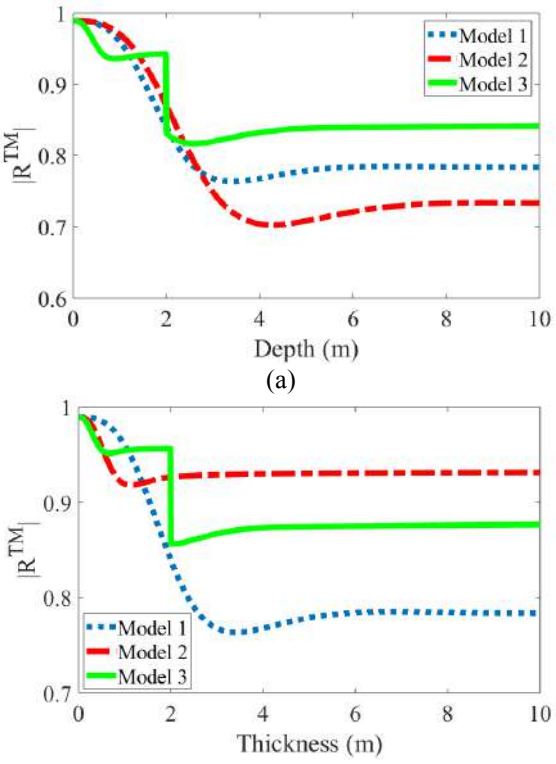

Figure 4: Graph of $|R^{TM}|$ vs. thickness (t) of the entire sea ice bulk for temperatures (a) $\theta = -20°C$ and (b) $\theta = -10°C$

From Fig. 4, it can be observed that $|R^{TM}|$ approaches a steady value with increasing thickness for all three models due to conductivity, which makes sea ice "lossy". The minimum point on $|R^{TM}|$ profile is due to a near phase matching effect (the surface impedance of the layered bulk approaches the intrinsic impedance of the source medium, air) of the whole ice bulk at that particular frequency and thicknesses, allowing maximum transmission. $|R^{TM}|$ is less in multiyear ice because frazil ice is more saline, and hence more conductive and more reflective. And model 3 has higher conductivities at different layers; hence $|R^{TM}|$ approaches a steady value at a lower thickness in model 3.

It is also observed that $|R^{TM}|$ is higher for models 2 and 3 in case of $\theta = -10°C$ compared to $\theta = -20°C$. From the equations of [7], it is expected that with the increase of temperature (for $\theta < 0°C$), the brine volume percentage V_{br} inside the bulk will keep increasing, which in turn, makes the bulk more saline in nature and increases its conductivity. Therefore, the value of $|R^{TM}|$ for each of the models generally increases with the increase in temperature. We also observe that $|R^{TM}|$ is less sensitive to change in thickness for $\theta = -10°C$ than for $\theta = -20°C$. The increase in conductivity with the increase in temperature makes the sea ice more lossy, and hence less sensitive to changes in the thickness. Hence, $|R^{TM}|$ approaches a steady value at lower thicknesses for models 2 and 3 in case of $\theta = -10°C$ compared to $\theta = -20°C$.

4. Conclusions

The dielectric behaviour of sea ice has been modelled and these models are used to determine the profiles of the reflection coefficient of the incident EM wave with varying thickness of sea ice bulk. In the models, the variations of salinity and porosity and their effects on the permittivity and conductivity of sea ice have been considered. Distinction has also been made between one-year old and multiyear ice.

The composition of sea ice and thus its electrical properties also depend on weather and seasonal variables, including phenomena such as brine drainage at the bottom or surface meltwater flushing [1] at the ice water interface. This demands complex models for sea ice with multiple characterizations. There is a scope for further research on these models.

The profiles of the reflection coefficient can be used to estimate the type of sea ice (frazil or multiyear), its thickness and its effect on electromagnetic radiation of different wave fronts (cylindrical, spherical or others). They can also be useful in the study of radio communications in cold regions of seas and oceans where sea ice is abundant.

Acknowledgements

This work has been supported by the Office of Naval Research Global, London, UK [grant N62909-19-1-2013] as part of the NICOP project "Non-invasive measurement of sea ice thickness using low frequency EM waves".

References

[1] D. N. Thomas and G. S. Dieckmann, Sea Ice, 2nd ed., Blackwell Publishing Ltd, 2010.

[2] V. V. Kharitonov, "Internal structure and porosity of ice ridges investigated at «North Pole-38» drifting station," *Cold Regions Science and Technology,* vol. 82, pp. 144-152, 2012.

[3] Z. N. Wing, B. Wang and J. W. Halloran, "Permittivity of Porous Titanate Dielectrics," *Journal of The American Ceramic Society,* vol. 89, no. 12, pp. 3696-3700, 2006.

[4] P. Hoekstra and P. Cappillino, "Dielectric Properties of Sea and Sodium Chloride Ice at UHF and Microwave Frequencies," *Journal of Geophysical Research,* vol. 76, no. 20, pp. 4922-4931, 1971.

[5] J. C. Cook, "RF Electrical Properties of Salty Ice and Frozen Earth," *Journal of Geophysical Research,* vol. 65, no. 6, pp. 1767-1771, 1960.

[6] M. R. Vant, R. B. Gray, R. O. Ramseier and V. Makios, "Dielectric properties of fresh and sea ice at 10 and 35 GHz," *Journal of Applied Physics,* vol. 45, no. 11, pp. 4712-4717, 1974.

[7] G. Frankenstein and R. Garner, "Equations for determining the brine volume of sea ice from -0.5° to -22.9°C," *Journal of Glaciology,* vol. 6, no. 48, pp. 943-944, 1967.

[8] J. R. Wait, Electromagnetic Waves in Stratified Media, Oxford: Pergamon Press Ltd, 1970.

[9] W. C. Chew, Waves and Fields in Inhomogenous Media, New Jersey: IEEE Press, 1995.

[10] M. R. Vant, R. O. Ramseier and V. Makios, "The complex-dielectric constant of sea ice at frequencies in the range 0.1-40 GHz," *Journal of Applied Physics,* vol. 49, no. 3, pp. 1264-1280, 1978.

[11] J. A. Kong, Electromagnetic Wave Theory, New York: John Wiley & Sons, 1986.

A Dual-Band TE_{10} – TM_{01} Mode Converter with a Rectangular to Circular Waveguide Transition

Ceyhan Turkmen[1,*], Mustafa Secmen[1]

[1]Department of Electrical and Electronics Engineering, Yasar University, Bornova, 35100, Izmir, Turkey
*corresponding author, E-mail: ceyhan.turkmen@yasar.edu.tr

Abstract

This study represents a dual-band mode converter structure between dominant TE_{10} mode of rectangular waveguide and first higher order mode (TM_{01} mode) of circular waveguide. The given waveguide transition contains a two-section cavity supported with irises at sections' boundaries for matching. The designed converter operates at the satellite communication's transmit/receive (transceiver) frequency bands of 11.75-12.14 GHz and 13.67-14 GHz with more than 10 dB return loss and 15 dB suppression of undesired TE_{11} and TE_{21} modes of circular waveguide.

1. Introduction

In the microwave channels of satellite communication, the waveguide structures are generally used for high power necessity especially at the transmitter part of the system. High microwave power is usually carried with rectangular waveguides in the channels. The satellite systems generally operate at Ku-Band in Europe with separate downlink (transmitter with respect to satellite) frequency band from 10.7 GHz to 12.75 GHz and uplink (receiver with respect to satellite) frequency band from 12.75 GHz to 14.5 GHz. Thus, rectangular waveguide of WR75 is frequently used in satellite communication applications due to its dimensions compatible with the given frequency bands.

The antennas placed at the end of the microwave channels of satellites have usually circular symmetries in geometry, and they should be fed by circular waveguides. Consequently, a rectangular-to-circular waveguide transition is needed inside the microwave channel to convey the microwave power carried in rectangular waveguide to the antennas fed by circular waveguide. Although, there are other feeding mechanisms such as coaxial pin feed of circular waveguides [1-3] or dielectric mode converters [4], these are not durable in terms of shock, vibrations and thermal stability, and they cannot provide required high power transmission. In most of the waveguide applications, these transition structures make mode conversion between the fundamental (dominant) TE_{10} mode of rectangular waveguide and a specific mode of circular waveguide. This specific mode for circular waveguide is mostly fundamental (dominant) TE_{11} mode that transition between rectangular-to-circular waveguides usually provides conversion between these fundamental modes [5, 6]. On the other hand, the conversion between rectangular TE_{10} mode and higher order mode of circular waveguide such as TM_{01} mode [7, 8] or TE_{01} mode [9] is also possible. Especially, in the applications of satellite communication such as telemetry and/or telecommand, which uses omnidirectional antennas, circular symmetry in field is needed inside the antennas in addition to circular symmetry in geometry. For these applications, rectangular-to-circular waveguide transition, which realizes mode conversion between rectangular TE_{10} mode and circular TM_{01} mode having circular symmetry in magnetic field by suppressing all other modes of circular waveguide including dominant TE_{11} mode, should be used. Although TE_{10} - TM_{01} mode converters operated at only transmitter or receiver frequency band exist [7, 8, 10]; in this study, a dual–band TE_{10} - TM_{01} mode converter operated at both frequency (transceiver) bands of satellite communication applications, is designed and presented for the first time in literature.

2. Single Band TE_{10} – TM_{01} Mode Converters for Transmitter and Receiver Structures

The proposed dual-band structure is developed from the single band transition given in Figure 1.

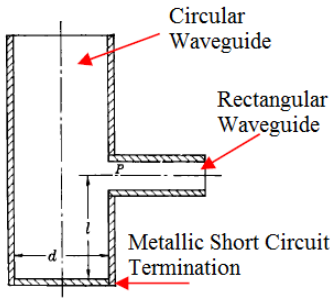

Figure 1: Single band rectangular-to-circular waveguide transition for TE_{10} – TM_{01} mode converter structure.

The transition structure in Figure 1 consists of two fundamental design parameters: the diameter of the circular waveguide (d), and the distance between point P and the short circuit termination (l).

For an effective TE_{10} – TM_{01} mode conversion in a wider bandwidth [7], d should be selected as the half of the guided wavelength of TM_{01} mode ($\lambda_{g,TM01}/2$) as given in (1), and l should be three-quarters of the guided wavelength of fundamental TE_{11} mode ($3\lambda_{g,TE11}/4$) as given in (2)

$$\beta = \sqrt{k^2 - \left(\frac{4.81}{d}\right)^2} = \frac{2\pi}{\lambda_{g,TM01}} = \frac{\pi}{d} \quad (1)$$

$$l = \frac{3\lambda_{g,TE11}}{4} = \frac{6\pi}{4\sqrt{k^2 - \left(\frac{3.68}{d}\right)^2}} \quad (2)$$

where $k = 2\pi f / c$ is the free-space wavenumber. The selection in (2) makes an effective suppression of dominant TE_{11} mode by transforming short circuit impedance at the bottom wall of the structure (metallic short circuit termination in Figure 1) into high impedance at point P for this mode. Therefore, the fields for TE_{11} mode are weakly excited in the circular waveguide.

In the previous work realized by the authors in [10], two separate single band TE_{10} – TM_{01} mode converters were designed at the transmit frequency of f_1 = 11.75 GHz and receive frequency of f_2 = 14 GHz. The calculated dimensions in Figure 1 are obtained by using (1) and (2) at the indicated frequencies, which are given in Table 1.

Table 1: The dimensions of the designed single band rectangular-to-circular waveguide transition structures for TE_{10} – TM_{01} mode converter.

Parameters	@ 11.75 GHz	@ 14 GHz
l (calculated)	25 mm	20.9 mm
l (optimized)	24.6 mm	20.1 mm
d (calculated)	23.3 mm	19.6 mm
d (optimized)	23.4 mm	19.6 mm

The designed structures are constructed in CST Microwave Studio as shown in Figure 2. As shown in Figure 2, circular waveguide in the structure has constant diameter of *d* along the propagation direction (+z axis in Figure 2) that there are no irises or tapered structures inside the circular waveguide for the given geometry.

The dimensions of the designed structures are optimized to give widest bandwidth around f_1 = 11.75 GHz and f_2 = 14 GHz as possible. The optimized *"d"* and *"l"* values obtained by CST Microwave Studio (CST MWS) are also given in Table 1 such that the parameter values are observed to be highly close to the theoretical ones.

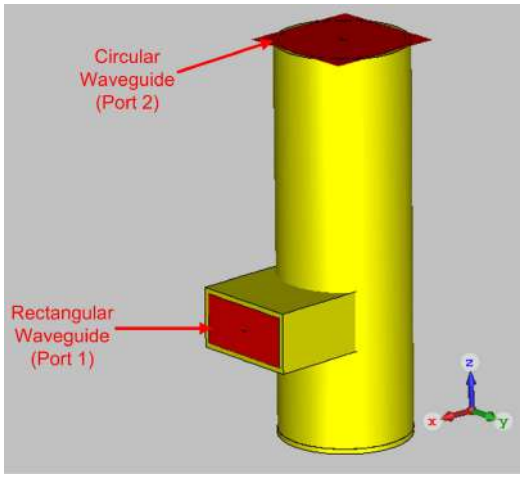

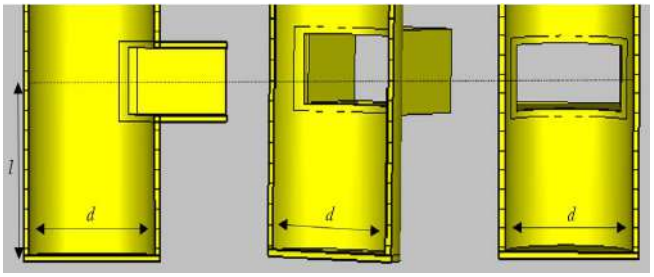

Figure 2: 3D and cut views (in CST Microwave Studio) of single band rectangular-to-circular waveguide transition for TE_{10} – TM_{01} mode converter structure at 11.75 and 14 GHz.

According to the results in [10], the single frequency bands were found as 11.25-12.1 GHz and 13.4-14.3 GHz for separate transmitter and receiver transition structures, respectively. Minimum 10 dB return loss, minimum 15 dB suppression of undesired modes (including fundamental TE_{11} mode), and maximum 0.25 dB transmission loss of desired TM_{01} mode were obtained within the given frequency bands.

3. Proposed Dual Band TE_{10} – TM_{01} Mode Converter for Transceiver Structure

In the proposed design of this study, individual mode converters, which are explained in the previous section and worked at different single frequency bands, are combined to give a sole transceiver structure. The cut views of the designed structure operated at multiple frequency bands around f_1 = 11.75 GHz and f_2 = 14 GHz are depicted in Figure 3. Since it is not possible to cover both frequency bands simultaneously with a uniform circular waveguide with constant diameter along propagation axis, the designed structure has circular waveguides with different diameters with additional irises. As shown in Figure 3, the cavities of single band transition structures below rectangular waveguide in Section 2 are cascaded to give a two-section cavity. This cavity contains circular waveguides with larger diameter of 23 mm and smaller diameter of 18 mm, which are highly close to the cavity diameters of transmitter and receiver structures of Section 2, respectively. In order to suppress the undesired fundamental TE_{11} mode at around 11.75 and 14 GHz, total electrical path length below rectangular waveguide in Figure 3 should be odd integer multiple of $\lambda_{g,TE11}/4$ (for high impedance transformation of TE11 mode explained in Section 2) at 11.75 GHz and 14 GHz. Although the cavity length dimensions of 19.7 mm and 7.1 mm, which are optimized by CST MWS, result in almost $3\lambda_{g,TE11}/4$ path length below rectangular waveguide at 11.75 GHz; total path length is about $\lambda_{g,TE11}$ at 14 GHz. However, the addition of two irises each having 1 mm thickness at the sections' boundaries, which increases the flexibility in the design parameters by bringing reactance effect in the equivalent circuit model, provides the sufficient suppression of TE_{11} mode also at 14 GHz. The diameters of irises are optimized to not only improve suppression of TE_{11} mode at 14 GHz but also give better return loss performance especially at around 11.75 GHz.

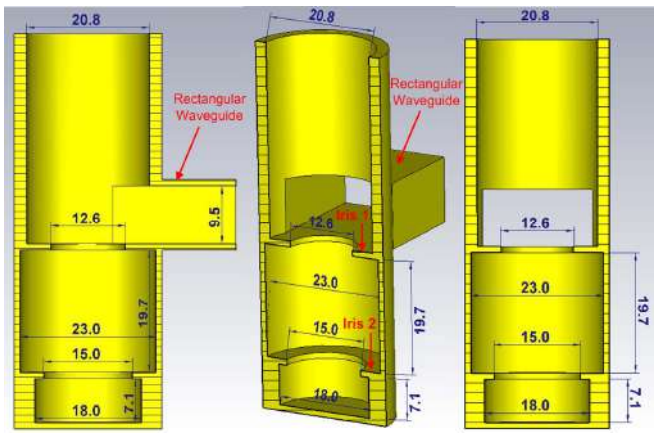

Figure 3: The cross-section simulation views of dual band rectangular-to-circular waveguide transition for $TE_{10} - TM_{01}$ mode conversion along with the dimensions of the realized design in this study. Dimensions are in mm.

The circular waveguide above rectangular waveguide, at which the desired TM_{01} mode at the frequency bands around 11.75 GHz and 14 GHz is carried, has an optimized diameter value of 20.8 mm. It is found from the simulations that if this diameter value is selected to be lower (close to 18 mm), the attenuation (loss) in the transmission of desired TM_{01} mode at 11.75 GHz increases since the cutoff frequency for TM_{01} mode increases towards 11.75 GHz within this waveguide. On the other hand, when the diameter above rectangular waveguide in Figure 3 is chosen to be higher (close to 23 mm), the suppression performance of TE_{21} mode (second higher order mode) at 14 GHz degrades as being lower than 15 dB since the cutoff frequency for TE_{21} mode becomes lower than 14 GHz allowing TE_{21} mode propagation inside the circular waveguide above rectangular waveguide. Therefore, the diameter of this circular waveguide is obtained to be between the diameters of cavity sections.

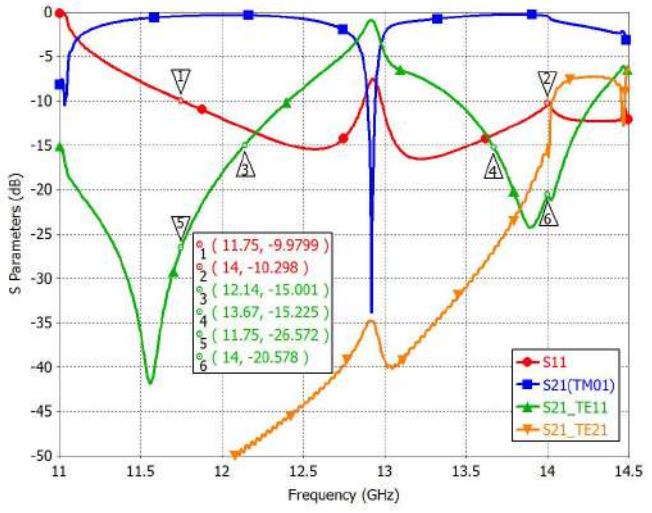

Figure 4: Reflection (S_{11}) and transmission (S_{21}) coefficients of the designed dual-band transition (transceiver) structure.

The scattering parameters of transceiver mode converter are given in Figure 4. It is obtained that the proposed transition structure performs more than 10 dB return loss, more than 15 dB suppression of undesired circular modes of TE_{11} and TE_{21} (other higher order modes have much better suppression values), and less than 0.5 dB transmission loss for the desired circular TM_{01} mode at transmitter and receiver frequency bands of 11.75 GHz - 12.14 GHz and 13.67 GHz - 14 GHz, respectively.

4. Conclusions

This study contains a dual-band rectangular-to-circular waveguide transition for the mode conversion between the rectangular waveguide's fundamental TE_{10} mode and circular waveguide's first higher TM_{01} mode having circular symmetry in terms of fields. This conversion is generally needed to excite circularly symmetric antennas with symmetric fields as in telemetry/telecommand (TTC) satellite communication applications. The designed structure contains a two-section cavity and two irises below rectangular waveguide in order to provide effective attenuation of undesired circular waveguide modes of TE_{11}, TE_{21} (and other higher order modes), and transmission of desired TM_{01} mode at dual band. The dual-band transition is verified for the frequency bands of around 11.75 GHz and 14 GHz, which are typical frequencies for transmitter and receiver channels at Ku-band of satellite communication. Therefore, the proposed transition structure can be useful for transceiver systems of satellite communications by providing simultaneous operations at both transmit and receive frequencies.

References

[1] C.A. Balanis, *Advanced Engineering Electromagnetics (2nd Edition)*, Wiley, Hoboken, New Jersey, pp.495-496, 2012.

[2] J.L. Masa-Campos, J.M. Fernandez, M. Sierra-Perez, J.L. Fernandez-Jambrina, Omnidirectional circularly polarized slot antenna fed by a cylindrical waveguide in millimeter band, *Microwave Opt. Technol. Lett.*, 49(3): 638-642, 2007.

[3] K. Iigusa, T. Teshirogi, M. Fujita, S.-I. Yamamoto, T. Ikegami, A slot-array antenna on a coaxial cylinder with a circularly polarized conical beam, *Electronics and Communications in Japan (Part I: Communications)*, 83(3): 74-87, 2000.

[4] B.C. Park, J.H. Lee, Dual-band omnidirectional circularly polarized antenna using zeroth-and first-order modes, *IEEE Antennas Wireless Propag. Lett.*, 11(1): 407-410, 2002.

[5] C. Turkmen, M. Secmen, Circularly polarized hemispherical antennas for telemetry and telecommand applications in satellite communications, *10th IEEE European Conference on Antennas and Propagation (EUCAP),* Davos, Switzerland, pp. 1828-1832, 2016.

[6] M.E. Carkaci, M. Secmen, The prototype of a wideband Ku-band conical corrugated horn antenna with 3-D

printing technology, *Advanced Electromagnetics (AEM)*, 8(2): 39-47, 2019.

[7] C. Turkmen, M. Secmen, Omnidirectional and circularly polarized slotted antenna array with increased bandwidth performance by using non-identical waveguide slots, *Radio Science*, 53(11): 1406-1418, 2018.

[8] C.B. Top, D. Dogan, A circularly polarized omni-directional low loss Ka-band slot antenna, *In IEEE International Symposium on Antennas and Propagation Society*, Chicago, USA, pp. 1-2, 2012.

[9] C.F. Yu, T.H. Chang, High-performance circular TE_{01} mode converter, *IEEE Transactions on Microwave Theory and Techniques*, 53(12): 3794-3798, 2005.

[10] C. Turkmen, M. Secmen, The variations of omnidirectional circularly polarized antennas for satellite telemetry/telecommand applications, *IU-JEEE*, 17(2): 3351–3359, 2017.

Homogenization of 3D Metamaterial Particle Arrays for Oblique Propagation via a Microscopic Analysis

Theodosios D. Karamanos[1], Theodoros T. Zygiridis[2], and Nikolaos V. Kantartzis[1,*]

[1]Department of Electrical and Computer Engineering, Aristotle University of Thessaloniki, Thessaloniki, Greece
[2]Department of Electrical and Computer Engineering, University of Western Macedonia, Kozani, Greece
*corresponding author, e-mail: kant@auth.gr

Abstract

In this work, a rigorous technique for the calculation of the effective parameters of infinite 3D metamaterial particle arrays in the case of oblique wave propagation, is presented. The extracted polarizabilities of the consisting scatterer and the numerically retrieved wavenumber for the obliquely propagating electromagnetic waves are inserted into a properly modified first-principles homogenization technique, thus leading to the characterization of the effective medium. Finally, the proposed methodology is applied on two popular, anisotropic metamaterial resonators.

1. Introduction

First-principles homogenization methods have gained increased popularity for either metamaterial assessment or design, due to their ability to retrieve accurate and "naturally"-behaving Lorentzian constitutive parameters of an effective medium. Contrary to parameter retrieval techniques [1, 2], these schemes compute the effective parameters of 2D/3D particle arrays [3, 4] in terms of the electromagnetic response of the consisting particles. Such methodologies originate from classical effective medium approximations, i.e. the Clausius-Mossotti or the Maxwell-Garnett one, for which the knowledge of the polarizability matrix of each scatterer is mandatory [5, 6]. It should be stressed that because of non-local phenomena in periodic structures, effective constitutive parameters, also, depend on the respective wavenumber of a wave propagating through them. Specifically, for the bulk metamaterial case, efforts have been made to retrieve the bulk constitutive parameters for normal wave propagation and infinite 3D arrays of isotropic magnetodielectric spheres [3] as well as of omega-type bianisotropic scatterers [7]. Similar attempts have been conducted to compute the effective parameters for the case of oblique propagation through an infinite array of magneto-dielectric spheres [8], involving wavenumbers from a retrieval or Nicolson-Ross-Weir (NRW) algorithm [9]. Consequently, in this scenario the possibility of deriving inaccurate results increases, and, furthermore, the existing formulation for the oblique propagation problem limits the potential applications to the idealized example of magnetodielectric spheres.

In this paper, we extend the concept of first-principles homogenization for oblique wave propagation in realistic metamaterial structures. The goal of the proposed methodology is to calculate bulk parameters of an effective medium comprising of planar resonators for oblique propagation, via the *a priori* knowledge of the polarizability matrix of each particle and the wavenumber of the propagating wave. First, the first-principles technique is reformulated in order to include a TE wave, and eventually the desired constitutive parameters are expressed with regard to the polarizabilities of the particles, the wavenumber and the angle of propagation. Unlike previous attempts, the required wavenumber is obtained via numerical eigensolvers for the sake of enhanced accuracy, while the polarizability matrix of the consisting particles is acquired through dynamic extraction schemes. The featured method is, finally, applied to two realistic, metamaterial resonators for various angles of propagation of a TEx wave, and the results, so derived, are thoroughly analyzed and discussed.

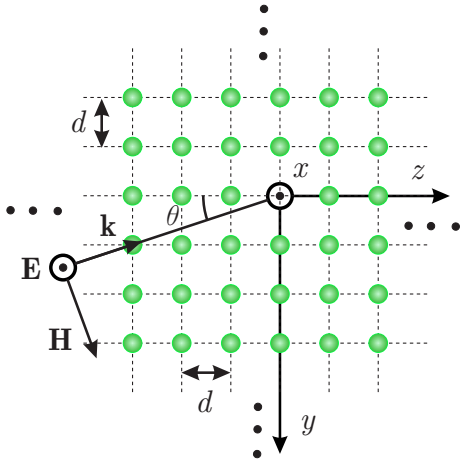

Figure 1: Transverse cut of an infinite cubic 3D array of omega-type bianisotropic scatterers and its corresponding Cartesian coordinates. The periodicity is set to $d = 10\,\text{mm}$ toward all axes.

2. Homogenization Algorithm

Let us assume the coordinate system of Fig. 1 at an infinite 3D array of identical, passive, omega-type bianisotropic scatterers particles, with vacuum as the background medium. If the particles are considered electrically-small, then they can be described by means of their respective polarizabilities, as a set of electric and magnetic

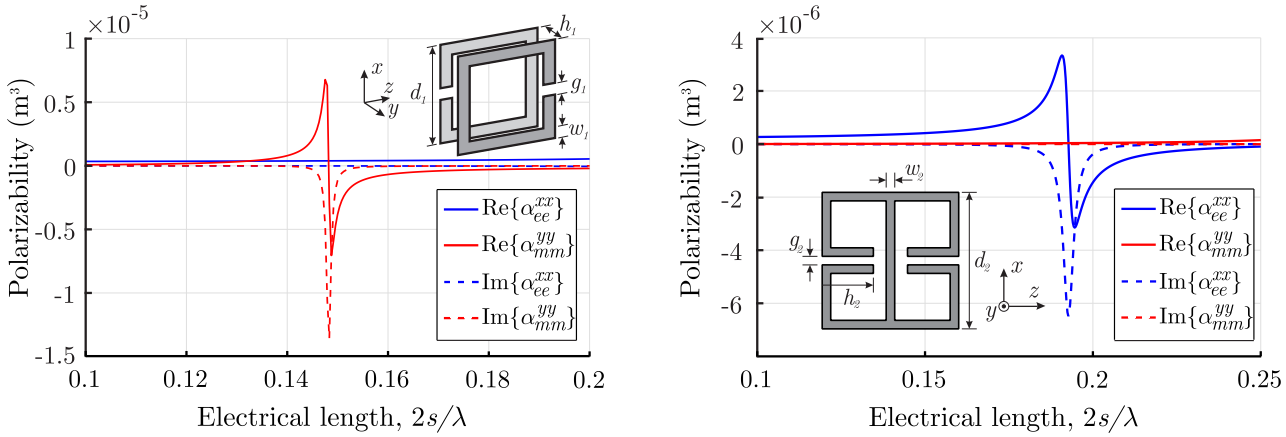

Figure 2: (a) The polarizabilites of the BC-SRR extracted via [10] (inlet shape: BC-SRR geometry, with $d_1 = 6\,\text{mm}$, $h_1 = 1\,\text{mm}$ and $w_1 = g_1 = 0.5\,\text{mm}$. The largest dimension is $s = 2r$.) and (b) the polarizabilites of the ERR extracted via [10] (inlet shape: ERR geometry, with $d_2 = 6\,\text{mm}$, $h_2 = 2\,\text{mm}$ and $w_2 = g_2 = 0.5\,\text{mm}$. The largest dimension is $s = \sqrt{2}d$.

dipoles. Additionally, if properly oriented planar scatterers are selected, the non-zero polarizabilities according to the axes of Fig. 1 are α_{ee}^{xx}, α_{em}^{xy}, and α_{mm}^{yy}, corresponding to the electric-electric, electric-magnetic, and magnetic-magnetic polarizabilities of the particle, respectively. Herein, they are extracted through the dynamic technique described in [10].

Considering the analysis of [8], the constitutive relations for the average fields, with regard to the axes of Fig. 1, are the following

$$D_{\text{av}}^{x} = \varepsilon_{\text{eff}}^{xx} E_{\text{av}}^{x} + (\chi_{\text{e,eff}}^{xy} - \chi_{\text{o,eff}}^{xy}) H_{\text{av}}^{y}, \tag{1a}$$

$$B_{\text{av}}^{y} = \mu_{\text{eff}}^{yy} H_{\text{av}}^{y} - (\chi_{\text{e,eff}}^{xy} + \chi_{\text{o,eff}}^{yx}) E_{\text{av}}^{x}, \tag{1b}$$

where the bianisotropy coefficient is split into an even and an odd part [3]. The relationship of the induced polarization with the average fields inside the equivalent medium can be written as

$$D_{\text{av}}^{x} = \varepsilon_0 E_{\text{av}}^{x} + P_{\text{av}}^{x}, \tag{2a}$$

$$B_{\text{av}}^{y} = \mu_0 H_{\text{av}}^{y} + \mu_0 M_{\text{av}}^{y}. \tag{2b}$$

In view of a microscopic analysis of the lattice, the induced polarization densities as a function of the fields, local to the constitutive particles, can be calculated at the origin of the axes in the form of

$$d^3 P_{\text{av}}^{x} = \alpha_{ee}^{xx} \varepsilon_0 (E_{\text{i}}^{x} + E_{\text{d}}^{x}) + \alpha_{em}^{xy} c_0^{-1} (H_{\text{i}}^{y} + H_{\text{d}}^{y}), \tag{3a}$$

$$d^3 M_{\text{av}}^{y} = -\alpha_{em}^{xy} \varepsilon_0 (E_{\text{i}}^{x} + E_{\text{d}}^{x}) + \alpha_{mm}^{yy} c_0^{-1} (H_{\text{i}}^{y} + H_{\text{d}}^{y}), \tag{3b}$$

with subscripts i and d referring to the respective incident and scattered fields on the particle at the origin of the axes. The latter can be expressed in terms of the induced polarization densities as

$$\varepsilon_0 E_{\text{d}}^{x} = C^{xx} d^3 P_{\text{av}}^{x} + D^{xy} d^3 c_0^{-1} M_{\text{av}}^{y}, \tag{4a}$$

$$c_0^{-1} H_{\text{d}}^{y} = C^{yy} d^3 M_{\text{av}}^{y} + D^{xy} d^3 P_{\text{av}}^{x}. \tag{4b}$$

where C^{xx}, C^{yy}, and D^{xy} are the 3D lattice co-field and cross-field interaction coefficients, correspondingly.

The effective parameters of (1) can, then, be derived by the modification of the homogenization formulas provided in [3, 8] for the case of normal and oblique incidence. In this paper, we consider the TEx wave case, with the wavevector of $\mathbf{k} = k_y \hat{\mathbf{y}} + k_z \hat{\mathbf{z}} = -k \sin\theta\, \hat{\mathbf{y}} + k \cos\theta\, \hat{\mathbf{z}}$, and a cubic lattice, as illustrated in Fig. 1. Thus, from Maxwell equations and the analysis in [3], it holds that

$$[k_0^2 - \mathbf{k}\times\mathbf{k}\times](\mathbf{E}_{\text{av}} - \mathbf{E}_{\text{i}}) = -k_0^2 \frac{\mathbf{P}_{\text{av}}}{\varepsilon_0} + k_0 \eta_0 \mathbf{k} \times \mathbf{M}_{\text{av}}, \tag{5a}$$

$$[k_0^2 - \mathbf{k}\times\mathbf{k}\times](\mathbf{H}_{\text{av}} - \mathbf{H}_{\text{i}}) = -k_0^2 \mathbf{M}_{\text{av}} - \frac{k_0}{\eta_0} \mathbf{k} \times \frac{\mathbf{P}_{\text{av}}}{\varepsilon_0}. \tag{5b}$$

Taking into account the geometry of the lattice and the particles of Fig. 1 and plugging $\mathbf{k}$, (4) become

$$E_{\text{av}}^{x} = E_{\text{i}}^{x} + \frac{k_0^2}{k^2 - k_0^2} \frac{P_{\text{av}}^{x}}{\varepsilon_0} + \frac{k_0 k \cos\theta}{k^2 - k_0^2} \eta_0 M_{\text{av}}^{y}, \tag{6a}$$

$$H_{\text{av}}^{y} = H_{\text{i}}^{y} + \frac{k_0^2}{k^2 - k_0^2} M_{\text{av}}^{y} + \frac{k_0 k \cos\theta}{k^2 - k_0^2} \frac{P_{\text{av}}^{x}}{\eta_0 \varepsilon}. \tag{6b}$$

Afterwards, (4) are inserted into (3), to express E_i^x and H_i^y with respect to the average polarization densities. Then, E_i^x and H_i^y are substituted into (6) and P_{av}^x and M_{av}^y are calculated as a function of the average fields. Finally, the average polarization densities are plugged into (2) and the constitutive parameters of the effective medium are obtained. Therefore,

$$\frac{\varepsilon_{\text{eff}}^{xx}}{\varepsilon_0} = 1 + N \frac{\text{A}_e - C_{\text{int}}^{yy}}{\Delta}, \tag{7a}$$

$$\frac{\mu_{\text{eff}}^{yy}}{\mu_0} = 1 + N \frac{\text{A}_m - C_{\text{int}}^{xx}}{\Delta}, \tag{7b}$$

$$c_0\, \chi_{\text{e,eff}}^{xy} = N \frac{A_{\text{em}}}{\Delta}, \quad c_0\, \chi_{\text{o,eff}}^{xy} = N \frac{D_{\text{int}}^{xy}}{\Delta}, \tag{7c}$$

with

$$\Delta = (\text{A}_e - C_{\text{int}}^{yy})(\text{A}_m - C_{\text{int}}^{xx}) - (D_{\text{int}}^{xy})^2 + \text{A}_{em}^2, \tag{8a}$$

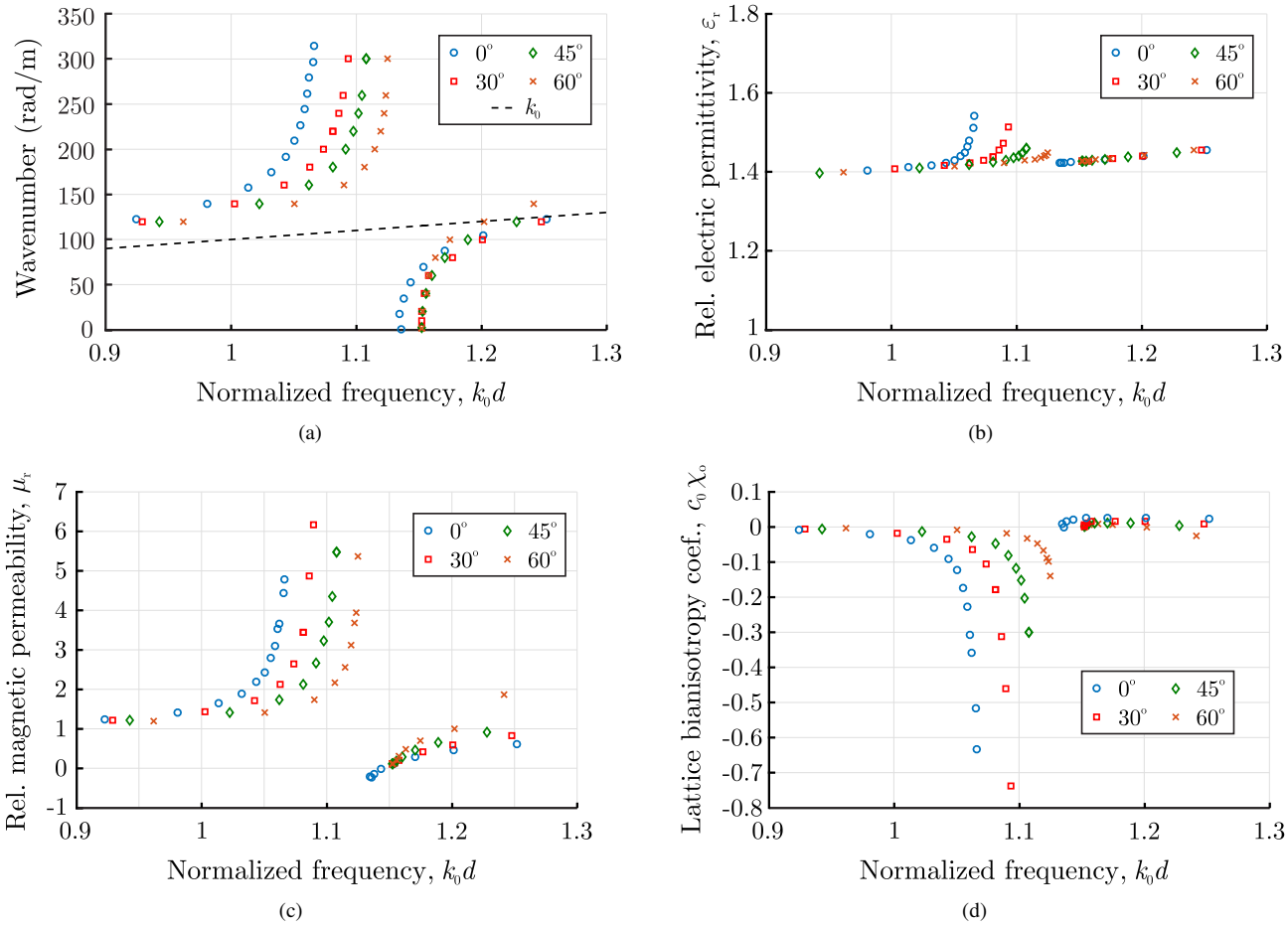

Figure 3: (a) Solutions of the eigenproblem for the BC-SRR resonator for different θ angles by means of [12]. Calculated (b) relative effective permittivity, (c) permeability, and (d) normalized odd part of the bianisotropy coefficient for various θ.

$$\mathrm{A}_e = \frac{\alpha_{ee}^{xx}}{\alpha_{ee}^{xx}\alpha_{mm}^{yy} + (\alpha_{em}^{xy})^2}, \tag{8b}$$

$$\mathrm{A}_m = \frac{\alpha_{mm}^{yy}}{\alpha_{ee}^{xx}\alpha_{mm}^{yy} + (\alpha_{em}^{xy})^2}, \tag{8c}$$

$$\mathrm{A}_{em} = \frac{\alpha_{em}^{xy}}{\alpha_{ee}^{xx}\alpha_{mm}^{yy} + (\alpha_{em}^{xy})^2}, \tag{8d}$$

and

$$C_{\mathrm{int}}^{ii} = C^{ii} - N\,\frac{k_0^2}{k^2 - k_0^2}, \qquad i = \{x, y\} \tag{9a}$$

$$D_{\mathrm{int}}^{xy} = D^{xy} - N\,\frac{k k_0 \cos\theta}{k^2 - k_0^2}, \tag{9b}$$

Coefficients C^{xx}, C^{yy}, and D^{xy} are computed in terms of rapidly converging Green function series [7, 11]. Moreover, from the symmetry of the problem, it is deduced that $C^{yy}(k_x, k_y, k_z, d) = C^{xx}(k_y, k_x, k_z, d)$ [11]. Notice in (7b), that the even part of the bianisotropy coefficient, $\chi_{\mathrm{e,eff}}^{xy}$, is associated with the bianisotropic effects caused by the attributes of the scatterer's geometry, or, the polarizability α_{em}^{xy}. Similarly, the odd part $\chi_{\mathrm{o,eff}}^{xy}$ refers to the bianisotropic effects, arising in the lattice geometry and the excitation on electric and magnetic dipoles perpendicular to each other, collectively expressed by the interaction coefficient D^{xy}.

As deduced from (9), the wavenumber k is required for our calculations. In the analysis of [8], the effective parameters for oblique propagation have been obtained utilizing extracted k values from a modified NRW technique [9]. However, since only a single unit-cell along z-axis is employed for the extraction of k, there exists a deviation from the featured problem of the infinite 3D scatterer array. In this work, to guarantee accuracy, the necessary wavenumber is numerically derived through the CST MWS™ computational package [12].

3. Results and Discussion

To verify its efficiency, the proposed homogenization technique is applied to two well-established metamaterial scatterers, i.e. the square broadside-coupled split-ring resonator (BC-SRR) [13] and the electric ring resonator (ERR) [14], as depicted in the inlet sketches of Fig. 2. Both scatterers employed, herein, are anisotropic and selected for their simplicity, without any loss of generality. Firstly, the polarizabilities of the particles are retrieved via the reflection/transmission coefficients using dynamic techniques [10, 15] and the results are displayed in Fig. 2. Figure 2(a) shows that the polarizabilities of the BC-SRR exhibit a magnetic resonator behavior at the first resonance, which is, basically, excited when a magnetic field is perpendicu-

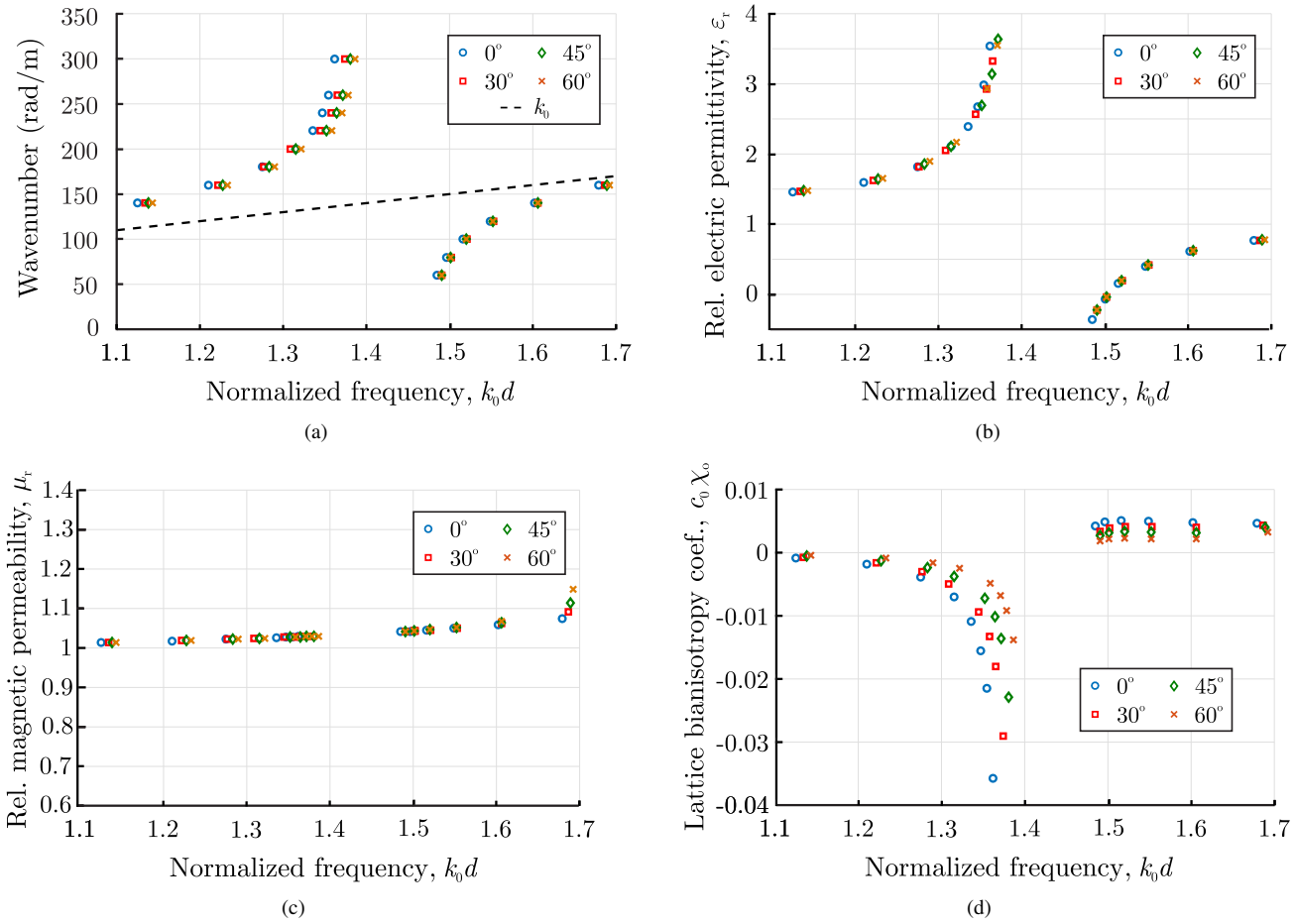

Figure 4: (a) Solutions of the eigenproblem for the ERR resonator for different θ angles by means of [12]. Calculated (b) relative effective permittivity, (c) permeability and (d) normalized odd part of the bianisotropy coefficient for various θ.

larly induced to its loop. Likewise, the outcomes of Fig. 2b reveal an electric resonator behavior for the ERR, primarily, excited when an incident electric field is parallel to the gaps of the resonator.

Subsequently, the constitutive parameters for the effective media comprising the respective resonators are calculated through the featured method. For the BC-SRR case, the eigensolver numerical simulation results for a periodic unit-cell along x-, y-, and z-axis and diverse angles of propagation θ, are provided in Fig. 3(a). The bandgap regions are associated with a reported μ-negative (MNG) or μ-near-zero (MNZ) behavior for the BC-SRR, when placed in 3D orthogonal periodic lattices, and become narrower with the increase of θ, as lower values of magnitude of H^y_{av} are coupled with the loop of the resonator. Next, the extracted polarizabilities of the particle (Fig. 2(a)) along with the retrieved k values are inserted into (7)-(9) to compute the effective parameters for the respective angles of propagation. The scatterer is reported to be anisotropic or $\alpha^{xy}_{em} = 0$, thus, $c_0\chi^{xy}_{\text{e,eff}} = 0$. The calculated homogenized medium parameters are illustrated in Figs. 3(b), 3(c), and 3(d), which confirm the expected MNG/MNZ behavior (Fig. 3(c)), indicated by the bandgap regions. Near-zero or negative values of the ε_r or μ_r relative parameters are associated with very low or imaginary wavenumbers, respectively, leading to a non-propagating and rapidly evanescent wave at these frequencies. Furthermore, the MNG attributes of the effective medium ($\mu < 0$) and the resonance amplitude diminish with the increase of θ, owing to the same magnetic field coupling reasons, mentioned above. One should observe the low, yet not negligible, $\chi^{xy}_{\text{o,eff}}$ values, produced by the non-zero cross-field interaction coefficient D^{xy}.

The second application investigates the ERR resonator, whose eigensolver simulation results for the same periodic unit-cell and angles of propagation θ, as in the BC-SRR configuration, are shown in Fig. 4(a). The bandgap regions are associated, herein, with a ε-negative (ENG) or ε-near-zero (ENZ) behavior for the first resonance, when placed in 3D orthogonal periodic lattices. Nonetheless, this phenomenon does not diminish significantly as θ increases, since it is reported that the ERR can function as an electric resonator for both y and z incidences [14]. Such a behavior can be justified by the fact that the local E^x field component of the a TEx wave is parallel to the gaps of the ERR, regardless of θ variation. However, a slight narrowing of the bandgap with the increase of θ is observed, which will be explained later on. Then, the extracted polarizabilities of the particle (Fig. 2(b)) as well as the simulated k values (Fig. 4(a)), are inserted into (7)-(9) to acquire the effective parameters for the respective angles of propagation. This

scatterer is, also, anisotropic, hence, $c_0\chi^{xy}_{\mathrm{e,eff}} = 0$. In this context, the calculated homogenized medium parameters are presented in Figs. 4(b), 4(c), and 4(d), which, again, certify the anticipated ENG/ENZ behavior (Fig. 4(b)), indicated by the bandgap regions and negative ε values. The ENG attributes of the effective medium remain unaffected with θ variation, in accordance with the reports of [14]. Nevertheless, the $\chi^{xy}_{\mathrm{o,eff}}$ values, related to the bianisotropy due to the lattice and expressed via the interaction coefficient D^{xy}, decrease with the increase of θ. As a consequence, the small decrease of the bandgap with the increase of θ, depicted in Fig. 4(a), considering the steady behavior of the effective ε and μ (Fig. 4(b) and Fig. 4(c)), can, therefore, be attributed to the respective behavior of $\chi^{xy}_{\mathrm{o,eff}}$. This important conclusion, to the best of the authors' knowledge, consists the first indication for the existence of distinct bianisotropic effects caused by the lattice, even if the effective medium consists of anisotropic particles, on the condition that electric and magnetic dipoles, perpendicular to each other, can be excited. Finally, as an overall evaluation, all artifacts that usually occur in NRW-based techniques, namely anti-resonances and non-passivity, are, herein, absent, hence, providing effective ε and μ consistent with a "natural" Lorentz-type dielectric medium.

4. Conclusions

An efficient technique for the precise effective parameter retrieval of metamaterial structures in the case of oblique propagation has been introduced in this paper. Initially, the consisting particles of the cubic lattice, under study, are considered to be equivalent to a collection of electric and magnetic dipoles placed at their shape center. The development of the featured method stems from the expansion of a popular first-principles algorithm for the case of oblique propagation inside the lattice, and, in particular, for a TEx wave. The required polarizabilities have been obtained via a dynamic extraction approach, while the wavenumber for propagation through the grid has been derived by means of a rigorous numerical solver. Finally, the proposed technique has been applied to two planar resonators for various propagation angles, with all results found to be physically meaningful and without or practically negligible artifacts. Also, the bianisotropy effects caused by the 3D array in the subsequent effective medium, even if it involves anisotropic particles, were identified and adequately discussed.

Regarding future endeavors, the presented algorithm will be extended to other types of obliquely propagating waves inside the infinite array, like the TM ones. Additionally, other classes of scatterers, e.g. helices or omega-type banisotropic particles, can be incorporated in the analysis, while, lastly, the featured methodology may be expanded to include interfaces rather than infinite arrays, thus moving toward practical, real-world implementations.

References

[1] U. C. Hasar, G. Buldu, Y. Kaya, and G. Ozturk, "Determination of effective constitutive parameters of inhomogeneous metamaterials with bianisotropy," *IEEE Trans Microw. Theory Techn.*, vol. 66, no. 8, pp. 3734–3744, Aug. 2018.

[2] K. Mnasri, A. Khrabustovskyi, M. Plum, and C. Rockstuhl, "Retrieving effective material parameters of metamaterials characterized by nonlocal constitutive relations," *Phys. Rev. B*, vol. 99, art. 035442, 2019.

[3] A. Alù, "First-principles homogenization theory for periodic metamaterials," *Phys. Rev. B*, vol. 84, no. 7, art. 075153, 2011.

[4] V. S Asadchy, A. Daz-Rubio, and S. A. Tretyakov, "Bianisotropic metasurfaces: Physics and applications," *Nanophoton.*, vol. 7, no. 6, pp. 1069–1094, 2018.

[5] A. Sihvola, "Homogenization principles and effect of mixing on dielectric behavior," *Photonics Nanostructures Fundamem. Appl.*, vol. 11, no. 4, pp. 364373, 2013.

[6] V. A. Markel, "Maxwell Garnett approximation (advanced topics): Tutorial," *J. Opt. Soc. Am. A*, vol. 33, no. 11, pp. 2237–2255 2016.

[7] T. D. Karamanos and N. V. Kantartzis, "Effective parameter calculation of 3D bianisotropic scatterer arrays through extracted polarizabilities," in Proc. *URSI International Symposium on Electromagnetic Theory (EMTS)*, Espoo, Finland, pp. 1–6, 2016.

[8] X.-X. Liu and A. Alù, "Generalized retrieval method for metamaterial constitutive parameters based on a physically driven homogenization approach," *Phys. Rev. B*, vol. 87, no. 23, art. 235136, 2013.

[9] C. Menzel, C. Rockstuhl, T. Paul, F. Lederer, and T. Pertsch, "Retrieving effective parameters for metamaterials at oblique incidence," *Phys. Rev. B*, vol. 77, no. 19, art. 195328, 2008.

[10] T. D. Karamanos and N. V. Kantartzis, "Full polarizability matrix extraction formulas for electrically small particles via reflection/transmission coefficients," *Progress in Electromagn. Res. B*, vol. 82, pp. 93–114, 2018.

[11] A. D. Scher, *Boundary effects in the electromagnetic response of a metamaterial using the point-dipole interaction model*, Ph.D. Thesis, University of Colorado at Boulder, CO, 2008.

[12] CST Microwave Studio™, *Computer Simulation Technology*, 2017.

[13] R. Marqués, F. Mesa, J. Martel, and F. Medina, "Comparative analysis of edge-and broadside-coupled split ring resonators for metamaterial design-theory and experiments," *IEEE Trans. Antennas Propag.*, vol. 51, no. 10, pp. 2572–2581, 2003.

[14] H. T. Chen, J. F. OHara, A. J. Taylor, R. D. Averitt, C. Highstrete, M. Lee, and W. J. Padilla, "Complementary planar terahertz metamaterials," *Opt. Express*, vol. 15, no. 3, pp. 1084–1095, 2007.

[15] A. D. Scher and E. F. Kuester, "Boundary effects in the electromagnetic response of a metamaterial in the case of normal incidence," *Progress in Electromagn. Res. B*, vol. 14, pp. 341-381, 2009.

Microwaves, Millimeter Waves, and THz

Towards Universality and Programmability in THz Chip-scale Sensors in CMOS

Kaushik Sengupta[1]

[1] Department of Electrical Engineering, Princeton University, NJ 08544.

Abstract

In this paper, we demonstrate an approach towards enabling a reconfigurable THz sensor interface that can be dynamically programmed for optimal response against spectrum (0.1-1.0 THz), angles of incidence and polarizations, while being operable at room temperature. We directly program the impressed current surface under THz incidence on the electromagnetic scattering interface depending on the incidence field properties. By allowing simultaneous sensing and reconfiguration at deep sub-wavelength scales, we create a map between the reconfigurable electromagnetic states to optimal reception for incident THz field properties. The approach allows us to overcome the limitations of singular devices at THz while allowing system-level reconfigurability, approaching a universal THz interface.

1. Introduction: THz Interface on Chip and Sub-wavelength Reconfiguration

Chip-scale Terahertz (THz) sensors operating at room temperature that are programmable across the incident field properties has transformative application potential in chemical sensing, biomedical imaging, spectroscopy and security. This is critically important since information at THz is often spread across multiple frequency points across the spectrum and therefore hyper-spectral sensing at THz is emerging as a powerful tool in this spectrum. In addition, the ability to reconfigure the sensor platform across various angles of incidence and polarization can allow fast electronic scanning and fast image acquisition [**?**].

Typically, such sensors are limited in their responsivity to all the three properties of the incident field. Allowing such reconfigurability in a chip-scale form is even more challenging since devices are typically inefficient in their sensitivity and reconfiguration at these frequencies. In this, CMOS-based integrated circuit technology is a powerful platform since it allows extremely high levels of integration giving the ability to realize highly complex systems in chip-scale form at low cost. This importance cannot be emphasized enough and an immediate success story can be seen in the revolution of modern day wireless connectivity that rests on highly integrated radio frequency integrated circuits (RFICs). However, cut-off frequencies of silicon-based transistors are much lower compared to III-V devices (such as InP), and therefore enabling such universality in the THz sensing interfaces is extremely challenging.

Here, we present a method to overcome limitations of singular devices through distributed approaches to sensing and reconfiguration. Integrating the THz electromagnetic interface in a CMOS chip allows direct interfacing with potentially millions of active devices. Here, we employ direct digital programming and absorption at the interface under incident THz fields to allow a universally programmable sensor interface across spectrum (0.1-1.0 THz), angle of incidence and polarization simultaneously [**?**, **?**].

2. Integrated Distributed THz Sensor and Interface

The overall concept behind the electromagnetic surface reconfiguration is shown in Fig. 1 [**?**]. The sensor responsivity is fundamentally dependent on the impressed surface current that is induced under the incident THz field. This is a function of the metal structure and the boundary conditions. In this work, we move away from a single-port antenna to a single detector to a distributed multi-port active THz sensing surface. The sensors and the reconfiguration sites are distributed over the antenna surface giving the ability to manipulate the surface current distribution at sub-wavelength scales that allows the incident power absorption at the reconfiguration sites. By moving away the traditional partitioned design approach, a new design space opens up to create a large set of THz sensor electromagnetic response. We map a subset of the reconfiguration states against the incident field properties to allow

- Spectral reconfigurability across 0.1-1.0 THz.
- Creation of a continuous phase surface to bend the receiver beam in a distributed non-coherent manner eliminating the need for complex phased arrays
- Rotate the polarization with sub-wavelength reconfiguration to allow for dynamic adaptability

3. Methods for the Multi-dimensional Optimization Process

The sensor interface with the log-periodic tooth surface and 16-subwavelength sensors is shown in Fig. 1. Each sensor site can be locally reconfigured with a 5-bit thermometer code, resulting in a total of $5^{16} = 152$ billion states. An example of this is shown in the simulated result in Fig.1, that demonstrates the bending of the reception beam with the programming of the digital states. The surface current is directly reconfigured creating a maximum responsivity at an off axis, similar to a phased array operating. In the process of enabling distributed reconfiguration with incoherent detectors, it avoids all the complexities of THz phased arrays and still achieves beam control. Therefore,

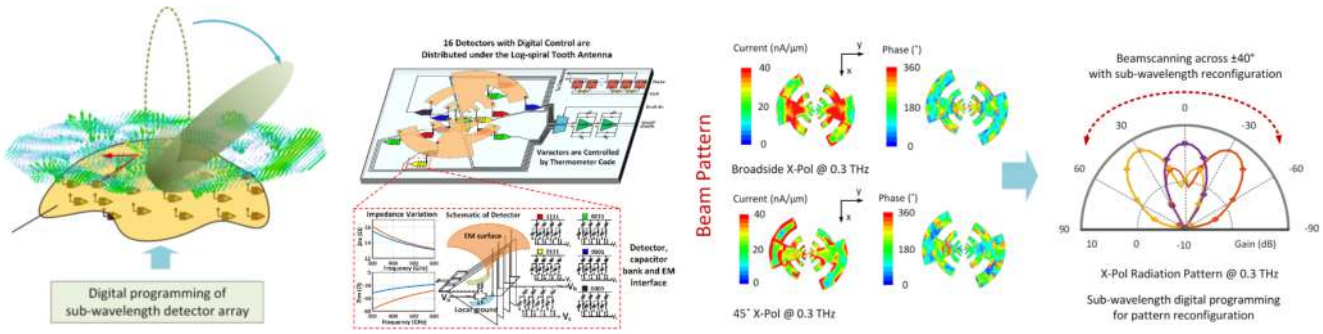

Figure 1: Single-chip THz sensor with distributed electromagnetic and sensor interface to allow for programmability against incident field properties to inject agility and universality in THz sensors [**?**, **?**].

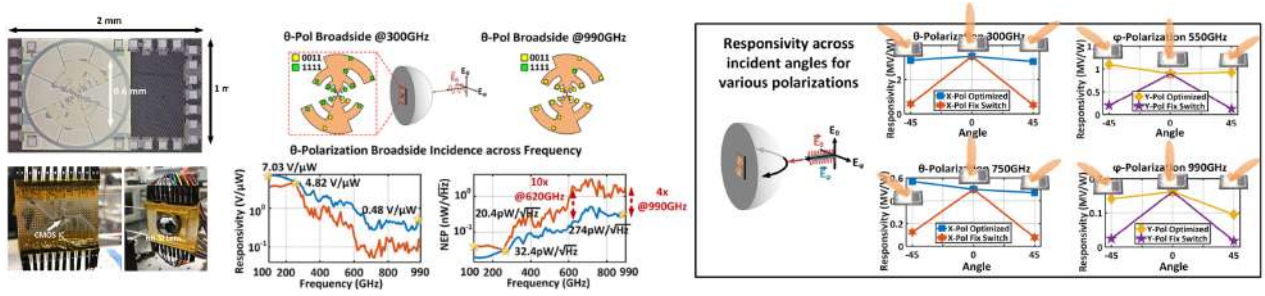

Figure 2: CMOS chip and measured reconfigurability with direct digital reconfiguration of the THz interface demonstrating 3x-10x enhancement across 0.1-1.0 THz, across various angles of incidence and polarization.

the aim of the sensor and interface design process is to maximize the range of reconfiguration across the three incident field properties. In this work, we follow a heuristic procedure to determine the number of detectors, their locations and sizes. In particular, we combine gradient decent optimization method with a random search algorithm in the 16-dimensional space. To randomize the effect of the intimal conditions, we allow the optimization to start with multiple random initial conditions and employ gradient descent to reach to the near optimal states. The entire interaction of the incident THz field at any frequency, angle of incidence ad polarization with the distributed scattering surface and detector impedance loading is taken into consideration in the design and optimization process.

4. Measurement Results

The chip is fabricated in a 65-nm industry standard CMOS process and is interfaced with a silicon lens and measured for reconfigurability with incident radiation across 0.1-1.0 THz, across various angles of incidence and polarization. Fig. 2 demonstrates the performance across the 900 GHz of reconfiguration space for both polarization. We compare the reconfigurable sensor response against a fixed baseline state optimized at 300 GHz. As can be seen, almost 4x-10x enhancement can be acheived through dynamic reconfiguration of the interface. The figure also shows two optimal states for the incidence at 300 GHz and 990 GHz. Evidently depending on the spectrum, different sensors contribute differently and the surface current need to be manipulated in a different fashion to allow optimal reception of the incident power. The chip also shows 3x-9x enhancement when measured across various angles of incidence across polarization and frequencies. The results demonstrates the key idea of beam and sensor manipulation through distributed in-coherent current manipulations. Through such methods of distributed sensing and field manipulation, new design spaces for chip-scale THz systems can open up to allow for efficient system-level programmability, critical for THz imaging and sensing applications.

References

[1] K. Sengupta, T.Nagatsuma, and D.Mittleman "Terahertz integrated electronic and hybrid electronicphotonic systems," *Nature Electronics*, vol. 1, pp. 622-635, Dec. 2018.

[2] X. Wu and K. Sengupta, "On-Chip THz Spectroscope Exploiting Electromagnetic Scattering With Multi-Port Antenna," *IEEE J.Solid-State Circuits*, vol. 51, no. 12, pp. 3049-3062, Dec. 2016.

[3] X.Wu and K.Sengupta, "Single-chip source-free terahertz spectroscope across 0.040.99 THz: combining sub-wavelength near-field sensing and regression analysis ," *Opt. Express*, vol. 26 (2018).

[4] X. Wu, H. Lu, X. Lu and K. Sengupta, "A Programmable Active THz Electromagnetic Surface on-Chip for Multi-functional Imaging," *IEEE Intl. Microw. Symp.*, pp. 1464-1467, 2018.

Thin film terahertz sources boosted by local field enhancement of pump laser and terahertz purcell effect

Zhanghua Han[1,*], Yuanmei Gao[1] and Sergey I. Bozhevolnyi[2]

[1]School of Physics and Electronic Engineering, Shandong Normal University, Jinan, China
[2]Center of Nano-optics, University of Southern Denmark, Odense M, Denmark
*corresponding author, E-mail: zhanghua.han@outlook.com

Abstract

We show that combing the dual effects of local field enhancement using bowtie antennas in a plasmonic slot waveguide for the pump lights and the Purcell effect using a split ring resonator for the generated terahertz field, efficient thin-film terahertz sources can be realized based on the nonlinear process of difference frequency generation using a nonlinear polymer embedded within the slot, showing an overall enhancement factor larger than 2×10^5 for the bare nonlinear polymer when the metallic structures are absent.

1. Introduction

Most terahertz (THz) continuous-wave (CW) sources nowadays are still inefficient and have low output powers, impeding the further development of THz science and its applications in various fields. Although solid state THz sources can provide mW level output for frequencies less than 200GHz and the frequency can be increased by a series of microwave amplifiers to around 1THz, the output power drops sharply as the frequency increases. On the high-frequency end, quantum well based quantum cascade lasers can provide high powers. But they are expensive, hard to use due the requirement of cryogenic conditions, and the frequency can be hardly below 2THz. Although THz pulsed sources have been more maturely developed thanks to the availability of high power ultra-fast lasers, the CW form of terahertz radiations are sometimes indispensable for applications like fast THz imaging, THz communications and high spectral resolution spectroscopy. Many approaches have been exploited to realize THz CW sources, among which difference frequency generation (DFG) based on the second order nonlinear process is conceptually the simplest one. However, the conventional DFG process based on nonlinear crystal usually needs to fulfill the phase-matching condition to realize high conversion efficiency and the crystal is usually quite bulky, hard to be incorporated into on-chip applications.

2. Structure and Results

While considerable research effort has been made on the conversion efficiency to terahertz radiations, to maximize the extraction of THz energy from the chip to the far field is of vital importance. In this work, we first show that a regular structure of split-ring resonator (SRR) can enhance the coupling of a dipole placed within this slit by 4 orders of magnitude compared to that when the case when the SRR is not present (see Fig. 1(a)). This dipole can be realized by using a bowtie antenna which is placed within the slit of the SRR, as schematically shown in Fig. 1(b). The bowtie antenna can also enhance the local electric field for both the two wavelengths of λ_1 and λ_2[1], which provide the frequency difference for the THz generation. Our calculations demonstrate that using a polymer material whose second order suseptibilty is set as $\chi^{(2)}$=200pm/V[2] and an incident power density of 0.013GW/cm2 for both λ_1 and λ_2 , a THz power of 13.75nW can be achieved with only one bowtie antenna structure. For comparison, we replaced all the gold structures in the simulations by the same thickness of the nonlinear polymer, and in this case the calculated THz output power is around 7×10^{-13} W, showing that the THz output boosted by both the pump light local field enhancement and the THz Purcell effect by a factor of 2×10^5. From the results in Fig. 1(a), one can see that the terahertz Purcell effect makes a contribution on the order of 10^4, and the rest enhancement comes from the hot spots of electric field within the bowtie antenna at the two pump wavelengths.

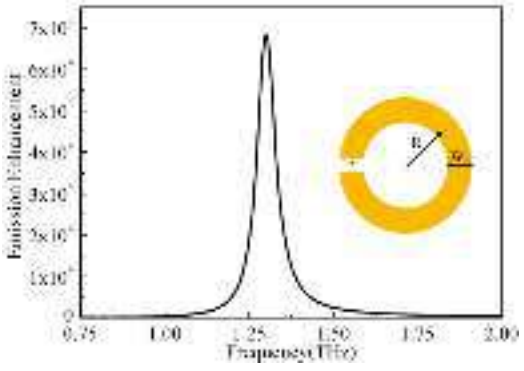

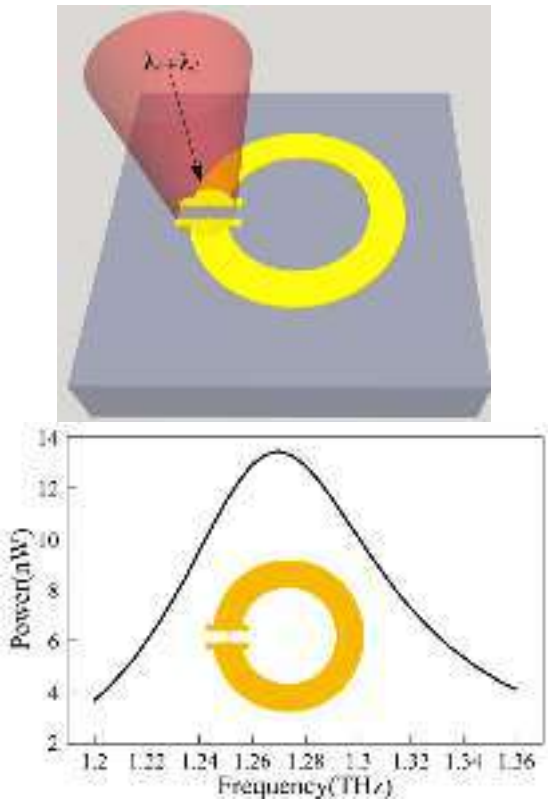

Fig. 1 (a) THz purcell effect using a SRR structure with a gap width of 600nm. (b) Schematic of the THz source incorporating both the bowtie antenna and the purcell effect. (c) Output power of the generated CW THz sources as a function of frequency.

3. Discussions and Conclusion

A higher power can be realized by incorporating more bowtie antennas within the same slit. Our results show that the dual effects of local field enhancement of the pump laser and the THz purcell effect can help together to realize efficent CW-form THz sources operating within 1-2THz, with a superior performance over most of the currently available THz souces.

As a conclusion, we have shown in this paper that the two resonators are used in the DFG process to help realize efficient THz sources, with one resonator (the bowtie antenna) used to enhance the local electric field of the pump lights and the subsequent optical-to-THz conversion, and the other resonator (the SRR) used to extract more power from the SRR slot the free space. An overall enhancement in the final THz output by a factor of 2×10^5 has been numerically demonstrated compared to the case when these two resonators are absent. Our results, together with other results reporting of manipulating THz radiation patterning and directionality by using a hyperbolic medium, show that some ideas in optical nanoantennas and optical metamaterials can be efficiently extended to the THz band. Such concepts may become helpful in the quest for realization of on-chip THz sources with acceptable output power. We expect that these results will assist in paving the way for further development of THz technology with the ultimate goal of bridging the THz gap.

References

[1] Moerner, W. E.; Kinkhabwala, A.; Yu, Z.; Fan, S.; Avlasevich, Y.; Mu, K. Large Single-Molecule Fluorescence Enhancements Produced by a Bowtie Nanoantenna. Nat. Photonics 2009, 3, 654–657.

[2] Salamin, Y.; Baeuerle, B.; Heni, W.; Abrecht, F. C.; Josten, A.; Fedoryshyn, Y.; Haffner, C.; Bonjour, R.; Watanabe, T.; Burla, M.; et al. Microwave Plasmonic Mixer in a Transparent Fibre – Wireless Link. Nat. Photonics 2018, 12, 749–753.

High gain Terahertz wave parametric amplifier using $LiNbO_3$ crystal

Kosuke Murate*, Guo Yunzhuo, Hikaru Sakai, Kodo Kawase

Nagoya University, Chikusa-ku, Nagoya 464-8603, Japan
E-mail: murate@nuee.nagoya-u.ac.jp
*corresponding author, E-mail: murate@nuee.nagoya-u.ac.jp

Abstract

In this research, we demonstrated a high-gain terahertz (THz) parametric amplifier for an extremely weak terahertz wave using MgO:$LiNbO_3$ crystal pumped by the microchip Nd:YAG laser. The amplification factor reached more than 100 dB by dividing the amplifier into two parts: the pre-amplifier and the main-amplifier.

1. Introduction

For several years, we have worked on the development of an injection-seeded Terahertz wave Parametric Generator (is-TPG) as a high-power terahertz wave source. Recently, the peak output power of is-TPG approached a few tens of kW after introducing a microchip Nd:YAG laser with a shorter pulse width [1]. It allows us to use is-TPG for many applications like illicit drug detection under thick envelopes and 3D computed tomography of plastics which is difficult with other systems[2,3].

In our previous work, we also achieved a 55-dB gain in terahertz wave amplification, based on the parametric process in MgO:$LiNbO_3$ crystals [4,5]. At that time, we attempted to amplify weak terahertz waves with frequencies around 1 THz; in this frequency range, the parametric gain was low, and our attempt was not successful. This was also attributed to energy losses associated with broadband spontaneous emission light, which we call Terahertz wave Parametric Generation (TPG) noise. In this research, we constructed a new type of terahertz parametric amplifier that suppressed TPG noise generation and improved the amplification gain.

2. Terahertz parametric amplification

When a high-power pump beam and seed beam are input into a MgO:$LiNbO_3$ crystal, a terahertz wave with a narrow line width and high brightness is generated by parametric wavelength conversion, an idler beam is also generated and amplified. This method is known as an is-TPG [1]. In an is-TPG, an infrared beam is used as the seed beam. On the other hand, in a terahertz parametric amplifier, a terahertz wave is used as the seed beam instead of an infrared beam. When a high-power pump beam and terahertz wave are input into a MgO:$LiNbO_3$ crystal, the terahertz wave is amplified by the parametric process in the crystal [4,5].

3. Experimental setup

Figure 1 shows the (a) previous and (b) new experimental setup for terahertz wave parametric amplification. In the previous setup, if the gain is increased by inputting higher energy pump beam or increasing the crystal length, most of gain is used for TPG noise generation, instead of amplified terahertz wave as shown in Fig.1 (a).

On the other hand, in the new configuration, the amplifier was divided into two parts, the pre-amplifier and the main-amplifier, to suppress TPG noise and enhance the amplification gain as shown in Fig.1(b). In the pre-amplifier, the terahertz wave of 1.05 THz from the is-TPG was input into the crystal along with a portion of the pump beam from a microchip Nd:YAG laser, satisfying the non-collinear phase-matching condition. Under nonlinear optical wavelength conversion, the terahertz wave was converted into a near infrared beam, i.e., the “idler beam”. The idler beam is dependent on the input terahertz wave. An iris

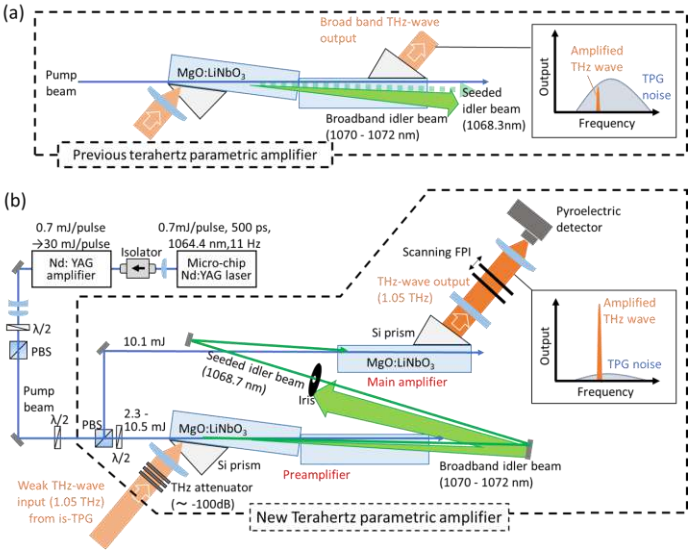

Figure 1: (a) Previous and (b) new setup for terahertz parametric amplifier.

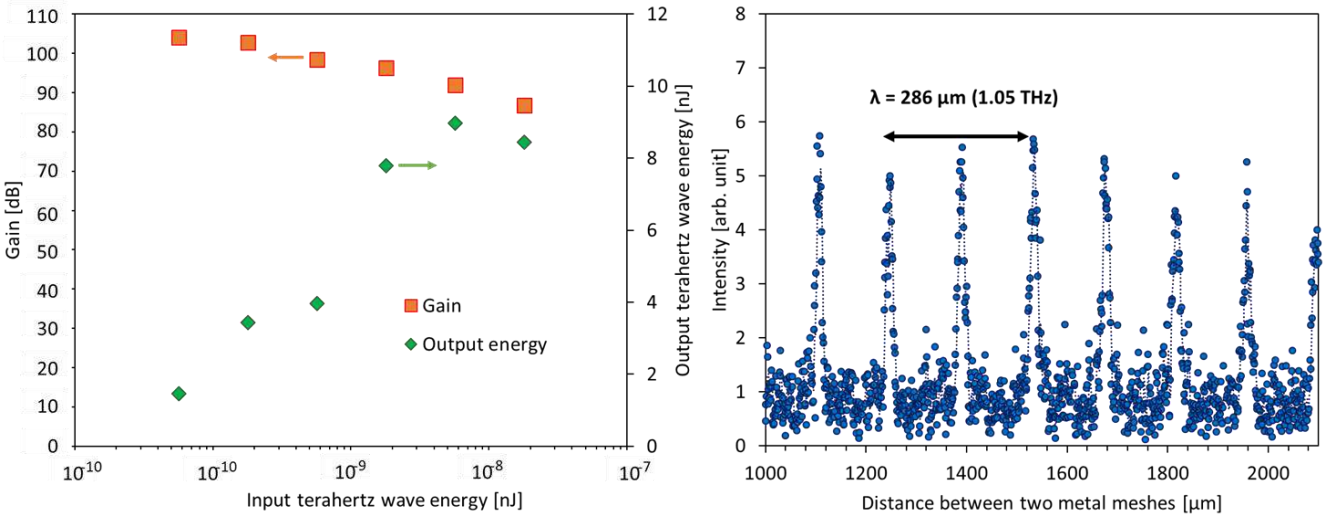

Figure 2: (a) The terahertz input energy dependence of the gain of the amplifier and output energy. (b) The transmission waveform of the scanning FPI inserted in the amplified terahertz wave path.

positioned behind the pre-amplifier isolated the idler beam and blocked the broadband TPG noise. Therefore, only the isolated idler beam can be injected into the crystal along with a portion of the pump beam to generate an amplified terahertz wave. The amplified terahertz wave was detected by a calibrated pyroelectric detector and the amplification factor of the system was measured.

We also placed a scanning Fabry–Pérot interferometer (FPI) in the output path to confirm whether the frequency of the input and output terahertz waves were the same. Two parallel metal meshes (97% reflectivity in 1 THz) were used as two mirrors in the interferometer. We observed the intensity of the transmitted terahertz wave while increasing the distance between the two meshes. We confirmed the frequency by observing the interference waveform.

4. Results

Figure 2 (a) shows the terahertz input energy dependence of the amplification factor and output energy. The amplification factor of the terahertz wave from the is-TPG with a frequency of 1.05 THz reached more than 10 billion (100 dB) when the input was 56 zJ (zJ=10^{-21}J), corresponding to an output of 1.45 nJ.

Figure 2 (b) shows the transmission waveform of the scanning FPI. A peak appeared every time the distance between the two meshes was an integer multiple of half-wavelength. Therefore, distance between two peaks indicates the wavelength of the transmitted terahertz wave. The wavelength of the output was confirmed to be 286 μm, corresponding to frequency of 1.05 THz, equal to the input.

Thus, we successfully demonstrated high-gain terahertz wave parametric amplification of extremely weak terahertz waves using the new amplification scheme.

5. Conclusion

In this research, we demonstrated a terahertz parametric amplifier with a gain of more than 100 dB for an extremely weak terahertz wave input. The amplification gain was low in our previous work due to broadband noise. This issue was resolved in the current study by dividing the amplifier into two parts to suppress noise and increase the parametric gain. We believe this work will contribute to the future development of terahertz applications.

Acknowledgements

The authors appreciate the fruitful discussions with Dr. S. Hayashi of NICT; Prof. T. Taira of IMS; Dr. H. Minamide and Dr. K. Nawata of Riken. This work was partially supported by JSPS KAKENHI Grant Number 18H03887, 18H05906.

References

[1] S. Hayashi, K. Nawata, T. Taira, J. Shikata, K. Kawase, and H. Minamide, Ultrabright continuously tunable terahertz-wave generation at room temperature, *Sci. Rep.* 4: 5045, 2014.

[2] M. Kato, S. R. Tripathi, K. Murate, K. Imayama, and K. Kawase, Non-destructive drug inspection in covering materials using a terahertz spectral imaging system with injection-seeded terahertz parametric generation and detection, *Opt. Express* 24: 6425, 2016.

[3] S. R. Tripathi, Y. Sugiyama, K. Murate, K. Imayama, and K. Kawase, Terahertz wave three-dimensional computed tomography based on injection-seeded terahertz wave parametric emitter and detector, *Opt. Express* 24: 6433, 2016.

[4] S. R. Tripathi, Y, Taira, S. Hayashi, K. Nawata, K. Murate, H. Minamide, and K. Kawase, Terahertz wave parametric amplifier, *Opt. Lett.* 39: 1649, 2014.

[5] Y. Taira, S. R. Tripathi, K. Murate, S. Hayashi, K. Nawata, H. Minamide, and K. Kawase, A Terahertz Wave Parametric Amplifier With a Gain of 55 dB *IEEE Trans. Terahertz Sci. Technol.* 4: 753, 2014.

Fiber-optic and Radio-wave Convergence for Ultra-Dense Small-cell and Moving-cell Networks

Pham Tien Dat[1,*], Atsushi Kanno[1], Naokatsu Yamamoto[1], and Tetsuya Kawanishi[1,2]

[1]National Institute of Information and Communications Technology, Tokyo 184-8795, Japan

[2]Waseda University, Tokyo 169-8050, Japan

*corresponding author: Email: ptdat@nict.go.jp

Abstract

We review our recently proposed systems for future mobile networks based on the seamless convergence of fiber-optic and radio-wave, including: a flexible and high-performance wireless fronthaul system in the millimeter-wave band, a system for generation and transmission of radio access signals in high-frequency bands, and a converged system for highly moving objects.

1. Introduction

Fifth generation (5G) and beyond networks with new requirements on data rate, latency, and ultra-dense radio cells pose many challenges to transport networks, especially fronthaul systems which transport radio signals from a cloud to antenna sites. The lack of fiber infrastructure in some dense urban and remote areas is another challenge for deployment of ultra-dense small-cell networks. It is also difficult to transmit radio access signals in high frequency bands to a large number of antenna sites, even with the use of the next generation fronthaul interface which is proposed to reduce the required data rate of fronthaul systems [1]. A convergence and cooperation of fiber transport and radio access networks would be very promising to resolve the challenges in the fronthaul systems. Furthermore, high-speed communications to highly moving users, such as those on high-speed trains, is considered one of the typical use cases in 5G and beyond networks [2]. Nevertheless, realization of such a high-speed and smooth communication network to highly moving users is extremely difficult because of frequent handovers, high penetration loss, and fast Doppler effects. A convergence of fiber-optic and radio-wave systems in high-frequency bands and the use of other advanced photonic technologies can be very useful to build such a network. Fig. 1 shows three different use cases of the convergence of fiber-optic and radio-wave systems. First, fiber–wireless systems can be used as an extension and/or a backup for an optical system for mobile fronthaul/backhaul transmission where the use of fiber cables is not possible or is too expensive (Fig. 1(a)). Second, a seamless fiber–wireless system can be attractive for generation and transmission of radio signals in high-frequency bands over fronthaul systems (Fig. 1(b)). In this case, the system can help to simplify antenna sites, and reduce the system cost, power consumption, and complexity. Third, the converged system with an adaptive signal routing technology can be very useful for high-speed and handover-free communications to highly moving objects, such as high-speed trains (Fig. 1(c)). In this paper, we review our recent systems and proof-of-concept demonstrations on the generation and transmission of radio signals over the converged fiber–radio systems.

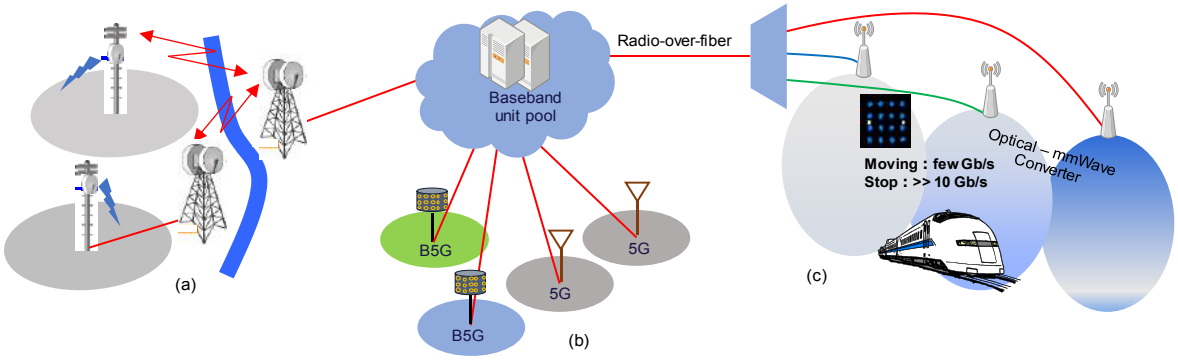

Fig. 1. Fiber–wireless converged systems: (a) converged fiber–mmWave bridge; (b) optical–wireless convergence for future radio access network; (c) optical–wireless system for moving-cell networks.

2. Example of convergence of fiber transport and radio access networks

In ultra-dense small-cell networks using radio signals in the millimeter-wave (mmWave) and sub-terahertz-wave bands, the transmission of signals over optical fronthaul systems is very challenging. Using digitized transmission methods, extremely high data rates are required for the transmission even to each antenna site. In addition, high-speed digital-to-analog and analog-to-digital converters are required at antenna sites, which significantly increase the system cost and complexity. Using analog radio-over-fiber systems, the transmission performance can be degraded because of impairments, such as fiber dispersion and nonlinear distortion effects. High-speed optical modulators should also be used for converting mmWave mobile signals to optical signals, which considerably increase the system cost. An optical heterodyne system is very attractive for generation, transmission, and up-conversion of radio signals to the mmWave bands.

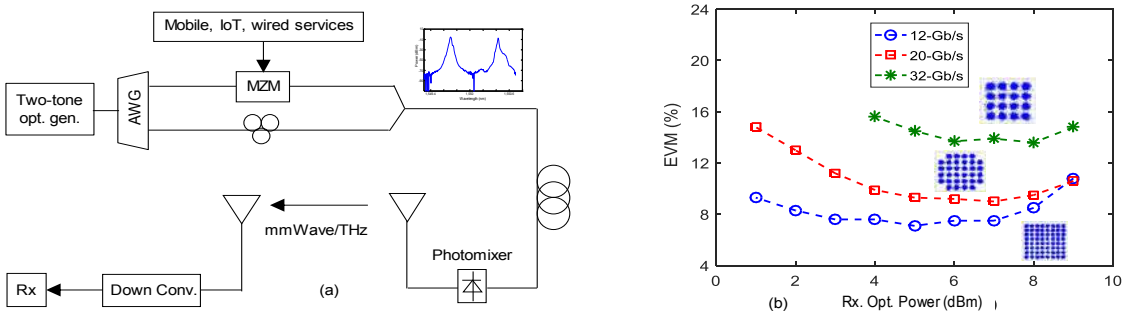

Fig. 2. (a) Schematic of an optical self-heterodyne system for generation and transmission of mmWave radio signals; (b) OFDM signal performance after being transmitted over the optical self-heterodyne system.

The schematic for the generation, transmission, and up-conversion of radio signals in the mmWave band over an optical fronthaul system is shown in Fig. 2(a). In this system, instead of transmitting directly radio signals in the mmWave band over the optical fronthaul, signals in low intermediate frequency bands are generated and transmitted over the fiber transport link. At the optical receiver, radio signals in the high frequency bands can be generated by up-converting the received optical signal using a high-speed photomixer [3]. First, a two-tone optical signal with a frequency separation between the sidebands of 89.6 GHz is generated using a high-precision optical modulation technology [4]. The two optical sidebands are separated by an arrayed waveguide grating, and one of them is modulated by an orthogonal frequency-division multiplexing (OFDM) signal. The modulated and unmodulated optical signals are then re-combined and amplified before being transmitted over a fiber to an optical receiver. The received optical signal is inputted to a high-speed photomixer for up-converting to the mmWave radio signal at 96.1 GHz. The signal is amplified before being transmitted into free space by a horn antenna. After being transmitted over approximately 1 m in free space, the signal is received by another horn antenna, down-converted by a coherent detection, and sent to a real-time oscilloscope. Fig. 2(b) shows the performance of the OFDM signal with different bandwidths and modulation levels. The results show that the converged system can provide a promising method for the transmission of mmWave radio signals over the optical fronthaul.

ACKNOWLEDGMENT

This work was support in part of the “Research and development for expansion of radio wave resources," by the Ministry of Internal Affairs and Communications (MIC), Japan, and in part by JSPS KAKENHI under grant 18K04156.

References

[1] J. Lee et al., “Spectrum for 5G: Global Status, Challenges, and Enabling Technologies,” IEEE Communication Magazine, Vol. 56, Iss. 3, pp. 12-18, March 2018.

[2] 3GPP TR 38.913 V14.2.0: “Study on Scenarios and Requirements for Next Generation Access Technologies,” Mar. 2017.

[3] P. T. Dat et al., “Seamless Convergence of Fiber and Wireless Systems for 5G and Beyond Networks,” IEEE J. Lightw. Technol., Vol. 37, Iss. 2, pp. 592 – 605, Jan. 2019.

[4] T. Kawanishi et al., “High-speed control of lightwave amplitude, phase, and frequency by use of electrooptic effect,” IEEE J. Sel. Topics Quantum Electron., Vol. 13, No. 1, pp. 79–91, Jan./Feb. 2007.

Ten Years of Terahertz Time-Domain Imaging in Heritage Science

Kaori Fukunaga

Electromagnetic Applications Laboratory, National Institute of Information and Communications Technology, Tokyo, Japan
*corresponding author, E-mail:kaori@nict.go.jp

Abstract

The biggest advantage of terahertz time domain imaging is that the technique can provide cross-section images of artworks non-destructively. The overview of 10 years terahertz time domain imaging activities in heritage science is discussed, by comparing with conventional and new imaging techniques in various frequency ranges.

1. Electromagnetic waves used in heritage science

Electromagnetic waves from microwave to X-ray are widely used in heritage science for material analyses as well as non-destructive internal structure imaging, although micro sampling can be required for precise chemical analyses to determine particular substance used in the work. Almost all instruments used in heritage science are based on well-established analytical techniques in industries. For example, Fourier transform infrared spectroscopy (FTIR), X-ray fluorescence (XRF) and X-ray diffraction (XRD) used in chemical industries, are essential tools for analyzing art materials. Recently developed multi- or hyper-spectral imaging systems are extremely useful for material mapping of paintings. [1, 2] Fig. 1 shows frequency bands and examples of images that can be obtained using those ranges. As shown in this figure, the band called far-infrared, sub-millimetre wave or terahertz (THz) exists between radio wave and ray, and thus the community is composed of various different research fields. Some art historians are interested in pigments which often prove the age, and the information can be obtained from very surface of an artwork. For conservators, on the other hand, its support and preparation layers are also important.

In the case of internal structure observation, the penetration depth and the spatial resolution are determined by a combination of the frequency and the object's physical properties (Fig. 2), and lower frequencies lead to deeper penetration depths at lower spatial resolutions. In general, microwave and millimetre wave imaging systems are based on radar technology, and photographic techniques include infrared (IR) and ultraviolet (UV) by choosing suitable wave lengths. X-ray radiography, especially X-ray CT has been commonly used to obtain three-dimensional structure at high resolution, although the object under test must be set in a particular place, and images are obtained in transmission mode. Thus, it is hardly applied to large scale objects such as wall paintings.

While THz technology is not yet commonly used in most industries, the THz time domain imaging technique has been adopted in heritage science, because it non-destructively reveals the internal layer structure from support to painted surface which is the most important part for conservation treatment. The activities for almost ten years around the world are mentioned in a mile-stone article of THz imaging by D. M. Mittleman [3]. Details of its technique are well-explained in previous papers and books. [4-6]

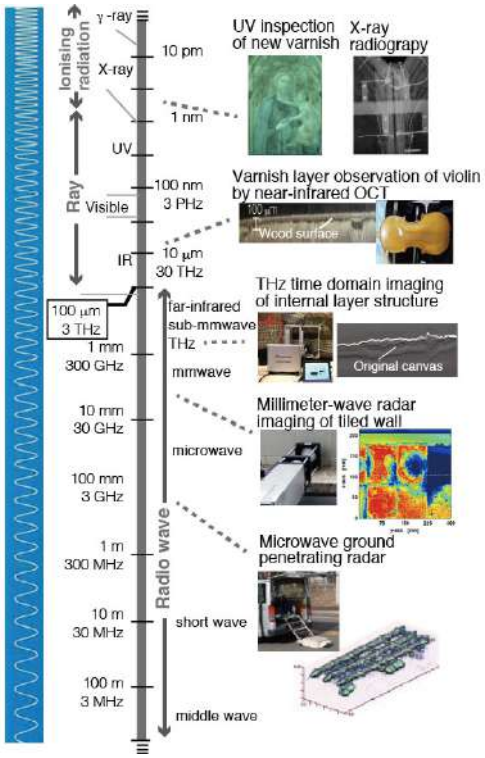

Figure 1: Examples of internal structure observation.

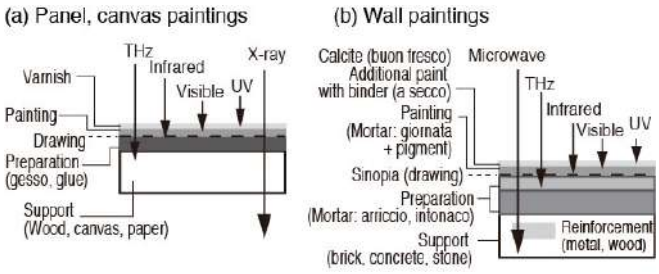

Figure 2: Typical structure of paintings and penetration depths of electromagnetic waves.

2. Internal structure observation by THz imaging

THz imaging technique has been applied to various museum objects, and some examples carried out by NICT are shown in Fig. 3, along the chronological table of art history. The first application was in 2008, during the conservation of "Polittico di Badia" (1300), a masterpiece of Giotto, at the Uffizi Gallery. The non-destructive cross-section image clearly showed that two gesso layers exist in the panel, which proved that the artist followed the medieval technique. In the case of Japanese panel screen, THz imaging is practically useful for condition check before conservation treatment. The panel is traditionally composed of three sets of supporting layers of paper on a latticed wooden mount. Full-scale conservation of a panel screen involves the replacement of supporting parts, and thus, the condition of their internal structure is important to estimate the works to be done. For example, THz imaging revealed many pieces of mending paper below the painting, which give the history of the artwork, as well as useful information for treatment planning. Among these examples, up to now, there are two unsolved issues. One is the painting technique of Bernt Notke's canvas painting "Danse Macabre" (15th century) in the Niguliste Museum in Estonia. Some parts have two painting layers. A conservation scientist suggested that the technique might be the glue-sized, which uses animal glue and pieces of thin fabric to paint. Further investigation is required to understand the experimental results and its painting technique. Another issue is over-paint layers of "Homme au Chapeau" (1915), by Pablo Picasso, in the Tokyo Station Gallery. The layer structure of the painting depends on the area. By extracting the second layer, the image becomes similar to a photograph shown in a catalogue [7], which is rather different from current image introduced in another catalogue and a book [8]. Art historians' viewpoints are required to understand these results.

We also discuss regulation issues that may cause some concerns in the telecommunication community.

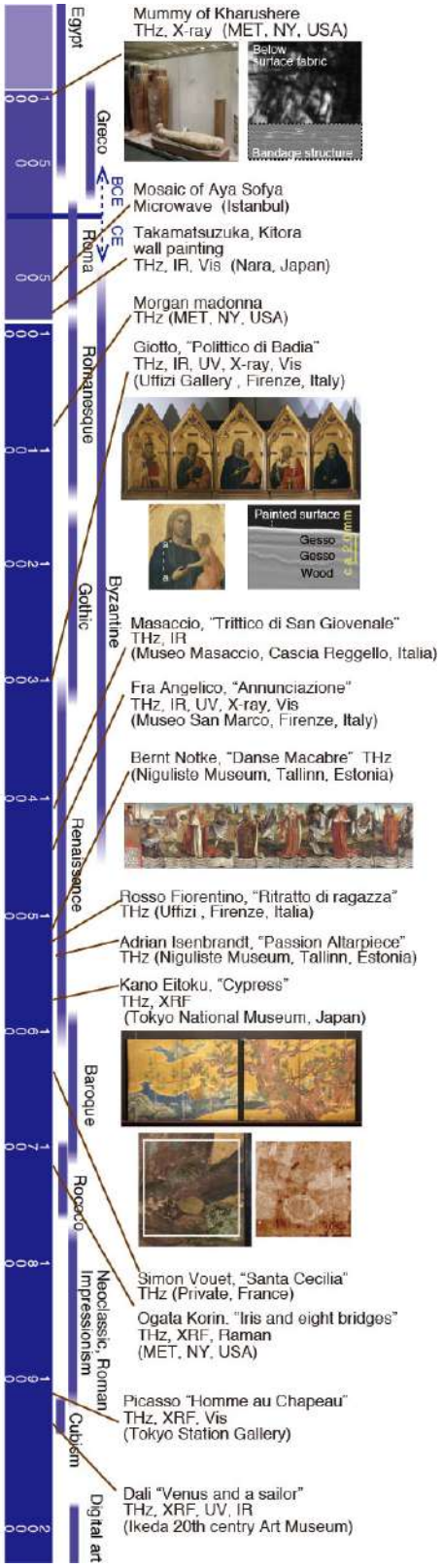

Figure 3: Examples of THz imaging activities.

References

[1] N. Masini, F. Soldovieri Eds., *Sensing the Past*, Springer, 2017.

[2] J. K. Delaney, et al., "Visible and infrared imaging spectroscopy of paintings and improved reflectography", Heritage Science, 2016. DOI: 10.1186/s40494-016-0075-4.

[3] D. M. Mittleman, "Twenty years of terahertz imaging", *Optics Express*, Vol. 26, pp. 9417-9431, 2018.

[4] B. B. Hu, M. C. Nuss, Imaging with terahertz waves, *Optics Letters*. Vol. 20, pp. 1716-1814, 1995.

[5] D. M. Mittleman, *Sensing with terahertz radiation*, Springer, 2003.

[6] K. Fukunaga, *THz Technology Applied to Cultural Heritage in Practice*, Springer, 2016.

[7] P. Daix, J. Rosselet, *Le Cubisme de Picasso*, Editions Ides et Calendes, Neuchâtel, p. 352, 1979.

[8] J. Richardson, *A Life of Picasso*, Jonathan Cape, London, p. 350, 1996.

Photoconductive germanium antenna emitting broadband THz pulses

Alexej Pashkin[1], Abhishek Singh[1], Stephan Winnerl[1], Manfred Helm[1,2], and Harald Schneider[1]

[1]Institute of Ion Beam Physics and Materials Research, Helmholtz-Zentrum Dresden-Rossendorf, Dresden, Germany
[2]Institute of Applied Physics, Technische Universität Dresden, Dresden, Germany

E-mail: a.pashkin@hzdr.de

Abstract

The spectral range between 5 and 10 THz is hardly accessible for time-resolved THz spectroscopy due to strong phonon absorption in many polar materials utilized for the generation of THz transients. We demonstrate that non-polar germanium is a promising semiconductor for a realization of a photoconductive THz emitter with a continuous spectrum spanning well above 10 THz.

1. Introduction

The THz frequency band is often referred to as *THz gap* due to difficulties faced by conventional microwave and optical technologies in this region of the electromagnetic spectrum. In spite of immense development in the last 3 decades to fill this gap, the 5-10 THz range within this band still remains elusive for most ultrafast spectroscopy techniques because of strong absorption bands in materials used for THz emission and detection [1, 2]. These absorption bands present in the radiated THz spectrum affect the THz intensity and the spectroscopy precision in their vicinity. The reason behind this is the polar nature of the solid state materials being used to fabricate the emitter and detector. The most common technique for a table-top room temperature emitter is the photoconductive technique, which relies on mainly two polar materials: GaAs and InGaAs. Due to polar crystal nature, their optical phonons are IR-active and hence absorb THz radiation at the phonon resonance frequency. Therefore, gapless spectra from GaAs and InGaAs photoconductive emitters are limited up to 7 THz. Other materials with second-order optical nonlinearity used for THz technology, e.g. ZnTe or GaP, are also polar and have phonon frequencies in the 5-10 THz band. For these reasons novel approaches for THz generation that do not rely on polar materials are highly demanded.

Here we demonstrate a Ge photoconductive emitter generating THz pulses with spectrum up to 13 THz which is free from any absorption bands if appropriate electro-optic detection is utilized. Ge is a centrosymmetric non-polar crystal and hence its phonons are not IR-active. Therefore, Ge shows high and almost uniform transmission of THz radiation up to frequencies more than 20 THz besides weak two-phonon absorption band near 10 THz [3]. On the other hand, the efficiency of THz emission from Ge antennae is similar to that of GaAs-based antennae due to the comparably high electron mobility.

2. Results

The studied photoconductive antennae are formed by bowtie-like electrode structures with 10 μm electrode gap deposited on a semiconductor substrate. Since the carrier lifetime in pure Ge is of the order of μs due to its indirect bandgap, we have utilized a Ti:sapphire amplified laser system operating at 250 kHz repetition rate in order avoid an accumulation of the photoexcited carriers. The pulse width was ~65 fs FWHM at the central wavelength of 800 nm.

The photoexcitation generates electron-hole pairs in the Ge substrate. These charge carriers are accelerated by the electric field between the electrodes biased by the voltage of 10 V. THz radiation emitted by the transient current passes through the Ge substrate and then it is collected and detected using off-axis parabolic mirrors in a standard time-domain spectroscopy setup. Electro-optic sampling using two different crystals, namely 40 μm ZnTe and 300 μm GaP, is used to record the THz waveforms and the spectra are obtained via Fourier transform. The results are shown in Fig. 1(a). However, the measured spectra are influenced by the frequency-dependent detector response. In addition, the finite pulse width of 65 fs of the pump and probe laser pulses gives rise to THz signal roll-off with increasing frequency. Detector response functions of both detector crystals are simulated according to reference [4]. Signal roll-off due to laser pulse widths is also included in the simulated response function and the results are shown in Fig. 1(b). In the observed spectra the GaP detector (blue curve) shows a gapless spectrum reaching up to 8 THz. This cutoff frequency is not the actual cut-off of the radiated THz pulse, but it is due to significant drop in the GaP detector response after 8 THz as shown in blue curve in Fig. 1(b).

The spectrum observed with the ZnTe detector shows a THz signal reaching up to frequencies more than 12.5 THz as shown with the black curve in Fig. 1(a). The simulated detector response of the ZnTe crystal has a sharp dip close

to 5 THz as shown in black in Fig. 1(b). Due to this dip in the detector response, the observed spectrum also has a dip close to 5 THz, otherwise the actual emitted THz radiation from Ge emitter is free from any sharp dips in the spectrum. The continuity of the spectrum observed with GaP also confirms that the actual emitted THz radiation does not have any dip in the spectrum close to 5 THz.

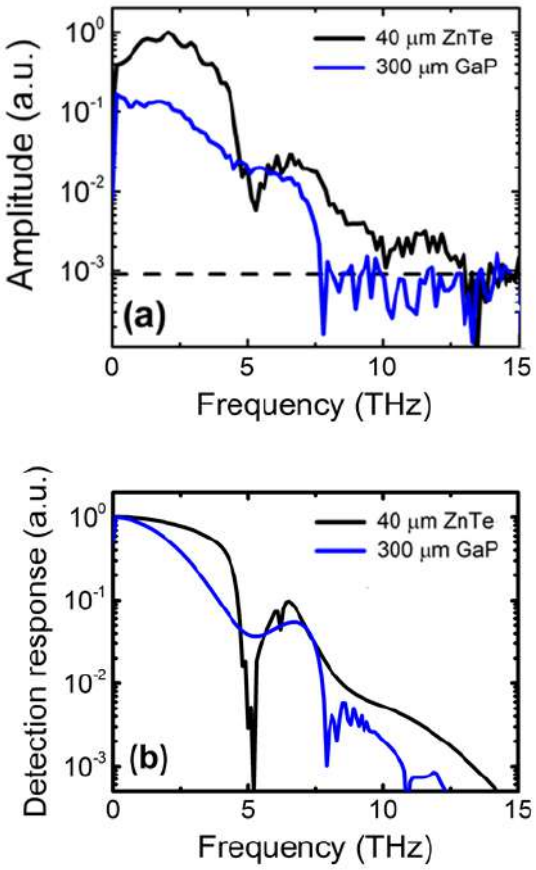

Figure 1: (a) Fourier transform of the THz pulse emitted from the Ge emitter and detected with GaP and ZnTe electro-optic detectors (adopted from [3].). (b) Simulated detector response function of both detectors including the roll-off contribution from the finite laser pulse width.

3. Conclusions

We have demonstrated that a Ge-based photoconductive emitter is capable to emit THz pulses covering frequency range beyond 10 THz. The efficiency of such emitter is comparable with its GaAs-based analog demonstrating a high potential of Ge for broadband THz technology. In addition, the relatively low bandgap energy of Ge ensures its compatibility with femtosecond fiber lasers operating at telecom wavelengths.

Acknowledgements

Support by the Nanofabrication Facilities Rossendorf at IBC is gratefully acknowledged.

References

[1] M. Tonouchi, Cutting-edge terahertz technology, *Nat. Photonics*, 1: 97–105, 2007.

[2] S. S. Dhillon, M. S. Vitiello, E. H. Linfield, A. G. Davies, M. C. Hoffmann, J. Booske, C. Paoloni, M. Gensch, P. Weightman, G. P. Williams, E. Castro-Camus, D. R. S. Cumming, F. Simoens, I. Escorcia-Carranza, J. Grant, S. Lucyszyn, M. Kuwata-Gonokami, K. Konishi, M. Koch, C. A. Schmuttenmaer, T. L. Cocker, R. Huber, A. G. Markelz, Z. D. Taylor, V. P. Wallace, J. A. Zeitler, J. Sibik, T. M. Korter, B. Ellison, S. Rea, P. Goldsmith, K. B. Cooper, R. Appleby, D. Pardo, P. G. Huggard, V. Krozer, H. Shams, M. Fice, C. Renaud, A. Seeds, A. Stöhr, M. Naftaly, N. Ridler, R. Clarke, J. E. Cunningham, M. B. Johnston, The 2017 terahertz science and technology Roadmap, *J. Phys. D: Appl. Phys*, 50: 043001, 2017.

[3] A. Singh, A. Pashkin, S. Winnerl, M. Helm, H. Schneider, Gapless broadband terahertz emission from a germanium photoconductive emitter, *ACS Photon.* 5: 2718−2723, 2018.

[4] A. Leitenstorfer, S. Hunsche, J. Shah, M. C. Nuss, W. H. Knox, Detectors and sources for ultrabroadband electro-optic sampling: Experiment and theory, *Appl. Phys. Lett.* 74: 1516−1518, 1999.

Deep Inverse Scattering

Uday K Khankhoje*, Yash Sanghvi, Yaswanth Kalepu

Department of Electrical Engineering,
Indian Institute of Technology Madras, Chennai, India
*corresponding author, e-mail: uday@ee.iitm.ac.in

Abstract

We study the problem of inverse scattering, where, the electrical properties of an object are inferred based on measurements of the electromagnetic fields scattered by the object. We incorporate deep neural networks into existing physics-based algorithms in order to achieve state of the art results. In particular, we extend the subspace optimization method and demonstrate the recovery of very high permittivity objects, and show how multi-frequency data can be leveraged for high resolution reconstructions beyond what is currently possible.

1. Introduction

In applications such as microwave breast cancer imaging or burried object detection, one is faced with the problem of determining the electrical properties of a remote system [1]. Typically, the object is illuminated with known electromagnetic fields and the scattered fields are collected at various points in space as permissible in the experimental setup. This leads to an inverse problem formulation between the known scattered fields and the unknown object permittivity.

The relationship between the object permittivity and the scattered fields is nonlinear; as a result, a non-convex optimization problem needs to be solved in order to determine the object permittivity. In addition, the problem is ill-posed and thus the solution strategy relies crucial on suitable a priori information which help regularize the problem.

For 'weak' scatterers (characterized by low values of permittivity), linear approximations give acceptable solutions [2]; however the more interesting proble arises when the permittivity is high (and thus mimicing realistic scenarios). Several solution strategies for these problems have been proposed in the past, for instance: [3, 4, 5, 6]. To overcome the ill-posedness of the problem, the above strategies have been ably assisted by various innovations in signal processing such as wavelet theory [7], compressive sensing approaches [8], and other related methods [9, 10]. Yet another approach has been to expand the scope of measurements to multiple frequencies and use lower frequency reconstructions (where the nonlinearity is less of an issue) as a priori information for the higher frequency reconstructions [11, 12].

2. Our Approach

In recent work [13] we have, through the use of deep learning techniques, proposed a framework for extended the range of existing inverse scattering algorithms such as the subspace optimization method (SOM) [9]. We recognized that the issue of nonlinearity becomes critical as the object permittivity increases, and thus the chances of an optimization problem settling into a local minima away from the true solution increases.

To overcome this, we start with a standard database of images [14], and suitably adapt it to a scattering problem, thereby generating a database of scattering objects and scattered fields. From this, we learn the relationship between the scattered field data and the null space of the scattering operator using a convolutional neural network. Now, we use any existing inverse scattering algorithm, but initialize it with the estimate provided by our custom neural network (NN). This strategy starts the optimization problem in the correct 'valley', thereby avoiding the issue of false minima. The NN takes negligible time to run, and fits in seamlessly into existing algorithms, thereby enhancing the range of object permittivities that can be retrieved . The results of the proposed method can be seen in Fig. 1, where a good recovery of the test object is observed. We have further validated the algorithm against experimental data.

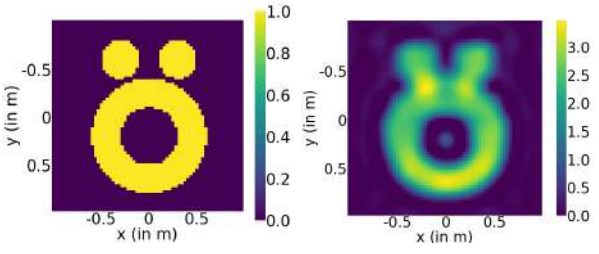

(a) True (b) Reconstruction

Figure 1: a) Generic *Austria* profile with contrast = 1 (b) Reconstruction for contrast = 3 using the proposed scheme. The colour bar represents the contrast values. Conventional methods fail for contrasts higher than 1.5.

We further extend this method to incorporate multi-frequency data. We observe two interesting consequences of doing so: in one case, the conventional frequency hoping approach [12] can be replaced by a deep learning enabled single frequency reconstruction; in another case, the range

of the multi-frequency approach can be extended by augmenting it with the deep learning approach.

3. Conclusion

We have shown an innovative extension of existing inverse scattering algorithms by augmenting them with ideas from deep learning. Apart from being able to recover strong scatterers, extensions to multi-frequency studies show that it is possible to reduce the experimental data collection time by collecting data at a single frequency and processing it via our proposed approach. These ideas hold a lot of promise for applications such as microwave breast cancer detection.

Acknowledgement

U K Khankhoje would like to acknowledge financial support from the Indian Institute of Technology Madras.

References

[1] N. K. Nikolova, "Microwave imaging for breast cancer," *IEEE microwave magazine*, vol. 12, no. 7, pp. 78–94, 2011.

[2] Y. Wang and W. C. Chew, "An iterative solution of the two-dimensional electromagnetic inverse scattering problem," *International Journal of Imaging Systems and Technology*, vol. 1, no. 1, pp. 100–108, 1989.

[3] W. C. Chew and Y.-M. Wang, "Reconstruction of two-dimensional permittivity distribution using the distorted born iterative method," *IEEE transactions on medical imaging*, vol. 9, no. 2, pp. 218–225, 1990.

[4] P. M. Van Den Berg and R. E. Kleinman, "A contrast source inversion method," *Inverse problems*, vol. 13, no. 6, p. 1607, 1997.

[5] X. Chen, "Subspace-based optimization method for solving inverse-scattering problems," *IEEE Transactions on Geoscience and Remote Sensing*, vol. 48, no. 1, pp. 42–49, 2010.

[6] Y. Zhong, M. Lambert, D. Lesselier, and X. Chen, "A new integral equation method to solve highly nonlinear inverse scattering problems," *IEEE Transactions on Antennas and Propagation*, vol. 64, no. 5, pp. 1788–1799, 2016.

[7] M. Li, O. Semerci, and A. Abubakar, "A contrast source inversion method in the wavelet domain," *Inverse Problems*, vol. 29, no. 2, p. 025015, 2013.

[8] G. Oliveri, M. Salucci, N. Anselmi, and A. Massa, "Compressive sensing as applied to inverse problems for imaging: Theory, applications, current trends, and open challenges." *IEEE Antennas and Propagation Magazine*, vol. 59, no. 5, pp. 34–46, 2017.

[9] Y. Zhong and X. Chen, "An fft twofold subspace-based optimization method for solving electromagnetic inverse scattering problems," *IEEE Transactions on Antennas and Propagation*, vol. 59, no. 3, pp. 914–927, 2011.

[10] G. Oliveri, P. Rocca, and A. Massa, "A bayesian-compressive-sampling-based inversion for imaging sparse scatterers," *IEEE Transactions on Geoscience and Remote Sensing*, vol. 49, no. 10, pp. 3993–4006, 2011.

[11] W. Chew and J. Lin, "A frequency-hopping approach for microwave imaging of large inhomogeneous bodies," *IEEE Microwave and Guided Wave Letters*, vol. 5, no. 12, pp. 439–441, 1995.

[12] O. M. Bucci, L. Crocco, T. Isernia, and V. Pascazio, "Inverse scattering problems with multifrequency data: reconstruction capabilities and solution strategies," *IEEE Transactions on Geoscience and Remote Sensing*, vol. 38, no. 4, pp. 1749–1756, 2000.

[13] Y. Sanghvi, Y. Kalepu, and U. K. Khankhoje, "Embedding deep learning in inverse scattering problems," *in revision, IEEE Transactions on Computational Imaging*, 2019.

[14] Y. LeCun, L. Bottou, Y. Bengio, and P. Haffner, "Gradient-based learning applied to document recognition," *Proceedings of the IEEE*, vol. 86, no. 11, pp. 2278–2324, 1998.

Current-Driven Plasmonic Instability in Graphene Metasurfaces for Terahertz Applications

Stephane Boubanga-Tombet[1], Deepika Yadav[1], Akira Satou[1], Wojciech Knap[2,3], Vyacheslav V. Popov[4], and Taiichi Otsuji[1]

[1]Research Institute of Electrical Communication, Tohoku University, Sendai, Japan
[2] Int'l Research Laboratory CENTERA, Institute of High Pressure Physics, Polish Academy of Sciences, Warsaw, Poland
[3]Laboratory Charles Coulomb, University of Montpellier and CNRS, Montpellier, France
[4] Kotelnikov Institute of Radio Engineering and Electronics (Saratov Branch), Russian Academy of Sciences, Saratov, Russia
*corresponding author, E-mail: otsuji@riec.tohoku.ac.jp

Abstract

We explore current-driven plasmon dynamics including perfect transparency and light amplification in monolayer graphene metasurfaces. Current-induced complete suppression of the graphene absorption is experimentally observed in a broad frequency range followed by a giant amplification (up to ~ 9 % gain) of an incoming terahertz radiation at room temperature.

1. Introduction

The generation and amplification of electromagnetic waves by plasmonic instabilities in conventional two-dimensional (2D) electron systems (2DESs) have been actively investigated since 1980 [1]. However, after about forty years, we are still a long way from the realization of efficient emitters and amplifiers based on those plasmonic instability-driven mechanisms. The intensity of radiation reported experimentally so far is weak, the plasmon resonances too broad and not tunable enough to be promising for device applications [2]. The rise of graphene and its extremely strong light-plasmon coupling and superior carrier transport properties [3] make this work worth to be revisited. We investigate dc current driven plasmonic instabilities in high mobility graphene meta-materials that combine the advantage of an efficient tunable absorber, emitter and amplifier at room temperature (RT).

2. Device structure and physics

Plasmon modes in our devices are excited in monolayer graphene on hexagonal boron nitride (hBN) with a periodic dual-grating gate structure [4] positioned above the graphene sheets. The grating gate modulates the incoming electromagnetic wave and defines the plasmonic wave vectors. The samples are fabricated as field effect transistors (Fig. 1) with structures featuring an interdigitated asymmetric-dual-grating-gate (ADGG) [5]. The plasmonic cavities are formed below the gates electrodes and designed with symmetric or asymmetric boundaries and electron mobilities around 50.000 cm^2/Vs at RT.

ADGG-bias-dependent electron density modulation causes spatial complementary modulation of the plasmon and drift velocities. This may cause Doppler-shift (DS) type, transit-time-modulation (TTM) type, Cherenkov (CK) type, and/or plasmonic boom (PB) type instabilities under asymmetric cavity boundaries [6][8]. When the instability-driven gain surpasses the Drude loss, the system yields the net gain, resulting in plasmon self oscillation at the resonant frequencies. The ADGG works as a broadband antenna that can convert the non-radiative plasma oscillations to radiative THz waves. This, in turn, enables spontaneous THz emission of radiation as well as coherent light amplification to the incident THz waves.

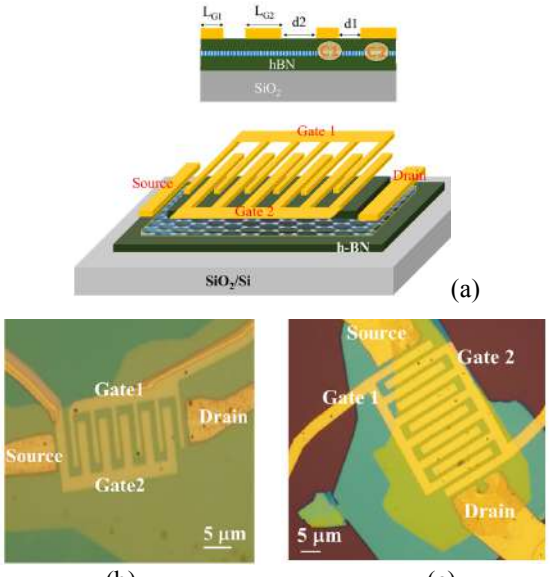

Figure 1: hBN/graphene/hBN FET with a DGG. (a) Bird's view schematic, (b) top view of an ADGG type sample, and (c) top view of a SDGG type sample.

3. Experimental results and discussion

We examined three samples: two ADGG type (ADGG1 (Fig. 1(b)) and ADGG2) and one symmetric DGG type (SDGG) alignment (Fig. 1(c)). With the applied gate

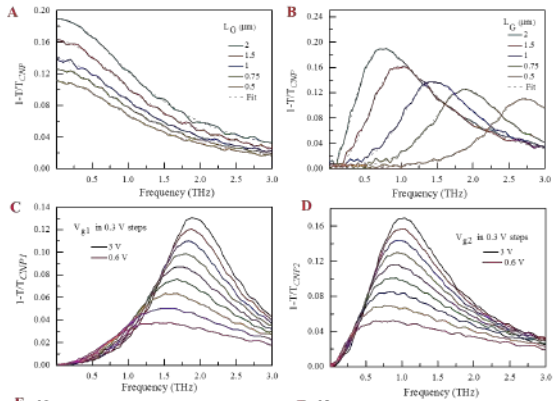

Figure 2: Measured extinction spectra at V_d = 0 V to the radiations with polarization parallel to the SDGG (a), perpendicular to the SDGG (b), ADGG-C1 (c), and ADGG-C2 (d).

voltages V_{g1} and V_{g2} each device supports the formation of two different plasmonic cavities (types C1 and C2) below the fingers of Gate 1 and Gate 2 in the DGG device structure (top part of Fig. 1). Terahertz (THz) time-domain spectroscopy (THz-TDS) was employed to measure the changes in the THz pulses transmitted through the graphene plasmonic cavities of type C1 (C2) when sweeping V_{g1} (V_{g2}) and keeping the voltage on the other gate electrode constant at the charge neutral point (CNP) $V_{g2} = V_{CNP2}$ ($V_{g1} = V_{CNP1}$). The source-to-drain voltage (V_d) dependent measurements were also conducted at a constant V_g. The transmission coefficient at a given V_g and V_d is referred to as T while T_{CNP} is the transmission coefficient at $V_g = V_{CNP}$. The measured extinction spectra ($1-T/T_{CNP}$) at V_d = 0 V exhibited similar tendencies of polarization-sensitive resonant absorptions among the three samples (Fig. 2).

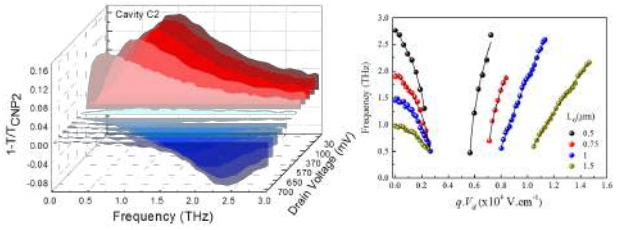

(a) (b)

Figure 3: Drain bias dependent extinction spectra of the graphene metamaterial. (a) Spectra measured in cavities C2 of device ADGG1 for fixed $V_{g2} - V_{CNP2}$ = 3 V and $V_{g1} = V_{CNP1}$ when varying V_d. (b) Drain bias dependent resonance frequencies, gain and phase spectra. Scaling laws of the measured graphene plasmon resonance frequency in the three devices as a function of characteristic field intensity qV_d and fits to data shown as solid lines, where q is the plasmon wave vector, $q = 2\pi/L_g$, and L_g is the gate length of one finger of the GG.

When V_d increases, the absorption peaks weakened with red shifting, only ADGG samples approaching perfect transparency over the measured entire frequency range (at V_d = 370 mV for C2 of ADGG1). Further increase in V_d for only ADGG samples gives rise to negative absorption peak, i.e. resonant amplification, appears in the extinction spectra with a noticeable blue shift, reaching the maximal gain (9%), which is far beyond the interband-transition-limited quantum efficiency (2.3%) (Fig. 3(a)). The measured frequency dependence of the extinction peaks perfectly traces the theory with sharp gain thresholds [7] (Fig. 3(b)). Considering the extracted plasmon and drift velocity relations, a mixture of DS and TTM instabilities may cause such phenomena.

4. Conclusions

We explored current-driven plasmon dynamics in monolayer graphene active metamaterials. Frequency tunable THz light amplification up to 9% gain at RT by current-driven plasmon instabilities produced in an ADGG-GFET structure has been successfully demonstrated.

Acknowledgements

We thank Dr. Dmitry Svintsov, Dr. Akira Satou, Pr. Michel Dyakonov, Pr. Victor Ryzhii and Pr. Michael S. Shur for helpful discussions. This work was supported by JSPS KAKENHI (#18H05331 and #16H06361), Japan.

References

[1] D. Tsui, E. Gornik, R. Logan, Far infrared emission from plasma oscillations of Si inversion layers. *Solid State Comm.* 35: 875–877, 1980.

[2] A. El Fatimy, N. Dyakonova, Y. Meziani, T. Otsuji, W. Knap, S. Vandenbrouk, K. Madjour, D. Theron, C. Gaquiere, M. Poisson, S. Delage, P. Prystawko, C. Skier- biszewsk, AlGaN/GaN high electron mobility transistors as a voltage-tunable room temperature terahertz sources. *J. Appl. Phys.* 107: 024504, 2010.

[3] L. Ju, B. Geng, J. Horng, C. Girit, M. Martin, Z. Hao, H. A. Bechtel, X. Liang, A. Zettl, Y. R. Shen, F. Wang, Graphene plasmonics for tunable terahertz metamaterials. *Nature Nanotechnol.* 6: 630–634, 2011.

[4] T. Otsuji, M. Hanabe, T. Nishimura and E. Sano, A grating-bicoupled plasma-wave photomixer with resonant-cavity enhanced structure, *Opt. Exp.* 14: 4815-4825, 2006.

[5] V. Popov, D. Fateev, T. Otsuji, Y. Meziani, D. Coquillat, W. Knap, Plasmonic terahertz detection by a double-grating-gate field-effect transistor structure with an asymmetric unit cell. *Appl. Phys. Lett.* 99: 243504, 2011.

[6] Y. Koseki, V. Ryzhii, T. Otsuji, V. V. Popov, and A. Satou, Giant plasmon instability in dual-grating-gate graphene field-effect transistor, *Phys. Rev. B* 93: 245408, 2016.

[7] S.A. Mikhailov, Plasma instability and amplification of electromagnetic waves in low-dimensional electron systems, *Phys. Rev. B* 58: 1517-1532, 1998.

[8] G. Aizin, J. Mikalopas, M. Shur, Current-driven plasmonic boom instability in three- dimensional gated periodic ballistic nanostructures. *Phys. Rev. B* 93: 195315, 2016.

Mirrorless backward terahertz-wave parametric oscillator with a slant-stripe-type PPLN

Hiroaki Minamide[1], Kouji Nawata[1], and Yu Tokizane[1]

[1]RIKEN center for Advanced Photonics, RIKEN, Sendai, Japan

*Corresponding author: Hiroaki Minamide, E-mail: minamide@riken.jp

Abstract

Backward optical parametric oscillators operating in the terahertz (THz)-frequency region have been developed with a mirrorless structure and a tunable wavelength. The robust and small (palmtop-sized) THz-wave source will facilitate the use of THz-frequency waves in many applications proposed in various fields.

1. Introduction

The backward optical parametric oscillator (OPO) is a promising light-source device offering many practical applications. A theory of the backward OPO was proposed as early as 1966 [1]. The wavelength conversion under a particular condition generates counter-propagating waves inside a nonlinear crystal, enabling a self-feedback effect without a cavity. In addition, the simple scheme of the backward OPO offers the benefits of compactness, stability, and light weight.

In particular, the backward OPO in the terahertz (THz) frequency region is attracting more attention because the development of a THz-wave source for general use has been long expected owing to its many proposed applications in nondestructive inspections. In addition, a wide tunability is necessary in such devices because of the THz finger-print spectra embedded in the THz-wave frequency region. However, the development of such a source is difficult due to the momentum mismatch between the propagating waves and the counter-propagating wave.

On the other hand, a quasi-phase-matching (QPM) device has the potential to generate backward THz-wave oscillation, and the momentum mismatch can be compensated by its use. A theoretical investigation conducted to realize a backward THz-wave parametric oscillation (TPO) was reported in a study [2]. The scheme of the optical configuration in the literature was based on a conventional optical condition, which is simplified to be a collinear phase matching when a pump beam irradiates normal to the grating period. Eventually, it could not be realized because an understanding of the detailed mechanism of backward OPO was necessary. However, the generation of backward THz-waves (excluding oscillation) using broadband femto-second lasers or dual-wavelength pump sources has been reported [3–6]. To generate backward TPO, the basis of stimulated polariton scattering in the lithium niobate nonlinear crystal must be understood clearly. Recently, the understanding has been gradually widened by the research on the high conversion efficiency between near-infrared light and THz-wave using MgO-doped lithium niobate, by following the reduction of a stimulated Brillouin scattering effect in the crystal [7–13]. Therefore, we can now investigate the actual potential of lithium niobate to generate THz waves.

In this study, we present a novel phenomenon of backward THz-wave oscillation and a new phase-matching condition using a slant-stripe-type periodically poled lithium niobate (PPLN) [14]. A wide tunability and narrow linewidth were achieved without any cavity. This backward TPO is expected to expand the practical applications of THz-wave.

2. Experimental setup and results

Figure 1 shows a mirrorless TPO based on backward oscillation. The system was consisted of a PPLN crystal and an off-axis parabolic mirror with a hole. The dimension of the PPLN crystal was 50 mm (L) × 1 mm (W) and, the dimension of the module was 80 mm (L) × 30 mm (W) × 30 mm (H)with weight of approximately 110 g, which provides a universal source for THz remote sensing.

To excite the oscillator, a single-longitudinal mode microchip Nd:YAG master oscillator power amplifier system was used in this experiment. The pump energy, pulse width, and spectrum linewidth were 8.9 mJ, 670 ps, and 0.01 nm, respectively. The polarization was aligned along the z-axis of the LN crystal such that the nonlinear coefficient d_{33} could

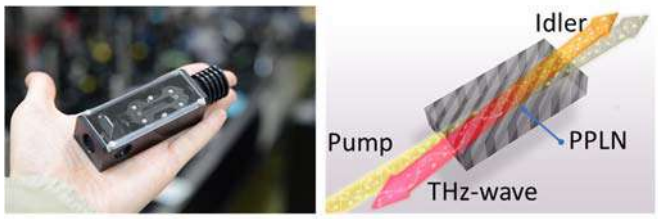

Fig. 1. (Left side) Photo of the backward THz-wave parametric oscillator. (Right side) Schematic illustration of the backward THz-wave parametric oscillation using a slanted stripe-type PPLN. The yellow, orange, and red arrows show propagating direction of the pump, idler, and THz-wave, respectively.

be used. The pump beam passed the parabolic mirror through a hole and the beam was irradiated to the PPLN. Backward THz-wave and a forward idler wave were generated inside the crystal. The counter-propagating THz-wave provided strong feedback effect to pump beam. The THz-wave was separated from the pump beam by the off-axis parabolic mirror, and subsequently measured by a pyro-electric detector.

In experiments, a PPLN crystal with poling period of 53 μm and angle of 23˚ was used. An output THz-wave frequency of 300 GHz was obtained with a pump intensity higher than 1.6 GW/cm^2. The frequency was measured by etalon scanning comprised of Si plates. To note, frequency difference between pump and idler wavelength was 300 GHz (measured by an optical spectrum analyzer). Frequency bandwidth of pump was approximately 3 GHz, therefore the THz-wave was generated by backward TPO process.

3. Conclusions

We presented a small (palmtop-sized) backward TPO. The TPO has wide tunability and a narrow oscillation linewidth. The frequency tuning method is implemented only by rotating the crystal, which provides fast and random access to desired frequency Mirrorless TPO has potential for many proposed applications of nondestructive inspection, from fundamental science to applications in industrial fields. The compact device can be installed on a rover or a drone in the future.

Acknowledgements

This work was partially supported by JSPS KAKENHI (Grant Nos. 17H01282, 18H01906, 16H03891, 17K18368, 17K14129, 17K18765) and the ImPACT Program of the Council for Science, Technology and Innovation (Cabinet Office, Government of Japan). Authors thank to Professor H. Ito of RIKEN and Professor M. Kumano of Tohoku University for their helpful discussions. Authors also thank to the colleagues of Teraphotonics Research Team, RIKEN.

References

[1] S. E. Harris, "Proposed backward wave oscillation in the infrared," *Appl. Phys. Lett.* **9**, 114–116 (1966).

[2] Y. J. Ding and J. B. Khurgin, "A new scheme for efficient generation of coherent and incoherent submillimeter to THz waves in periodically-poled lithium niobate," *Opt. Commun.* **148**, 105–109 (1998).

[3] Y. S. Lee, T. Meade, V. Perlin, H. Winful, T. B. Norris, and A. Galvanauskas, "Generation of narrow-band terahertz radiation via optical rectification of femtosecond pulses in periodically poled lithium niobate." *Appl. Phys. Lett.* **76**, 2505–2507 (2000).

[4] C. Weiss, G. Torosyan, J. Meyn, R. Wallenstein, and R. Beigang, "Tuning characteristics of narrowband THz radiation generated via optical rectification in periodically poled lithium niobate.", *Opt. Express* **8**, 497–502 (2001).

[5] N. E. Yu, C. Kang, H. K. Yoo, C. Jung, Y. L. Lee, C. S. Kee, D. K. Ko, J. Lee, K. Kitamura, and S. Takekawa, "Simultaneous forward and backward terahertz generations in periodically poled stoichiometric LiTaO3 crystal using femtosecond pulses.", *Appl. Phys. Lett.* **93**, 41104 (2008).

[6] T. D. Wang, S. T. Lin, Y. Y. Lin, F. Y. Lin, and Y. C. Huang, "Forward and backward terahertz-wave difference-frequency generations from periodically poled lithium niobate.", *Opt. Express*. **16**, 6471 (2008).S. Hayashi, K. Nawata, T. Taira, J. Shikata, K. Kawase, and H. Minamide, "Ultrabright continuously tunable terahertz-wave generation at room temperature," *Sci. Rep.*, **4**, 5045 (2014).

[7] H. Minamide, S. Hayashi, K. Nawata, T. Taira, J. Shikata, and K. Kawase, "Kilowatt-peak terahertz-wave generation and sub-femtojoule terahertz-wave pulse detection based on nonlinear optical wavelength-conversion at room temperature," *J. Infrared Millim. Terahertz Waves*, **35**, 25–37 (2014).

[8] K. Nawata, T. Notake, H. Ishizuki, F. Qi, Y. Takida, S. Fan, S. Hayashi, T. Taira, and H. Minamide, "Effective terahertz-to-near-infrared photon conversion in slant-stripe-type periodically poled $LiNbO_3$," *Appl. Phys. Lett.* **104**, 1–4 (2014).

[9] Y. Takida, J. I. Shikata, K. Nawata, Y. Tokizane, Z. Han, M. Koyama, T. Notake, S. Hayashi, and H. Minamide, "Terahertz-wave parametric gain of stimulated polariton scattering," *Phys. Rev. A* **93**, 4–7 (2016).

[10] K. Nawata, S. Hayashi, H. Ishizuki, K. Murate, K. Imayama, Y. Takida, V. Yahia, T. Taira, K. Kawase, and H. Minamide, "Effective Terahertz Wave Parametric Generation Depending on the Pump Pulse Width Using a $LiNbO_3$ Crystal," *IEEE Trans. Terahertz Sci. Technol.* **7**, 617–620 (2017).

[11] Y. Takida, K. Nawata, S. Suzuki, M. Asada, and H. Minamide, "Nonlinear optical detection of terahertz-wave radiation from resonant tunneling diodes," *Opt Express* **25**, 5389–5396 (2017).

[12] Y. Moriguchi, Y. Tokizane, Y. Takida, K. Nawata, T. Eno, and S. Nagano, "High-average and high-peak output-power terahertz-wave generation by optical parametric down-conversion in MgO:$LiNbO_3$," *Appl Phys Lett* **113**, 121103 (2018).

[13] K. Nawata, Y. Tokizane, Y. Takida, and H. Minamide, "Tunable Backward Terahertz-wave Parametric Oscillation," *Sci. Rep*. **9**, 726 (2019).

A 30-GHz compact resonator structure based on Folded Slow-wave CoPlanar Waveguides on a 55-nm BiCMOS technology

Marc Margalef-Rovira*[,1,2], Olivier Occello[2], Abdelhalim A. Saadi[2], Manuel J. Barragán[1], Christophe Gaquière[3], Emmanuel Pistono[2], Sylvain Bourdel[2], and Philippe Ferrari[2]

[1]Université Grenoble Alpes, CNRS, Grenoble INP*, TIMA F-38000 Grenoble, France
[2] Université Grenoble Alpes, Grenoble INP*, RFIC-Lab F-38000 Grenoble, France
[3]Université de Lille, IEMN, 59652 Villeneuve d'Ascq, France
*corresponding author, E-mail: marc.margalef-rovira@univ-grenoble-alpes.fr

Abstract

Miniaturization of transmission lines is a subject of major interest in the microelectronics community. This work presents, for the first time, an innovative miniaturization technique based on the use of folded Slow-wave CoPlanar Waveguides. The proposed miniaturization technique enables a length reduction of more than 80% as compared to a classical μ-strip line. On-wafer measurements are provided with a demonstrator integrated on a 55-nm BiCMOS technology.

1. Introduction

In the past years, miniaturization has played a major role in the development of the microelectronics industry. This reduction in size has increased the maximum frequency of transistors, reduced the minimal feature size, decreased the area overhead and thus, reduced the fabrication cost per transistor. For instance, the cutting-edge technology node in the '80s was around 1 μm while nowadays it is around 10 nm. However, the miniaturization that active devices have benefited has not been reproduced in the same scale for the passive circuitry since its size is mainly frequency dependent. In this scenario, several authors have addressed the issue of miniaturization of passive devices. An early proposal in this field was given in [1] where the authors present the slow-wave concept. The authors in this work proposed to lower the propagation velocity of a wave in a given medium (i.e. substrate) in order to increase the phase constant of the propagated wave and thus, obtain a greater phase shift for a given length. This principle was later extended to the so-called Slow-wave CoPlanar Waveguides (S-CPW) structures in [2]. In this work, the authors modified the classical CoPlanar Waveguide (CPW) structure by adding floating fingers below the signal and ground strips to artificially increase the effective dielectric constant seen by the propagated wave. Deeper comprehension of the physics behind the S-CPWs was brought by authors in [3]. In this paper, a first proposal of an equivalent electrical model was given. This first model was subsequently implemented in [4]. The works presented in [3,4] show that S-CPWs not only help in the miniaturization process but might allow the designer to achieve a larger range of characteristic impedances and a greater quality factor as compared to classical μ-strip lines.

In this work, a new implementation of S-CPW is proposed, with a folded S-CPW. The folding permits to dramatically reduce the physical length for a given electrical length, for two reasons, (i) folding that divides by two the length, and (ii) use of different characteristic impedances to achieve stepped-impedance resonator, as firstly proposed in [5], and couplings in the folded region.

This paper is organized as follows: in section 2, the proposed folded S-CPW architecture is presented. Section 3 provides with the on-wafer measurements. Finally, in section 4 the main conclusions of this work are discussed.

2. Proposed architecture

Classical μ-strip structures integrated in CMOS Back-End-Of-Lines (BEOL) tend to use the top metal for the signal strip and the lower metal for the ground plane. This approach is taken in order to be able to use wider signal strips for a given impedance and minimize metallic losses, since rising the ground plane increases the linear capacitance and thus a narrower signal line is needed to achieve the same characteristic impedance. However, the fingers in a S-CPW tend to be close to the signal and ground strips in order to boost the slow-wave effect while the linear inductance is almost that of a CPW.

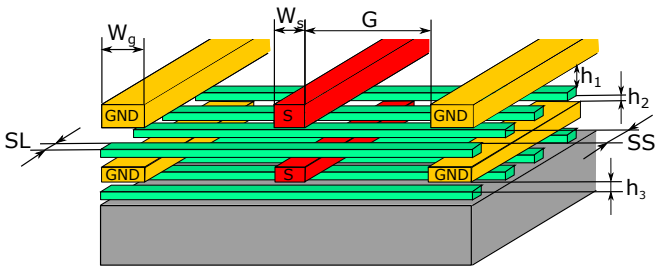

Fig. 1 Proposed folded S-CPW architecture.

In this work, it is proposed to use the lower metal layers of a classical S-CPW in order to achieve a greater integration level. Fig. 1 presents the proposed folded S-CPW

architecture. This structure consists in two stacked S-CPWs connected through vias at far end. This provides with a device with an input and output in the same z-plane. The parameters that allow to size this structure as depicted in Fig. 1 are: G that correspond to the distance between ground (*GND*) and signal strips (*S*), W_s and W_g that correspond to the signal and ground strips' width, respectively. *SS* and *SL* represent the separation between fingers and their width, respectively. Finally, h_1 , h_2 and h_3 correspond to the distance between the strips and the fingers around them. These architecture parameters provide the designer with a structure featuring several degrees of freedom. This allows the tuning of the characteristic impedance and propagation velocity as two independent variables.

3. Results

As a case of study, the Device Under Test (DUT) was placed as an open-circuit stub between two 50-Ω ports. Stubs are a widely used component at RF and mm-wave frequencies to perform impedance matching, filtering and for biasing purposes. However, at the low-end of the mm-wave spectrum, designers tend to use lumped components (i.e. inductors and capacitors) in order to perform the desired function since the required size for the stub is much greater than the size of the lumped devices.

The proposed folded S-CPW architecture, which solves the size issue, was implemented in STM 55-nm BiCMOS technology with a total length (feeding µ-strip lines and folded S-CPW) of 240 µm. This technology features 8 metal layers. The two top metals were stacked and used for the signal and ground strips of the top S-CPW. Metals 4 and 3 were stacked and used for the signal and ground strips of the lower S-CPW. The fingers were placed on metal 5 and 2, respectively. Regarding the lateral dimensions, the signal and ground strips W_s and W_g are equal to 12 µm. They are separated by a gap G of 50 µm. Finally, the fingers width *SL* and spacing *SS* were set to 1 µm for both finger layers.

The presented folded S-CPW was measured using an Anritsu VectorStar® ME7838A4 VNA from 70 kHz up to 145 GHz. The non-de-embedded measurement results are depicted in Fig. 2. The magnitude of the reflection and transmission coefficients (i.e. $|S_{11}|$ and $|S_{21}|$) are depicted versus frequency.

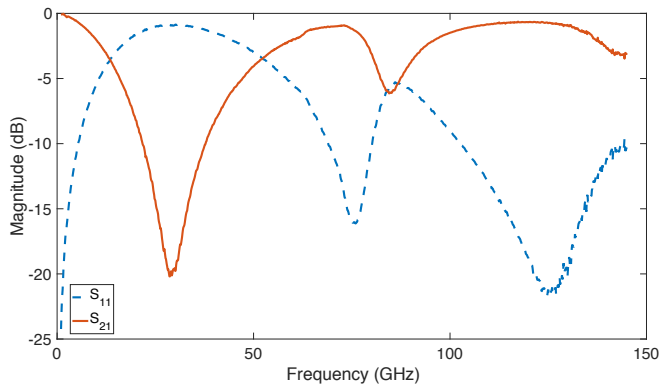

Fig. 2 Measured S-Parameters magnitude.

These measurements show that a first resonance appears at 29 GHz. In the configuration of an open-circuit stub, this means that, at this frequency, the DUT is equivalent to a stub with an electrical length of 90°. At this frequency, the DUT shows an attenuation of 20 dB and a return loss of 0.9 dB. It is easy to demonstrate that the folded S-CPW behaves as a transmission line with an effective dielectric constant equal to 109 using the following expression:

$$\lambda/_4 = \frac{1}{4} \cdot \frac{c_0}{f \cdot \sqrt{\varepsilon_{reff}}} \quad (1)$$

where λ represents the guided wavelength, c_0 the speed of light in vacuum, f the working frequency and $\varepsilon_{r,eff}$ the effective dielectric constant, respectively.

Let us consider an equivalent structure built using a classical µ-strip line. In this scenario, considering the same technology, the relative effective dielectric constant of the µ-strip line would be around 4. With this kind of structure, and using the expression given by (1), a µ-strip line measuring 1.25 mm would be needed in order to perform the same function as the folded S-CPW. Therefore, a reduction of more than 80% in length of the structure is demonstrated through the use of folded S-CPWs as compared to a classical µ-strip line.

4. Conclusions

In this paper, the concept of folded S-CPWs has been presented for the first time. The proposed architecture takes advantage of the unused lower metal layers under a classical S-CPW to enhance the miniaturization effect. On-wafer measurements up to 145 GHz have been provided and a length miniaturization greater than 80% has been demonstrated as compared to a classical µ-strip line. Further details will be given during the conference, along with an electrical model of the folded S-CPW, to be used by circuits designers.

Acknowledgements

This work has been funded by the TARANTO project.

References

[1] H. Hasegawa, M. Furukawa and H. Yanai, "Slow wave propagation along a microstrip line on Si-SiO_2 systems," in *Proceedings of the IEEE*, vol. 59, no. 2, pp. 297-299, Feb. 1971.

[2] T. S. D. Cheung, J. R. Long, K. Vaed, R. Volant, A. Chinthakindi, C. M. Schnabel, J. Florkey, and K. Stein, "On-chip interconnect for mm-wave applications using an all-copper technology and wavelength reduction," *2003 IEEE International Solid-State Circuits Conference, ISSCC2003'*, San Francisco, CA, USA.

[3] A. L. Franc, E. Pistono, G. Meunier, D. Gloria and P. Ferrari, "A lossy circuit model based on physical interpretation for integrated shielded slow-wave CMOS coplanar waveguides structures," *IEEE Trans. on Mic. Theory and Tech.*, vol. 61, no. 2, pp. 754-763, Feb. 2013.

[4] A. Bautista, A. L. Franc, and P. Ferrari, "Accurate parametric electrical model for slow-wave CPW and application to circuits design," *IEEE Trans. on Mic. Theory and Tech.*, vol. 63, no. 12, pp. 4225-4235, Dec. 2015.

[5] M. Makimoto, and S. Yamashita, "Bandpass Filters Using Parallel Coupled Stripline Stepped Impedance Resonators," *IEEE Trans. on Mic. Theory and Tech.*, vol. 2, no 12, Dec. 1980.

Highly intense THz vortex generation and its applications

Katsuhiko Miyamoto[1,2], Fabian Rotermund[3], Takashige Omatsu[1,2]

[1]Graduate School of Engineering, Chiba University, Chiba, 263-8522, Japan
[2]Molecular Chirality Research Center, Chiba University, Chiba 263-8522, Japan
[3]Department of Physics, Korea Advanced Institute of Science and Technology, Daejeon 34141, Korea

*corresponding author, E-mail: k-miyamoto@faculty.chiba-u.jp

Abstract

We report on the development of a monocycle THz vortex source by utilizing a polymeric Tsurupica vortex phase plate in combination with tilted-pulse-front optical rectification in $LiNbO_3$ crystal. The system produces a 0.6 THz optical vortex pulse with an energy of 2.3 μJ. We also investigate unique nonlinear transmission behaviours of a bilayer graphene by utilizing our THz vortex source.

1. Introduction

Optical vortices[1], having an annular intensity profile, a spiral wavefront and orbital angular momentum characterized by a topological charge ℓ, and they provide us a variety of potential research opportunities, such as ultra-high speed optical communication, advanced optical manipulation, and chiral materials fabrication [2], [3]. In particular, they enable us to develop super-resolution microscopes (with a spatial resolution beyond the diffraction-limit) based on fluorescence depletion via simulated emission[4].

An optical vortex beam in a terahertz (THz) frequency region, including eigen frequencies of the molecular (or cluster-cluster) interactions, will have the potential to develop THz imaging systems with a micrometer-scale spatial resolution beyond the diffraction-limit by applying it to materials with nonlinearities such as graphene. To date, we reported the generation of 2, 4 THz vortex beam at topological charge of $\ell = \pm 1, 2$ by a Tsurupica vortex phase plate (Tsurupica-VPP)[5].

In this presentation, we demonstrate monocycle THz vortex pulse generation by utilizing a Tsurupica-VPP. Furthermore, unique nonlinear transmission behaviors in bilayer graphene were investigated by utilizing our THz vortex source [6].

2. Experiments and discussion

The schematic diagram of the experimental setup is shown in Fig.1. A broadband THz source based on optical rectification in a MgO-doped prism-cut stoichiometric $LiNbO_3$ crystal pumped by a femtosecond Ti; sapphire laser (pulse width: 100fs, pulse repetition frequency: 1kHz, average power: 4W, wavelength: 800nm) was used, and its maximum average power was measured to be 3.3mW by a room temperature pyroelectric detector (Gentec THZ5B-MT-USB). The THz output also exhibited a near Gaussian spatial form and a center frequency of 0.6 THz with a bandwidth (FWHM) of 0.7 THz. A Tsurupica-VPP was designed for a 0.6 THz vortex output with a topological charge of ℓ =1; it had dimensions of φ50.4 mm (aperture) and 2 mm (thickness) azimuthally divided into 18 segments

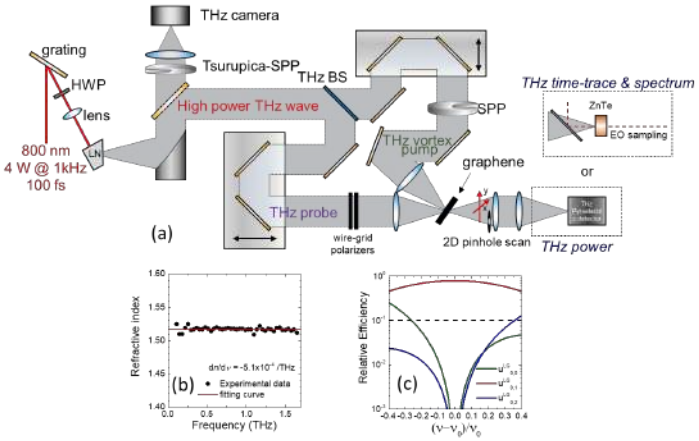

Fig. 1 (a) Experimental setup of THz pump-probe system to measure nonlinear absorption of graphene.
(b) Experimental refractive index of Tsurupica polymer. (d) Simulated relative intensity of the LG modes as a function of the frequency of the THz output (ν_0 = 0.6 THz).

with a total step height of ~980 μm. The Tsurupica polymer has a good advantage in the THz region such as high transmission (absorption coefficient ~ 0.4 cm^{-1}) and extremely low frequency dispersion ($dn/dv = -5.1 \times 10^{-4}$/THz) at a frequency range of 0.1 – 6 THz (Fig. 1 (b)). Therefore, Tsurupica-VPP has essentially the potential to convert the THz output with a relatively broad spectrum bandwidth, i.e., a bandwidth of at least 50% center frequency (Fig. 1 (c)).

The THz output shows a 1.7-mm annular spatial form with a <450 μm slightly off-center dark core arising from a phase singularity in the near field, as shown in Fig. 2(a). The simulated THz vortex exhibited an annular intensity distribution and an expected value of the topological charge of 1.15. The astigmatic aberration of the tilted lens also broke the cylindrical symmetry, thereby converting the focused vortex output into a twin mode such as Hermite-Gaussian HG_{01} mode as shown in Fig. 2(b).

The unsaturated absorption measurement of a bilayer graphene deposited on a quartz plate with saturation intensity of ~76 MW/cm^2 at a frequency of 0.6 THz (Fig. 3(a)) was performed by utilizing vortex pump and Gaussian probe beams. The transmitted probe output through the bilayer graphene exhibits a small dip owing to the phase singularity of the THz vortex pump beam, indicating that the unsaturated absorption of 0.62 was measured at a spatial resolution of 0.38 mm beyond the diffraction limit (1/8) as shown in Fig. 3(b). The experimental two-dimensional mapping of the modulated spatial form with the vortex pump beam exhibits a slightly off-axial dip around the core of the vortex pump beam (Fig. 3(c)).

3. Conclusions

We have successfully demonstrated a highly intense 0.6 THz vortex generation by using a Tsurupica-VPP. The maximum average output power of the THz vortex was measured to be 2.3 mW, corresponding to peak power of 2.3MW. Also, we have successfully measured unsaturated absorption of a bilayer graphene by employing the vortex pump and Gaussian probe beams, evidencing that the THz vortex output enables us to develop a super resolution THz imaging system with a spatial resolution beyond the diffraction-limit.

Acknowledgements

The authors acknowledge support in the form of Grants-in-Aid for Scientific Research (16K04971) from the Japan Society for the Promotion of Science (JSPS). This work was also financially supported by a Kakenhi Grant-in-Aid (No. JP 16H06507) for Scientific Research on Innovative Areas "Nano-Material Optical-Manipulation".

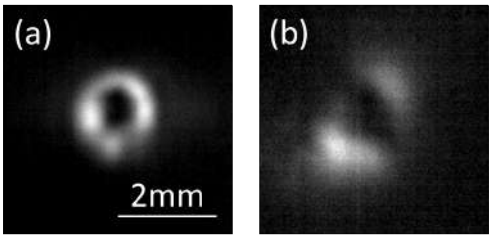

Fig. 2. (a) Experimental near field of the THz vortex output. (b) THz vortex output produced by a tilted lens.

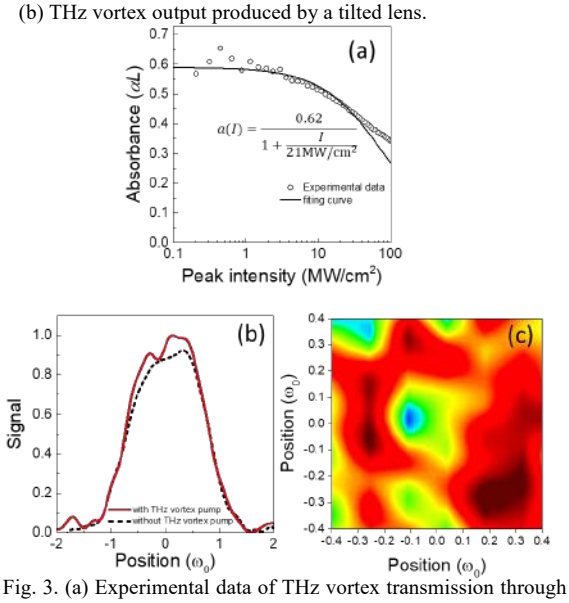

Fig. 3. (a) Experimental data of THz vortex transmission through bilayer graphene sample as a function of incident THz vortex intensity. (b, c) Intensity profiles of the THz probe output through bilayer graphene with or without vortex pump beam.

References

[1] L. Allen, M. W. Beijersbergen, R. J. C. Spreeuw, and J. P. Woerdman, "Orbital angular momentum of light and the transformation of Laguerre-Gaussian laser modes," *Phys. Rev. A*, vol. 45, no. 11, pp. 8185–8189, Jun. 1992.

[2] K. Toyoda, K. Miyamoto, N. Aoki, R. Morita, and T. Omatsu, "Using optical vortex to control the chirality of twisted metal nanostructures," *Nano Lett.*, vol. 12, no. 7, pp. 3645–3649, 2012.

[3] F. Takahashi, S. Takizawa, H. Hidai, K. Miyamoto, R. Morita, and T. Omatsu, "Optical vortex pulse illumination to create chiral monocrystalline silicon nanostructures," *Phys. Status Solidi Appl. Mater. Sci.*, vol. 213, no. 4, pp. 1063–1068, Apr. 2016.

[4] S. Bretschneider, C. Eggeling, and S. W. Hell, "Breaking the diffraction barrier in fluorescence microscopy by optical shelving," *Phys. Rev. Lett.*, vol. 98, no. 21, p. 218130/1-4, 2007.

[5] K. Miyamoto, K. Suizu, T. Akiba, and T. Omatsu, "Direct observation of the topological charge of a terahertz vortex beam generated by a Tsurupica spiral phase plate," *Appl. Phys. Lett.*, vol. 104, no. 26, p. 261104, 2014.

[6] K. Miyamoto *et al.*, "Highly intense monocycle terahertz vortex generation by utilizing a Tsurupica spiral phase plate," *Sci. Rep.*, vol. 6, p. 38880, 2016.

Development of a New Microwave Tomography System for Medical Diagnostic Applications: Design, Testbeds, and Algorithms

Panagiotis Kosmas

Faculty of Natural and Mathematical Sciences, King's College London, London, UK
E-mail: panagiotis.kosmas@kcl.ac.uk

Abstract

We present an overview of our past and current work on developing a novel microwave tomography (MWT) system for medical imaging. This involves innovative solutions to the design and fabrication of the prototype, the implementation of imaging algorithms, as well as the development of suitable numerical and experimental testbeds to evaluate the imaging prototype and algorithms.

1. Introduction

Motivated by continuously increasing hardware and computing capabilities, reduction in cost, and smaller form factors, the application of microwave technologies for medical imaging and diagnostics is gaining renewed interest within the electromagnetic (EM) engineering community [1]. As a result, researchers worldwide are developing a new generation of safe, low-cost, portable, and accurate microwave sensing and imaging systems which could tackle various current challenges in medical diagnostics.

In quantitative microwave medical imaging, the dielectric properties of human tissues are estimated within the body region of interest using a tomography setup and inverse EM scattering algorithms [2]. A pathological condition can be detected if the dielectric contrast between healthy and disease-affected tissues is non-negligible. To ensure clinically acceptable performance, microwave tomography (MWT) systems must feature a reliable experimental setup [3] and robust reconstruction techniques which can safeguard against measurement errors and uncertainties [4]. To optimise performance, EM inverse scattering algorithms must be tuned specifically for a given prototype and imaging application [5]. Consequently, it is imperative that microwave imaging prototypes and algorithms are co-developed and optimised in a synergistic manner.

This paper and invited presentation will present an overview of our past and current work towards developing a robust, efficient, and accurate microwave tomography prototype for medical imaging. The remainder of this paper provides a brief summary of different research issues addressed towards the development of this prototype.

2. MWT prototype design

Details on the initial design of our wideband MWT system for medical imaging have been presented in [3]. The prototype uses printed monopole antennas which can operate in the 1.0-3.0 GHz range when fully immersed in liquids commonly used in MWT, such as a 90% glycerine-water mixture. Operation in lower frequencies can be easily achieved by scaling the antenna's dimensions.

A photo of the prototype is presented in Figure 1. The setup consists of two concentric cylindrical tanks with 100 and 200 mm diameters. The outer cylinder is surrounded with an absorber and is covered with a metallic shield. An eight-antenna circular ring transmits and records data inside the outer acrylic tank, which is filled with the 90% glycerine-water mixture. The system uses a multiport PXI VNA technology by Keysight to record the signals received by all eight antennas when one of them transmits, and this process is repeated sequentially for all eight antennas as transmitters. Vertical and horizontal mounts allow us to control the antenna positions and vary their height as well as the array diameter.

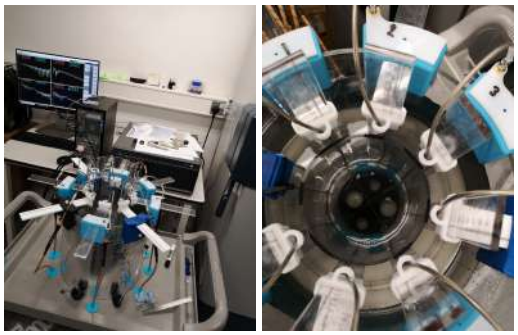

(a) (b)

Figure 1: Photos of the MWT prototype: (a) side, and (b) top view.

3. Testbeds for evaluation

To evaluate the experimental prototype, we conducted measurements first with a target of 16 mm diameter placed inside the inner tank, which was filled with water. The "background-only" case of no water target was also recorded. The setup and experiments have also been simulated using commercial EM solvers(CST Microwave Studio) [3]. This allows us to benchmark performance in various imaging scenarios, such as cases of multiple targets. More importantly, the CST simulation models also allow

us to optimise the system design, for example by minimising the impact of multipath signals with respect to antenna locations or the choice of the immersion liquid [3]. An example of these CST models is shown in Figure 2(a), and the experimental setup for imaging multiple targets is shown in Figure 2(b).

In addition to assessing performance by imaging cylindrical or spherical targets in homogeneous backgrounds, we have constructed phantoms to approximate simplified brain models and blood targets. A picture of an ellipsoidal phantom for this purpose is shown in Figure 2(b). To confirm that the dielectric properties of these phantoms resemble literature values for brain tissue and blood, we have conducted dielectric spectroscopy measurements using Keysight's dielectric probe kit and slim form probes.

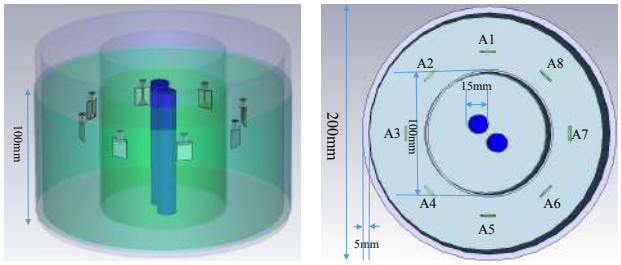

(a)

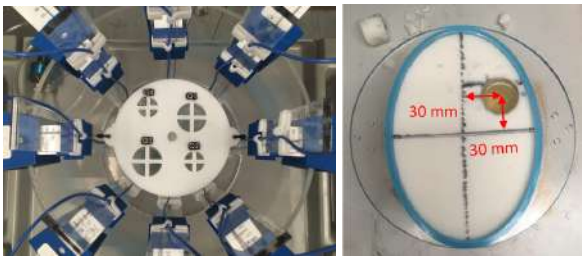

(b) (c)

Figure 2: Examples of different testbeds for evaluating our MWT system: (a) a CST model of two cylindrical targets filled with water, and (b) its experimental realization; (c) an ellipsoid with an inclusion mimicking average brain tissue and a blood target, respectively.

4. Imaging algorithm and results

Our DBIM-TwIST imaging algorithm [5] is based on the distorted Born iterative method (DBIM), which solves the nonlinear scattering problem iteratively by applying a Born approximation at each iteration. The linear problem at each DBIM iteration is solved by our own optimised implementation of the two-step iterative shrinkage thresholding algorithm. The algorithm's forward solver uses the finite-difference time-domain (FDTD) method, which is applied to a simplified two-dimensional (2-D) model of the tank with line sources at the same locations as the monopoles. To calibrate data from our forward model with CST or experimental data, we apply a standard calibration procedure using the "empty tank" datasets [4]. Examples of reconstructions using our setups and testbeds are provided in Figure 3.

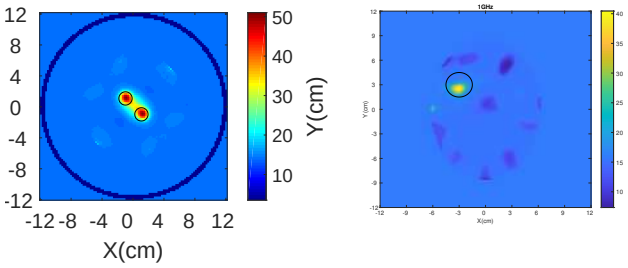

Figure 3: Example of reconstructions using the DBIM-TwIST algorithm. The left image corresponds to the estimated dielectric constant for the simulation setup of Figure 2(a), while the right image represents the dielectric constant reconstruction for the experimental phantom (rotated) shown in Figure 2(c).

Acknowledgement

This research was funded in part by Innovate UK grant number 103920, and in part by the Engineering and Physical Sciences Research Council grant number EP/R013918/1. The author would like to thank his past and present PhD students and research associates who have contributed to this research: Syed Ahsan, Zhenzhuang Miao, Ziwen Guo, Yannis Sotiriou, Pan Lu, Olympia Karadima, Navid Ghavami, Maria Koutsoupidou, and Mohammad Rahman.

References

[1] P. Kosmas, L. Crocco, Introduction to special sssue on electromagnetic technologies for medical diagnostics: Fundamental issues, clinical applications and perspectives, *Diagnostics* 9:1, 2019.

[2] P. M. Meaney, M. W. Fanning, T. Raynolds, C. J. Fox, Q. Fang, C. A. Kogel, S. P. Poplack, K. D. Paulsen, Initial clinical experience with microwave breast imaging in women with normal mammography, *Academic Radiology* 14:2, pp. 207-218, 2007.

[3] S. Ahsan, Z. Guo, Z. Miao, I. Sotiriou, M. Koutsoupidou, E. Kallos, G. Palikaras, P. Kosmas, Design and experimental validation of a multiple-frequency microwave tomography system employing the DBIM-TwIST algorithm, *Sensors* 18:10, 2018.

[4] Z. Miao, S. Ahsan, P. Kosmas, Impact of information loss on reconstruction quality in microwave tomography for medical imaging, *Diagnostics* 8:3, 2018.

[5] Z. Miao, P. Kosmas, Multiple-frequency DBIM-TwIST algorithm for microwave breast imaging, *IEEE Trans. Antennas Propag.* 65:5, pp. 2507-2516, 2017.

Complex fiber Bragg gratings designed and fabricated for optical pulse manipulation

Xuewen Shu[1,*]

[1]Wuhan National Laboratory for Optoelectronics, Huazhong University of Science and Technology, Wuhan, China
*corresponding author, E-mail: xshu@hust.edu.cn

Abstract

Fiber Bragg gratings can be used to directly manipulate optical pulses in optical fiber. We will review our past and recent research on the design and fabrication of fiber Bragg gratin devices used for optical pulse manipulations with various functionalities.

1. Introduction

Fiber Bragg gratings (FBGs) have attracted considerable research interests and also found many applications in the areas of optical communications and optical sensing. They are typically periodical or quasi-periodical refractive index structures, which can be permanently inscribed in optical fibers with laser inscription techniques. Due to the their natural compatibility, FBGs can directly process optical signals in optical fiber without the need for coupling/re-coupling alignments thus provide a low-loss, stable, cost-effective and ultra-fast solution for optical pulse manipulations.

In this paper, we review our past and recent research work on fiber grating based optical signal manipulation techniques. We will discuss their various processing functionalities including optical differentiators, optical pulse shapers and modulation format converters etc[1-5].

2. Device examples

Generation and control of ultrahigh-repetition-rate optical pulse bursts have become increasingly important in many areas including ultrahigh-speed optical communication, photonic signal processing and optical computing. Figure 1 shows an example of the design of phase-modulated FBG (PM-FBG) operating in transmission to generate ultrahigh-repetition-rate optical pulse bursts from a single pulse. We employ a two-step nonlinear optimization method we previously proposed to design such PM-FBG [3]. The coupling coefficient amplitude is defined as a raised cosine function with roll-off factor of 0.05, where the maximum amplitude is $400m^{-1}$. The error feedback to the numerical optimization is calculated in a defined band of interest of 4 nm around the central wavelength. The grating profile of the designed PM-FBG is presented in Fig.1a. The objective and numerical spectrum responses are shown in Fig.1b. Fig.1c shows the obtained pulse burst results when a single Gaussian pulse launched to the gratings, in which we can clearly see that 4 pulses are burst.

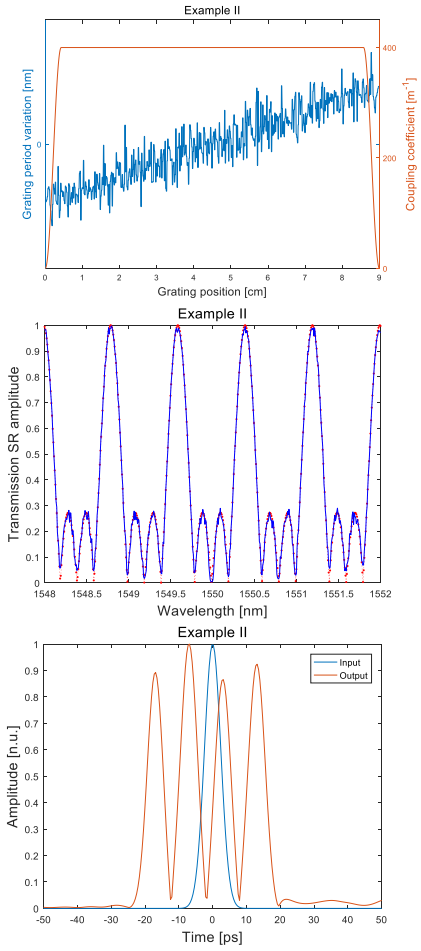

Figure 1: PM-FBG designed for generating ultrahigh-repetition-rate optical pulse bursts.

The proposed technique brings potential technological feasibility advantages since the coupling strengths of such gratings remain uniform along most of the grating lengths. Also, since these PM-FBGs work in transmission, the use of a coupler or circulator is not

required, which can offer the optimum energy efficiency and reduce the cost and complexity of the system.

3. Conclusions

In conclusions, fiber Bragg gratings are versatile passive devices and have very flexible design capability. They can be designed to manipulate optical signals directly in optical fiber with ultra fast speed, therefore have great potential in future high-speed optical communication systems.

Acknowledgements

The author would thank Mr Xing Liu, Dr Miguel A. Preciado, Dr Adenowo Gbadebo and Dr Hui Cao for their contributions and discussions. This work is supported by National Natural Science Foundation of China (NSFC) (61775074) .

References

[1] M. A. Preciado, X. Shu, and K. Sudgen, "Proposal and design of phase-modulated fiber gratings in transmission for pulse shaping," *Opt. Lett.*, vol. 38, no. 1, 70-72, 2013.

[2] H. Cao, X. Shu, J. Atai, Q. Dong, J. Zuo, G. Chen, and Y. Yu, "RZ-OOK to NRZ-OOK format conversion based on a single fiber Bragg grating," *Chinese Opt. Lett.,* 12, 090603, 2014.

[3] X. Liu and X. Shu, "Design of Arbitrary-Order Photonic Temporal Differentiators Based on Phase-Modulated Fiber Bragg Gratings in Transmission," *J. Lightwave Technol.* 35, 2926-2932，2017.

[4] X. Liu X. Shu and H. Cao, "Proposal of a phase-shift fiber Bragg grating as an optical differentiator and an optical integrator simultaneously," *IEEE Photonics J*., 10(3), 7800907, 2018

[5] X. Liu and X. Shu, "Design of an all-optical fractional-order differentiator with terahertz bandwidth based on a fiber Bragg grating in transmission," *Appl. Opt*. 56, 6714-6719, 2017.

Additive Manufacturing of Rectangular Waveguide Devices for Teaching Microwave Laboratory

Enrique Márquez-Segura[1]
[1]Departamento de Ingeniería de Comunicaciones, E.T.S. Ingeniería de Telecomunicación,
Universidad de Málaga, Málaga, Spain.
E-mail: ems@ic.uma.es

Abstract

In this paper the outline of using of low-cost additive manufacturing FDM/FFF technology to build waveguide devices is presented. The focus is set in a full design from specifications to final measurements in a microwave teaching laboratory. Final results obtained asses that this experience is an extraordinary opportunity for students to get involved in waveguide technology. In addition, the use of 3D design software enriches the curricula of electronic engineering students.

1. Introduction

Waveguide technology is still nowadays a very important technology in microwave and millimetre-wave applications. The main advantages of metallic waveguides over other transmission media are, among others, its low-loss and power-handling capabilities. The fabrication of conventional metallic waveguide devices has been traditionally based in expensive and long time-consuming mechanical procedures using different aluminum alloys. The emergence of additive manufacturing processes is changing some paradigms in waveguide fabrication for certain applications [1]. In this paper, focus is set in educational aspects of these new technologies.

For plastics and resins, additive manufacturing term encloses several technologies, from the most affordable fused filament fabrication -hundred dollars nowadays- to polyjet systems -hundred thousand dollars. Additionally, additive manufacturing of metallic mechanical parts is also available, for instance using selective laser sintering (SLM), but in this work has not been considered as it is not an affordable technology for academic porpoises. In general, additive manufacturing technologies grow parts from scratch adding layers of material one on top of the other. In this work, fused filament fabrication (FFF) or, as it is also known filament deposition modeling (FDM), is considered. Lately, this technology has been spread enormously and a huge community of developers provide software and repositories of parts ready to be fabricated. Some students even have a 3D printer available at home.

Waveguide fabrication has traditionally carried out in external facilities where the device emerges from a cube of aluminum. FDM technology is appropriate for plastic polymers whereas waveguide fabrication requires high conductivity materials. So, a final metal coating is necessary to fabricate waveguides. In this paper, the experience of introducing waveguide 3D printed waveguide devices in a teaching environment is presented.

2. Rectangular Waveguide devices

In order to design real prototypes with dimensions that can be big enough but small enough, the WR62 waveguide, for its dimensions, has been chosen. This waveguide is usable in our teaching laboratories as the frequency range of the ENA Vector Network Analyser available for students is 18 GHz, so the nominal bandwidth (12-18GHz) is completely cover by measurement equipment.

Waveguide parts and devices can be complex and 3D modeling software is important. Open source software OpenSCAD has been used. This is a programming language for creating 3D mechanical parts that is available for different operating system. It has no interactive modeler but in case a more complex structures are needed FreeCAD is fully compatible with OpenSCAD code so both of them can be used for this laboratory. Fig. 1 shows the code and rendering of a TRL calibration kit and a half-wavelength section of rectangular waveguide.

When a 3D part is going to be printed using FDM, special care has to be taken with overhanging surfaces, mainly to avoid support material. In case there are surfaces or cavities support material is necessary unless you keep this fact throughout the design process. In spite of everything, some devices have no solution for this problem unless they are divided into several parts. Waveguide parts library will be available for downloading in parametric format so different waveguide sizes can be fabricated using the same code.

For mechanical reasons and availability, ABS polymer filament is used for FDM [2-3]. Special care has to be taken when coating with metallic layer and it is carried out by instructors, not by students (Fig. 2(a)). TRL calibration is introduced to students and a 3D model of a short and a line is designed as shown in Fig. 2(b). Student are encouraged to develop their own code. As can be seen in Fig. 2(c) different irises shapes can be easily developed and printed [4]. Using these simple elements, a more complex iris-based h-plane filter can be design, simulated, build stacking waveguide sections and measured.

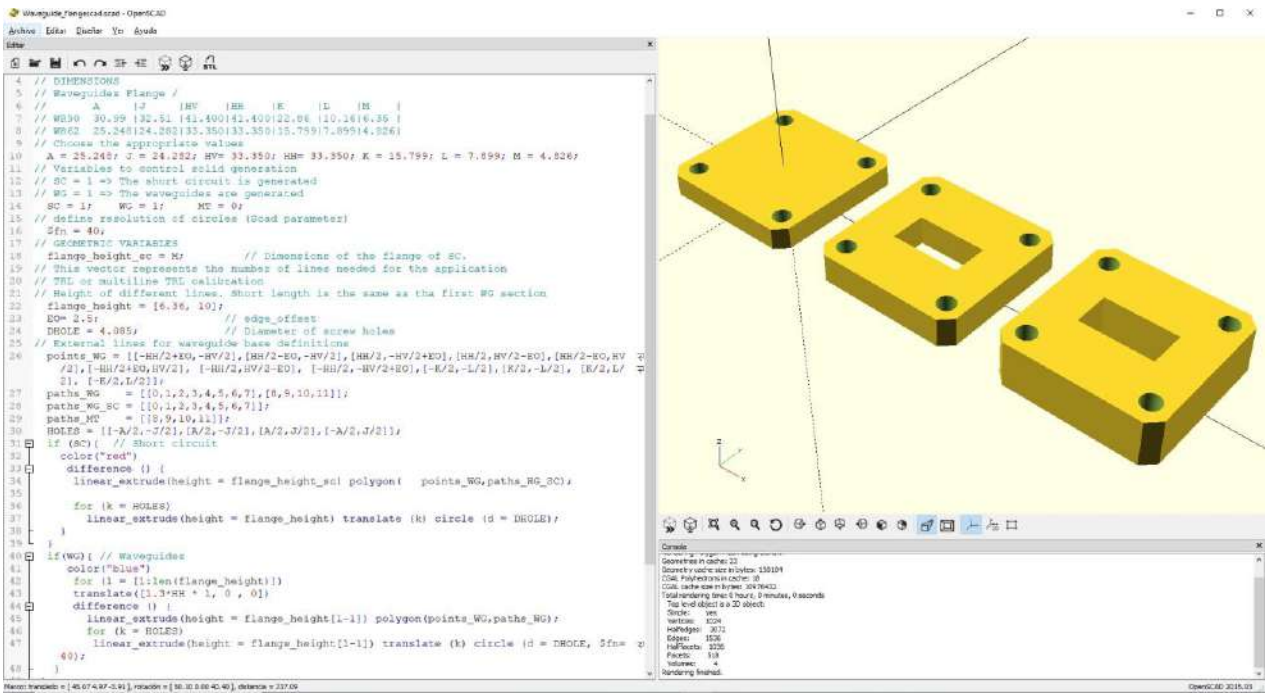

Figure 1: OpenSCAD software environment shown TRL calibration code and rendering of waveguide parts.

(a) (b)

Figure 2: (a) Nickel Spraying process for ABS coating with air extraction. (b) WR62 TRL calibration kit once metallized compared with aluminium one. (c) Different irises fabricated. (c) 1 out of 3 measurement bench available for students.

3. Discussion

Additive manufacturing technology has been introduced in a master level subject entitled Microwave Laboratory. The experience has been introduced in a project-based learning scheme where students actively explore the issues associated with the final fabrication technologies and the necessary loop from specifications to prototype in a CAD environment. The academic outcomes of the project excessed original expectations and students get involved in the process intensively. The analysis of the perception of the activity among students is excellent, mainly because they get a product designed and build by themselves in contrast with the use of expensive prefabricated commercial available waveguide kits.

References

[1] R. Bahr, B. Tehrani, M.M. Tentzeris, “Exploring 3-D printing for new applications”, IEEE Microwave magazine, January/February 2018, pp. 57-66.

[2] W. J. Otter and S. Lucyszyn, “3-D printing of microwave components for 21st century applications”, Proc. IEEE MTT-S Int. Microw. Workshop Ser., Adv. Mater. Process RF Terahertz Appl. (IMWS-AMP), Changdu, China, Jul. 2016.

[3] M. D’Auria, W. Otter, J. Hazell, B. Gillatt, C. Long-Collins, N. Ridler, S. Lucyszyn, “3D printed metal-pipe rectangular waveguides”, IEEE Trans. Comp. Packag. Manufact. Technol., vol. 5, no. 9, 2015, pp. 1339-1349.

[4] N. Marcuvitz, Waveguide Handbook, Peter Peregrinus Ltd., 1986.

Subcycle THz near-field control of spin switching

C. Lange[1*], S. Schlauderer[1], S. Baierl[1], T. Ebnet[1], C. P. Schmid[1], D. C. Valovcin[2], A. K. Zvezdin[3,4], A. V. Kimel[5,6], R. V. Mikhaylovskiy[6], and R. Huber[1]

[1]*Department of Physics, University of Regensburg, 93040 Regensburg, Germany*
[2]*Department of Physics and the Institute for Terahertz Science and Technology, University of California at Santa Barbara, Santa Barbara, California 93106, USA*
[3]*Prokhorov General Physics Institute and P.N. Lebedev Physical Institute of the Russian Academy of Sciences, Moscow 119991, Russia.*
[4]*Moscow Institute of Physics and Technology (State University), Dolgoprudny 141700, Russia.*
[5]*Moscow Technological University (MIREA), Moscow 119454, Russia.*
[6]*Radboud University, Institute for Molecules and Materials, Nijmegen 6525 AJ, The Netherlands.*

*corresponding author, E-mail: Christoph.Lange@physik.uni-regensburg.de

Abstract

Future information technologies rely on ultimately fast, low-dissipation quantum control. The fastest and least dissipative way to switch spins is to trigger precessional dynamics as is possible by resonant light fields in the THz spectral range. Here, we demonstrate ballistic dynamics and coherent switching of spins between metastable states in $TmFeO_3$, triggered by strong THz pulses enhanced in custom-cut metallic nanoresonators. We reveal a characteristic phase flip of the transient polarization rotation as a fingerprint of all-coherent spin switching.

1. Introduction

Landauer's principle [1] states a lower limit for the energy dissipation required to process one bit of information as $Q = k_B T \ln 2$, where T is the temperature and k_B denotes the Boltzmann constant. At room temperature, $Q \sim$ meV, which entails picosecond time scales for minimally dissipative switching, resonantly triggered by THz pulses.

Optical pulses have enabled remarkable progress from subpicosecond laser-induced spin dynamics [2] to all-optical non-thermal recording [3]. Yet, THz-induced spin control is still in its infancy. While the energies of magnons of antiferromagnets lie in the meV range [4] and can be directly excited by the magnetic field component of intense THz pulses [5,6], the underlying Zeeman interaction is relatively weak, limiting the attainable spin deflections to a few mrad. A much more promising route has been opened up by exciting crystal-field-split electronic states which control the magnetic anisotropy and enable much more effective energy transfer from the light field to the spin system, while minimizing dissipation. Corresponding strong-field THz excitation with amplitudes of ~1 MV/cm has enabled large-amplitude magnon oscillations with spin deflections of up to 2.5°, observed directly in the time domain [7].

Here, we use custom-cut gold nanoantennas processed on antiferromagnetic $TmFeO_3$ crystals to generate pulsed THz near-fields in excess of 20 MV/cm, inducing extremely strong transient spin oscillations measured by a femtosecond Faraday probe. The dynamics entail a characteristic phase flip, an asymmetric spectral splitting of the magnon resonance, and a long-lived offset, which we identify as novel hallmarks of all-coherent spin switching in accordance with a numerical simulation.

2. Experimental setup

In the Γ_{24} transition phase, spins in $TmFeO_3$ undergo a reorientation phase transition within $80\,K < T < 90\,K$, which may also be driven by strong THz excitation of the crystal field split states [7]. Our idea is to abruptly alter the anisotropy potential by strong THz pulses enhanced in the near-field of an antenna structure to switch spins ballistically. We fabricate custom-tailored gold bowtie antennas on a single crystal of $TmFeO_3$ by electron-beam lithography (Fig. 1a). Strong, single-cycle THz pulses of up to 1 MV/cm of amplitude induce near-field amplitudes in excess of 20 MV/cm (Fig. 1b), which are spectrally shaped by the antenna to strongly excite the crystal-field-split states of $TmFeO_3$. We time-resolve the spin dynamics by a femtosecond Faraday probe which propagates collinearly with the THz pulse and is transmitted through the antenna feed gap. The sample is kept in a cryostat at a temperature of 83 K. The THz pulse abruptly sets off coherent magnon oscillations. For THz far-field amplitudes of 0.4 MV/cm (Fig. 1c, blue circles), we observe a monochromatic oscillation related to the material's quasi-ferromagnetic (q-fm) mode [8] centered at 0.09 THz (Fig. 1d, blue circles). The amplitude exceeds that obtained for the unstructured substrate (not shown) by more than an order of magnitude, and we estimate a spin deflection angle of up to 24°, in the antenna center. Most remarkably, for a THz far-field amplitude exceeding 0.75 MV/cm, qualitatively novel

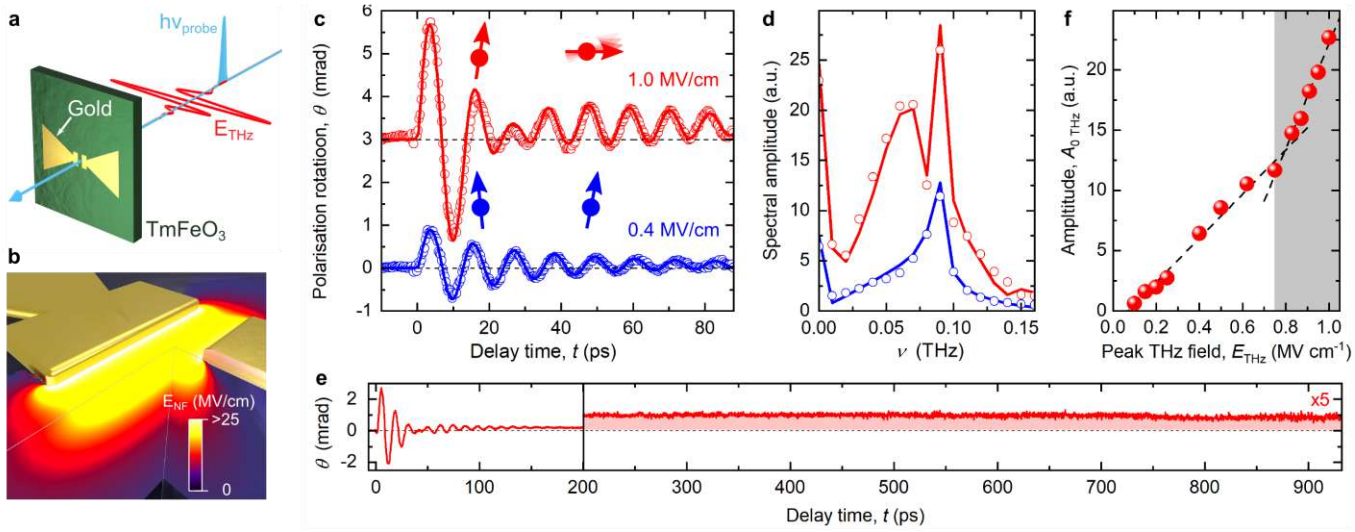

Figure 1 | THz spin switching in the near field of a THz antenna. a, THz gold antenna, THz transient (red curve), and Faraday probe pulse (blue shade). **b,** Near-field profile in the feed gap of the antenna calculated by the finite-difference frequency-domain method. **c,** Transient polarization rotation after strong-field excitation for various THz amplitudes (dots), and theory (curves). **d,** Fourier transform of the data shown in **c**. **e,** Faraday rotation up to large delay times showing the residual dc component. **f,** Scaling of the dc component as a function of the THz amplitude.

signatures emerge. At 1 MV/cm (Fig. 1c, red circles), the period of the first oscillation cycle is distinctly stretched (vertical dashed line), and a beating feature is observed at delay times 25 ps < t < 35 ps. These features correspond to a broadening of the frequency spectrum and an asymmetric splitting of the q-fm mode, reminiscent of the signature of carrier-wave Rabi flopping (Fig. 1d, red circles). Moreover, a long-lived offset of the polarization rotation develops (Fig. 1e), leading to a dc spectral component $A_{0\,THz}$, which grows more rapidly for E_{THz} > 0.75 MV cm^{-1} (Fig. 1f).

We show that the first two features hallmark all-coherent, non-perturbative spin trajectories crossing the energy barrier between stable spin orientations, while the dc offset directly reads out the switched state. To this end, we quantitatively calculate the spin dynamics in the entire near-field region by solving the sine-Gordon equation based on the local THz near-field determined by frequency-domain finite difference calculations (Fig. 1b). Summing up all microscopic contributions to the polarization rotation of the probe pulse, we obtain the net polarization rotation signal. The calculation reproduces all features of the experiment both in the time (Fig. 1c, solid curves) and frequency domain (Fig. 1d, solid curves), including the quasi-monochromatic magnon oscillation, for 0.4 MV/cm, as well as the phase retardation of the first magnon oscillation period and the pronounced beating signature at $t \approx 25$ ps, in the strong-field regime. Moreover, the model unambiguously links the asymmetric splitting of the q-fm resonance to THz-driven all-coherent spin switching: While spins further away from the strong field enhancement of the central antenna part essentially perform monochromatic oscillations, spins exposed to fields exceeding 10 MV/cm acquire sufficient momentum to ballistically cross the potential barrier to the adjacent minimum of the anisotropy potential. The phase accumulated in this process relative to spins which do not switch leads to the pronounced beating signature in the time domain, and the splitting of the resonance, which we identify as novel fingerprints of all-coherent spin switching. Moreover, our theory directly relates the different slopes of $A_{0\,THz}(E_{THz})$ to spin switching, as an intentional tilt of 1.25° of the sample surface normal with respect to the near-infrared k-vector slightly modifies the Faraday rotations induced by spins which switch, and spins which remain in their original orientation [8].

In conclusion, we have observed all-coherent THz spin control and switching in an antiferromagnet in the near-field of a THz antenna, and identified corresponding unique fingerprints in the time and frequency domain. The extremely low dissipation of less than 1 μeV, per spin, and the excellent spatial definition achievable with THz antennas render this scheme highly scalable and thus a promising platform for future storage devices operating at THz rates.

References

[1] R. Landauer, Irreversibility and heat generation in the computing process. IBM Journal of Research and Development **5**, 183 (1961).

[2] E. Beaurepaire, et al., Ultrafast spin dynamics in ferromagnetic nickel. Phys. Rev. Lett. **76**, 4250 (1996).

[3] A. Stupakiewicz, et al., Ultrafast nonthermal photo-magnetic recording in a transparent medium. Nature **542**, 71 (2017).

[4] T. Jungwirth, et al., Antiferromagnetic spintronics. Nature Nanotechnology **11**, 231 (2016).

[5] T. Kampfrath, et al., Coherent terahertz control of antiferromagnetic spin waves. Nature Photonics **5**, 31 (2011).

[6] T. F. Nova, et al., An effective magnetic field from optically driven phonons. Nature Physics **13**, 132 (2017).

[7] S. Baierl, et al., Nonlinear spin control by terahertz-driven anisotropy fields. Nature Photonics **10,** 715 (2016).

[8] S. Schlauderer et al., Nature, in press.

Spatiotemporal Dynamics in Multimode Nonlinear Optical Fibers

Stefan Wabnitz[1], Alioune Niang[2], Daniele Modotto[2], Alain Barthélémy[3], Alessandro Tonello[3], Vincent Couderc[3], Katarzyna Krupa[4], Guy Millot[4]

[1]DIET, Sapienza University of Rome, Via Eudossiana 18, 00184 Rome, Italy
[2]Dipartimento di Ingegneria dell'Informazione, Università di Brescia, via Branze 38, 25123, Brescia, Italy
[3]Université de Limoges, XLIM, UMR CNRS 7252, 123 Avenue A. Thomas, 87060 Limoges, France
[4]Université Bourgogne Franche-Comté, ICB UMR CNRS 6303, 9 Avenue A. Savary, 21078 Dijon, France
*corresponding author, E-mail: stefan.wabnitz@uniroma1.it

Abstract

We overview experiments associated with nonlinear beam propagation in multimode optical fibers. We show that complex spatio-temporal phenomena permit to control the nonlinear beam reshaping across its spatial, temporal and spectral dimensions.

1. Introduction

Although nonlinear optical effects in multimode optical fibers (MMFs), such as the modal-phase matching of four-wave mixing (FWM), have been known since a long time, the manipulation of the temporal and spectral properties of ultrashort pulses combined with the degrees of freedom provided by fiber multimodality is a research field which has only emerged over recent years.

2. Spatiotemporal beam control

In this talk, we review a set of recent experiments associated with the nonlinear propagation of multimode optical pulses. It has been observed that the effect of periodic intensity oscillations associated with self-imaging in graded-index (GRIN) MMFs leads, via the Kerr effect, to a longitudinal grating that may scatter far-detuned optical sidebands over multiple octaves. Moreover, self-imaging also leads to nonlinear mode coupling that, in combination with random linear mode coupling, surprisingly favors the stable emergence of low-order transverse spatial modes at the MMF output, a process that has been named beam self-cleaning.

2.1. Multimode solitons and dispersive wave generation

Multimode solitons (MMSs) are the most natural object within the spatiotemporal dynamics of optical pulses in nonlinear MMFs. In the anomalous dispersion regime, any pulse modal component sees a force of attraction towards the center of mass of the multimode pulse, which may bind all modes together into a single self-trapped entity: the MMS [1].

Early experimental studies of soliton propagation in MMFs by Grudinin et al. [2] showed that femtosecond Raman solitons are produced in GRIN MMFs with a clean beam size, close to that of the fundamental mode of the fiber.

More recent experiments by Renninger and Wise [3] demonstrated that, because of cross-phase modulation, higher-order modes (HOMs) exhibit a nonlinearity-induced blue shifting in the spectral domain, so that they slow down, and propagate with the same group velocity along with the fundamental mode.

Dispersive wave (DW) emission from MMSs, which can be interpreted in analogy with Cherenkov radiation in electrodynamics, leads to ultra-wideband series of unequally spaced sharp spectral peaks extending from the visible into the mid-infrared regions [4]. The mechanism of DW sideband series generation is the resonant phase-matching with MMS, owing to their spatio-temporal intensity oscillations, or self-imaging [5] .

2.2. Geometric Parametric Instabiilities

The periodic self-imaging of a beam in MMFs also leads to a geometric parametric instability (GPI) [6]: a series of visible sidebands were generated with large frequency detuning (123.5 THz) from a 1064 nm pump [7]. GPI permits to convert a near-infrared multimode laser directly into the visible and mid-infrared range. Remarkably, both pump and sideband peaks were carried by a well-defined and stable bell-shaped spatial profile. The position of GPI sidebands can be engineered by fiber design, e.g., varying the MMF core size, or concatenating different fibers [8]. The sideband widths and positions may also be slightly controlled by the pump power level [9].

2.3. Supercontinuum Generation

By pumping GRIN fibers with sub-ns pulses in the normal dispersion regime, efficient high-brightness supercontinuum generation extending into the visible spectral range was reported [10, 11]. The generated spectra span more than two octaves, from below 450 nm up to 2500 nm, and exhibit a high-quality, bell-shaped beams.

2.4. Spatial beam self-cleaning

Because of random linear mode coupling, multimode optical fibers spread a light pulse among its many transverse modes, leading to a severe loss of beam quality and speckled output transverse patterns. Recent experiments have demonstrated that the Kerr effect may overcome speckle distortions, and lead to spatially clean output beams, which are robust against fibre bending. Initial observations of this spatial beam self-cleaning effect involved long, subns pulses [12, 13], and where later extended to the case of femtosecond pulses, propagating in the normal dispersion regime of a GRIN MMF [14]. The polarization dynamics of Kerr beam self-cleaning was recently investigated by Krupa et al., showing that spatial beam cleaning is accompanied by significant nonlinear polarization rotation of the beam, along with an increase of the degree of linear polarization [15].

3. Conclusions

Multimode nonlinear optics is a promising and flexible new platform for developing a whole new class of optical signal processing devices. These are very promising for the upscaling of the energy of coherent fiber laser sources.

Acknowledgement

This work was supported by the European Research Council (ERC), under the European Union's Horizon 2020 research and innovation programme (grant No. 740355)

References

[1] A. Hasegawa, "Self-confinement of multimode optical pulse in a glass fiber," *Opt. Lett.*, vol. 5, no. 10, pp. 416–417, Oct 1980.

[2] A. B. Grudinin, E. Dianov, D. Korbkin, M. P. A, and D. Khaidarov, "Nonlinear mode coupling in multimode optical fibers; excitation of femtosecond-range stimulated-Raman-scattering solitons," *J. Exp. Theor. Phys. Lett*, vol. 47, pp. 356–359, 1988.

[3] W. H. Renninger and F. W. Wise, "Optical solitons in graded-index multimode fibres," *Nat. Commun.*, vol. 4, p. 1719, 2012.

[4] L. G. Wright, D. N. Christodoulides, and F. W. Wise, "Controllable spatiotemporal nonlinear effects in multimode fibres," *Nat. Photonics*, pp. 1–5, April 2015.

[5] L. G. Wright, S. Wabnitz, D. N. Christodoulides, and F. W. Wise, "Ultrabroadband dispersive radiation by spatiotemporal oscillation of multimode waves," *Phys. Rev. Lett.*, vol. 115, p. 223902, Nov 2015.

[6] S. Longhi, "Modulational instability and space time dynamics in nonlinear parabolic-index optical fibers," *Opt. Lett.*, vol. 28, no. 23, pp. 2363–2365, Dec 2003.

[7] K. Krupa, A. Tonello, A. Barthélémy, V. Couderc, B. M. Shalaby, A. Bendahmane, G. Millot, and S. Wabnitz, "Observation of geometric parametric instability induced by the periodic spatial self-imaging of multimode waves," *Phys. Rev. Lett.*, vol. 116, p. 183901, May 2016.

[8] Z. S. Eznaveh, M. A. Eftekhar, J. E. A. Lopez, M. Kolesik, A. Schülzgen, F. W. Wise, D. N. Christodoulides, and R. A. Correa, "Tailoring frequency generation in uniform and concatenated multimode fibers," *Opt. Lett.*, vol. 42, no. 5, pp. 1015–1018, Mar 2017.

[9] H. E. L. Aviles, F. O. Wu, Z. Eznaveh, M. A. Eftekhar, F. Wise, R. Correa, and D. N. Christodoulides, "A systematic analysis of parametric instabilities in nonlinear parabolic multimode fibers," *APL Photonics*, vol. 4, no. 2, p. 022803, 2019.

[10] G. L. Galmiche, Z. S. Eznaveh, M. A. Eftekhar, J. A. Lopez, L. G. Wright, F. Wise, D. Christodoulides, and R. A. Correa, "Visible supercontinuum generation in a graded index multimode fiber pumped at 1064 nm," *Opt. Lett.*, vol. 41, no. 11, pp. 2553–2556, Jun 2016.

[11] K. Krupa, C. Louot, V. Couderc, M. Fabert, R. Guenard, B. M. Shalaby, A. Tonello, D. Pagnoux, P. Leproux, A. Bendahmane, R. Dupiol, G. Millot, and S. Wabnitz, "Spatiotemporal characterization of supercontinuum extending from the visible to the midinfrared in a multimode graded-index optical fiber," *Opt. Lett.*, vol. 41, no. 24, pp. 5785–5788, Dec 2016.

[12] K. Krupa, A. Tonello, B. M. Shalaby, M. Fabert, A. Barthélémy, G. Millot, S. Wabnitz, and V. Couderc, "Spatial beam self-cleaning in multimode fibres," *Nat. Photonics*, vol. 11, pp. 234–241, 2017.

[13] L. G. Wright, Z. Liu, D. A. Nolan, M.-J. Li, D. N. Christodoulides, and F. W. Wise, "Self-organized instability in graded-index multimode fibres," *Nat. Photonics*, vol. 10, pp. 771–776, November 2016.

[14] Z. Liu, L. G. Wright, D. N. Christodoulides, and F. W. Wise, "Kerr self-cleaning of femtosecond-pulsed beams in graded-index multimode fiber," *Opt. Lett.*, vol. 41, no. 16, pp. 3675–3678, Aug 2016.

[15] K. Krupa, G. G. Castañeda, A. Tonello, A. Niang, D. S. Kharenko, M. Fabert, V. Couderc, G. Millot, U. Minoni, D. Modotto, and S. Wabnitz, "Nonlinear polarization dynamics of Kerr beam self-cleaning in a graded-index multimode optical fiber," *Opt. Lett.*, vol. 44, no. 1, pp. 171–174, Jan 2019.

A 0.5 - 12 GHz Ultra-wide Band Low Noise Amplifier with Transformer Coupled Technique in 180 nm CMOS

Guan-Jhong Syu, and Hwann-Kaeo Chiou*

Department of Electrical Engineering, National Central University, Jhongli Distr., Taoyuan, Taiwan
*corresponding author, E-mail: hkchiou@ee.ncu.edu.tw

Abstract

This paper presents a 0.5-12 GHz ultra-wide band (UWB) low noise amplifier (LNA) by using transformer coupled technique in an inverted-type amplifier in tsmc™ 180 nm CMOS. The uses of bifilar and trifilar transformers not only boost the trans-conductance, broaden the bandwidth but also save the chip area. The measured peak gain is 11.97 dB over a 3-dB bandwidth from 0.5 to 12 GHz with a minimum noise figure (NF) of 3.89 dB. The measured peak P_{1dB} and IIP3 are -12 dBm and -2 dBm, respectively. The total power consumption is 12.74 mW.

1. Introduction

Ultra-wideband (UWB) communication techniques have been applied in short-range and high-speed wireless mobile systems. The frequency band of UWB system is adopted from 3.1-10.6 GHz which can be implemented as single-band impulse and multi-band radio approaches. The former approach operates in pulse mode that occupies a full 7.5-GHz spectrum. The required spectrum of the latter one is split into fourteen 528-MHz sub-bands with OFDM modulation from 3.1-10.6 GHz. Thus, an ultra-wide band LNA is asked for operating over full 7.5-GHz band with performance of low NF, flat gain, low power and compact area in multi-band UWB system. Recently, many literature researches regarding broadband low noise amplifiers have been proposed [1]-[6]. In reference [1], the authors presented a linearization technique in UWB common gate (CG) and cascode LNAs that provided linearity analysis using Volterra series. Since the uses of source inductive and drain gain peaking techniques, the chip areas for both linearized CG and cascode LNAs are large as 0.58 mm^2. Work [2] adopted resistive feedback and current-reuse techniques for a compact UWB LNA. The fabriacted LNA only occupies a small core area of 0.031 mm^2. Thus, this paper introduced a FoM that considered the chip area as a performance indicator. Work [3] proposed a two-stage inverted-type UWB LNA that used a third order π-match input network to obtain gain and NF flatness. In reference [4], the authors employed dual reactive feedbacks and an LC ladder matching network to accommodate a wide bandwidth. The proposed dual reactive feedback was implemented in the first stage inverted-type amplifier with transformer feedback manner. Work [5] proposed g_m-boosted feedback with two different transformer feedback topologies, *i.e.*, shunt-series and shunt–shunt, to tradeoff the performance of input matching and noise matching. Work [6] adopted cascaded gain cell, that constituted an inductively parallel-peaking cascode stage with a low-Q RLC load and an inductively series-peaking CS stage, as a distributed amplifier for UWB LNA design. However, due to the limitations of the distributed type amplifier, this kind of amplifier consumes much dc power and large chip area. Some observations from above mentioned UWB LNA designs are listed as below, (1) current reused technique, such as inverted type amplifier, is commonly used to save dc power. (2) Transformer feedback topology is usually used to save chip area. (3) High order input matching network, such three-order ladder network or dual loop feedback, is used to flatten the frequency response of the gain, and noise figure. (4) g_m-boosting technique is used to enhance the gain performance. This paper proposed a 0.5 to 12 GHz two-stage inverter-type amplifier with bifilar and trifilar transformers feedback technique to comply these requirements.

2. Circuit Design

Fig. 1 shows the schematic diagram of the proposed LNA which employs a current reuse inverter-type topology to save dc power consumption. A gate-source transformer coupled technique is applied in the first stage to boost the trans-conductance (g_m) and match the minimal NF. A simplified calculation treats the PMOS as a complementary transistor and ignores R_1. The equivalent trans-conductance can be shown as (1),

$$\frac{i_o}{v_i} = \frac{g_m}{j\omega L_s g_m - \omega^2(L_g + L_s) - M\left\{\left[\omega^2 C_{gs}\left(\frac{L_s}{L_g} + \frac{L_g}{L_s}\right) + j\omega g_m \frac{L_g}{L_s}\right]\right\}} \quad (1)$$

g_m is the trans-conductance without transformer feedback. M is the mutual coupling of the transformer. As can be seen, in $M > 0$ case, the transformer offers a positive feedback which boosts the g_m but reduces the bandwidth of input match. In $M < 0$ case, transformer offers a negative feedback which reduces the g_m and enhances the bandwidth of input match. Therefore, this design chooses $M > 0$ to boost the g_m to enhance power gain of the LNA. Meanwhile, the values of self-inductances of the source, gate inductors

(L_s, L_g) and its mutual coupling factor M need to be appropriately chosen. Fig. 2 shows the transformer characteristics of the proposed UWB LNA. The input matching network of the first stage is used a gate-source bifilar transformer to offer positive feedback which provides wideband input and noise matching conditions. The matching network of the second stage is used a trifilar transformer feedback topology to enhance the bandwidth and flatten the gain. The drain inductor can be resonated out the parasitic capacitance of the transistor which enhances the gain at high frequencies. Moreover, the drain inductor and gate-source transformer are combined into as a trifilar transformer to save the chip area. A simplified calculation in the same way as the first stage, and the equivalent output impedance can be shown as (2),

$$Z_{out} = sL_s\left[-\frac{sC_{gs}}{g_m}\left(1+\frac{M_{gs}}{L_g}+\frac{M_{sd}L_d}{Ls^2}-\frac{M_{gd}L_s}{L_dL_g}\right)+1+\frac{L_d}{L_s}+\frac{M_{sd}L_d}{{L_s}^2}+\frac{M_{sd}}{L_d}\right] \quad (2)$$

The use of trifilar transformer reduces the frequency dependence of the output impedance in high frequency regime and enhanced the bandwidth of output matching. Fig. 3 shows the trifilar characteristics. The precisely control of the coupling factors M of these transformers is the key of this UWB LNA design. The effects of M on the gain and return loss are extensively investigated by the simulations and verified by measurements. The transistor sizes for M_1 to M_4 of the first and second stages are selected as below, 5×19 μm, 5×17 μm, 5×20 μm, and 2×20 μm. The values of the shunt-shunt feedback resistors R_1 and R_2 are 270 Ω and 308 Ω, respectively. The optimal current density for minimal noise figure is chosen as 0.04 mA/μm which is obtained by simulating NF performance versus current density in various transistor sizes.

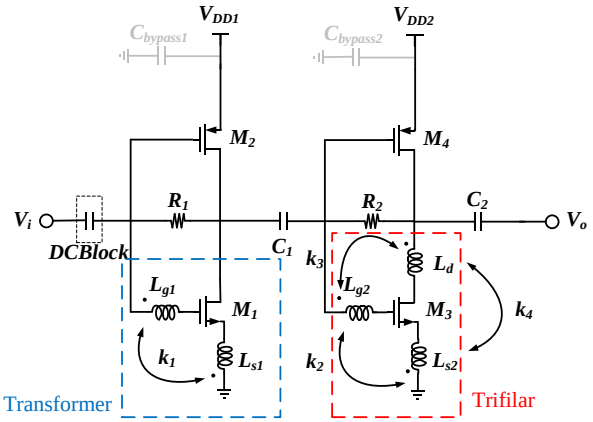

Figure 1: The schematic diagram of the transformer feedback UWB LNA.

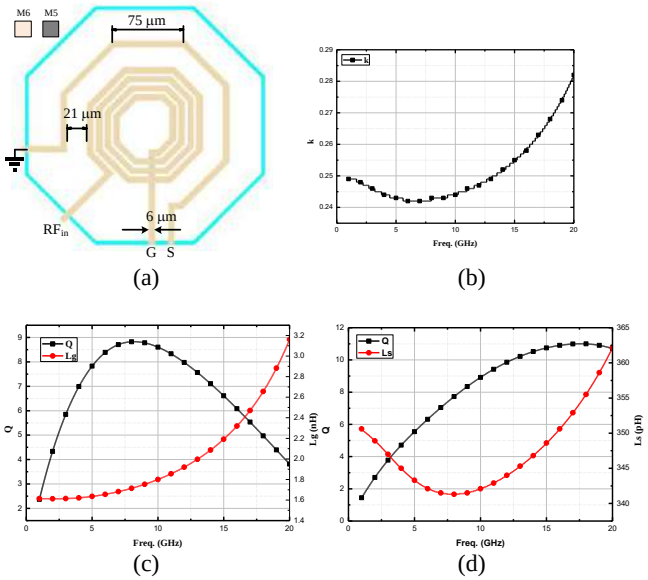

Figure 2: (a) The layout of the bifilar transformer, (b) coupling coefficient k ($k = M/\sqrt{L_sL_g}$), (c) self-inductance L_g and its Q factor, (d) self-inductance L_s and its Q factor.

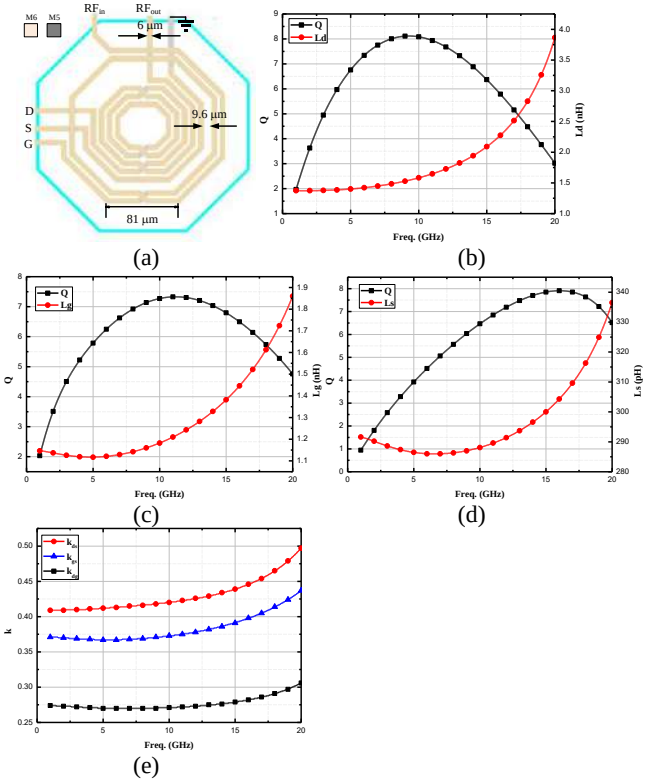

Figure 3: (a) The layout of the trifilar, (b) self-inductance L_d and its Q factor, (c) self-inductance L_g and its Q factor, (d) self-inductance L_s and its Q factor, (e) mutual coupling coefficients k.

3. Measurements

Fig. 4 shows the fabricated chip of the proposed LNA. The LNA was measured by on-wafer probing system. The LNA

consumes a dc power of 12.48 mW under V_{DD1} = 1.63 V, I_{D1} = 3.82 mA and V_{DD2} = 1.8 V, I_{D2} = 3.62 mA. Fig. 5 shows the simulated and measured gains. The peak gain is 11.97 dB and its 3-dB gain bandwidth is from 0.5 to 12.0 GHz. Figures 6 and 7 shows the simulated and measured input and output return losses. As can be seen, good return losses below 10 dB are achieved across 0.5 to 12 GHz. Fig. 8 shows the simulated and measured *NF* which lowest *NF* is 3.89 dB at 9 GHz. Meanwhile, the measurements and simulations are in good agreements on gain, return losses and *NF*. The simulated and measured P_{1dB} and IIP3 are shown in figures 9 and 10 which are better than -16 dBm and -6 dBm from 3 to 12 GHz, respectively.

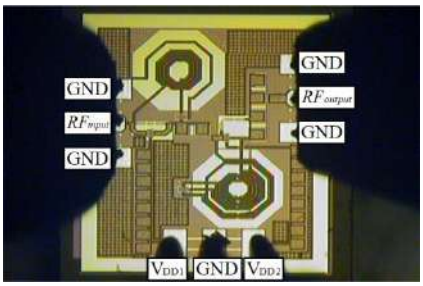

Figure 4: The photo of the fabricated chip with the area of 0.55×0.68 mm^2.

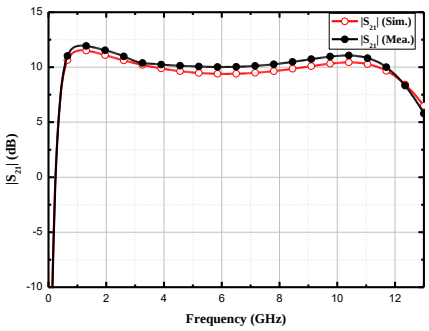

Figure 5: The simulated and measured gains.

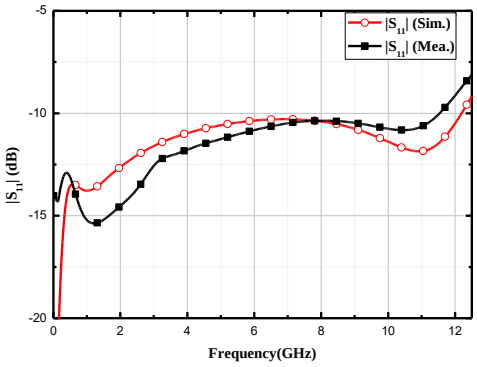

Figure 6: The simulated and measured $|S_{11}|$.

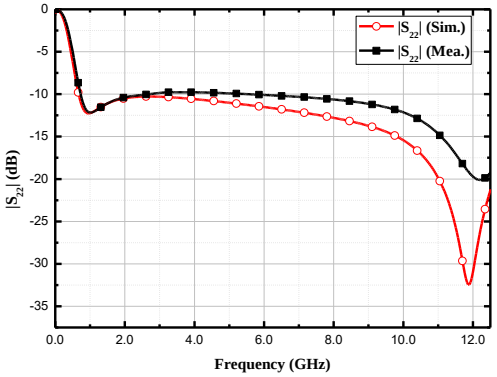

Figure 7: The simulated and measured $|S_{22}|$.

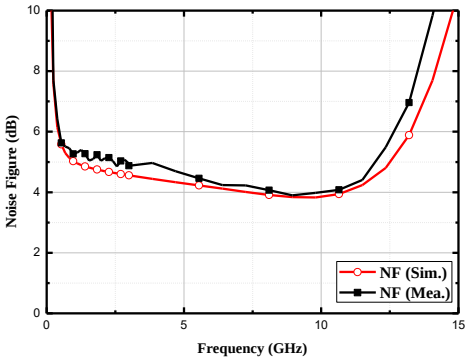

Figure 8: Measured and simulated noise figures.

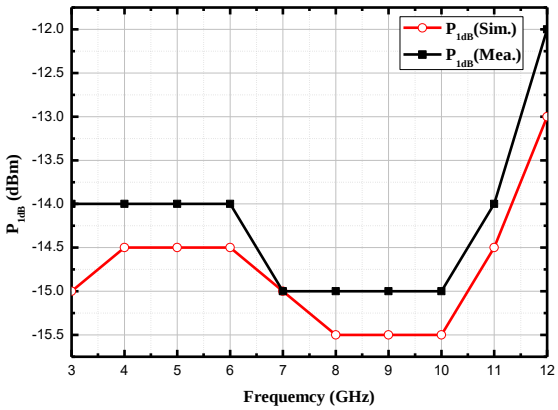

Figure 9: Measured and simulated P_{1dB}.

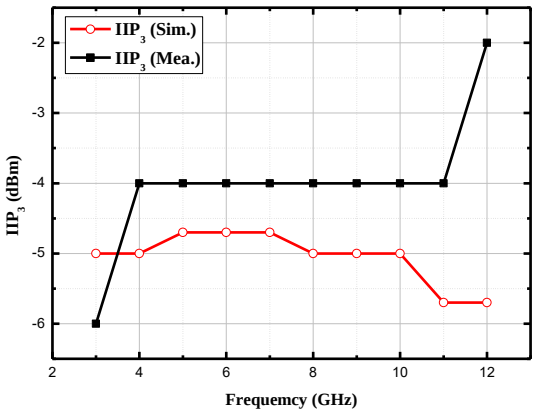

Figure 10: Measured and simulated IIP3.

4. Discussions

Table I benchmarks the performance of the prior state-of-the-arts works, [1] suggested a figure-of-merit (FoM) for the fair comparison of the overall performance. Since this work uses bifilar and trifilar transformers, the realized chip size is reduced significantly. [2] proposed a FoM that considered the chip area as a performance indicator. Although the gain and *NF* of our LNA are worse than [3,5,6], the performance of our LNA outperforms in the bandwidth that covers the entire C/X frequency band with smaller chip area.

Table 1 benchmark of recently published UWB LNA:

Ref.	[3]	[4]	[5]	[6]	This work
CMOS process	180 nm	180 nm	180 nm	130 nm	180 nm
Freq. (GHz)	3-10	3.1-10.6	2.2-12.2	0.4-10.5	0.5-12.1
Gain (dB)	13.7	14	13	20.47	11.97
NF (dB)	2.3	4.5	1.9	3.29	3.89
P_{DC} (mW)	18	21	10.8	37.8	12.48
IIP_3 (dBm)	-0.2	-12	2.1	-11.5	-2
Area (mm^2)	0.39	0.46	1.11	0.879	0.372
FoM	2.697	0.984	7.534	2.489	2.54
FoM(A)	6.6	0.135	11	0.2	4.32

$FoM = (|S_{21}| \times BW[GHz])/((NF-1)\times P_{DC}[mW])$
$FoM(A) = (|S_{21}| \times BW[GHz])/((NF-1)\times P_{DC}[mW]\times Area[mm^2])$

5. Conclusion

A low power wideband LNA in 180 nm CMOS technology has been successfully designed and measured. The transformer coupled technique is adopted to achieve the g_m boosting, wide bandwidth matching, and chip size reduction. Its achieved ultra-wide bandwidth with good gain flatness will find applications in wideband wireless communications.

Acknowledgements

This work is supported by the Ministry of Science and Technology, Taiwan, R.O.C under Contract MOST 106-2221-E-008-007-MY3. National Chip Implementation Center (CIC) of National Applied Research Laboratories, Taiwan, R.O.C., is also acknowledged for chip fabrication.

References

[1] Heng Zhang, Xiaohua Fan, and Edgar Sánchez Sinencio, "A low-power, linearized, ultra-wideband LNA design technique," *IEEE J. Solid-State Circuits.*, vol. 44, no. 2, Feb. 2009, pp. 320-330.

[2] Po-Yu Chang and Shawn S. H. Hsu, "A compact 0.1–14-GHz ultra-wideband low-noise amplifier in 0.13-μm CMOS," *IEEE Trans. Microw. Theory Tech*., vol. 58, no. 10, Oct. 2010, pp. 2575 - 2581.

[3] Yo-Sheng Lin, Chien-Chin Wang, Guan-Lin Lee, and Chih-Chung Chen , "High-performance wideband low-noise amplifier using enhanced-π match input network," *IEEE Microw. Wireless Compon. Lett.*, vol. 24, no. 3, pp. 200 – 202, Mar. 2014.

[4] Chang-Tsung Fu, Chien-Nan Kuo and Stewart S. Taylor , "Low-noise amplifier design with dual reactive feedback for broadband simultaneous noise and impedance matching, " *IEEE Trans. Microw. Theory Tech.*, vol. 58, no. 4, Apr 2010, pp. 795 - 806.

[5] Rong-Fu Ye, Tzyy-Sheng Horng, and Jian-Ming Wu, "Two CMOS dual-feedback common-gate low-noise amplifiers with wideband input and noise matching, "*IEEE Trans. Microw. Theory Tech*., vol. 61, no. 10, Oct. 2013, pp. 3690 - 3699.

[6] Yo-Sheng Lin , Jin-Fa Chang, and Shey-Shi Lu, "Analysis and design of CMOS distributed amplifier using inductively peaking cascaded gain cell for UWB systems, "*IEEE Trans. Microw. Theory Tech*., vol. 59, no. 10, Oct. 2011, pp. 2513- 2524.

Optical Imaging using Deep Neural Networks

Demetri Psaltis*

Ecole Polytechnique Federale de Lausanne (EPFL)
Optics Laboratory, School of Engineering
Lausanne, Switzerlandand
* E-mail: demetrri.psaltis@epfl

Abstract

We will describe optical imaging systems that operate with the help of neural networks. One of the examples is imaging using multiple mode fibers where the modal scrambling due to propagation in the fiber is inverted using a network trained on a database of images transmitted through the fiber. A comparison of neural networks with conventional inverse scattering methods will be reported.

Summary

Learning to execute tasks in optics by training neural networks has a long history [1]. The recent emergence of "deep learning" networks has resulted in new developments for how to use learning techniques in the design and operation of optical systems [2,3,4,5,6]. We will present our results related to this recent activity and describe how deep neural networks can be applied to imaging systems including systems in which multi-ode fibers are used as imaging elements.

References

[1] Abu-Mostafa, Yaser S., and Demetri Psaltis. "Optical Neural Computers." *Scientific American*, vol. 256, no. 3, 1987, pp. 88–95.,

[2] U. Kamilov, I. Papadopoulos, M. Shoreh, A. Goy, C. Vonesch, M. Unser, and D. Psaltis, "Learning approach to optical tomography," Optica 2, 517-522 (2015).

[3] Ayan Sinha, Justin Lee, Shuai Li, and George Barbastathis, "Lensless computational imaging through deep learning," Optica 4, 1117-1125 (2017)

4] Rivenson, et. al. , "Phase recovery and holographic image reconstruction using deep learning in neural networks", Light Science and Applications 7,17141, Feb 2018

[5] N. Borhani, E. Kakkava, C. Moser, and D. Psaltis, "Learning to see through multimode fibers," Optica 5, 960-966 (2018).

1. [6] Shen, et. al, "Deep learning with coherent nanophotonic circuits", Nature Photonics, 11 (2017).

EMC & EMI

Ethernet interface with RJ45 connector in the process of electromagnetic infiltration

Rafał Przesmycki[1], Marek Bugaj[1], Marian Wnuk[1]

[1] Faculty of Electronics, Military University of Technology, Gen. Sylwestra Kaliskiego 2 str., 00-908 Warsaw, Poland
*corresponding author, E-mail: rafal.przesmycki@wat.edu.pl

Abstract

The article deals with problems related to electromagnetic compatibility and the compromising emission, i.e. information security. The article focuses on the Ethernet data transfer interface using the RJ45 (Registered Jack - type 45) connector for which the extortion signals used in the emission measurements of the revealing are presented and the results of the emission measurements from the Ethernet interface are discussed. In addition, the article discusses the laboratory stand for measuring the compromising emission.

1. Introduction

Emission of the electromagnetic field is a phenomenon inherent in the flow of electric current, which in turn is the basis for the operation of all electronic and electric devices. On the basis of field changes it is possible to deduce about the operation of the devices being its source. What's more, the properties of the electromagnetic field enable its remote registration and analysis. The phenomenon of the formation of electromagnetic waves carrying information about the operation of electrical and electronic devices is called a compromising emission or electromagnetic leakage Since the electrical and electronic equipment has begun to be used to process information, often of a confidential nature, the existence of a disclosure issue has become particularly important [2].

Information security against electromagnetic permeability of devices and electromagnetic systems (IT) is of great importance. This problem is growing with the increasing use of tele information devices to process and transmit information that should not fall into the wrong hands. It results from the fact that every electronic device is a source of undesirable (secondary) emission of electromagnetic energy induced in the surrounding space and in all close electrical conductors and metal constructions [3].

When the signals of undesirable emission are correlated with unclassified information, they can be used to reconstructing that information by the intelligence services. The phenomenon of such an undesirable emission is called the revealing emission, and its use by the intelligence - penetration or electromagnetic infiltration. Undertakings aimed at hindering the recognition of systems based on the revealing emission are called protection of information against electromagnetic penetration or emission safety [4].

Electromagnetic emissions having the character of a compromising emission may arise at every stage of the processing of coded information in the form of electric currents. There is also no possibility to research both the source itself and the channel of information penetration. However, in laboratory conditions, it is possible to carry out such tests, in which the tested devices are introduced into working modes allowing to learn their infiltration susceptibility. This article presents an example of such experiments. It seems that the most suitable for illustrating the electromagnetic problem of information penetration are devices or their components that process information in a serial manner, and the coding rule is uncomplicated and widely known.

2. Ethernet interface

Ethernet is a technique in which standards used in the construction of mainly local computer networks are included. It includes the specification of wires and the signals transmitted. Ethernet also describes the frame format and protocols of the two lowest layers of the OSI Model. Its specification is given in the IEEE 802 standard.

Ethernet was developed by Robert Metcalfe at Xerox PARC in the Xerox research center, and published in 1976. It is based on the idea of nodes connected to a common medium and sending and receiving special messages (frames). All nodes have a unique MAC address.

Classic Ethernet networks have four common features. These are: time parameters, frame format, transmission process and basic rules for designing them.

Ethernet is the general name for a set of technologies containing standards used in the construction of computer networks. Describes the cabling specification, methods of signal transmission in networks. Ethernet is currently the most popular standard for local area networks. Among the technologies included in Ethernet, we can distinguish: Ethernet i IEEE 802.3, Fast Ethernet, Gigabit Ethernet and 10 Gigabit Ethernet.

All standards are compatible, so there are no problems with the use of several technologies in one network. Ethernet as a method of access to the transmission medium uses the CSMA / CD method, which was developed in the seventies by Xerox. In February 1980, the IEEE institute took responsibility for transforming Ethernet into a valid network

standard. IEEE 802.3, like its predecessor, used the CSMA / CD method developed by Xerox. However, the next version of Ethernet was already a joint work of companies, Xerox, DEC and Intel. This version is already compatible with IEEE 802.3. The first Ethernet was based on a coaxial cable and operated in half duplex mode. There are 4 frame standards used in Ethernet transmission:

- Ethernet version 1 - no longer used,
- Ethernet version 2 (Ethernet II) - also called the DIX frame from DEC, Intel and Xerox, which developed this frame type together and published in 1978. It is currently the most widely used,
- IEEE 802.x LLC,
- IEEE 802.g LLC,

In Ethernet networks, devices communicate with frames. The frame consists of a sequence of bits organized in fields, which include address fields, data field and error control field, whose task is to ensure the correctness of data. The minimum frame length is 64 bytes, while the maximum is 1518 including the data field. Frames differ in header lengths, maximum frame length (MTU) and other details. Different types of frames can simultaneously use the same network. The construction of the Ethernet version 1 frame is shown in Fig. 1.

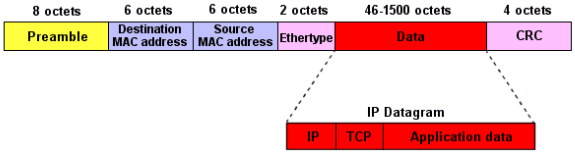

Figure 1. Ethernet version 1 frame

In Ethernet networks, devices are most often connected using the RJ-45 (Registered Jack - type 45) connector. This is the type of connector most commonly used to connect modems or network cards. The plug is similar to 8P8C, but it is equipped with an additional tab that prevents inserting it into the usual socket. The view of RJ45 plug is shown on Figure 2. Pins 4 and 5 are used. - line connection and 7 and 8 - resistor placed in the socket, controlling the power of the modem. It comes in two versions: RJ 45S - single socket and RJ45M - up to eight sockets.

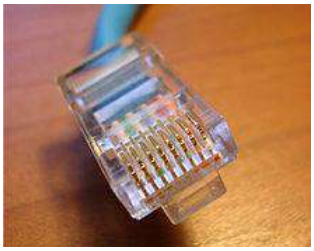

Figure 2. View of the RJ45 plug

3. The laboratory stand for compromising emission measurements

In order to determine the sources of compromising emission from the Ethernet interface, the content of the test signal, intentionally generated by the interface (Ethernet cable), should be estimated in the signal received by the measurement stand as radiative or conductive emission. The laboratory stand for the implementation of the research to determine the sources of compromising emissions should enable the receipt of the generated test signal propagating as emission of radiation or conducted. This article focuses only on the radiated emission [2][3][4]. An exemplary system for testing extortion signals for compromising emissions based on the equipment available on the market is shown in Fig. 3.

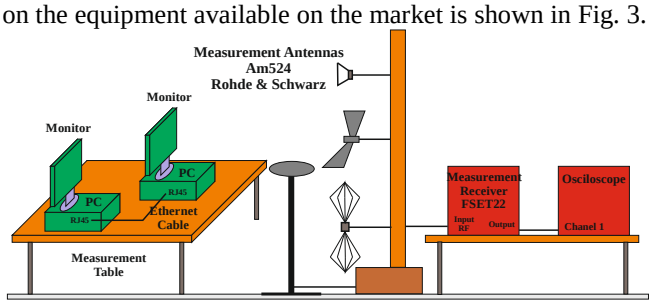

Figure 3. Block diagram of the laboratory stand for testing compromising emission

For the Ethernet interface, as a forced emission for the compromising emission was used the transmission of test binary information sequences between two PCs connected with an Ethernet cable using RJ45 connectors. The signal received by a particular antenna is transmitted through the antenna commutator to the FSET 22 broadband receiver. In the receiver, this signal is filtered and it is converted into a lower frequency range (to the intermediate frequency of the measuring receiver of 10 MHz). The signal after detection is fed to the VIDEO output on the receiver and then it is fed to the external channel input of the oscilloscope, where it is possible to visualize the information received in the time domain [2][3][4].

4. Measurement results

The usual observation of the spectrum obtained during operation of the Ethernet interface in the mode of transmission of selected binary sequences does not give an answer as to the possibility of compromising emission. It is not even possible to observe the beginning and end of data transfer. It is not possible to observe the phenomenon confirming the operation of the Ethernet interface in the form of data transmission.

During the emissivity tests of the Ethernet interface, only interface work can be identified after connecting the device through this interface, but there is no possibility to observe the beginning and end of data transmission by comparing the time course and its spectrum on transmission lines after transmission is switched on and in idle state (no data transmission forced to given interface). In order to show the above phenomenon, the results of measurements for states are presented below, when the data transmission on the interface lines is forced and when such transmission is not forced.

The results of measurements in the form of frequency spectra for a pseudo-random binary sequence at a transmission speed of about 1 Gbit / s are shown in Fig. 4, Fig. 5, Fig. 6 and Fig. 7.

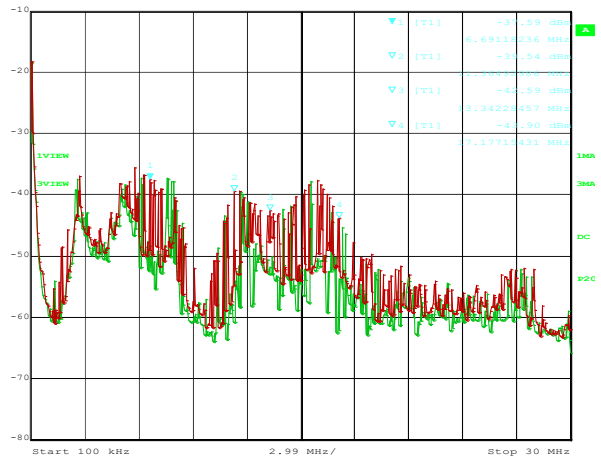

Figure 4. Radiated emission deriving from the Ethernet interface while the transmission data is OFF(green color) and during transmission of a binary sequence with transmission speed of about 1 Gbit / s (red color) in the frequency range 100kHz - 30MHz

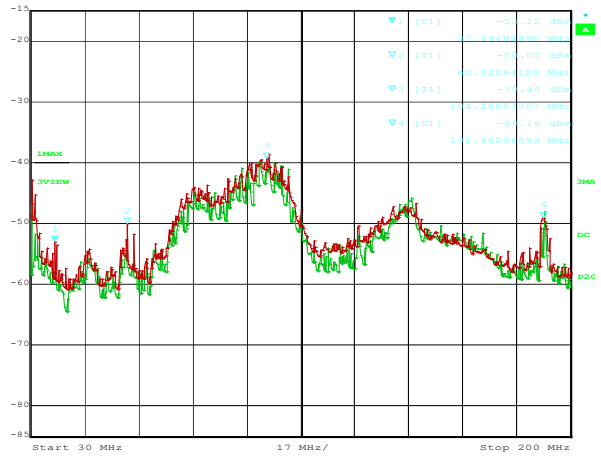

Figure 5. Radiated emission deriving from the Ethernet interfa-ce while the transmission data is OFF(green color) and during transmission of a binary sequence with transmission speed of about 1 Gbit / s (red color) in the frequency range 30MHz – 200MHz

Very often the assessment of the spectrum itself is insufficient due to the difficulties resulting from qualifying appearing signals on particular frequencies. For this reason, it is necessary to use other methods involving the use of more sophisticated measuring devices. Either way, in most cases the qualification of emissions takes place by visual method. However, it should be remembered that in doubtful cases or in cases where visual assessment is impossible, assessment methods based on digital processing of recorded signals are used [1].

Identification is a process or result of the processes of identifying a given object with another object. It may include distinguishing common features, grasping the similarities between the examined object and other objects of this class, estimating the values of observed parameters of a given object [1]. The use of any method of identification of compromising emission signals requires the identification of distinctive features of reference signals and the determination of the degree of similarity of these characteristics to analogous parameters of the tested signals. Based on the analysis of radiated emission levels for the Ethernet interface, the probable receiving frequencies of the compromising emission signals were determined. In order to check whether the signals radiated in this frequency range actually have the character of a compromising emission, a series of recording of these signals was made using a digital oscilloscope and analyzed. Measurements were made when data was transmitted in the form of pseudo-random binary sequences between two PCs connected via Ethernet cable using RJ45 connectors. The sample results are shown in Fig. 8 and Fig. 9.

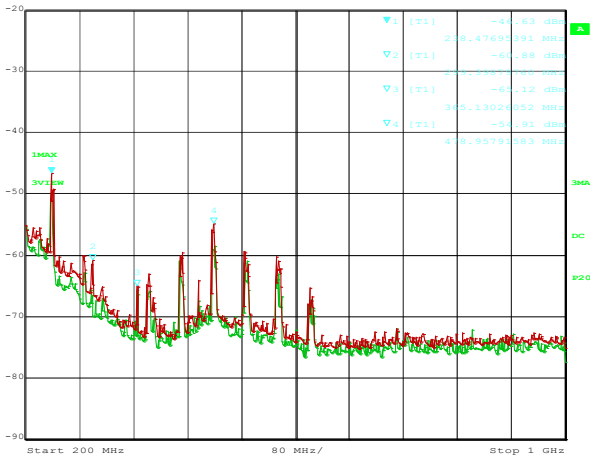

Figure 6. Radiated emission deriving from the Ethernet interface while the transmission data is OFF(green color) and during transmission of a binary sequence with transmission speed of about 1 Gbit / s (red color) in the frequency range 200MHz – 1000MHz

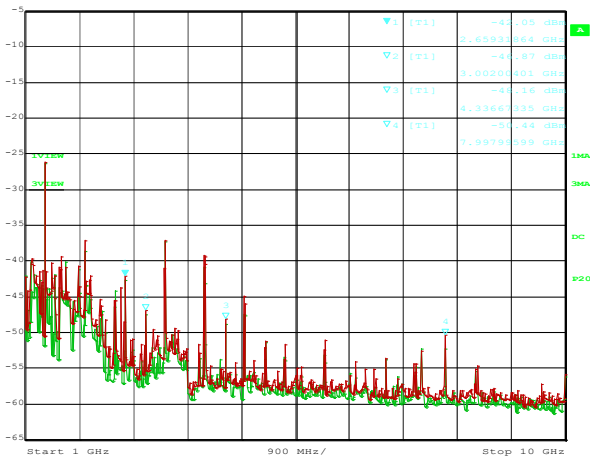

Figure 7. Radiated emission deriving from the Ethernet interface while the transmission data is OFF(green color) and during transmission of a binary sequence with transmission speed of about 1 Gbit / s (red color) in the frequency range 1000MHz – 10000MHz

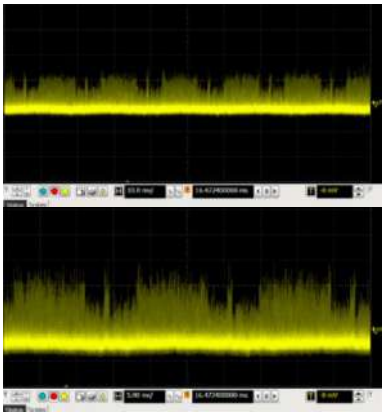

Figure 8. Oscillogram for the Ethernet interface during data transmission is off. The signal received by the antenna for f = 1.73 GHz given from the VIDEO output FSET22 receiver

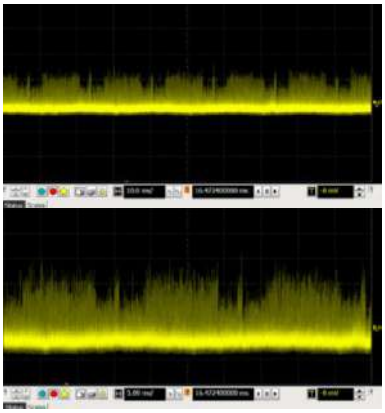

Figure 9. Oscillogram for the Ethernet interface during data transmission is on. The signal received by the antenna for f = 1.73 GHz given from the VIDEO output FSET22 receiver

In order to show the possibility of identifying the operation of the Ethernet interface, measurements were made during data transmission in the form of pseudo-random binary sequences between two PCs connected via Ethernet with the use of RJ45 connectors, using intermittent transmission. This transmission consisted in sending certain size files (binary sequences) between two PCs connected via an Ethernet cable with certain forced interruptions in transmission. Thanks to this, on the oscilloscope it was possible to observe the signal containing the data transmission, and after determining the FFT for this signal in the frequency spectrum, the bands spaced apart from each other by the frequency resulting from the interruption of data transmission are visible. In order to show the above phenomenon, Fig. 10, Fig. 11 and Fig. 12 show examples of measurement results for specific measurement conditions. During the measurements, data transmission was carried out, consisting of transferring a 100 MB file between two PCs connected by Ethernet cable using RJ45 connectors with two specified transmission intervals – 30 ms and 100 ms. For a 30 ms transmission gap in the frequency spectrum, we expect spectrum frequency component spaced from each other by f = 33 Hz, while for a transmission gap equal to 100 ms in the frequency spectrum we expect spectrum frequency component spaced from each other by f = 10 Hz. These values were estimated based on the dependence f = 1 / ts where ts is the duration of the interruption in transmission.

5. Conclusions

From the presented in the article the time courses of radiated emission signals for the Ethernet interface, it can be seen that these signals do not have a clear relationship with the content of the transmitted binary sequences with a given transmission speed, and therefore they do not have the character of compromising emission signals. It is not possible to identify the content of the transmitted information in the time series. However, it is possible to identify the operation of the Ethernet interface using intermittent transmission. Due to such transmission on the oscilloscope it was possible to observe the signal containing the data transmission and after determining the FFT for this signal in the frequency spectrum one can see the spectrum frequency component separated from each other by the frequency resulting from the duration of the data transmission interval. On the basis of measurements obtained on the transmission lines of the interface and their spectrograms obtained during the use of intermittent transmission, it can be stated that: by choosing the appropriate break time in data transmission we can shape the form of the signal waveform on the transmission lines of Ethernet interfaces in such a way that it can be easily identified.

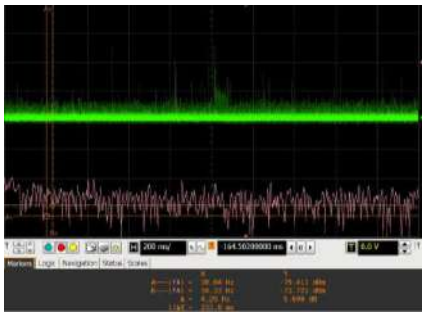

Figure 10. Oscillogram for the Ethernet interface during data transmission is off or on. The signal received by the antenna for f = 1,453 GHz given from the VIDEO output of the FSET22 receiver

Figure 11. Oscillogram for the Ethernet interface during data transmission (transmission of a 100MB file) with transmission intervals of 30 ms. The signal received by the antenna for f = 1,453 GHz given from the VIDEO output of the FSET22 receiver

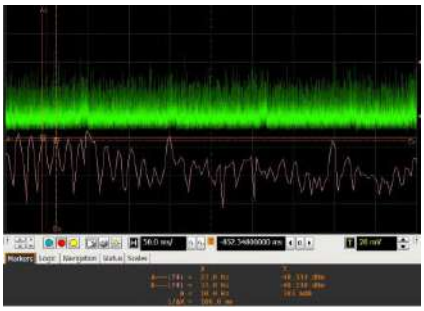

Figure 12. Oscillogram for the Ethernet interface during data transmission (transmission of a 100MB file) with transmission intervals of 100 ms. The signal received by the antenna for f = 1,453 GHz given from the VIDEO output of the FSET22 receiver

6. References

[1] K. Grzesiak, I. Kubiak, S. Musiał, A. Przybysz, Elektromagnetyczne bezpieczeństwo informacji, Wydawca: WAT, Zegrze 2012,

[2] Rafał Przesmycki Measurement and Analysis of Compromising Emanation for Laser Printer, Guangzhou, China, PIERS Proceedings 2014, str. 2661-2665, ISSN 1559-9450,

[3] L. Nowosielski, R. Przesmycki and M. Nowosielski, "Compromising Emanations from VGA and DVI Interface," *2016 Progress in Electromagnetic Research Symposium (PIERS)*, Shanghai, 2016, pp. 1024-1028. doi: 10.1109/PIERS.2016.7734570,

[4] R. Przesmycki and L. Nowosielski, "USB 3.0 interface in the process of electromagnetic infiltration," *2016 Progress in Electromagnetic Research Symposium (PIERS)*, Shanghai, 2016, pp. 1019-1023. doi: 10.1109/PIERS.2016.7734569